UNIVERSITY OF CALIFORNIA, SAN DIEGO

SIMULATION OF THE VACUUM ASSISTED RESIN TRANSFER MOLDING (VARTM) PROCESS AND THE DEVELOPMENT OF LIGHT-WEIGHT COMPOSITE BRIDGING

A Dissertation submitted in partial satisfaction of the requirements for the degree

Doctor of Philosophy

in

Structural Engineering

by

Marc J. Robinson

Committee in charge:

Professor John Kosmatka, Chair
Professor David Benson
Professor Vistasp Karbhari
Professor Petr Krysl
Professor Hidenori Murakami

2008

The Dissertation of Marc J. Robinson is approved, and it is acceptable in quality and form for publication on microfilm and electronically:

_____

_____

_____

_____

_____
Chair

University of California, San Diego

2008

To my wife Christy and our children

A journey of a thousand miles must begin with a single step.

–Lao-Tzu

TABLE OF CONTENTS

LIST OF FIGURES

LIST OF TABLES

ACKNOWLEDGEMENTS

I would like to acknowledge the support and encouragement of my advisor Dr. John Kosmatka over the past six years. His thoughts and guidance both related to my research as well other have been invaluable.

I would also like to acknowledge support provided by Riley Woodham at Seemann Composites Inc. in sharing insights into the VARTM (SCRIMP) process.

I would like to acknowledge the financial support provided by the Office of Naval Research (ONR) as well as US Army TACOM which made this research possible.

Chapter 9, in part, is a reprint of the material which appears in the *Journal of Composites for Construction* 2008 volume 12 issue 3 pages 344-354 titled "Light-Weight Fiber-Reinforced Polymer Composite Deck Panels for Extreme Applications." The dissertation author was the primary investigator and author with advisor J. B. Kosmatka as co-author.

Chapter 10, in part, is a reprint of the material which appears in the *Journal of Bridge Engineering* 2008 volume 13 issue 4 pages 388-397 titled "Development of a Short-Span Fiber-Reinforced Composite Bridge for Emergency Response and Military Applications." The dissertation author was the primary investigator and author with advisor J. B. Kosmatka as co-author.

VITA

1998	B.S., Utah State University
1998-2000	Graduate Research Assistant, Utah State University
2001	M.S., Utah State University
2000-2002	Design Engineer, Allen and Bailey/EQE/ABS Consulting Firms
2002-2008	Graduate Research Assistant, University of California, San Diego
2007	Professional Engineer Licensure, State of Utah
2008	Ph.D., University of California, San Diego

PUBLICATIONS

Journal Papers

Robinson, M. J. and Kosmatka, J. B. 2006. Improved Damping in VARTM Composite Structures using Perforated Viscoelastic Layers, *Journal of Composite Materials*, 40 (23): 2157-2173.

Robinson, M. J. and Kosmatka, J. B. 2008. Light-Weight Fiber-Reinforced Polymer Composite Deck Panels for Extreme Applications. *Journal of Composites for Construction* 12 (3): 344-354.

Robinson, M. J. and Kosmatka, J. B. 2008. Development of a Short-Span Fiber-Reinforced Composite Bridge for Emergency Response and Military Applications. *Journal of Bridge Engineering* 13 (4): 388-397.

Kai, H. H., Halling, M. W., Barr, P. J., and Robinson, M. J. 2008. Structural Damage Detection Using Dynamic Properties Determined from Laboratory and Field Testing. *Journal of Performance of Constructed Facilities* 22 (4): 238-244.

Conference Proceedings

Robinson, M. J. and Kosmatka, J. B. 2005. Embedding Viscoelastic Damping Materials in Low-Cost VARTM Composite Structures. *SPIE Proceedings on Smart Structures and Materials* 5760: 349-360.

Robinson, M. J. and Kosmatka, J. B. 2005. Low-Cost VARTM Processing of Thin Laminate Composites with Embedded Impervious Layers. *Proceedings of SAMPE 2005, Long Beach California*, (cd-rom) 14 pages.

Robinson, M. J. and Kosmatka, J. B. 2006. An Alternative Method for Measuring Permeability for the VARTM Process. *Proceedings of SAMPE 2006, Long Beach, California*, (cd-rom) 15 pages.

Velazquez, E., Klein, D. J., Robinson, M. J., and Kosmatka, J. B. 2008. Acoustic Emissions (AE) Monitoring of Large-scale Composite Bridge Components. *SPIE Proceedings on Smart Structures and Materials*,

Robinson, M. J., and Kosmatka, J. B. 2008. Vacuum Assisted Resin Transfer Molding Simulation for Thick Laminate Structures. Proceedings of the 49th AIAA/ASME/ASCE/AHS/ASC Structures, Structural Dynamics, and Materials Conference, Paper No SDM Conference

Robinson, M. J., and Kosmatka, J. B. 2008. Resin Bleeding Simulation for the VARTM Process. *Proceedings of SAMPE 2008, Long Beach, California*, (cd-rom) 15 pages.

Reports

Robinson, M. J., Stravidis, A., Kosmatka, J. B., and Ashford, S. A. 2004. "Rapidly Deployable Composite Bridge Project" final report submitted to the Office of Naval Research Under Contract No. N00014-02-C-0374, UCSD SSRP-04/07.

Kosmatka, J. B. and Robinson, M. J. 2007. "Rapidly Deployable Composite Bridge: ONR 1-4 m Bridge Final Report" final report submitted to the Office of Naval Research, UCSD Dept. of Structural Engineering.

ABSTRACT OF THE DISSERTATION

SIMULATION OF THE VACUUM ASSISTED RESIN TRANSFER MOLDING (VARTM) PROCESS AND THE DEVELOPMENT OF LIGHT-WEIGHT COMPOSITE BRIDGING

by

Marc J. Robinson

Doctor of Philosophy in Structural Engineering

University of California, San Diego, 2008

Professor John Kosmatka, Chair

A continued desire for increased mobility in the aftermath of natural disasters, or on the battlefield, has lead to the need for improved light-weight bridging solutions. This research investigates the development of a carbon/epoxy composite bridging system to meet the needs for light-weight bridging. The research focuses on two main

topics. The first topic is that of processing composite structures and the second is the design and testing of these structures.

In recent years the Vacuum Assisted Resin Transfer Molding (VARTM) process has become recognized as a low-cost manufacturing alternative for large Fiber Reinforced Polymer (FRP) composite structures for civil, military, and aerospace applications. The success of the VARTM process (complete wet-out) is very sensitive to the resin injection strategy used and the proper placement of flow distribution materials and inlet and vacuum ports. Predicting the flow front pattern, the time required for infusing a part with resin, and the time required to bleed excess resin at the end of filling, is critical to ensure that the part will become completely impregnated and desired fiber volume fractions achieved prior to the resin gelling (initiation of cure). In order to eliminate costly trial and error experiments to determine the optimal infusion strategy, this research presents a simulation model which considers in-plane flow as well as flow through the thickness of the preform. In addition to resin filling, the current model is able to simulate the bleeding of resin at the end of filling to predict the required bleeding time to reach desired fiber volume fractions for the final part.

In addition to processing, the second portion of the dissertation investigates the design and testing of composite bridge deck sections which also serve as short-span bridging for gaps up to 4 m in length. The research focuses on the design of a light-weight core material for bridge decking as well as proof loading of short-span bridge sections in the lab and extensive field testing using a variety of wheeled and tracked vehicles at different crossing speeds and crossing conditions.

CHAPTER 1

INTRODUCTION

As the desire for light-weight aerospace [1], marine [2], military [3, 4, 5], and civil structures [6, 7, 8, 9] continues to grow, more and more applications are being found for Fiber Reinforced Polymer (FRP) composite materials. Currently, the Office of Naval Research (ONR) is sponsoring a project at the University of California, San Diego to develop modular, light-weight, composite bridging for the US Military to be used on the battlefield or in the aftermath of natural disasters. Composites offer many advantages over conventional metallic materials used in existing modular bridging, such as reduced weight, increased fatigue life, and improved resistance to corrosive environments. However, great care must be taken to ensure that primary load bearing composite structures are fabricated in such a way that the integrity of the structure is not compromised.

FRP composites are a unique building material in that there are a number of different materials (fibers and matrix) and fabrication processes. It is imperative when designing composite structures that the designer not only consider the structural design but the materials and processing methods which will be used to achieve the final product. One of the main focus points of this work is to identify and investigate a manufacturing process which is conducive for the manufacturing of composite bridge components to be used in modular bridging. Although there are different manufacturing methods for composite structures, this research only considers methods

which utilize fabrics and are capable of creating large complex geometries. Based on manufacturing costs and the quality of parts produced, four different fabrication methods were reviewed from which a manufacturing process was selected for further investigation.

1.1 COMPOSITE PROCESSING METHODS

The processes reviewed include, 1) wet layup, 2) Resin Transfer Molding (RTM), 3) Vacuum Assisted Resin Transfer Molding (VARTM), and 4) Autoclave processing. A description of each process including advantages and disadvantages is presented.

1.1.1 Wet Layup

The most basic processing method is wet layup. This method has been used for many years in the boat building industry. The method consists of laying dry reinforcing fabric (preform) on a rigid mold surface and then applying resin using hand tools such as rollers and squeegees to force the resin into the preform and to remove any trapped air (voids). An illustration of this process is presented in Figure 1-1. One of the major advantages of this method is cost. Due to the basic nature of the process, tooling and material costs are very low. Unlike some of the other methods, the mold tool does not need to be air tight greatly reducing tooling costs. This process is conducive to using most preform materials and resins. The major disadvantage to this method is part quality and exposure to potentially harmful

emissions. The wet layup method is capable of fiber volume fractions between 40% and 45% with the quality (complete wetting) being dependent on the experience of the fabricator. In addition, since this is an open molding process workers are exposed to potentially harmful emissions from the matrix resin.

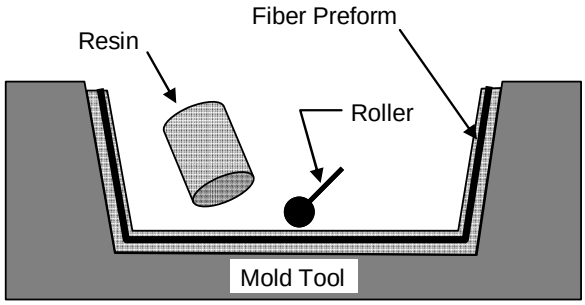

Figure 1-1 Illustration of the wet lay-up process.

1.1.2 Resin Transfer Molding

Industries which produce a large number of small to medium parts having the same geometry primarily use the Resin Transfer Molding (RTM) process. The RTM process uses two rigid matching mold halves. The dry fiber preform is placed in the mold and high clamping pressure is used to hold the two mold halves together. With the mold clamped together resin is injected into the mold cavity under positive pressure typically between 50 and 100 psi. A vent located in the mold allows air within the preform to be forced out of the mold cavity as it is replaced by the injected resin. Heated molds are used to quickly cure the part after which the mold is opened and the part is removed and replaced with the next dry preform. An illustration of the

RTM process is presented in Figure 1-2. The main advantage of this process is the ability to quickly produce large numbers of parts, the consistency of part quality, and containment of harmful emissions. Fiber volume fractions for the RTM process are typically between 50% and 60%. Due to the high injection pressures used, the molds must be extremely rigid to resist deformation during the injection process. The mold rigidity requirements limit this process to the production of small to medium sized parts and is cost prohibitive for producing large scale bridging components.

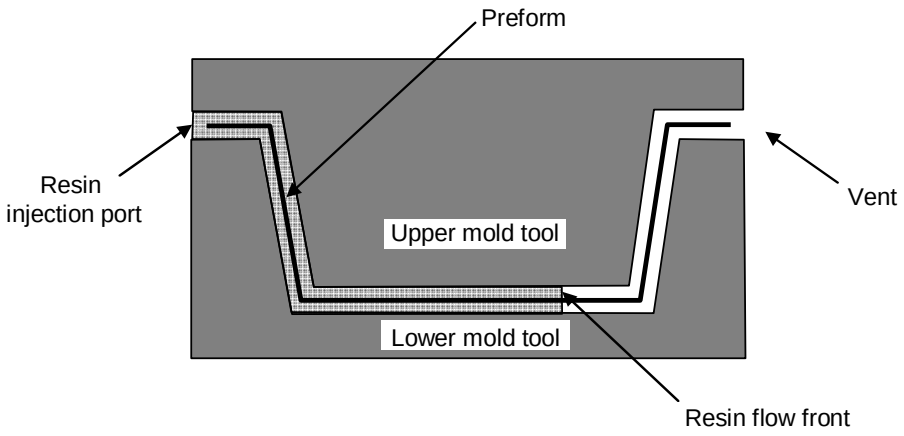

Figure 1-2 Illustration of the Resin Transfer Molding (RTM) process.

1.1.3 Vacuum Assisted Resin Transfer Molding

The Vacuum Assisted Resin Transfer Molding Process (VARTM) has taken the concept of the RTM process and made it applicable to large structures which were traditionally produced using wet layup. The VARTM process consists of placing a dry fiber preform in a rigid one sided mold and covering the other side with a flexible vacuum bagging material which is sealed around the perimeter. Following the

placement of the bagging material, a vacuum pump is used to draw a vacuum within the mold cavity and resin is injected into the preform under atmospheric pressure. An illustration of the VARTM process is presented in Figure 1-3. Due to the low driving pressure, relatively large structures have been fabricated with this process such as boats and wind turbine blades [10]. The VARTM process also provides a closed system which reduces exposure to harmful emissions. The process is typically limited to resins which have a viscosity below 0.4 Pa•s. Depending on the reinforcing fabric, the fiber volume fraction of parts fabricated using this process is typically 50% to 55%.

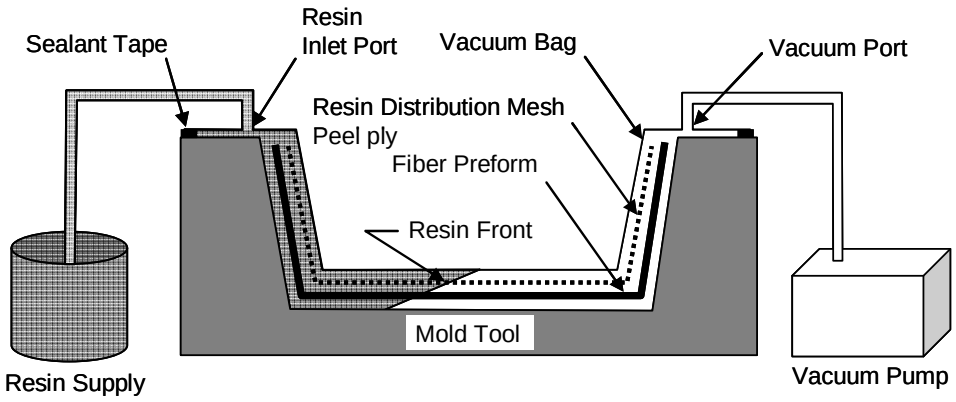

Figure 1-3 Illustration of the Vacuum Assisted Resin Transfer Molding (VARTM) process.

1.1.4 Autoclave Processing

Autoclave processing is typically used in the aerospace and sporting goods industries. Parts fabricated using the autoclave process use reinforcing fabrics (prepreg) which are preimpregnated with resin and then stored at below freezing temperatures to prevent the resin from curing prematurely. An illustration of the Autoclave process is shown in Figure 1-4. From the figure it is seen that the preimpregnated preform is laid on a rigid mold followed by a layer of peel ply and a layer of breather material. The mold is then covered with a vacuum bag and sealed around the perimeter. The entire assembly is then placed in an autoclave which applies heat and pressure to consolidate and cure the part. During curing the vacuum bag is connected to an external vacuum pump which is used to remove any volatiles during out gassing of the resin. The breather layer provides uniform vacuum pressure across the part surface as well as provides a path for excess resin to bleed out of the part greatly increasing the fiber volume fraction of the part. Cure temperatures and pressure are typically on the order of 300° F with compaction pressures between 75 and 100 psi. Expected fiber volume fractions for the autoclave process are from 60% to 65%. The autoclave process is capable of producing parts of excellent quality, however the cost of prepreg materials as well as operation of autoclaves is very high.

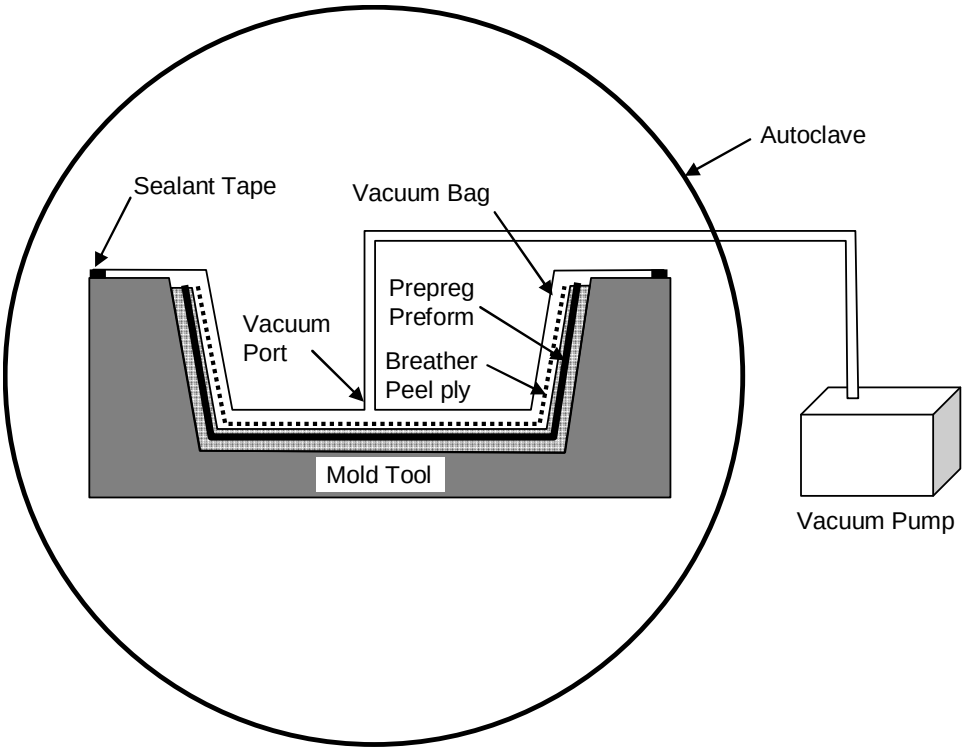

Figure 1-4 Illustration of the autoclave process.

A comparison of each of the reviewed manufacturing methods, based on relative cost and part quality, is given in Table 1-1. From the table it is seen that autoclave processing offers the best quality and repeatability, however the associated costs with materials, tooling, and autoclave processing make this process uneconomical for consideration in composite bridging. At the other end of the spectrum, wet lay-up is very low cost, however the quality (fiber volume fraction and repeatability) is very dependent on the fabricators capabilities and variations occur from part to part. In addition, unlike the other methods where the preform and resin are enclosed in a mold, the wet layup process leaves workers exposed to potentially

harmful emissions from resins. The RTM process offers good quality and high production rates, however due to the high injection pressures tooling large enough to accommodate bridging components is impractical. The VARTM process offers good quality as well as low to medium costs and is conducive to the fabrication of complex shapes. Of the four methods reviewed the VARTM process was the selected based on relative cost, part quality, repeatability, and ease of fabrication.

Table 1-1 Fabrication Method Comparison

Process	*Material Cost*	*Equipment Cost*	*Fiber volume fraction*	*Quality and Repeatability*
VARTM	Low	Medium	50-55%	Good
RTM	Low	High	50-60%	Good
Wet Lay-up	Low	Low	40-45%	Poor
Autoclave (prepreg)	High	High	60-65%	Excellent

1.2 COMPOSITE STRUCTURES PROCESSING AND DESIGN

The quality of parts produced through the VARTM process is dependent on complete wetting of the fabric preform. Complete wetting of the preform is very sensitive to the location of resin injection and vacuum ports as well as the layout of the resin distribution network (infusion strategy) with relationship to the geometry of the part including varying laminate thickness. For this reason it is critical during the design phase to consider the strategy which will be used to infuse the part with resin. A diagram illustrating this interdependence between processing and structural design

is given in Figure 1-5. Although the diagram illustrates the development of the composite modular bridge currently under investigation, the concepts apply to any composite structure.

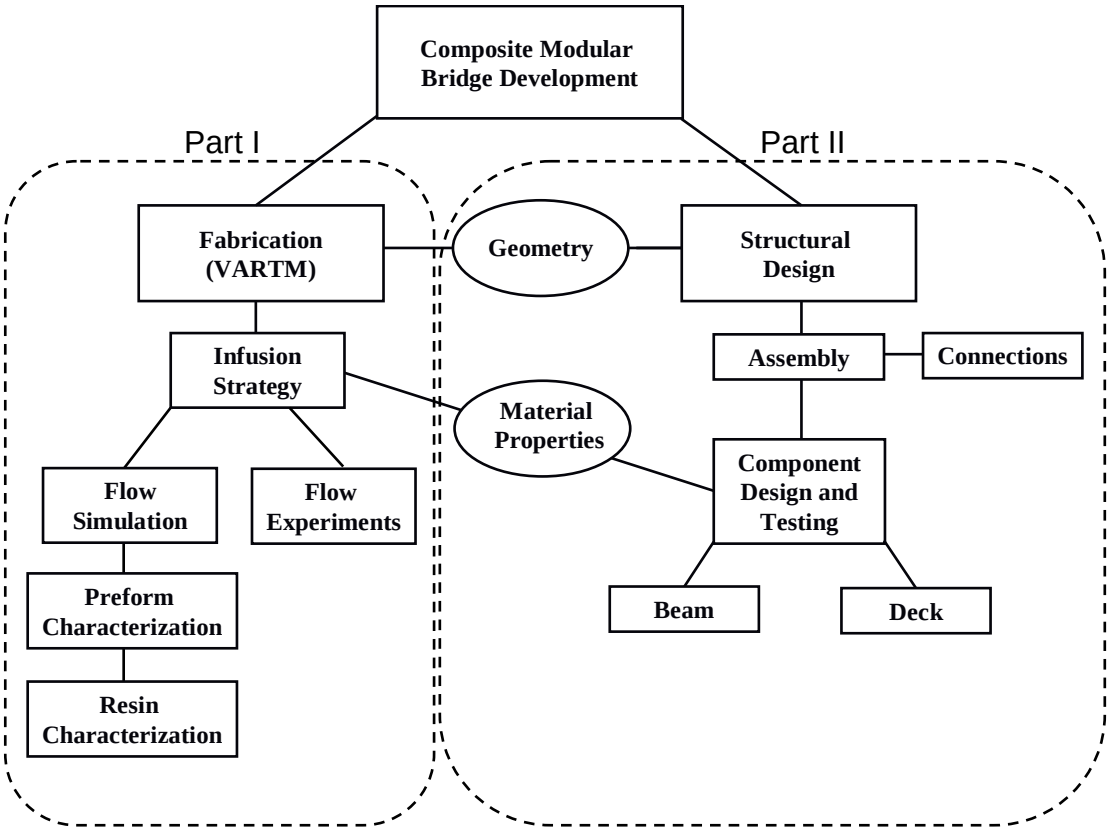

Figure 1-5 Diagram illustrating the supporting efforts to develop a composite modular bridge.

From the diagram it is seen that there are two main efforts involved in the development of the composite modular bridge. The first effort (Part I) is the fabrication process (VARTM) and the other effort (Part II) is the structural design. From the figure it is seen that these two efforts are interdependent on each other

through the geometry and material properties. When considering the geometry of the structural components the designer must keep in mind which geometries will offer the highest probability of a successful infusion of resin into the part (complete wet out). In addition to geometry, the material properties used in design are dependent on the fiber volume fraction achieved as well as the quality of the parts (minimal voids).

The structural design effort (Part II) of this research includes the design and testing of beam, deck, and joint elements. The bridge design follows a building block approach [11] in which material properties obtained from coupon testing are used to design each individual component (beam and deck). Each of these components is individually tested prior to being tested as an assembly. To date the bridge deck system has been developed and extensively tested both in the lab as well as the field. The beam and joint components are currently under development and are not considered in this dissertation.

The main focus of this dissertation is dedicated to the fabrication effort (Part I). The focus is to further develop the VARTM process through better understanding of preform material properties which influence resin flow and to develop improved simulation tools for simulating the VARTM process. From Figure 1-5 it is seen that the success of the VARTM process is dependent on developing an infusion strategy which will produce quality parts. To reduce the need and expense of trial and error experiments to determine the optimal infusion strategy this research presents a simulation model to accurately simulate the VARTM process as well as the characterization of preform materials to be used in flow modeling.

In accordance with the diagram shown in Figure 1-5 the dissertation is divided into two main topics. The first topic addresses the enhancement of the VARTM process through characterization of resin and preform materials and the development of a model to simulate both the resin filling and resin bleeding stages of the VARTM process. The second part of the dissertation is dedicated to the structural design and testing of the deck component of the bridge which also serves as short-span bridging for spanning gaps up to 4 m in length.

1.3 DISSERTATION OUTLINE

Part I of the dissertation is covered by chapters 2 through 7 and addresses improved simulation tools for the VARTM process including characterization of preform materials to be used in simulation. A brief description of the contents of each chapter is presented.

Chapter 2 presents a literature review of the development of the VARTM process including a description of the many variations of the VARTM process which are currently in use. A discussion of preform material properties which affect resin flow are presented along with methods for measuring these properties is presented. An overview of the methods for simulating resin flow through porous materials is presented along with current methods for simulating the VARTM process is presented. The chapter finishes with a discussion of the main research objectives of Part I of the dissertation.

Chapter 3 introduces the general equations used to simulate the VARTM process as well as an explanation of the finite element/control volume (FE/CV) method which is used to track the resin flow front during the VARTM process. The proposed model accounts for the changing preform porous volume due to compaction and relaxation of the preform allowing the bleeding phase of the VARTM process to be simulated in addition to the infusion.

Chapter 4 describes an alternative method for measuring the permeability and compaction characteristics of fiber preforms. The experimental procedure is outlined along with development of permeability and compaction constitutive models which are used in simulations.

Chapter 5 presents the validation of the developed flow simulation model through experimental studies. The validation experiments consider resin filling and resin bleeding for three different laminates with different lay-ups as well as the use of resin distribution layers.

Chapter 6 presents the case study of the infusion of a beam section used in the composite modular bridge. The study utilizes the developed simulation tool to develop an infusion strategy for fabricating the beam using the VARTM process.

Chapter 7 summarizes the conclusions of the VARTM research considered in Part I of the dissertation.

Part II is covered by chapters 8 through 11 and includes the design and testing of the composite deck/short-span bridge developed as part of the composite modular bridge research.

Chapter 8 describes the current mobile bridging systems used by the US Military and presents the composite modular bridging system considered in this research.

Chapter 9 describes the development and testing of several different structural core materials which were considered for the composite deck/short-span bridge system.

Chapter 10 presents the development of the deck/short-span bridging system. A list of performance, as provided by the US Army, is reviewed along with a description of the design and fabrication of the deck/bridge. Laboratory proof testing of the system is presented along with extensive field testing including an investigation of impact factors due to various military vehicles at different crossing speeds and approach conditions.

Chapter 11 provides a summary of the conclusions derived from the development of the short-span bridge system.

PART I

VARTM SIMULATION

CHAPTER 2

BACKGROUND AND OBJECTIVES

In recent years the Vacuum Assisted Resin Transfer Molding (VARTM) process has become recognized as a low-cost manufacturing alternative for large Fiber Reinforced Polymer (FRP) composite structures for civil, military, and aerospace applications. The success of the VARTM process (complete wet-out) is very sensitive to the resin injection strategy used and the proper placement of flow distribution materials and inlet and vacuum ports. Predicting the time required for infusing a part with resin, and bleeding excess resin at the end of filling is critical to ensure that the part will become completely impregnated during the filling phase and desired part fiber volume fractions are achieved through resin bleeding prior to the resin gelling (initiation of cure). In order to eliminate costly trial and error experiments to determine the optimal infusion strategy, numerical simulation codes have been developed. The usefulness of these models is dependent on the accuracy of the input parameters such as the permeability of the fiber preform and viscosity of the resin. This chapter presents a historical review of the development of the VARTM process as well as a literature review of previous research focused on simulating the VARTM process and methods for characterizing prefom materials. Finally, the research objectives in relationship to simulating the VARTM process and experimental methods for characterizing preform materials are set forth.

2.1 HISTORICAL DEVELOPMENT OF THE VARTM PROCESS

Williams, Summerscales, and Gove [12] presented a historic overview of Resin Injection under Flexible Tooling (RIFT) in which they describe the development of the VARTM process. The VARTM process, sometimes referred to as the Vacuum Infusion Process (VIP) or Resin Infusion under Flexible Tooling (RIFT), was first introduced in 1950 and was referred to as the Marco method [13]. The Marco method, developed for manufacturing boat hulls, consisted of laying up dry reinforcing fabric over a rigid male mold and then placing a semi-flexible female tool over the surface. Resin was placed in a trough around the perimeter of the mold which was then drawn into the preform by application of vacuum pressure to the mold cavity. The method was not widely used due to the preference of wet layup in the boat building industry. An illustration of the Marco method is shown in Figure 2-1.

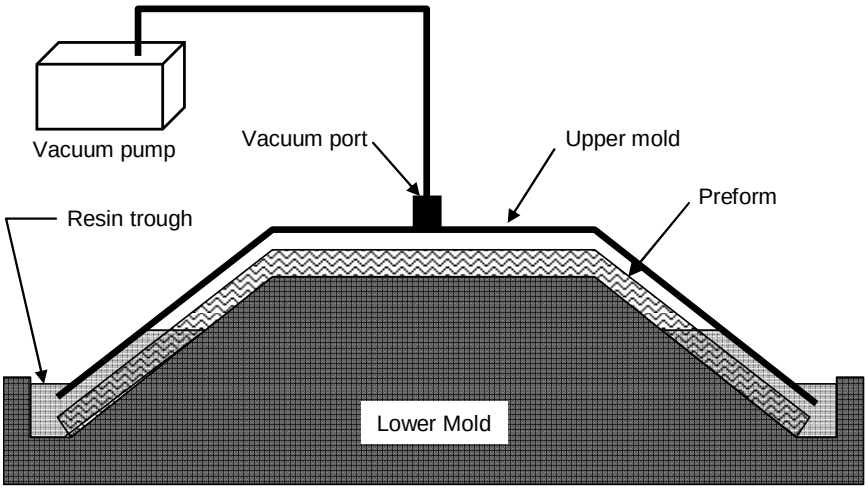

Figure 2-1 Illustration of the Marco method.

In 1972 a method for producing FRP auto components was patented by Group Lotus Car Ltd [14]. The process consisted of a closed mold composed of two halves. Dry reinforcing fabric was placed into the mold with a measured amount of resin poured on the fiber preform after which the mold was sealed. Vacuum pressure was applied to the mold to evacuate the air and draw the two halves of the mold together to provide consolidation and diffusion of the resin within the mold.

In 1978, as a response to the introduction of the Health and Safety Act to reduce styrene emissions, Gotch [15] followed a similar approach to the Lotus Group, replacing one half of the rigid mold with a silicone rubber bagging material. Again a measured amount of resin was poured onto the preform surface followed by the placement and sealing of the silicone vacuum bag after which vacuum pressure was applied to consolidate the laminate and draw out excess air. Gotch reported that the quality of molded parts was higher than that achieved for wet lay-up with better consistency due to the removal of the operator experience required for wet lay-up. Later in 1980 [16] and 1985 [17] Gotch revisited the process using the silicone vacuum bag but now used vacuum pressure to draw the resin into the dry preform from a resin supply rather than pouring the resin onto the dry preform prior to placement of the vacuum bag.

In 1990 Seemann patented the Seemann Composite Resin Infusion Molding Process (SCRIMP) [18] which is currently widely used in manufacturing large composite structures. The SCRIMP process is a variant of the VARTM process which uses a highly permeable resin distribution mesh which is placed on the surface of the laminate preform allowing the resin to quickly flow across the surface of the laminate

and then permeate through the thickness (see Figure 2-2). Full vacuum pressure is applied at the outlet with the inlet hose closed. When the mold cavity is under full vacuum the inlet hose is opened and resin is allowed to flow into the dry preform under atmospheric pressure. The resin distribution mesh is stopped just short of the vacuum outlet to prevent resin from flowing directly into the outlet and allowing the preform to become completely wetted through the thickness. At the end of filling (resin reaches the outlet) the inlet line is clamped and excess resin is allowed to bleed from the preform as the resin pressure reaches equilibrium. By placing a layer of peel ply or release fabric between the laminate and the resin distribution mesh, the distribution mesh may be removed from the final part following cure. Drawbacks of the SCRIMP process are the increase in waste materials (flow distribution mesh and peel ply) and print through of the distribution mesh onto the surface of the finished part. To overcome this, Seemann developed reusable bagging systems which have a resin distribution network printed into the surface of the bag eliminating the need for a resin distribution layer [19]. The introduction of the SCRIMP process has greatly increased the use of the VARTM process over the past 15 years.

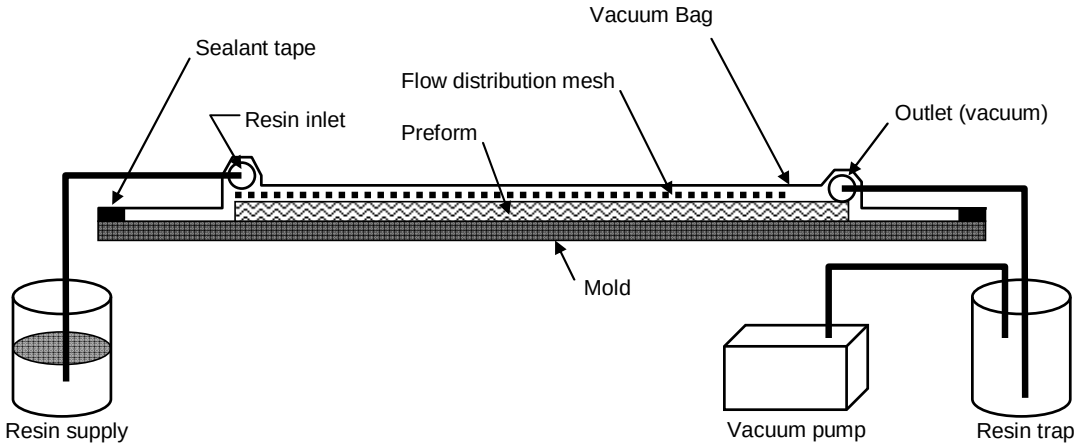

Figure 2-2 Illustration of the Seemann Composite Resin Injection Molding Process (SCRIMP).

One of the unique features of the VARTM process in comparison to processes which use a two sided rigid mold, such as the RTM process, is the ability of the preform to compact or relax under the flexible bagging material as the pressure within the mold changes. During the SCRIMP process, prior to the inlet hose being opened, the preform is under full vacuum pressure and the preform is fully compacted (minimum thickness). When the inlet hose is opened the resin coming into the mold is near atmospheric pressure which results in the preform relaxing (thickness increase) as the flow front progresses. Thus at the end of filling there is a pressure gradient from the inlet to the outlet leading to a gradient in the part thickness and fiber volume fraction. By closing the inlet at the end of filling, excess resin is allowed to escape through the outlet as the preform compacts and pressure equilibrium is reached. However, depending on the infusion strategy used the time required to bleed excess resin could be very long, potentially resulting in the resin curing before full compaction is achieved. To reduce the time to bleed excess resin and achieve uniform

preform compaction Rigas and Thomas [20] received a patent in 2006 for the concept of applying vacuum pressure at the resin inlet at the end of filling to remove excess resin. At the end of filling the inlet hose is attached to a resin trap with a vacuum pump such that excess resin is removed through both the inlet and outlet allowing preform compaction to be achieved more quickly resulting in parts which have a uniform laminate thickness.

Woods, Modin, Hawkins, and Hanks [21] received a patent in 2008 for a process entitled “Controlled Atmospheric Pressure Resin Infusion” (CAPRI) which is used by Boeing to manufacture aerospace parts. The process follows the same procedure as the SCRIMP process with the exception that the resin is not injected at atmospheric pressure. Prior to introducing the resin into the mold a vacuum pump is used to compact the preform fibers through several cycles of applied vacuum pressure to increase the final fiber volume fraction. To maintain the fiber compaction during the infusion process a vacuum line is attached to the resin supply container such that vacuum pressure can be applied independently at both the inlet and outlet (see Figure 2-3). As an example, while full vacuum (0 kPa) is applied at the outlet only half vacuum (50 kPa) is applied at the inlet to maintain fiber compaction. By maintaining moderate vacuum pressure at the inlet, the compaction of the fiber preform is able to be maintained throughout the infusion. One of the disadvantages of applying vacuum pressure to the inlet is the reduced pressure gradient provided to drive the resin into the dry preform leading to longer processing times.

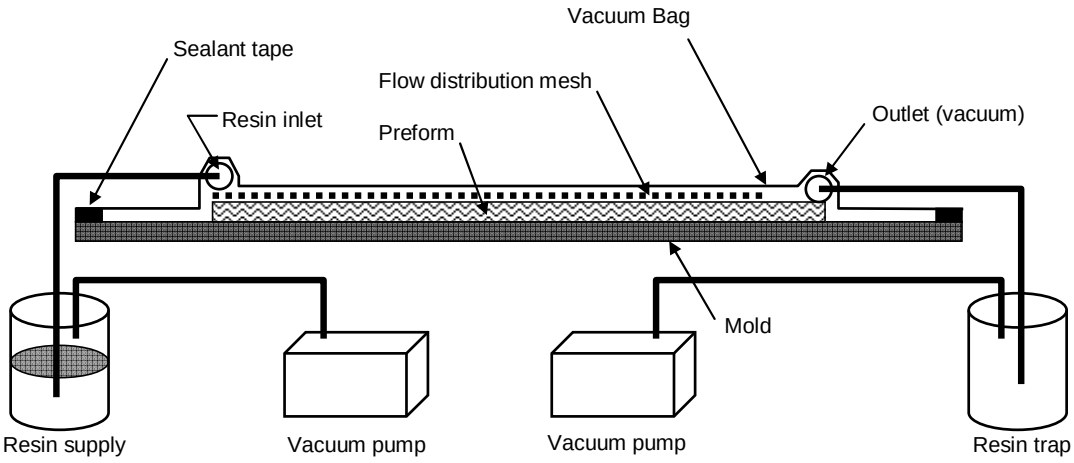

Figure 2-3 Illustration of the Controlled Atmospheric Pressure Resin Infusion (CAPRI) process.

In an effort to improve the quality (increased fiber volume fraction and reduced void content) of parts the Vacuum-Assisted Process (VAP) was developed by Filsinger, Lorenz, Stadler, and Utecht and patented by EADS Deutschland [22]. The process uses a gas-permeable membrane to allow for uniform vacuum pressure distribution and provides continuous degassing of the resin during the infusion process. An illustration of the process is shown in Figure 2-4. Like the SCRIMP process, a flow distribution layer is placed on top of the fiber preform to assist with the flow of resin. Following the placement of the flow distribution layer the assembly is sealed under a gas-permeable membrane. A breather cloth layer is then placed on top of the membrane with the outlet (vacuum) hose which is covered with a final vacuum bag layer which is sealed around the entire assembly. The breather layer allows even vacuum pressure to be applied over the entire surface providing uniform preform compaction as well as continuous degassing of the resin during the infusion process. Li, Krehl, Gillespie, Heider, Endrulat, Hochrein, Dunham, and Dubois [23] performed

an evaluation of the VAP process comparing it with the SCRIMP process. During the evaluation they compared infusion times, changes in the preform thickness after infusion and after cure, and fiber volume fractions and void fractions of finished panels. The study showed the fill time and flow progression for both the VAP and SCRIMP processes to be very similar, however the VAP process was shown to be more robust in terms of eliminating the formation of dry spots due to the ability to continuously remove air through the gas permeable layer. At the end of filling the VAP panel showed uniform thickness along the length of the panel while the SCRIMP panel showed a thickness gradient from thicker at the inlet to thinner at the outlet. At the end of the filling stage the inlet hoses were closed and excess resin was allowed to bleed from the preform. At the end of bleeding both the VAP and SCRIMP panels showed uniform thicknesses throughout the panel with the SCRIMP panel being thinner (higher fiber volume fraction) in comparison to the VAP panel. The authors contribute the higher thickness of the VAP panel to over filling of the mold since there is no path for bleeding excess resin at the end of filling. A second panel was fabricated using the VAP process in which the resin supply bucket was lowered 1.3 m below the mold to reduce the pressure at the inlet resulting in a higher fiber volume fraction. Fiber volume fraction and void content testing in accordance with ASTM D3171-99 and ASTM D2734-99 respectively were performed on ten samples from each panel. Fiber volume fraction and void content values along with standard deviations are shown for each panel in Table 2-1. From the table it is seen that the SCRIMP panel showed a higher fiber volume fraction in comparison to the VAP process, however due to the ability of the VAP process to continue to degas the resin

throughout the process the VAP panels showed considerably lower void content. Short beam shear testing (ASTM D2344) of the panels showed the VAP and SCRIMP panels to have similar strengths with the VAP panel being slightly higher with a lower coefficient of variation.

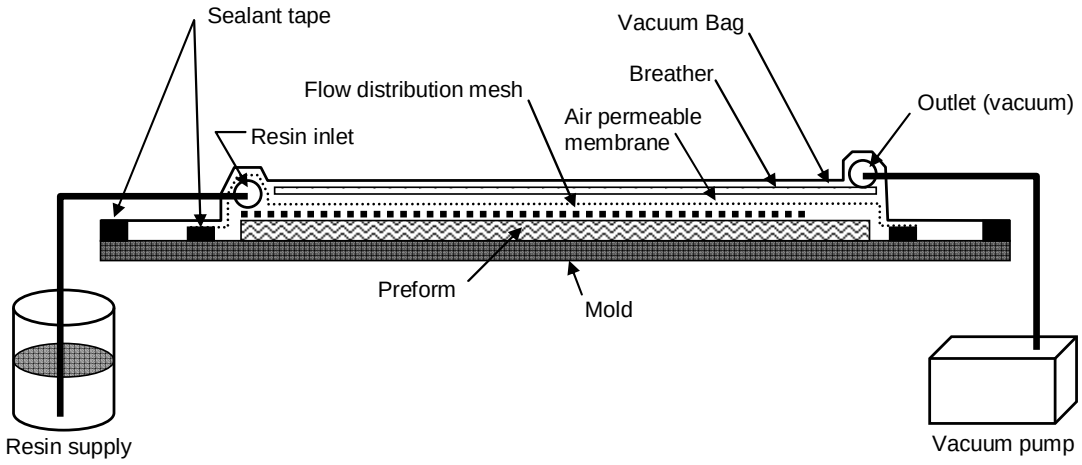

Figure 2-4 Illustration of the Vacuum Assisted Process (VAP).

Table 2-1 Fiber Volume Fraction and Void Content

Process	*Fiber Volume fraction (%) Standard Deviation (%)*	*Void Content (%) Standard Deviation (%)*
VAP	50.9/0.5	0.37/0.3
VAP_{low}	54.0/0.3	0.6/0.3
SCRIMP	56.0/1.0	1.64/1.2

Many of the VARTM processes described incorporate resin distribution or breather layers which become saturated with resin during the infusion process and become waste at the end of processing. In an effort to reduce waste, Walsh (U.S.

Army Research Laboratory) [24] developed a process and received a patent for an "Apparatus and Method for Selectively Distributing and Controlling a means for Impregnation of fibrous articles". The process has become known as FASTRAC which refers to Fast Remotely Actuated Channels. An illustration of the FASTRAC process is presented in Figure 2-5. The basic concept of the FASTRAC method is similar to the other VARTM processes described with the exception that a flow distribution layer is not employed. For FASTRAC the preform is laid on a rigid mold with inlet and outlet lines which are covered and sealed by a primary vacuum bag. On the surface of the primary vacuum bag a resin distribution tool (FASTRAC layer) is placed. The FASTRAC layer has a network of channels formed into the surface which is in contact with the primary vacuum bag. A second vacuum bag is then placed and sealed over the entire assembly. Vacuum pressure is applied to the preform through the outlet and a second vacuum is applied to the FASTRAC layer. By applying a slightly higher vacuum pressure to the FASTRAC layer the primary bag is lifted up into the channels of the FASTRAC layer creating a resin distribution network across the surface of the preform. At this point resin is allowed to flow through the channels across the surface and then penetrate through the thickness of the preform. At the end of filling the vacuum pressure applied to the FASTRAC layer is released allowing the primary bag to pull back down to the surface of the preform and compact the preform as excess resin bleeds through the outlet. By controlling the vacuum pressure differential between the preform and the FASTRAC layer the rate of infusion can be controlled. The primary advantage of this method is the reduction in waste materials since there is no distribution layer which becomes saturated with resin. Allende,

Mohan, and Walsh [25] performed a set of experiments to compare the fill time of the FASTRAC process with the SCRIMP process. The study considered the infusion of a panel 55.9 cm long and 41.1 cm wide consisting of 10 layers of 24 oz. weaved fiber glass. The infusion was performed on a glass mold such that the flow front could be tracked on both the top and bottom surfaces of the panel. The experimental results showed the FASTRAC infusion time to be about 17% of the infusion time for the SCRIMP process. The authors also point out that due to the low resistance to flow through the open channels created by the FASTRAC layer, resins with lower viscosity which would not be considered for conventional VARTM processes could be used in the FASTRAC process.

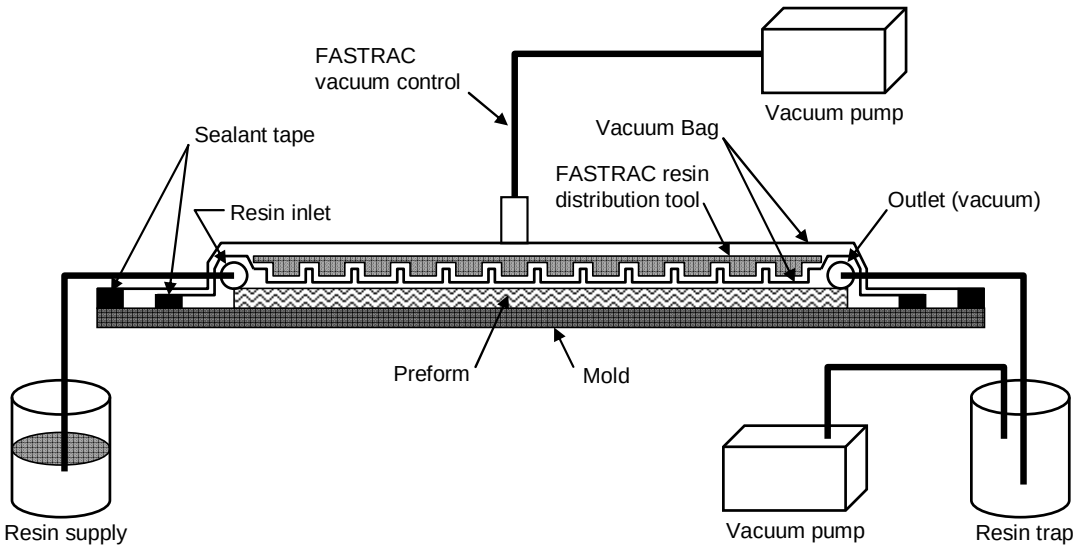

Figure 2-5 Illustration of the Fast Remotely Actuated Channels (FASTRAC) process.

2.2 SIMULATION

There have been several variations of the VARTM process developed for fabricating composite structures. The success of each of these processes (complete wet-out) is very sensitive to the resin injection network used and the proper placement of inlet ports, resin distribution materials, and vacuum ports. In order to eliminate costly trial and error experiments to determine the optimal infusion strategy, numerical simulation models have been developed. In general these simulation models are based on the flow of an incompressible viscous fluid through a fibrous preform which is modeled using Darcy's Law [26] expressed as

$$q = -\frac{[\kappa]}{\mu}\nabla P\,, \tag{2.1}$$

where, q is the superficial resin velocity, $[\kappa]$ is the preform permeability tensor, μ is the resin viscosity, and P is the pressure. The usefulness of these models is dependent on the accuracy of the input parameters such as the permeability of the fiber preform and viscosity of the resin. The intent of the remainder of this chapter is to provide an overview of the current flow modeling methods being used in literature as well as methods for characterizing preform materials for simulation and finally establishing the objectives of the current research. Additional details of the flow simulation model considered in this research as well as methods for characterizing preform materials are presented in Chapter 3 and Chapter 4 respectively.

2.2.1 RTM Simulation

Most current VARTM technologies are variants of the RTM process. As such, most models for simulating the VARTM process have emerged from simulation models developed for the RTM process. Therefore the review of flow simulation for VARTM begins with a review of simulation models developed for the RTM process.

Based on conservation of mass Dave [27] presented a "Unified Approach to Modeling Resin Flow During Composite Processing" which with the correct boundary conditions can be modified to describe a variety of composite manufacturing processes. The model is based on the following assumptions:

1. There exists continuity for both the resin phase and air phase at all times.
2. Resistance to flow due to air is negligible.
3. The individual fibers are incompressible.
4. The resin flow through a porous material obeys Darcy's Law.
5. The process is quasi-static.
6. Body forces such as self weight are negligible.

The unified model is expressed as

$$\frac{\partial(\phi\psi\rho)}{\partial t} + q \bullet \nabla(\phi\psi\rho) + (\phi\psi\rho)\nabla \bullet q = 0, \qquad (2.2)$$

where ϕ is the porosity, ψ is the degree of saturation or also known as the fill factor, ρ is the resin density, t is time, and q is the superficial velocity given by Darcy's Law (2.1). For the RTM process the mold thickness is fixed such that the porosity remains constant throughout the process. By making other logical assumptions, such as the resin is incompressible (constant density) and the preform behind the flow front is completely saturated, the governing equation for the RTM process reduces to

$$\nabla \bullet q = 0. \tag{2.3}$$

It has been shown by others [28] that for some laminate fiber architectures complete saturation behind the flow front may not be a valid assumption and the partial derivative of saturation with respect to time on the left hand side of Eq. (2.2) should be considered. However for many materials the RTM process is adequately described by Eq. (2.3).

To solve the governing differential equation (2.3) a variety of numerical techniques have been used including finite difference [29, 30], boundary element [31], and finite element methods [32-45]. Of the finite element methods considered the Finite Element/Control Volume (FE/CV) is the most widely used.

In the FE/CV approach [32, 33] the mold geometry is descretized into finite elements over which the pressure distribution may be solved using the finite element method. The finite elements are further divided into smaller sub volumes such that a control volume is constructed around each node. An illustration of the control volumes associated with each node is given in Figure 2-6. Each node (control

volume) is assigned a fill factor (ψ) representing the degree of saturation of the control volume, where the fill factor is defined as the ratio of the volume of fluid in the control volume to the total volume of the control volume. The fill factor takes on values from 0 to 1, where 0 signifies an empty control volume and a value of 1 represents a completely filled control volume. The flow front is represented by partially filled control volumes having a fill factor value between 0 and 1. Based on prescribed boundary conditions (flow rate or pressure) the flow rate at each unfilled control volume at the flow front is calculated from Darcy's Law. The shortest time to fill one control volume is determined and the flow front is advanced to completely fill the control volume after which the time step is advanced. Following the advancement of the flow front, the boundary conditions are modified to include the newly filled control volume and the pressure is once again solved for each node where the control volume is completely filled ($\psi = 1$). This process is repeated until all of the control volumes are filled or until the resin has gelled and flow is terminated. A flow chart illustrating the numerical procedure is given in Figure 2-7.

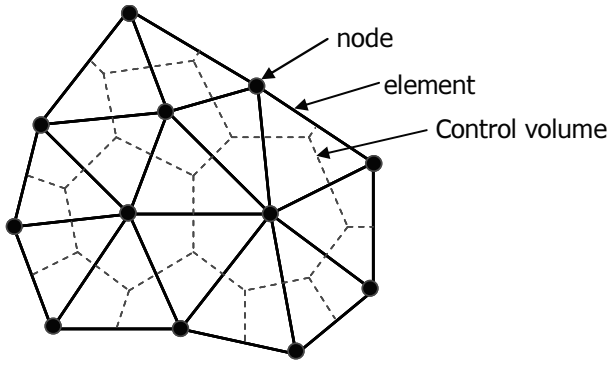

Figure 2-6 Illustration of a finite element mesh showing nodes, elements, and control volumes.

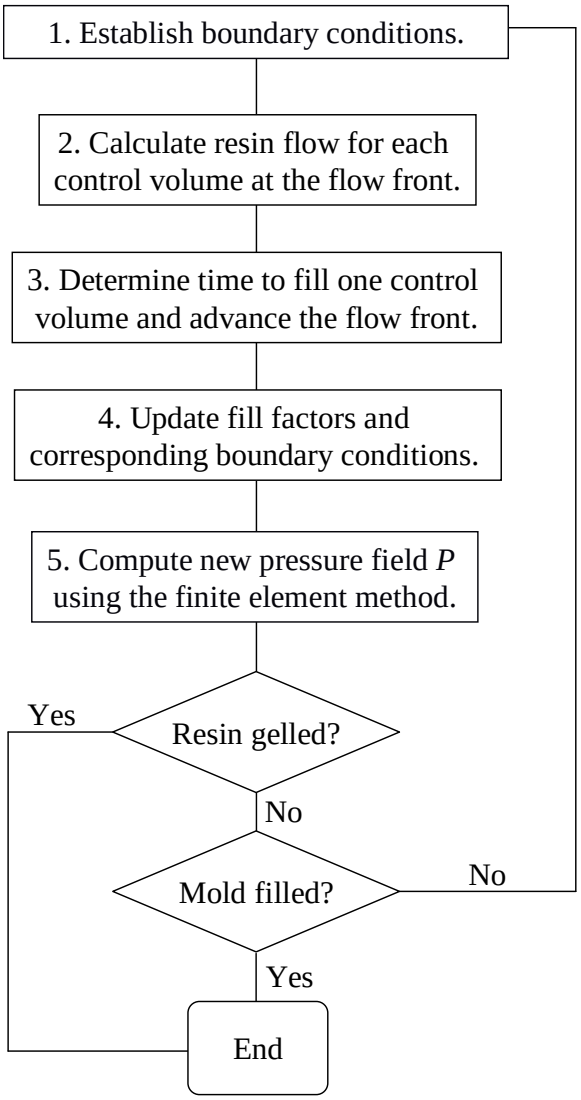

Figure 2-7 Flow chart of the Finite Element/Control Volume procedure for simulating the resin filling process.

Based on the continuity expression given in Eq. (2.3) Several authors [34-40] have used the FE/CV method to simulate the RTM process for two and three-dimensional anisotropic performs. Typically in the RTM process the thickness of the preform is very thin in comparison to the in-plane dimensions and the through thickness flow is neglected. In two dimensions Darcy's Law is described by

$$\begin{pmatrix} q_x \\ q_y \end{pmatrix} = -\frac{1}{\mu}\begin{bmatrix} \kappa_{xx} & \kappa_{xy} \\ \kappa_{yx} & \kappa_{yy} \end{bmatrix}\begin{pmatrix} \partial P/\partial x \\ \partial P/\partial y \end{pmatrix}, \tag{2.4}$$

where κ_{xx} is the permeability in the *x* direction, κ_{yy} is the permeability in the *y* direction, κ_{xy} is coupling of the permeability in the *x* and *y* directions, q_x is the superficial velocity in the *x* direction, and q_y is the superficial velocity in the *y* direction.

In general the preform is composed of several layers with each layer having a different principle permeability value and direction. For two-dimensional analysis it has been proposed [34] that an equivalent averaged permeability be used to represent such laminates. The equivalent permeability ($\overline{\kappa_{ij}}$) is expressed by

$$\overline{\kappa_{ij}} = \frac{1}{H}\sum_{l=0}^{n} h^l \kappa_{ij}^l , \tag{2.5}$$

where $\overline{\kappa_{ij}}$ is the equivalent permeability tensor, *H* is the laminate thickness, *h* is the individual lamina thicknesses and the subscript *l* is the lamina number.

Applying continuity (2.3) to the two-dimensional expression for Darcy's Law leads to

$$\frac{\partial}{\partial x}\left(\kappa_{xx}\frac{\partial P}{\partial x}\right)+\frac{\partial}{\partial x}\left(\kappa_{xy}\frac{\partial P}{\partial y}\right)+\frac{\partial}{\partial y}\left(\kappa_{yx}\frac{\partial P}{\partial x}\right)+\frac{\partial}{\partial y}\left(\kappa_{yy}\frac{\partial P}{\partial y}\right)=0. \qquad (2.6)$$

The Galerkin finite element method is applied using linear shape functions leading to a system of linear equations which can be expressed by

$$[K]\{P\}=\{b\}, \qquad (2.7)$$

were *K* represents the permeability "stiffness" matrix and *b* is the boundary condition based on a prescribed pressure or flow rate. The boundary conditions consist of a zero pressure condition at the flow front with a prescribed injection pressure or flow rate at the inlet.

Bruscke and Advani [34] at the University of Delaware presented a two-dimensional flow model based on the described FE/CV procedure to simulate the RTM process under isothermal conditions using a non reactive resin. The developed code is referred to as LIMS (Liquid Injection Molding Simulation) [35]. A set of four experiments were conducted to validate the results of the simulation. A flat rectangular mold having dimensions of 46 cm x 46 cm with a gap height of 5.5 mm was used. A glass top plate was used to seal the mold such that the flow front could visually be monitored during the injection process. A Newtonian fluid (oil) was injected at the center of the mold under constant pressure. Four different experiments were performed to validate the simulation code and achieve better understanding of the physics of the process. The first experiment used a preform of uni-directional

layers oriented in different directions ([0/±45/90/0/90/±45/0]) to study the effects of the ply orientations on the flow field. An equivalent permeability based on Eq. (2.5) was used in the simulation. The second experiment used a random glass mat preform with an impermeable circular insert to study the influence of the geometric complexity on the flow field. In the third experiment the preform consisted of two separate pieces of uni-directional material put together side by side. The line where the two layers meet is refered to as the cutline. The permeability along the interface of the two pieces is different from the bulk permeability of each mat. The purpose of the experiments was to study the effects of local permeability non homogeneity on the flow field. The last experiment used random mats in a mold with two different gap heights to study the effects of preform compaction on the flow field. In general the simulations were in good agreement with the experimental results. For the third experiment with the cut line it was observed that the flow along the direction of the cut line was faster than predicted by the simulation suggesting that the permeability was higher than predicted along the cut line. In the last experiment the flow in the area of the reduced mold height was much faster than the simulation.

Young, Han, Fong, Lee and Liou [36] at Ohio State University developed a simulation code using the FE/CV method to investigate two and three-dimensional flow for the RTM process. The authors considered the infusion of a rectangular mold (20.32 cm x 80.01 cm) under isothermal conditions using a non reactive fluid (oil). Two sets of experiments were preformed using a combination of random fiber mats and stitched bi-directional mats which were used to validate numerical simulations. The first experiment considered three different arrangements of fiber mats. For the

first case, six layers of random fiber mat filled the entire mold having a mold thickness of 0.58 cm. In the second case four layers of random fiber mat were placed in the mold with two more layers of random fiber mat being added in two smaller rectangular areas creating areas of local lower porosity and permeability leading to a mold thickness of 0.50 cm. In case three, four layers of random mat and six layers of bi-directional mat were placed side by side having a mold thickness of 0.47 cm. For each case the resin was injected at the center of the mold at a constant flow rate. For cases one and three, two runs were conducted with the same fiber mat configurations. For one run a 2.5 cm hole was cut through the fiber mats such that there was no resistance to flow through the thickness and the flow can be treated as two-dimensional. For the second run there was no hole provided resulting in a three-dimensional flow pattern. For the second set of experiments 12 layers of random fiber mat (R) and 8 layers of bi-directional mat (B) were used to study the effects of two different stacking sequences, $[R_6/B_8/R_6]$ and $[B_4/R_{12}/B_4]$, which were each 1.5 cm thick. All experiments were performed using clear acrylic sheets such that the flow front on the top and bottom surfaces could be observed. For the first case of the first set of experiments, the predicted flow field and pressure correlated with experimental measurements with and without the hole through the fiber mat. The two-dimensional and three-dimensional models gave similar results suggesting that the pressure drop through the thickness of the random fiber mat was insignificant. For the second case it was observed that the flow front slowed as it passed through the areas of local low permeability created by the additional layers of fiber mat. The experimental measurements and simulation showed good agreement. For the third case it was

observed that resin flow was slower through the bi-directional fabric which has a lower permeability than the random fiber mat. Again simulation predictions showed good agreement with experimental results. For the second set of experiments it was observed that the stacking sequence had significant effects on the flow progression. For the mat in which the bi-directional layers were on the top and bottom surfaces the flow front on the two surfaces was very similar and showed good agreement with three-dimensional simulations, however for the other stacking sequence in which the random fiber mats were on the top and bottom surfaces the flow front on the bottom surface significantly lagged the flow front on the top surface. It was concluded that an average permeability through the thickness was not adequate to capture the effects of the stacking sequence.

Young, Rupel, Han, and Lee [37] used the model developed at Ohio State University [36] to demonstrate the simulation of complex geometries. In the study they demonstrate the two-dimensional filling of an automotive hood with multiple injection points. The model showed areas in which flow fronts merged indicating locations where vents should be placed to remove excess air from the mold cavity.

Calhoun, Yalvac, Wetters, Wu, Wang, Tsai, and Lee [38] conducted RTM experiments at Dow Chemical to validate the simulation model developed at Ohio State University [36]. The experiments were conducted independent of the flow simulations to remove any bias. Isothermal filling of a rectangular mold measuring 33.02 cm by 45.72 cm by either 0.28 cm or 0.56 cm for either 7 plies or 14 plies of fiber mat respectively was conducting using two different injection strategies. The first injection was one-dimensional using a line injection at one edge and line venting

at the opposite edge. The second injection strategy was two-dimensional with flow converging from the mold edges with a vent at the center of the mold. It was found that mold filling times could be predicted within in experimental error but the pressure field required scaling to match experimental data. It was also noted that the model was extremely sensitive to the preform porosity and permeability values used in the simulation. By increasing the edge permeability by 100 times the bulk preform, permeability to represent the increased permeability at the mold edges, the experimental pressures could be closely predicted through simulation.

Koorevaar [39] presented RTM-Worx, a commercially available flow simulation code based on the FE/CV method. Koorevaar showed that rather than determining the flow into each control volume using Darcy's Law and then determining the flow rate through each face of the control volume one can simply multiply the permeability (stiffness) matrix by the pressure field to calculate the residual flow at each node. A comparison of the simulation predictions with analytical one and two-dimensional solutions showed convergence to the exact solution.

Recognizing the need for three-dimensional simulation and considerations of nonisothermal effects and resin kinetics Young [40] at National Cheng-Kung University in Taiwan developed a three-dimensional simulation model for nonisothermal mold filling for the RTM process. The model utilizes the same FE/CV method used by previous authors introducing heat transfer as well as resin reaction through the appropriate choice of resin kinetic and viscosity models. Numerical simulations were performed to demonstrate the model for complicated three-dimensional parts, however the model was not validated by experiments.

Trochu, Gauvin, Gao, and Boudreault [41, 42] at Ecole Polytechnique, Montreal, Canada, developed an RTM simulation code using the FE/CV method with nonconforming finite elements. The simulation code is referred to as RTMFLOT [41, 42]. The RTMFLOT simulation code follows the same FE/CV procedure for advancing the flow front as previously described with the exception that it is not required to define control volumes around each node. An illustration of a nonconforming triangular element with interpolating function *W* is seen in Figure 2-8.

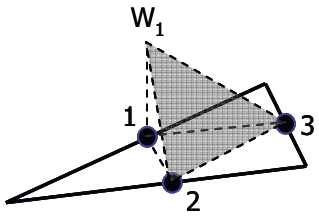

Figure 2-8 Illustration of a nonconforming linear triangle element.

Using the nonconforming element allows the element itself to represent the control volume and the secondary work of formulating control volumes around each node is not necessary. A comparison between experimental results and numerical simulations using RTMFLOT showed good agreement.

Mohan, Ngo, Tamma [43, 44, 45], and Shires [45] presented an implicit "Pure Finite-Element Based Methodology for Resin Transfer Mold Filling Simulations." In this formulation the mass balance is described by

$$\frac{\partial \psi}{\partial t} = \nabla \bullet \left(\frac{\kappa}{\mu} \nabla P \right), \tag{2.8}$$

where the time derivative of the fill factor is given explicitly as

$$\frac{\partial \psi}{\partial t} = \frac{\psi^{n+1} - \psi^{n}}{\Delta t}, \tag{2.9}$$

where *n* is the time step. Based on this formulation an iterative method is used at each time step until convergence is reached for the fill factor. The significant advantage of this method highlighted by the authors is that the flow front progression is independent of the time step as opposed to the limitation of the FE/CV where the time step is limited to the filling of a single control volume. However the authors do point out that the pressure solution is dependent on the time step size. The authors went on to expand the method to three dimensional performs and did a comparison between the implicit pure finite element method and the explicit FE/CV method showing good agreement [44, 45].

The previous models considered have all treated the flow of resin through a fibrous preform as saturated flow of a Newtonian fluid through a single scale porous medium. It has been shown by Pillai and Advani [28] that this assumption of saturated flow through a single scale porous medium may break down for the case of woven and stitched fiber mats which exhibit characteristics of a dual scale porous medium. A two layer model which considers inter-tow and intra-tow flow was

developed with these flows being coupled by a sink term which accounts for the loss of resin due to unsaturated control volumes behind the flow front. The model was demonstrated for a simple one-dimensional case. Later Pillai and Advani [46] adapted a pre-existing FE/CV code (LIMS) to model flow in woven fiber mats considering the dual scale inter-tow and intra-tow flow enabling one to simulate unsaturated flow in complex geometries representative of the RTM process. Similar to previous models, this model is based on Darcy's Law and mass conservation (continuity). However, where previous models have considered complete saturation behind the flow front leading to Eq. 2.3, the assumption of unsaturated flow leads to the addition of a sink term (S) to describe the loss of resin behind the flow front as resin penetrates the intra-tow fibers. Thus the governing equation is expressed as

$$\nabla \bullet q = S \ , \tag{2.10}$$

where the sink term (S) is a function of pressure. Because the sink term is a function of pressure, at each time step an iterative scheme is used until pressure convergence is reached before advancing the flow front and going to the next time step.

In summary the Finite Element/Control Volume method with Darcy's Law has been used extensively to simulate the RTM process.

2.2.2 VARTM Simulation

VARTM differs from RTM in several aspects which must be considered during simulation. Unlike the RTM process, the mold cavity thickness during the VARTM process is not fixed and the preform thickness varies as a function of pressure and flow front progression. Furthermore the relationship between preform thickness and compaction pressure is material dependent where the transient nature of the preform thickness affects other dependent material properties such as fiber volume fraction and permeability. The compaction or relaxation of the preform also leads to a decrease or increase in porous volume which must be considered if one is to simulate resin bleeding for the VARTM process which has only recently been considered in literature [64]. A review of current techniques for simulating the VARTM process is presented.

To address the transient thickness during the VARTM process Kempner [47] presented a unified model to describe mass and momentum balance between the resin and the fibers. The model is given as

$$\frac{1}{V_f}\frac{\partial V_f}{\partial t}+\frac{1}{V_f}\nabla V_f \bullet u^f = \nabla \bullet q\,, \tag{2.11}$$

where V_f is the fiber volume fraction, u^f is the actual fiber velocity, and q is the superficial velocity described by Darcy's Law. The model accounts for the time dependence of the fiber volume fraction (changing volume) which may be important

for accurately simulating the filling stage of the VARTM process and is essential in simulating the resin bleeding stage.

Using Kempner's unified model, Kang, Lee, and Hahn [48] developed a two-dimensional model to simulate the Vacuum Bag Resin Transfer Molding (VBRTM) process. This process is a variant of the VARTM process in which no flow enhancing layers are used. An illustration of the VBRTM process showing the cross section of the preform is given in Figure 2-9. Because a flow distribution layer is not used it is assumed that the pressure and fiber volume fraction are constant through the thickness of the preform. In addition the model assumes the velocity of the fibers in the plane of the laminate can be neglected such that

$$u_x^f = u_y^f = \frac{\partial P}{\partial z} = \frac{\partial V_f}{\partial z} \approx 0. \tag{2.12}$$

Based on these assumptions Eq. (2.11) is simplified to

$$-\frac{1}{V_f}\frac{\partial V_f}{\partial t} = \nabla\left(\frac{[\kappa]}{\mu}\nabla P\right), \tag{2.13}$$

where Darcy's Law has been introduced. The right hand side of Eq. (2.13) is descretized using the finite element method and the left hand side is descretized explicitly as

$$-\frac{1}{V_f^{n-1}}\left(\frac{V_f^n - V_f^{n-1}}{\Delta t}\right), \tag{2.14}$$

where *n* represents the current time step and *n*-1 represents the previous time step. An iterative approach is used at each time step until convergence of the fiber volume fraction and pressure field is achieved. Constitutive models relating the fiber volume fraction to compaction pressure and the permeability to fiber volume fraction are introduced to update the fiber volume fraction and permeability at each time step. The FE/CV method previously described is used to advance the flow front. The authors presented numerical simulations demonstrating the model but did not make any comparisons with experimental results.

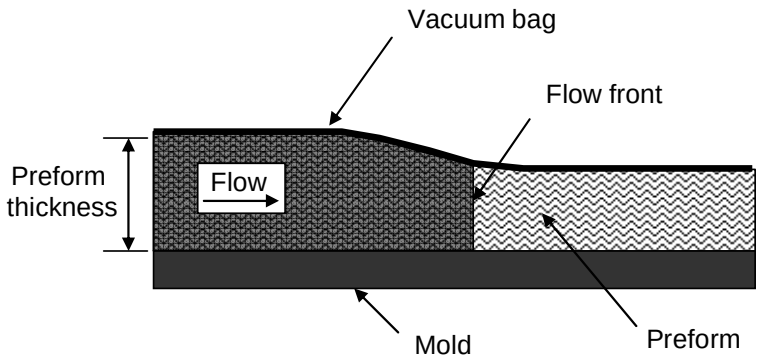

Figure 2-9 Illustration of the VBRTM process showing the relaxation of the preform.

Joubaud, Achim, and Trochu [49] arrived at the same governing equation derived by Kempner but expressed the fiber volume fraction in terms of the laminate height leading to

$$\frac{1}{h}\frac{\partial h}{\partial t} = \nabla\left(\frac{[\kappa]}{\mu}\nabla P\right), \tag{2.15}$$

where h is the height of the preform. The mass conservation equation is then expressed as

$$\frac{1}{h^{n-1}}\left(\frac{h^n - h^{n-1}}{\Delta t}\right) = \nabla\left(\frac{[\kappa]}{\mu}\nabla P\right). \tag{2.16}$$

The authors compared flow front progression and preform thickness predictions with experimental results from the infusion of an irregularly shaped preform. The preform consisted of a Rovicore fiber glass mat for which permeability and compaction measurements were performed to provide the appropriate compaction and permeability constitutive models for the simulation. The flow front progression and preform thickness predictions showed good agreement with experimental results. No pressure data was recorded to assess the capacity of the model to accurately predict pressures. The authors note that the key issue for obtaining good results is to provide accurate constitutive models for both the permeability as well as compaction characteristics of the preform. The authors also note that the approach is limited by the assumption that no flow occurs through the thickness of the preform.

A one-dimensional analytical solution for the VARTM process was developed by Correia, Robitaille, Long, Rudd, Simacek, and Advani [50] and compared with

simulation results using LIMS [35]. For the one-dimensional case the LIMS simulation showed good agreement with analytical results. Again it was assumed that no flow through the thickness of the preform was present and only in-plane flow was considered. The simulation model was not compared with experimental results. Based on the same assumption that through thickness flow is negligible, other one-dimensional analytical solutions have been developed to study the VARTM process [51, 52].

Walsh and Freese [53] developed a simulation technique for the VARTM process based on the pure finite element approach developed by Mohan, Ngo, and Tamma [43, 44] for simulating the RTM process. Through the implementation of compaction and permeability constitutive models the simulation accounts for the transient thickness nature of the VARTM process. Like the previous models described, through thickness flow was neglected and only in-plane flow was considered. A comparison of simulation predictions and analytical results showed good agreement, however no comparisons were made with experimental measurements. The authors suggest that future work is need to validate the model with experimental results and to extend the model to include through thickness flow such that the use of flow distribution layers may be considered.

The VARTM simulation work which has been reviewed describes two dimensional models in which the pressure and fiber volume fraction are assumed constant through the thickness. For thick laminates with flow distribution layers the constant pressure and fiber volume fraction through the thickness are not valid assumptions and a three-dimensional model is required. Song [54] and others [55, 56,

57] have implemented compaction and permeability constitutive models for selected materials into an existing three-dimensional FE/CV simulation package entitled 3DINFIL [58, 59]. The model handles full three-dimensional flow as well as incorporating resin kinetics (temperature and degree of cure). The model is based on the governing equation for the RTM process given by Eq. 2.3 where the sink/source terms are not considered. At each time step the permeability is updated in accordance with a permeability constitutive model and a compaction model is only used for predicting the fiber volume fraction of the preform. Song [54] compared experimental flow front progression experiments with simulation results to validate the model. Two experiments consisted of rectangular preforms consisting of SAERTEX fabric and a flow distribution layer. The first panel consisted of one layer of fabric having a thickness of 19 mm and the second panel consisted of 4 layers of material having an initial thickness of 82 mm. A comparison of the flow front progression of each experiment was compared with simulation predictions. The simulation predictions showed good agreement with the experimental results for the thinner preform with much greater error being observed for the thicker preform. It was also shown that the inlet boundary condition significantly affected the simulation results.

Hsiao, Mathur, Advani, Gillespie, and Fink [60] developed a closed form solution for flow during the VARTM process with the presence of a high permeability flow mesh. The formulation assumes that the flow is fully developed where the flow is divided into to a flow front region and a saturated region. In the saturated region it is assumed that that there is no cross flow between the high permeability layer and the preform and in the flow front region the flow is assumed to flow in the plane of the

high permeability layer and transverse into the preform. The results from the analytical solution are compared with simulations from LIMS [35]. It was found that the solution showed the lowest error when the lead-lag distance (*d*) was much greater than the preform thickness (*h*) (flow dominated by high permeability flow mesh).

Other work [61, 62, 63] in simulating the VARTM process has been performed to simplify the three-dimensional flow problem to a two-dimensional in-plane problem. Yoon and Dolan [61] proposed a model which reduces the three-dimensional flow problem to a two-dimensional flow problem by developing equivalent in-plane homogenous permeability and porosity values which are used to simulate the flow front progression in an average sense. The equivalent permeability and porosity properties are obtained from the closed form solution proposed by Hsiao, Mathur, Advani, Gillespie, and Fink [60]. The flow front shape can be found at any time during the filling simulation by recreating the flow front profile from the closed form solution. The flow front location and fill times showed good agreement with three-dimensional simulations with errors increasing for very thick laminates and laminates in which the through thickness permeability was very high.

Sun, Li, and Lee [62] investigated the flow in the SCRIMP process when a flow distribution layer is used. Visual observations under various molding conditions showed that the in-plane flow of resin was dominated by the flow distribution layer and that the flow front lead-lag through the thickness of the preform remained nearly constant during the filling process. A three-dimensional model was employed to simulate the flow of resin for experiments with and without flow distribution layers. A parametric study was performed to investigate the influence of the flow distribution

layer and the preform on the total filling time. The study showed that the filling time was a strong function of the permeability of the flow distribution layer and was much less sensitive to the permeability of the preform. Simulation results in combination with experimental measurements demonstrated that the in-plane flow in the preform could be neglected when the permeability of the preform is much less than that of the flow distribution layer and the length along the flow direction is much larger than the thickness of the part. Based on these observations the authors presented a leakage flow model which considers the flow as two-dimensional in the plane of the flow distribution layer with sink terms accounting for the resin flow through the thickness of the preform. The leakage flow model reduced computation time by more than 90% while still showing good agreement with three-dimensional simulation results and experimental measurements. Similar work was performed by Ni, Li, Sun, and Lee [63] to address SCRIMP based on grooves.

Song and Youn [64] recently proposed a one-dimensional model to simulate the bleeding of resin for the VARTM process. The study uses a non-rigid control volume to formulate the governing equation for the simulation. The governing equation is based on work done by Loptnikov, Simacek, Gillespie, and Advani [52] where the average fluid velocity is used and not the superficial velocity which is typically considered in literature. It should be noted that the since the fluid averaged velocity is used one must divide the permeability by the porosity to to obtain results consistent with other models from literature where the superficial velocity is used [52]. The governing equation is solved using the finite difference method where the results

are used to investigate the effects of processing parameters and different processing scenarios during the bleeding phase of the VARTM process.

2.3 PREFORM CHARACTERIZATION

The success of accurately simulating the VARTM process is dependent on the preform compaction and permeability constitutive models which are used in the simulations. Although analytical models have been introduced such as the Kozeny-Carman model [65, 66] for predicting permeability as a function of fiber volume fraction and Gutowski's model [67, 68, 69] for predicting fiber volume fraction as a function of compaction pressure these properties are very dependent on fabric architectures and stitching and cannot be fully described by analytical models. The best results are obtained through empirical models based on measurements using the actual materials under consideration.

2.3.1 Permeability

In general the permeability of a fiber preform may be anisotropic in which the three-dimensional permeability of the preform may be described as a fully populated third order tensor given by

$$[\kappa] = \begin{bmatrix} \kappa_{xx} & \kappa_{xy} & \kappa_{xz} \\ \kappa_{yx} & \kappa_{yy} & \kappa_{yz} \\ \kappa_{zx} & \kappa_{zy} & \kappa_{zz} \end{bmatrix}. \tag{2.17}$$

By determining the permeability along the principal directions only three independent values are required. For an orthotropic preform material the principle directions are along the fibers (κ_{11}), transverse to the fibers (κ_{22}) and through the thickness of the preform (κ_{33}) where the principal permeability tensor is given by

$$[\kappa'] = \begin{bmatrix} \kappa_{11} & 0 & 0 \\ 0 & \kappa_{22} & 0 \\ 0 & 0 & \kappa_{33} \end{bmatrix}, \tag{2.18}$$

where the prime indicates the principle coordinate system. By determining the permeability in each of the three principle directions the permeability in any direction may be determined by a simple coordinate transformation. Measurement of the principle permeability values have typically been performed by one of two methods which are based on Darcy's Law.

The first method for measuring permeability is the advancing front permeability measurement technique in which resin is injection into a dry fiber preform. By applying a constant pressure differential (ΔP) from the inlet to flow front the permeability is determined by the flow front location (x) as a function of time as given by

$$\kappa_{xx} = \frac{x^2 \mu \phi}{2 \Delta P t}, \tag{2.19}$$

where ϕ is the preform porosity and t is time. Alternatively the volumetric flow rate (Q) can be held constant in which case the permeability is determined from the derivative of the pressure at the inlet with respect to time as given by [70]

$$\kappa_{xx} = \frac{\mu}{\frac{dP_i}{dt}\phi}\left(\frac{Q}{hw}\right)^2 \tag{2.20}$$

where h is the height of the preform and w is the width of the preform.

The preform permeability may also be measured using a saturated preform in which flow has reached steady state. For the steady state case the permeability is given by [70]

$$\kappa_{xx} = \frac{\mu Q l}{hw\Delta P}, \tag{2.21}$$

where l is the length of the preform. For this case the permeability may be measured by either applying a constant flow rate and measuring the change in pressure over the length of the preform or by applying a constant pressure differential and measuring the volumetric flow rate. Greater detail showing the derivations for the permeability equations for both advancing flow front and steady state methods are presented in Chapter 4.

Based on these two methods researchers have presented permeability measurements for a variety of performs [70-80]. The permeability measurement methods were primarily developed for characterizing materials for the RTM process where the test setup uses a two sided rigid mold similar to that used in the RTM process.

Based on the described measurement techniques several authors [78, 79, 80] have investigated the effects of multilayer performs. The findings have shown that the permeability of these performs is dependent on the fabric architecture of the individual plies as well as the stacking sequence. Materials which are less compressible and have significant surface undulations showed higher effective permeability values when multiple layers were assembled. The increased permeability is due to the large interlaminar pores created between layers. The magnitude of the increase in permeability decreases fractionally as the ratio of interlaminar regions to fabric layers approaches unity. Additional findings showed that the high permeability layers greatly increase the effective permeability with the highest effective permeabilities occurring when the high permeability layers are between layers of the other fabric and not at the top or bottom of the stack.

To address the need for permeability measurements for different fabric architectures and fabric types, Parnas, Flynn, and Dal-Favero [71] created a permeability database through the National Institute of Standards and Technology (NIST). The database consists of permeability measurements for both saturated and unsaturated flows in glass fabrics for various fabric architectures. From their studies the authors have shown that permeability measurements for unstructured performs

such as random fiber mats may vary by as much as 50% while permeability measurements for structured fabrics such as weaved and stitched fabrics show measurement variations which are typically 15% or less.

In order to address the need of obtaining permeability measurements over a wide range of fiber volume fractions Stadtfeld, Erninger, Bickerton, and Advani [70] have proposed a method for continually measuring permeability of fiber performs as a function of fiber volume fraction. The method uses the saturated measurement technique where the test fabric is place in a rigid mold in which the mold height may be adjusted to provide a range of fiber volume fractions without replacing the test fabric. Experimental measurements using the method showed good repeatability.

2.3.2 Compaction

The VARTM process differs from the RTM process in that it utilizes a flexible vacuum bag with one sided rigid tooling allowing the laminate to compress or relax with changing compaction pressure. Tackitt and Walsh [81] performed an experimental study to investigate the formation of thickness gradients during the VARTM process. The study investigated the infusion of a 61 cm x 61 cm plate using both line as well as point injections. The experimental results confirmed a gradient in the thickness of the laminate from the resin inlet to the vacuum outlet with reduction in thickness gradient when the pressure at the inlet was reduced (resin supply level position lower than mold).

In order to better understand the compaction characteristics of fiber performs for predicting part thicknesses and fiber volume fractions, analytical compaction models have been developed by several authors [67-69, 82-92]. The proposed models are primarily based on physical mechanics which relate compaction pressure to fiber volume fraction. While the analytical models provide a relationship between compaction pressure and fiber volume fraction, the relationship is independent of whether the preform is undergoing compaction or relaxation. Song [54] has shown that the constitutive relationship between fiber volume fraction and compaction pressure can be very different depending on whether the preform is undergoing compaction or relaxation. Furthermore the relationship between compaction pressure and fiber volume fraction is dependent on whether the preform is dry or saturated. Much higher levels of compaction are achieved for wetted fibers due to lubricating effects [54].

Robitaille and Gauvin [89] have developed compaction pressure versus fiber volume fraction relationships for a variety of materials in which a power lay curve is fit to experimental measurements. From the testing the authors observed that as the number of layers increases the initial fiber volume fraction is increased and the compaction stiffness is decreased. It was also observed that for repeated cycles the stiffness decreased. Although analytical models may provide general insight into preform compaction behavior, experimental testing is required to fully characterize specific fabric architectures.

2.4 RESEARCH OBJECTIVES

Several different models for simulating the VARTM process have been reviewed. However the models [48, 49, 50, 53] which account for the transient nature of the preform thickness, do not consider through thickness flow which is critical in cases where flow distribution layers are used, and the models [54, 62] which do consider through thickness flow do not consider the transient nature of the thickness. While all of the models reviewed simulate the resin filling stage of the VARTM process, the bleeding stage, which is critical in obtaining final part dimensions and fiber volume fractions, has received little attention. Furthermore there is a shortage of experimental results, especially pressure measurements, which are needed to validate these models.

Preform compaction and permeability characteristics are material dependent requiring experimental measurements to determine accurate properties. Currently the measurement techniques being used are based on the RTM process in which a two-sided rigid mold is used. Measurement procedures which more closely represent the physics of the VARTM process need to be investigated. Based on the identified needs for VARTM simulation and material characterization the following research objectives were identified:

1. Development a simulation model for the VARTM process which considers the transient thickness effects coupled with through thickness flow.

2. Include the capability to simulate resin bleeding in the model.

3. Development an alternative method for characterizing preform materials which more closely represent the physics of the VARTM process.

4. Validate the simulation model for both filling and bleeding stages of the VARTM process through experimental measurements which include flow front progression, fill time, pressure measurements, and preform thickness measurements.

5. Use the developed model to investigate infusion strategies for components to be used in composite bridging.

Each research objective is addressed in the following chapters.

CHAPTER 3

MODEL DEVELOPMENT

A three-dimensional simulation model for the VARTM process has been developed. The model accounts for transient permeability effects as well as transient fiber volume fraction effects for full three dimensional flow in which the flow through the thickness of the preform is included. The model is implemented numerically using the finite element/control volume (FE/CV) method which is predominately used in the literature and will be described in detail. By properly considering the transient nature of the fiber volume fraction, one is not only able to simulate the filling phase of the VARTM process but the resin bleeding stage as well as will be demonstrated in Chapter 5. A presentation of the general equations, numerical implementation using finite elements and the control volume method are presented followed by a discussion on solution convergence and verification of the simulation code through simple one, two, and three-dimensional flow problems for which analytical solutions are available.

3.1 GENERAL EQUATIONS

The flow of resin through a fibrous preform is typically modeled as flow through a porous media in which the resin is considered to be a Newtonian fluid and the resin flow is described by Darcy's Law given by

$$q = -\frac{[\kappa]}{\mu}\nabla P\,, \tag{3.1}$$

where q is the superficial resin velocity, $[\kappa]$ is the permeability tensor, μ is the resin viscosity, and P is the pressure. Darcy's Law for full three dimensional flow is expressed in matrix form by

$$q = -\frac{1}{\mu}\begin{bmatrix} \kappa_{xx} & \kappa_{xy} & \kappa_{xz} \\ \kappa_{yx} & \kappa_{yy} & \kappa_{yz} \\ \kappa_{zx} & \kappa_{zy} & \kappa_{zz} \end{bmatrix}\begin{bmatrix} \frac{\partial P}{\partial x} \\ \frac{\partial P}{\partial y} \\ \frac{\partial P}{\partial z} \end{bmatrix}, \tag{3.2}$$

where it is seen that for the three-dimensional case the permeability tensor is a fully populated third order tensor which is diagonalized when the coordinate system is aligned with the principle permeability directions. The superficial velocity (q) is related to the interstitial resin velocity (u^r) by

$$q = \phi u^r\,, \tag{3.3}$$

where ϕ is the preform porosity. The porosity is defined by

$$\phi = \frac{Vol_\phi}{Vol}\,, \tag{3.4}$$

where *Vol* is the total volume and Vol_ϕ is the porous volume (total volume minus the volume of fibers). The differential equation needed to model resin flow through a fibrous preform is obtained by applying conservation of mass [93]. In general, conservation of mass for resin flow in the presence of fibers may be expressed by

$$\begin{pmatrix}\text{Rate of resin}\\ \text{mass increase}\end{pmatrix}+\begin{pmatrix}\text{Rate of fiber}\\ \text{mass increase}\end{pmatrix}=\begin{pmatrix}\text{Rate of resin}\\ \text{mass inflow}\end{pmatrix}+\begin{pmatrix}\text{Rate of fiber}\\ \text{mass inflow}\end{pmatrix}-\begin{pmatrix}\text{Rate of resin}\\ \text{mass outflow}\end{pmatrix}-\begin{pmatrix}\text{Rate of fiber}\\ \text{mass outflow}\end{pmatrix}, \tag{3.5}$$

where the rate of change in resin and fiber mass over a fixed volume is equal to the inflow of resin and fiber mass minus the outflow of resin and fiber mass. An illustration of mass conservation over a fixed volume is illustrated in Figure 3-1. The control volume is defined by $\Delta x\Delta y\Delta z$ where the resin and fiber mass inflow and outflow fluxes through each face of the volume are shown in Figure 3-1. Based on the mass inflow and outflow fluxes the conservation of resin mass is expressed by

$$\begin{aligned}\Delta x\Delta y\Delta z\frac{\partial(\phi\rho_r)}{\partial t} &= \Delta y\Delta z\left[\left(\phi\rho_r u_x^a\right)\Big|_x-\left(\phi\rho_r u_x^a\right)\Big|_{x+\Delta x}\right]\\ &+\Delta x\Delta z\left[\left(\phi\rho_r u_y^a\right)\Big|_y-\left(\phi\rho_r u_y^a\right)\Big|_{y+\Delta y}\right]\\ &+\Delta x\Delta y\left[\left(\phi\rho_r u_z^a\right)\Big|_z-\left(\phi\rho_r u_z^a\right)\Big|_{z+\Delta z}\right]\end{aligned}, \tag{3.6}$$

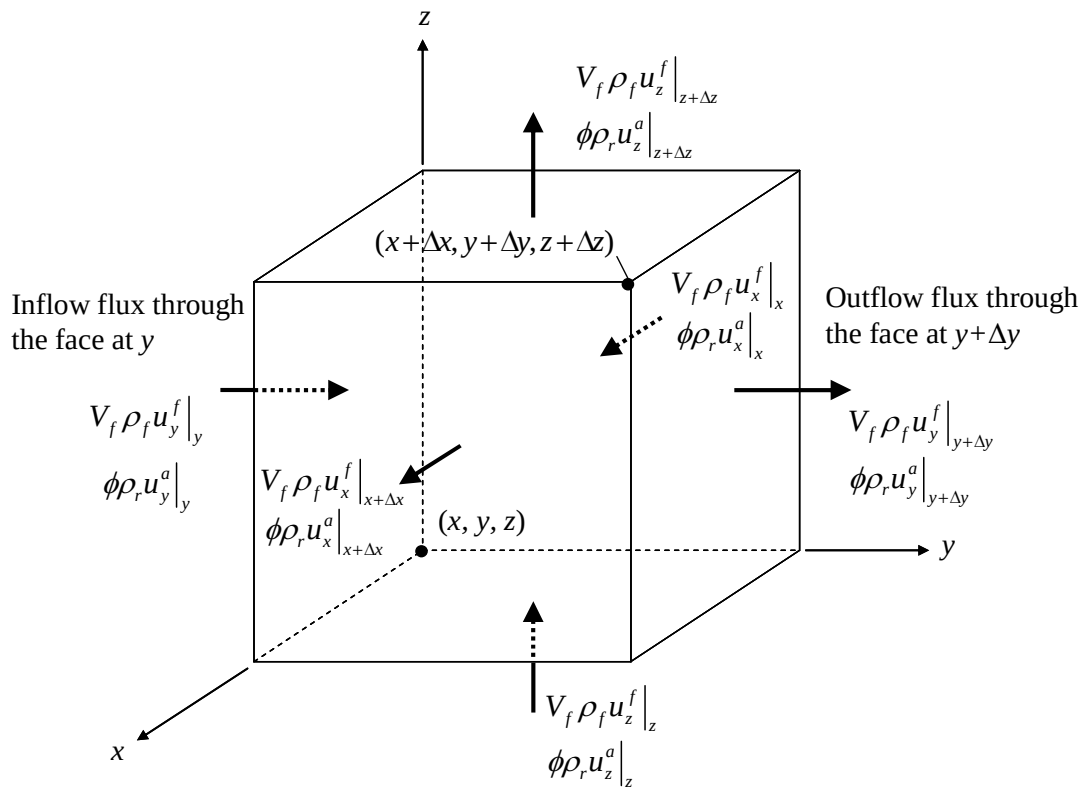

Figure 3-1 Illustration of a fixed volume showing the conservation of mass.

where ρ_r is the resin density and u^a is the absolute resin velocity which is the summation of the fiber velocity (u^f) and resin interstitial velocity (u^r) given by

$$u^a = u^r + u^f . \tag{3.7}$$

The conservation of fiber mass over the control volume is given by

$$\begin{aligned}\Delta x\Delta y\Delta z\frac{\partial\left(V_f\rho_f\right)}{\partial t} &= \Delta y\Delta z\left[\left(V_f\rho_f u_x^f\right)\Big|_x-\left(V_f\rho_f u_x^f\right)\Big|_{x+\Delta x}\right]\\ &+\Delta x\Delta z\left[\left(V_f\rho_f u_y^f\right)\Big|_y-\left(V_f\rho_f u_y^f\right)\Big|_{y+\Delta y}\right]\\ &+\Delta x\Delta y\left[\left(V_f\rho_f u_z^f\right)\Big|_z-\left(V_f\rho_f u_z^f\right)\Big|_{z+\Delta z}\right]\end{aligned}, \tag{3.8}$$

where ρ_f is the fiber density and V_f is the fiber volume fraction which is related to the porosity (ϕ) by

$$V_f = 1-\phi\,. \tag{3.9}$$

Dividing both sides of Eq. (3.6) and Eq. (3.8) by the volume ($\Delta x\Delta y\Delta z$) and taking the limit as Δx, Δy, $\Delta z \to 0$ leads to

$$\frac{\partial\phi_r}{\partial t} = -\frac{\partial}{\partial x}\left(\phi u_x^a\right)-\frac{\partial}{\partial y}\left(\phi u_y^a\right)-\frac{\partial}{\partial z}\left(\phi u_z^a\right) = -\nabla\bullet\left(\phi u^a\right), \tag{3.10}$$

and $$\frac{\partial V_f}{\partial t} = -\frac{\partial}{\partial x}\left(V_f u_x^f\right)-\frac{\partial}{\partial y}\left(V_f u_y^f\right)-\frac{\partial}{\partial z}\left(V_f u_z^f\right) = -\nabla\bullet\left(V_f u^f\right) \tag{3.11}$$

respectively. Summing Eq. (3.10) and Eq. (3.11) to obtain the conservation of mass as given by Eq. (3.5) leads to

$$\frac{\partial V_f}{\partial t}+\frac{\partial\left(1-V_f\right)}{\partial t}+\nabla\bullet\left(\left(1-\phi\right)u^f\right)+\nabla\bullet\left(\left(\phi\right)\left(u^r+u^f\right)\right)=0, \tag{3.12}$$

where Eq. (3.9) is used to express the fiber volume fraction in terms of porosity and vice-versa and Eq. (3.7) is used to express the absolute resin velocity in terms of the fiber velocity and interstitial resin velocity. Applying the chain rule to the gradients and summing like terms reduces Eq. (3.12) to

$$\nabla\bullet\left(u^{f}\right)+\nabla\bullet\left(\phi u^{r}\right)=0. \tag{3.13}$$

By applying the chain rule to Eq. (3.11) it is recognized that

$$\nabla\bullet\left(u^{f}\right)=-\frac{1}{V_f}\frac{\partial V_f}{\partial t}-\frac{1}{V_f}\left(\nabla V_f\right)u^{f}, \tag{3.14}$$

and from equations (3.1) and (3.3) it is seen that

$$\nabla\bullet\left(\phi u^{r}\right)=-\nabla\bullet\left(\frac{[\kappa]}{\mu}\nabla P\right). \tag{3.15}$$

Directly substituting Eq.(3.14) and Eq. (3.15) into Eq. (3.13) leads to the equation given by

$$-\frac{1}{V_f}\frac{\partial V_f}{\partial t}-\frac{1}{V_f}\left(\nabla V_f\right)u^{f}=\nabla\bullet\left(\frac{[\kappa]}{\mu}\nabla P\right). \tag{3.16}$$

This is the same expression which was developed by Kempner [47] and has been used by several authors [48, 49] to model the VARTM process. For the VARTM process the amount of fibers within the mold cavity remains constant. Thus, in order to preserve mass conservation the fiber velocity relative to the control volume considered in Figure 3-1 must be equal to zero ($u_x^f = u_y^f = u_z^f = 0$). Applying this assumption leads to the governing equation given by

$$-\frac{1}{V_f}\frac{\partial V_f}{\partial t} = \nabla \bullet \left(\frac{[\kappa]}{\mu} \nabla P \right). \tag{3.17}$$

Other authors [48, 49] have used the same governing equation but have applied assumptions which limit the models to two-dimensional flow within the plane of the preform and neglect flow through the thickness of the preform laminate. The left hand side of the governing equation may be expressed over an explicit time step by

$$\frac{1}{V_f}\frac{\partial V_f}{\partial t} = \frac{1}{V_f^{t-1}}\frac{V_f^t - V_f^{t-1}}{\Delta t} \tag{3.18}$$

where *t* is the current time step and *t-l* is the previous time step. Substituting Eq. (3.18) into Eq. (3.17) leads to the governing equation over an explicit time step given by

$$\nabla \bullet \left(\frac{[\kappa]}{\phi \mu} \nabla P \right) + \frac{1}{V_f^{t-1}} \frac{V_f^t - V_f^{t-1}}{\Delta t} = 0 \tag{3.19}$$

To solve the governing equation the weighted residual method [94] is used in which the pressure is expressed as an approximation based on a combination of linearly independent shape functions (N) given by

$$\tilde{P} = NP, \tag{3.20}$$

where $\tilde{P}$ is the approximated pressure field. Introducing this approximation for the pressure into Eq. (3.19) leads to an error or residual (R) which is not zero due to the inability of the approximated pressure to satisfy the equation. The residual is expressed by

$$R = \nabla \bullet \left(\frac{[\kappa]}{\mu} \nabla \tilde{P} \right) + \frac{1}{V_f^{t-1}} \frac{V_f^t - V_f^{t-1}}{\Delta t}. \tag{3.21}$$

The method of weighted residuals seeks to determine the unknown pressure field such that in an average sense Eq. (3.19) is satisfied over the entire solution domain. This is accomplished by multiplying the residual by linearly independent weighting functions such that the residual goes to zero when integrated over the domain as given by

$$\int_{\Omega} RW \, d\Omega = 0 \,, \tag{3.22}$$

where W are the weighting functions and Ω is the solution domain. Applying the Galerkin method [94], in which the weighting functions (W) are taken to be the same as the previously defined shape functions (N), leads to a "weak form" of the governing equation given by

$$\int_{\Omega} N \left[\nabla \bullet \left(\frac{[\kappa]}{\mu} \nabla N \right) P + \frac{1}{V_f^{t-1}} \frac{V_f^t - V_f^{t-1}}{\Delta t} \right] d\Omega = 0 \,. \tag{3.23}$$

Integrating Eq. (3.23) by parts to reduce the shape function derivatives to first order derivatives leads to a system of nonlinear equations, where the nonlinearity is due to the dependence of the fiber volume fraction (V_f) on pressure. The system of equations is expressed by

$$[K] P = d + f \,, \tag{3.24}$$

where $[K]$ is the "stiffness" matrix expressed as

$$[K] = \frac{1}{\mu} \int_{\Omega} \nabla N^T \, [\kappa] \nabla N \, d\Omega \,. \tag{3.25}$$

The term d is the natural boundary condition (flow across the boundary surface Γ) which is only non-zero at injection points and the flow front and is given by

$$d = \int_{\Gamma} \left(N^T q \right) \bullet n \, d\Gamma , \tag{3.26}$$

where n is the normal vector to the boundary surface. In the case of resin bleeding simulations where the preform is already filled with resin, d is only non-zero at the inlet or outlet. The "loading" term (f) which accounts for resin flow due to the change in volume of the preform resulting from compaction and relaxation is given by

$$f = \int_{\Omega} N \left(\frac{1}{V_f^{t-1}} \frac{V_f^t - V_f^{t-1}}{\Delta t} \right) d\Omega . \tag{3.27}$$

An illustration describing this change in volume due to compaction and relaxation of the fiber preform is given in Figure 3-2. The initial preform volume (Vol^o) consists of the fiber volume (Vol_f) and the initial porous volume (Vol_ϕ^o) such that the initial fiber volume fraction is given by

$$V_f^o = \frac{Vol_f}{Vol^o} \tag{3.28}$$

At time *t* the volume of the preform changes due to compaction or relaxation of the preform as a result of a change in the applied pressure. The fiber volume (Vol_f) remains constant, thus the new volume (Vol^t) is the sum of the fixed fiber volume (Vol_f) plus the new porous volume (Vol_ϕ^t) at time *t*. The fiber volume fraction is now given by

$$V_f^t = \frac{Vol_f}{Vol^t} \tag{3.29}$$

From Eq. (3.28) and Eq. (3.29) the current volume at time *t* can be related to the initial volume by

$$Vol^t = \frac{V_f^o}{V_f^t} Vol^o . \tag{3.30}$$

This relationship will be used in the finite element development to relate the true change in volume over the fixed element volume. Assuming that the preform is only able to compact and relax in the thickness direction the current preform thickness (h^t) is related to the initial thickness (h^o) by

$$h^t = \frac{V_f^o}{V_f^t} h^o \tag{3.31}$$

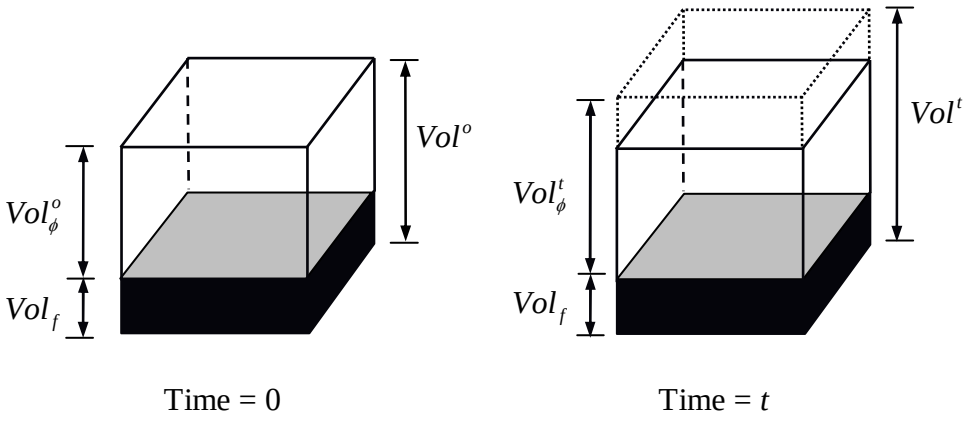

Figure 3-2 Illustration showing the change in volume of due to the compaction or relaxation of the preform.

To gain additional insight into how much the preform thickness (volume) varies due to a change in the fiber volume fraction, a plot of the ratio of the current preform thickness to the initial thickness (h^t/h^o) versus the current fiber volume fraction (V_f^t) for initial fiber volume fractions (V_f^o) of 0.4, 0.5, and 0.6 is given in Figure 3-3. As the current fiber volume fraction approaches zero the thickness ratio tends to infinity. For an initial fiber volume fraction of 0.4 the thickness increases by a factor of two for a current fiber volume fraction of 0.2. Similarly for an initial fiber volume fraction of 0.5 the thickness doubles for a current fiber volume fraction of 0.25 and for an initial fiber volume fraction of 0.6 the thickness doubles for a current fiber volume fraction of 0.3. For the material considered in this research the fiber volume fractions typically range from 0.55 for fully compacted (initial fiber volume fraction) to 0.3 at full relaxation (current fiber volume fraction). Thus one can see that the thickness or the

porous volume of the preform can vary widely due to compaction and relaxation during the resin filling and bleeding phases of the VARTM process.

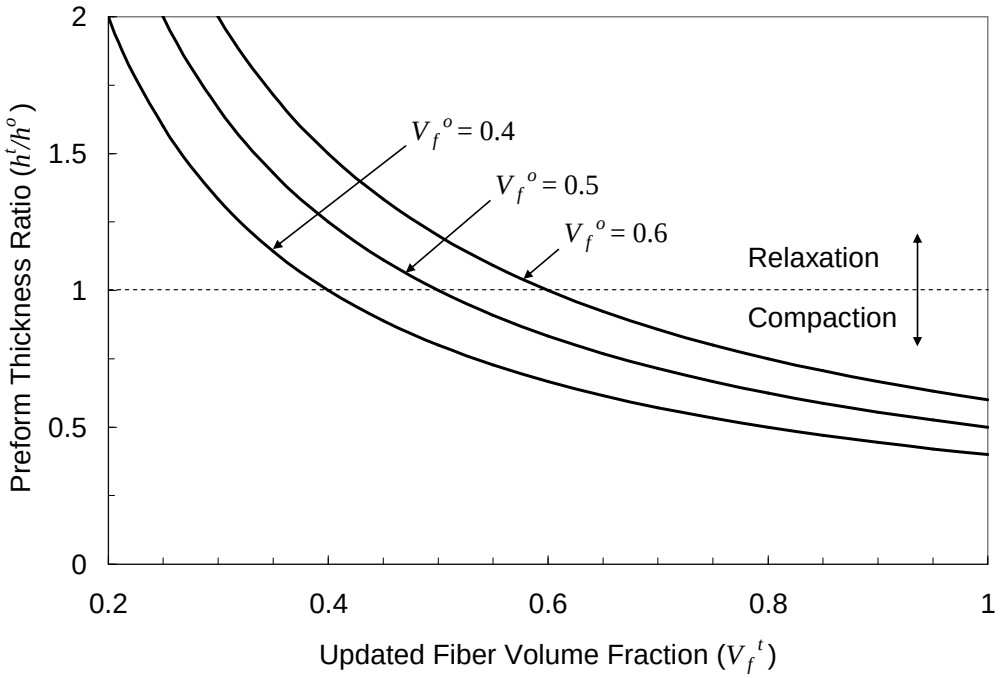

Figure 3-3 Plot of thickness ratio versus updated fiber volume fraction for initial fiber volume fractions of 0.4, 0.5, and 0.6.

3.2 NUMERICAL IMPLEMENTATION

Although there are several different approaches for numerically solving resin flow through a porous volume [29-43], due to ease of implementation and ability to model complex geometries, the finite element/control volume method [32] is used in this study. The implementation of the finite element method is described followed by a description of the control volume method which is used to track the progression of the resin flow front.

3.2.1 Finite Element Method

The finite element method is preferred over other numerical methods due to the ability to model complex geometries using a combination of one, two, and three-dimensional elements. Examples of how different elements may be used in VARTM process problems are presented. For a full three-dimensional model, as shown in Figure 3-4, three-dimensional elements are used to model the preform, two-dimensional elements are used to model the flow distribution mesh, and the resin distribution line is modeled with one-dimensional line elements. In cases where the preform is thin and the through thickness flow can be neglected (pressure through the thickness is constant), the three-dimensional model can be reduced to two dimensions where the preform is modeled using two-dimensional elements as shown in Figure 3-5 [48, 93, 49]. In cases where the through thickness flow cannot be neglected but the in-plane flow can be considered one-dimensional in the plane of the preform, as shown in Figure 3-4, the three-dimensional model can be reduced to two-dimensional flow through the thickness of the preform. In this case the preform is modeled with two-dimensional elements, the flow distribution mesh is modeled using one-dimensional elements and the resin distribution line is treated as a point source (see Figure 3-6). This last case is used to validate and show the capabilities of the model in chapter 5. The developed code incorporates a variety of different elements which include one-dimensional line elements (2 node), two-dimensional triangle (3 node) and quadrilateral (4 node) elements, and three-dimensional tetrahedral (4 node), wedge (6 node), and hexahedral (8 node) elements. Illustrations of each of these elements are given in Figure 3-7. The code utilizes FEMAP as a pre and post processor to develop

finite element meshes and to view results with the main FE/CV code being developed in FORTRAN.

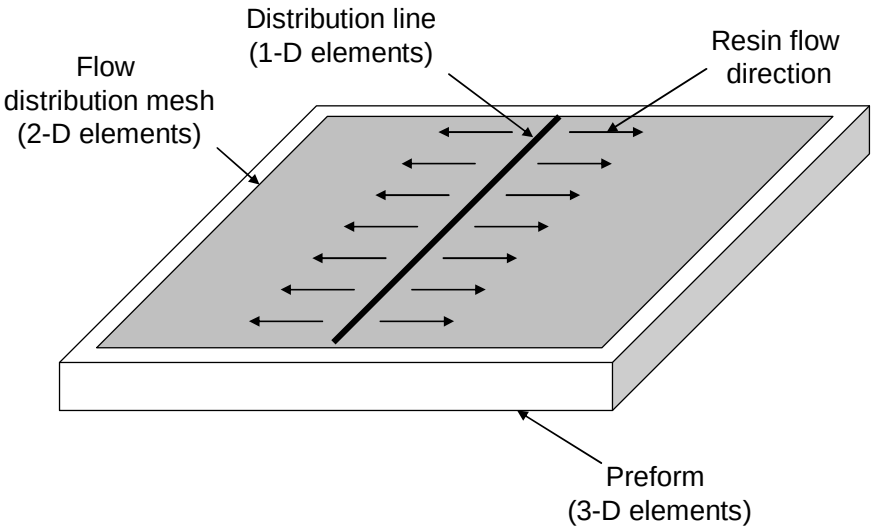

Figure 3-4 Illustration of full three dimensional flow model showing preform (3-D elements), flow distribution mesh (2-D elements), and resin distribution line (1-D elements).

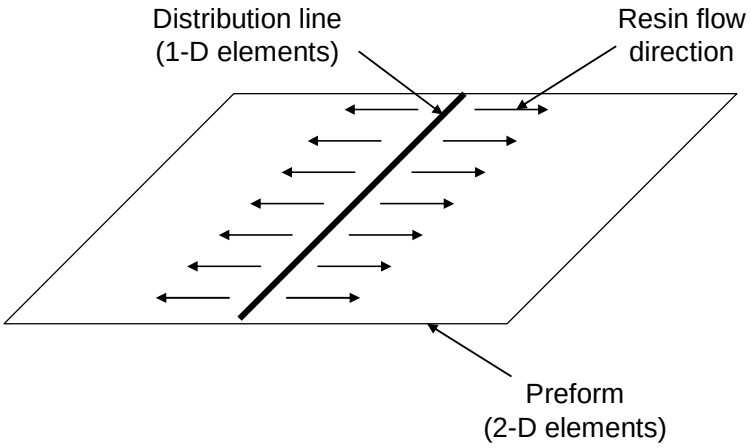

Figure 3-5 Illustration of reduced two dimensional flow model (through thickness flow neglected) showing preform (2-D elements) and resin distribution line (1-D elements).

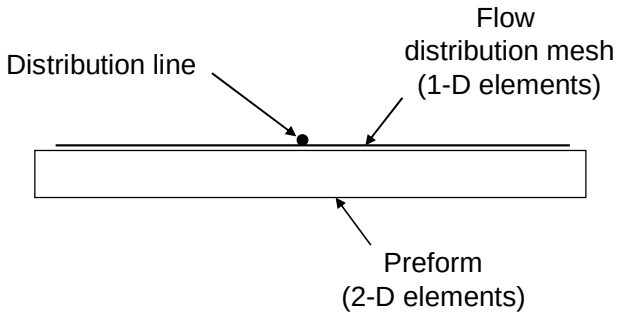

Figure 3-6 Illustration of a reduced two dimensional flow model (in-plane flow considered one dimensional) showing preform (2-D elements), flow distribution mesh (1-D elements), and distribution line (point injection).

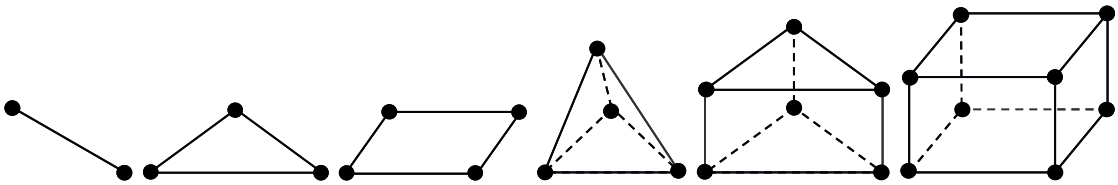

(a) (b) (c) (d) (e) (f)

Figure 3-7 Illustration of linear finite elements (a) two node line, (b) three node triangle, (c) four node quadrilateral, (d) four node tetrahedral, (e) six node wedge, and (f) eight node hexahedral.

For ease of application to general finite element meshes, isoparametric elements are used in which simple geometric elements in a local coordinate system are mapped onto more general geometric elements in the global coordinate system. As an example we refer to the isoparametric triangle element shown in Figure 3-8 where a local coordinate system (r, s) is used to define the element. The triangle is a right triangle with nodes at the origin (0,0), (0,1), and (1,0). The integral formulation for this simple element can then be mapped to the more general element in the global

coordinate system given in Figure 3-9. In general, to develop the stiffness matrix given by Eq. (3.25) we need to integrate a function over the volume of the element which consists of derivatives of the shape functions in terms of the global coordinate system. Using isoparametric elements we are able to solve this integral over the simplified isoparametric element which is then mapped to the more general element in global coordinates. For the purpose of explanation, the formulation of the stiffness matrix using the triangle isoparametric element is presented. Development of the stiffness matrix for other elements is presented in Appendix A.

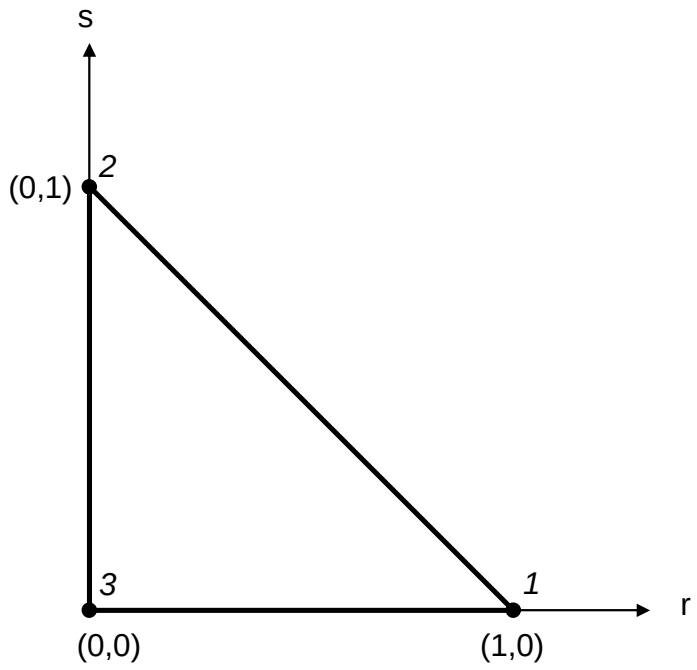

Figure 3-8 Illustration of a three node triangle isoparametric element.

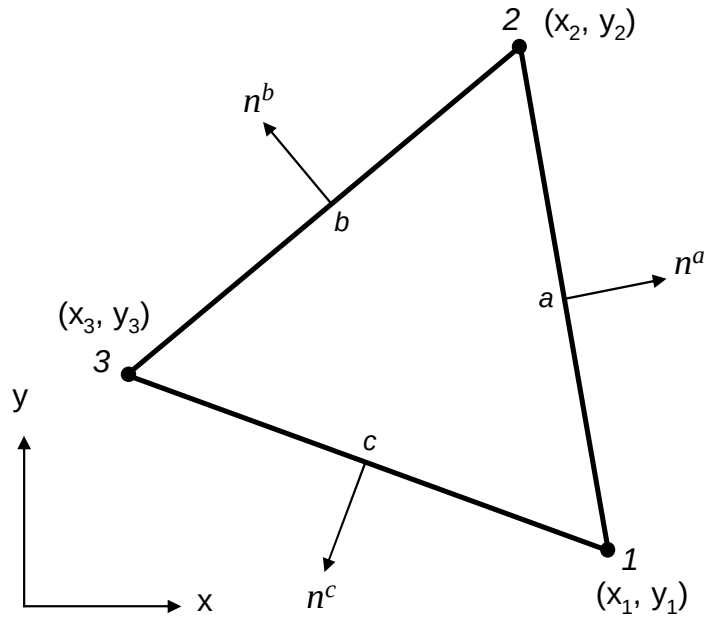

Figure 3-9 Illustration of a general three node triangle element in global coordinates.

The derivatives of the shape functions with respect to global coordinates *x* and *y* can be evaluated using the chain rule and are given by

$$\frac{\partial N_i}{\partial x} = \frac{\partial N_i}{\partial r}\frac{\partial r}{\partial x} + \frac{\partial N_i}{\partial s}\frac{\partial s}{\partial x}, \tag{3.32a}$$

and

$$\frac{\partial N_i}{\partial y} = \frac{\partial N_i}{\partial r}\frac{\partial r}{\partial y} + \frac{\partial N_i}{\partial s}\frac{\partial s}{\partial y}, \tag{3.32b}$$

where *i* goes from 1 to the number of nodes for the element, and *N* are the linear shape functions expressed in local coordinates *r* and *s*, which for the triangle isoparametric element are given by

$$N_1 = r\,, \tag{3.33a}$$

$$N_2 = s\,, \tag{3.33b}$$

and

$$N_3 = 1 - r - s\,. \tag{3.33c}$$

For convenience the shape function derivatives from Eq. (3.32) are recast in the following matrix form:

$$\begin{bmatrix} \dfrac{\partial N_1}{\partial x} & \dfrac{\partial N_1}{\partial y} \\ \dfrac{\partial N_2}{\partial x} & \dfrac{\partial N_2}{\partial y} \\ \dfrac{\partial N_3}{\partial x} & \dfrac{\partial N_3}{\partial y} \end{bmatrix} = \begin{bmatrix} \dfrac{\partial N_1}{\partial r} & \dfrac{\partial N_1}{\partial s} \\ \dfrac{\partial N_2}{\partial r} & \dfrac{\partial N_2}{\partial s} \\ \dfrac{\partial N_3}{\partial r} & \dfrac{\partial N_3}{\partial s} \end{bmatrix} \begin{bmatrix} \dfrac{\partial r}{\partial x} & \dfrac{\partial r}{\partial y} \\ \dfrac{\partial s}{\partial x} & \dfrac{\partial s}{\partial y} \end{bmatrix}. \tag{3.34}$$

The shape function derivatives with respect to local coordinates may be explicitly computed and are given by

$$\begin{bmatrix} \dfrac{\partial N_1}{\partial r} & \dfrac{\partial N_1}{\partial s} \\ \dfrac{\partial N_2}{\partial r} & \dfrac{\partial N_2}{\partial s} \\ \dfrac{\partial N_3}{\partial r} & \dfrac{\partial N_3}{\partial s} \end{bmatrix} = \begin{bmatrix} 1 & 0 \\ 0 & 1 \\ -1 & -1 \end{bmatrix}, \tag{3.35}$$

However the terms in the far right matrix of Eq. (3.34) cannot be determined since we do not have explicit expressions for *r* and *s* as functions of global coordinates *x* and *y*. We do however have the inverse relationships given by

$$x(r,s) = N_i(r,s)x_i = N_1(r,s)x_1 + N_2(r,s)x_2 + N_3(r,s)x_3, \qquad (3.36a)$$

and

$$y(r,s) = N_i(r,s)y_i = N_1(r,s)y_1 + N_2(r,s)y_2 + N_3(r,s)y_3, \qquad (3.36b)$$

which enables us to calculate the Jacobian matrix which can be expressed in terms of global coordinates as

$$[J] = \begin{bmatrix} \frac{\partial x}{\partial r} & \frac{\partial x}{\partial s} \\ \frac{\partial y}{\partial r} & \frac{\partial y}{\partial s} \end{bmatrix} = \begin{bmatrix} x_1 - x_3 & x_2 - x_3 \\ y_1 - y_3 & y_2 - y_3 \end{bmatrix}, \qquad (3.37)$$

where

$$\frac{\partial x}{\partial r} = \frac{\partial N_i}{\partial r} x_i . \qquad (3.38)$$

The derivatives of global coordinates x and y which respect to local coordinates r and s is obtained by taking the inverse of the Jacobian matrix given by

$$\left[J\right]^{-1}=\begin{bmatrix}\dfrac{\partial r}{\partial x} & \dfrac{\partial r}{\partial y}\\ \dfrac{\partial s}{\partial x} & \dfrac{\partial s}{\partial y}\end{bmatrix}=\frac{1}{\left|J\right|}\begin{bmatrix}\dfrac{\partial y}{\partial s} & -\dfrac{\partial x}{\partial s}\\ -\dfrac{\partial y}{\partial r} & \dfrac{\partial x}{\partial r}\end{bmatrix}=\frac{1}{\left|J\right|}\begin{bmatrix}y_1-y_3 & x_3-x_2\\ y_3-y_1 & x_1-x_3\end{bmatrix}, \tag{3.39}$$

where $\left|J\right|$ is the determinant of the Jacobian matrix. The determinant of the Jacobian matrix may be expressed in global coordinates as

$$\left|J\right|=\left\{(x_1-x_3)(y_2-y_3)-(x_2-x_3)(y_1-y_3)\right\}=2A_e, \tag{3.40}$$

where A_e is the area of the element. The inverse of the Jacobian matrix is substituted into the right hand side of Eq. (3.34) to obtain the derivatives of the shape functions in global coordinates. This leads to what is typically referred to in the finite element method as the B-matrix given by

$$\left[B\right]^T=\begin{bmatrix}\dfrac{\partial N_1}{\partial x} & \dfrac{\partial N_1}{\partial y}\\ \dfrac{\partial N_2}{\partial x} & \dfrac{\partial N_2}{\partial y}\\ \dfrac{\partial N_3}{\partial x} & \dfrac{\partial N_3}{\partial y}\end{bmatrix}=\begin{bmatrix}\dfrac{\partial N_1}{\partial r} & \dfrac{\partial N_1}{\partial s}\\ \dfrac{\partial N_2}{\partial r} & \dfrac{\partial N_2}{\partial s}\\ \dfrac{\partial N_3}{\partial r} & \dfrac{\partial N_3}{\partial s}\end{bmatrix}\left[J\right]^{-1}=\begin{bmatrix}(y_2-y_3) & (x_3-x_2)\\ (y_3-y_1) & (x_1-x_3)\\ (y_1-y_2) & (x_2-x_1)\end{bmatrix}\frac{1}{\left|J\right|}. \tag{3.41}$$

For convenience in expressing the stiffness matrix K in closed form the terms in the B matrix are expressed in compact form by

$$a_1 = x_3 - x_2, \tag{3.42a}$$

$$a_2 = x_1 - x_3, \tag{3.42b}$$

$$a_3 = x_2 - x_1, \tag{3.42c}$$

$$b_1 = y_2 - y_3, \tag{3.42d}$$

$$b_2 = y_3 - y_1, \tag{3.42e}$$

and $$b_3 = y_1 - y_2, \tag{3.42f}$$

where the B-matrix can now be expressed by

$$[B] = \frac{1}{2A_e}\begin{bmatrix} b_1 & b_2 & b_3 \\ a_1 & a_2 & a_3 \end{bmatrix}. \tag{3.43}$$

The area of the element (A_e) is given by

$$A_e = \frac{1}{2}\left(a_2 b_1 - a_1 b_2\right). \tag{3.44}$$

The element stiffness matrix can now be expressed in integral form (integrating over the isoparametric element) by

$$[K]_e = \frac{1}{2\mu}\int_0^1\int_0^1 \left([B]^T [\kappa]_e [B] |J|\right) h_e \, dr\,ds, \tag{3.45}$$

where the permeability matrix is given by

$$\left[\kappa\right]_e = \begin{bmatrix} \kappa_{xx} & \kappa_{xy} \\ \kappa_{xy} & \kappa_{yy} \end{bmatrix}. \tag{3.46}$$

In general the integral in Eq. (3.45) can be solved numerically using Gaussian quadrature [94]. However, for the linear triangle element considered, the shape function derivatives are constant and a closed form solution can be obtained directly. Substituting Eq. (3.40), Eq. (3.43), and Eq. (3.46) into Eq. (3.45) leads to a closed form expression for the element stiffness matrix given by

$$\left[K\right]_e = \frac{h_e}{4A_e\mu}\left\{\kappa_{xx}\left[K_{xx}\right]_e + \kappa_{yy}\left[K_{yy}\right]_e \kappa_{xy}\left[K_{xy}\right]_e\right\}, \tag{3.47}$$

where

$$\left[K_{xx}\right]_e = \begin{bmatrix} b_1^2 & b_1b_2 & b_1b_3 \\ b_1b_2 & b_2^2 & b_2b_3 \\ b_1b_3 & b_2b_3 & b_3^2 \end{bmatrix}, \tag{3.48}$$

$$\left[K_{yy}\right]_e = \begin{bmatrix} a_1^2 & a_1a_2 & a_1a_3 \\ a_1a_2 & a_2^2 & a_2a_3 \\ a_1a_3 & a_2a_3 & a_3^2 \end{bmatrix}, \tag{3.49}$$

$$\left[K_{xy}\right]_e = \begin{bmatrix} 2a_1b_1 & a_1b_2 + a_2b_1 & a_1b_3 + a_3b_1 \\ a_1b_2 + a_2b_1 & 2a_2b_2 & a_2b_3 + a_3b_2 \\ a_1b_3 + a_3b_1 & a_2b_3 + a_3b_2 & 2a_3b_3 \end{bmatrix}, \tag{3.50}$$

and h_e is the thickness of the element.

The resin flow across the flow front boundary and at the inlet and outlet given by Eq. (3.26) is expressed for each element node by

$$d_1 = \frac{h_e l_a}{2} q \bullet n^a + \frac{h_e l_c}{2} q \bullet n^c , \tag{3.51a}$$

$$d_2 = \frac{h_e l_a}{2} q \bullet n^a + \frac{h_e l_b}{2} q \bullet n^b , \tag{3.51b}$$

and

$$d_3 = \frac{h_e l_b}{2} q \bullet n^b + \frac{h_e l_c}{2} q \bullet n^c , \tag{3.51b}$$

where l is the length of each side of the element and n is the normal as given in Figure 3-9. The normal for each side of the triangle is given by

$$n^a = \frac{1}{l_a}\left[\left(y_2 - y_1\right)\ \left(x_1 - x_2\right)\right], \tag{3.52a}$$

$$n^b = \frac{1}{l_b}\left[\left(y_3 - y_2\right)\ \left(x_2 - x_3\right)\right], \tag{3.52b}$$

and

$$n^c = \frac{1}{l_c}\left[\left(y_1 - y_3\right)\ \left(x_3 - x_1\right)\right]. \tag{3.52c}$$

Substituting Eq. (3.52) into Eq. (3.51) and utilized the expressions from Eq. (3.42) leads to a closed form expression for the boundary flow given by

$$d_e = \frac{h_e}{2}\begin{bmatrix} b_1 & a_1 \\ b_2 & a_2 \\ b_3 & a_2 \end{bmatrix}\begin{bmatrix} q_x \\ q_y \end{bmatrix}. \tag{3.53}$$

The consistent load vector describing the rate of change in volume of the element is given by

$$f_e = A_e h_e \begin{bmatrix} \frac{1}{3} \\ \frac{1}{3} \\ \frac{1}{3} \end{bmatrix}\left(\frac{1}{V_f^{t-1}} \frac{V_f^t - V_f^{t-1}}{\Delta t} \right), \tag{3.54}$$

where one-third of the rate of volume change is lumped at each node of the element. For models in which two-dimensional elements are used to model flow in the plane of the preform laminate, and through thickness flow is neglected, the current thickness of the element may be expressed using Eq. (3.31). In the case where three-dimensional elements are used, or two-dimensional elements are used to model flow through the thickness of the preform, the element volumes are fixed and the true change in preform volume cannot be captured by the finite element mesh. In this case it is necessary to multiply the fixed element volume by the ratio of the initial fiber volume

fraction to current fiber volume fraction (V_f^o / V_f^t) as given by Eq. (3.30) to capture the true change in volume. The consistent load for each node (*n*) may also be obtained by simply multiplying the fiber volume fraction change rate by the control volume (CV) associated with each node as given by

$$f_n = \frac{V_f^o}{V_f^t} CV_n \left(\frac{1}{V_f^{t-1}} \frac{V_f^t - V_f^{t-1}}{\Delta t} \right). \tag{3.55}$$

The control volume is defined in the next section.

The element stiffness matrices from Eq. (3.47) are assembled to form the global stiffness matrix where the assembly of the element stiffness matrices is given by

$$[K]_{Global} = \sum_{e=1}^{nel} [K]_e , \tag{3.56}$$

where *e* is the element number and *nel* is the total number of elements. The global boundary flow vector and consistent loading vector are assembled in a similar fashion and are given by

$$d_{Global} = \sum_{e=1}^{nel} d_e , \tag{3.57}$$

and $$f_{Global} = \sum_{e=1}^{nel} f_e \, . \qquad (3.58)$$

3.2.2 Control Volume Method: Resin Filling

The control volume method allows one to track the location of the free surface of a fluid using a fixed mesh, eliminating the need for redefining the mesh as the flow front progresses. In order to implement the method, the mold cavity geometry is descretized into elements which occupy the total volume of the mold cavity. These elements may be one, two or three-dimensional elements depending on the nature of the problem to be solved. For the sake of discussion a two-dimensional triangle element will be considered here. Following element discretization, a control volume is associated with each node of the mesh. The control volumes are defined such that the entire mold cavity is captured by the control volumes with no overlapping of individual control volumes. The portion of the element volume contributing to the control volume associated with each node of a triangle element is shown in Figure 3-10. The quadrilateral defined by points *1, c, d,* and *a* (*1cda*) is the portion of the control volume from this element which is associated with node 1. In a like manner the quadrilateral defined by *2bda* is associated with node 2 and the quadrilateral defined by *3cdb* is associated with node 3. The triangle element is divided into control volumes by bisecting each side of the triangle with lines which are perpendicular to the edges and converge at a point within the triangle. This method of dividing the

triangle element into control volumes requires that the triangle has no interior angles which exceed 90 degrees (limited to acute or right triangles).

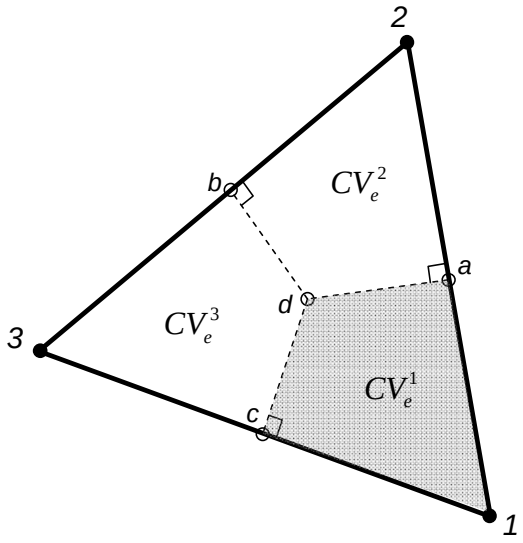

Figure 3-10 Illustration of a triangle elements showing the area of the control volume associated with node number 1.

The area of each control volume within the triangle element is expressed by

$$CV_e^1 = \frac{1}{2}\left(\frac{l_a}{2}\left(\sqrt{r^2 - \frac{l_a^2}{2}}\right)\right) + \frac{1}{2}\left(\frac{l_c}{2}\left(\sqrt{r^2 - \frac{l_c^2}{2}}\right)\right), \qquad (3.59a)$$

$$CV_e^2 = \frac{1}{2}\left(\frac{l_a}{2}\left(\sqrt{r^2 - \frac{l_a^2}{2}}\right)\right) + \frac{1}{2}\left(\frac{l_b}{2}\left(\sqrt{r^2 - \frac{l_b^2}{2}}\right)\right), \qquad (3.59b)$$

and $$CV_e^3 = \frac{1}{2}\left(\frac{l_b}{2}\left(\sqrt{r^2 - \frac{l_b^2}{2}}\right)\right) + \frac{1}{2}\left(\frac{l_c}{2}\left(\sqrt{r^2 - \frac{l_c^2}{2}}\right)\right), \qquad (3.59c)$$

where CV_e^1 is the control volume contribution in which the subscript *e* identifies the element under consideration and the superscript defines the node associated with the control volume. l is the length of each side of the triangle which is expressed in terms of the nodal coordinates with the length of each side being given by

$$l_a = \sqrt{\left(x_2 - x_1\right)^2 + \left(y_2 - y_1\right)^2}\,, \tag{3.60a}$$

$$l_b = \sqrt{\left(x_3 - x_2\right)^2 + \left(y_3 - y_2\right)^2}\,, \tag{3.60b}$$

and

$$l_c = \sqrt{\left(x_1 - x_3\right)^2 + \left(y_1 - y_3\right)^2}\,. \tag{3.60c}$$

The variable *r* is the distance (radius) from each of the nodes to the point within the element where the control volumes converge, where *r* is expressed in terms of the lengths of each side of the triangle by

$$r = l_a l_b l_c \Big/ \sqrt{\left|l_a l_b l_c \left(l_a + l_b + l_c\right)\left(l_b + l_c - l_a\right)\left(l_a + l_b - l_c\right)\right|}\,. \tag{3.61}$$

An illustration of a triangle element showing the length of each side as well as the radius (*r*) is given in Figure 3-11. The total control volume associated with each node is determined by summing the contributing volume from each element which is associated with a specific node as given by

$$CV^{node} = \sum_{e=1}^{nel} CV_e^{node} \quad . \tag{3.62}$$

where *nel* is the number of elements which share the node under consideration in common. A general finite element mesh using triangle elements showing the control volumes associated with each node is presented in Figure 3-12.

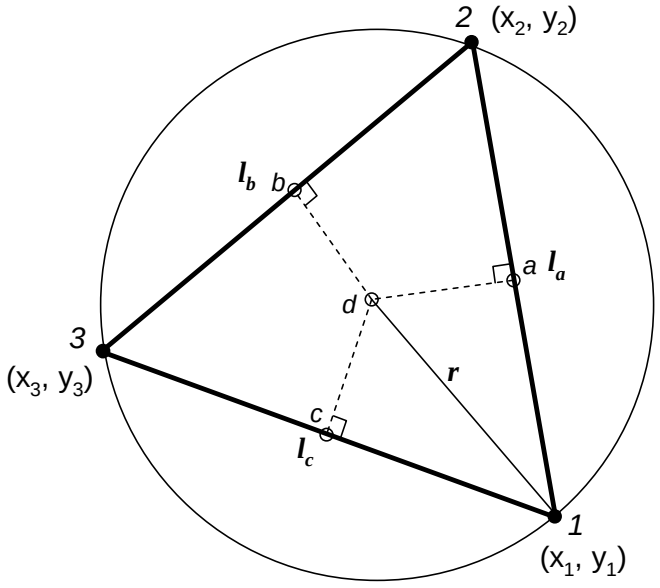

Figure 3-11 Illustration of a triangle element with control volume subdivisions defining the length of each side of the element as well as the radius (*r*) defined by a circle passing through each point of the element.

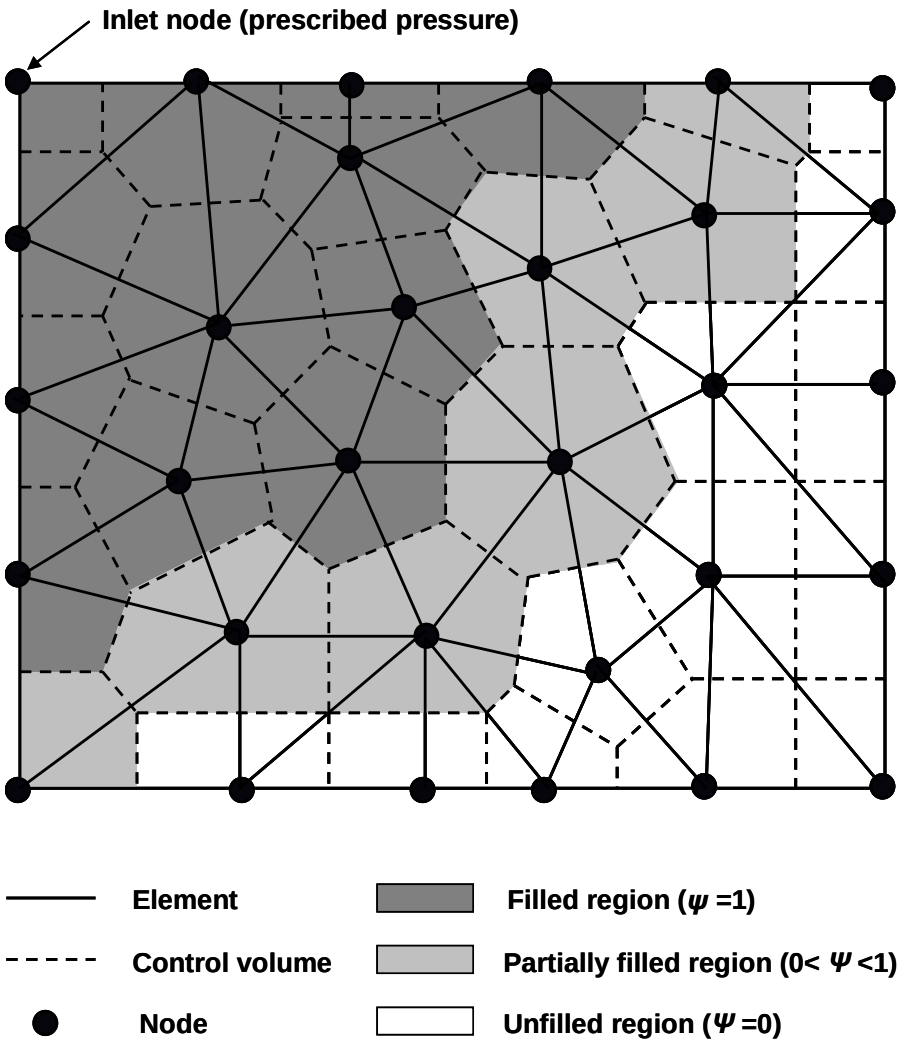

Figure 3-12 Illustration of general finite element mesh using triangle elements with control volumes showing filled, partially filled, and unfilled regions.

Alternatively the control volumes may be defined by division lines from the mid-point of each side of the triangle to the centroid such that one-third of the element volume is associated with each node. In the case of an equilateral triangle the two methods result in identical control volumes. However, in the case of right triangles it is observed that the alternative method using the element centroids to define the

control volumes is dependent on the mesh discretization (Figure 3-13) whereas the previously described method using division lines which are perpendicular to the triangle sides results in control volumes which are independent of the mesh discretization (Figure 3-14). Further it is observed from Figure 3-13 that the distribution of the control volumes is not uniform when the element centroids are used. Alternatively using perpendicular lines to divide the element volume results in control volumes which are uniformly distributed across the mesh (Figure 3-14). The control volumes for other element geometries are presented in Appendix A.

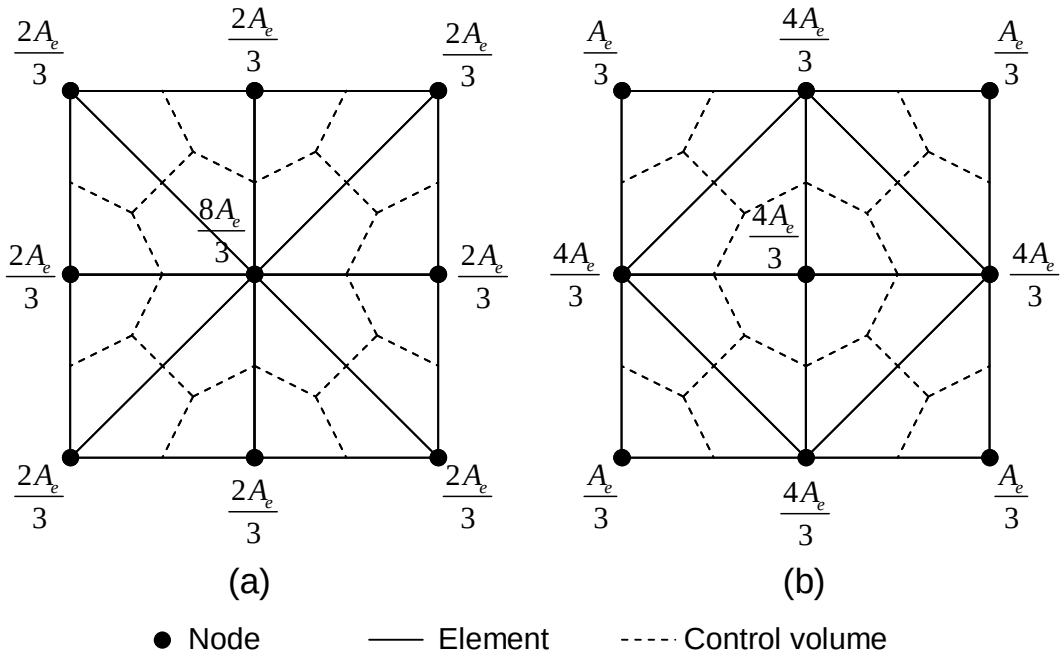

Figure 3-13 Illustration of control volumes defined using the element centroids for two different mesh discretizations.

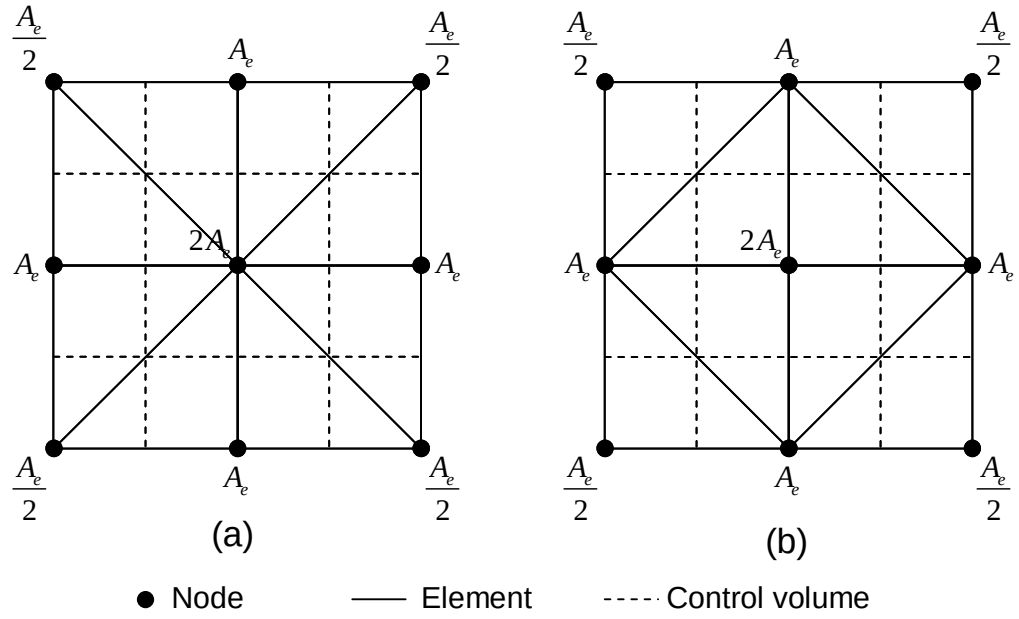

Figure 3-14 Illustration of control volumes defined using perpendicular dividing lines for two different mesh discretizations.

The flow front progression over a fixed mesh is tracked using fill factors which are associated with each control volume. The fill factors (ψ) range from zero (empty) to one (completely filled) with partially filled control volumes having a fill factor value between zero and one. Initially all of the control volumes are empty (ψ=0) with the exception of the inlet nodes where the pressure is prescribed (ψ=1). An illustration of this flow front tracking method is shown in Figure 3-12. The figure depicts a partially filled finite element mesh where the flow originates at the inlet node. The dark shaded area represents control volumes which are completely filled (ψ=1), the lightly shaded region represents control volumes which are partially filled ($0<\psi<1$) (flow front), and the unshaded region represents control volumes which are

empty (ψ =0). An algorithm outlining the method for advancing the flow front is given in Figure 3-15 with the procedure being described by the following steps:

1. Establish solution parameters and boundary conditions, K, V_f, P, and μ. The pressure is specified at the inlet and outlet, where the pressure at the inlet is typically atmospheric pressure (P = 101 kPa) and the pressure at the outlet is full vacuum pressure (P = 0 kPa).

2. Calculate the residual flow rate (d) at the flow front (unfilled or partially filled control volumes). the residual flow rates are calculated from the derived stiffness matrix (K) and the known pressure field (P) as given by

$$[K]P = d \tag{3.63}$$

3. Determine the largest time increment to fill exactly one control volume determined by

$$time\,to\ fill\,control\,volume = \frac{control\,volume}{residual\ \ flow\,rate} \tag{3.64}$$

and advance the flow front filling exactly one control volume.

4. Update the fill factors where the control volume which was completely filled in step 3 is assigned a value of one and the partially filled control volumes are assigned fill factor values in accordance with the degree to which they are filled. The boundary conditions are updated in accordance with the new fill factors such that all nodes which have a fill factor equal to one are part of the solution domain.

5. Based on the updated boundary conditions compute the new pressure field using Eq. (3.24) (nodes with a fill factor ψ <1 are ignored). Due to the nonlinearity introduced by the load vector (f) in Eq. (3.24) an iterative approach is followed to determine the pressure field which satisfies the load vector (f) due to compaction or relaxation of the fiber preform. An example of a constitutive model describing the compaction of a fiber preform is given in Figure 3-16.

6. Check if all of the control volumes are filled (ψ =1). If all of the control volumes are filled the simulation is complete, otherwise continue to the next step.

7. Reassemble the stiffness matrix with updated permeability, fiber volume fraction, and viscosity values based on material constitutive relationships and advance the time step then go back to step 1. Examples of constitutive models for preform permeability and resin

viscosity are given in Figure 3-17 and Figure 3-18 respectively. Although this research assumes constant temperature and only considers the viscosity changing as a function of time, it is also common for temperature to be changing during the VARTM process either due to an exotherm from the resin or processing in an oven. For these cases a more complex model which relates both time and temperature to the viscosity is required [95].

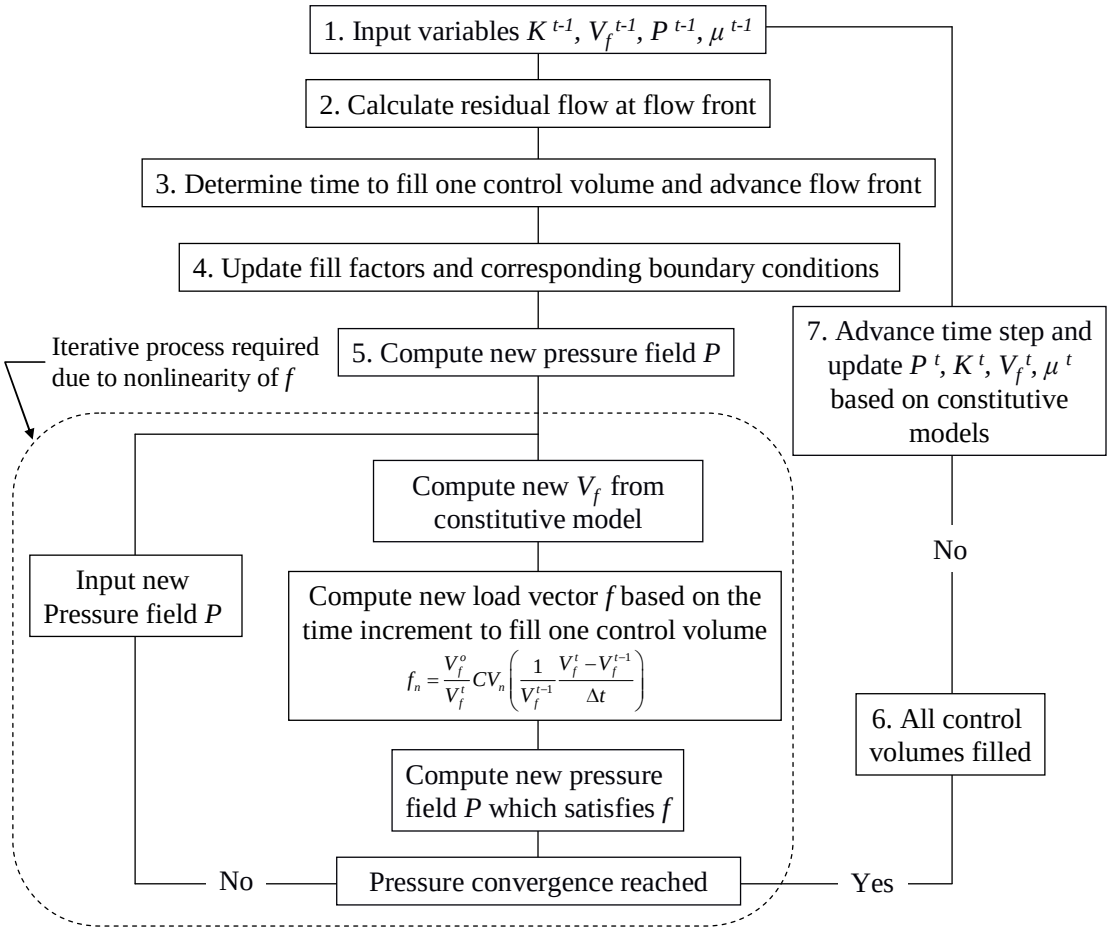

Figure 3-15 **A**lgorithm for advancing flow front (resin filling).

The described method is quasi-static in that the pressures remain constant at each time step while the flow front is advanced. In step 2 the residual flow at the flow front can also be determined by computing the resin velocity for each element using Darcy's Law and then summing the local flux across each surface of the control volume to determine the total flow into the control volume [32]. However it has been shown that the residual flow can also be determined by a simple matrix vector multiplication as shown in step 2, see references [96] and [39].

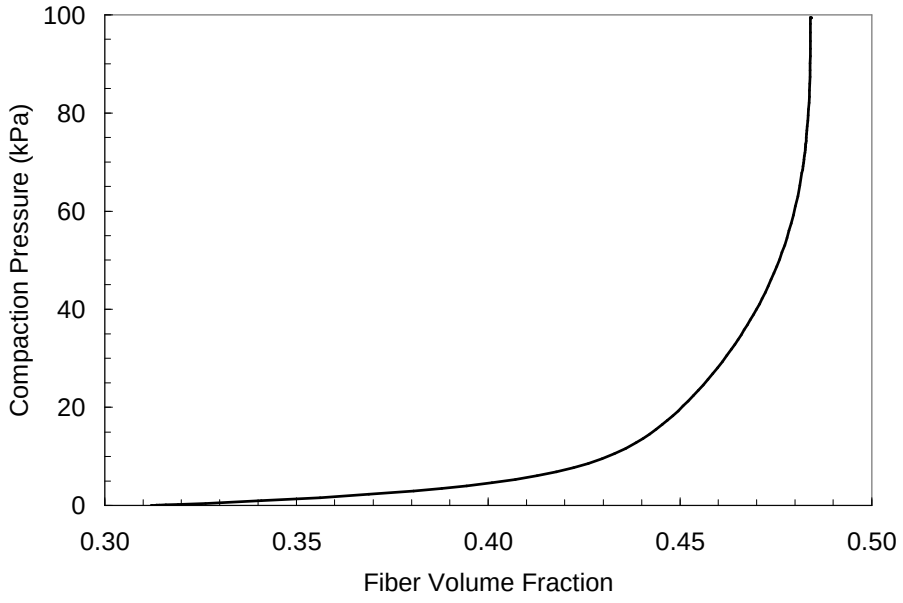

Figure 3-16 Compaction pressure versus fiber volume fraction constitutive model for uni-directional stitched carbon fabric.

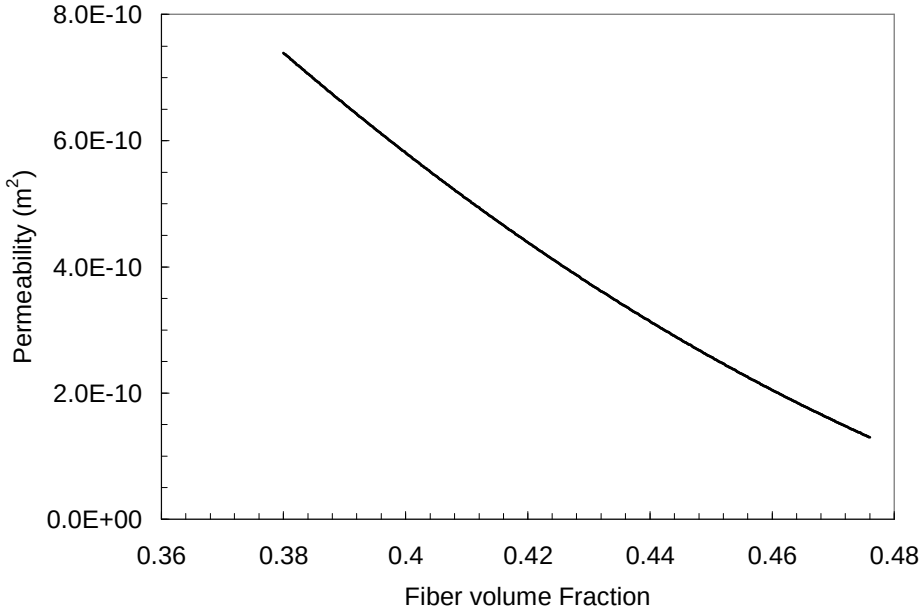

Figure 3-17 Permeability versus fiber volume fraction constitutive model for uni-directional stitched carbon.

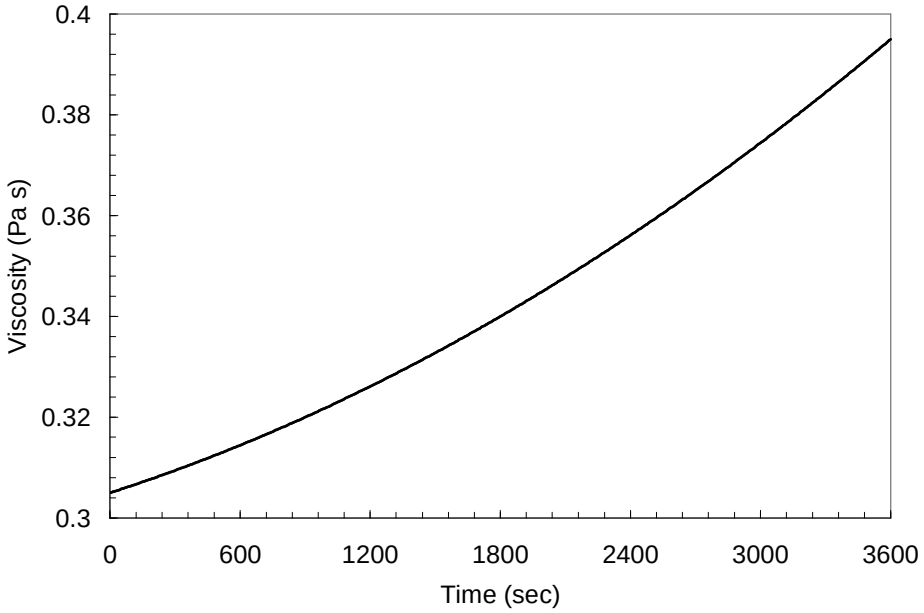

Figure 3-18 Viscosity versus time constitutive model for epoxy resin at fixed temperature.

3.2.3 Resin Bleeding Simulation

The procedure for simulating the resin bleeding phase of the VARTM process is similar to resin filling with the exception that there is no flow front to track. During the bleeding phase the preform is completely saturated, therefore all of the control volumes are filled (ψ =1) and there is no need for calculating the longest time to fill a control volume or updating the boundary conditions based on fill factors. An algorithm outlining the resin bleeding simulation is given in Figure 3-19 with the procedure steps given as follows:

1. Establish solution parameters and boundary conditions, K, V_f, P, and μ. At the beginning of the bleeding simulation the input parameters are based on the conditions at the end of filling. Prescribe boundary conditions for resin bleeding which may include vacuum pressure applied at the inlet or discontinuing flow at the inlet as well as reduced vacuum pressure at the outlet.

2. Based on the prescribed bleeding pressure boundary conditions compute the new pressure field. Due to the nonlinearity introduced by the load vector (f) in Eq. (3.24) an iterative approach is followed to determine the pressure field with satisfies the load vector (f) due to compaction or relaxation of the fiber preform.

3. Check if pressure equilibrium is reached. If equilibrium is achieved the simulation is ended otherwise continue to the next step.

4. Reassemble the stiffness matrix with updated permeability, fiber volume fraction, and viscosity values based on material constitutive models, advance the time step, and go back to step 1.

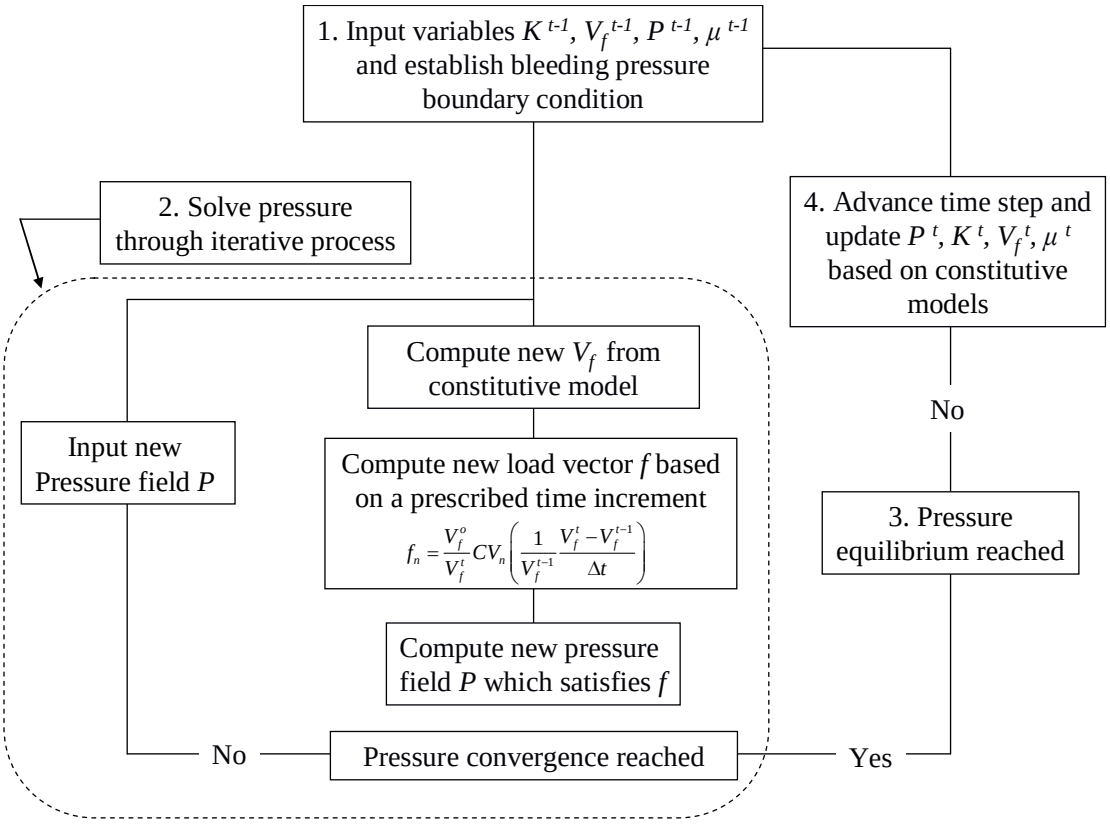

Figure 3-19 Algorithm for simulating resin bleeding.

3.2.4 Pressure Solution

For both the resin filling and resin bleeding simulations an iterative process is required to solve the pressure field due to the nonlinearity introduced by the load vector (f). During this iterative process it is observed that there exists more than one solution to which the solution may converge. To better understand the convergence of the solution, a one degree of freedom model to simulate resin bleeding was investigated. The model consists of a two node line element in which the initial pressure at node 1 (inlet) is prescribed to be 100 kPa and the pressure at node 2 (vacuum outlet) is prescribed to be 0 kPa. An illustration of the model is presented in Figure 3-20. At time zero the flow rate into node 1 is prescribed to be zero (clamped inlet hose) and the resin is allowed to flow through the outlet (node 2) as the preform compacts. Assuming a unit volume, the system of equations describing the model is given by

$$\begin{bmatrix} K_{11} & K_{12} \\ K_{21} & K_{22} \end{bmatrix} \begin{Bmatrix} P_1 \\ P_2 = 0 \end{Bmatrix} = \begin{Bmatrix} f_1 \\ d_2 \end{Bmatrix}. \tag{3.65}$$

Based on the prescribed boundary conditions the system of equations reduce to

$$P_1 = f_1 / K_{11} \tag{3.66}$$

where f is described by

$$f = \frac{V_f^o}{V_f^t}\left(\frac{1}{V_f^{t-1}}\frac{V_f^t - V_f^{t-1}}{\Delta t}\right). \tag{3.67}$$

The preform is assumed to have a fully compacted fiber volume fraction of 0.5. For this investigation the volume fraction is expressed as is a linear function of pressure given by

$$V_f = 0.5 - 0.001P\,, \tag{3.68}$$

such that the initial fiber volume fraction at the inlet (node 1) is 0.4 and the fiber volume fraction at the outlet (node 2) is 0.5. The stiffness parameter K is given an assumed value of 1.0e-3 m/(kPa•s) which is consistent with the materials considered in this research. Substituting Eq. (3.67) into Eq. (3.66) and rearranging leads to an expression for the time increment as a function of pressure given by

$$\Delta t = \frac{1}{PK}\left(\frac{V_f^t}{V_f^{t-1}} - \frac{V_f^{t-1}}{V_f^t}\right). \tag{3.69}$$

It should be remembered that the fiber volume fraction is also a function of the pressure as given by Eq. (3.68). From Eq. (3.69) a plot of pressure versus time step size is given in Figure 3-21. The plot shows that for a time step of 1 second the pressure decreases to 74.6 kPa, for a time step of 2 seconds the pressure decreases to 58.7 kPa and for a time step of 3 seconds the pressure goes to 48.0 kPa. As expected,

the pressure continues to decrease as larger time steps are used. As the time step goes to 0 seconds the pressure goes to 100 kPa which is the initial pressure at time zero. It is also observed that a second incorrect solution exists which is shown in Figure 3-22. From this plot it is seen that for a time step of 1 second the pressure is 1680 kPa, for a time step of 2 seconds the pressure is 1070 kPa, and for a time step of 3 seconds the pressure is 870 kPa none of which are achievable for the VARTM process. As the time step increment goes to zero the solution asymptotically goes to infinity.

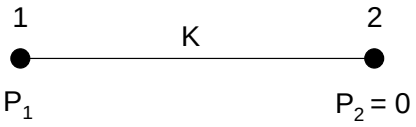

Figure 3-20 Illustration of one-dimensional resin bleeding model with one degree of freedom.

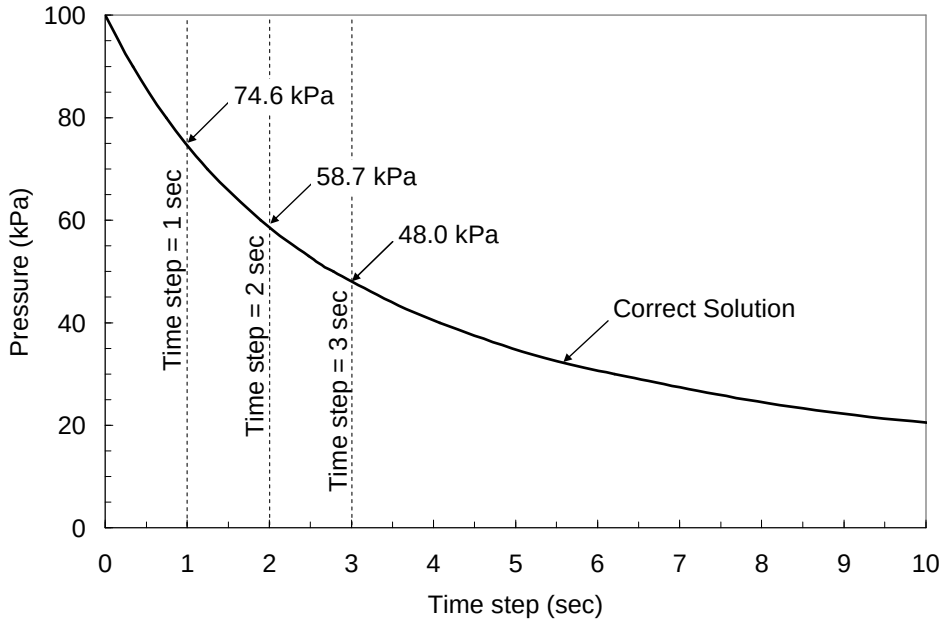

Figure 3-21 Plot of pressure versus time step showing the correct solution.

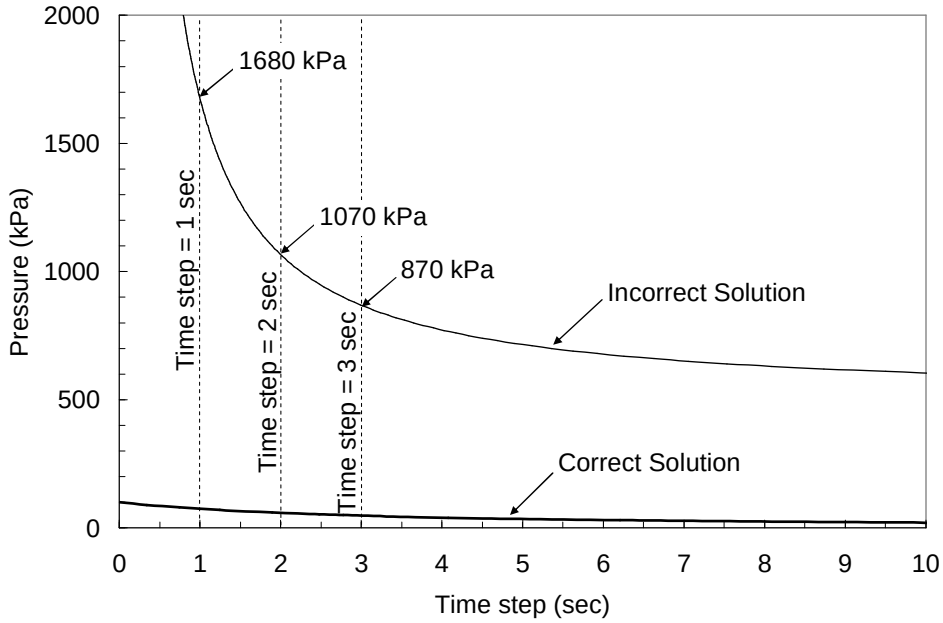

Figure 3-22 Plot of pressure versus time step showing the two values for which the solution converges.

To further study the solution convergence, the iterative process described previously in the resin bleeding section (see Figure 3-19) for solving for the pressure field was carried out using time step sizes of 1, 2, and 3 seconds. A plot of pressure versus the number of iterations for each time step is presented in Figure 3-23. For all three time steps P is equal to zero at the first iteration resulting in zero flow ($f = 0$) because the equivalent fiber volume fraction at the initial time step (t-1) and current time step (t) are equal. For the 1 second time step the pressure at the second iteration exceeds 200 kPa and continues to diverge until it converges to the wrong solution (1680 kPa) after 10 iterations. For the 2 second time step the solution diverges at a slower rate but still converges to the wrong solution (1070 kPa). For the 3 second time step the solution converges to the correct solution of 48 kPa.

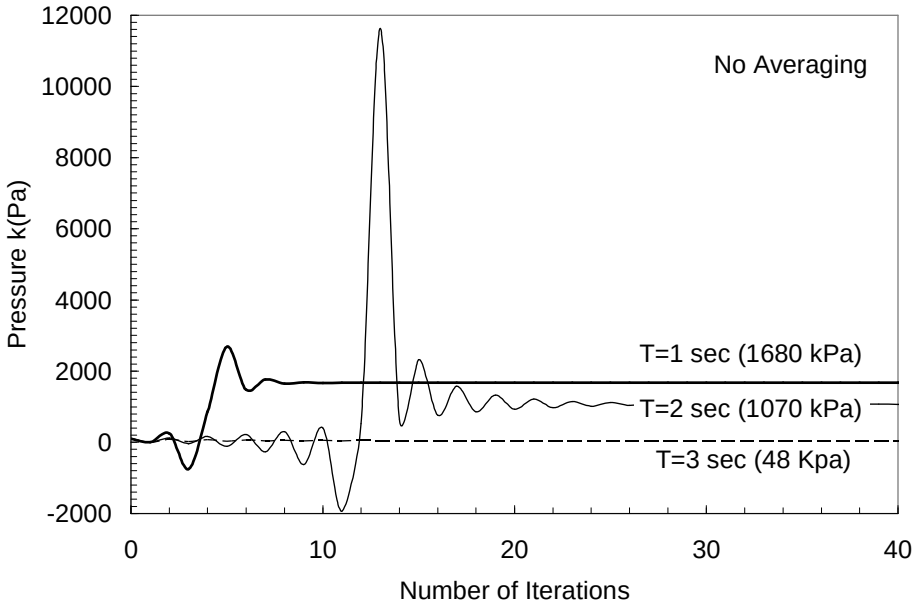

Figure 3-23 Plot of pressure versus the number of iterations to reach pressure convergence (alternate solution) with no averaging.

To achieve convergence to the correct solution an averaging technique is used. The averaging technique keeps the newly calculated pressure field closer to the previously known pressure field preventing divergence from the correct solution. The averaging method is given by

$$P_i \overset{m}{\underset{n=1}{\leftarrow}} \frac{P_i + P_{i-1}}{2} \tag{3.70}$$

where $P_{i\text{-}1}$ is the known pressure from the previous iteration and P_i is the solved pressure for the current iteration and m is the number of averages to be taken for which P_i is updated. For example at the beginning of the solution $P_{i\text{-}1}$ is equal to 100 kPa and the first solution for P_i is 0 kPa. Taking one average leads to a P_i = 50 kPa, two averages leads to P_i = 75 kPa, and three averages leads to 87.5 kPa. More

averages can be taken to bring the pressure solution closer to the know solution from the previous time step. The proper number (m) of averages can prevent the solution from diverging, leading to convergence to the correct solution. A plot of pressure versus the number of iterations for a time step of 1 second using 1, 2, 3, and 4 averages is presented in Figure 3-24. From the plot it is observed that using one average causes the solution to converge after about 40 iterations (numerically under damped) where using two averages convergences in two iterations (numerically critically damped). Using a higher number of averages (3 and 4) still converge to the correct solution but takes several iterations due to being numerically over damped. For a time step of two seconds a plot of pressure versus number of iterations is given in Figure 3-25. From the plot it is observed that for one average convergence is achieved in 3 iterations where for higher numbers of averages the solution takes longer to converge due to being over damped. Although actual problems to be solved have many more degrees of freedom, and the fiber volume fraction to pressure constitutive relationship is much more complex, this method of averages proves to be effective in achieving solution convergence at each time step. For the problems considered in this research typically 6 to 10 averages are sufficient to achieve convergence. It should also be noted that taking a higher number of averages than necessary leads to convergence but the computation time may be increased significantly.

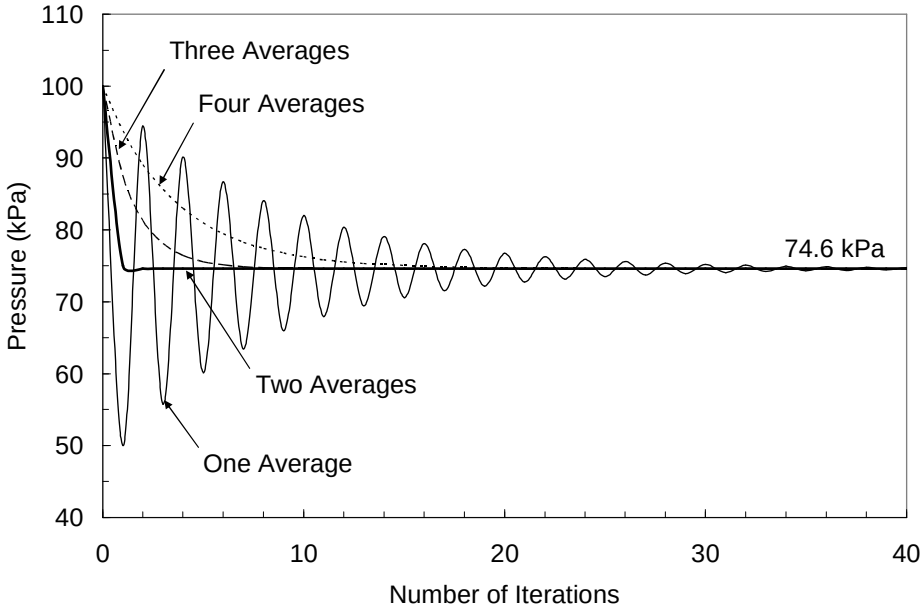

Figure 3-24 Plot of pressure versus number of iterations to reach convergence using one, two, three, and four averages for a time step of one second.

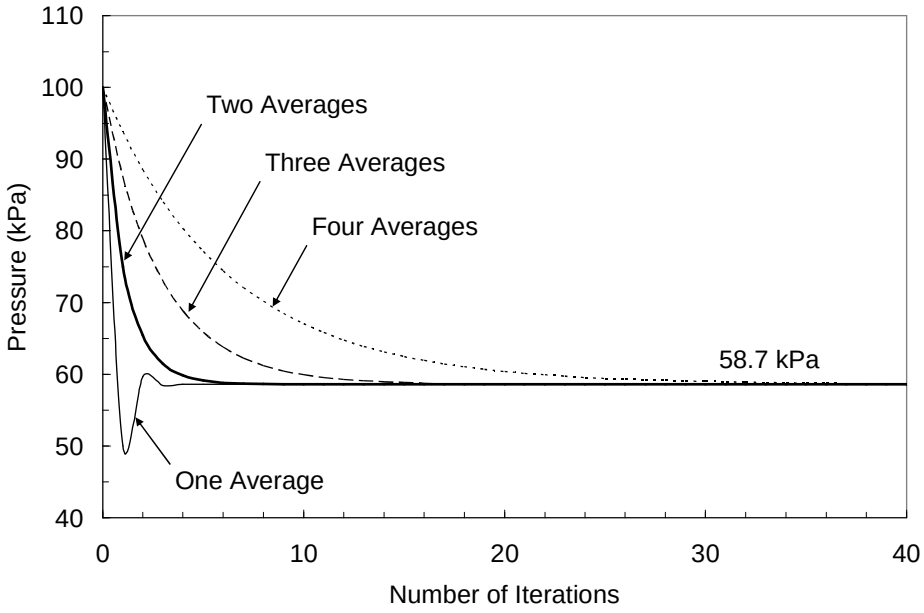

Figure 3-25 Plot of pressure versus number of iterations to reach convergence using one, two, three and four averages for a time step of two seconds.

3.3 MODEL VERIFICATION

One, two and three-dimensional flow simulations using fixed permeability and fiber volume fraction were performed and compared with analytical solutions to verify the developed code. Depictions of the-one dimensional flow, two-dimensional radial flow, and three-dimensional spherical flow are shown in Figure 3-26, Figure 3-27, and Figure 3-28 respectively. The black areas represent control volumes which are completely filled (ψ =1), the gray areas represent control volumes which are partially filled (0<ψ <1), and the white areas represent control volumes which are empty (ψ =0) The analytical solutions for one-dimensional flow, two-dimensional radial flow, and three-dimensional spherical flow for constant pressure are [39,44]

$$t = \frac{\phi \mu l^2}{2\kappa P_0}, \tag{3.71}$$

$$t = \frac{\phi \mu r^2}{4\kappa P_0}\left(\frac{R}{r}\right)^2\left[2\ln\left(\frac{R}{r}\right)+\left(\frac{R}{r}\right)^2-1\right], \tag{3.72}$$

and

$$t = \frac{\phi \mu (R^3 - r^3)}{3\kappa r P_0} - \frac{\varphi \mu (R^2 - r^2)}{2\kappa P_0}, \tag{3.73}$$

where t is the fill time, ϕ is the preform porosity, μ is the fluid viscosity, l is the flow distance, κ is the preform permeability, P_0 is the inlet pressure, r is the inlet radius and R is the flow front radius. A summary of fill times normalized with respect to the

analytical fill times are presented in Table 3-1. The numerical fill time predictions all show convergence to the analytical solution.

Figure 3-26 Finite element model of one-dimensional flow using three node triangle elements.

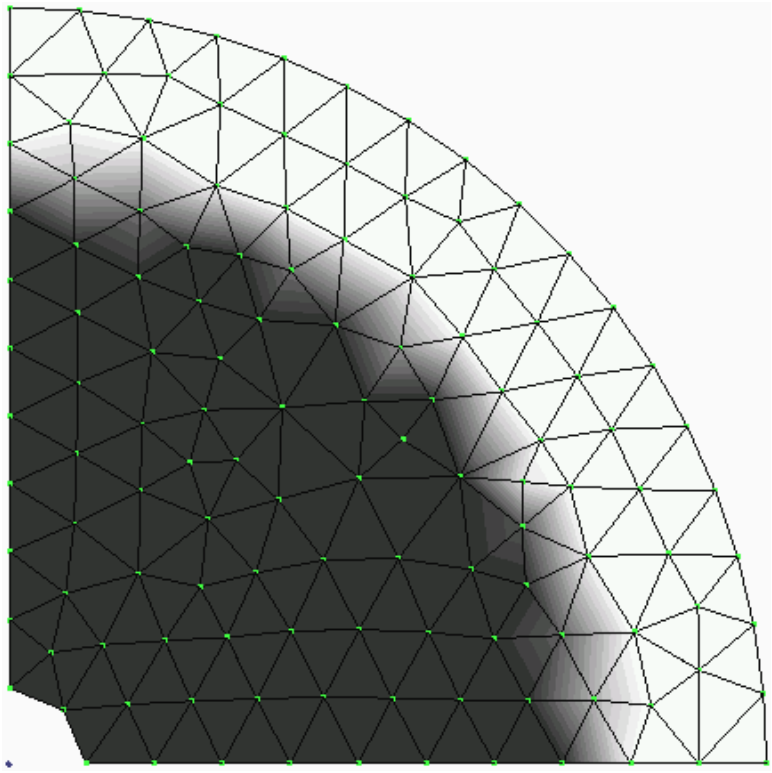

Figure 3-27 Finite element model of two-dimensional radial flow using three node triangle elements.

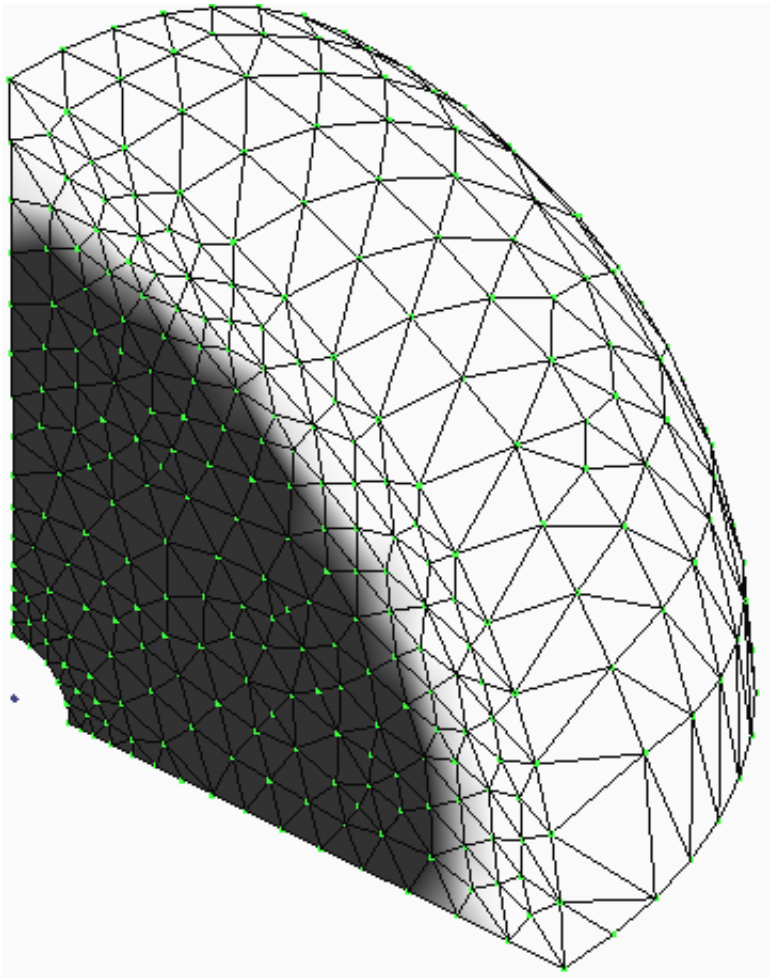

Figure 3-28 Finite element model of three-dimensional spherical flow using four node tetrahedral elements.

Table 3-1 Analytical vs. Numerical Flow Results

Flow	*1D*	*2D*	*3D*
Analytical fill time (sec)	1.0	1.0	1.0
Simulation fill time (sec)	1.0	0.99	0.96

3.4 SUMMARY

The development of a three-dimensional model to simulate the VARTM process has been presented. The model considers transient permeability and fiber volume fraction effects due to preform compaction without neglecting flow through the thickness of the preform. By considering the transient nature of the fiber volume fraction, the change in preform volume is accounted for allowing one to simulate the bleeding phase of the VARTM process as well as the filling phase. Simulation algorithms for both resin filling as well as resin bleeding have been presented with the introduction of an averaging technique which is used to obtain convergence of the pressure solution due to the nonlinearities introduced through the transient fiber volume fraction. Finally the developed simulation model has been verified with one, two, and three-dimensional flow studies for which analytical solutions are available.

The next chapter discusses a procedure for characterizing preform and resin materials to develop permeability, fiber volume fraction, and viscosity constitutive models which are used in the simulation.

CHAPTER 4

MATERIAL CHARACTERIZATION

It has been established that the flow of resin through a fibrous preform is governed by three material properties: (1) the permeability of the fiber preform (κ_{ij}), (2) the fiber volume fraction (V_f), and (3) the viscosity of the resin (μ). The purpose of this chapter is to discuss the procedures for measuring these material properties and to introduce an alternative method for characterizing the preform material which more closely represents the VARTM process. The general theory for determining the permeability and compaction properties of fiber performs is presented followed by a description of the experimental procedures used in this research for characterizing the fiber preform and resin. Finally, there is a discussion about the material characterization results and presentation of the experimentally developed constitutive models which will be used for simulation in the following chapters.

4.1 PREFORM CHARACTERIZATION

VARTM simulation requires two preform material models which describe: (1) the relationship between the preform permeability and the fiber volume fraction and (2) the relationship between the fiber volume fraction and the compaction pressure.

4.1.1 Permeability

In general, for an anisotropic preform the three dimensional permeability tensor is fully populated and expressed as

$$[\kappa] = \begin{bmatrix} \kappa_{xx} & \kappa_{xy} & \kappa_{xz} \\ \kappa_{yx} & \kappa_{yy} & \kappa_{yz} \\ \kappa_{zx} & \kappa_{zy} & \kappa_{zz} \end{bmatrix}. \tag{4.1}$$

To characterize the material one needs to determine nine permeability values. By assuming the preform is orthogonal and symmetric the number of values reduces to six, i.e. $\kappa_{ij} = \kappa_{ji}$ if $i \neq j$ [70]. However by determining the permeability along the principal directions only three independent values are required. For an orthotropic preform material the principle directions are along the fibers (κ_{11}), transverse to the fibers (κ_{22}) and through the thickness of the preform (κ_{33}) where the principal permeability tensor is given by

$$[\kappa'] = \begin{bmatrix} \kappa_{11} & 0 & 0 \\ 0 & \kappa_{22} & 0 \\ 0 & 0 & \kappa_{33} \end{bmatrix}, \tag{4.2}$$

where the prime indicates the permeability along the principal directions. The permeability tensor $[\kappa]$ in the general coordinate system is obtained by the transformation given by

$$[\kappa] = [C]^T [\kappa'][C], \tag{4.3}$$

where $[C]$ is the matrix of direction cosines of the general coordinate axes *x*, *y*, *z* with respect to the principal axes *x'*, *y'*, *z'*. [97,98]. Parnas [99] has shown good correlation between permeability tensors obtained from transformations of principal permeability tensors and experimental infusion experiments. By aligning the *z* and *z'* axes the permeability in the general coordinate system is given by

$$[\kappa] = \begin{bmatrix} \kappa_{11}\cos^2\theta + \kappa_{22}\sin^2\theta & (-\kappa_{11} + \kappa_{22})\sin\theta\cos\theta & 0 \\ (-\kappa_{11} + \kappa_{22})\sin\theta\cos\theta & \kappa_{11}\sin^2\theta + \kappa_{22}\cos^2\theta & 0 \\ 0 & 0 & \kappa_{33} \end{bmatrix}, \tag{4.4}$$

where θ is the rotation angle in reference to the principal axes [99]. Additional transformations to align *z'* with *z* are given in Appendix B.

The general theory to determine the principal permeability values is presented. Permeability measurements for composite reinforcing fabrics have been primarily accomplished by one of two methods. The first method consists of monitoring the flow front of the resin under a constant pressure differential from the inlet to the flow front and recording the progression of the flow front as a function of time. This is referred to as advancing flow front or unsaturated flow [100]. The permeability is calculated from Darcy's Law which is expressed in one dimension by

$$q_x = -\frac{\kappa_{xx}}{\mu}\frac{dP}{dx}, \tag{4.5}$$

where q_x is the superficial velocity in the *x* direction, κ_{xx} is the permeability in the *x* direction, μ is the resin (test fluid) viscosity, and P is the resin (pore) pressure. The superficial fluid velocity (q_x) is expressed in terms of the interstitial fluid velocity (u_x) and the porosity (ϕ) of the preform material by

$$q_x = u_x\phi = \frac{dx}{dt}\phi\,. \tag{4.6}$$

Substituting Eq. (4.6) into Eq. (4.5) and expressing the pressure gradient in the *x* direction as the difference in pressure over the infused length leads to

$$\frac{dx}{dt}\phi = \frac{\kappa_{xx}}{\mu}\left(\frac{P_i - P_o}{l}\right), \tag{4.7}$$

where P_i is the pressure at the inlet, P_o is the pressure at the flow front, and l is the infused length. An illustration of unsaturated flow condition showing the infused length and inlet and flow front pressures is given in Figure 4-1. By applying separation of variables and integrating the left hand side from time zero to the time for the flow front to reach length *l* and the right hand side from zero to the length of the flow front leads to the following expression

$$\kappa_{xx} \int_{o}^{t} dt = \frac{\mu \phi l}{P_i - P_o} \int_{0}^{l} dx \,. \tag{4.8}$$

Carrying out the integration and solving for the permeability (κ_{xx}) leads to

$$\kappa_{xx} = \frac{l^2 \mu \phi}{2 \Delta P t} \,, \tag{4.9}$$

where ΔP is the pressure differential between the inlet and the flow front. For constant viscosity, pressure differential, and porosity the infused length can be measured as a function of time to determine the permeability.

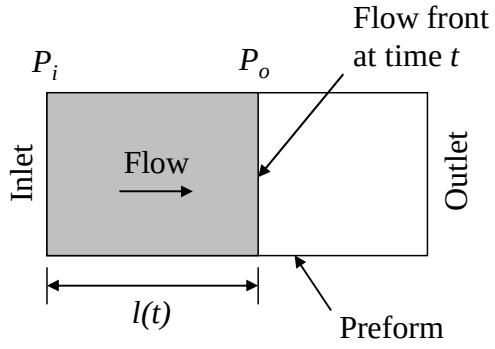

Figure 4-1 Illustration of the unsteady (unsaturated) flow condition.

The permeability may also be determined by plotting $l^2\mu\phi/(2\Delta P)$ versus time (t) where the permeability is given as the slope of the line. An example of the described plot is given in Figure 4-2.

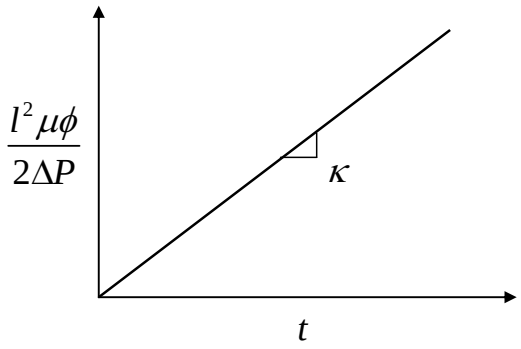

Figure 4-2 Plot of $l^2\mu\phi/(2\Delta P)$ versus time where the permeability is given by the slope of the line.

The second method for measuring the permeability of a fiber preform is a steady-state condition in which the preform is completely saturated and the flow rate has reached steady-state [100]. By applying separation of variables to Eq. (4.5), at steady-state, Darcy's Law is expressed in the following integral form

$$q_x\mu\int_0^l dx = -\kappa_{xx}\int_{P_i}^{P_o} dP\ . \tag{4.10}$$

On the left hand side integration is carried out over the length of the saturated preform and on the right hand side the integral is taken from the pressure at the inlet (P_i) to the

pressure at the outlet (P_0). Following integration the permeability for the steady-state flow condition is expressed as

$$\kappa_{xx} = \frac{q_x \mu}{\Delta P} l \,, \tag{4.11}$$

where l is now the total length of the perform and ΔP is the pressure differential from the inlet to the outlet. At constant viscosity and pressure differential the volumetric flow rate (Q) is measured to determine the permeability. The volumetric flow rate is related to the superficial flow rate (q_x) by

$$q_x = \frac{Q}{h\,w}, \tag{4.12}$$

where h is the thickness of the preform and w is the width of the preform. An illustration of the steady-state flow condition showing the preform dimensions and inlet and outlet pressures is given in Figure 4-3. The expressions for the permeability from Eq. (4.9) and Eq. (4.11) are dependent on a linear pressure field from the inlet to the outlet. The validity of this assumption is shown to agree well with experimental measurements as will be shown in the results section.

It is well known [68, 69, 82] that the permeability of a fiber preform is dependent on the fiber volume fraction of the preform. Thus to fully characterize the permeability of a given preform material, measurements must be performed over a

range of fiber volume fractions which are representative of the VARTM process. Due to the need for repeated testing, the saturated (steady-state) method is often preferred over the unsaturated method for permeability measurements because the same preform sample can be used throughout all of the testing at different fiber volume fractions while a new preform sample is required for each measurement using the unsaturated method.

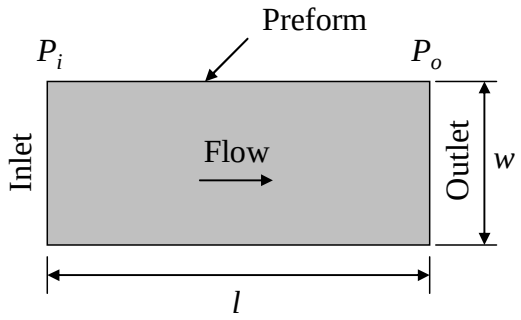

Figure 4-3 Illustration of the steady-state (saturated) flow condition.

Both of these measurement methods assume that the flow rate is uniform and constant across the width of the preform sample. This condition can be verified during the first filling of the dry preform. If the flow front is linear then the flow can be assumed to be uniform with constant flow rate across the width of the preform. However if a parabolic flow front is observed this indicates the presence of non uniform flow rate across the width of the preform. This may be due to edge runners (open channels) or other conditions which may result in inaccurate measurements. This condition will be further discussed in the experimental procedure section. An

illustration depicting uniform flow with constant flow rate versus parabolic flow due to non uniform flow rate across the width of the preform is presented in Figure 4-4.

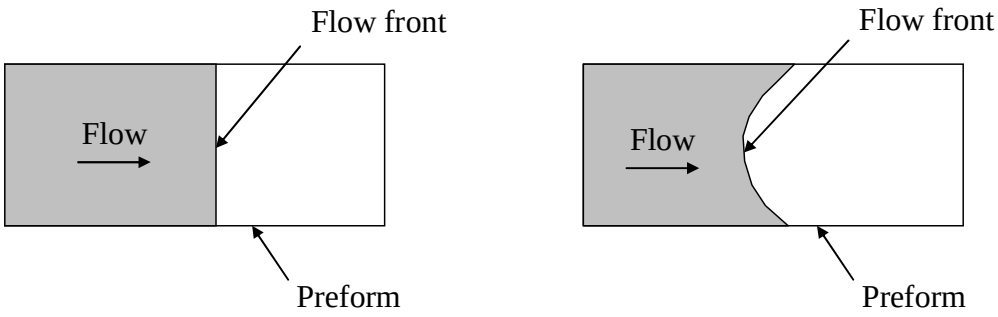

Figure 4-4 Illustration of one-dimensional flow with constant resin velocity (linear flow front) versus non uniform resin velocity resulting in a parabolic flow front.

Several models have been proposed to describe the relationship between the permeability and the fiber volume fraction [65, 66, 101-103] with the Kozeny-Carman [65, 66] model being the most commonly used. However due to the permeability dependence on fabric architecture, empirical constitutive models developed from experimental measurements offer the highest accuracy.

4.1.2 Compaction

In addition to a constitutive model to relate the permeability to the fiber volume fraction, a second model is required to relate the preform fiber volume fraction to the compaction pressure. This relationship can be determined by first understanding the pressures which are present during the VARTM process. During

the VARTM process atmospheric pressure is acting on the vacuum bag surface which is held in equilibrium by the resin (pore) pressure and the stress (compaction pressure) within the fiber preform. This equilibrium condition is expressed by

$$P_{atm} = P_c + P, \tag{4.13}$$

where P_{atm} is atmospheric pressure, P_c is the fiber preform stress (compaction pressure), and P is the resin pressure. An illustration showing the pressure equilibrium within the mold is given in Figure 4-5. At any time during the VARTM process the atmospheric pressure acting on the vacuum bag surface must be in equilibrium with the resin pressure and the pressure carried by the fiber preform. Typically full vacuum pressure is used to infuse resin into the dry fiber preform. Initially when there is no resin in the preform (resin pressure is zero) the stress in the fiber preform is equal to atmospheric pressure. As resin is infused into the preform and the resin pressure increases and the preform stress (compaction pressure) decreases in accordance with Eq. (4.13). The preform acts as a spring such that as the preform stress (compaction pressure) decreases the preform increases in thickness and as the compaction pressure increases the preform decreases in thickness. The fiber volume fraction is related to the preform thickness by

$$V_f = \frac{Areal\ weight}{h\,\rho_f}. \tag{4.14}$$

where *h* is the preform thickness, ρ_f is the fiber density, and the *Aerial weight* is the weight per unit area of the preform.

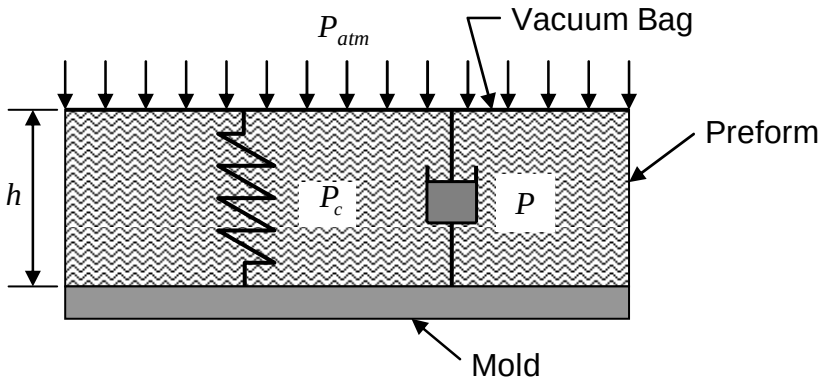

Figure 4-5 Illustration of the relationship between atmospheric pressure, preform stress (compaction pressure), and resin pressure for the VARTM process.

Song [54] has shown that the relationship between preform compaction pressure and fiber volume fraction is very different depending on whether the preform is undergoing compaction or relaxation. An illustration of this is shown in Figure 4-6. Although only the relaxation curve is needed during the infusion process the compaction curve is important if one is to consider the compaction of the preform due to the bleeding of excess resin at the end of filling. It has also been observed that saturated fiber preforms undergo greater compaction in comparison to dry performs due to the lubricating effect between wetted fibers [54].

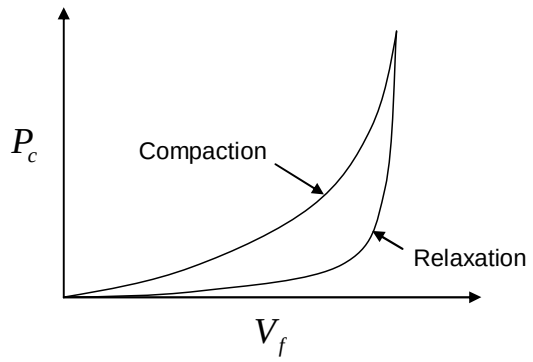

Figure 4-6 Plot showing relationship between preform compaction and fiber volume fraction during preform compaction and relaxation.

Several authors [67-69, 82-92] have examined compaction effects on fiber volume fraction and proposed different models for relating compaction pressure to fiber volume fraction. There are two compaction models commonly used in the literature [67-69, 89]. The first model was developed by Gutowski [67-69] and is given by

$$P_c = A_s \frac{\left(\sqrt{\frac{V_f}{V_o}} - 1\right)}{\left(\sqrt{\frac{V_a}{V_f}} - 1\right)^4} \tag{4.15}$$

where A_s is an empirical spring constant, V_f is the fiber volume fraction, V_o is the unloaded fiber volume fraction, and V_a is the maximum possible fiber volume fraction. The model is based on the compaction of a layer of uni-directional fibers. The author notes that if the fibers are all straight and aligned that the observed

compaction behavior cannot be explained. However by assuming that the fibers have an assumed small curvature then the observed compaction behavior can be explained. Gutowski's model is based on the assumption that each fiber is initially curved and partially restrained at the ends to transverse motion. As the fiber is compressed it buckles forming two arches with the double arch now being 16 times stiffer than the initial arch. As compaction continues the arches continue to divide resulting in progressively higher stiffness.

The second model is a simple power law fit used by Robitaille et al. [89] which is given by

$$V_f = V_o \sigma_{zz}^B, \tag{4.16}$$

where B is referred to as the stiffening index which is adjusted to fit experimental data. The accuracy of these models in predicting fiber volume fractions for the materials considered in this research will be shown in the results section. Alternatively one can directly develop resin pressure versus fiber volume fraction constitutive models by fitting curves consisting of a combination of polynomials and exponential terms to experimental data for both preform relaxation as well as preform compaction. This research uses the latter approach for relating fiber volume fraction to resin pressure.

4.2 RESIN CHARACTERIZATION

For simulation of the VARTM process it is required to know the relationship between the resin viscosity, temperature, and degree of cure over time. For this research the resin viscosity is measured using a cone/plate viscometer (Brookfield). The viscometer has a hot plate such that the viscosity is measured over a range of temperatures. For the VARTM process the ideal viscosity is typically considered to be less than 0.4 Pa•s [104]. For the permeability measurements considered in this study corn oil having a viscosity of 0.06 Pa•s at room temperature is used. The oil is used for two reasons: (1) The oil exhibits constant viscosity at a fixed temperature and (2) the oil is not harmful to the pressure transducers. A plot of viscosity versus temperature for the corn oil used in this research is given in Figure 4-7. For the fabrications considered in this research EPON 862 resin with Lindride 6 hardener is used. A viscosity versus temperature profile for this resin is given in Figure 4-8. From the plot it is observed that ideally this resin would be used at a temperature greater than 90° F to achieve a viscosity less than 0.4 Pa•s.

In addition to temperature dependence, the viscosity of epoxy resin is also dependent on the degree of cure. A plot of viscosity versus time for EPON 862 epoxy with Lindride 6 hardener at a constant temperatures of 95° and 120° F are given in Figure 4-9 and Figure 4-10 respectively. From the plots it is observed that at 95 F the viscosity remains near linear over entire measurement period while at 120 F the viscosity remains linear for only the first two hours.. It is also interesting to observe that over the first two hours the viscosity of the resin increased at a faster rate at 95° F in comparison to 120° F.

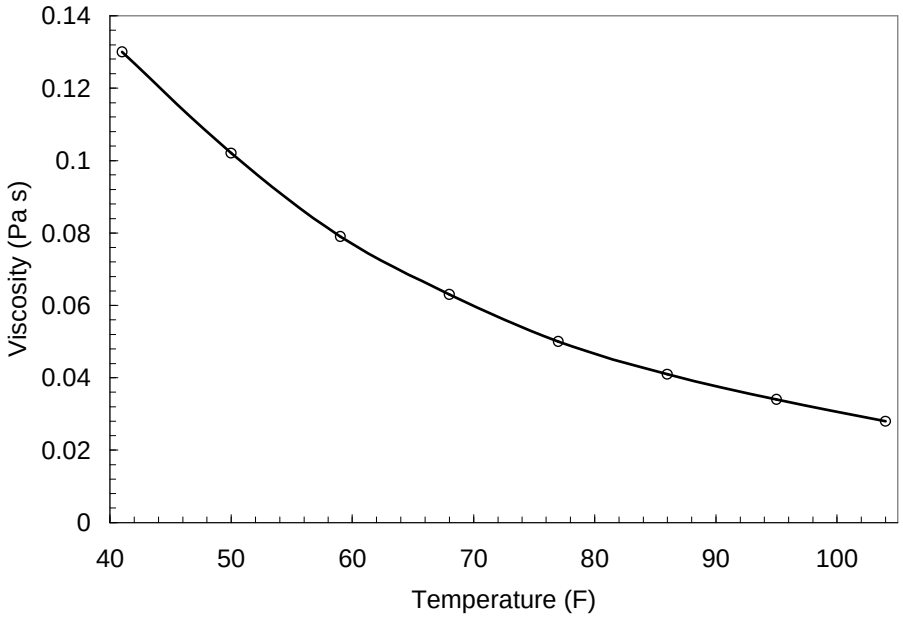

Figure 4-7 Plot of viscosity versus temperature for corn oil.

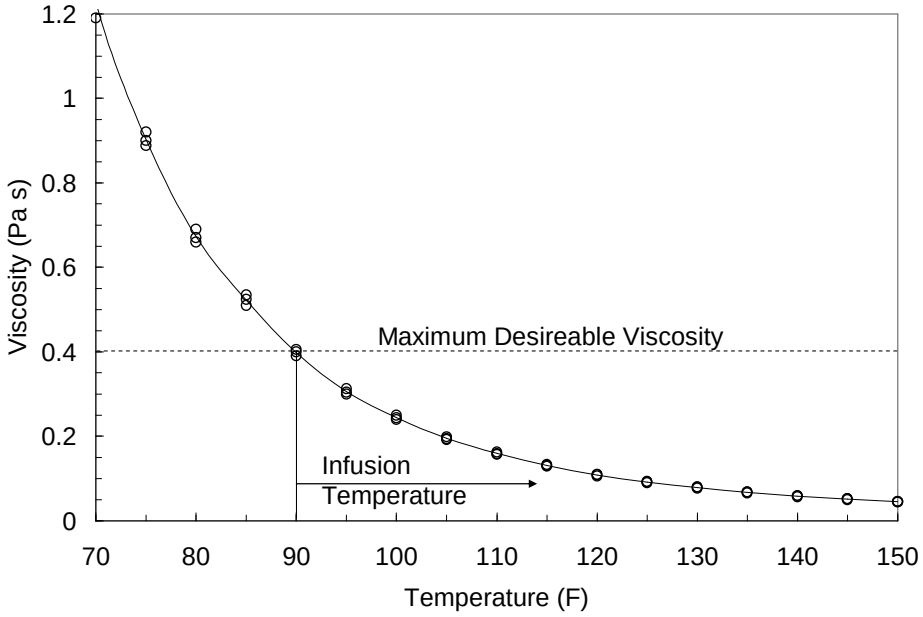

Figure 4-8 Plot of viscosity versus temperature for EPON 862 epoxy with Lindride 6 hardener.

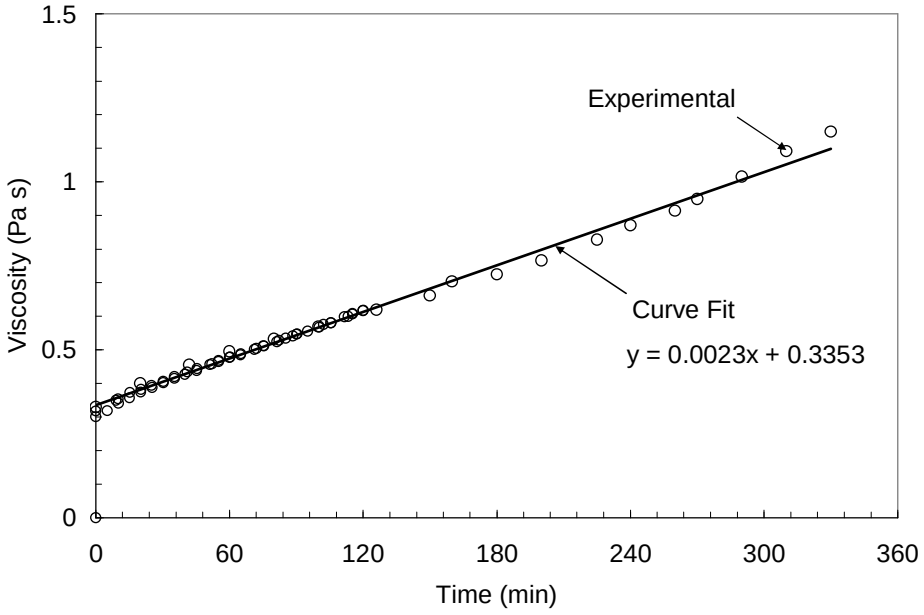

Figure 4-9 Plot of viscosity versus time for EPON 862/Lindride 6 epoxy at 95 F.

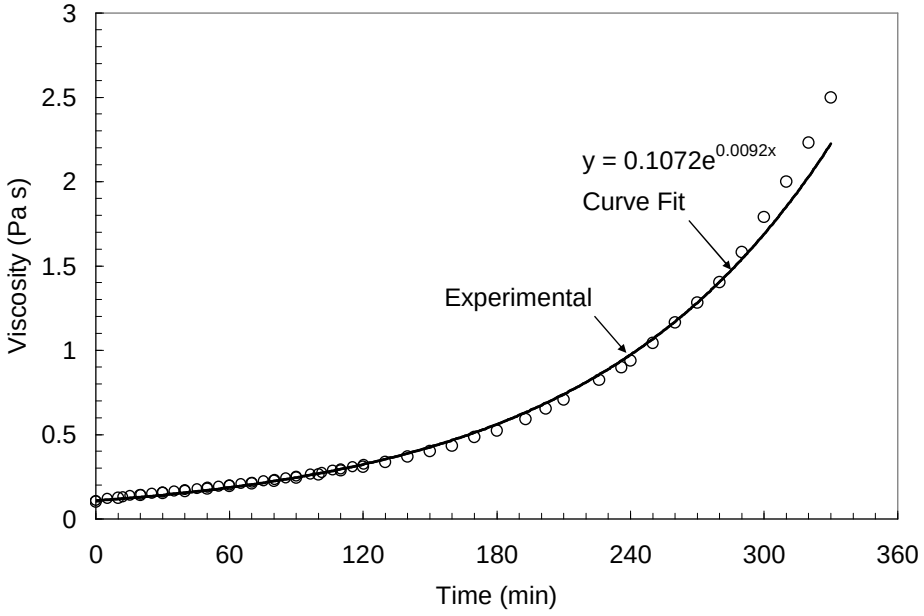

Figure 4-10 Plot of viscosity versus time for EPON 862/Lindride 6 epoxy at 120 F.

4.3 EXPERIMENTAL PROCEDURE

Preform permeability measurements have typically been performed using a two sided rigid mold, similar to the RTM process, with a fixed mold thickness (h) representing known fiber volume fractions [70-78]. An illustration showing a fiber preform between two rigid tool surfaces with a fixed thickness (h) is given in Figure 4-11. Permeability measurements are performed over a range of fiber volume fractions (preform thicknesses) which are representative of the VARTM process. Additional measurements are then performed to relate the preform fiber volume fraction to compaction pressure. These two data sets are used to develop preform permeability and compaction constitutive relationships which are used to simulate the VARTM process. Unlike the RTM process, the VARTM process uses a single sided rigid tool with a compliant vacuum bag on one surface (Figure 4-12). From the illustration in Figure 4-12 it is seen that the interface between the compliant vacuum bag and preform fiber tows is different than the interface between the rigid mold surface and the preform fiber tows (Figure 4-11). This chapter presents an alternative experimental method for developing permeability and compaction relationships using a measurement procedure and test fixture which more closely represents the conditions of the VARTM process and allows the compaction pressure, permeability, and fiber volume fraction to be related in a single experimental setup. A description of the measurement procedure along with a demonstration of the procedure is presented to study repeatability and to understand some of the limitations of the method.

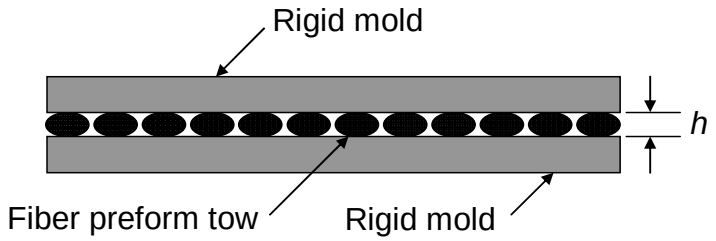

Figure 4-11 Illustration of a typical rigid matched mold test fixture for measuring preform permeability.

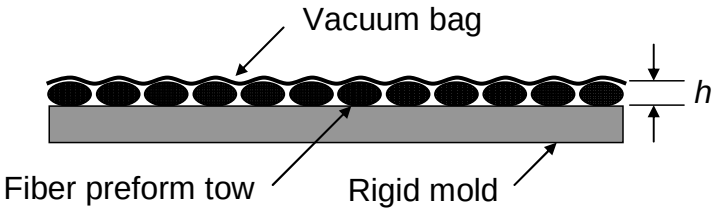

Figure 4-12 Illustration depicting the conditions during the VARTM process.

The experimental procedure consists of placing a 160 mm x 190 mm preform sample on a rigid aluminum plate having a machined channel along one edge of the preform serving as the fluid inlet channel and another channel along the opposite edge serving as the fluid outlet channel (see Figure 4-13 and Figure 4-14). The inlet and outlet channels have a tapered slope such that the edges of the preform do not become blocked by the vacuum bag at the inlet or the outlet (see Figure 4-15). Three Omega PX 302 pressure transducers mounted to the underside of the mold with 3 mm holes through the mold are used to record the fluid pressure at the inlet, outlet and at the center of the preform sample. A vacuum bag is placed over the preform sample and sealed around the perimeter. A vacuum pot filled with the test fluid is connected to

the fluid inlet channel and a second vacuum pot is attached to the fluid outlet channel. A volumetric measuring cylinder is placed in the hose between the outlet channel and the vacuum pot which is used to measure the volumetric flow rate of the test fluid through the preform sample. Three 10 mm displacement transducers are mounted on a strut at a fixed height above the aluminum mold surface allowing the thickness of the preform sample to be measured at three locations. The displacement transducers are located at the center of the preform and 60 mm either side of center. Prior to the placement of the preform sample the displacement transducers are set to zero at the surface of the mold such that the thickness of the perform sample plus the vacuum bag thickness can be measured directly. A pressure differential is established by controlling the pressure in each vacuum pot independently. Once a pressure differential is established the fluid inlet line is opened and the test fluid is allowed to flow through the preform sample. It was observed during the first experiment that the test fluid raced along the edges of the preform resulting in a parabolic flow front leading to superficially high permeability values. This problem was solved by placing modeling clay along the preform edges which prevented resin from racing down the open channels along the edges (Figure 4-14). Subsequent experiments using the modeling clay resulted in linear flow fronts. A photograph of the complete test setup is shown in Figure 4-16.

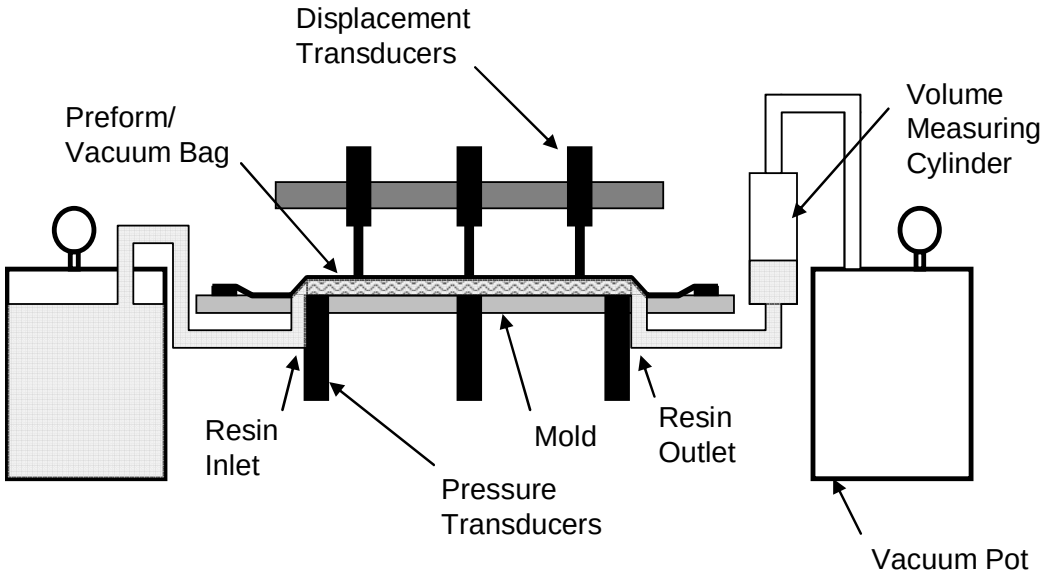

Figure 4-13 Side view of setup for measuring in-plane permeability for saturated (steady state) flow.

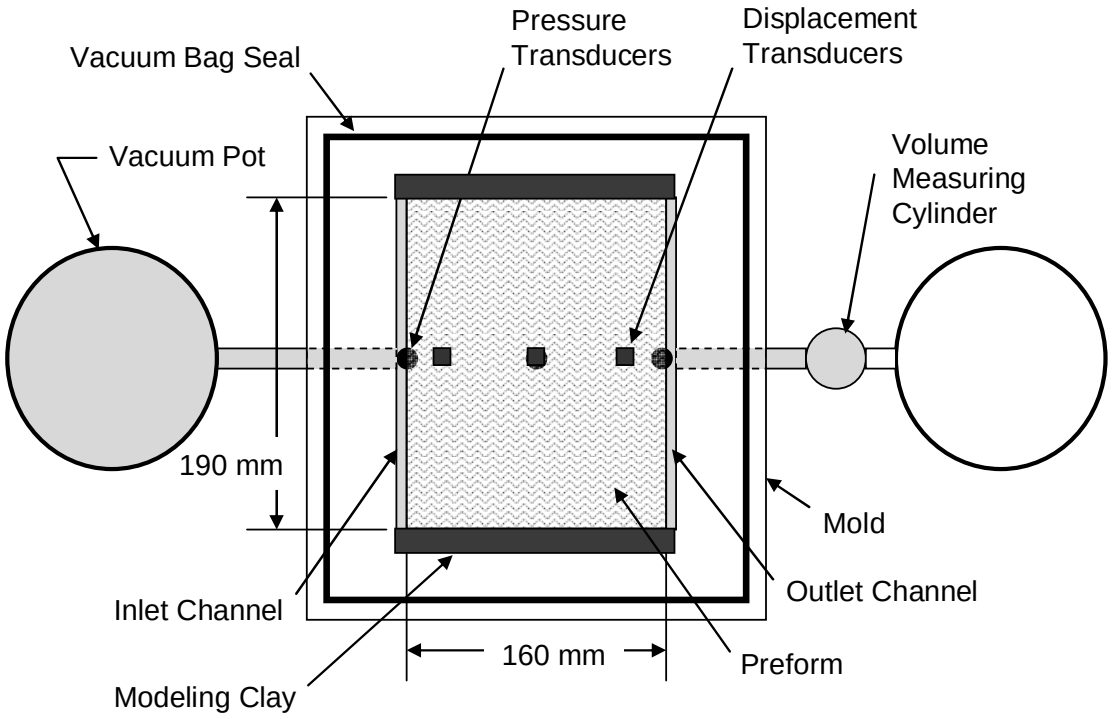

Figure 4-14 Plan view of setup for measuring in-plane permeability for saturated (steady state) flow.

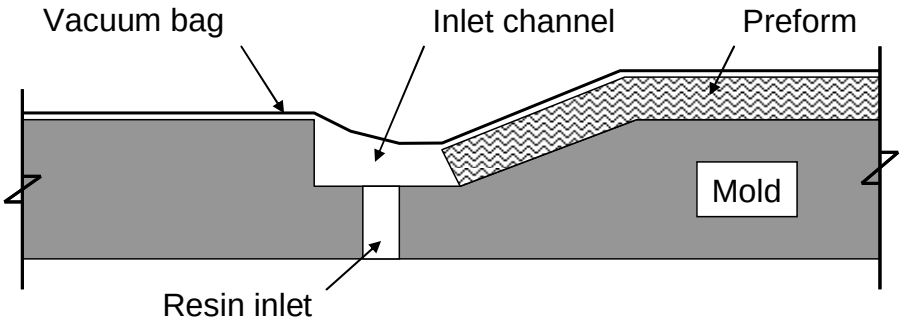

Figure 4-15 Illustration of the cross section of the inlet channel showing the edge of the preform sample.

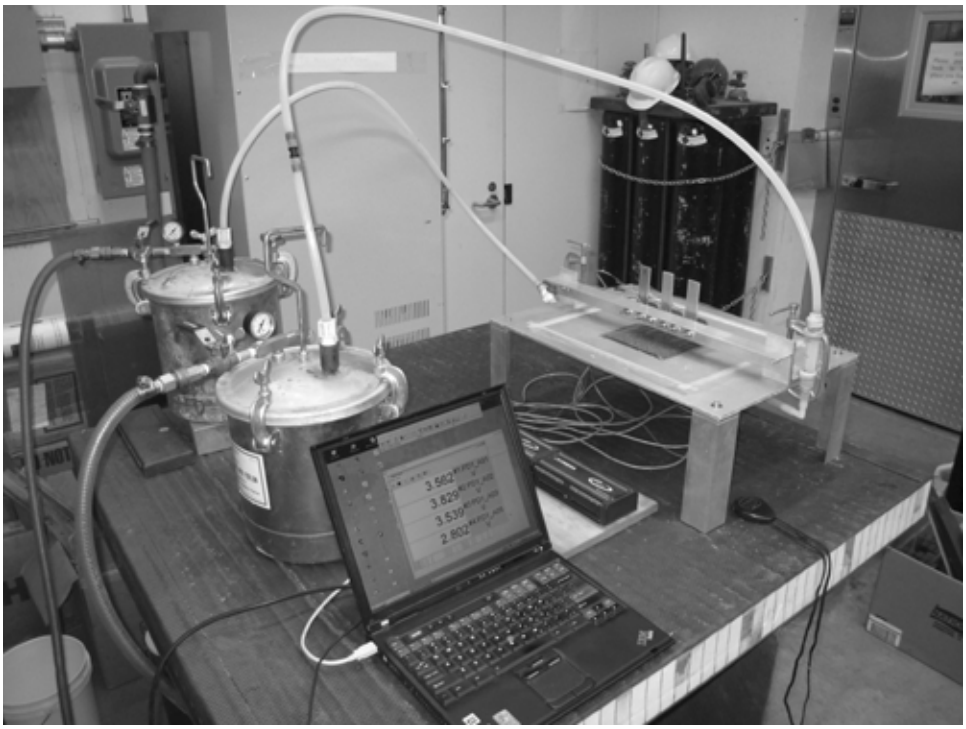

Figure 4-16 Photograph of permeability measurement fixture and test setup.

Once one-dimensional uniform flow has been confirmed through visual inspection during the initial filling of the dry preform sample, one can begin making measurements using the saturated preform based on Eq. (4.11). The procedure is described by the following steps:

1. Establish constant pressure differential from the inlet to the outlet and record the average pressure from the three pressure transducers. The pressure differential should be small enough that a constant pressure gradient can be assumed along the length of the preform.

2. Determine the volumetric flow rate (Q) by measuring the time to fill a known volume in the volumetric measuring cylinder.

3. Record the average preform thickness from the measurements of the three displacement transducers.

4. From the preform thickness use Eq. (4.14) to determine the fiber volume fraction for the given pressure level.

5. Based on the thickness of the preform and the known width of the preform sample, determine the superficial velocity (q_x) from Eq. (4.12).

6. With the calculated superficial velocity, known pressure differential, and known fluid viscosity use Eq. (4.11) to determine the permeability.

7. Repeat the procedure for the full range of compaction pressures (0-100 kPa) which are representative of the VARTM process. In this study the flow rate at each pressure level was measured a minimum of four times to assess the variability of the measurements.

In each case the measurements were made by beginning at the highest compaction pressure levels and progressively taking measurements at lower compaction pressures. It was observed by Stadtfeld et al [70] that measurements beginning at low compaction pressures and going to higher compaction pressures resulted in hysteresis in the permeability data. An example of resin pressure intervals which are used is shown in Table 4-1. At low compaction pressure levels the fiber volume fraction and permeability are very sensitive to changes in pressure, therefore as seen in Table 4-1 at the higher pressure levels (6 and 7) smaller pressure increments are used. Note that the compaction pressure is the difference between atmospheric pressure and the resin pressure as given by Eq. (4.13). By measuring the permeability in each of the principle directions (along the fibers and transverse to the fibers) the permeability in any direction in the plane of the preform can be determined through a coordinate transformation of the permeability tensor (Eq. 4.4).

Table 4-1 Resin Pressure Measurement Levels

Pressure Level	P_{inlet} *(kPa)*	P_{outlet} *(kPa)*	P_{avg}
1	40	30	35
2	60	50	55
3	70	60	65
4	80	70	75
5	90	80	85
6	95	90	92.5
7	100	95	97.5

Following the in-plane permeability versus fiber volume fraction measurements the relationship between the compaction pressure and fiber volume fraction is obtained by slowly cycling the compaction pressure from zero compaction to full compaction (101 kPa) and then relaxing the pressure back to zero. During the cycling the pressure and preform thickness are recorded. The thickness data is then converted to fiber volume fraction using Eq. (4.14) from which the compaction versus fiber volume fraction relationship is established.

The through thickness permeability is measured in a similar manner as previously described for the in-plane permeability. A highly permeable flow distribution layer is placed above and below the preform, as shown in Figure 4-17, allowing the fluid to flow across the surface of the preform and then permeate through the thickness. Again a volumetric measuring cylinder attached to the fluid outlet is

used to measure the volumetric flow rate. Modeling clay is placed along the edges to prevent any racing of the fluid around the preform edges. The permeability is determined from Eq. (4.11) where now the length (l) is the thickness of the preform which varies with compaction pressure and must be determined at each pressure interval and the superficial velocity (q_x) is found from

$$q_x = \frac{Q}{b\,w} \tag{4.17}$$

where b and w are the preform in plane length and width respectively. The pressure differential across the thickness of the preform is taken from the measured pressure from each vacuum pot. Therefore it is important to ensure that the fluid surface in the inlet vacuum pot is at the same level as the resin inlet point to minimize the pressure difference between the vacuum pot and the resin inlet point. The same steps presented for measuring the in-plane permeability values are followed for the through-thickness directions where the flow length (l) is determined from the compaction pressure versus thickness data obtained from the in-plane permeability preform sample.

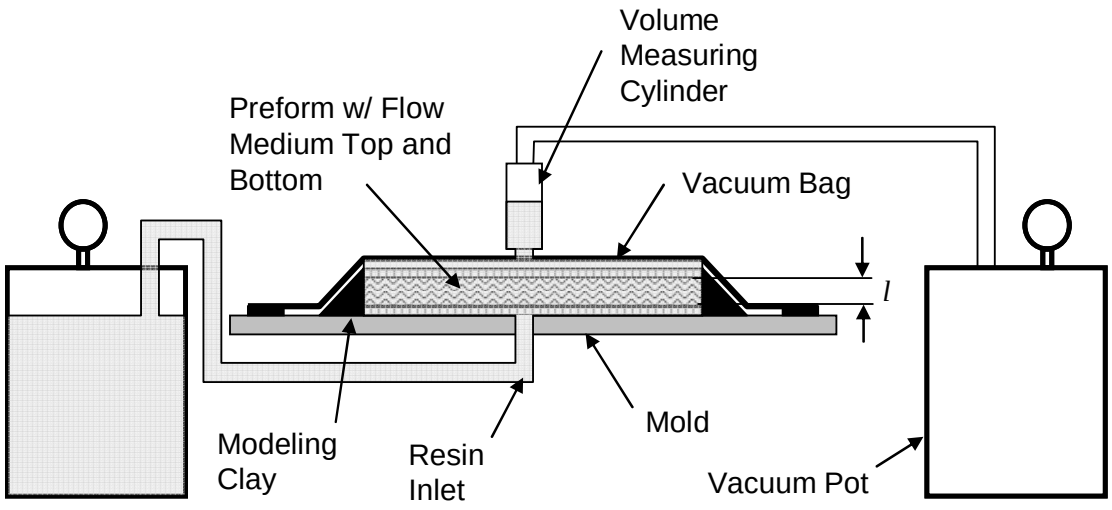

Figure 4-17 Setup for measuring through thickness permeability for saturated (steady) flow.

4.4 COMPACTION AND PERMEABILITY RESULTS

To demonstrate the developed measurement procedure, permeability and compaction measurements were conducted for a uni-directional stitched carbon fabric. Permeably measurements were performed in the three principle directions: Parallel to the fibers (κ_{11}), transverse to the fibers (κ_{22}), and through the thickness of the preform (κ_{33}). To investigate the repeatability of the method, measurements were performed on two different samples for each in-plane principle direction with three measurements being performed on each sample. The material is a 0.69 kg/m^2 24k tow stitched carbon fabric (C-LA 1812-7) supplied by Vectorply Inc (for complete fabric details see Table 4-2). To prevent damage to the test fixture vegetable oil having a viscosity of 0.06 Pa$\bullet$s at room temperature (70°F) was used as the test fluid.

Prior to making any permeability measurements the pressure gradient at several pressure levels was measured to verify that the pressure field along the length of the preform was linear. Figure 4-18 shows the resin pressure versus sensor location for a saturated preform sample. It is seen from the plot that the pressure is essentially linear along the length of the preform sample for each pressure level. The measurements confirm the constant pressure gradient assumption used in the development of Eq. (4.9) and Eq. (4.11). From the plot it is seen that for the resin pressure interval from 95 to 100 kPa the "R-squared" value is the lowest having a value of 0.97 which still shows a very good linear fit. R-squared is a statistical measure of how well a regression line approximates experimental data points R-squared ranges from zero to one where a value of one indicates an exact correlation [105]. R-squared is defined by

$$R^2 \equiv 1 - \frac{SS_{err}}{SS_{tot}}, \tag{4.18}$$

where SS_{tot} is the total sum of squares given by

$$SS_{tot} = \sum_i \left(y_i - \bar{y} \right)^2, \tag{4.19}$$

where y_i are the experimental measurements and $\bar{y}$ is the is the mean of the experimental measurement and SS_{err} is the sum of the squared error given by .

$$SS_{err} = \sum_i \left(y_i - f_i \right)^2 , \tag{4.20}$$

where f_i are the model or curve fit values. As will be seen from the compaction testing later in the section the preform thickness is very sensitive to pressure at low compaction (high resin) pressure and less sensitive at high compaction (low resin) pressure. Based on the results given in Figure 4-18 it was determined that the a linear pressure field was a valid assumption when using pressure differentials not exceeding 10 kPa.

During initial experiments is was observed that at low resin pressure (high vacuum) that any dissolved air within the oil underwent significant growth as it migrated toward the fluid outlet resulting in fluid flow rates which were difficult to measure. This problem was reduced by degassing the oil prior to infusion, however at resin pressures below 20 kPa measurements were still difficult to obtain.

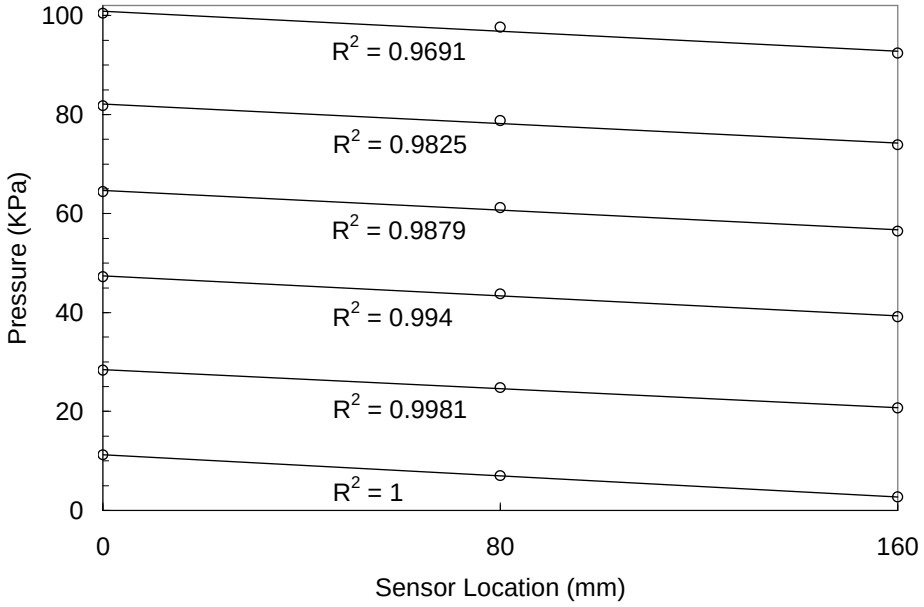

Figure 4-18 Plot of pressure gradients for six pressure levels ranging from 0 to 100 kPa.

The in-plane permeability measurements were preformed using three plies of the preform material and the through thickness permeability measurement was performed using six plies of the material Figure 4-19 shows the compaction pressure versus fiber volume fraction for the saturated preform. It is observed that the compaction and relaxation curves are highly nonlinear with much higher levels of compaction for the compaction pressure range from 0 to 40 kPa and less compaction occurring at higher pressure levels. Figure 4-20 and Figure 4-21 show the repeatability of the experimental method for the uni-directional material. At each pressure level two preform samples were tested three times each resulting in a total of six tests at each pressure level. Figure 4-20 shows the permeability vs. fiber volume fraction in the direction parallel to the fibers. In the plot legend κ_{11} (1/1) represents

the principle permeability (κ_{11}) in the fiber direction of test one of the first preform sample and κ_{11} $(1/2)$ represents the principle permeability of the first test of the second preform sample. Figure 4-21 shows the permeability vs. fiber volume fraction for the direction transverse to the fibers. It is observed for both plots that the measured permeability values show the greatest variation at low fiber volume fractions (low compaction pressure) where the fiber volume fraction is very sensitive to small variations in pressure. At higher compaction pressures the fiber volume fraction becomes less sensitive to changes in pressure and therefore leads to more repeatable measurements. From Figure 4-20 it is seen that there is some variation in measurements at high fiber volume fraction (low resin pressure). As was discussed previously, at very low resin pressures, measurements become more difficult as dissolved air in the resin expands making flow rates difficult to measure

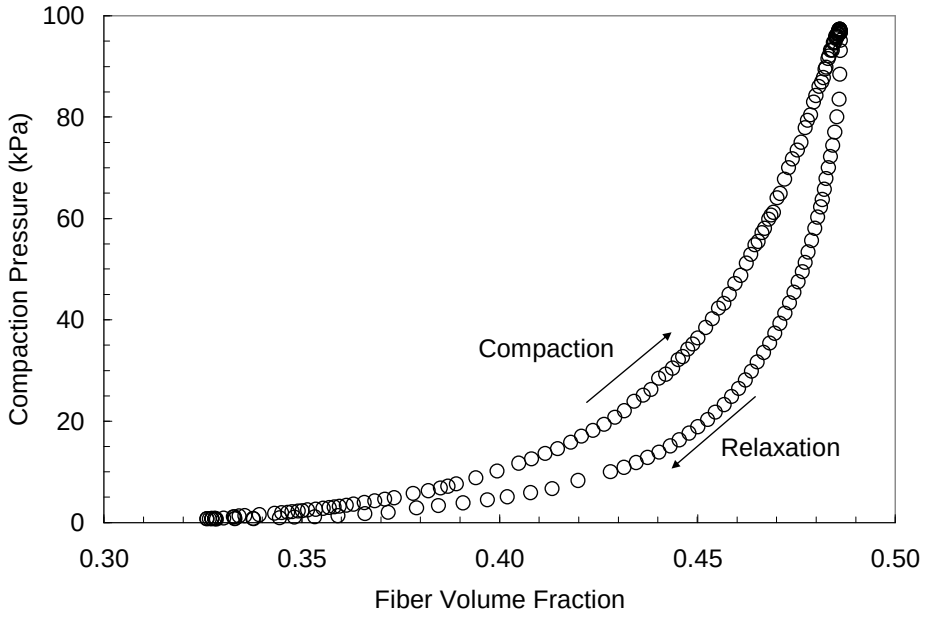

Figure 4-19 Compaction pressure versus fiber volume fraction for saturated uni-directional carbon preform.

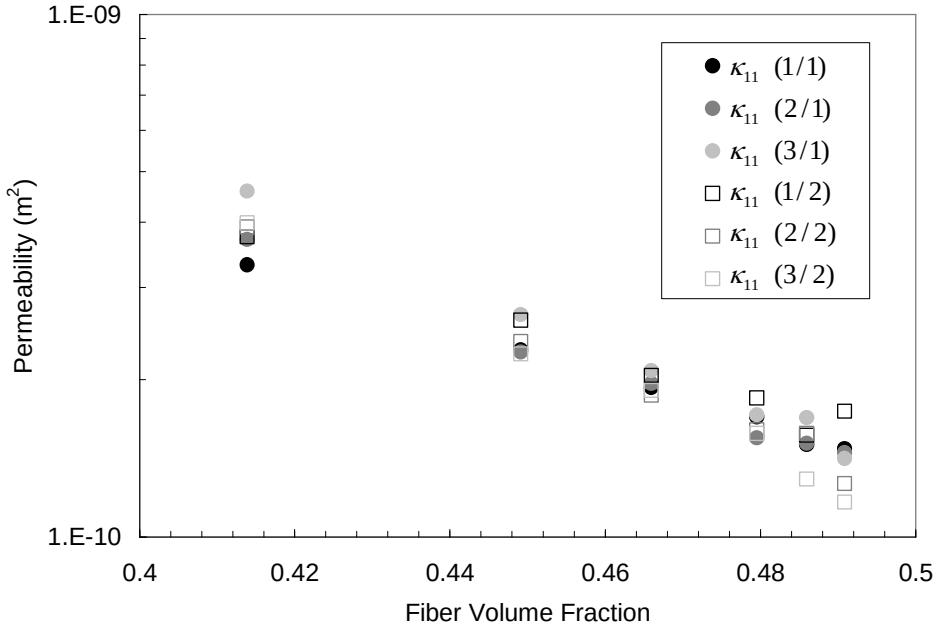

Figure 4-20 Uni-directional preform longitudinal (κ_{11}) permeability versus fiber volume fraction showing measurement repeatability.

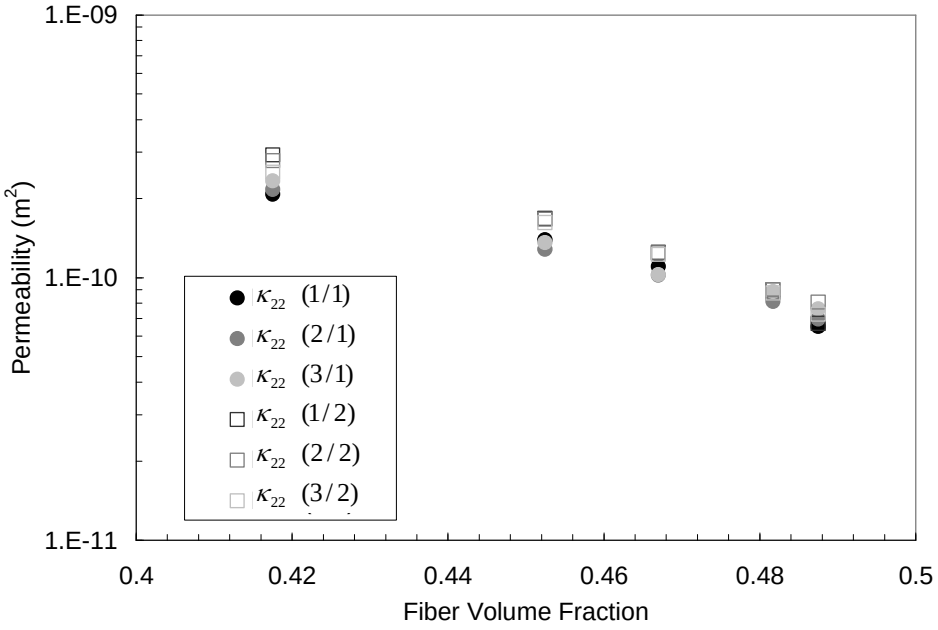

Figure 4-21 Uni-directional preform transverse permeability (κ_{22}) versus fiber volume fraction showing measurement repeatability.

Figure 4-22 shows the through thickness permeability versus fiber volume fraction at each pressure level for the uni-directional material. It is observed from the plot that the through thickness permeability is largely independent of the fiber volume fraction in comparison to the in-plane permeability. Some increase in permeability is observed for low fiber volume fraction values.

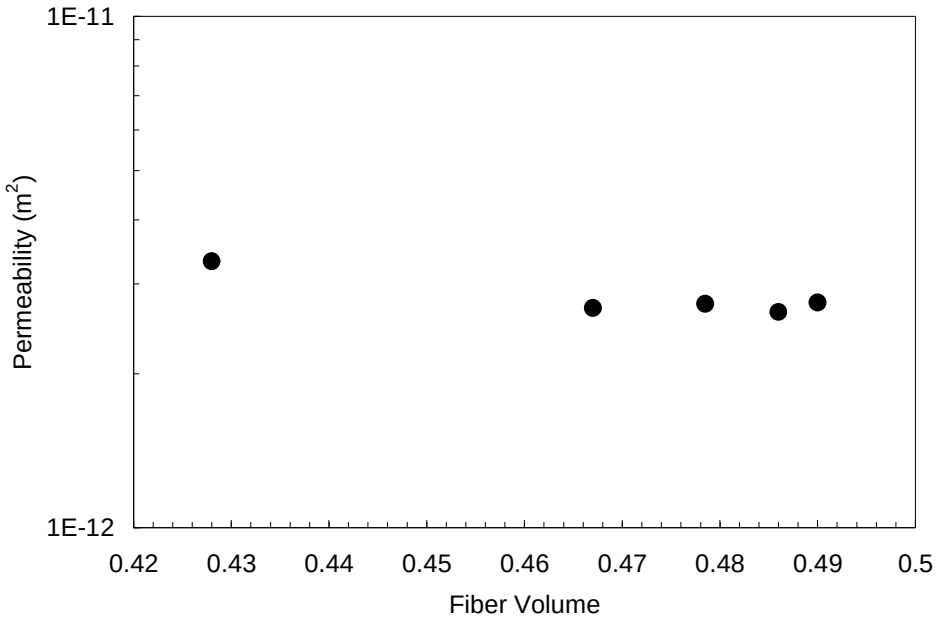

Figure 4-22 Through-thickness permeability (κ_{33}) for uni-directional fabric.

To investigate the effects of the deformable vacuum bag mold surface, a piece of acrylic was cut to the size of the preform sample and placed over the preform prior to the placement of the vacuum bag. Three permeability measurements were performed using the same uni-directional preform sample along the fiber direction with and without the acrylic plate. Modeling clay was used along the edges of the preform and acrylic plate to eliminate any racing of the test fluid along the edges. The permeability measurements for each case are shown in Figure 4-23. It is observed that the presence of the acrylic plate resulted in permeability values which were slightly higher than the permeability of the sample without the presence of the acrylic plate. The presence of the acrylic plate does not allow the vacuum bag to conform to the surface of the preform resulting in additional channels between the fiber tows at the

interface between the preform and the acrylic plate. It is expected that this effect would be less apparent in preforms having architectures with smooth surfaces. However, using a rigid surface to measure the permeability of flow distribution mediums, which have a very rough surface, would be expected to significantly alter the permeability measurements.

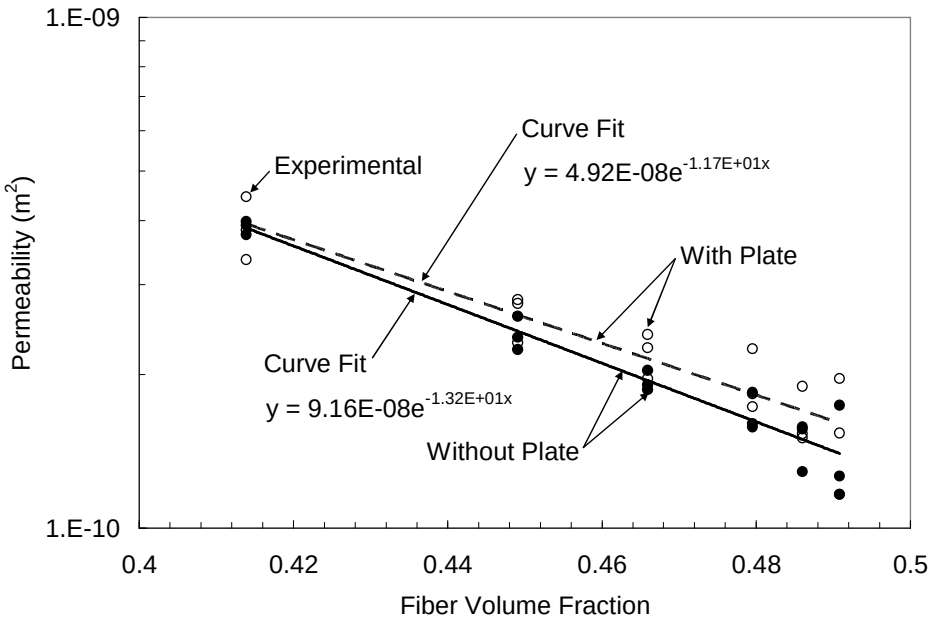

Figure 4-23 Uni-directional preform permeability versus fiber volume fraction with and without the rigid acrylic mold plate.

To assess the validity of the saturated flow permeability measurements a comparison was made with permeability measurements obtained using the unsaturated approach from Eq. (4.9). Unsaturated permeability measurements were performed longitudinal (κ_{11}) to the fibers as well as transverse (κ_{22}). Plots of $l^2\mu\phi/(2\Delta P)$

versus time for flow longitudinal and transverse to the fibers are shown in Figure 4-24 and Figure 4-25 respectively. The slope of the linear curve fit for infusions at five different fiber volume fractions represent the permeability at each fiber volume fraction. Figure 4-26 shows a comparison between the measured permeability values using the saturated and unsaturated flow conditions. It is seen from the figure that there is good agreement between the two measurement methods. The saturated measurement allows the same preform sample to be used throughout the entire procedure where as the unsaturated case requires the preparation and placement of a dry preform at each pressure level measurement. Using the saturated measurement significantly reduces time and effort to characterize the permeability of a material.

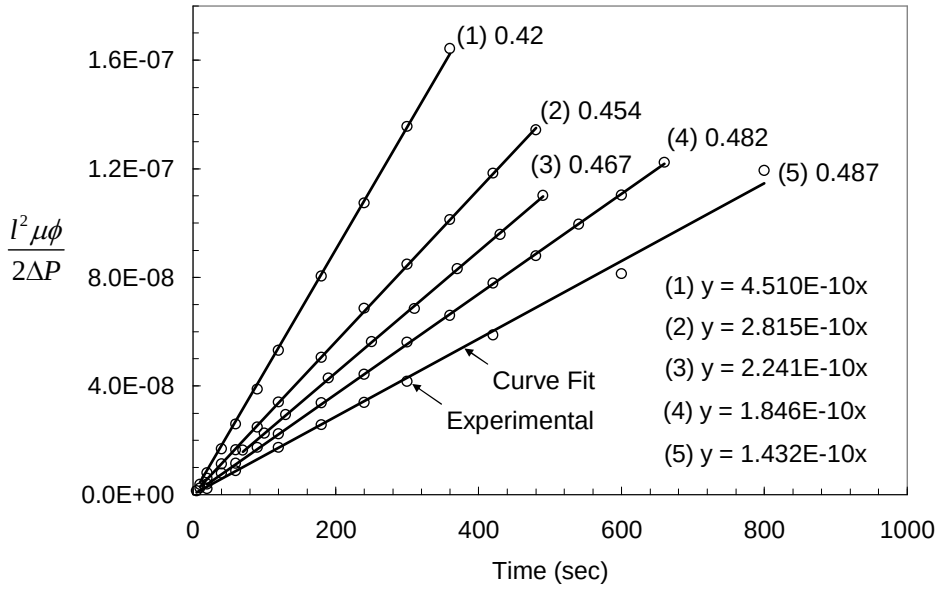

Figure 4-24 Plot of $l^2\mu\phi/(2\Delta P)$ versus time for five different fiber volume fractions where the slope of the linear curve fit represents the longitudinal permeability (κ_{11}).

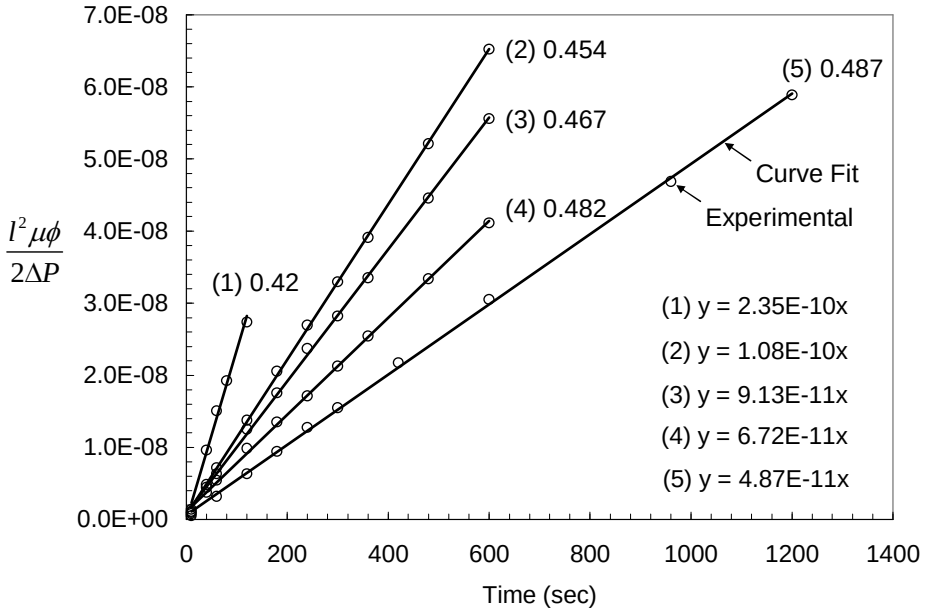

Figure 4-25 Plot of $l^2\mu\phi/(2\Delta P)$ versus time for five different fiber volume fractions where the slope of the linear curve fit represents the transverse permeability (κ_{22}).

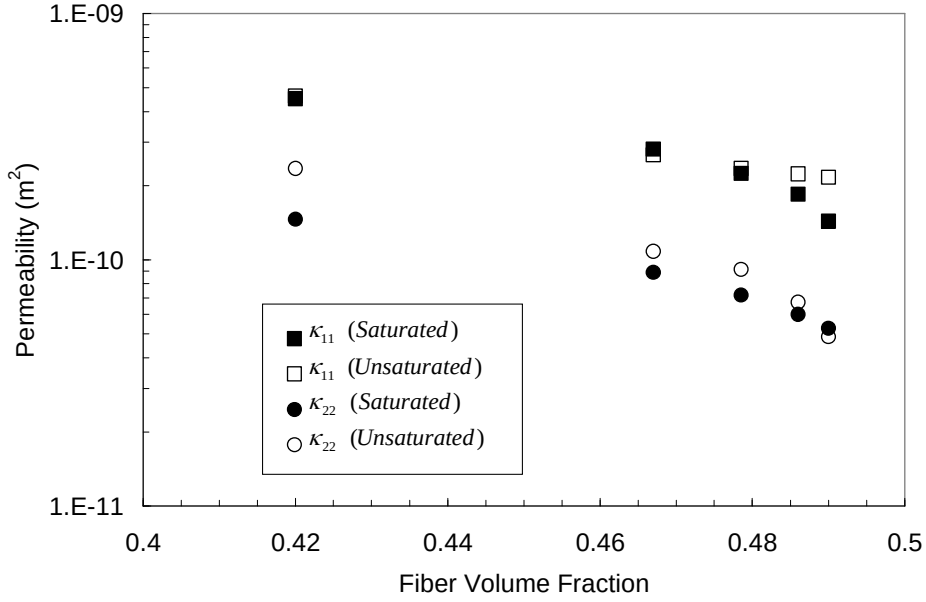

Figure 4-26 C-LA 1812-7 permeability vs. fiber volume comparison between saturated and unsaturated measurements.

4.4.1 Preform Materials

Compaction and permeability constitutive models are developed for two different preform materials and a laminate preform composed of these two preform materials. The preform materials consist of (1) uni-directional stitched carbon fabric and (2) triax stitched carbon fabric. The preform laminate is composed of 3 plies of triax material and 10 plies of uni-directional material such that the longitudinal fibers of the uni-directional material are transverse to the longitudinal fibers of the triax material. A description of each preform material is given in Table 4-2. Photographs of the uni-directional material showing the front and back surface of the fabric are given in Figure 4-27 and Figure 4-28 respectively. From the photos it is observed that the stitching on the top surface runs transverse to the fiber tows while the stitching on the bottom surface runs parallel to the longitudinal fiber tows. It is also observed from the back surface that the fiber tows are stitched to a light mat of random fiberglass fibers to hold the carbon fiber tows together. Photographs of the front and back surfaces of the triax material are shown in Figure 4-29 and Figure 4-30 respectively. From the figures it is observed that on the top surface the stitching runs transverse to the longitudinal fiber tows. On the back surface, where the fibers are oriented at a 45 degree angle, it is observed that the stitching runs parallel with the longitudinal fiber tows. The uni/triax laminate preform layup is given by $[\text{triax}/\text{uni}_4/\text{triax}/\text{uni}_4/\text{triax}/\text{uni}_2]$, where 33% of the laminate thickness consists of triax material and 67% of the thickness is uni-directional material. The preform represents half the thickness of a symmetric laminate which is considered in the following chapter.

Table 4-2 Preform Materials

Preform Material	*Laminated Ply Thickness (mm)*	*Areal Weight (kg/m^2)*	*Carbon Percent by Weight (0°/±45°/90°)*	*0° Fiber Type/Size*	*±45° Fiber Type/Size*
Uni	0.76	0.69	100/0/0	Tenax 24kSTS/24k	NA
Triax	1.27	1.23	50/50/0	T700/24k	T700/12k

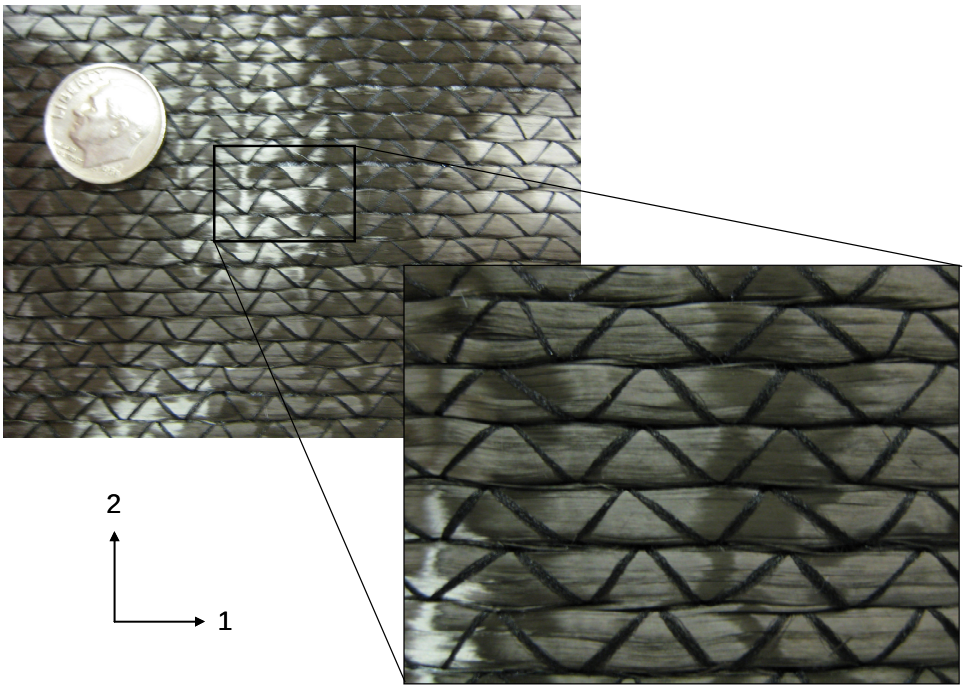

Figure 4-27 Photograph of the top surface of the uni-directional material showing the orientation of the fibers and stitching.

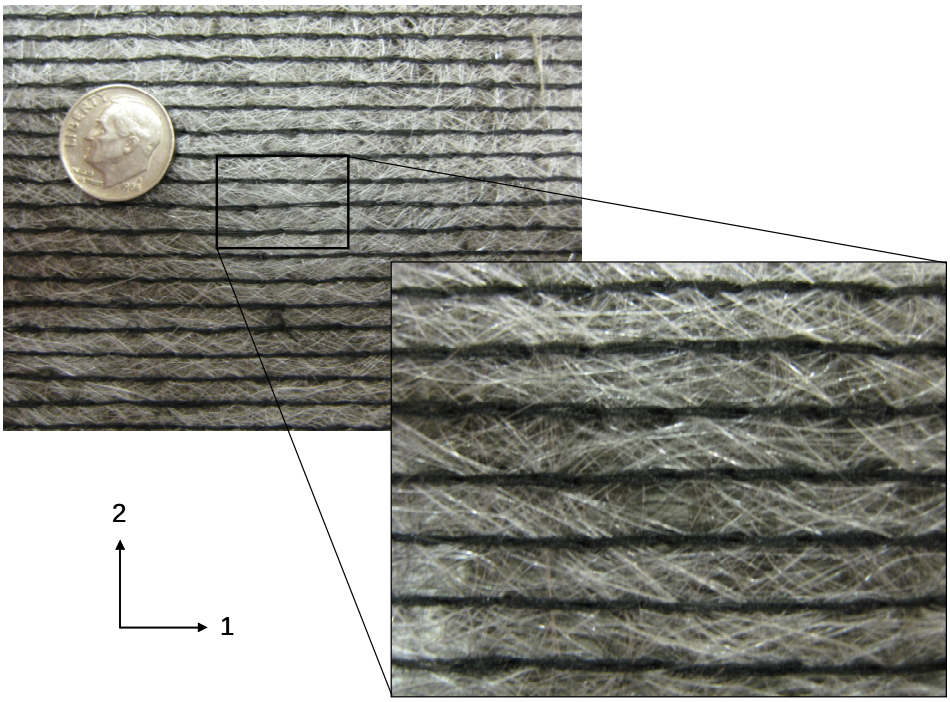

Figure 4-28 Photograph of the bottom surface of the uni-directional material showing the chopped fiber mat and the orientation of the stitching.

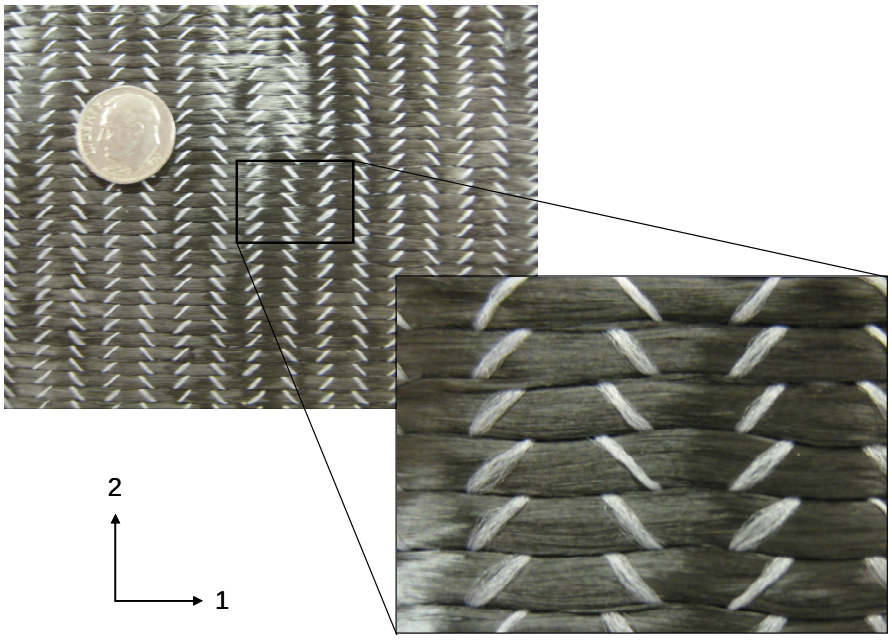

Figure 4-29 Photograph of the top surface of the triax material showing the fibers in the longitudinal direction as well as the stitching.

.

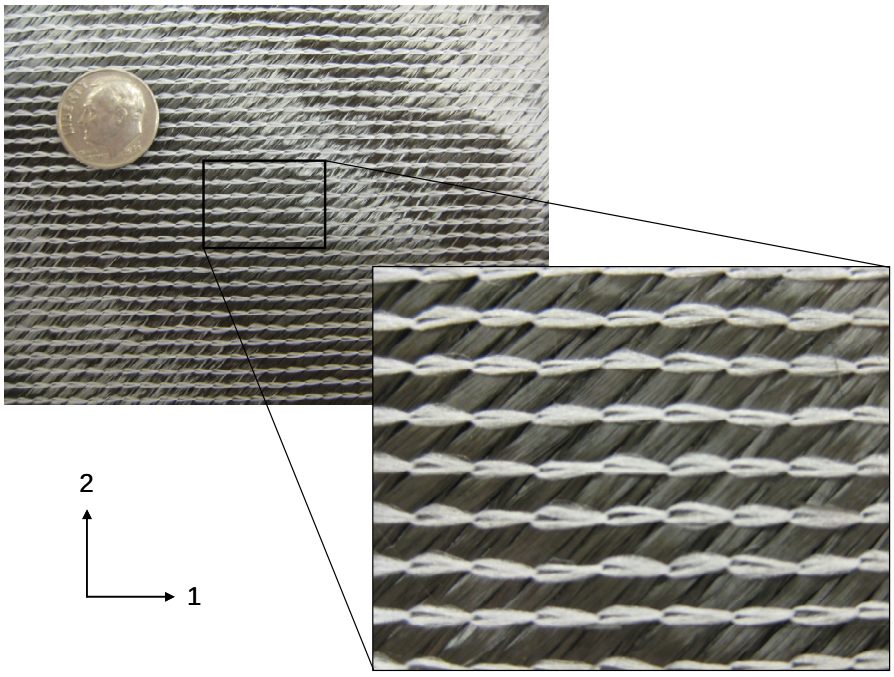

Figure 4-30 Photograph of the bottom surface of the triax material showing the fibers oriented at 45° as well as the stitching.

4.4.2 Compaction Models

Compaction models were developed for the three different preforms: (1) Three plies of uni-directional stitched carbon, (2) tow plies of triax stitched carbon, and (3) the uni/triax laminate consisting of 33% triax stitched carbon and 67% uni-directional carbon. To investigate the accuracy of existing models, experimental measurement were compared with curve fits using Gutowski's model [67] Eq. (4.15) as well as the power law model Eq. (4.16) previously described. The compaction experiments are performed using saturated preform samples. Plots of compaction pressure (P_c) versus fiber volume fraction for each of the preforms showing both compaction as well as

relaxation is given in Figure 4-31 through Figure 4-36. For each preform the experimental compaction and relaxation results are compared with Gutowski's model and a power law curve fit. From the plots it is observed that the relationship between the compaction pressure and fiber volume fraction is very dependent on whether the preform is undergoing compaction or relaxation. This is important to note since the fibers are undergoing relaxation during the resin filling stage of the VARTM process and then undergo compaction during the resin bleeding stage. Therefore it is important to have models for both compaction and relaxation curves. From Figure 4-31, Figure 4-33, and Figure 4-35 it is observed that Gutowski's model does a very poor job of matching the experimental compaction data. However from the same figures it is seen that the power law curve fit does a good job of matching the experimental data for all three preforms. Although Gutowski's model was developed for preform compaction, from Figure 4-32 and Figure 4-36 it is seen that Gutowski's model does a fair job of matching the experimental relaxation data for the uni-directional and uni/triax laminate preforms while from Figure 4-34 it is seen that Gutowski's model does a poor job of matching the experimental relaxation data for the triax preform. It is also observed that the power law curve fit does a poor job of matching the experimental relaxation data for any of the preforms. The parameters used for Gutowski's model as well as the power law curve fit are given in Table 4-3.

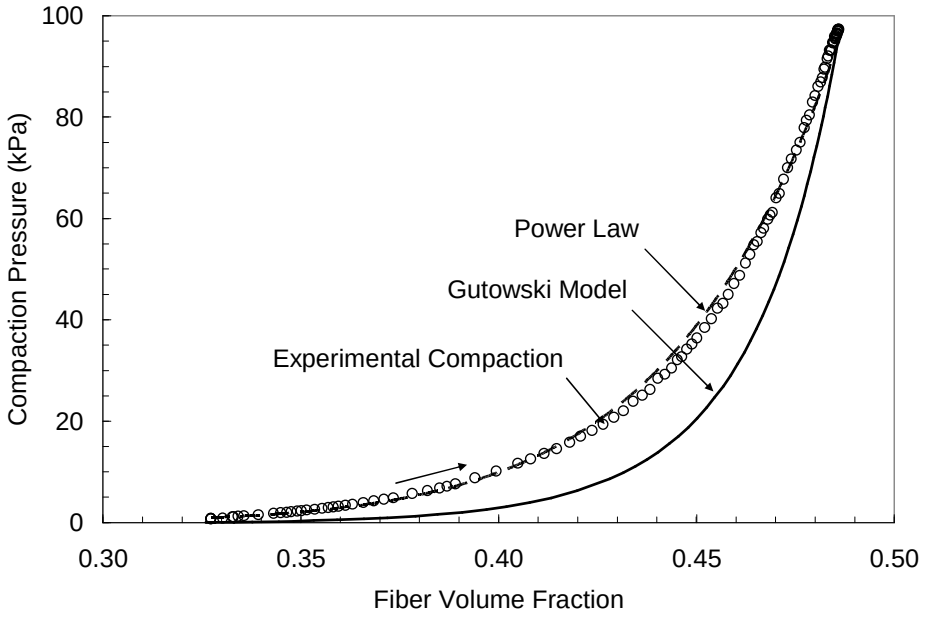

Figure 4-31 Plot of compaction pressure versus fiber volume fraction for uni-directional stitched carbon showing experimental compaction results as well as power law and Gutowski's models.

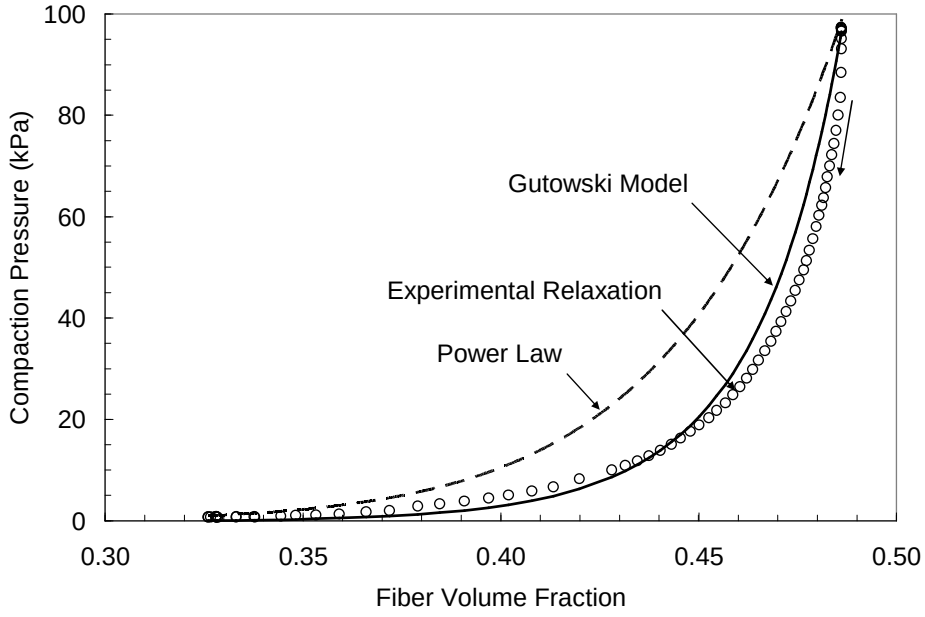

Figure 4-32 Plot of compaction pressure versus fiber volume fraction for uni-directional stitched carbon showing experimental relaxation results as well as power law and Gutowski's models.

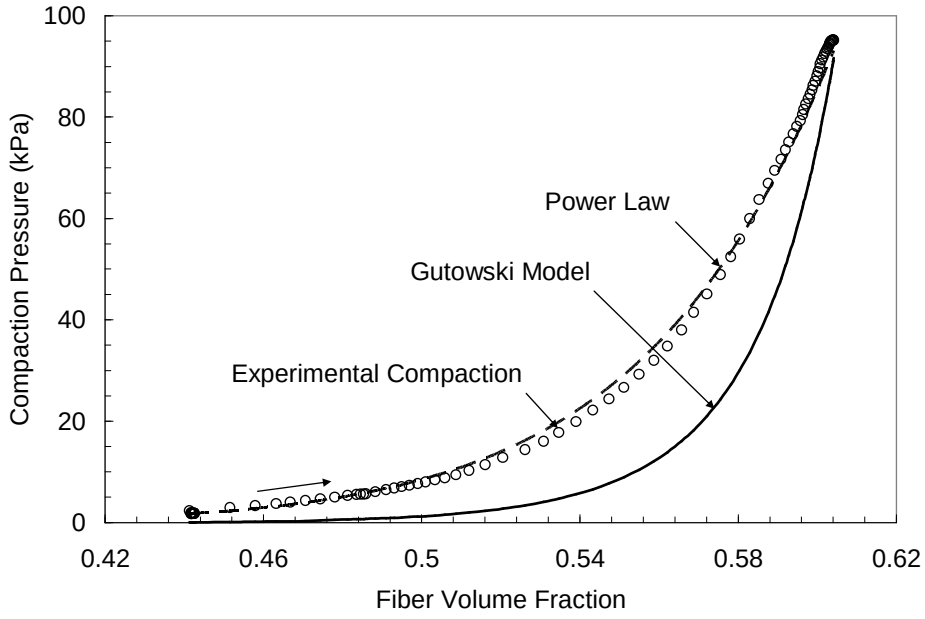

Figure 4-33 Plot of compaction pressure versus fiber volume fraction for triax stitched carbon showing experimental compaction results as well as power law and Gutowski's models.

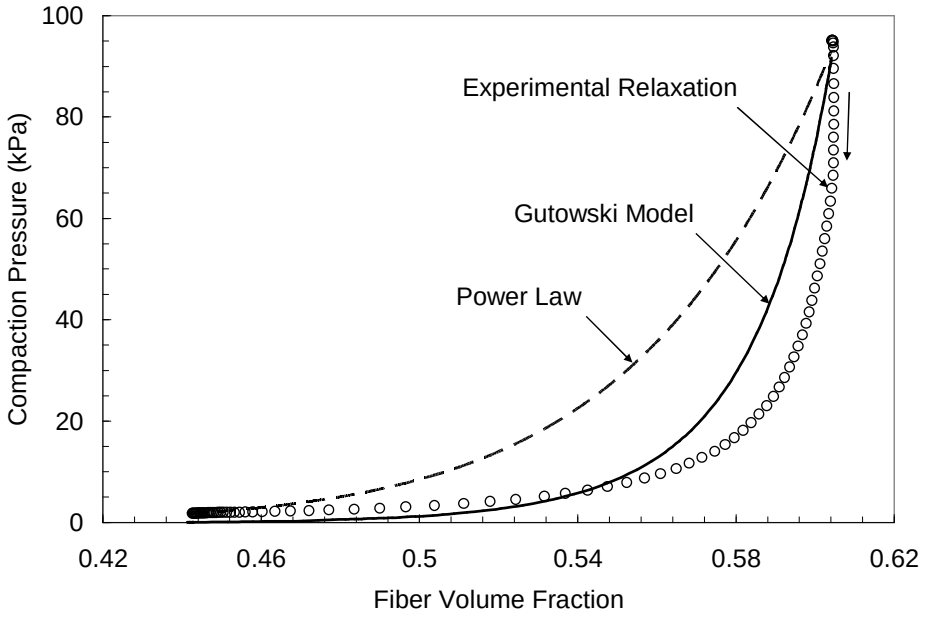

Figure 4-34 Plot of compaction pressure versus fiber volume fraction for triax stitched carbon showing experimental relaxation results as well as power law and Gutowski's models.

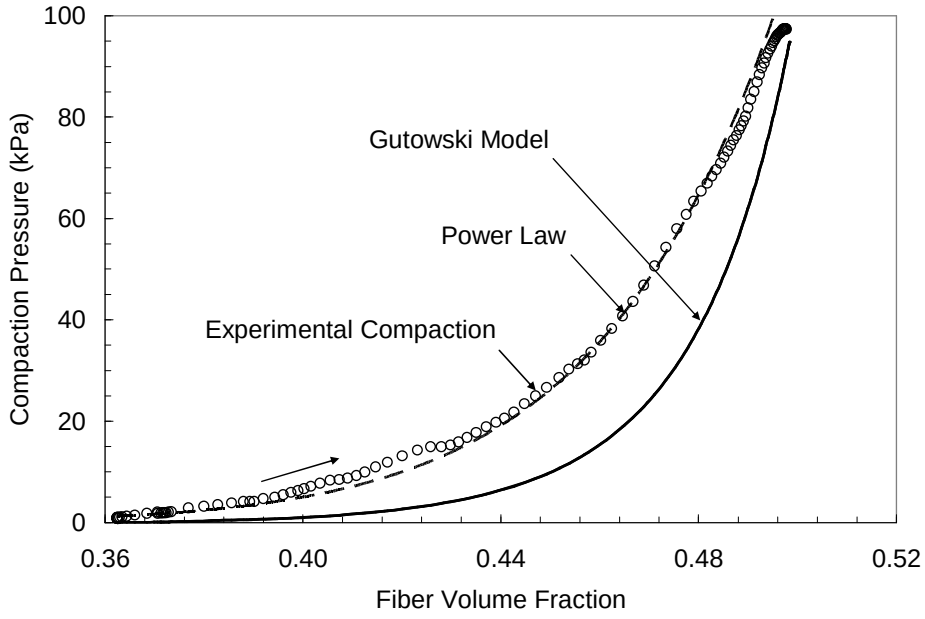

Figure 4-35 Plot of compaction pressure versus fiber volume fraction for uni/triax laminate showing experimental compaction results as well as power law and Gutowski's models.

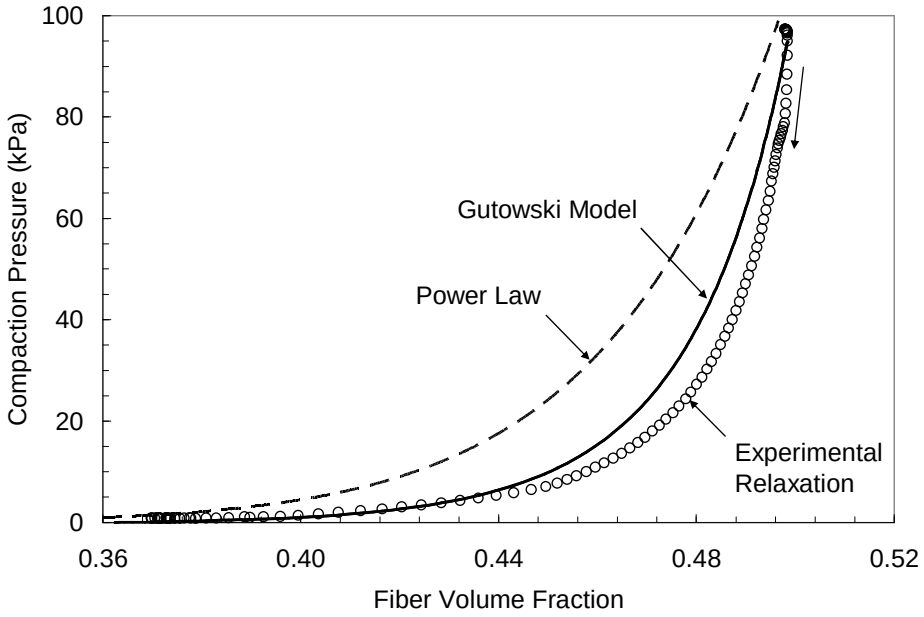

Figure 4-36 Plot of compaction pressure versus fiber volume fraction for uni/triax laminate showing experimental relaxation results as well as power law and Gutowski's models.

Table 4-3 Compaction model parameters

Preform Material	A_s	V_o	V_a	B
Uni-directional	0.63	0.32	0.6	0.087
Triax	0.019	0.43	0.7	0.084
Uni/Triax Laminate	0.048	0.36	0.6	0.070

To increase the accuracy of the simulations to be performed, manual curve fitting for both the compaction and relaxation curve for each material was performed using a combination of polynomials and exponential terms. Plots showing the experimental measurements with the curve fits for each preform type are given in Figure 4-37 through Figure 4-39. It is seen from the plots that the curve fits match the experimental data very well. The expression for each of the curve fits is given in Table 4-4. For convenience for simulation the curve fits are expressed in terms of resin pressure rather than compaction pressure. It is also observed that the triax preform (Figure 4-38) shows a much higher degree of hysteresis in comparison to the uni-directional preform (Figure 4-37). Not surprising, the uni/triax which is composed of 67% uni-directional material, shows a hysteresis patterns (Figure 4-39) which closely resembles that for the uni-directional material. It is also observed that the triax material achieves much higher fiber volume fraction levels in comparison to the uni-directional material. The effects of the higher fiber volume fraction on the permeability of the material will be shown.

Table 4-4 Compaction and Relaxation Constitutive Models

Model	***Uni-directional***	***Eq.***
Compaction	$V_f = 0.486 - 0.035\left(\frac{P}{100}\right) - 0.058\left(\frac{P}{100}\right)^3 + \left(1 - e^{0.226P}\right)\left(10^{-11}\right)$	(4.21)
Relaxation	$V_f = 0.486 - 0.066\left(\frac{P}{100}\right)^3 + \left(1 - e^{0.2975P}\right)\left(10^{-14}\right)$	(4.22)
Model	***Triax***	***Eq.***
Compaction	$V_f = 0.605 - 0.037\left(\frac{P}{100}\right) - 0.008\left(\frac{P}{100}\right)^2 - 0.053\left(\frac{P}{100}\right)^3 + \left(1 - e^{0.229P}\right)\left(10^{-11}\right)$	(4.23)
Relaxation	$V_f = 0.605 - 0.01\left(\frac{P}{100}\right)^2 - 0.015\left(\frac{P}{100}\right)^4 - 0.054\left(\frac{P}{100}\right)^9 + \left(1 - e^{0.51P}\right)\left(10^{-23}\right)$	(4.24)
Model	***Uni/Triax Laminate***	***Eq.***
Compaction	$V_f = 0.498 - 0.035\left(\frac{P}{100}\right) - 0.046\left(\frac{P}{100}\right)^3 + \left(1 - e^{0.178P}\right)\left(10^{-9}\right)$	(4.25)
Relaxation	$V_f = 0.498 - 0.0035\left(\frac{P}{100}\right) - 0.046\left(\frac{P}{100}\right)^3 + 0.02\left(\frac{P}{100}\right)^8 + \left(1 - e^{0.185P}\right)\left(10^{-9}\right)$	(4.26)

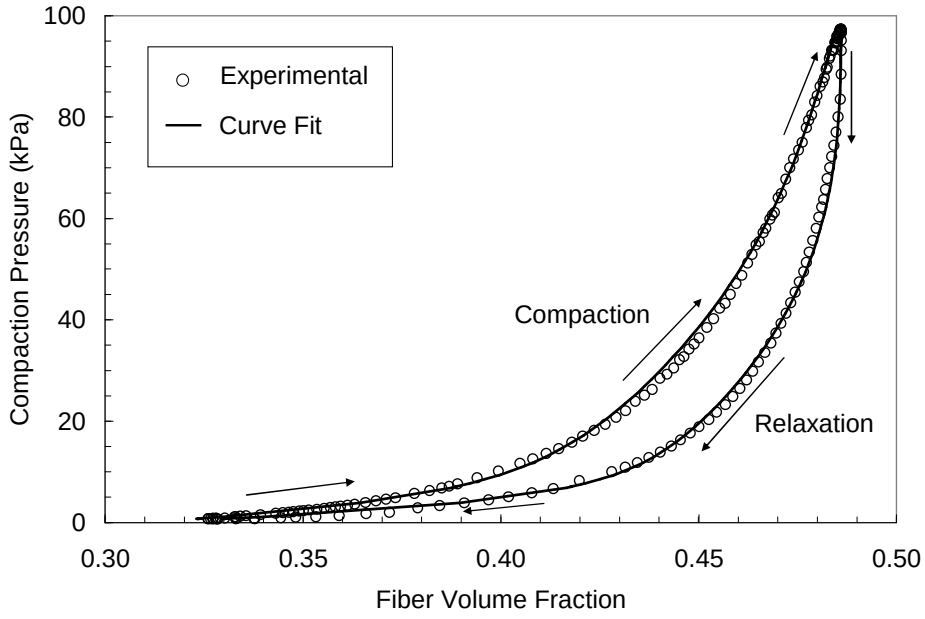

Figure 4-37 Compaction pressure versus fiber volume fraction with curve fits for the uni-directional carbon preform.

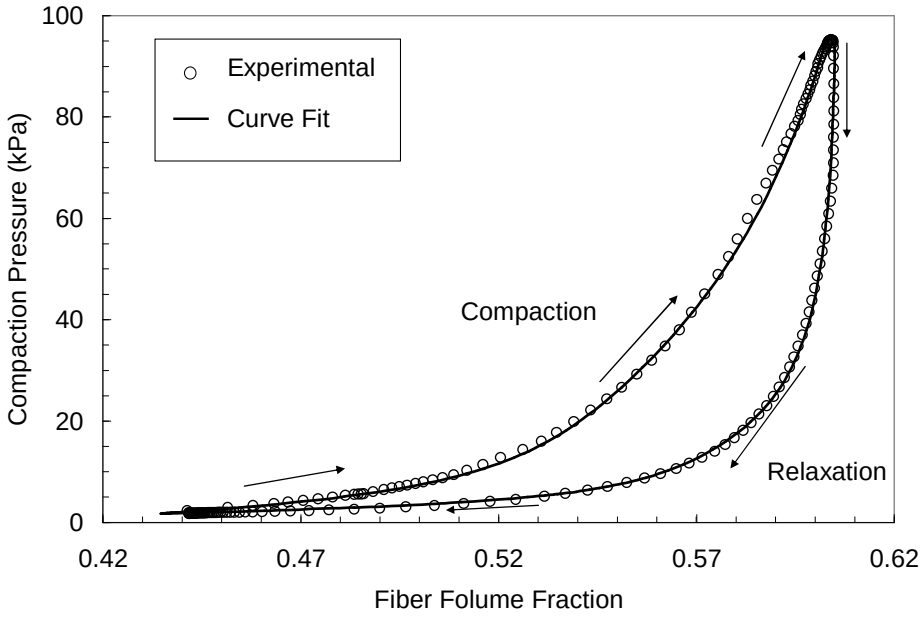

Figure 4-38 Compaction pressure versus fiber volume fraction with curve fits for the triax carbon preform.

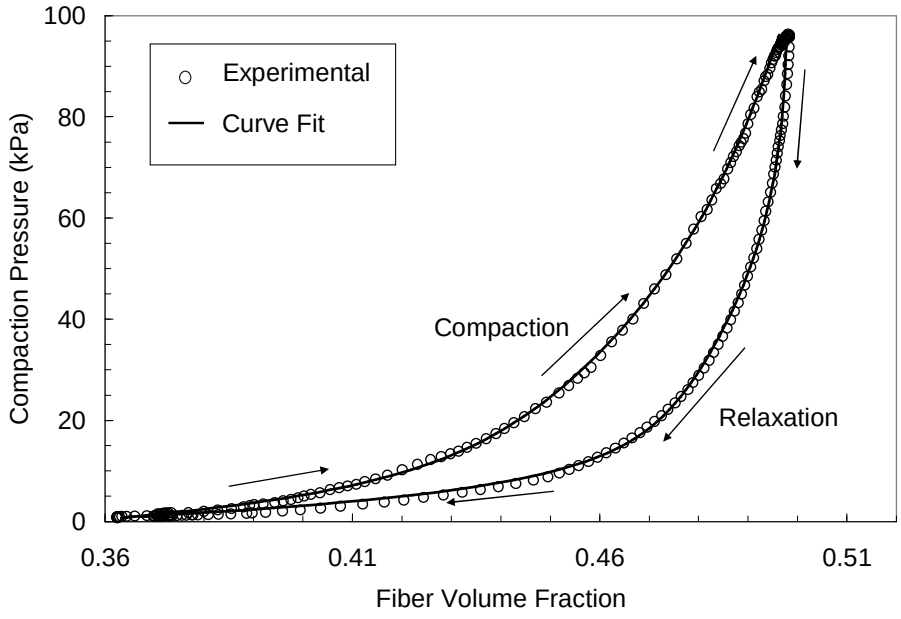

Figure 4-39 Compaction pressure versus fiber volume fraction with curve fits for the uni/triax laminate preform.

As has been shown there are separate curves for compaction and relaxation of the preform. Additional compaction experiments show that there are an infinite number of compaction and relaxation curves for each preform bounded by the compaction and relaxation curves shown in Figure 4-37 through Figure 4-39. To reveal these other curves additional compaction experiments were performed using the saturated triax preform. For this experiment the preform was compacted under full vacuum pressure at which point the compaction pressure was partially reduced allowing the preform to relax before being compacted again under full vacuum. This was repeated for several compaction pressure levels with the experimental measurements being given in Figure 4-40. From the plot two observations are made. First it is seen that as the preform goes through each additional compaction cycle

greater compaction occurs leading to higher ultimate fiber volume fractions. Secondly it is observed that for each new starting point a compaction curve exists which does not follow the original compaction or relaxation curve. To better understand this observation the additional compaction from each cycle is subtracted from the data to create a common ultimate compaction level. The results are plotted in Figure 4-41. For clarity the compaction cycles from Figure 4-41 are illustrated in Figure 4-42. From the figure it is seen that for each starting pressure corresponding to points B through F a different compaction curve exists which originates on the relaxation curve and goes to the maximum compaction level at point G. Similarly as shown in Figure 4-43 there are an infinite number of relaxation curves which originate along the compaction curve and go to the unloaded fiber volume fraction given by point A.

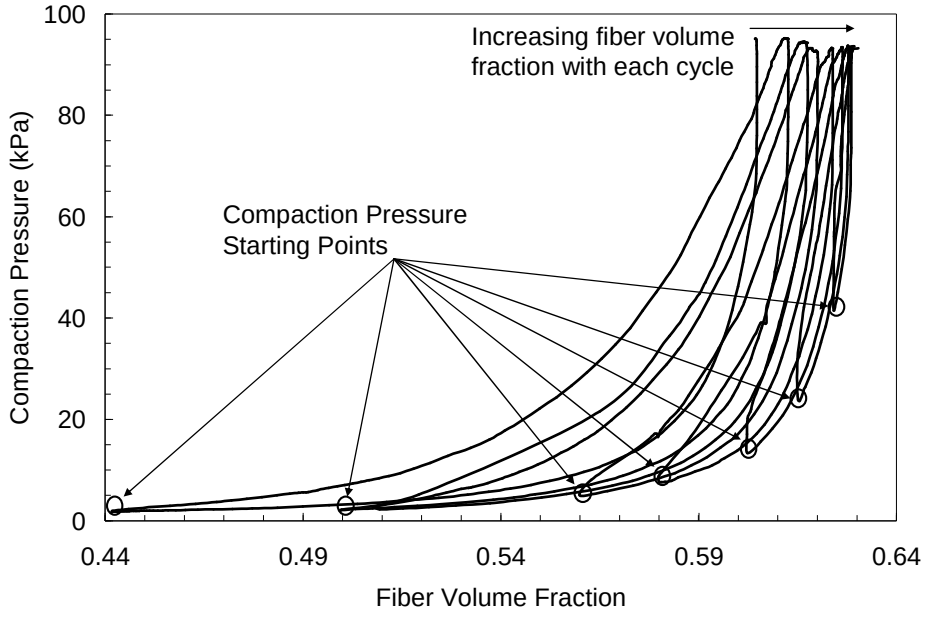

Figure 4-40 Experimental measurements showing alternative compaction curves for stitched triax carbon preform.

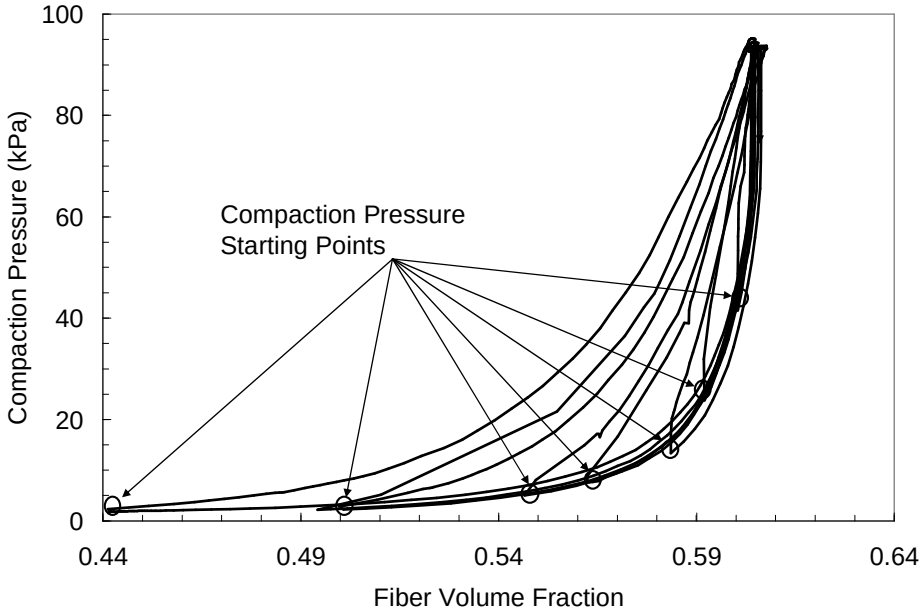

Figure 4-41 Experimental measurements showing alternative compaction curves for stitched triax carbon preform with common ultimate compaction point.

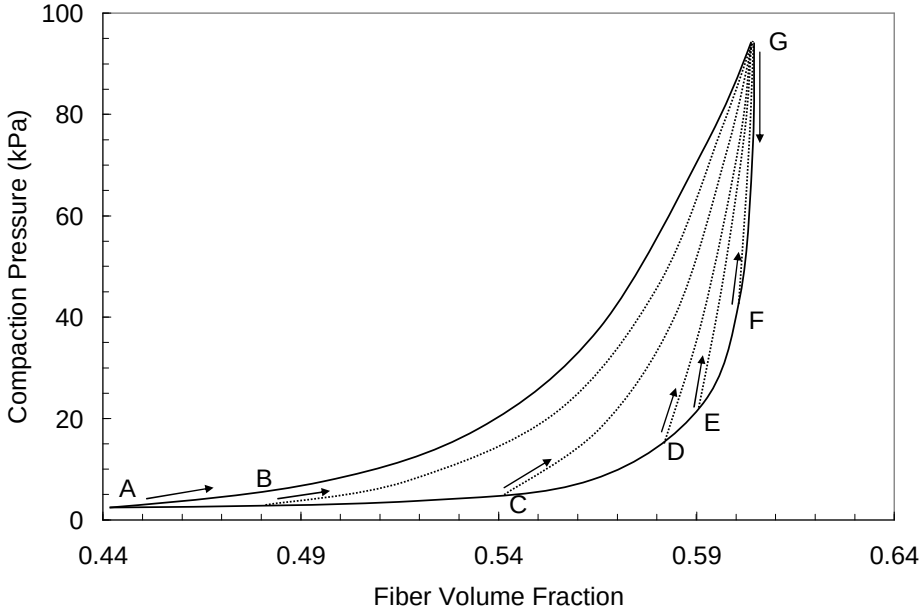

Figure 4-42 Illustration of alternate compaction paths for the stitched triax carbon preform.

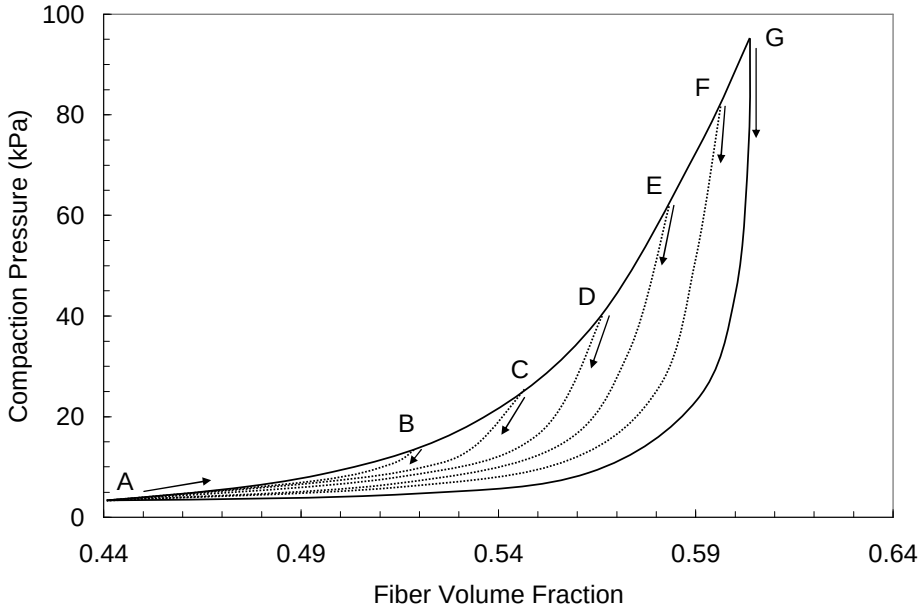

Figure 4-43 Illustration of alternate relaxation paths for the stitched triax carbon preform.

Additional compaction experiments were conducted using the uni/triax laminate preform to study the effects of compaction cycling of dry performs and saturation. The dry preform was cycled five times through full compaction followed by one compaction cycle after being infused with oil. A plot of compaction pressure versus fiber volume fraction for the dry and wet compaction cycles is given in Figure 4-44. From the figure it is observed that very little additional compaction occurs for compaction cycling of the dry preform with significant additional compaction occurring for one compaction cycle of the wetted preform. As has been shown by others [54,55], saturated preforms show higher levels of compaction due to the lubrication of preform fibers.

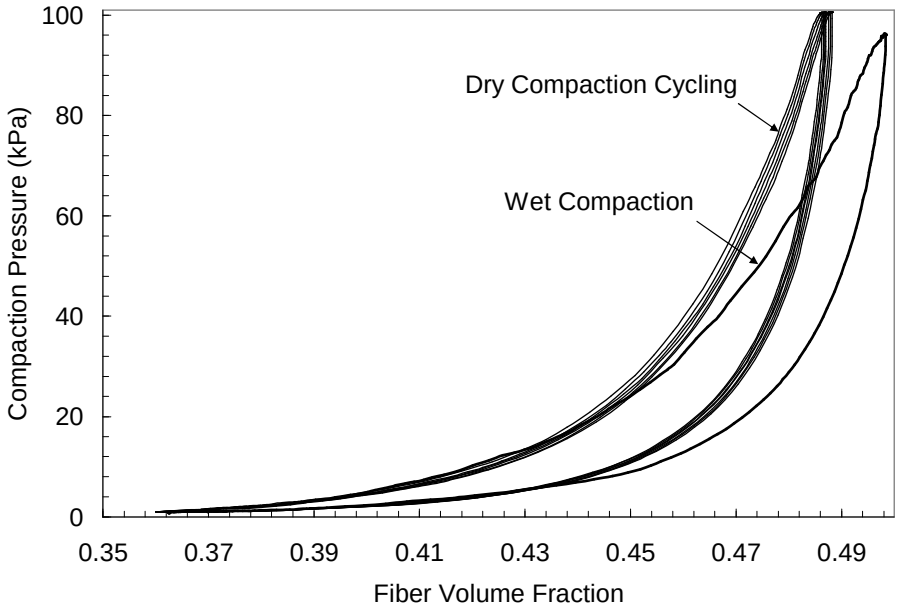

Figure 4-44 Experimental compaction measurements for a dry and saturated preform sample of the uni/triax laminate.

4.4.3 Permeability Models

Permeability versus fiber volume fraction models have been developed for each of the three preforms. Permeability models were developed for all three principal directions (κ_{11}, κ_{22}, and κ_{33}) for all three performs (uni, triax, and uni/triax). Photographs of the test setup for the triax and uni/triax laminate preforms are shown in Figure 4-45 and Figure 4-46 respectively. From Figure 4-45 it is seen that a thin metal shim is attached to the surface of the vacuum bag to provide a smooth surface for the displacement measurements. The thickness of the shim is accounted for in determining the fiber volume fraction of the preform. From Figure 4-46 it is observed that due to the thickness (11.41 mm) of the uni/triax laminate preform, flow springs having a diameter of 12.5 mm were used at the inlet and outlet to provide in-plane

flow across the total thickness of the laminate. It is also observed from the figure that the flow front is uniform across the width of the preform during initial filling.

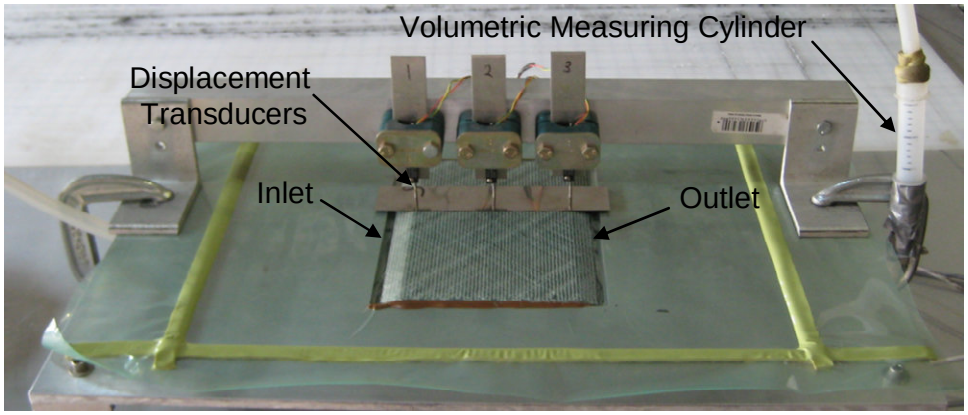

Figure 4-45 Photograph of the test setup for measuring in-plane permeability for the triax preform.

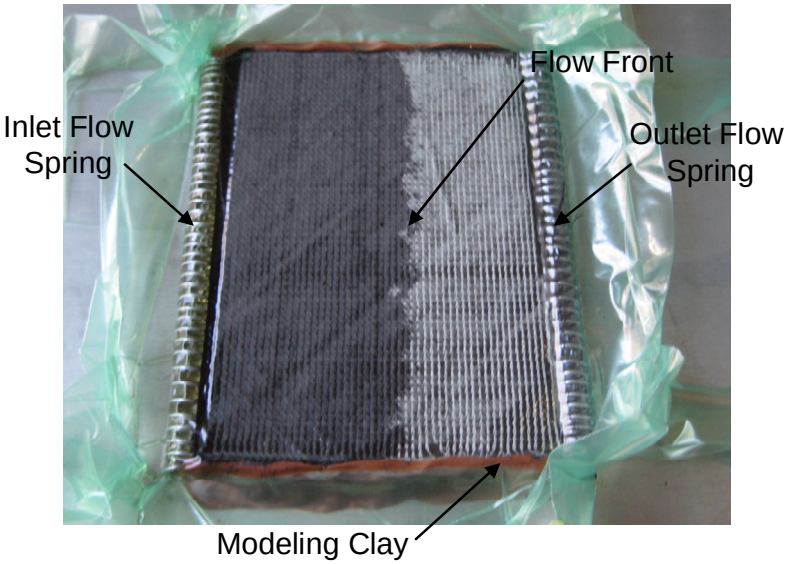

Figure 4-46 Photograph of the test setup for measuring the in-plane permeability of the uni/triax laminate preform.

To verify that the pressure field is linear along the length of the preform sample in accordance with Eq. (4.11) a plot of the measured resin pressure at the inlet, center of the preform, and outlet for each measurement at each pressure level for the triax and uni/triax performs are presented in Figure 4-47 and Figure 4-48 respectively. As was observed for the uni-directional material, the pressure field is shown to be very near linear at each pressure level for both performs.

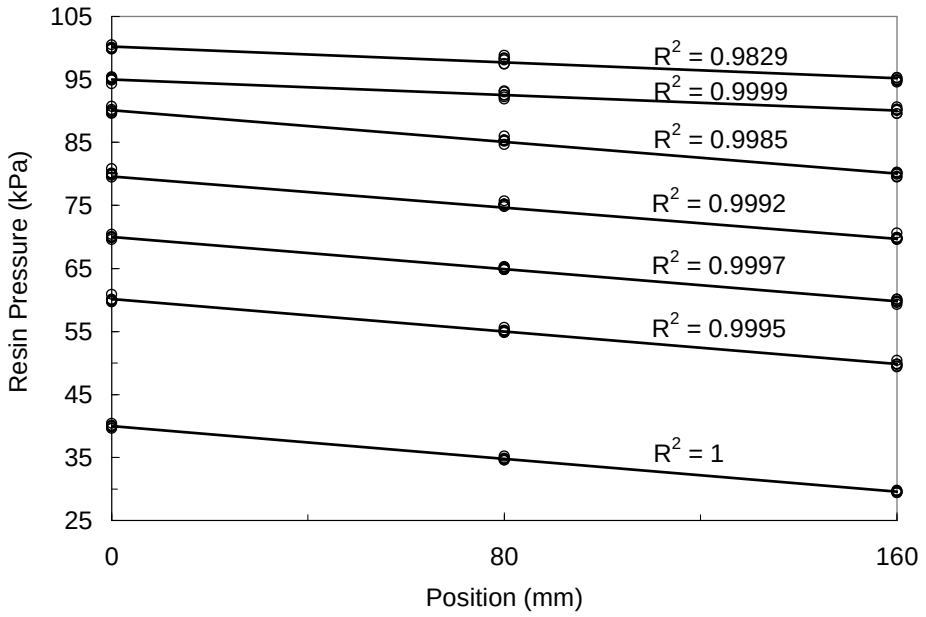

Figure 4-47 Plot of the resin pressure along the length of the triax test sample at each pressure level.

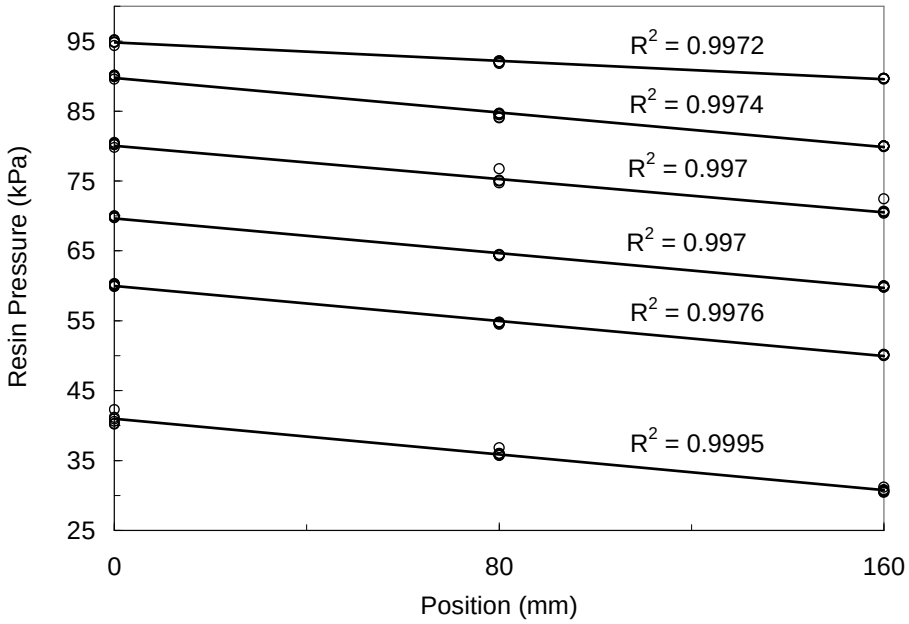

Figure 4-48 Plot of the resin pressure along the length of the uni/triax laminate test sample at each pressure level.

Plots of experimental permeability measurements along with the curve fits for each preform material are presented. The principle in-plane longitudinal (κ_{11}), transverse (κ_{22}), and through-thickness (κ_{33}) permeability measurements for the uni-directional preform are given in Figure 4-49, Figure 4-50, and Figure 4-51 respectively. The principle in-plane longitudinal (κ_{11}), transverse (κ_{22}), and through-thickness (κ_{33}) permeability measurements for the triax preform are given in Figure 4-52, Figure 4-53, and Figure 4-54 respectively. The principle in-plane longitudinal (κ_{11}), transverse (κ_{22}), and through-thickness (κ_{33}) permeability measurements for the uni/triax preform are given in Figure 4-55, Figure 4-56, and Figure 4-57 respectively. Each permeability model is described by an exponential curve fit [70]. The curve fit expressions for each material are given in the plots as well as Table 4-5.

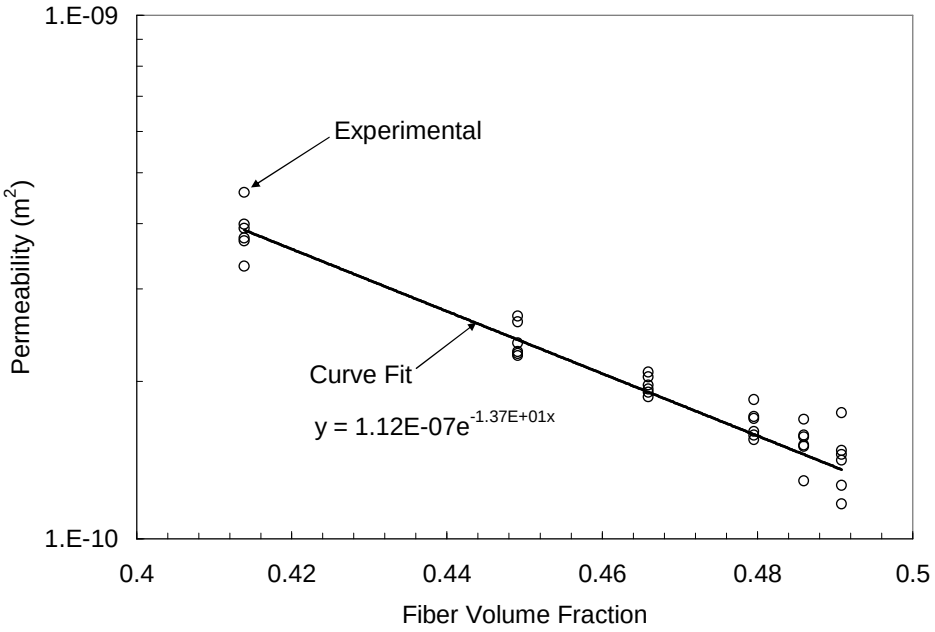

Figure 4-49 Uni-directional material longitudinal (κ_{11}) permeability versus fiber volume fraction.

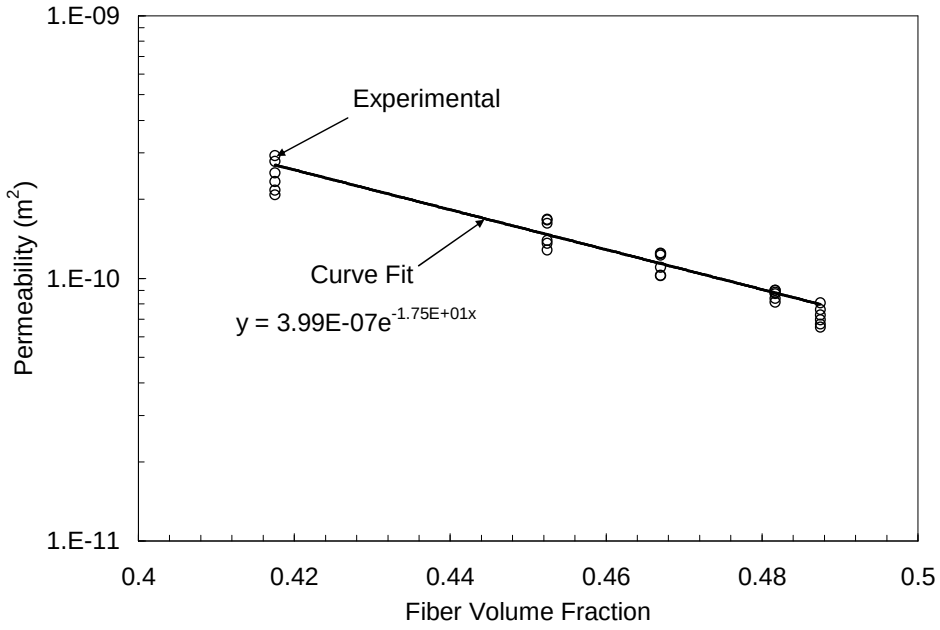

Figure 4-50 Uni-directional material transverse (κ_{22}) permeability versus fiber volume fraction.

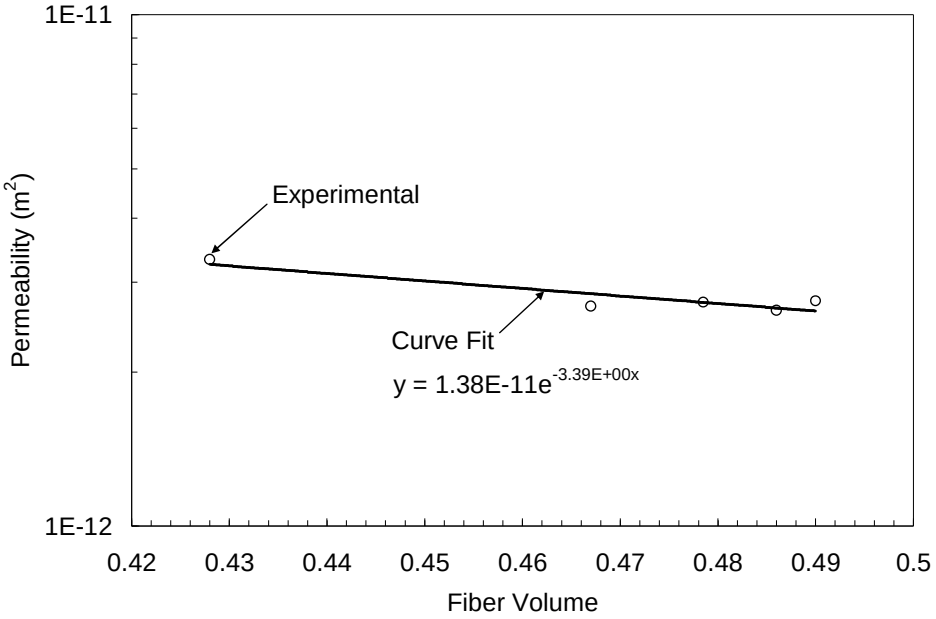

Figure 4-51 Uni-directional material through-thickness (κ_{33}) permeability versus fiber volume fraction.

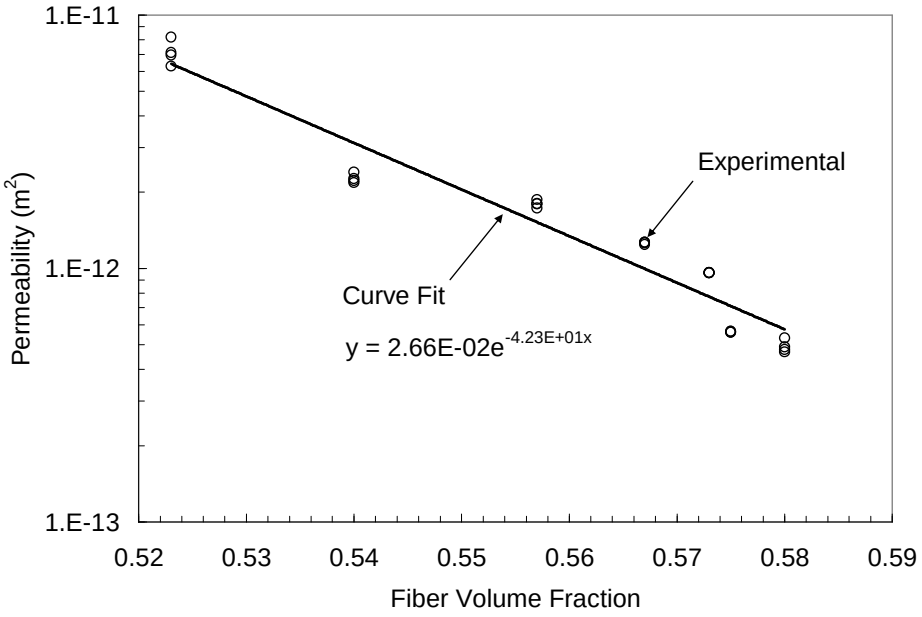

Figure 4-52 Triax material longitudinal (κ_{11}) permeability versus fiber volume fraction.

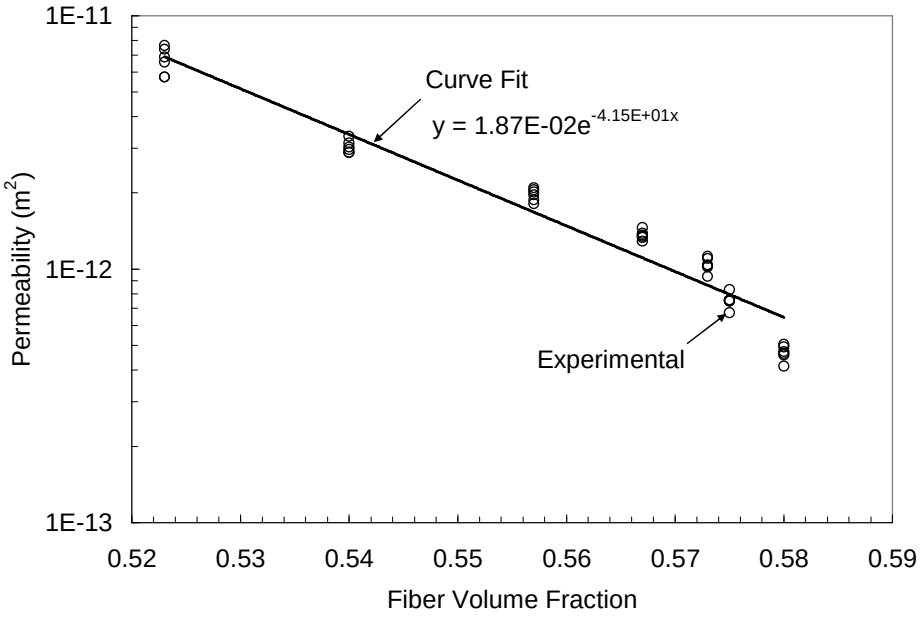

Figure 4-53 Triax material transverse (κ_{22}) permeability versus fiber volume fraction.

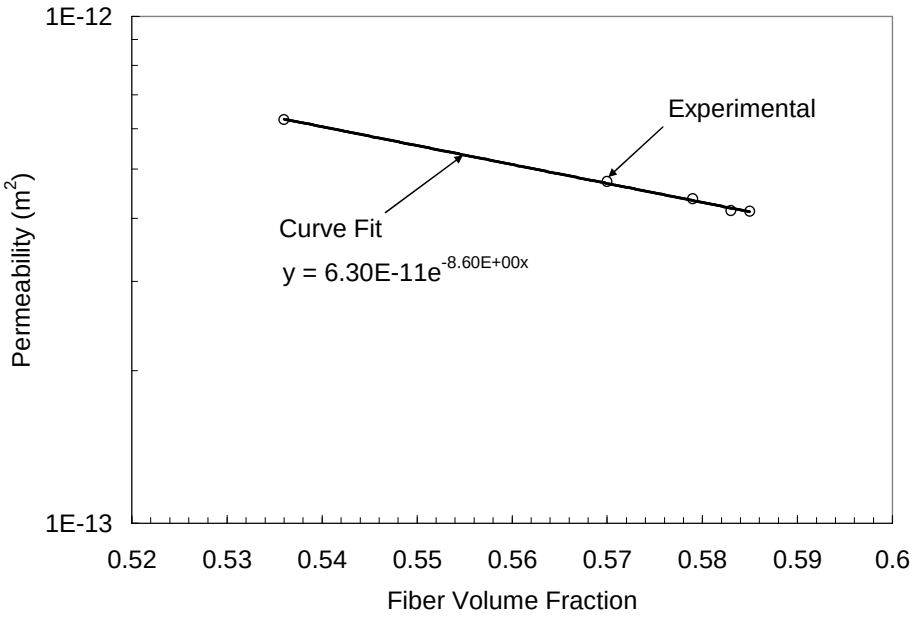

Figure 4-54 Triax material through-thickness (κ_{33}) permeability versus fiber volume fraction

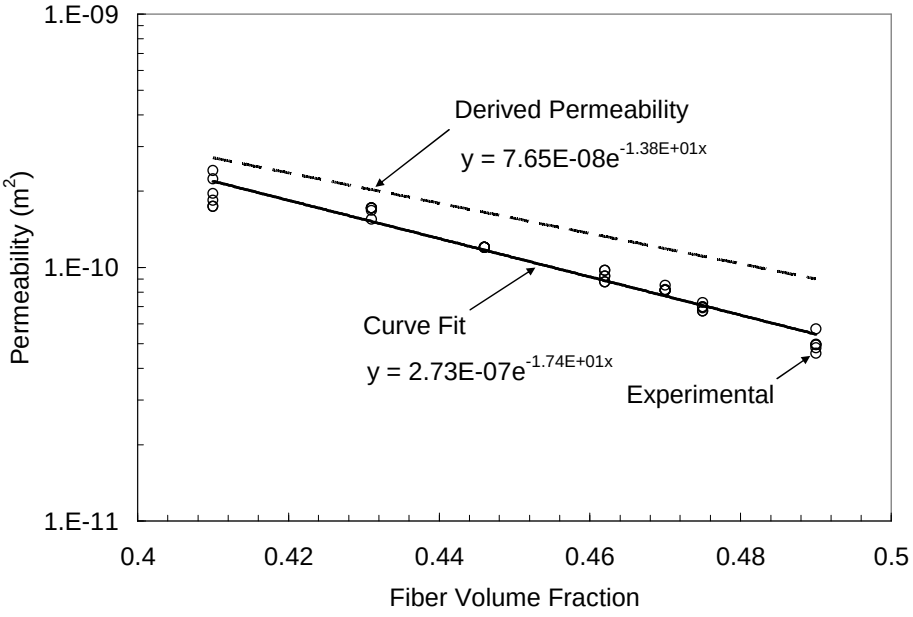

Figure 4-55 Uni/Triax laminate transverse (κ_{11}) measured and derived effective permeability versus fiber volume fraction.

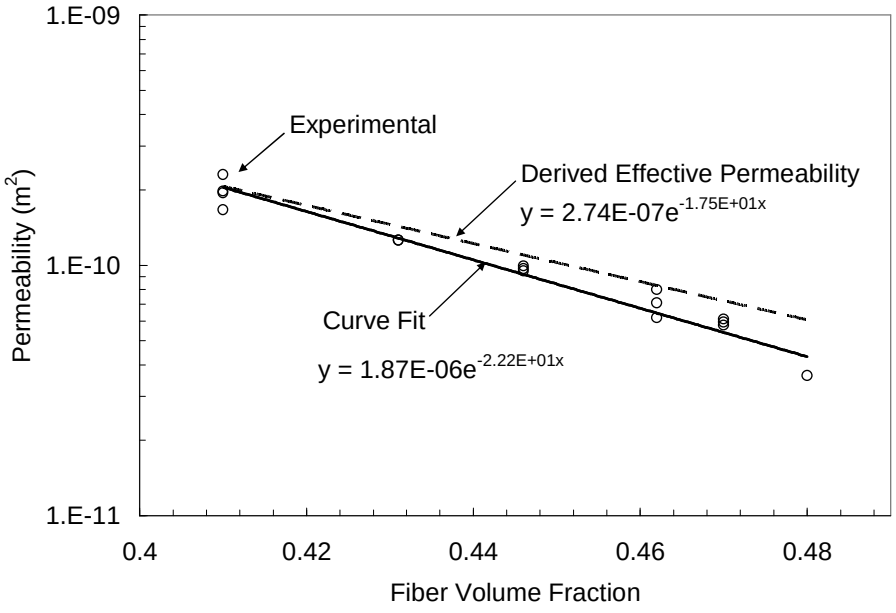

Figure 4-56 Uni/Triax laminate transverse (κ_{22}) measured and derived effective permeability versus fiber volume fraction.

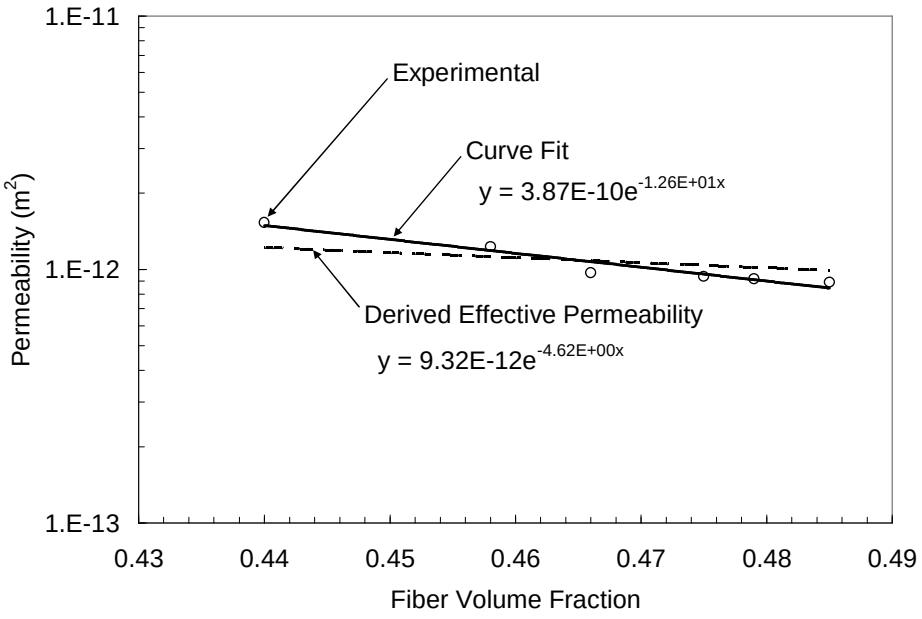

Figure 4-57 Uni/Triax laminate through-thickness (κ_{33}) measured and derived effective permeability versus fiber volume fraction.

Due to the need for permeability data for the many available fiber architectures the National Institute of Standards and Technology (NIST) has developed a database of permeability measurements for different materials. Currently the database is limited to glass materials [71]. However for comparison purposes a uni-directional glass fabric (ACC57) has a permeability along the fiber direction of 1.6e-10 m^2 at a fiber volume fraction of 0.45. A different uni-directional glass fabric (MDSR06) has a permeability transverse to the fibers of 2.0e-10 m^2 at a fiber volume fraction of 0.52. This same material has a through thickness permeability of 4.0e-12m^2 at a fiber volume fraction of 0.5.

Table 4-5 Permeability Model Expressions

Material	*Constitutive Model*	*Eq.*
Uni-directional	$\kappa_{11} = \left(1.12e^{-13.7V_f}\right)\left(10^{-7}\right)$	(4.27)
	$\kappa_{22} = \left(3.99e^{-17.5V_f}\right)\left(10^{-7}\right)$	(4.28)
	$\kappa_{33} = \left(1.38e^{-3.39V_f}\right)\left(10^{-11}\right)$	(4.29)
Triax	$\kappa_{11} = \left(2.66e^{-42.3V_f}\right)\left(10^{-2}\right)$	(4.30)
	$\kappa_{22} = \left(1.87e^{-41.5V_f}\right)\left(10^{-2}\right)$	(4.31)
	$\kappa_{33} = \left(6.30e^{-8.6V_f}\right)\left(10^{-11}\right)$	(4.32)
Uni/Triax Laminate	$\kappa_{11} = \left(2.73e^{-17.4V_f}\right)\left(10^{-7}\right)$	(4.33)
	$\kappa_{22} = \left(1.87e^{-22.2V_f}\right)\left(10^{-6}\right)$	(4.34)
	$\kappa_{33} = \left(3.87e^{-12.6V_f}\right)\left(10^{-10}\right)$	(4.35)

A "Rule of Mixtures" [106] approach may be used to derive effective in-plane and through-thickness permeability values for preforms consisting of multiple layers having different permeabilities. For in-plane flow, the flow rate (Q) in each layer will differ depending on the thickness (t) and the permeability (κ) of each layer. Considering a preform consisting of two different layers as shown in Figure 4-58 the flow rate in each layer is described by

$$Q_1 = \frac{t_1 \kappa_1}{\mu} \frac{dP}{dx}, \tag{4.36}$$

and

$$Q_2 = \frac{t_2 \kappa_2}{\mu} \frac{dP}{dx}. \tag{4.37}$$

The effective flow rate (Q_{eff}) for the preform is the summation of the flow rate from each individual layer expressed as

$$Q_{eff} = Q_1 + Q_2. \tag{4.38}$$

The effective flow rate is expressed in terms of the total preform thickness and an effective in-plane permeability given by

$$Q_{eff} = \frac{t \kappa_{eff}}{\mu} \frac{dP}{dx}. \tag{4.39}$$

By substituting equations (4.36), (4.37), and (4.39) into (4.38) and recognizing that the pressure gradient and viscosity in each layer are equal, the in-plane effective permeability is expressed by

$$\kappa_{eff} = \frac{t_1}{t} \kappa_1 + \frac{t_2}{t} \kappa_2. \tag{4.40}$$

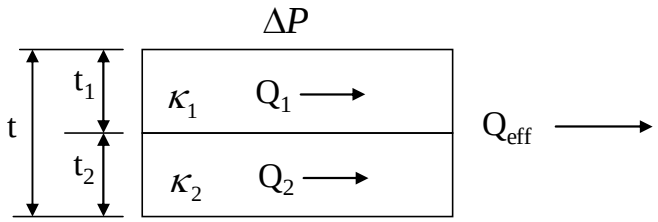

Figure 4-58 Illustration of in-plane flow for a preform with multiple layers having different permeability.

The through-thickness effective permeability is derived by recognizing that the superficial flow rate (q) is constant through the entire preform thickness as shown in Figure 4-59 and is expressed by

$$q = \frac{\kappa_1}{\mu}\frac{\Delta P_1}{t_1} = \frac{\kappa_2}{\mu}\frac{\Delta P_2}{t_2} = \frac{\kappa_{eff}}{\mu}\frac{\Delta P}{t}. \tag{4.41}$$

The pressure change across each layer is given by

$$\Delta P_1 = \frac{q\mu t_1}{\kappa_1}, \tag{4.42}$$

and

$$\Delta P_2 = \frac{q\mu t_2}{\kappa_2}, \tag{4.43}$$

The pressure drop across the entire thickness is expressed by

$$\Delta P = \frac{q\mu t}{\kappa_{eff}}, \tag{4.44}$$

where the effective through-thickness permeability is introduced. The total pressure drop through the thickness of the preform is the summation of the pressure change across each layer given by

$$\Delta P = \Delta P_1 + \Delta P_2 . \tag{4.45}$$

Substituting equations (4.42), (4.43), and (4.44) into (4.45) and recognizing that the superficial flow rate and viscosity are equal for each layer, the effective permeability is expressed as

$$\frac{1}{\kappa_{eff}} = \frac{t_1}{t\kappa_1} + \frac{t_2}{t\kappa_2} . \tag{4.46}$$

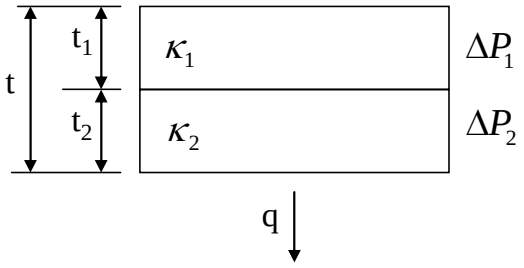

Figure 4-59 Illustration of through thickness flow for a perform with multiple layers having different permeability

By using the Rule of Mixtures the effective in-plane and through-thickness permeabilities were calculated for the uni/triax laminate preform and compared with experimental measurements. The effective principle permeabilities for the uni/triax laminate are shown in Figure 4-55 through Figure 4-57. The predicted effective permeability values show good agreement with the experimental measurements with the longitudinal effective permeability showing the greatest discrepancy.

For comparison purposes the curve fits for each principle direction for each preform type are plotted at the same scale. The curve fits for the uni-directional, triax, and uni/triax laminate preforms are given in Figure 4-60, Figure 4-61, and Figure 4-62 respectively. From Figure 4-60 and Figure 4-61 it is observed that the permeability of the uni-directional material is considerably greater than that for the triax material. From looking at the slope of the curves it is also observed that the triax material is much more sensitive to fiber volume fraction. From the compaction results it was observed that the triax preform fiber volume fraction was much higher than the uni-directional material explaining the difference in permeability for the two materials For the uni-directional material it is seen that the longitudinal permeability (κ_{11}) is slightly higher than the transverse permeability (κ_{22}). For the triax and uni/triax performs the longitudinal (κ_{11}) and transverse (κ_{22}) permeabilities are very similar. The through-thickness permeability (κ_{33}) for each preform is found to be much less sensitive to fiber volume fraction in comparison to the in-plane permeability values.

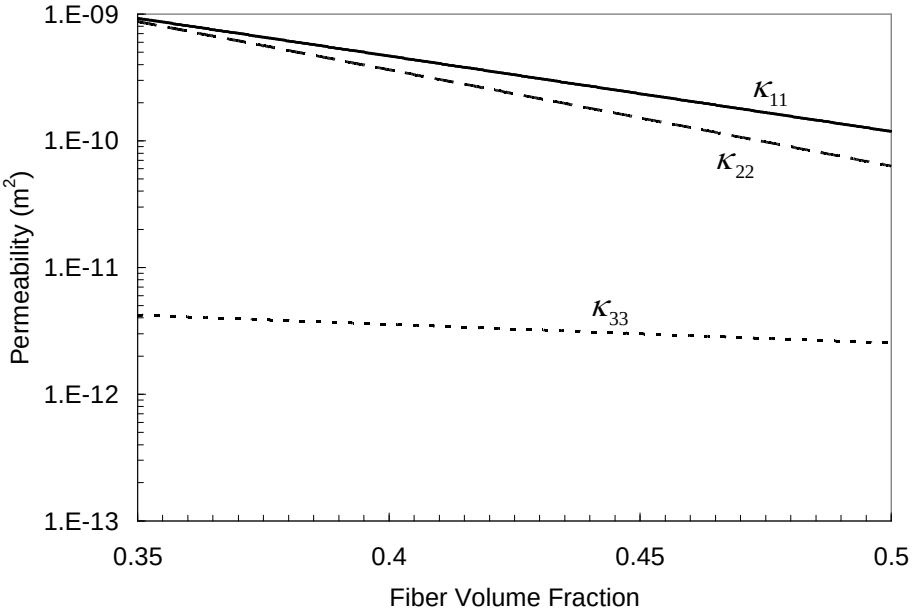

Figure 4-60 Plot of permeability versus fiber volume fraction showing curve fits for all three principle directions for the uni-directional preform.

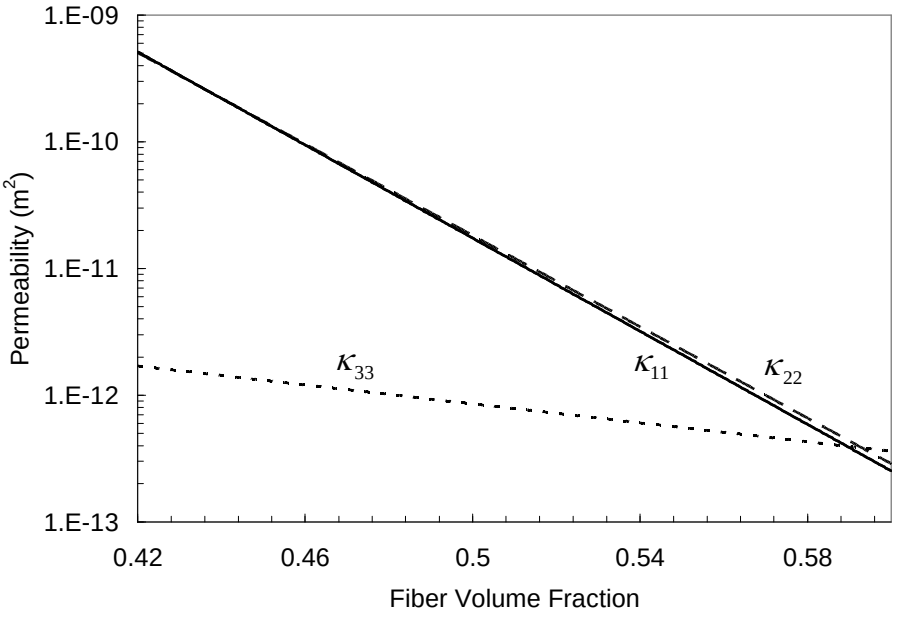

Figure 4-61 Plot of permeability versus fiber volume fraction showing curve fits for all three principle directions for the triax preform.

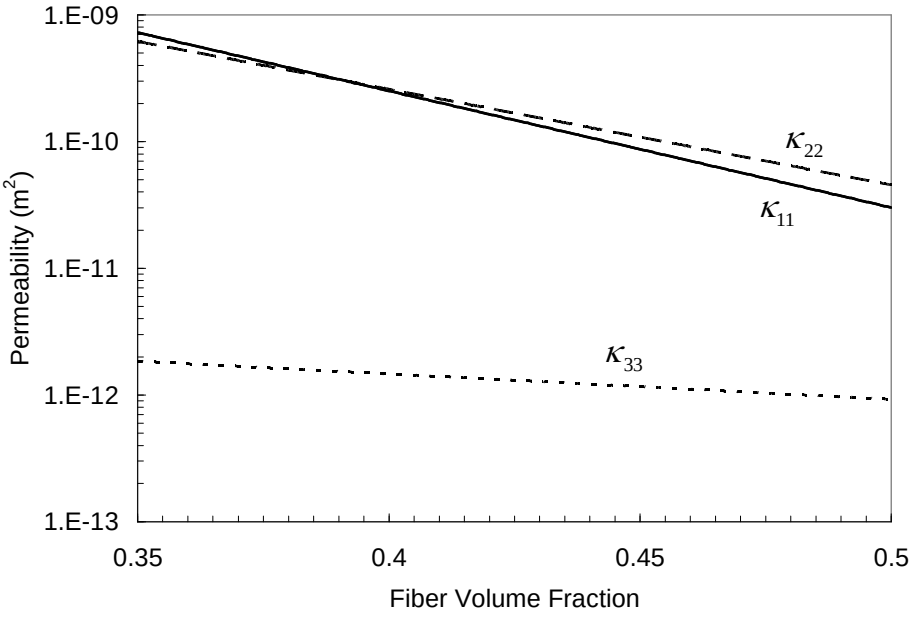

Figure 4-62 Plot of permeability versus fiber volume fraction showing curve fits for all three principle directions for the uni/triax laminate preform.

4.4.4 Flow Distribution Mesh

In addition to characterizing the preform compaction and permeability, the permeability of the resin distribution mesh must also be known to simulate VARTM processes such as SCRIMP which use flow distribution layers. Several different types of flow distribution mesh may be used in the SCRIMP process, ranging from highly porous random fiber mats, knitted nylon materials, to open mesh materials. The first two types of flow distribution materials are compressible similar to fiber preforms whereas the open mesh materials are relatively non compressible unless several layer are used in which case some compaction may occur due to nesting. This research considers non compressible open mesh flow distribution layers. A photograph of the flow distribution mesh considered in this study is given in Figure 4-63.

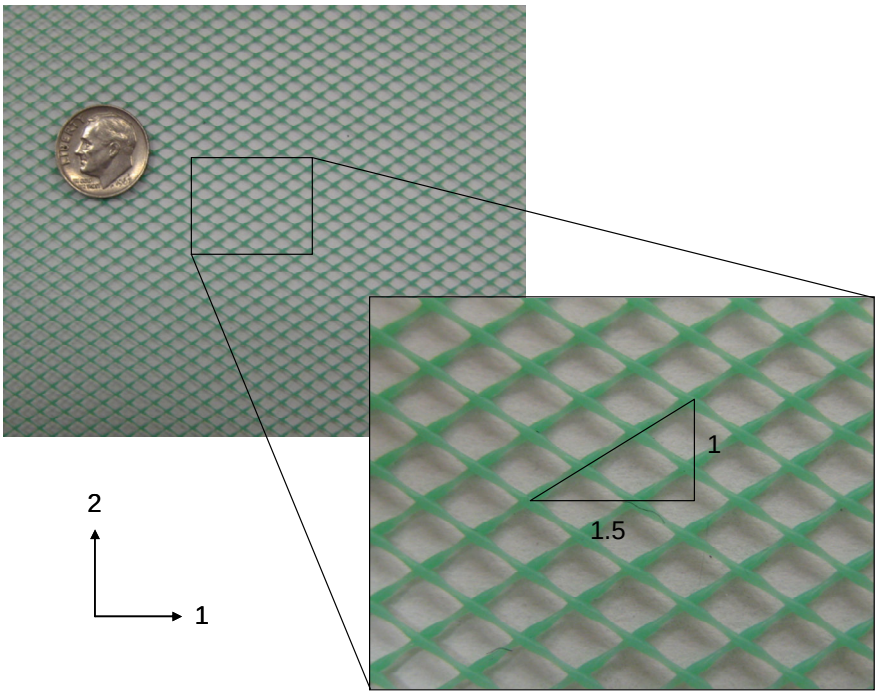

Figure 4-63 Photograph of the flow distribution mesh showing principle directions 1, and 2.

Due to the inelastic nature of the distribution mesh the thickness (*h*) of the mesh remains constant under increasing compaction pressure. An illustration showing the cross section of a layer of distribution mesh between a rigid mold and vacuum bag with no compaction pressure applied is shown in Figure 4-64. Due to the elastic nature of the vacuum bag material the bag deforms as vacuum pressure is applied reducing the porous volume within the flow distribution mesh layer (Figure 4-65). Although the overall thickness of the distribution mesh remains constant under vacuum pressure the thickness of the porous region between the mesh fibers is reduced as vacuum pressure is applied. Furthermore the porous area within the flow distribution layer becomes further reduced when a fiber preform is present. Due to the

deformable nature of the preform under compaction pressure the flow distribution mesh nests into the preform further reducing the porous area (see Figure 4-66).

To study these effects three different permeability measurement experiments were performed as follows: (1) One ply of flow distribution mesh without a preform, (2) one ply of flow distribution mesh with a triax preform and a layer of release fabric, and (3) two plies of flow distribution mesh with a triax preform and a layer of release fabric. A photograph of the test setup with one layer of flow distribution mesh, triax preform, and release fabric is shown in Figure 4-67. For each of the three experiments the flow mesh was oriented such that the permeability was measured in the transverse direction (κ_{22}). The results of the experiments are shown in Figure 4-68. From the figure it is seen that as compaction pressure increases and the vacuum bag conforms to the distribution mesh the permeability decreases and remains near constant for compaction pressures above 35 kPa. It is also observed from comparing experiments one and two that the presence of the fiber preform greatly decreases the permeability of the flow distribution mesh. For the third experiment, where two plies of flow distribution mesh are used, a greater range of permeability is observed likely due to nesting of the flow distribution plies. However due to the presence of the preform, the permeability values are similar to those for the first experiment where only one layer of distribution mesh is used without the presence of a preform layer. Due to the difficulties in measuring the actual fiber volume fraction of the distribution layer due to the conforming of the vacuum bag and nesting of the preform, the permeability of the flow distribution layer is related directly to the compaction pressure. The relationship between the permeability and compaction pressure for the flow

distribution mesh in the presence of a preform layer in the longitudinal (κ_{11}) and transverse (κ_{22}) directions is given in Figure 4-69 and Figure 4-70 respectively. The permeability versus compaction pressure constitutive relationships for the flow distribution mesh are given in Table 4-6.

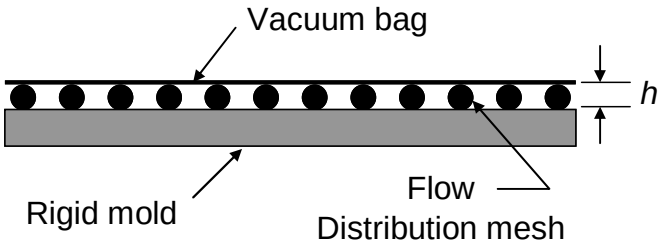

Figure 4-64 Illustration of resin distribution mesh between rigid mold surface and pliable vacuum bag without vacuum pressure applied showing porous cross section.

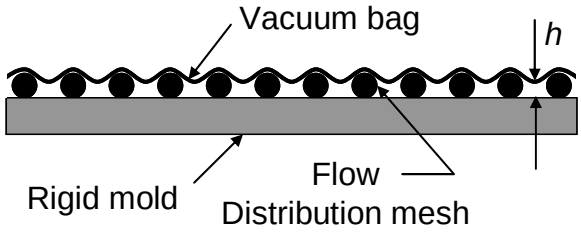

Figure 4-65 Illustration of resin distribution mesh between rigid mold surface and pliable vacuum bag with vacuum pressure applied showing reduced porous area.

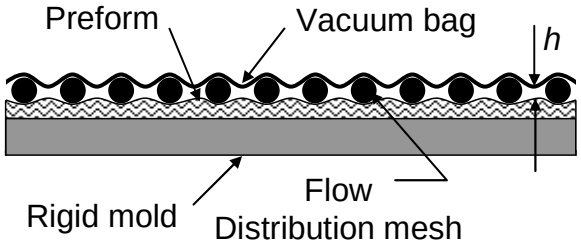

Figure 4-66 Illustration of resin distribution mesh with preform layer between rigid mold surface and pliable vacuum bag with vacuum pressure applied showing reduced porous area.

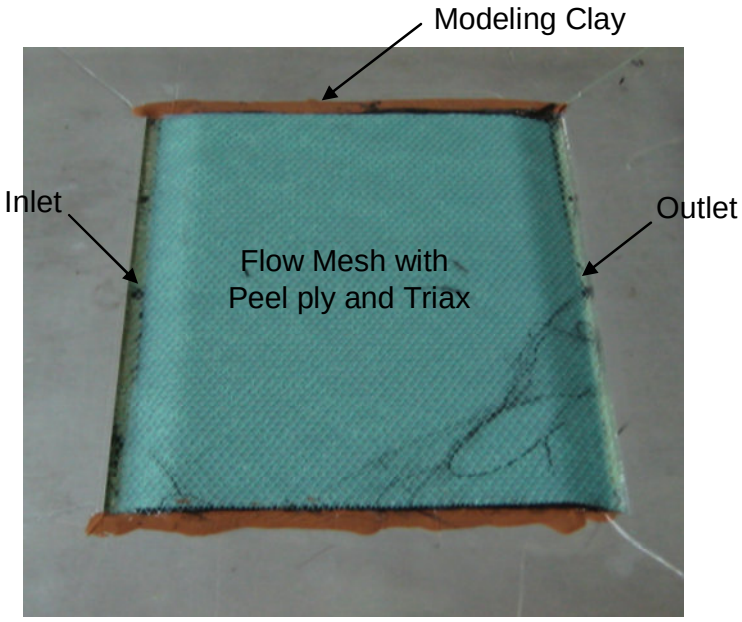

Figure 4-67 Photograph of the test setup for measuring the permeability of the flow mesh with release fabric and triax preform.

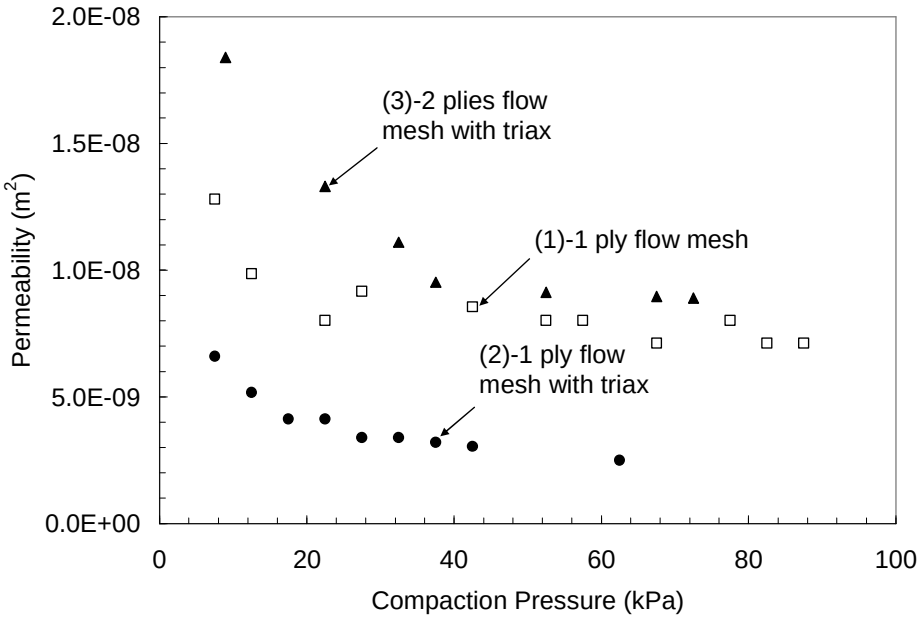

Figure 4-68 Flow distribution mesh transverse permeability (κ_{22}) versus compaction pressure.

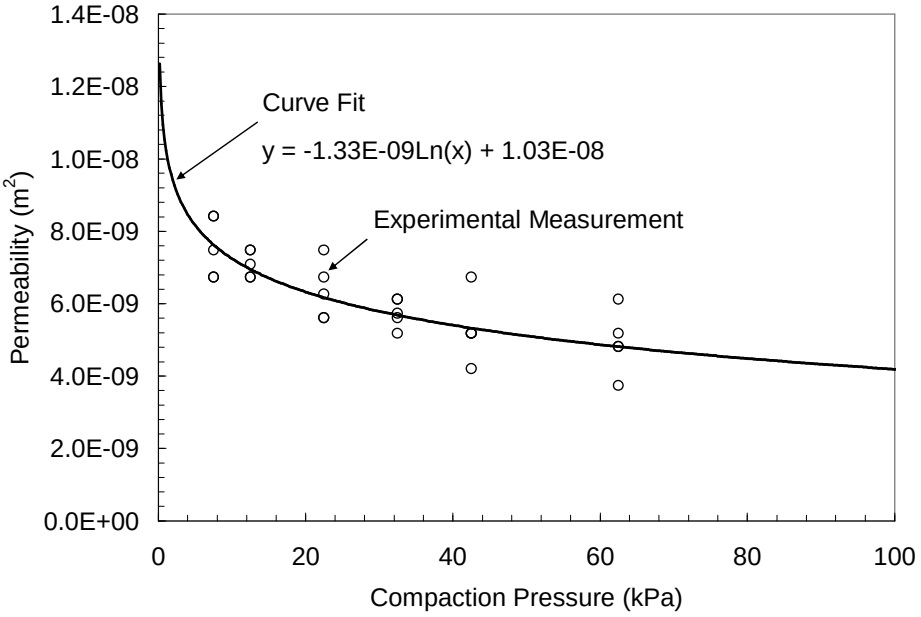

Figure 4-69 Flow distribution mesh permeability (κ_{11}) versus compaction pressure constitutive model.

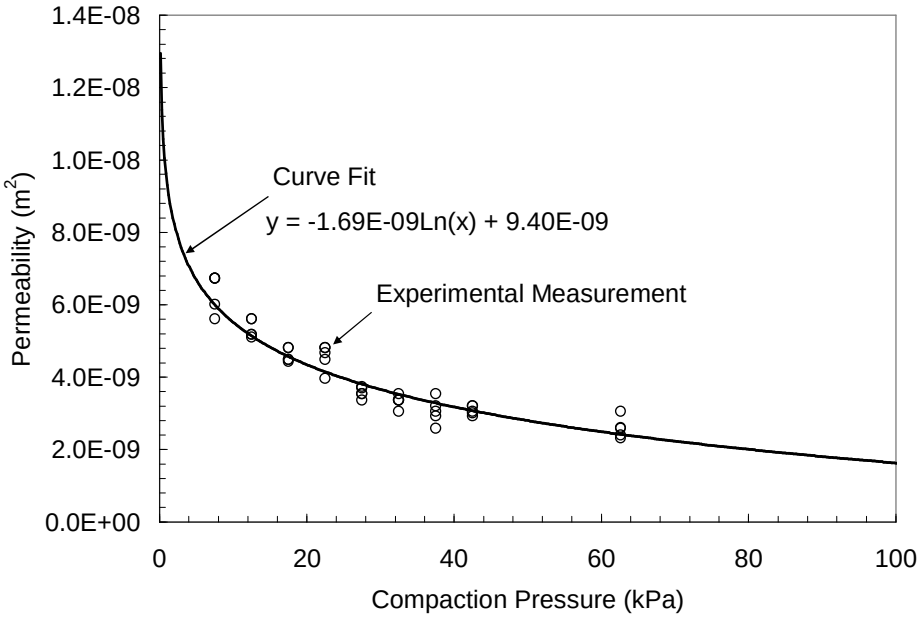

Figure 4-70 Flow distribution mesh permeability (κ_{22}) versus compaction pressure constitutive model.

Table 4-6 Flow Mesh Permeability Models

Orientation	*Constitutive Model*	*Eq.*
Longitudinal (κ_{11})	$\kappa_{11} = \left(10.3 - 1.33\ln\left(P_c\right)\right)\left(10^{-9}\right)$	(4.47)
Transverse (κ_{22})	$\kappa_{22} = \left(9.4 - 1.69\ln\left(P_c\right)\right)\left(10^{-9}\right)$	(4.48)

4.5 SUMMARY

An alternative method for characterizing the compaction and permeability characteristics of fiber performs has been introduced. The method was used to develop compaction pressure versus fiber volume fraction and permeability versus fiber volume fraction constitutive models to be used in simulations. The studies showed that the fiber volume fraction versus compaction pressure curves during the compaction and relaxation stages are very different and must be represented by separate constitutive models.

Permeability models were also developed for the flow distribution medium in which it was observed that the presence of the preform with the flow distribution mesh significantly affected the permeability measurements and must be taken into consideration. Due to nesting effects between the preform and flow distribution mesh the permeability of the flow distribution layer was significantly reduced with the permeability varying as a function of compaction pressure.

In addition to characterizing the preform materials a constitutive models was developed for the epoxy resin considered in this research which is also used in the simulation.

CHAPTER 5

MODEL VALIDATION

To validate the developed simulation model a series of experiments were performed in which the experimental results are compared with numerical simulations. The experiments include: (1) one-dimensional flow through a uni-directional stitched carbon preform, (2) two-dimensional flow, including through the thickness flow, for a thick uni-directional stitched carbon preform laminate in which a flow distribution layer is used, and (3) two-dimensional flow, including through the thickness flow, for a thick preform laminate consisting of uni-directional and triax stitched carbon layers and a flow distribution layer. The experiments and simulations include resin filling as well as resin bleeding. Comparisons of filling times, bleeding times, pressure fields, and laminate thickness and fiber volume fractions during the filling and bleeding stages are made with simulation results to assess the validity of the simulation model and to gain further insight into the VARTM process.

A description of the test setup and procedure for each experiment along with a comparison of experimental and simulation results is presented.

5.1 ONE-DIMENSIONAL (UNI)

Experiments were performed and compared with simulations to investigate one-dimensional resin flow. The simulations employ the previously established compaction and permeability constitutive models to simulate the resin filling and

bleeding stages of the VARTM process. A description of the experimental setup and procedures is presented followed by a presentation of the experimental results and comparison with simulation predictions.

5.1.1 Experimental Setup

The flow experiment was performed using a preform consisting of three plies of uni-directional carbon fabric with the flow being parallel to the direction of the fibers. The properties for the preform material are given in Table 4-2 with the compaction and permeability models being given in Table 4-4 and Table 4-5 respectively. The thickness of each ply under full compaction was approximately 0.75 mm with the total thickness of the preform being 2.25 mm. The preform was 0.2 m wide and 1.0 m long with a flow spring connected to an inlet hose at one end and a second flow spring connected to an outlet hose at the opposite end. The preform was placed on a mold instrumented with 11 pressure transducers (Omega PX 302) spaced at 0.1 m on center. An illustration of the plan view of the mold with the preform showing the dimensions of the preform and locations of the pressure transducers is shown in Figure 5-1. A side view of the test setup is given in Figure 5-2 and a photograph of the bottom surface of the mold showing the pressure transducers is given in Figure 5-3. A vacuum bag is placed over the preform and sealed around the perimeter with the inlet and outlet hoses each being attached to vacuum pots such that the pressure can be controlled independently at both the inlet and the outlet. A photograph of the complete experimental setup is seen in Figure 5-4. The experiments were all performed at room temperature in which corn oil having a viscosity 0.06 $Pa \cdot s$

was used as the infusion fluid. In all of the experiments oil is used in place of epoxy resin to prevent damage to the pressure sensors.

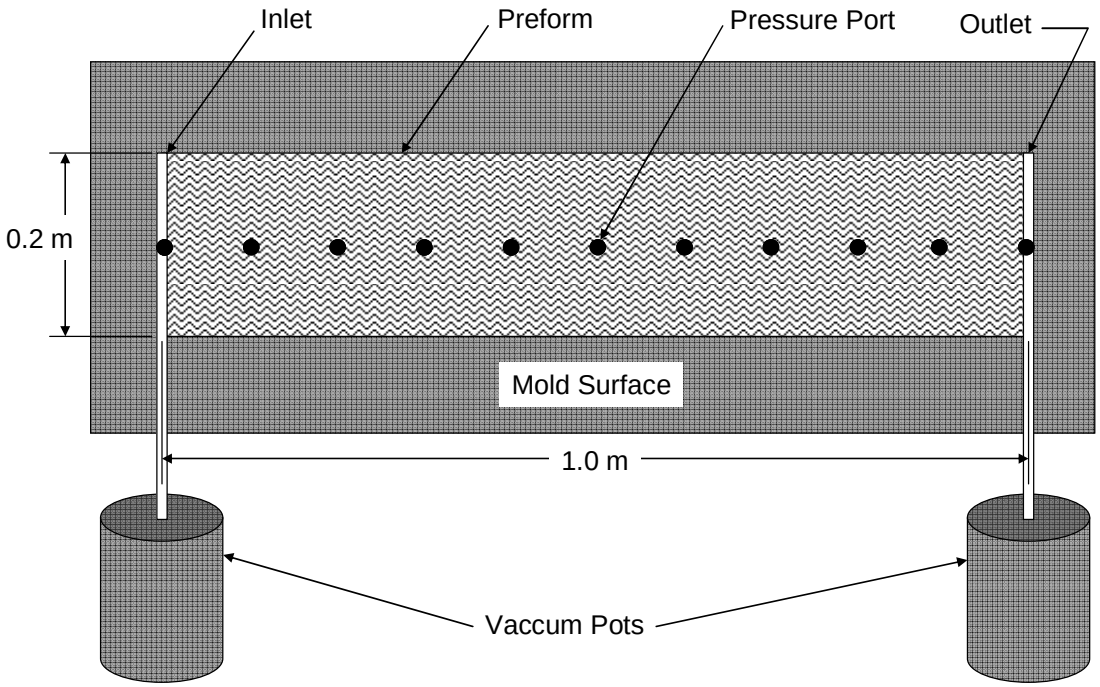

Figure 5-1 Illustration of the plan view of the one-dimensional flow experiment showing the dimensions of the preform and locations of the pressure transducers and resin inlet and outlet lines.

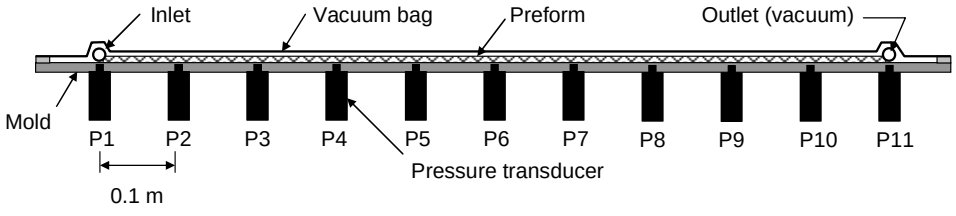

Figure 5-2 Illustration of the side view of the one-dimensional flow experiment showing the spacing of the pressure sensors.

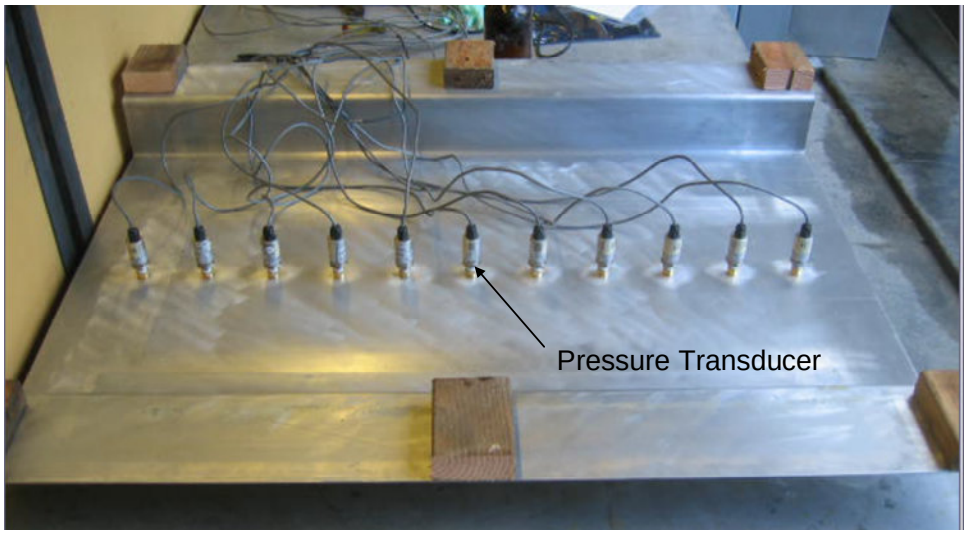

Figure 5-3 Photograph showing the pressure transducers on bottoms side of mold.

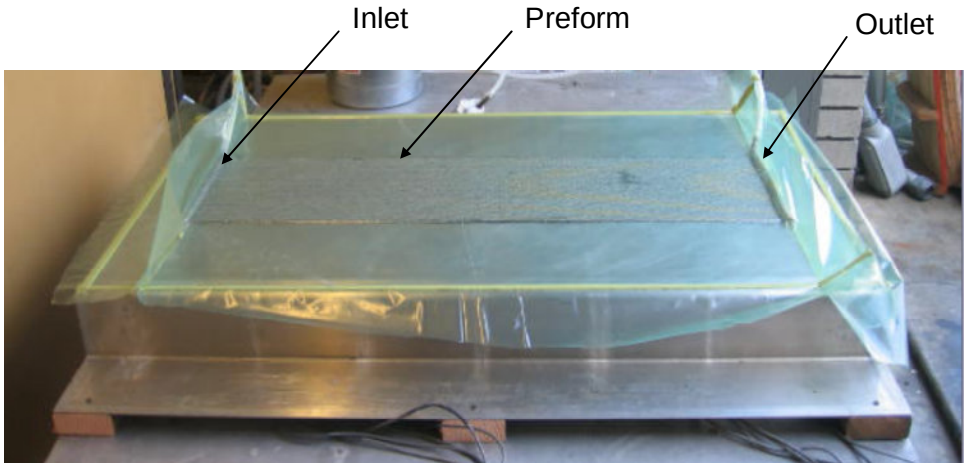

Figure 5-4 Photograph showing the dry fiber preform on the mold surface covered with a vacuum bag. Pressure sensor ports cannot be seen due to presence of preform.

5.1.2 Experimental Procedure

It is common practice in VARTM processing to infuse parts at full vacuum pressure after which the vacuum pressure is reduced to about 50% of full vacuum at

the end of filling to minimize the presence of micro voids due to any dissolved air in the resin. In addition to reducing the vacuum pressure at the outlet, vacuum pressure may be applied at the inlet to remove (bleed) excess resin in order to increase the fiber volume fraction of the part and achieve uniform laminate thickness [20].

The one-dimensional flow experiment considered both the resin filling and bleeding stages of the VARTM process. For the filling stage the resin inlet hose is closed while full vacuum pressure (0 kPa) is applied at the outlet. When full vacuum is achieved within the mold cavity the resin inlet hose is opened and the oil is allowed to flow into the preform under atmospheric pressure (101 kPa). The progression of the flow front is visually monitored using a stop watch and marking the location of the flow front. A photograph of the resin filling stage is given in Figure 5-5. From the photograph it is seen the flow is uniform across the width of the preform. In addition to visually monitoring the flow, the pressure within the mold cavity is also recorded at each pressure sensor location. At the end of filling the pressure at the outlet is reduced to 50 kPa and the pressure within the mold is allowed to reach equilibrium. Once the pressure has reached equilibrium, vacuum pressure of 50 kPa is applied at the inlet and excess oil is bled from the mold cavity as the preform compresses. Pressure measurements at each sensor location are recorded throughout the bleeding process. A summary of the initial pressure conditions at the inlet and outlet prior to resin filling and bleeding as well as the inlet and outlet pressures during the resin fill and bleeding processes are given in Table 5-1.

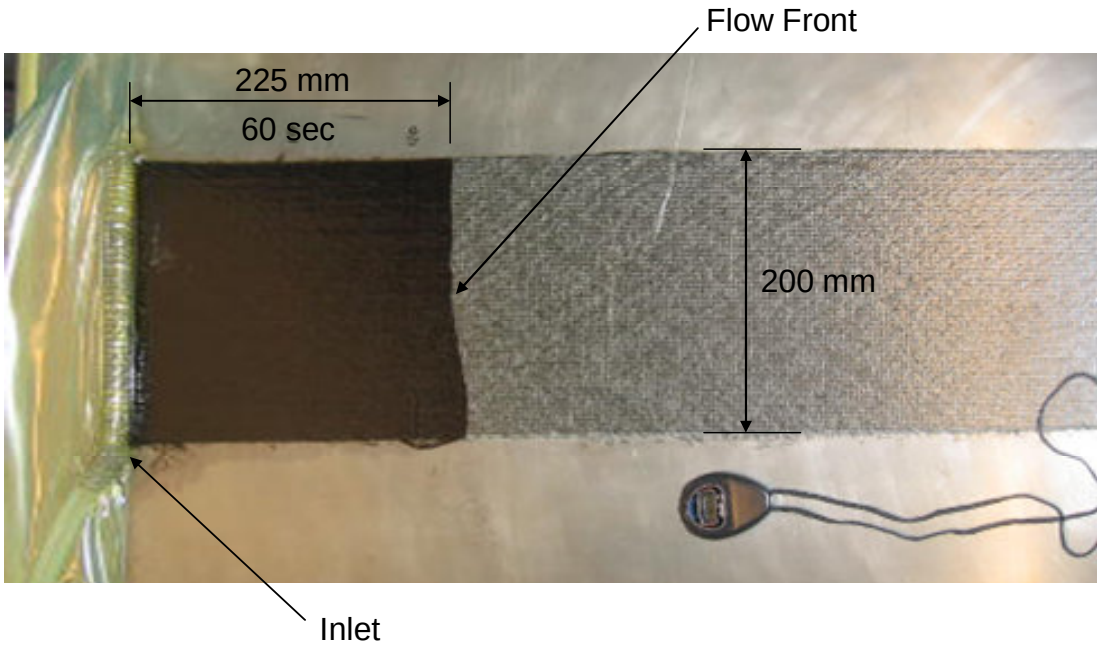

Figure 5-5 Photograph of the one-dimensional flow experiment showing the progression of the flow front.

Table 5-1 Inlet and Outlet Pressures

	Initial Conditions		*Process Conditions*	
Process	*Inlet (kPa)*	*Outlet (kPa)*	*Inlet (kPa)*	*Outlet (kPa)*
Resin Filling	0	0	101	0
Resin Bleeding	101	50	50	50

5.1.3 Results and Discussion

Resin filling and bleeding simulations were performed using a finite element model consisting 100 one-dimensional line elements. The finite element model is shown in Figure 5-6. The simulations are performed using the established

permeability and compaction constitutive models for the uni-directional material. The results of the experimental measurements and simulations for both the resin filling and resin bleeding experiments are presented.

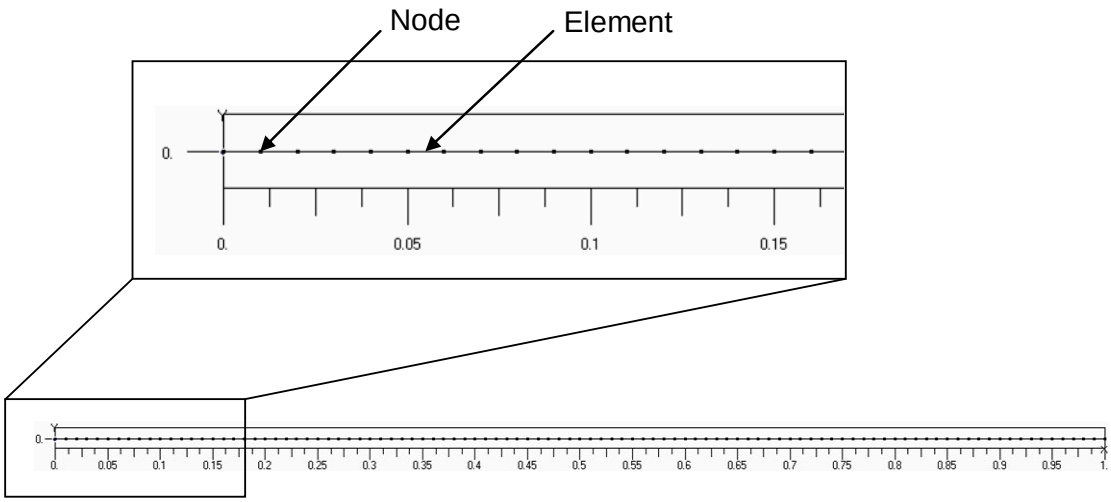

Figure 5-6 Finite element mesh used to simulate resin flow and bleeding for the uni-directional laminate without flow mesh.

Resin Filling

To illustrate the difference between the RTM (fixed preform thickness) and VARTM (transient preform thickness) processes, simulations of each process were performed using the material properties from the uni-directional material. The simulations are performed using the preform relaxation constitutive model for the uni-directional preform as well as the previously established permeability constitutive model. A comparison of the predicted pressure fields along the length of the preform are shown in Figure 5-7. From the figure it is observed that the pressure field for the

RTM process is linear due to the fixed preform thickness and permeability. Due to the transient nature of the preform thickness during the VARTM process the pressure is highest at the inlet and decreases in a nonlinear fashion to the outlet. Plots of the normalized fiber volume fraction versus location along the length of the preform as well as normalized permeability versus location are given in Figure 5-8 and Figure 5-9 respectively. From the plots it is seen that due to the reduced compaction pressure near the inlet the fiber volume fraction is decreases and subsequently the permeability increases. However, for the RTM process the preform thickness is fixed and the permeability and fiber volume fraction are constant along the length of the preform. Based on the permeability value at full compaction of the preform, a comparison of the flow front location versus fill time for both the VARTM and RTM processes is given in Figure 5-10. From the plot it is seen that the filling time for the VARTM process is less than half the time as that for the RTM process due to the transient nature of the preform thickness.

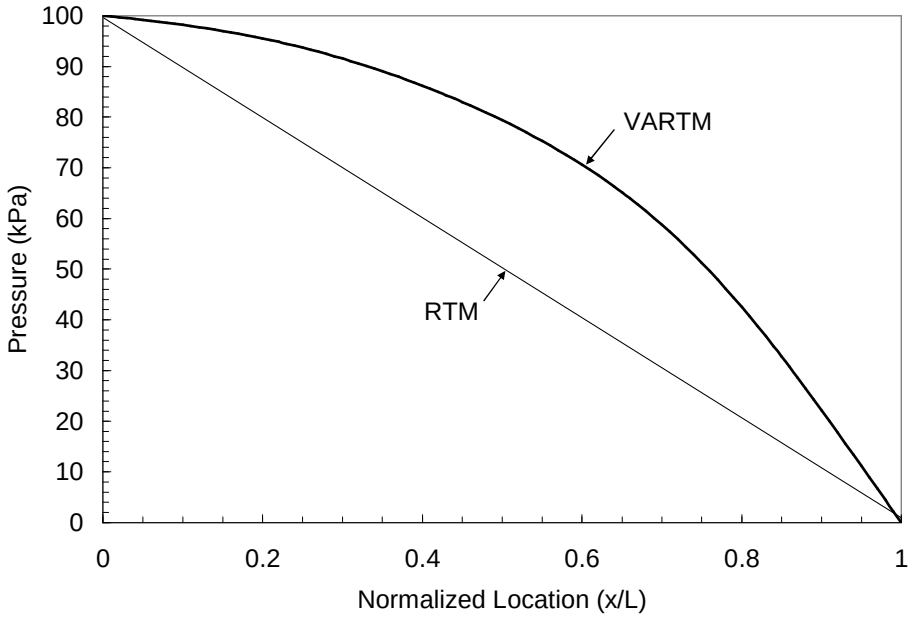

Figure 5-7 Comparison of pressure versus normalized location for the VARTM and RTM processes.

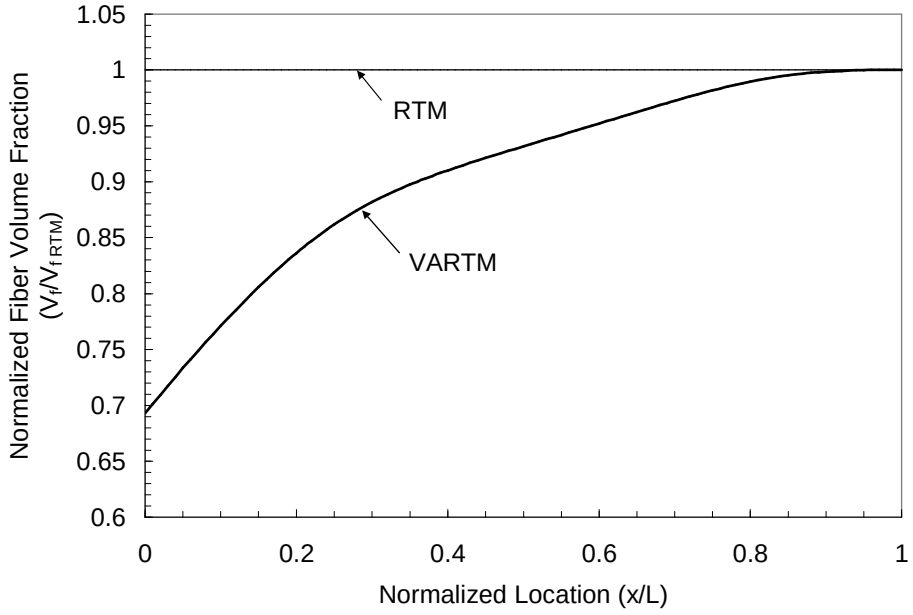

Figure 5-8 Comparison of normalized fiber volume fraction versus normalized location for the VARTM and RTM processes.

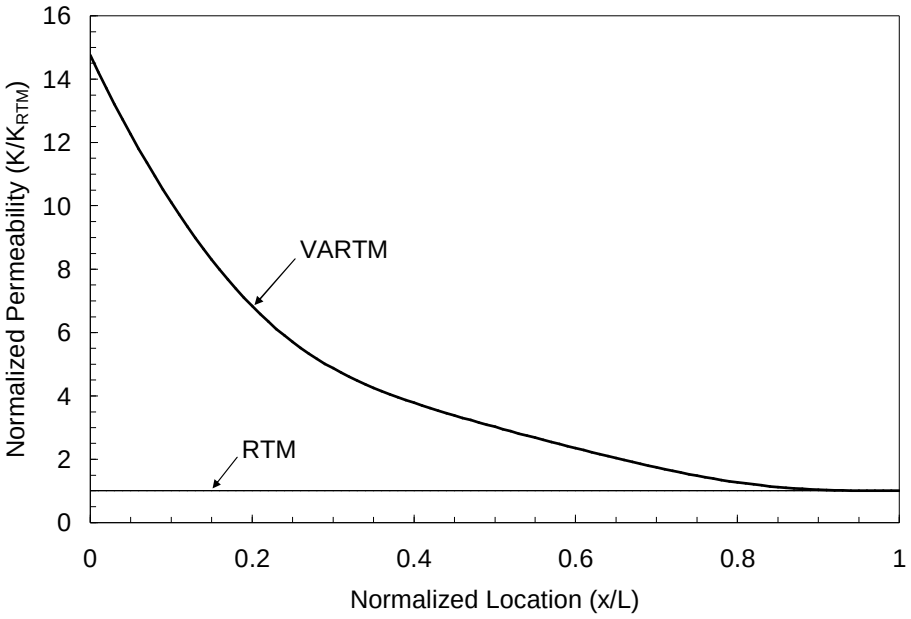

Figure 5-9 Comparison of normalized permeability versus normalized location for the VARTM and RTM processes.

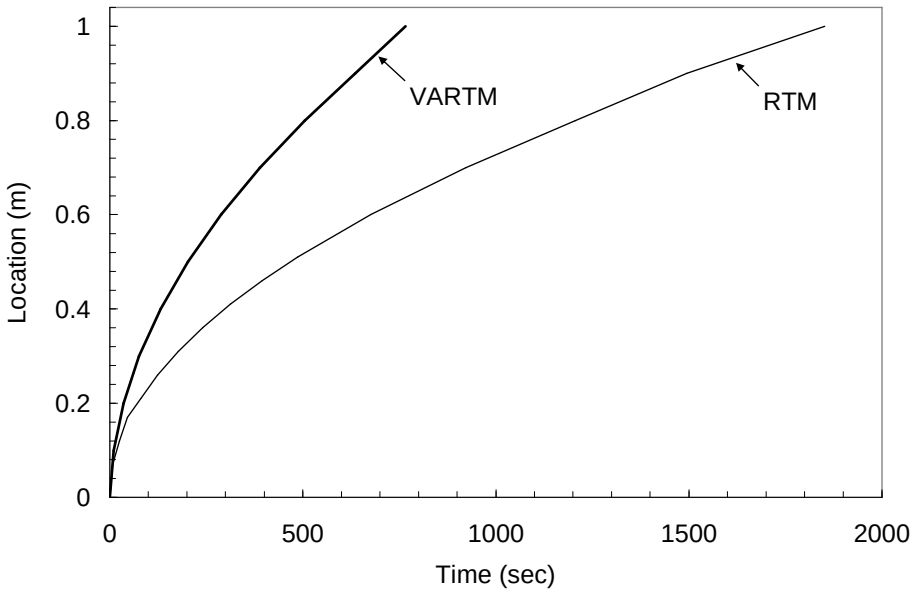

Figure 5-10 Comparison of flow front location versus fill time for the VARTM and RTM processes.

In addition to comparing the VARTM and RTM processes a parametric study was conducted to understand the effects of preform thickness and resin sinks due to the relaxation of the preform during filling. As the thickness of the laminate increases the cross sectional area over which the resin flows is increased. For one-dimensional flow this thickness can be accounted for by updating the thickness (h_e) of the elements in the finite element model as given in Eq. (3.47). Furthermore as the preform relaxes and the porous volume increases resin sinks are created which account for the increased resin volume as given by Eq. (3.54). To study the effects of these parameters, five different cases were considered in which different combinations of the parameters were implemented. In each case, with the exception of case 5, the permeability is updated as a function of fiber volume fraction (Table 4-5). For the first case the thickness is held constant and the sink terms are neglected. These are the same conditions considered by Song [54]. For the second case the transient preform thickness is considered with the sink terms neglected. For the third case the sink terms are considered with the thickness held constant. For case four both the transient thickness as well as sink terms are considered which are the conditions considered by Kang, Lee, and Han [48], Joubaud, Achim, and Trochu [49], Lopatnikov, Simacek, Gillespie, and Advani [52], and Walsh and Freeze [53]. These are also the same conditions considered in the current research when the through thickness flow is neglected. When through thickness flow is considered and elements through the thickness are required the model in the current research is represented by case 3 where the sink due to volume changes are considered but the changing preform thickness in the stiffness matrix is neglected. Finally the fifth case, reprenting the RTM process,

considers the condition in which the permeability is held constant at the initial compacted value and the changing thickness and sink terms are neglected. A summary of the five cases is given in Table 5-2. A plot of the flow front location versus fill time for each case along with experimental results is given in Figure 5-11. From the plot it is seen that case 2 resulted in the shortest fill time while case 5 resulted in the longest fill time. The consideration of the transient thickness in case 2 leads to a gradient in the element thicknesses from the inlet to the outlet where the thickness is greater at the inlet and lower at the outlet leading to higher flow rates. Consideration of the sink term in case 3 resulted in a reduction in the resin flow rate due to the additional resin consumed by the sinks. Cases 1 and 4 predicted similar fill times which showed good correlation with the experimental results. It appears that the increased flow rate due to considering the transient thickness of the preform is countered by the decreased flow rate when the sink terms are considered. As expected, case 5 which held the permeability fixed at the initial compacted value, showed the longest fill time. The actual fill time from the experiment was 780 seconds. The fill time for each case along with the percent error is given in Figure 5-3. From the table it is seen that the maximum error is 61.5% for case 5 while the other four cases had errors less than 7%. From the parametric study it is shown that for resin filling the consideration of transient thickness and sink terms has little effect on the predicted filling times especially when one considers that permeability measurements are reported to have an uncertainity as has as $\pm$ 15% [71].

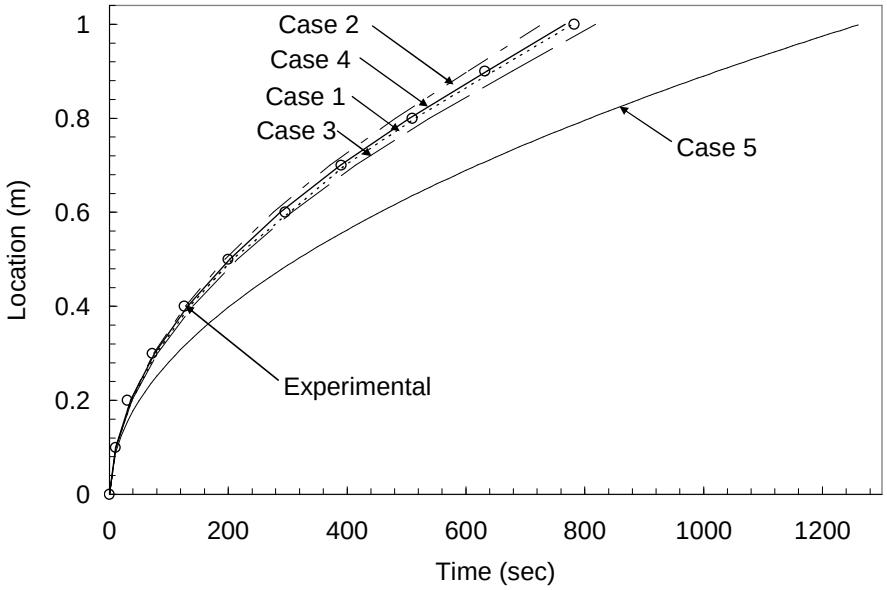

Figure 5-11 Plot of the flow front location versus filling time comparing the four different simulation cases with experimental results.

Table 5-2 Active Simulation Parameters

Case	*Thickness*	*Sink*
1	no	no
2	yes	no
3	no	yes
4	yes	yes
5 (fixed permeability)	no	no

Table 5-3 Simulation Fill Times

Case	*Fill Time (sec)*	*Error (%)*
1	780	0
2	728	-6.7
3	818	+4.9
4	767	-1.7
5	1260	+61.5

In addition to measuring the flow front progression, the pressure at each sensor location (P2 through P10) was also recorded. A plot of the experimental measurements along with the predicted pressure at each sensor location as a function of filling time is give in Figure 5-12. The predicted pressures are based on a filling simulation which considers both the transient thickness of the preform as well as the sink terms (case 4). From the figure it is seen that that the predicted pressures show very good agreement with the experimental measurements.

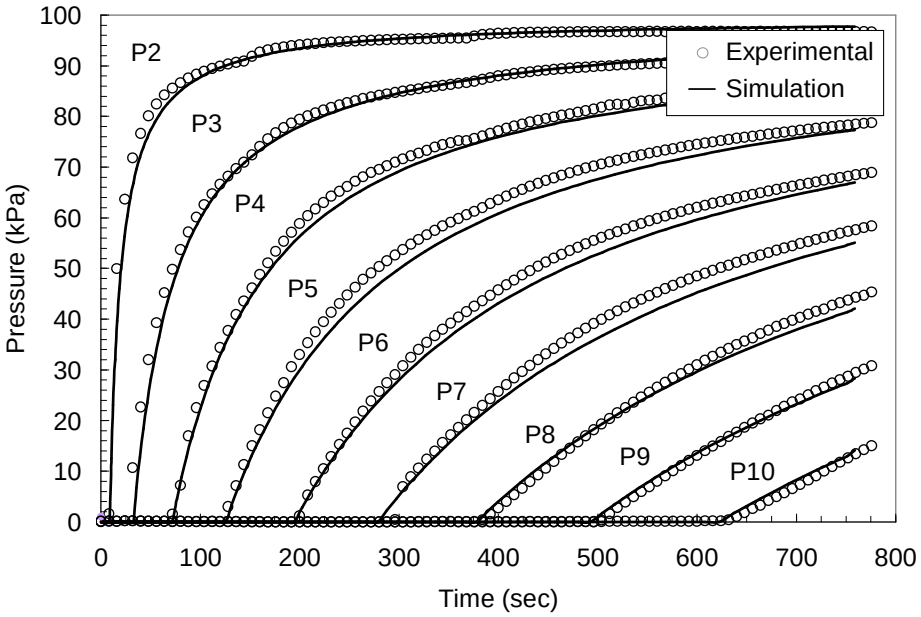

Figure 5-12 Plot of pressure versus filling time for the uni-directional preform showing the measured and predicted pressure at each sensor location.

Resin Bleeding

Although consideration of the transient nature of the preform thickness (volume) had little effect on the filling phase of the VARTM process it is vital in simulating the bleeding phase. Using the established algorithm for resin bleeding,

pressure predictions from simulations are compared with experimental measurements. At the end of filling the pressure at the outlet was reduced to 50 kPa at which time a pressure of 50 kPa was applied at the inlet to bleed excess resin. A convergence study was performed to determine an appropriate time increment to be used in the simulation. A time history plot of pressure versus time for time steps ranging from 1 to 20 seconds is seen in Figure 5-13. From the plot it is seen that for time steps less than 5 seconds the solution converges very quickly. In the current study a time step of 2 seconds is used for the resin bleeding simulations.

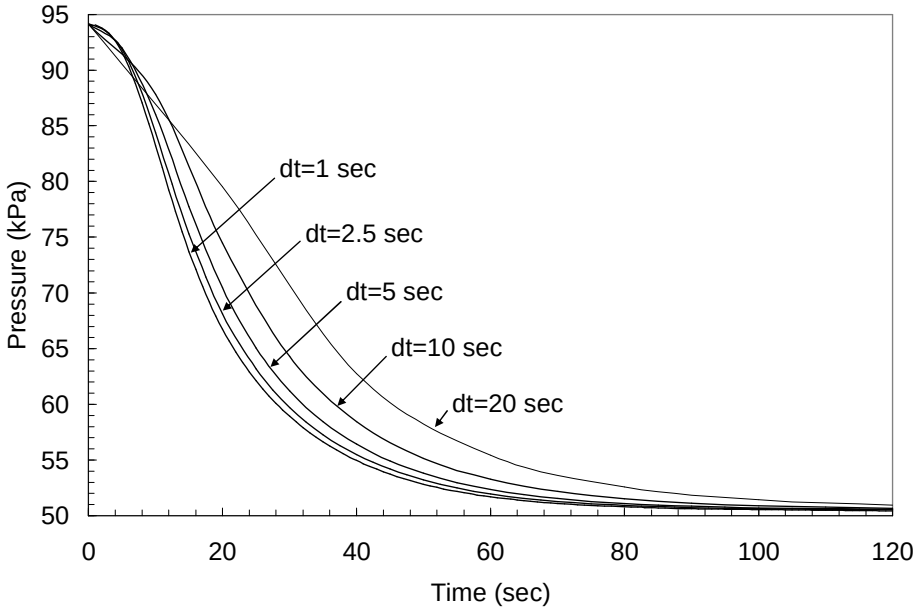

Figure 5-13 Plot of pressure versus time showing curves for several bleeding simulations using time steps ranging from 1 to 20 seconds.

A plot of the experimentally measured pressure at each sensor along the length of the preform combined with simulation results at bleeding times of 0, 30, 60, and 120 seconds is given in Figure 5-14. From the plot it is seen that the predicted pressures match the experimental results very well. However as the bleeding time increases above 60 seconds the simulation gives a near symmetric pressure field about the mid point (0.5 m) of the preform while the experimental results are non symmetric with higher pressures toward the outlet end of the preform. Since the same pressure is applied at both the inlet and the outlet one would expect that as the bleeding progresses the pressure field would become symmetric about the mid point of the preform. This is true if one assumes that there is a one to one relationship between the preform compaction pressure and the fiber volume fraction. However, as has already been established, the relationship between compaction pressure and fiber volume is dependent on whether the preform is undergoing compaction or relaxation and furthermore is dependent on the initial starting point as it transitions from relaxation to compaction or vise versa. To better understand this phenomenon a plot of compaction pressure versus fiber volume fraction for the uni-directional material showing the location of each pressure sensor on the relaxation curve at the end of resin filling is given in Figure 5-15. Remember that compaction pressure is the difference between atmospheric pressure and resin pressure. At the end of filling the outlet pressure is reduced to 50 kPa and the preform continues to relax with the points representing each pressure sensor moving down the relaxation curve as seen in Figure 5-16. Finally after the pressure has reached equilibrium a pressure of 50 kPa is applied at the inlet and the preform undergoes compaction. During the bleeding process the simulation

uses the compaction model and assumes that all the points follow this curve and eventually arrive at the same point. However in reality, as shown in Figure 5-17, each point starts at a different location on the relaxation curve and follows a compaction curve with lies somewhere between the relaxation curve and the compaction curve with each point arriving at a different fiber volume fraction corresponding to a pressure of 50 kPa. Higher fiber volume fraction values correspond to lower permeability through the permeability versus fiber volume fraction constitutive relationship. Thus, even though the inlet and outlet are at the same pressure level the preform permeability is higher near the inlet and lower near the outlet resulting in a non symmetric pressure field as the resin bleeding progresses.

In addition to validating the bleeding model with experimental measurements a comparison was also made with the one-dimensional model proposed by Song and Youn [64]. Upon recognizing that the fluid averaged velocity is used in the formulation and dividing the permeability by the porosity as noted by Lopatnikov, Simacek, Gillespie, and Advani [52], it was discovered that the system of equations produced by the finite difference approach used by Song and Youn are identical to the system of equations arrived at using the finite element method in the current research. Thus the simulation results from the current research are identical with those of Song and Youn for the one-dimensional model.

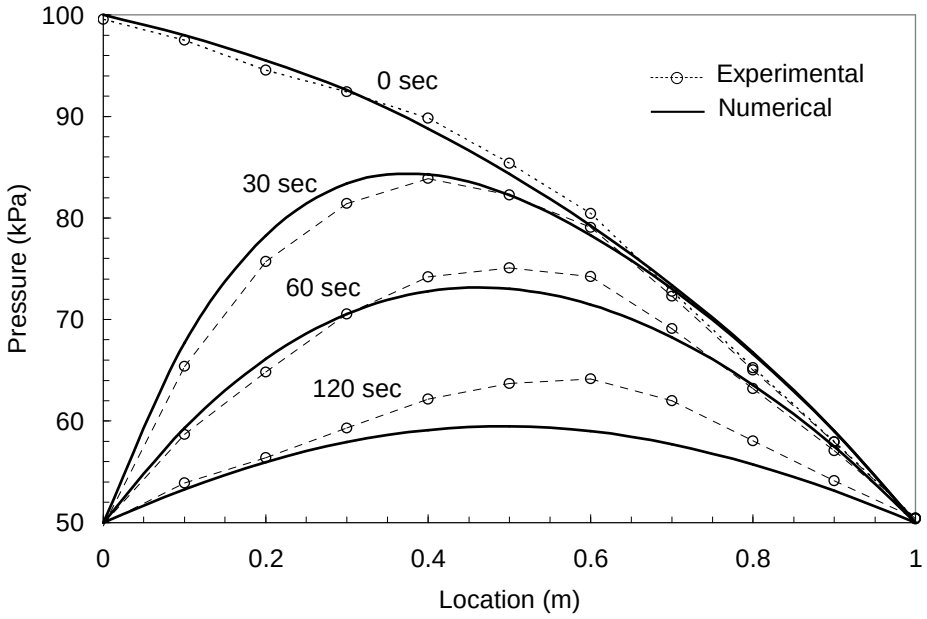

Figure 5-14 Plot of pressure versus location at different bleeding times for the uni-directional preform comparing experimental measurements with simulation for an applied pressure of 50 kPa at the inlet.

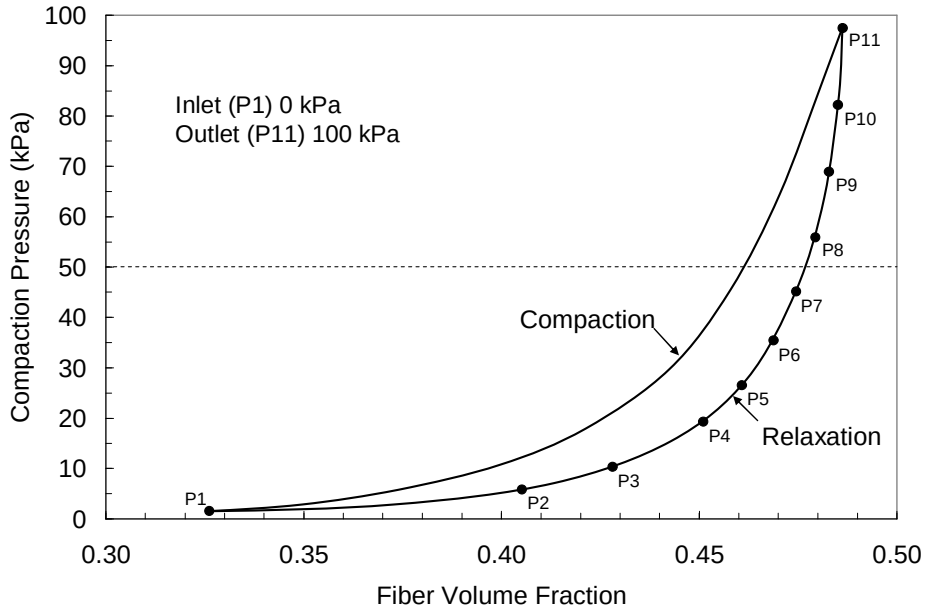

Figure 5-15 Plot of the compaction constitutive model for the uni-directional material showing the pressure and corresponding fiber volume fraction at each sensor location at the end of filling.

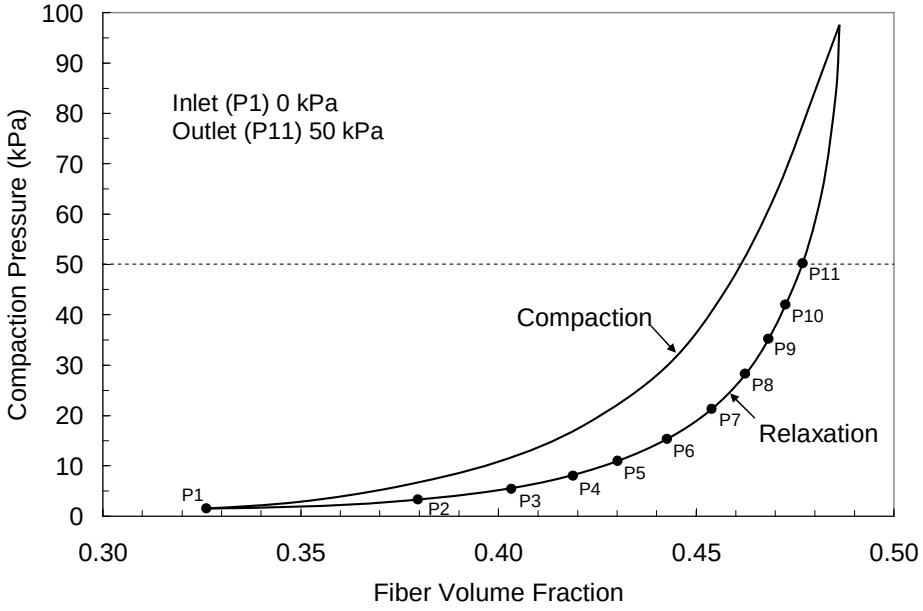

Figure 5-16 Plot of the compaction constitutive model for the uni-directional material showing the pressure and corresponding fiber volume fraction at each sensor location following the reduction of vacuum pressure at the outlet.

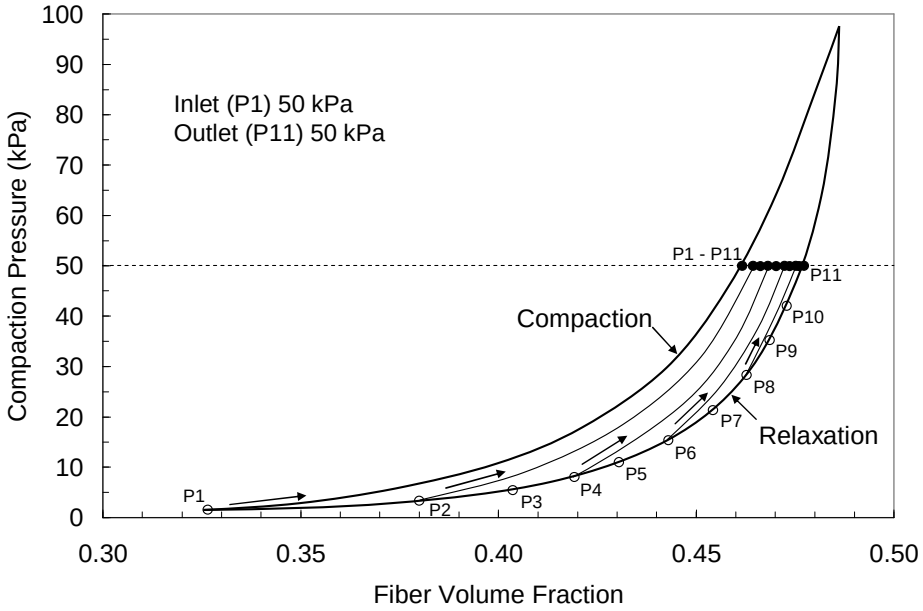

Figure 5-17 Plot of the compaction constitutive model for the uni-directional material showing the compaction versus fiber volume fraction path for each sensor location following the application of 50 kPa pressure at the inlet.

Realizing that the true constitutive relationship lies somewhere between the relaxation and compaction curves, the bleeding simulation was performed using both the relaxation as well as compaction curves and compared with experimental measurements. A time history of the pressure during the bleeding process for each pressure sensor P2 through P10 is given in Figure 5-18 through Figure 5-26 respectively. P1 and P11 are at 50 kPa throughout the test and are therefore not shown. From the plots shown in Figure 5-18 through Figure 5-20 it is seen that the pressure predictions based on the compaction curve shows much better agreement with experimental measurements than pressure predictions based on the relaxation curve. This is not surprising since, as was seen in Figure 5-17, these three points follow curves which are more representative of the compaction curve than the other points which are closer to the outlet. For the remaining sensor locations (P5-P10) it appears that some combination of the predicted pressures using the compaction and relaxation curves shows the best fit with the experimental measurements.

Using FEMAP as a post processor the predicted pressure field as well as predicted fiber volume fractions at bleeding times of 2, 20, 40, 60, 90, and 120 seconds are given in Figure 5-27 and Figure 5-28 respectively.

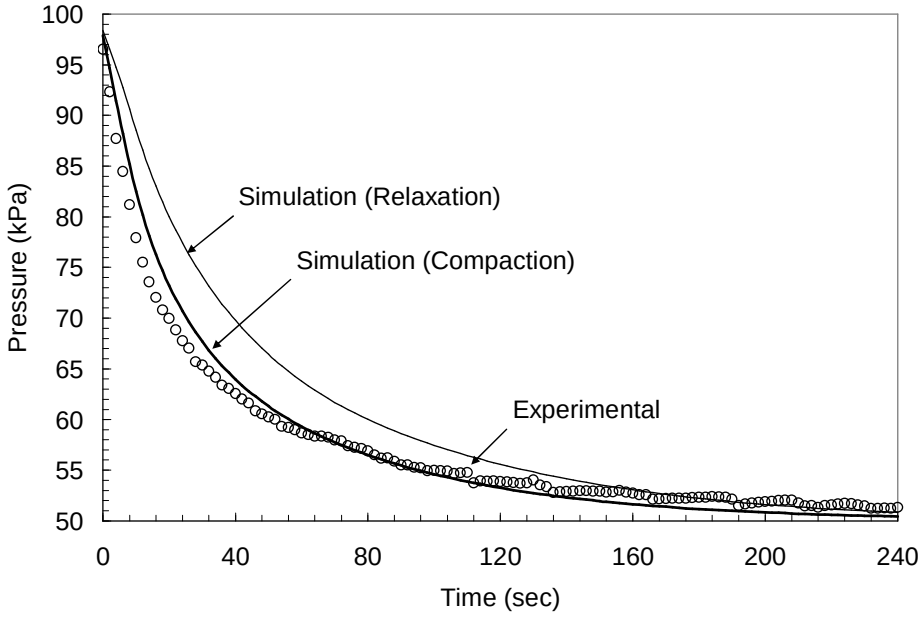

Figure 5-18 Plot of pressure versus bleeding time at pressure sensor P2 (0.1 m) showing experimental measurements as well as simulation results using both the relaxation and compaction models.

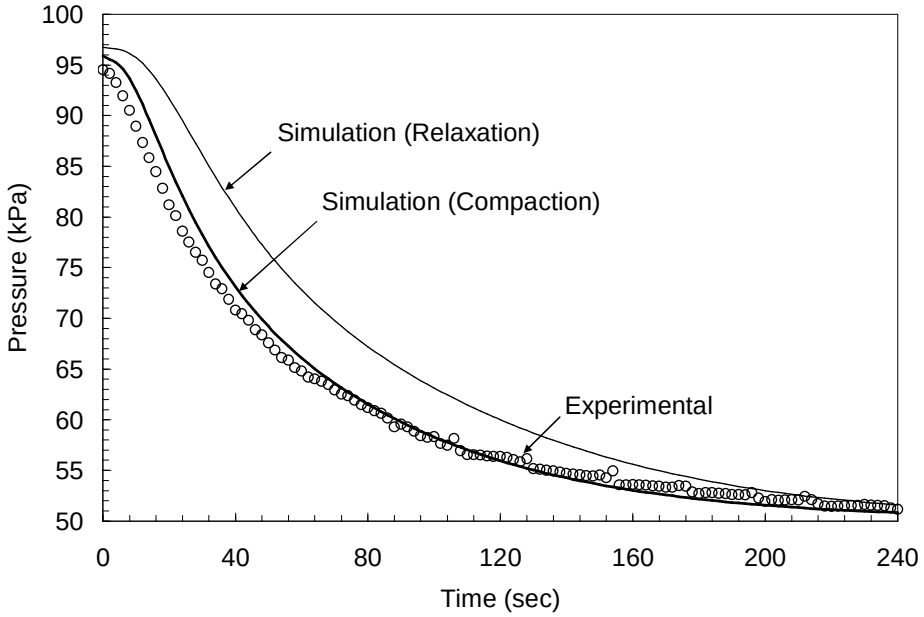

Figure 5-19 Plot of pressure versus bleeding time at pressure sensor P3 (0.2 m) showing experimental measurements as well as simulation results using both the relaxation and compaction models.

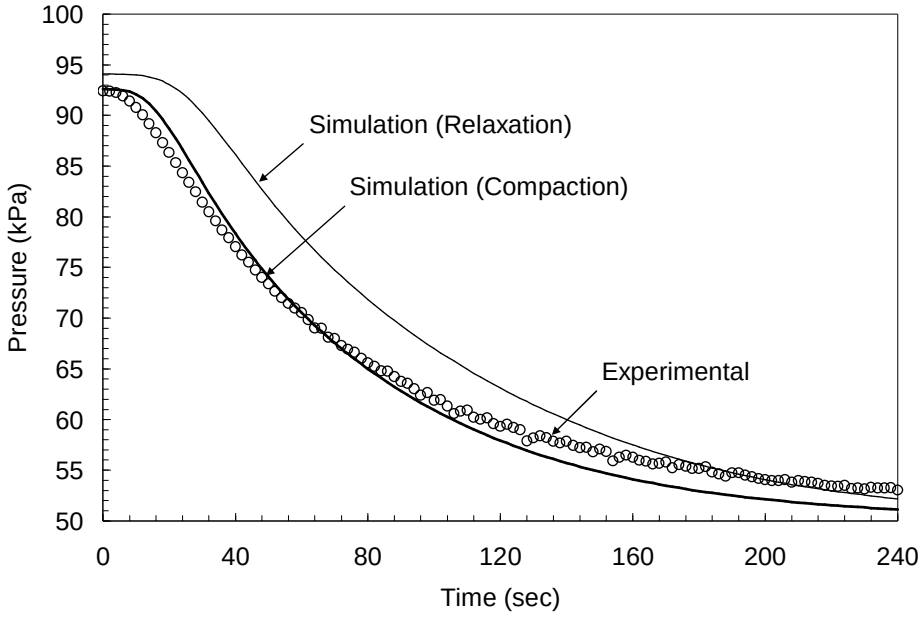

Figure 5-20 Plot of pressure versus bleeding time at pressure sensor P4 (0.3 m) showing experimental measurements as well as simulation results using both the relaxation and compaction models.

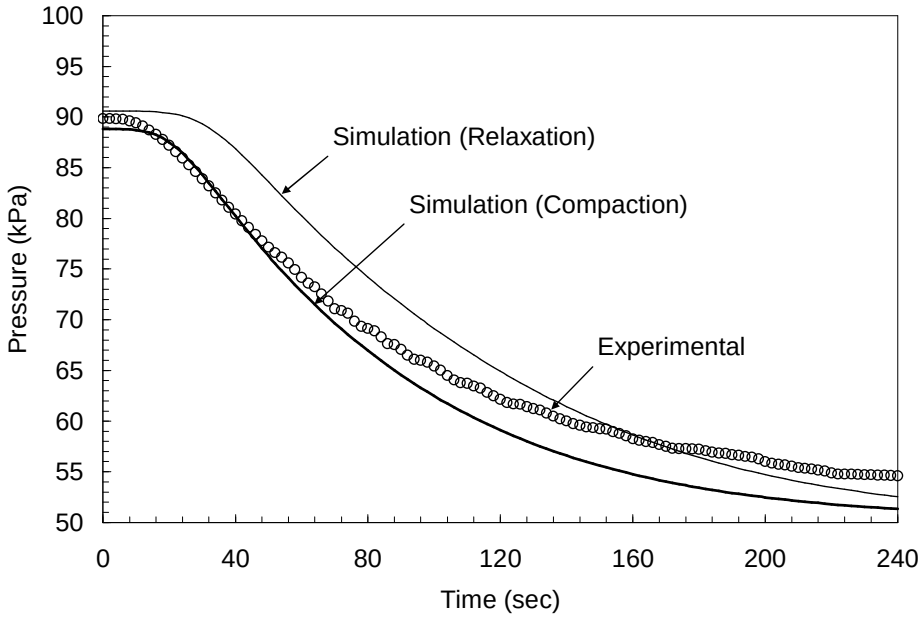

Figure 5-21 Plot of pressure versus bleeding time at pressure sensor P5 (0.4 m) showing experimental measurements as well as simulation results using both the relaxation and compaction models.

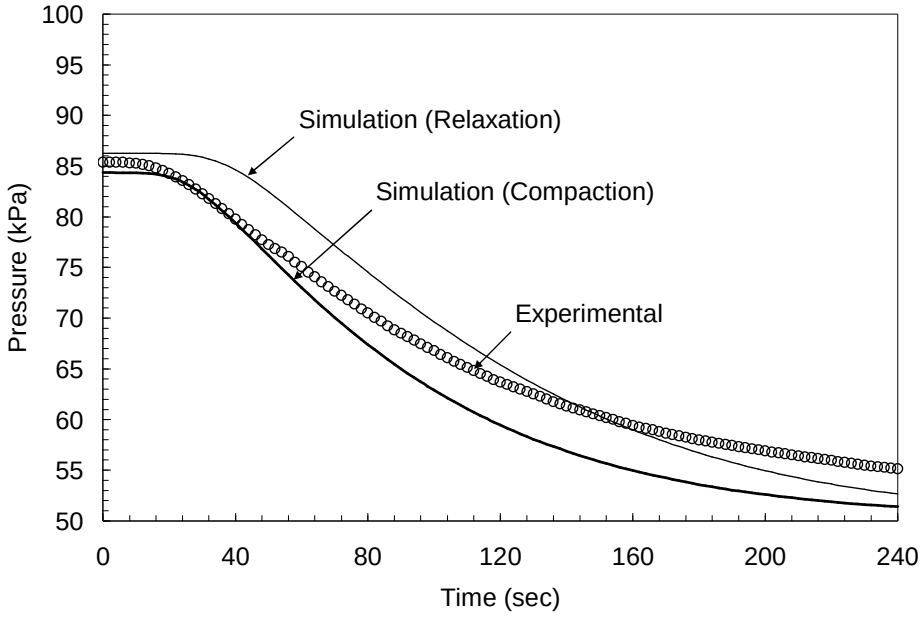

Figure 5-22 Plot of pressure versus bleeding time at pressure sensor P6 (0.5 m) showing experimental measurements as well as simulation results using both the relaxation and compaction models.

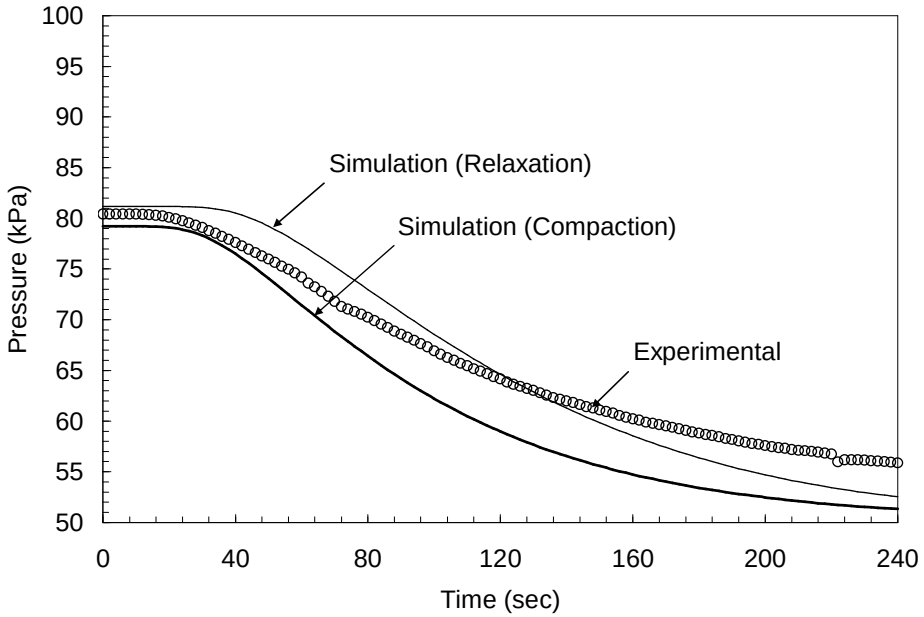

Figure 5-23 Plot of pressure versus bleeding time at pressure sensor P7 (0.6 m) showing experimental measurements as well as simulation results using both the relaxation and compaction models.

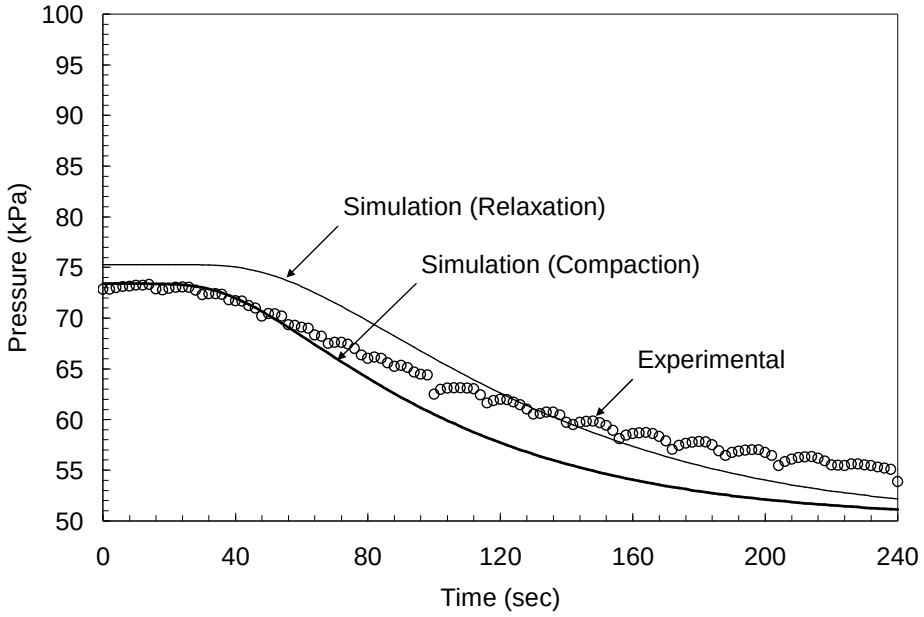

Figure 5-24 Plot of pressure versus bleeding time at pressure sensor P8 (0.7 m) showing experimental measurements as well as simulation results using both the relaxation and compaction models.

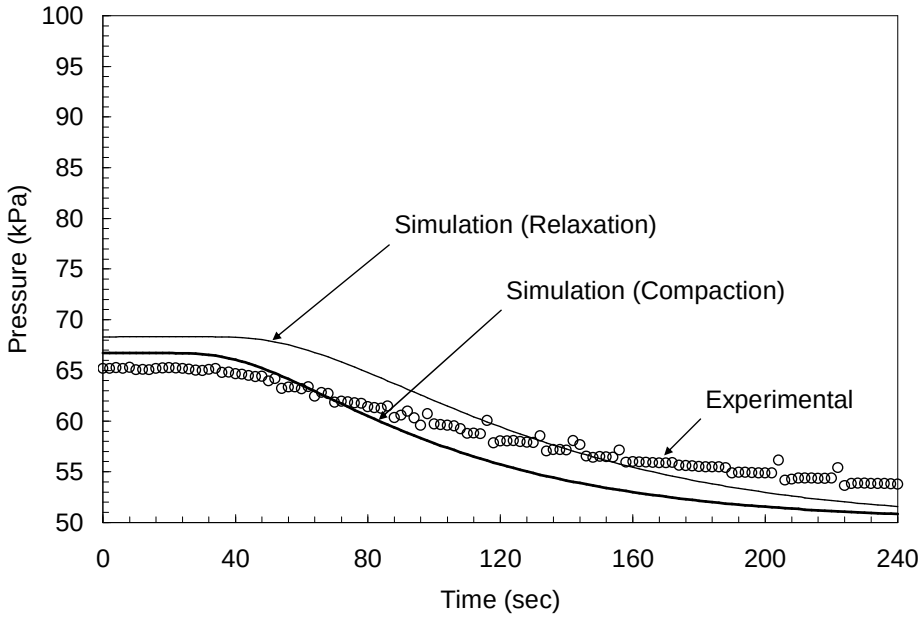

Figure 5-25 Plot of pressure versus bleeding time at pressure sensor P9 (0.8 m) showing experimental measurements as well as simulation results using both the relaxation and compaction models.

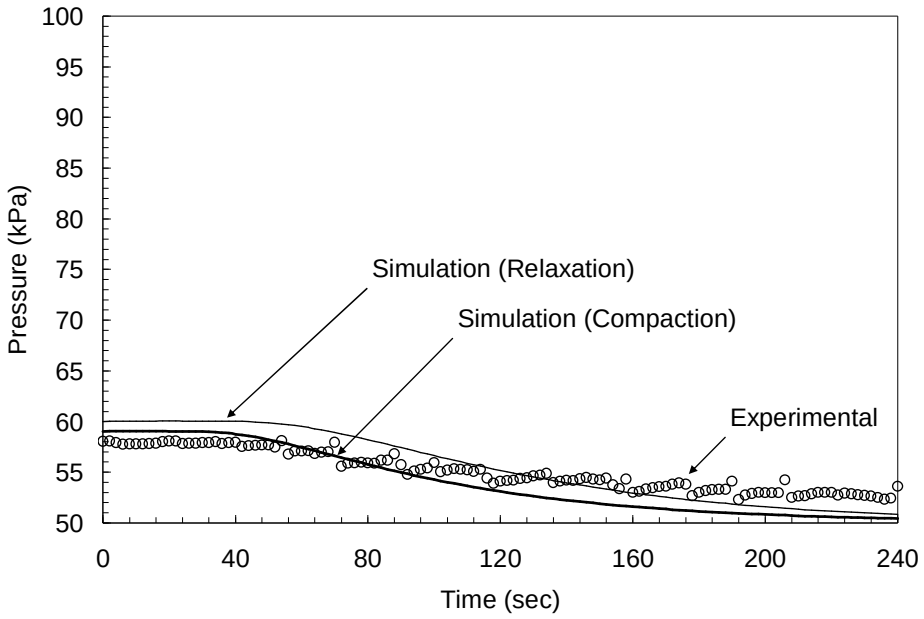

Figure 5-26 Plot of pressure versus bleeding time at pressure sensor P10 (0.9 m) showing experimental measurements as well as simulation results using both the relaxation and compaction models.

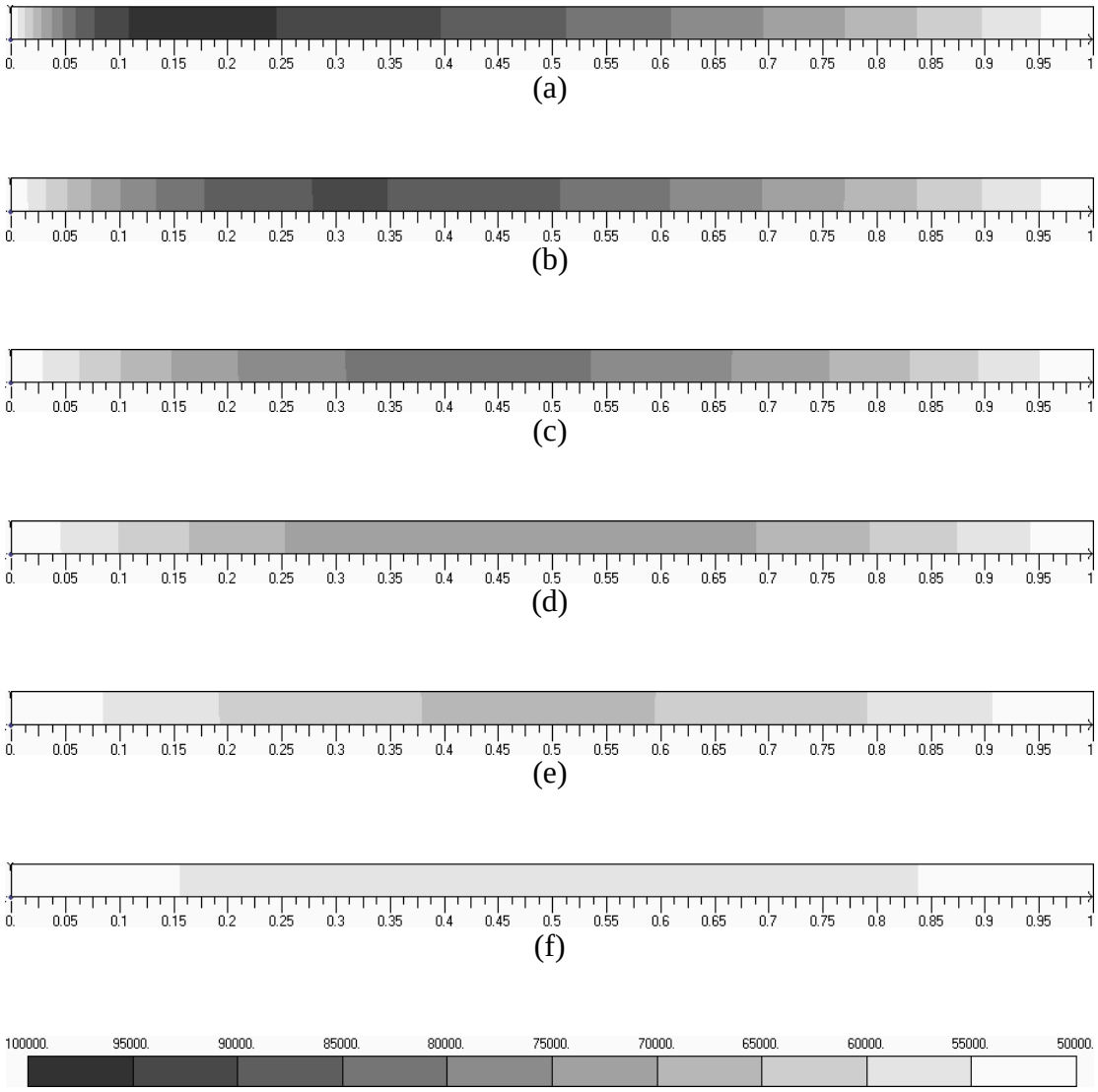

Figure 5-27 Contour plots of resin pressure for the uni-directional laminate without flow mesh at (a) 2 seconds, (b) 20 seconds, (c) 40 seconds, (d) 60 seconds,(e) 90 seconds, and (e) 120 seconds.

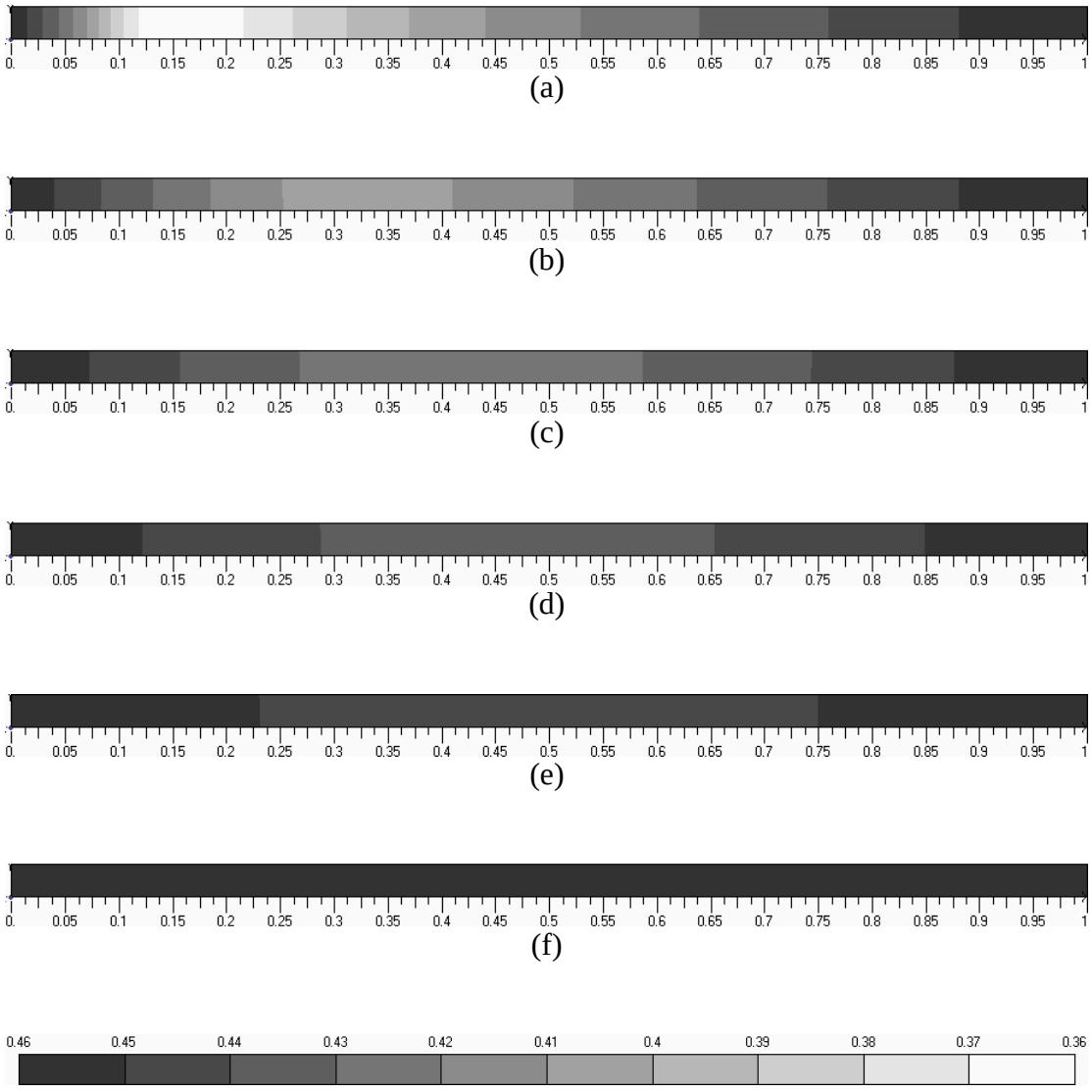

Figure 5-28 Contour plots of fiber volume fraction for the uni-directional laminate without flow mesh at (a) 2 seconds, (b) 20 seconds, (c) 40 seconds, (d) 60 seconds, (e) 90 seconds, and (f) 120 seconds.

5.2 TWO-DIMENSIONAL (UNI)

To study the effects of flow distribution layers a two-dimensional flow experiment was performed using a thick laminate consisting of the uni-directional material and one layer of flow distribution mesh. A description of the experimental setup along with the procedures is presented followed by a discussion of the experimental and simulation results.

5.2.1 Experimental Setup

This experiment used the same mold and pressure sensors that were used for the one-dimensional flow study. In addition to the pressure sensors, three displacement transducers were used to measure the thickness changes of the preform. The locations of the pressure sensors as well as the displacement transducers in relationship to the preform are given in Figure 5-29. The uni-directional laminate consisted of 30 plies of the uni-directional material resulting in a fully compacted laminate thickness of approximately 24 mm. The laminate was 0.6 m long and 0.2 m wide. The laminate was oriented such that the flow is parallel to the direction of the fibers. A layer of peel ply was placed over the entire laminate followed by a single layer of flow distribution mesh which was 0.55 m long and 0.2 m wide. The flow distribution mesh was oriented such that the flow was in the transverse direction, for which a permeability constitutive model was previously established (Table 4-6). The flow mesh ended 0.05 m before the end of the laminate. A flow spring was in contact

with the flow distribution mesh at the inlet with the vacuum (outlet) hose being placed at the end of the preform. Vacuum pots were attached to both the inlet and outlet hoses such that the pressure could be controlled at each end of the laminate. The locations of the preform, flow distribution mesh, and inlet and outlet lines are seen in Figure 5-29. Photographs of the test setup are given in Figure 5-30 and Figure 5-31.

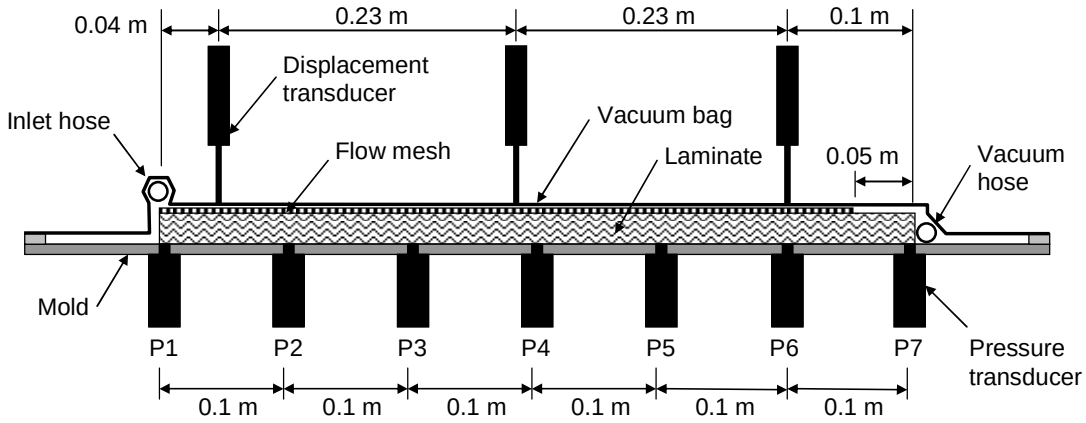

Figure 5-29 Illustration of the test setup for the uni-directional laminate with flow distribution mesh showing the locations of pressure and displacement transducers.

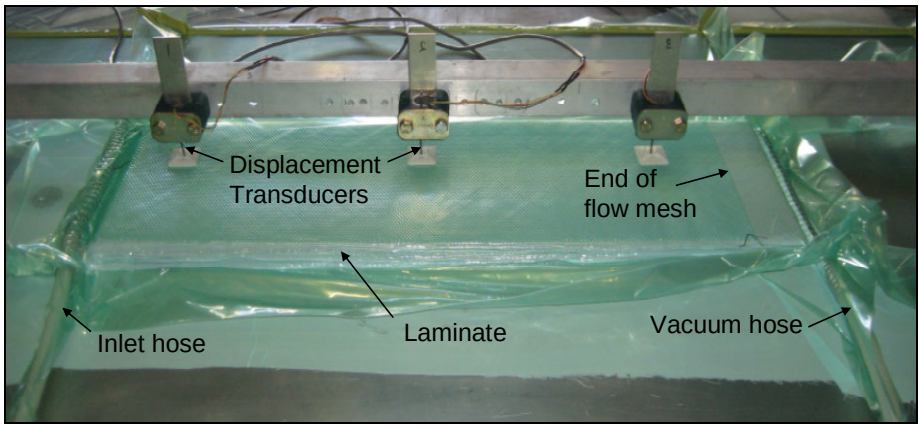

Figure 5-30 Photograph of the test setup for the uni-directional laminate with flow distribution mesh showing inlet and vacuum (outlet) hoses as well as displacement transducers.

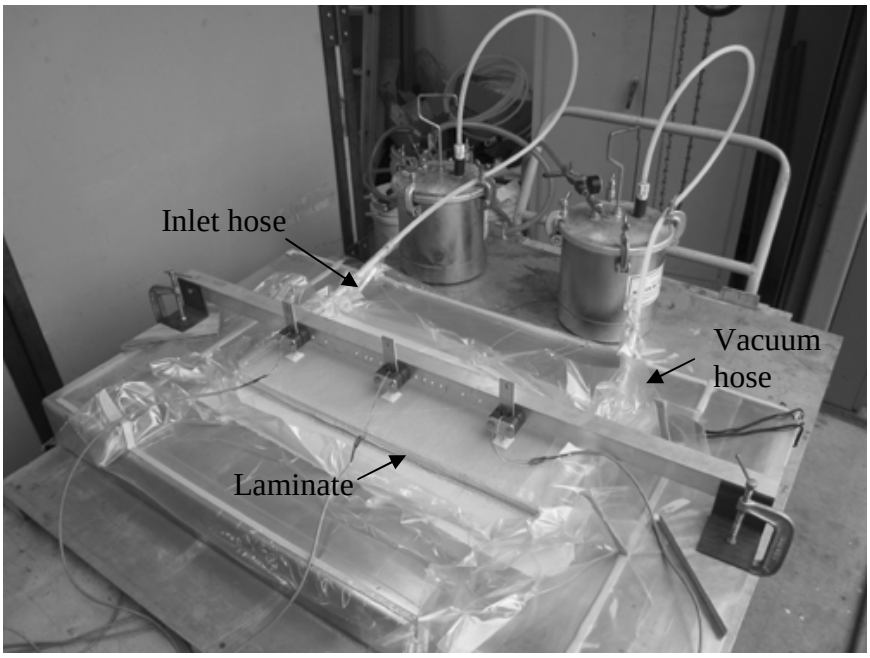

Figure 5-31 Photograph of the test setup showing the vacuum pots with the inlet and vacuum (outlet) hoses.

5.2.2 Experimental Procedure

Four different experiments were performed using the uni-directional laminate with flow distribution mesh. The first experiment consisted of resin filling in which the inlet line was closed while full vacuum pressure was applied at the outlet. When the mold cavity was at full vacuum the inlet line was opened and oil was allowed to flow into the preform under atmospheric pressure. Visual inspection was used to track the flow front progression along the top surface and the pressure sensors where used to track the flow front along the mold surface and to record the pressure data. The displacement of the laminate surface was measured using the displacement sensors. At the end of filling the outlet pressure was reduced to 50 kPa and the pressures within

the mold were allowed to reach equilibrium prior to the beginning of the second experiment.

With the outlet pressure reduced to 50 kPa the second experiment consisted of applying a vacuum pressure of 50 kPa at the inlet and allowing oil to be removed (bled) through the inlet. Pressure and displacement data were recorded until an equilibrium pressure of 50 kPa was achieved throughout the preform.

The third experiment began with the same initial pressure conditions as the previous bleeding experiment (50 kPa at the outlet and 101 kPa at the inlet). With the pressure at equilibrium the inlet hose was closed to prevent oil from flowing into the preform. The oil was bled through the outlet hose until a pressure of 50 kPa was achieved throughout the preform. Again pressure data was recorded during the bleeding process.

Unlike the previous two bleeding experiments the fourth experiment investigated the flow of resin into an already saturated preform due to relaxation of the preform. The experiment began with a pressure of 48 kPa applied at both the inlet and outlet with a uniform pressure of 48 kPa throughout the mold cavity. Next the inlet hose was opened allowing oil to flow into the preform under atmospheric pressure as the preform relaxed (thickened) due to the reduced compaction pressure. Pressure and laminate thickness measurements were recorded until pressure equilibrium was achieved. A summary of the initial pressure conditions and pressure conditions during the experiments are given in Table 5-4.

Table 5-4 Inlet and Outlet Pressures

	Initial Conditions		*Process Conditions*	
Process	*Inlet (kPa)*	*Outlet (kPa)*	*Inlet (kPa)*	*Outlet (kPa)*
Resin Filling	0	0	101	0
Resin Bleeding	101	50	50	50
Resin Bleeding	101	50	Closed	50
Preform Relaxation	48	48	101	48

5.2.3 Results and Discussion

Simulations of each experiment were performed using a finite element model consisting of 287 nodes and 523 elements. One-dimensional line elements were used to simulate the resin distribution mesh as well as edge effects at the ends of the preform. Two-dimensional triangle elements were used to model the preform. During the filling experiment it was observed that the flow rate along preform/vacuum bag interface at the ends of the preform was faster than the measured flow rate through the thickness of the preform. To account for this increased permeability along the laminate edges one-dimensional line element having a permeability of 1e-10 m^2 were used. An illustration of the finite element mesh showing the extent of the flow distribution elements is given in Figure 5-32. The simulations are performed using the established permeability and compaction constitutive models for the uni-directional and flow distribution mesh materials (Table 4-4, Table 4-5, and Table 4-6). The results of each of the four experiments along with simulation predictions are presented.

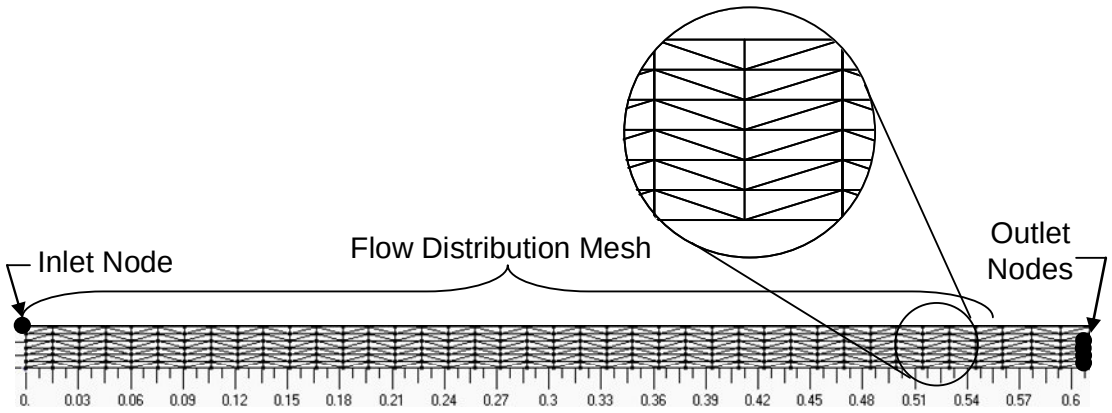

Figure 5-32 Finite element mesh showing the extent of the flow mesh elements and boundary nodes.

Resin Filling

During the resin filling experiment the flow front progression along the top and bottom surfaces were recorded and compared with simulation results. A plot of flow from location versus filling time for the top and bottom surfaces of the laminate is given in Figure 5-33. Two simulation cases were considered. The first case neglected the sink terms due to the changing volume representative of the model used by Song [54] and the second case considered the sink terms due to the changing volume as presented in the current research. In Figure 5-33 Song's model is shown by the dashed line while the current model is depicted by the solid line. From the plot it is seen that the predictions are very similar, with in only a 1% difference in predicted fill times. Again this suggests that for resin filling simulations considereation of the sink terms has little affect on the predicted filling time. From the plot it is observed that the simulation results show good agreement with the experimental measurements.

The experimental measurements show a maximum lag of 0.2 m between the flow front location at the top and bottom of the laminate near the inlet reducing to 0.14 m as the flow becomes established. The simulation shows a maximum lag of 0.23 m near the inlet reducing to 0.18 m as the flow becomes established. Contour plots showing the predicted flow front shape and location for filling times of 20, 60, 120, 200, and 240 seconds are given in Figure 5-34. Although the model proposed by Song agrees well with the current model it is not capable of simulating the bleeding of excess resin at the end of filling since the transient preform volume is not considered.

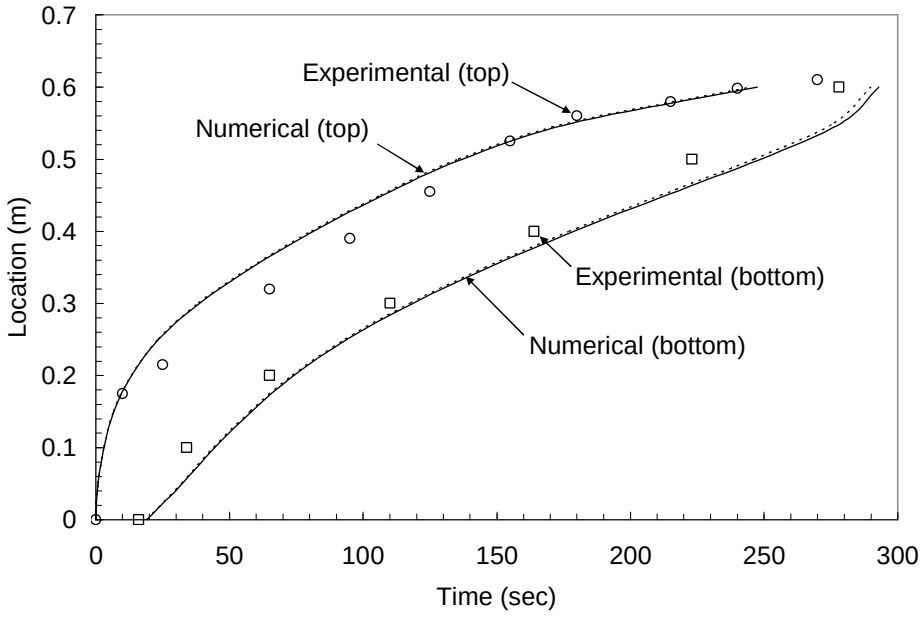

Figure 5-33 Plot of flow front location versus time showing experimental and simulation results.

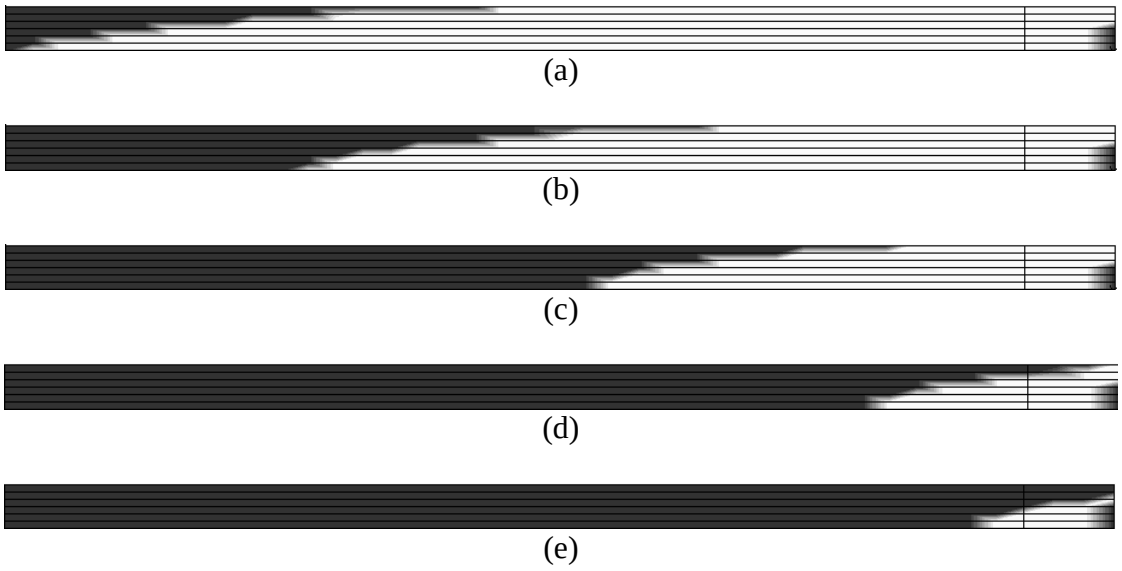

Figure 5-34 Resin filling simulation of the uni-directional preform showing elapsed times of a) 20, b) 60, c) 120, d) 200, and e) 240 seconds.

The recorded pressure at each sensor during the filling process is compared with the predicted pressures from the simulation in Figure 5-35. From the plot it is seen that the simulation and experimental results show good agreement with the exception of sensor P1 where the pressures are under predicted by about 8 kPa. The discrepancy at sensor P1 may be explained by the fact that the permeability along the edge of the preform at sensor P1 is unknown and the assumed value may be too low.

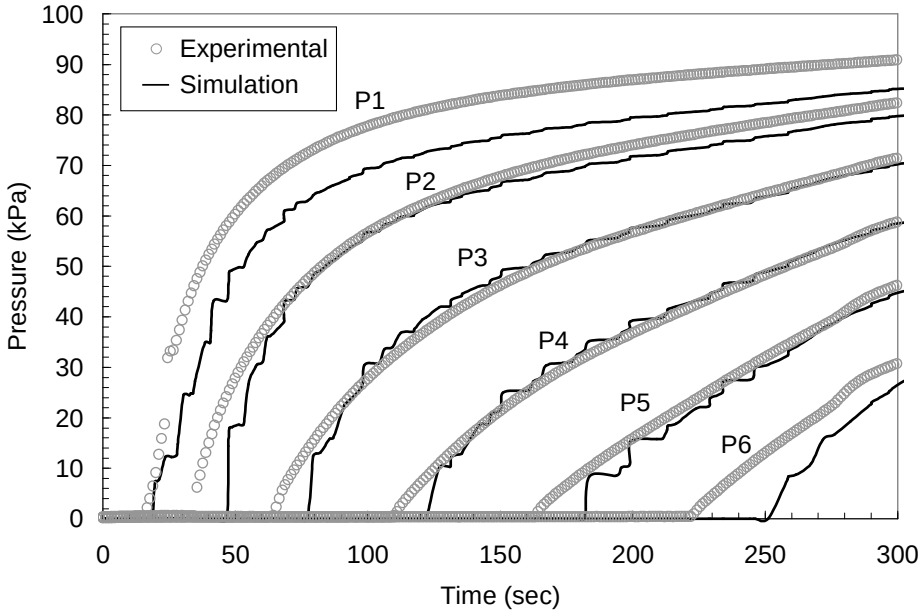

Figure 5-35 Plot of Pressure versus filling time at each pressure sensor (P1-P6) comparing experimental measurements and simulation results.

In addition to pressure, the predicted laminate thickness during the filling process is compared with the experimentally measured thickness. Through the compaction versus fiber volume fraction constitutive relationship previously established the predicted laminate thickness may be determined. From the initial fiber volume fraction (V_f^o) at full compaction and the initial preform thickness (h^o) the current average fiber volume through the thickness of the laminate may be used with Eq. (3.31) to determine the current laminate thickness. The initial fully compacted fiber volume fraction was found to be 0.486 with the initial thickness being 24 mm. A comparison of the predicted and experimentally measured laminate thickness at sensor locations D1, D2, and D3 during the filling process is shown in Figure 5-36. From the figure it is seen that the predicted thicknesses and measured thicknesses show good agreement.

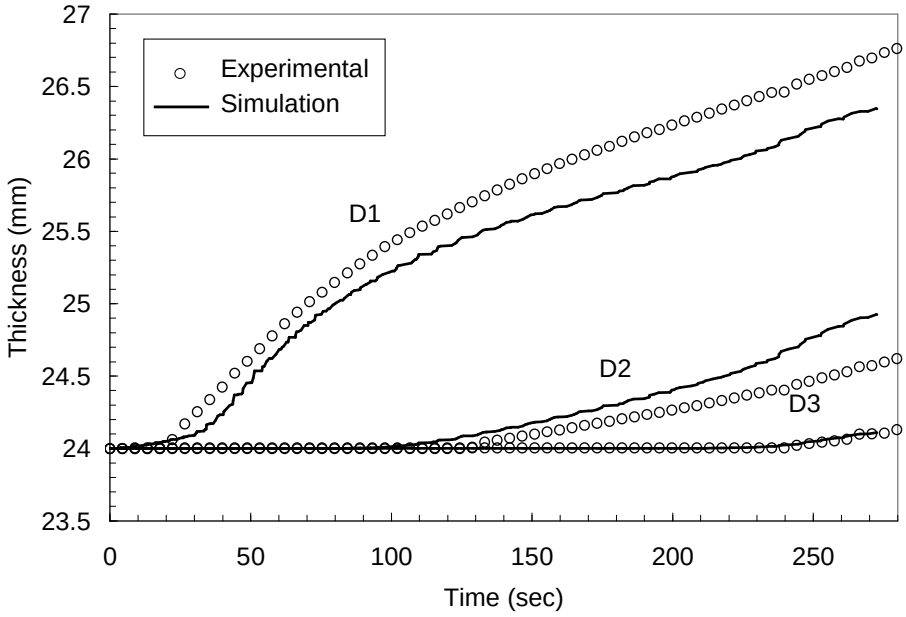

Figure 5-36 Plot of laminate thickness versus filling time showing experimental measurements as well as simulation predictions at each displacement transducer location.

Resin Bleeding (50 kPa Applied at Inlet)

For the first bleeding experiment, in which a pressure of 50 kPa was applied at the inlet, plots of the experimental and predicted pressures along the length of the preform at different bleeding times are given in Figure 5-37 and Figure 5-38 respectively. The plot in Figure 5-37 shows simulation results obtained using the compaction curve from the constitutive model and Figure 5-39 shows simulation results using the relaxation curve from the constitutive model. It is observed that the compaction model predicts pressures which are initially lower than experimental values but come closer to matching experimental measurements at longer bleeding times. On the other hand the relaxation model does a good job of matching initial pressure measurements but over predicts pressures at longer bleeding times.

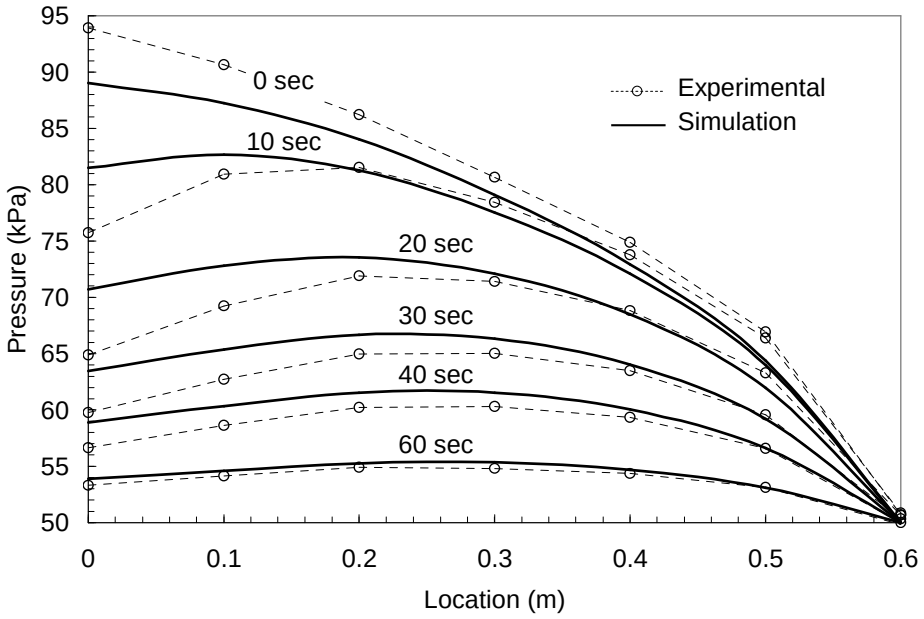

Figure 5-37 Plot of experimentally measured pressures and predicted pressures using the compaction curve from the constitutive model versus location at different bleeding times for an applied pressure of 50 kPa at the inlet.

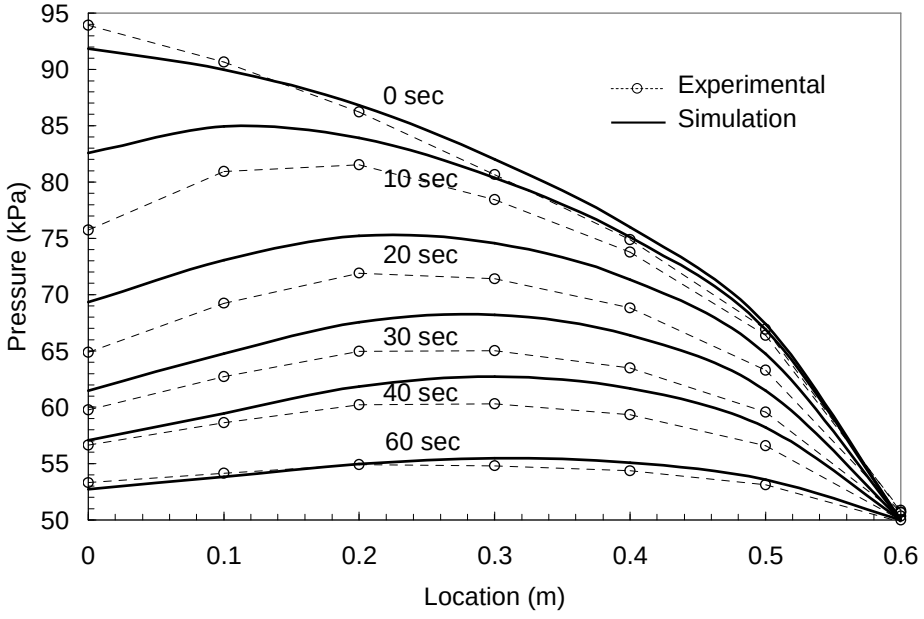

Figure 5-38 Plot of experimentally measured pressures and predicted pressures using the relaxation curve from the constitutive model versus location at different bleeding times for an applied pressure of 50 kPa at the inlet.

Plots of the pressure time history for pressure sensors P1 through P6 are given in Figure 5-39 through Figure 5-44 respectively. Each plot shows the experimental measurements along with simulation predictions using both the compaction and relaxation constitutive model curves. As was noted previously, the predictions using the compaction curve underestimate the initial pressures but do a good job of capturing the pressures at longer bleeding times. From the plots it is observed that the simulations using the relaxation curve capture the initial pressures very well but slightly over predict the pressures at longer bleeding times. During the filling stage the preform undergoes relaxation therefore the predicted pressures at the end of filling and the beginning of the bleeding phase are the same and are be best predicted using the relaxation curve from the constitutive model. During the bleeding stage the preform undergoes compaction and the simulation utilizes the compaction curve from the constitutive model. However, as was seen in Figure 5-17, there are infinitely many unique compaction curves which are dependent on the starting point from the relaxation curve. In reality the correct pressure is based on curves which fall between the established relaxation and compaction constitutive curves.

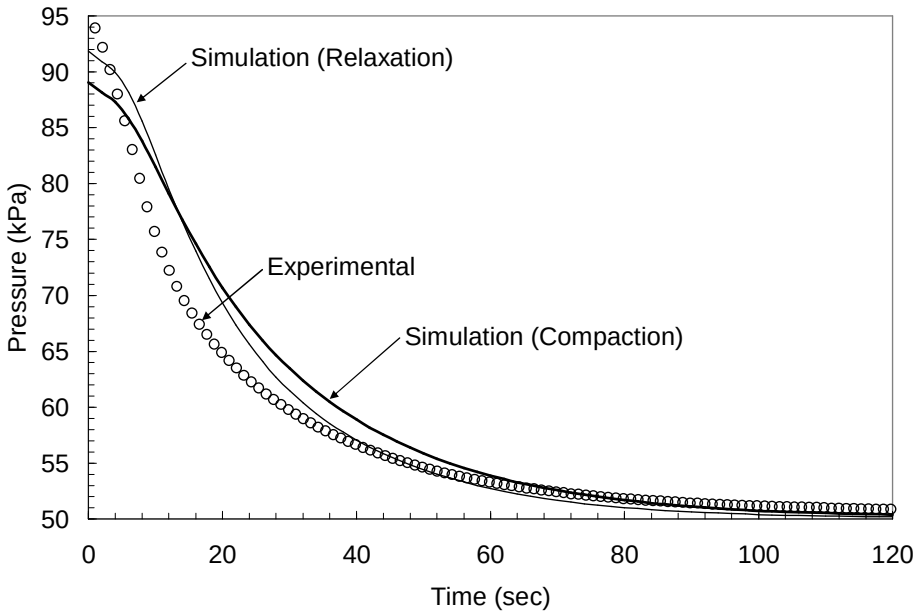

Figure 5-39 Plot of pressure versus time at pressure sensor P1 (0 m) showing experimental data as well as numerical results using relaxation and compaction constitutive models.

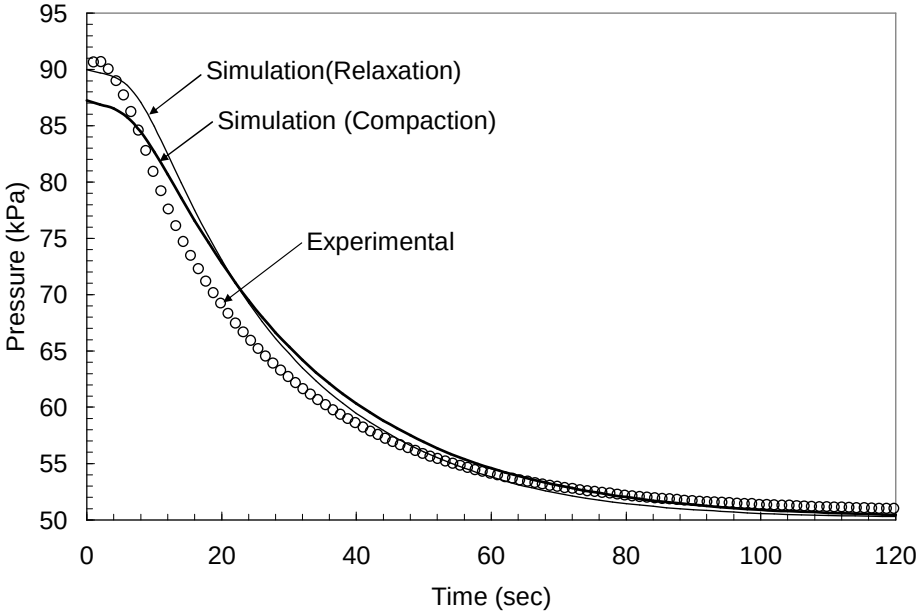

Figure 5-40 Plot of pressure versus time at pressure sensor P2 (0.1 m) showing experimental data as well as simulation results using relaxation and compaction constitutive models.

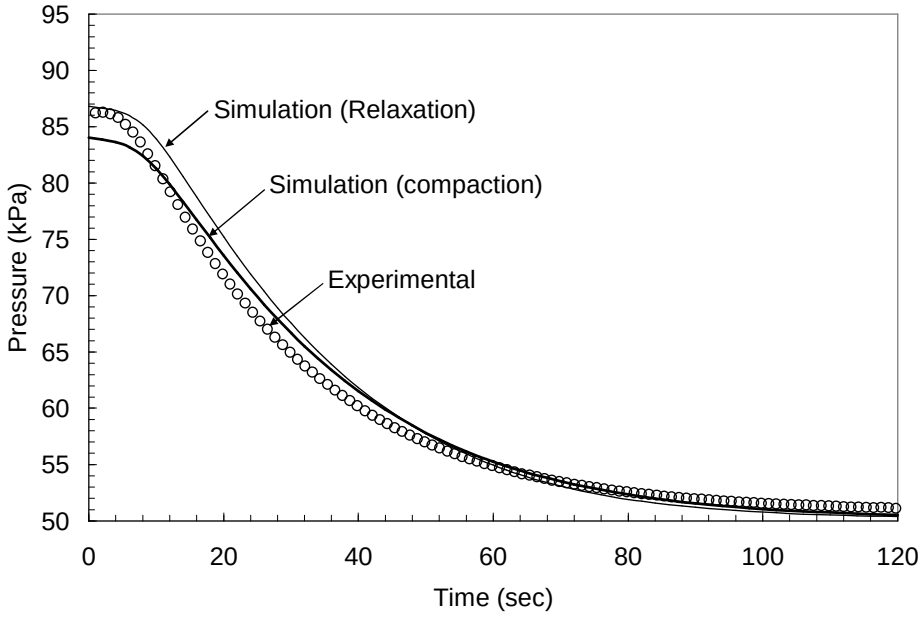

Figure 5-41 Plot of pressure versus time at pressure sensor P3 (0.2 m) showing experimental data as well as simulation results using relaxation and compaction constitutive models.

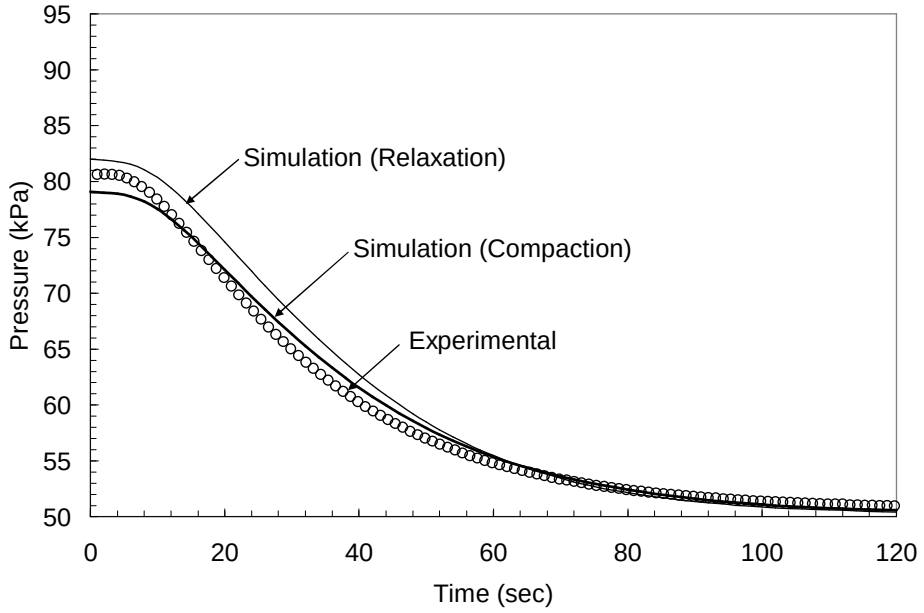

Figure 5-42 Plot of pressure versus time at pressure sensor P4 (0.3 m) showing experimental data as well as simulation results using relaxation and compaction constitutive models.

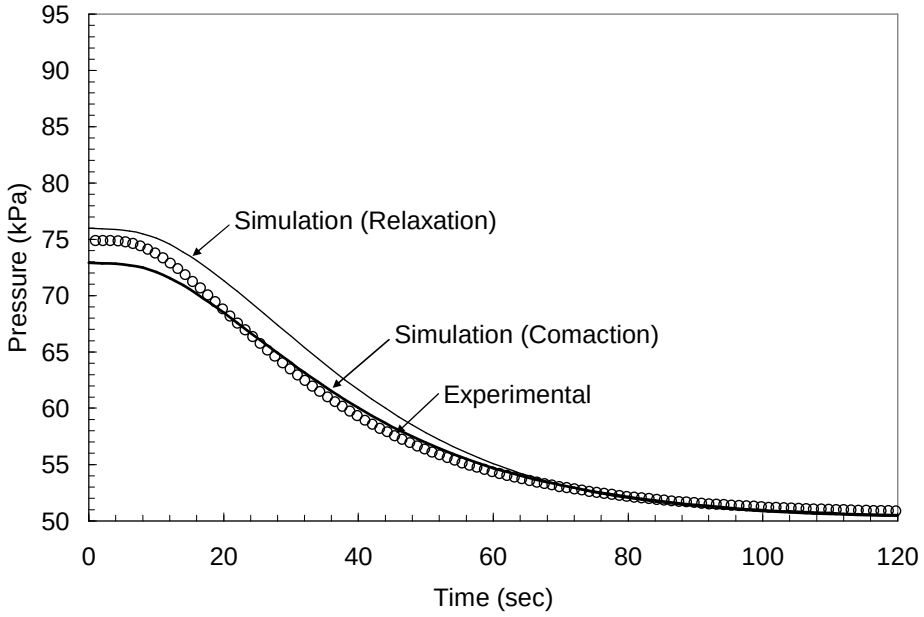

Figure 5-43 Plot of pressure versus time at pressure sensor P5 (0.4 m) showing experimental data as well as simulation results using relaxation and compaction constitutive models.

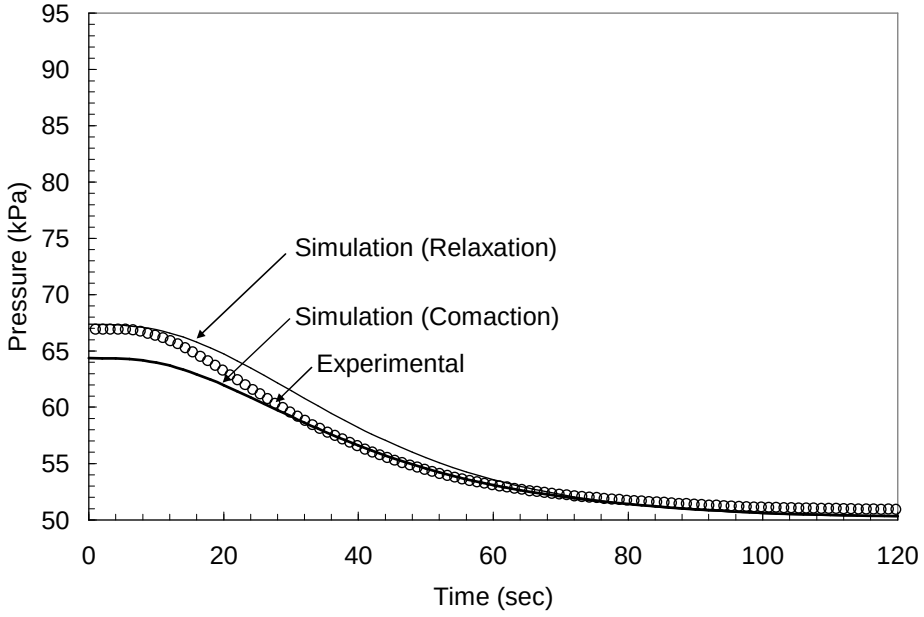

Figure 5-44 Plot of pressure versus time at pressure sensor P6 (0.5 m) showing experimental data as well as simulation results using relaxation and compaction constitutive models.

Plots showing the pressure field and corresponding fiber volume fractions within the preform for elapsed bleeding times of 0, 10, 20, 30, 40, and 60 seconds are given in Figure 5-45 and Figure 5-46 respectively. From Figure 5-45 it is observed that at the beginning of the bleeding process the pressure gradient through the thickness is minimal. However, due to the pressure applied at the inlet a significant pressure gradient is created through the thickness of the laminate causing oil to flow from the preform into the flow distribution mesh and then out through the inlet hose. Bleeding through the inlet hose leads to a very short bleeding time (100 seconds).

The fiber volume fraction plots given in Figure 5-46 are used to predict the thickness of the laminate at each of the displacement sensor locations D1 through D3. Plots of the predicted displacement using both the compaction and relaxation curves from the constitutive model are given in Figure 5-47 through Figure 5-49 respectively. From the plots it is observed that the experimental measurements lie between the lower thickness predicted by the relaxation curve and higher thickness prediction using the compaction curve. The predicted thicknesses show the correct trends, however in general the total predicted change in thickness at each location exceeds the actual measured change in thickness. A summary of the preform thickness changes of the preform at each displacement sensor location is given in Table 5-5 at the end of this section. From the table it is seen that the predicted thicknesses based on the relaxation curve shows the best agreement with experimental measurements. Surprisingly the experimental measurements at sensor location D3 showed no change in the thickness of the preform while a thickness change of 0.5 mm was predicted. This discrepancy could be due to deformation of the mold as vacuum is applied to the

vacuum bag (the mold is only 3 mm thick) or it may be due to the thickness of the preform. The compaction constitutive model for the uni-directional preform was based on measurements performed on a preform consisting of three plies of material while the preform under consideration consists of 30 plies of material. It has been shown by others [86, 87, 89, 90, 91] that the number of plies of the material affects the relationship between compaction pressure and fiber volume fraction.

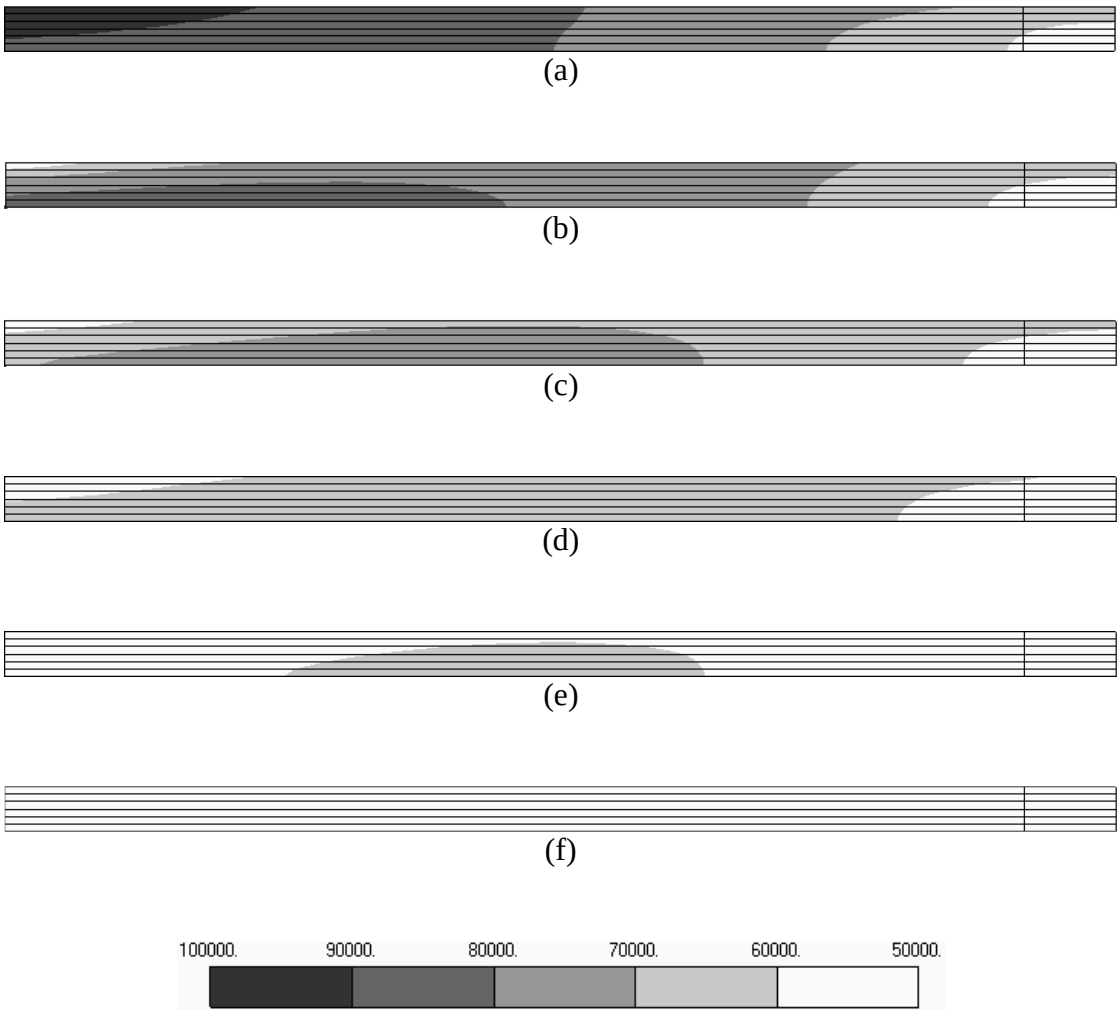

Figure 5-45 Contour plots of resin pressure for the uni-directional laminate using the compaction model with vacuum pressure applied at inlet showing pressures at (a) 0, (b) 10, (c) 20, (d) 30, (e) 40, and (f) 60 seconds.

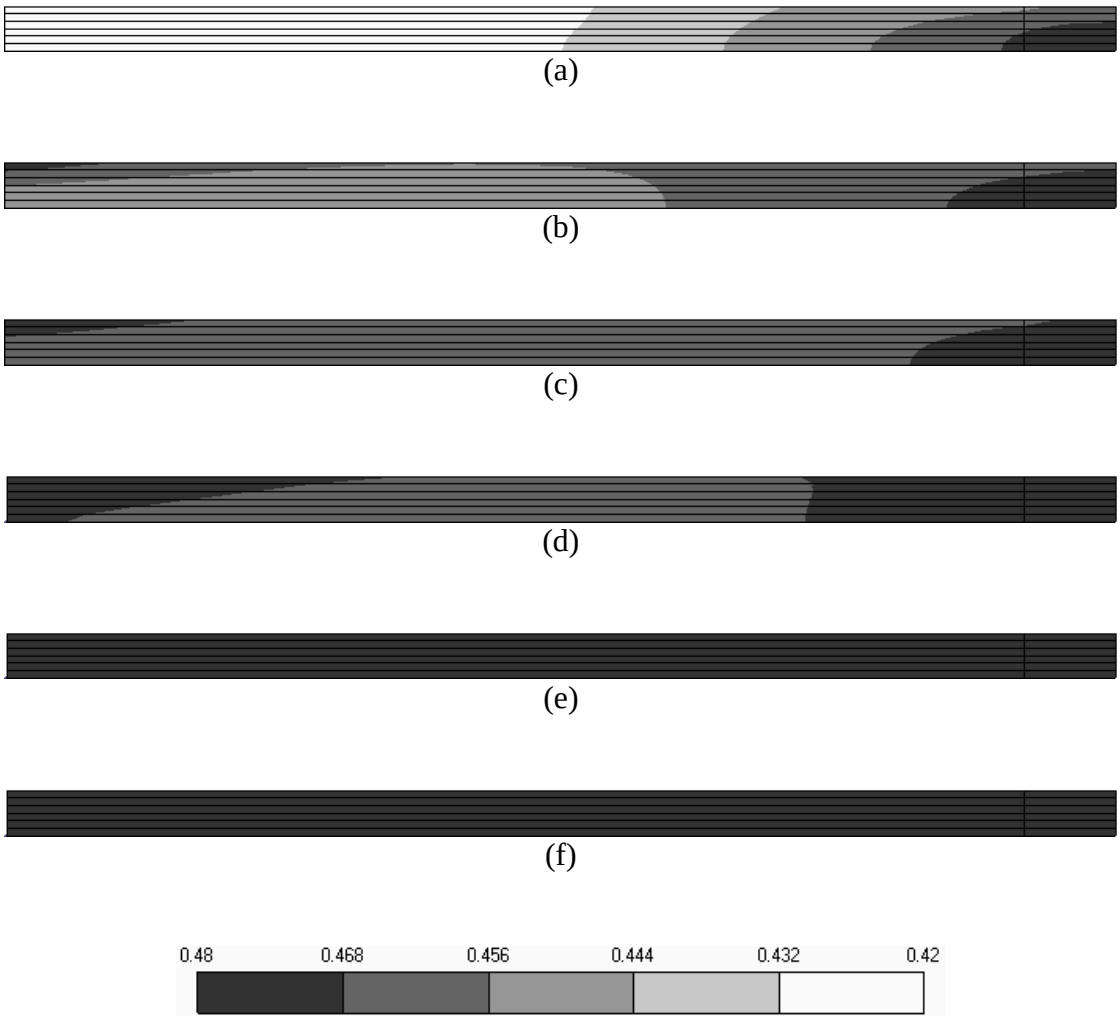

Figure 5-46 Contour plots of fiber volume fraction for the uni-directional laminate using the compaction model with vacuum pressure applied at the inlet showing pressures at (a) 0, (b) 10, (c) 20, (d) 30, (e) 40, and (f) 60 seconds.

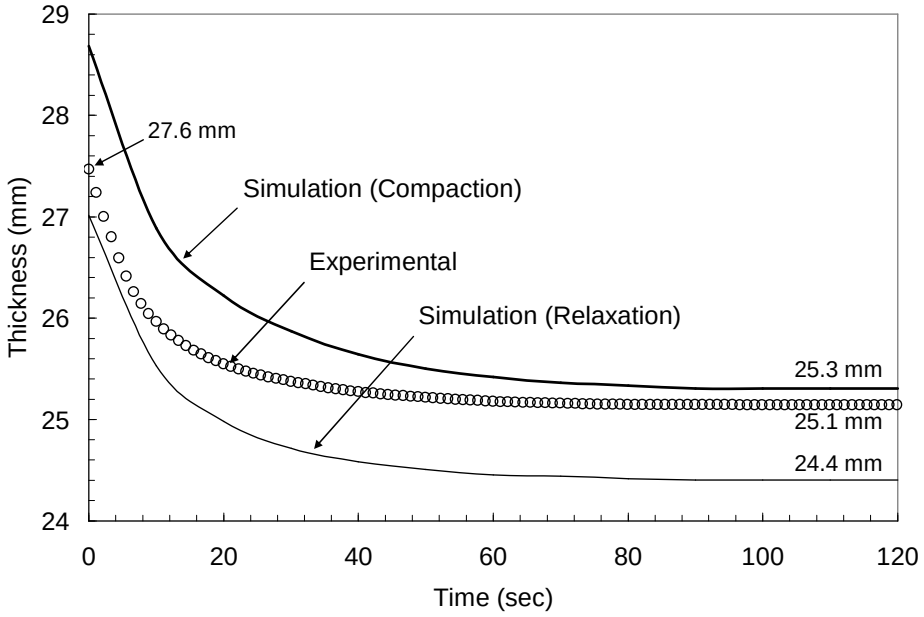

Figure 5-47 Plot of thickness versus bleeding time with 50kPa applied at the inlet comparing the predicted laminate thickness at sensor D1 with the experimentally measured thickness.

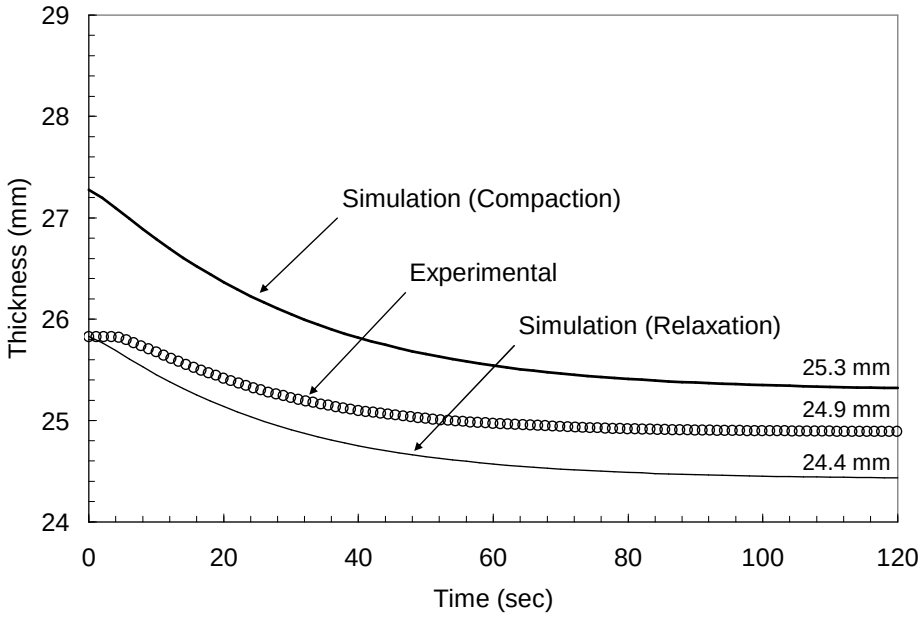

Figure 5-48 Plot of thickness versus bleeding time with 50kPa applied at the inlet comparing the predicted laminate thickness at sensor D2 with the experimentally measured thickness.

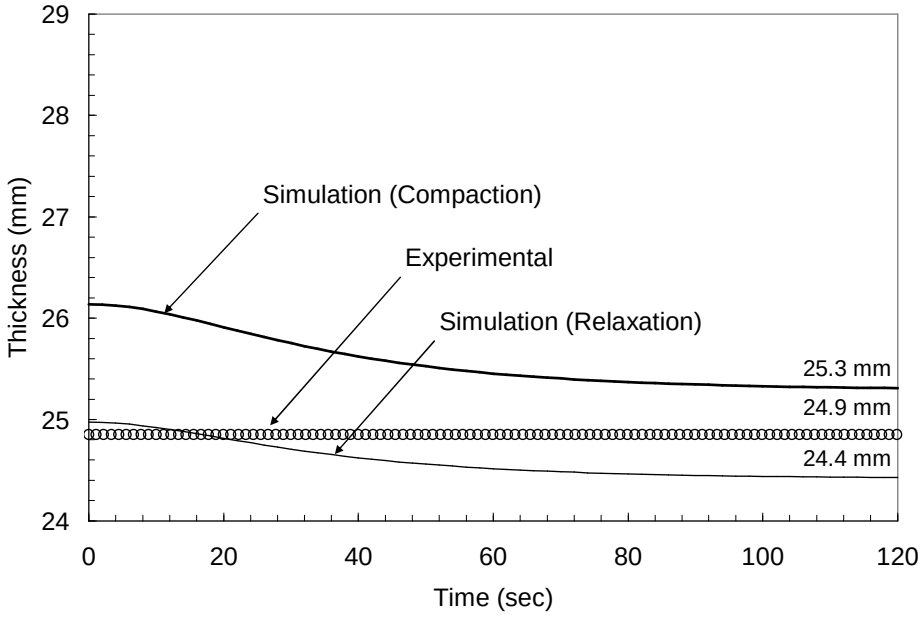

Figure 5-49 Plot of thickness versus bleeding time with 50kPa applied at the inlet comparing the predicted laminate thickness at sensor D3 with the experimentally measured thickness.

Resin Bleeding (Inlet Closed)

The second bleeding experiment is identical to the first bleeding experiment with the exception that rather than applying vacuum pressure at the inlet, the inlet is simply closed and oil is allowed to exit through the outlet hose only. A plot of the predicted pressures based on the compaction curve from the constitutive model along with experimental measurements at different bleeding times is given in Figure 5-50. From the figure it is seen that for all bleeding times the predicted pressures underestimate the measured pressures.

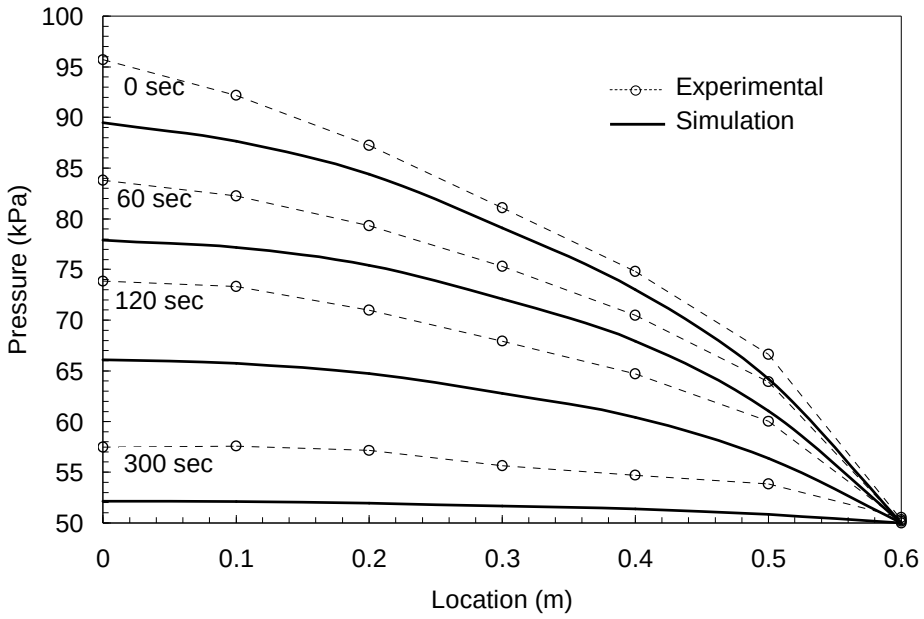

Figure 5-50 Comparison of experimental and predicted pressures using the compaction curve from the constitutive model versus location at different bleeding times with the inlet hose closed.

Time history plots of the pressure versus bleeding time for each pressure sensor are given in Figure 5-51 through Figure 5-56. Each plot shows the experimentally measured pressures along with the predicted pressures using both the compaction and relaxation curves from the constitutive model. From the plots it is seen that both predictions using the two different constitutive curves show very similar results with the relaxation curve predicting slightly higher pressures at the beginning of the bleeding process. In all cases the simulated pressures under predict the actual measured pressures with the simulation reaching equilibrium (50 kPa) much sooner than experimental data. One explanation may be that when the inlet hose is clamped there still remains some excess oil in the flow spring at the inlet which continues to

flow in to the preform as the vacuum bag compresses around the spring. The simulation does not account for any resin coming into the preform after the inlet hose is closed.

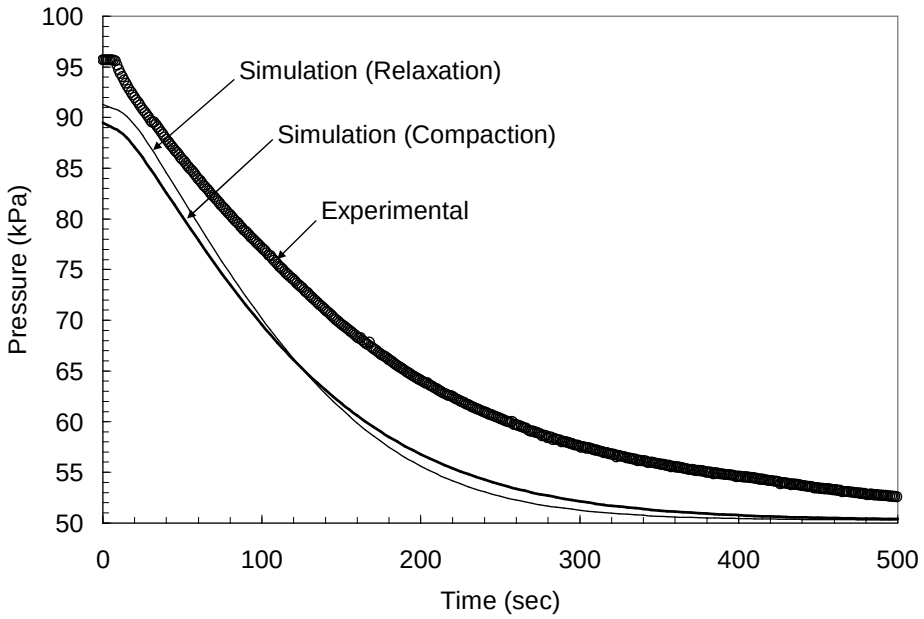

Figure 5-51 Plot of pressure versus time at pressure sensor P1 (0 m) showing experimental results as well as simulation results using both relaxation and compaction models.

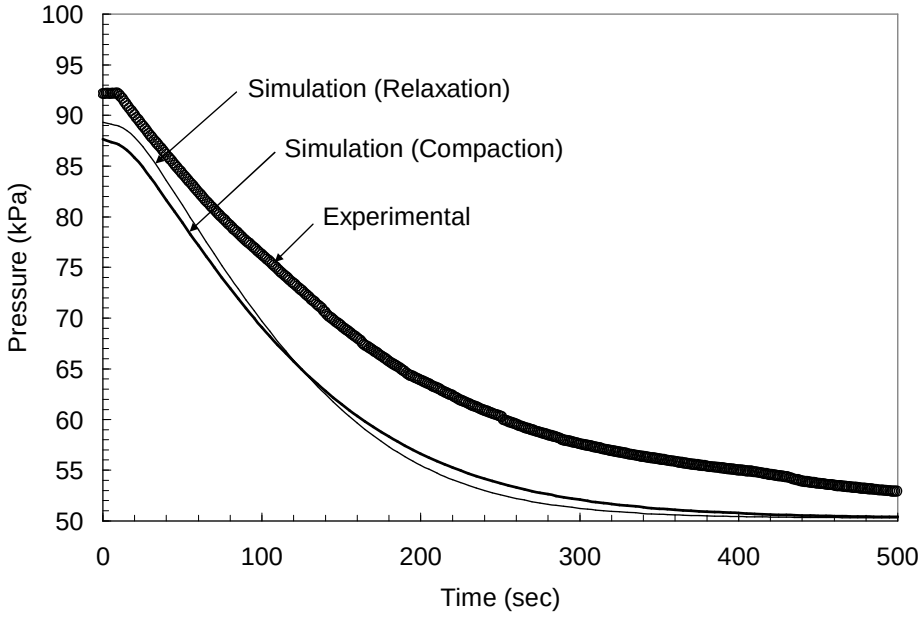

Figure 5-52 Plot of pressure versus time at pressure sensor P2 (0.1 m) showing experimental results as well as simulation results using both relaxation and compaction models.

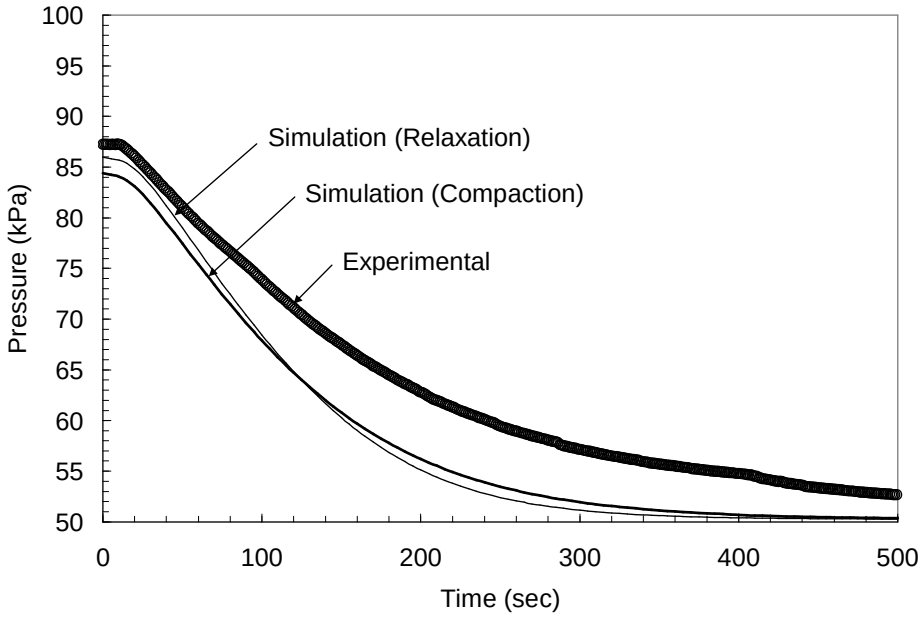

Figure 5-53 Plot of pressure versus time at pressure sensor P3 (0.2 m) showing experimental results as well as simulation results using both relaxation and compaction models.

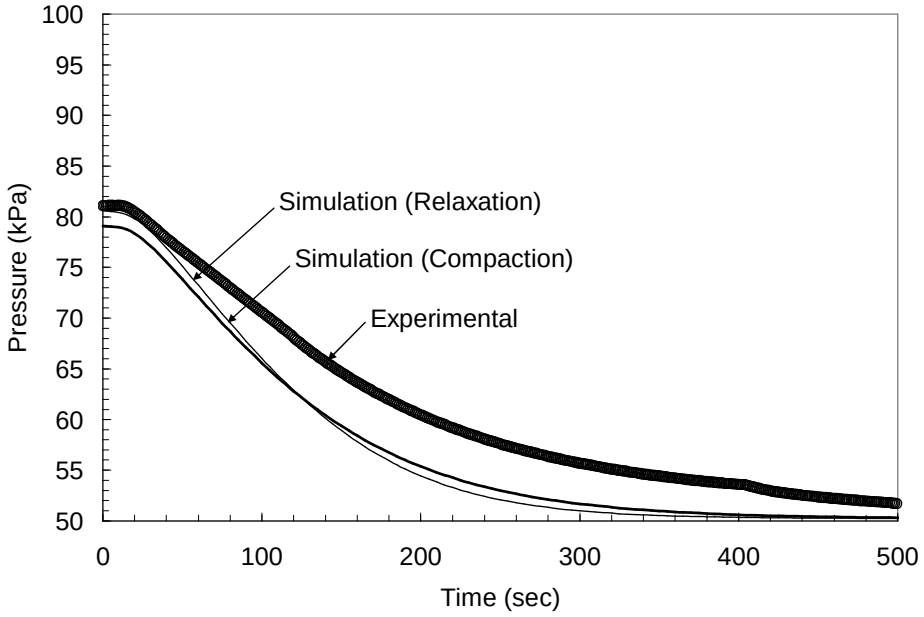

Figure 5-54 Plot of pressure versus time at pressure sensor P4 (0.3 m) showing experimental results as well as simulation results using both relaxation and compaction models.

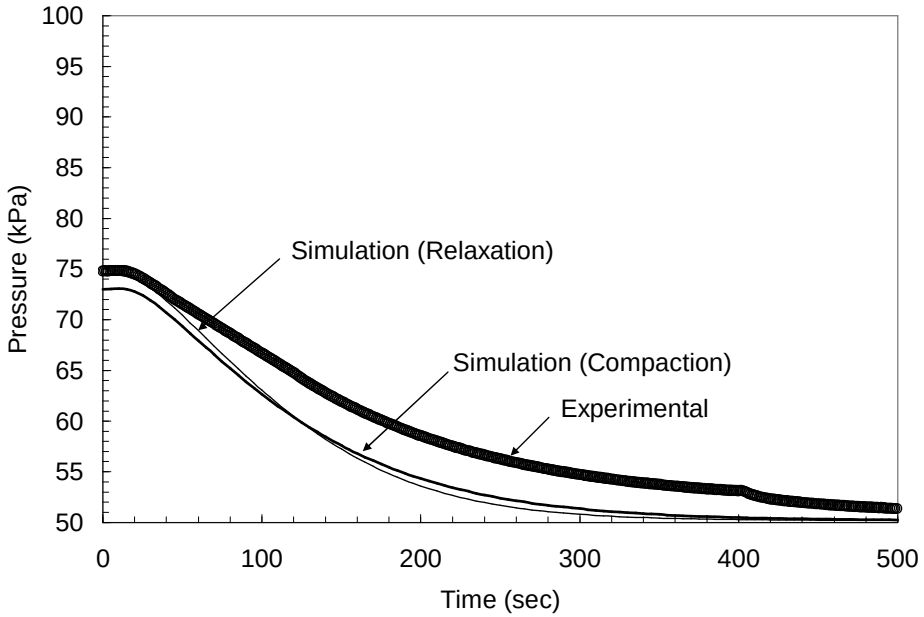

Figure 5-55 Plot of pressure versus time at pressure sensor P5 (0.4 m) showing experimental results as well as simulation results using both relaxation and compaction models.

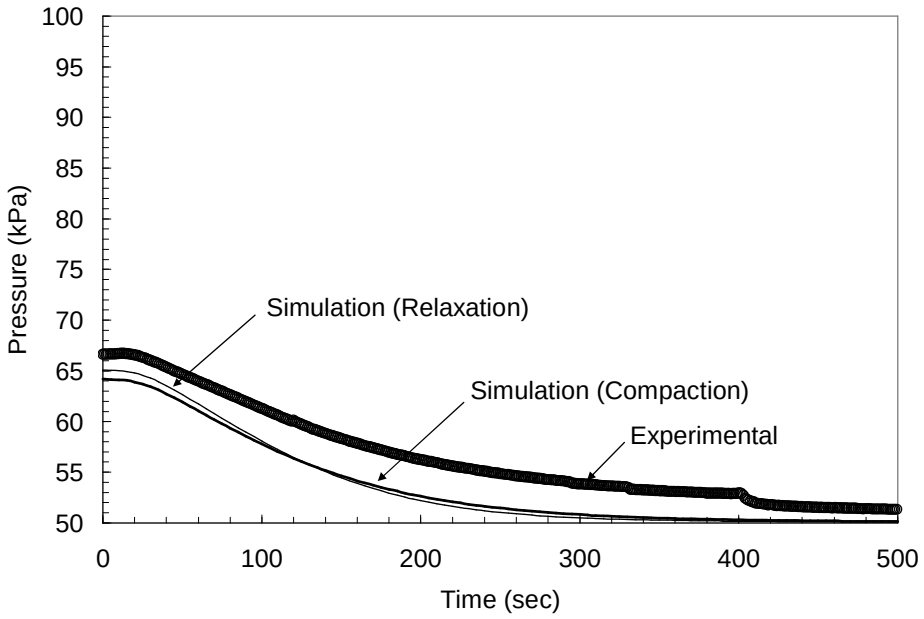

Figure 5-56 Plot of pressure versus time at pressure sensor P6 (0.5 m) showing experimental results as well as simulation results using both relaxation and compaction models.

Pressure as well as fiber volume fraction contour plots of the preform at bleeding times of 0, 20, 40, 60, 90, 120, and 180 seconds are given in Figure 5-57 and Figure 5-58 respectively. From Figure 5-57 it is seen that throughout the bleeding process the pressure gradient is predominately along the length of the preform with a very small pressure gradient through the thickness. Due to the nature of the pressure gradient the flow of resin is predominately taking place within the preform with the flow distribution mesh doing little to aid in the bleeding process. For this bleeding experiment the time to reach equilibrium was approximately 500 seconds compared to 100 seconds for the case when vacuum pressure is applied at the inlet.

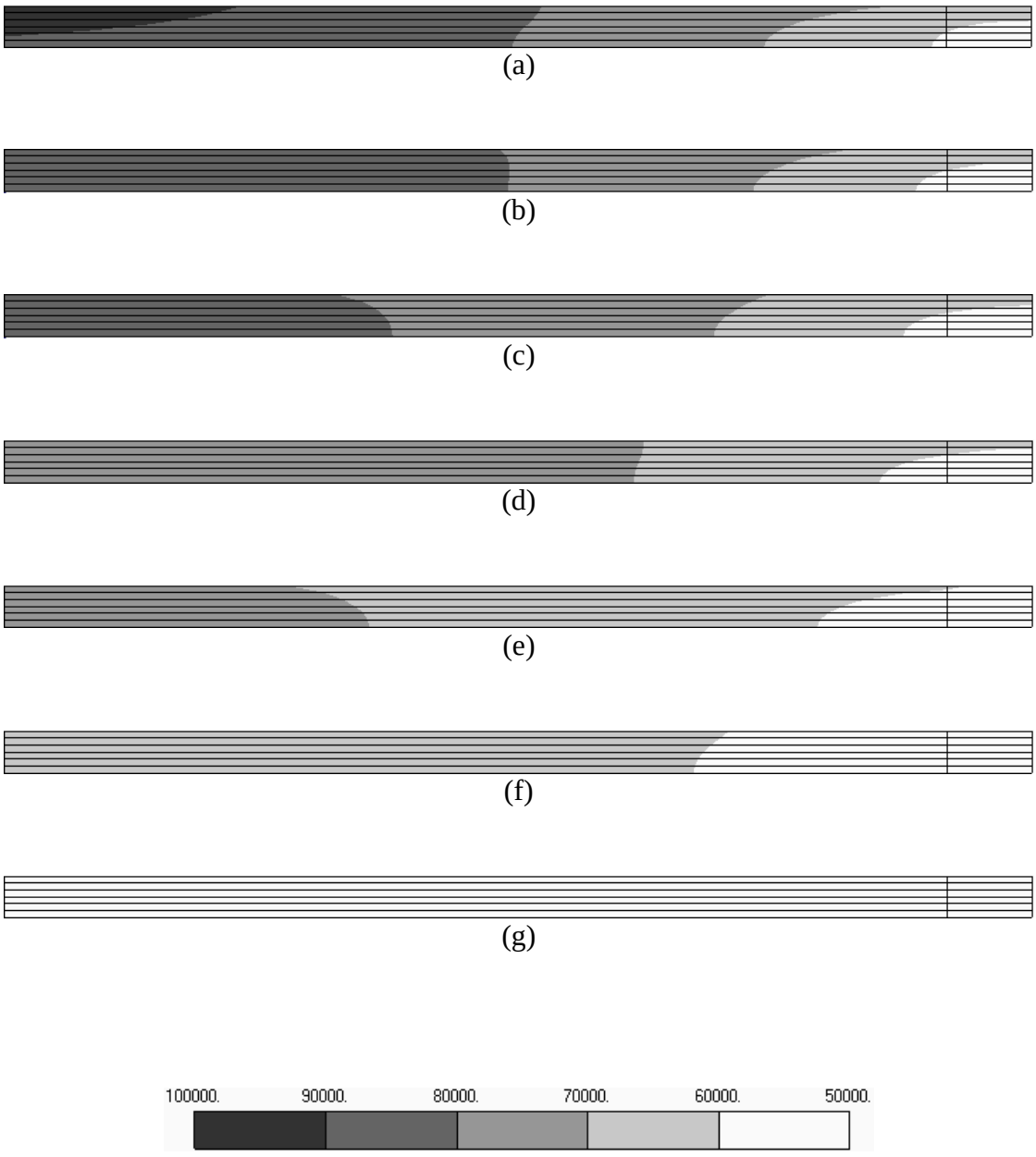

Figure 5-57 Contour plots of resin pressure for the uni-directional laminate with the inlet closed showing pressures at (a) 0, (b) 20, (c) 40, (d) 60, (e) 90, (f) 120, and (g) 180 seconds.

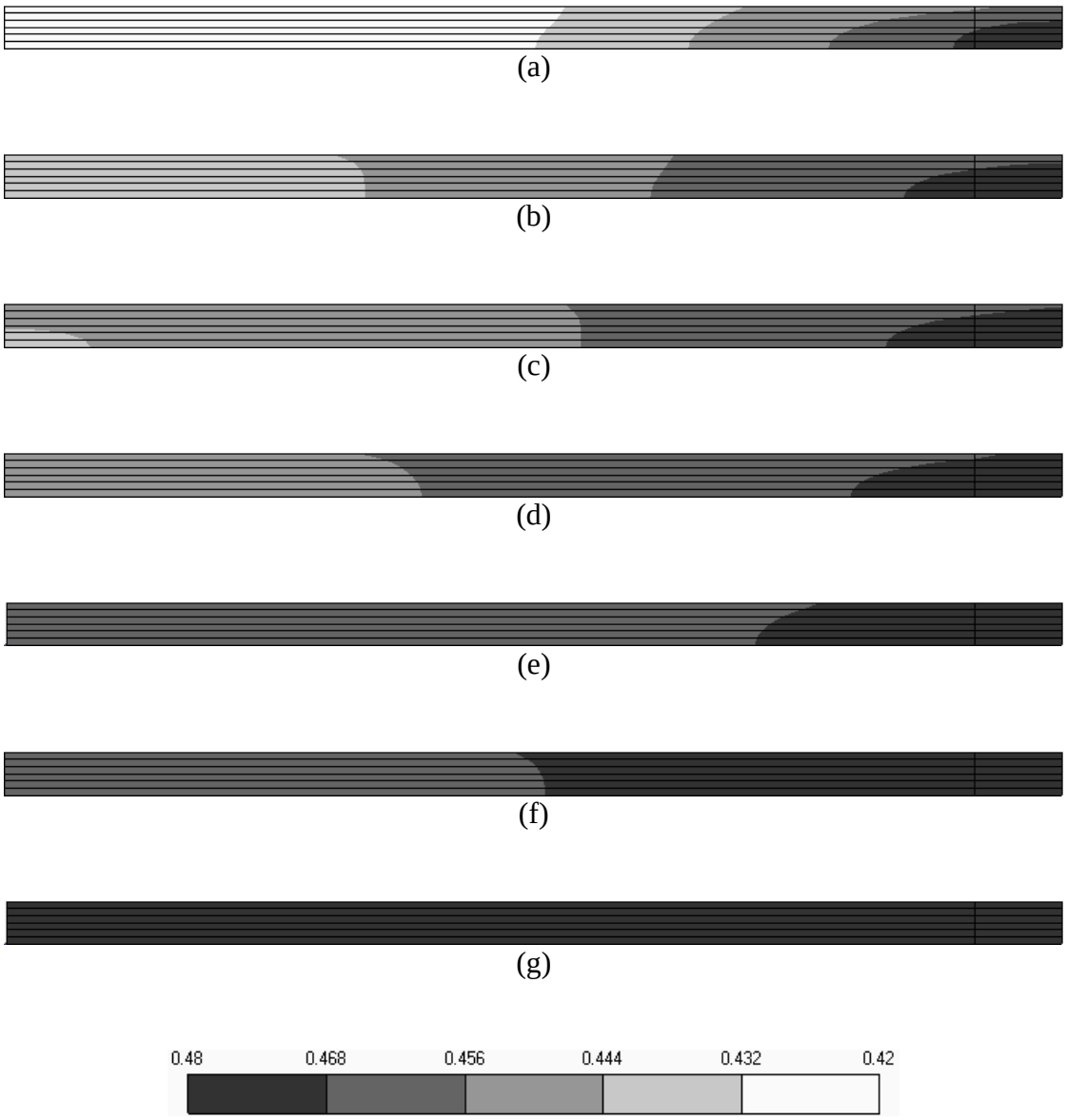

Figure 5-58 Contour plots of fiber volume fraction for the uni-directional laminate with the inlet closed showing pressures at (a) 0, (b) 20, (c) 40, (d) 60, (e) 90, (f) 120, and (g) 180 seconds.

From the predicted fiber volume fractions the laminate thicknesses are predicted at each displacement sensor location using both the compaction and

relaxation constitutive models. Plots of the predicted thickness along with experimental measurements for sensors D1, D2, and D3 are shown in Figure 5-59 through Figure 5-61 respectively. At all three sensor locations the final laminate thickness is best predicted by the compaction simulation. Again the predicted trends match the experimental results however at all three locations the simulation predicts larger overall changes in thickness in comparison with the experimental measurements. Unlike previous observations, the experimentally measured thickness at D1 is not bounded by the compaction and relaxation predictions but exceed both curves. This is most likely due to an offset in the measurement due to disturbance of the sensor or offsets in the data acquisition. From Figure 5-47, Figure 5-48, and Figure 5-49 it is observed that when the pressure is uniform (50 kPa) at the end of bleeding the thickness measurements at each sensor location are nearly the same (D1=2.51 mm, D2=2.49 mm, and D3=2.49 mm). However from Figure 5-59, Figure 5-60, and Figure 5-61 it is seen that at a uniform pressure of 50 kPa at the end of bleeding the thickness measurement at D2 and D3 are uniform at 2.51 mm while the thickness at D1 is much higher having a measured thickness of 25.8 mm. It is believed that the measurements at D1 are approximately 0.6 to 0.7 mm too high. A summary of the measured and predicted thickness changes are given in Table 5-5 at the end of this section. From the results it is seen that while the compaction curve best predicts the final thickness the relaxation constitutive model best captures the change in preform thickness. Again the discrepancy in measurements and predictions may be due to the thickness of the preform in comparison to the thin preform used to develop the compaction constitutive model.

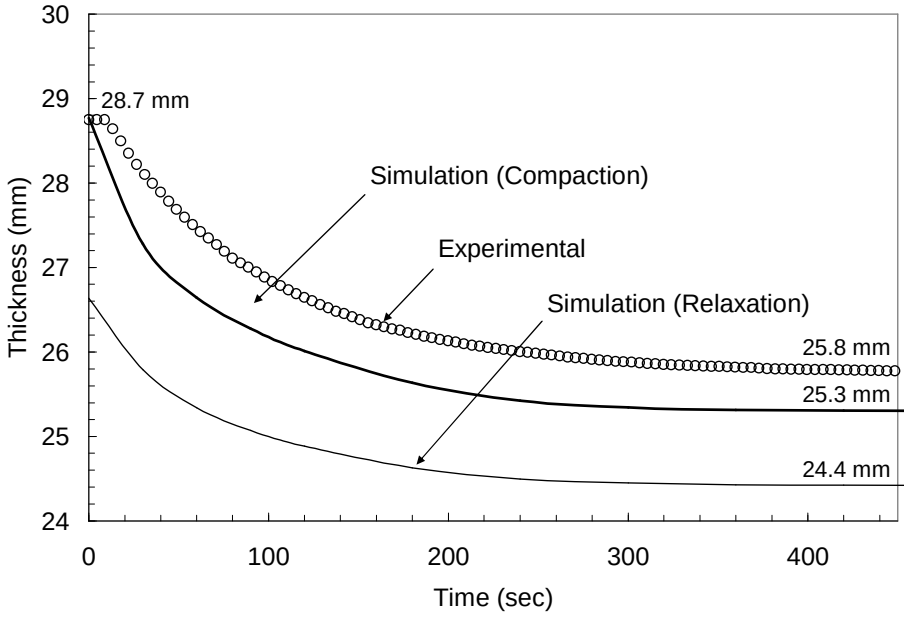

Figure 5-59 Plot of thickness versus bleeding time with the inlet closed comparing the predicted laminate thickness at sensor D1 with the experimentally measured thickness.

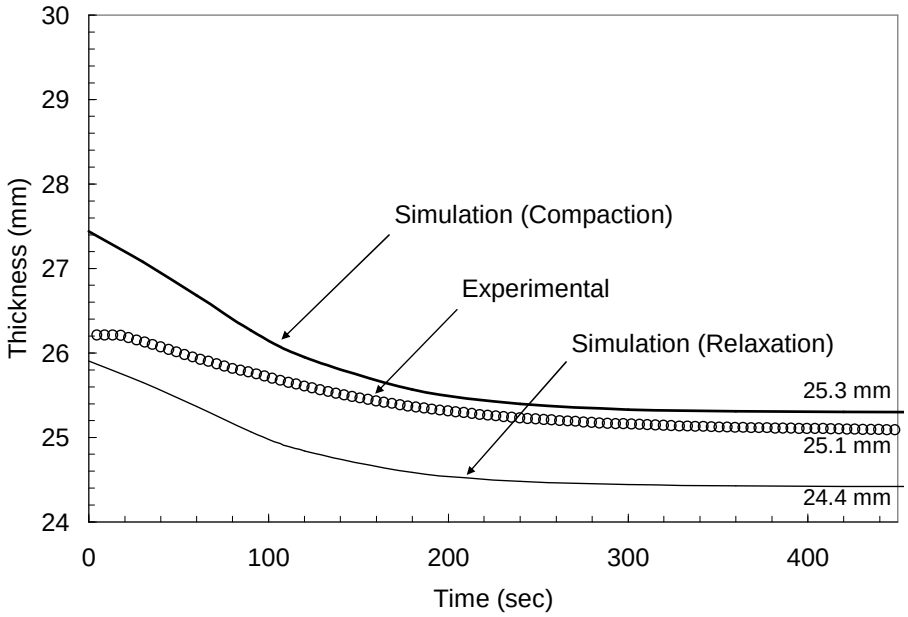

Figure 5-60 Plot of thickness versus bleeding time with the inlet closed comparing the predicted laminate thickness at sensor D2 with the experimentally measured thickness.

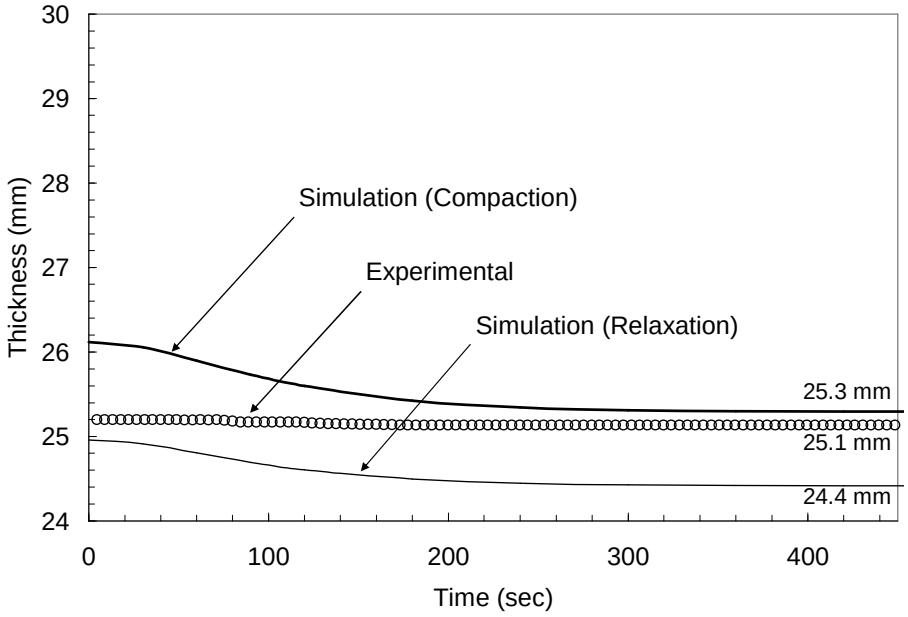

Figure 5-61 Plot of thickness versus bleeding time with the inlet closed comparing the predicted laminate thickness at sensor D1 with the experimentally measured thickness.

Preform Relaxation (Atmospheric Pressure at Inlet)

The final experiment for the uni-directional preform with flow distribution mesh consisted of allowing resin to flow back into the preform from an initial uniform pressure of 48 kPa. Oil was allowed to flow back into the preform under atmospheric pressure at the inlet. A plot of the pressure along the length of the preform during the relaxation process is given in Figure 5-62. The plot shows experimental measurements as well as simulation results using the relaxation curve from the constitutive model for elapsed times of 0, 10, 30, and 60 seconds. From the plot it is seen that the simulation does a very good job of predicting the pressures except near the inlet. Again this is likely due to using too low of a permeability along the preform/vacuum bag interface near the inlet.

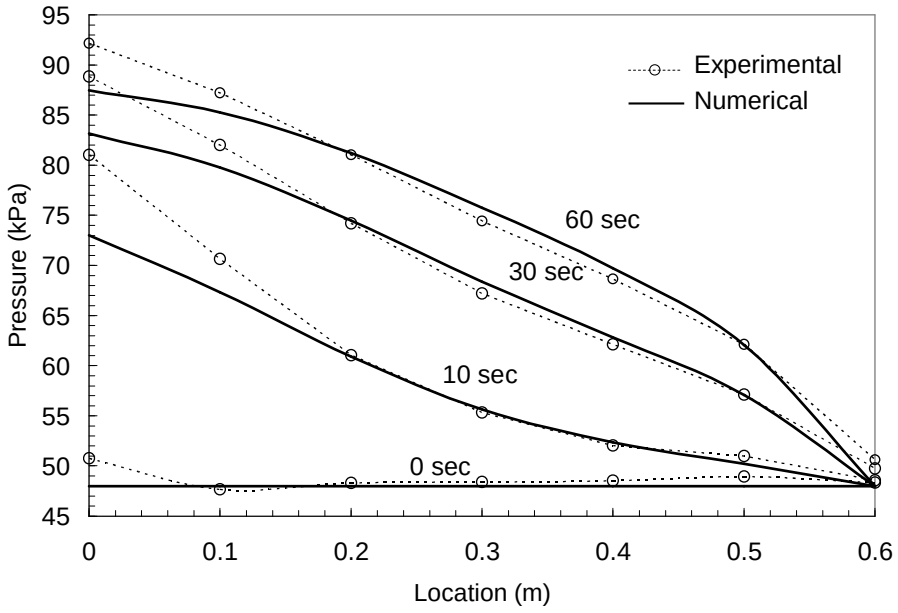

Figure 5-62 Comparison of simulation and experimental pressure versus location at different times during relaxation of the preform.

Time history plots of pressure versus time for pressure sensors P1 through P6 are given in Figure 5-63 through Figure 5-68 respectively. Each plot shows the experimental measurements as well as the simulation results using both the compaction and relaxation constitutive models. With the exception of sensor P1 the simulation results using the relaxation model show very good agreement with the experimental measurements. This is not surprising since the preform started at a uniform constant pressure and then underwent relaxation.

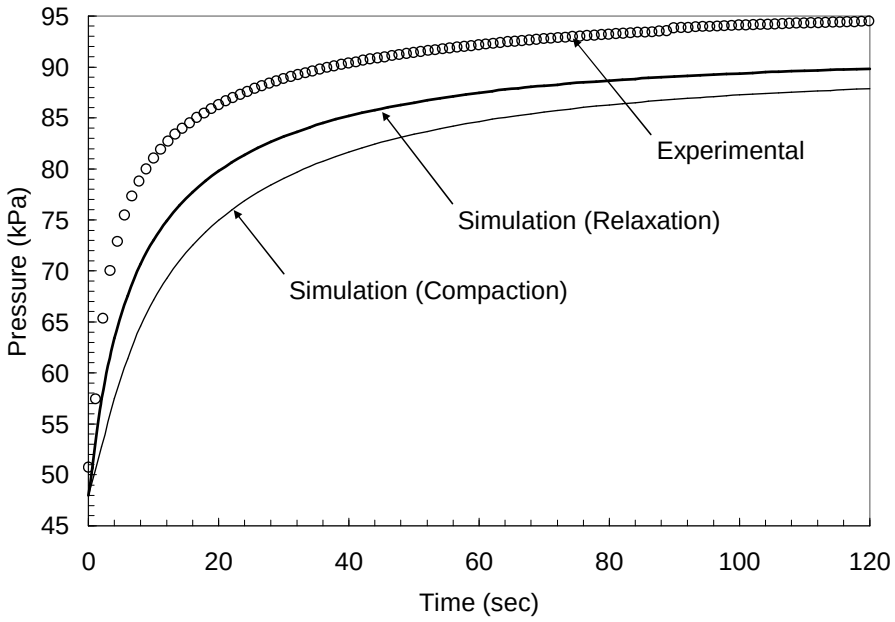

Figure 5-63 Plot of pressure versus time at pressure sensor P1 (0.0 m) showing experimental results as well as simulation results for both relaxation and compaction models.

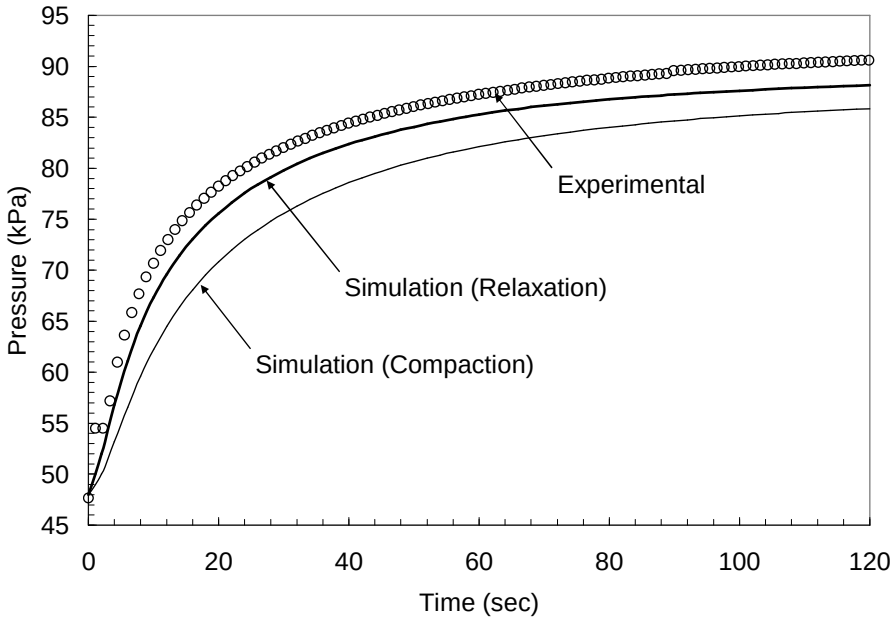

Figure 5-64 Plot of pressure versus time at pressure sensor P2 (0.1 m) showing experimental results as well as simulation results for both relaxation and compaction models.

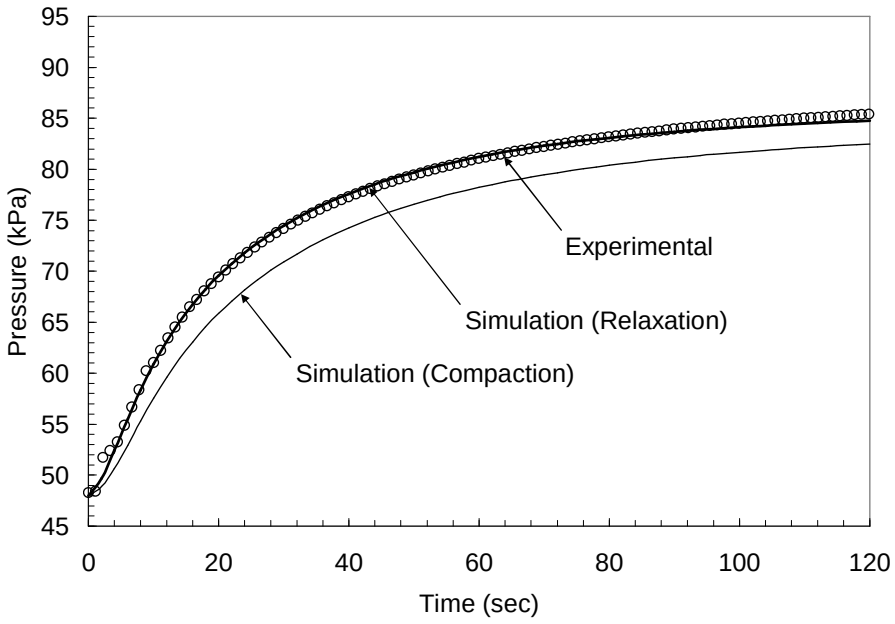

Figure 5-65 Plot of pressure versus time at pressure sensor P3 (0.2 m) showing experimental results as well as simulation results for both relaxation and compaction models.

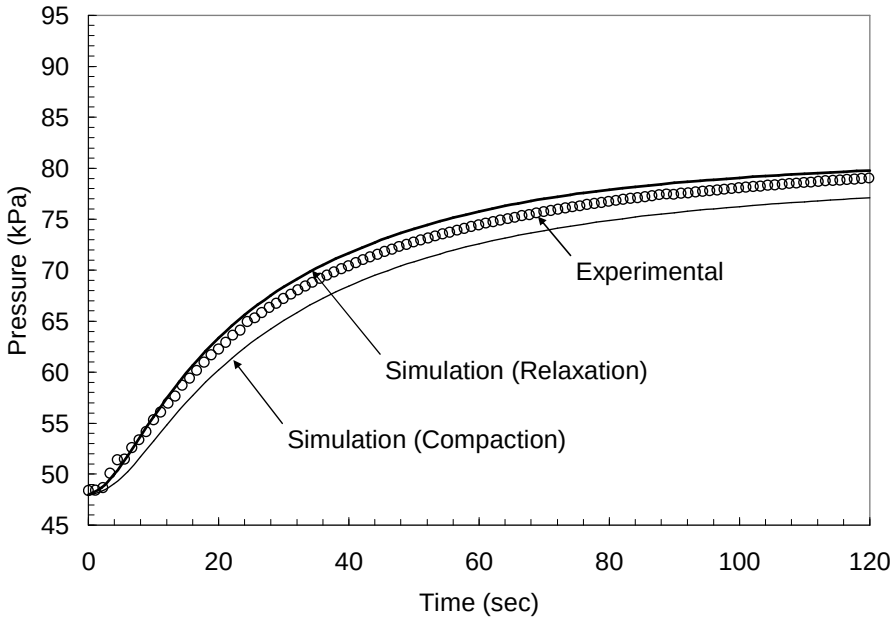

Figure 5-66 Plot of pressure versus time at pressure sensor P4 (0.3 m) showing experimental results as well as simulation results for both relaxation and compaction models.

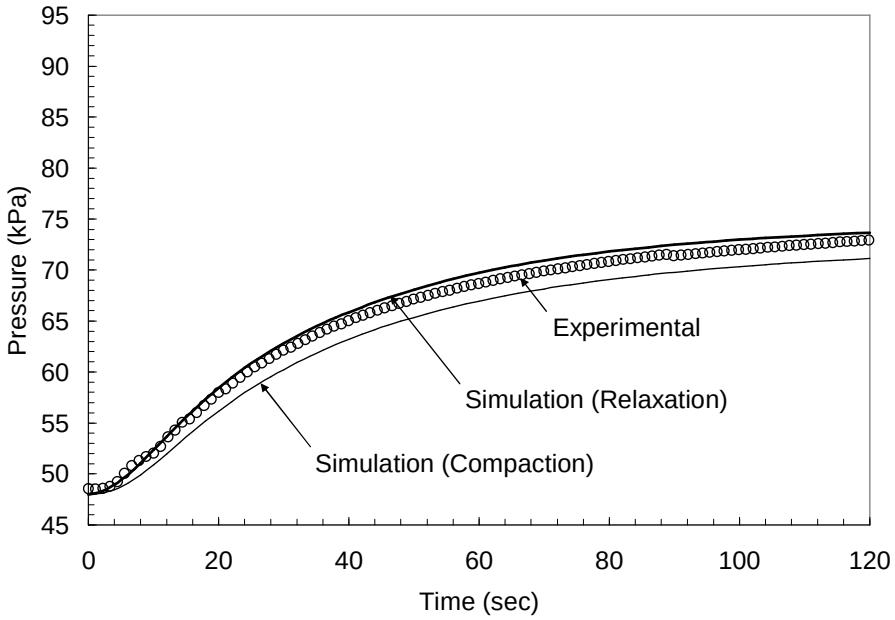

Figure 5-67 Plot of pressure versus time at pressure sensor P5 (0.4 m) showing experimental results as well as simulation results for both relaxation and compaction models.

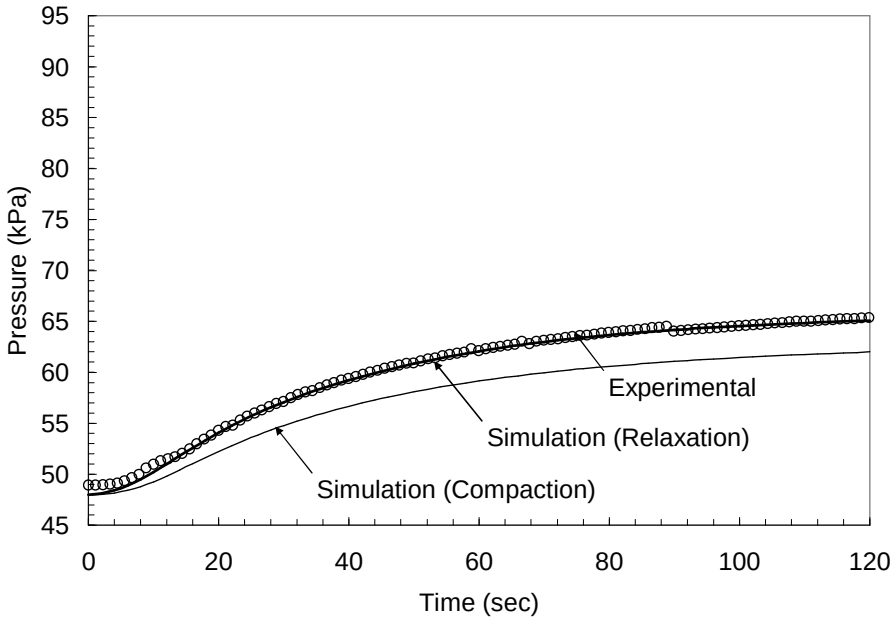

Figure 5-68 Plot of pressure versus time at pressure sensor P6 (0.5 m) showing experimental results as well as simulation results for both relaxation and compaction models.

Contour plots of predicted pressure and fiber volume fraction during the relaxation process for elapsed times of 0, 10, 20, 30, 40, 60, and 120 seconds are shown in Figure 5-69 and Figure 5-70 respectively.

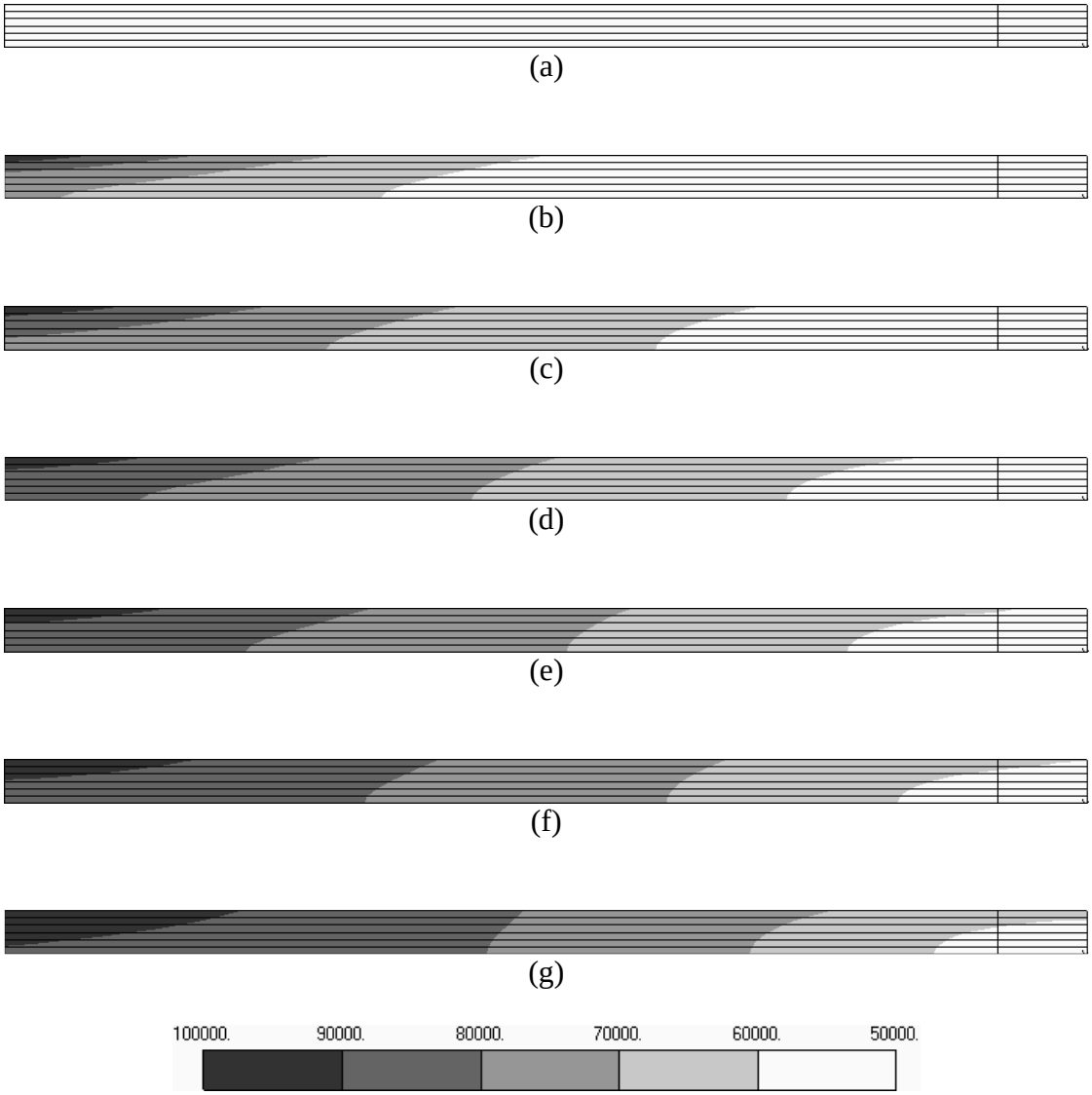

Figure 5-69 Contour plots of resin pressure for the uni-directional laminate during relaxation showing pressures at (a) 0, (b) 10, (c) 20, (d) 30, (e) 40, (f) 60, and (g) 120 seconds.

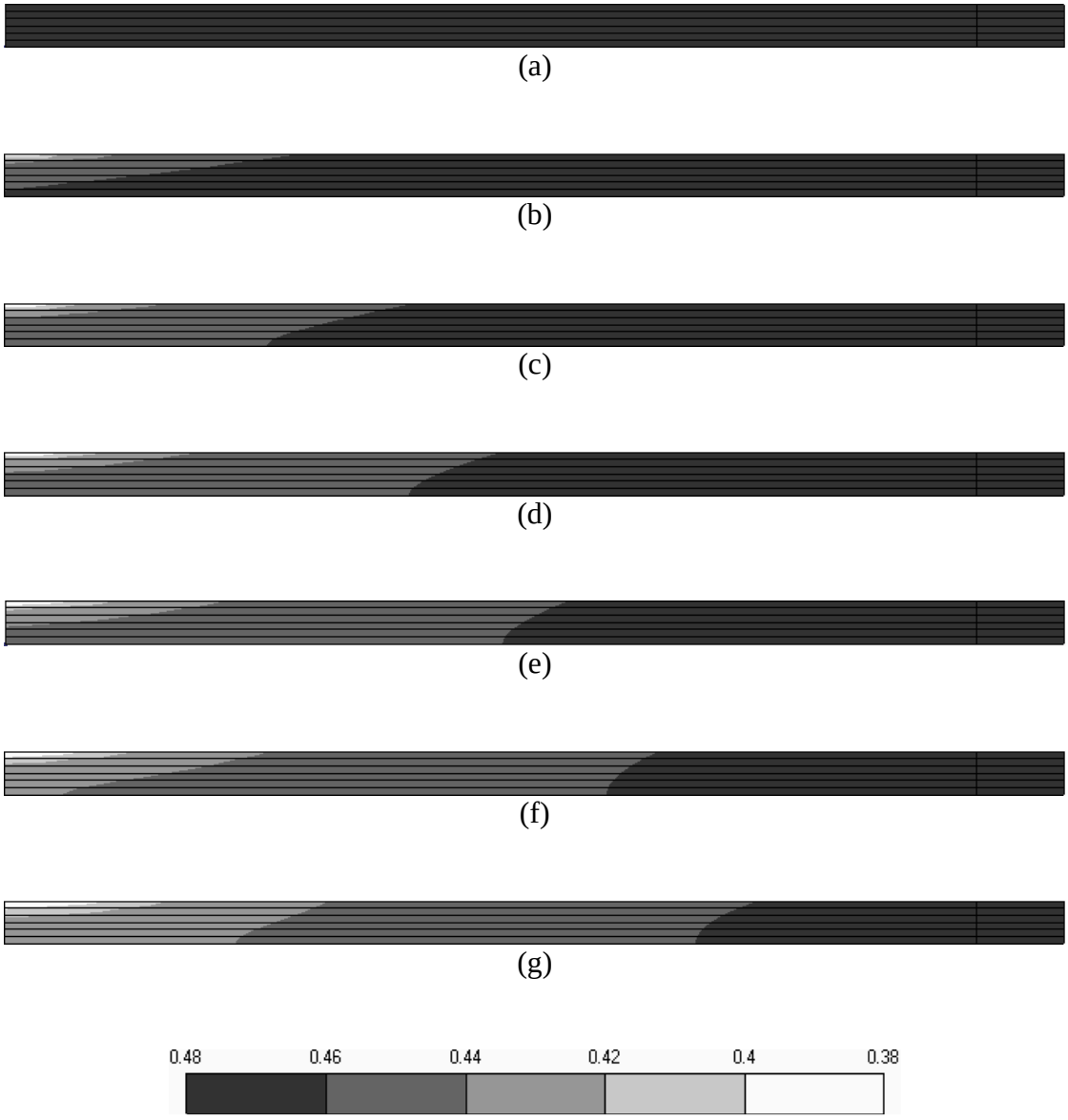

Figure 5-70 Contour plots of fiber volume fraction for the uni-directional laminate during relaxation showing pressures at (a) 0, (b) 10, (c) 20, (d) 30, (e) 40, (f) 60, and (g) 120 seconds.

From the predicted fiber volume fractions the laminate thicknesses are predicted at each displacement sensor location using both the compaction and relaxation constitutive models. Plots of the predicted thickness along with experimental measurements for sensors D1, D2, and D3 are shown in Figure 5-71 through Figure 5-73 respectively. From the plots it is seen that for sensor locations D2 and D3 the relaxation simulation does the best job of predicting the final laminate thickness. At D1, although the relaxation simulation under predicts the magnitude of the thickness it does a good job capturing the trend of the experimental data as well as the total change in thickness. Looking at the initial measured thickness at time zero (50 kPa uniform pressure) the measured thickness at D1 is 25.7 mm which is about 0.7 mm higher than the thickness measured at D2 and D3. Again it is believed that the curve should be shifted downward 0.7 mm such that the experimental measurements are more closely represented by the relaxation curve. It is observed that the predicted thickness change at D2 and D3 are large in comparison with experimental measurements. Again, as discussed previously, the compaction constitutive relationship was developed from a preform consisting of 3 plies of material while the preform used in these experiments was 30 plies thick. Based on experimental measurements performed by others [86, 87, 89, 90, 91] the compaction constitutive model is dependent on the thickness of the preform. A summary of the measured and predicted thickness changes is given in Table 5-5. Overall for all three experiments the predictions based on the relaxation constitutive model showed better agreement with measured preform thickness changes in comparison to predictions using the compaction curve from the constitutive model.

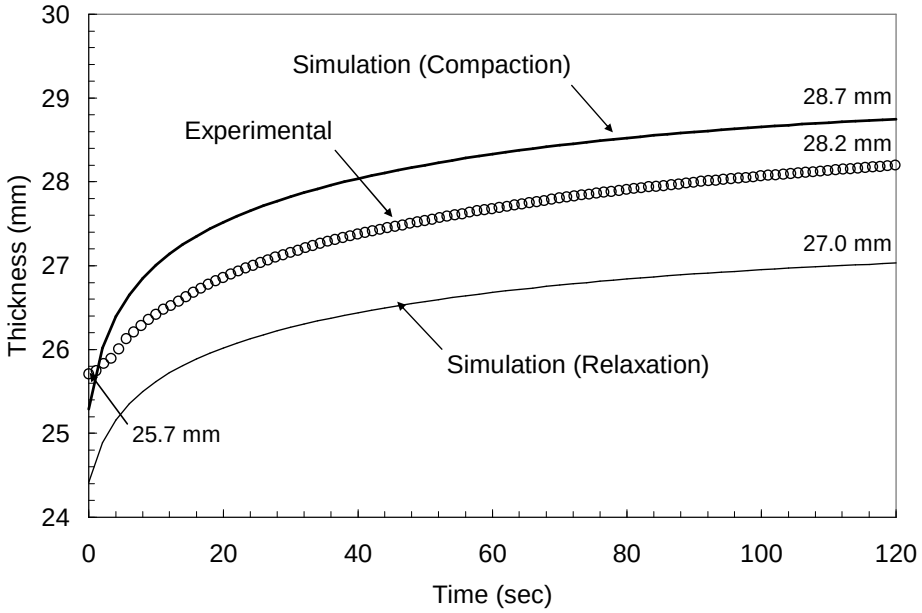

Figure 5-71 Plot of thickness versus time during relaxation comparing the predicted laminate thickness at sensor D1 with the experimentally measured thickness.

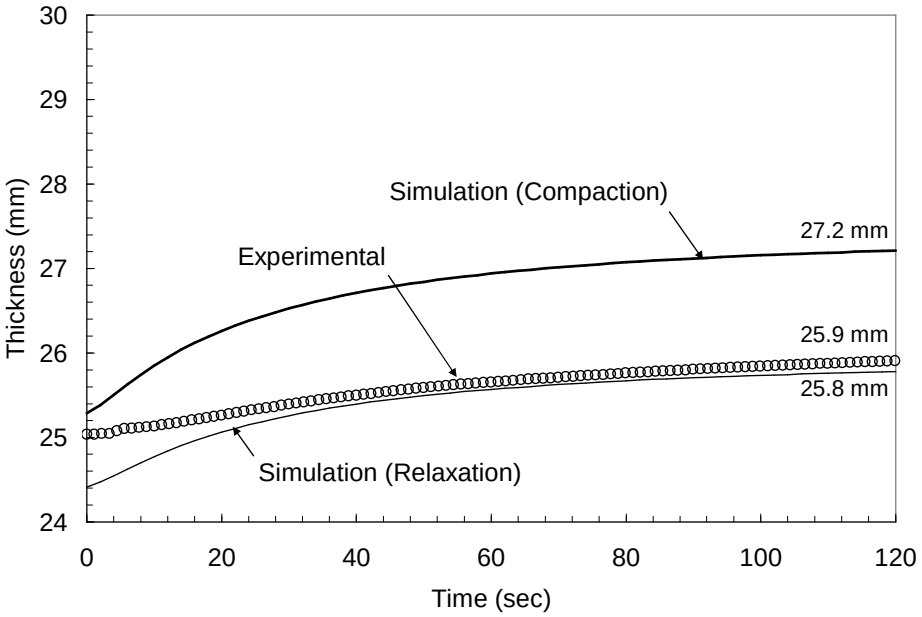

Figure 5-72 Plot of thickness versus time during relaxation comparing the predicted laminate thickness at sensor D2 with the experimentally measured thickness.

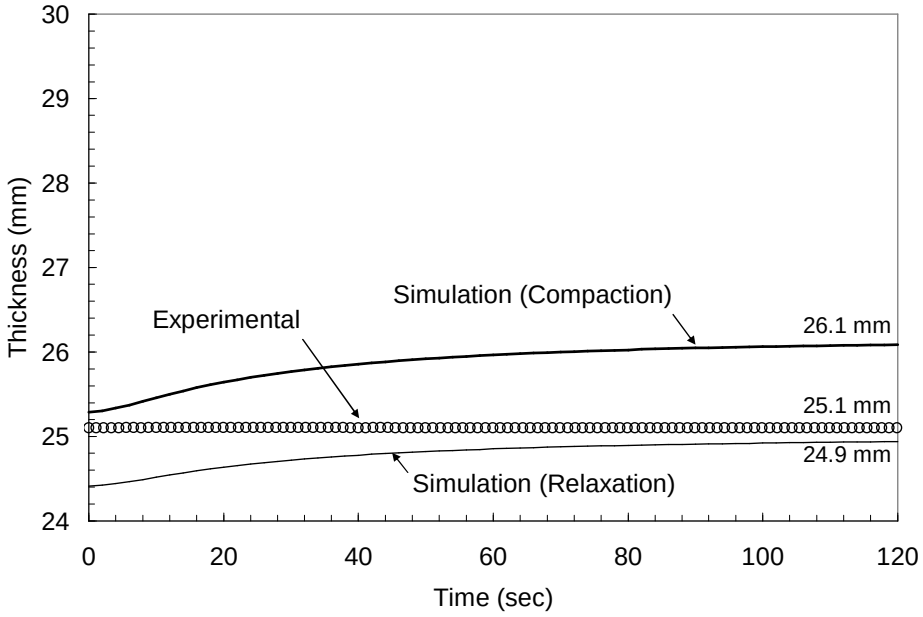

Figure 5-73 Plot of thickness versus time during relaxation comparing the predicted laminate thickness at sensor D3 with the experimentally measured thickness.

Table 5-5 Summary of Thickness Predictions

	D1		*D2*		*D3*	
Case	Δt *(mm)*	*Error (%)*	Δt *(mm)*	*Error (%)*	Δt *(mm)*	*Error (%)*
			Bleed (50 kPa @ Inlet)			
Experimental	2.4	NA	0.9	NA	0.0	NA
Compaction	3.4	+25	2.9	+122	0.8	NaN
Relaxation	2.6	+8	1.4	+55	0.5	NaN
			Bleed (Inlet Closed)			
Experimental	2.9	NA	1.1	NA	0.1	NA
Compaction	3.4	+17	2.0	+82	0.8	+700
Relaxation	2.6	-10	1.4	+27	0.5	+400
			Relax (100 kPa @ Inlet)			
Experimental	2.5	NA	0.9	NA	0.0	NA
Compaction	3.4	+36	2.0	+122	0.8	NaN
Relaxation	2.6	+4	1.4	+56	0.5	NaN

5.3 TWO DIMENSIONAL (UNI/TRIAX)

To study the effects of plies with differing permeability values a two-dimensional flow experiment was performed using a thick laminate consisting of uni-directional as well triax materials with a layer of flow distribution mesh. A description of the experimental setup along with the procedures is presented followed by a discussion of the experimental and simulation results.

5.3.1 Experimental Setup

This experiment used the same mold, pressure sensors, and displacement transducers which were used for the previous experiment. The locations of the pressure sensors as well as the displacement transducers in relationship to the preform are given in Figure 5-74. The laminate consisted of 20 plies of the uni-directional material and 6 plies of the triax material. The lay up was such that the uni-directional material was sandwiched between the triax materials with 3 plies of triax material on either side (Figure 5-75). The uni-directional plies were oriented 90° to the flow direction and the triax plies were oriented with the longitudinal fibers parallel to the flow direction (Figure 5-75). The orientations were chosen to best represent laminates which are to be infused as part of the development of the composite beam sections for the composite modular bridge. The resulting laminate was approximately 20 mm thick under full compaction with two-thirds of the thickness consisting of the uni-directional plies and one-third of the thickness being triax. The laminate was 0.63 m long and 0.2 m wide. A layer of peel ply was placed over the entire laminate followed

by a single layer of flow distribution mesh which was 0.59 m long and 0.2 m wide. The flow distribution mesh was oriented such that the flow was in the transverse direction. The flow mesh ended 0.04 m short of the end of the preform. Like the previous experiment a resin flow spring was in contact with the flow distribution mesh at the inlet with the outlet flow spring being placed at the end of the preform. Vacuum pots were attached to both the inlet hose as well as the outlet hose such that the pressure could be controlled at each end of the laminate. The locations of the preform, flow distribution mesh, and inlet and outlet hoses are seen in Figure 5-74. A photograph of the test setup is given in Figure 5-76.

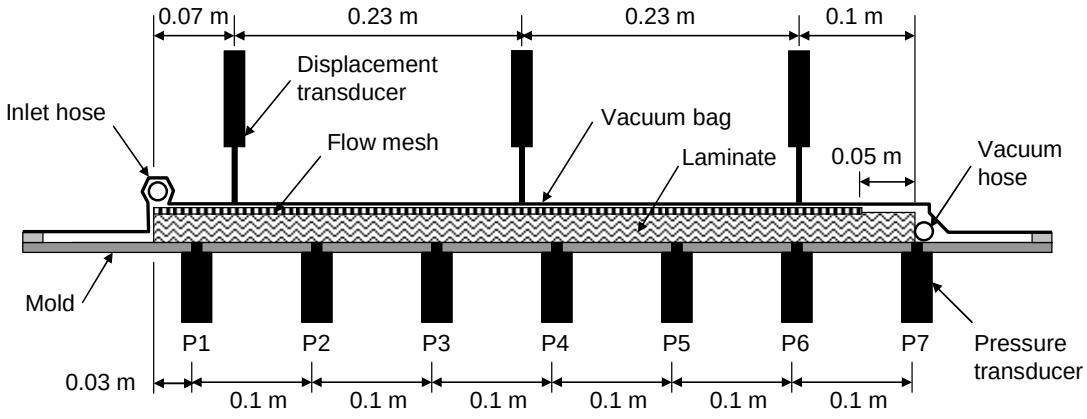

Figure 5-74 Illustration of the test setup for the uni/triax laminate showing the locations of pressure and displacement transducers.

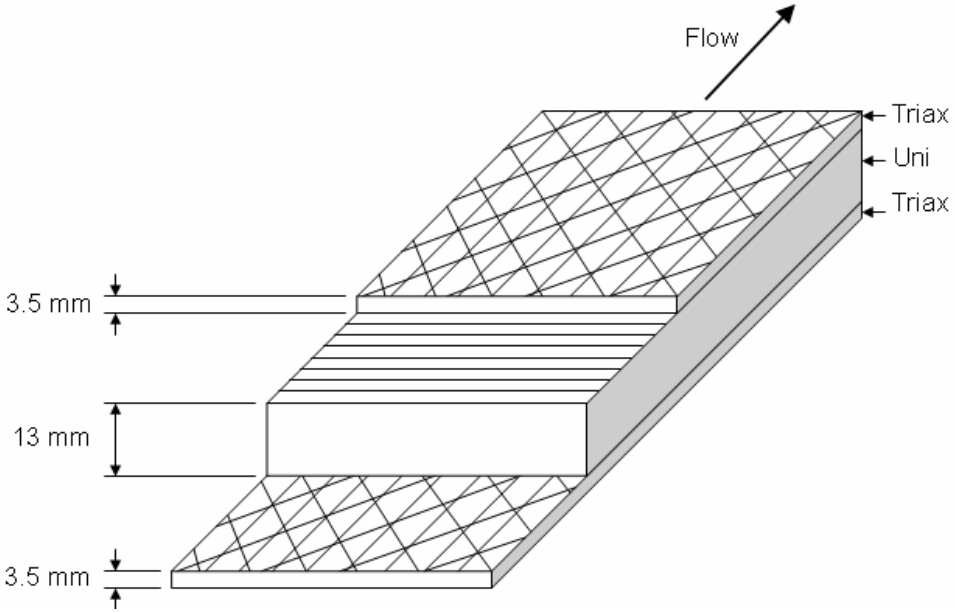

Figure 5-75 Illustration showing the lay up of the uni/triax laminate.

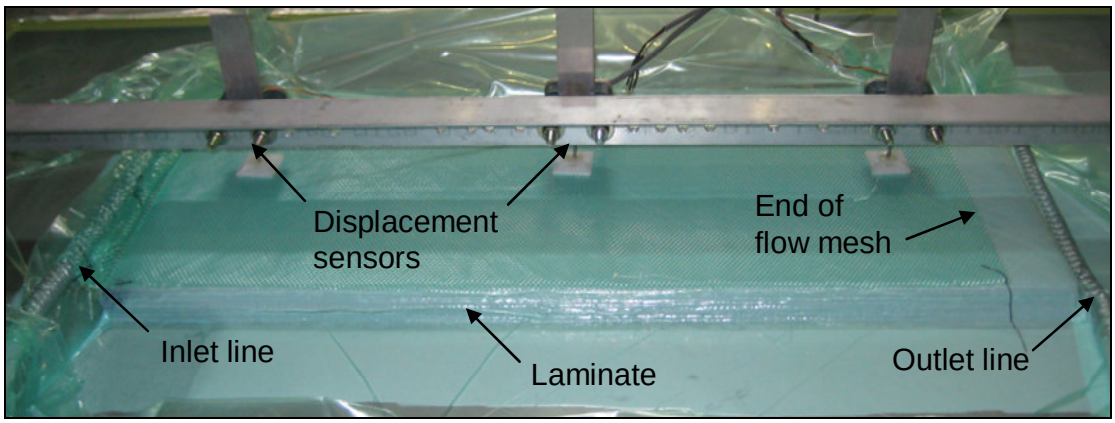

Figure 5-76 Photograph of the test setup showing the inlet and outlet lines, laminate, flow distribution mesh and displacement sensors.

5.3.2 Experimental Procedure

This study repeats the same four experiments which were used for the two-dimensional flow experiment using the uni-directional preform. Namely: resin filling,

resin bleeding with vacuum pressure applied at the inlet, resin bleeding with the inlet hose closed, and preform relaxation with the inlet opened to atmospheric pressure. The pressure conditions applied during the experiments and simulations is given in Table 5-6.

Table 5-6 Inlet and Outlet Pressures

	Initial Conditions		*Process Conditions*	
Process	*Inlet (kPa)*	*Outlet (kPa)*	*Inlet (kPa)*	*Outlet (kPa)*
Resin Filling	0	0	101	0
Resin Bleeding	101	50	50	50
Resin Bleeding	101	52	Closed	52
Preform Relaxation	50	50	101	50

5.3.3 Results and Discussion

Simulations of each experiment were performed using a finite element model consisting 288 nodes and 530 elements. One-dimensional line elements were used to simulate the resin distribution mesh and edge effects at the inlet and outlet ends and two-dimensional triangle elements were used to model the preform. Like the previous experiment a permeability of 1e-10 m^2 was applied at the preform/vacuum bag interface at each end of the preform. In this study simulation results using layerwise permeability values are compared with results using measured effective permeability values for the laminate. An illustration of the geometry of the laminate is given in

Figure 5-77. The model is divided into six different layers which may be assigned different permeability and compaction constitutive relationships. For the layerwise simulations, layers 1 and 6 are assigned triax permeability and compaction properties and layers 2 through 5 are assigned uni-directional permeability and compaction properties. For the effective permeability simulations all six layers are assigned uni/triax laminate effective permeability and compaction properties. The compaction and permeability constitutive models for each material are given in Table 4-4 and Table 4-5 respectively. An illustration of the finite element mesh showing the extent of the flow distribution elements as well as the inlet and outlet nodes is given in Figure 5-78. The results of the experimental measurements and simulations for each experiment are presented.

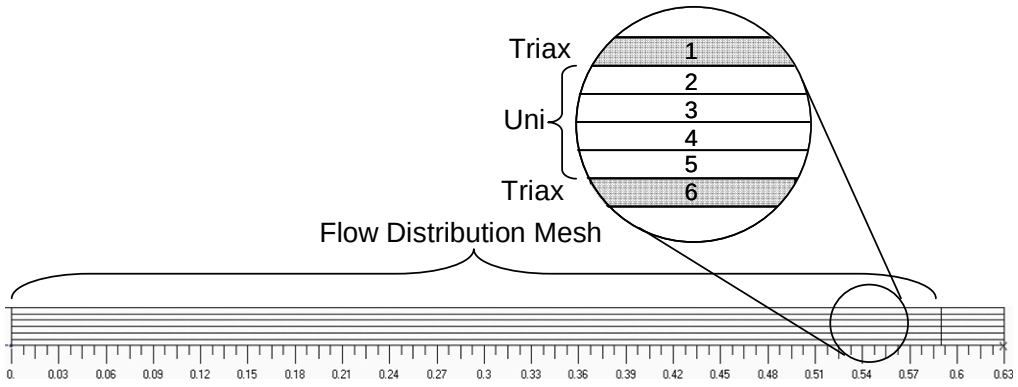

Figure 5-77 Illustration of the model geometry showing each of the different layers.

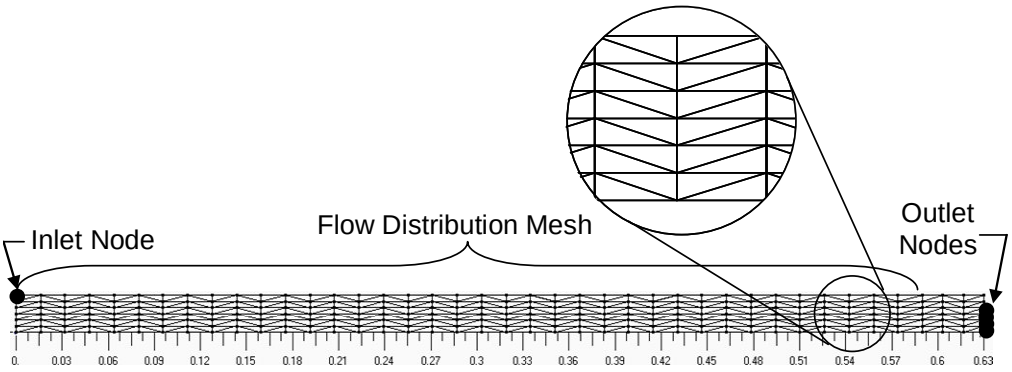

Figure 5-78 Illustration of the finite element mesh showing the locations of the inlet and outlet nodes as well as the flow distribution mesh.

Resin Filling

Resin filling simulations using both the layerwise as well as effective permeability models were performed and compared with experimental results in Figure 5-79. From plot it is seen that the predicted flow front using the layerwise model matches the experimental results for both the top and bottom surfaces of the preform up to a fill time of 200 seconds at which point the flow front at the mold surface lags behind the experimental results. It is also observed that the effective model does a fair job of predicting the flow front progression in the flow distribution layer (top surface) but does a poor job of predicting the flow front along the mold surface. The relaxation curve from the constitutive model was used for the filling simulations. A photograph of the laminate during the filling process is given in Figure 5-80.

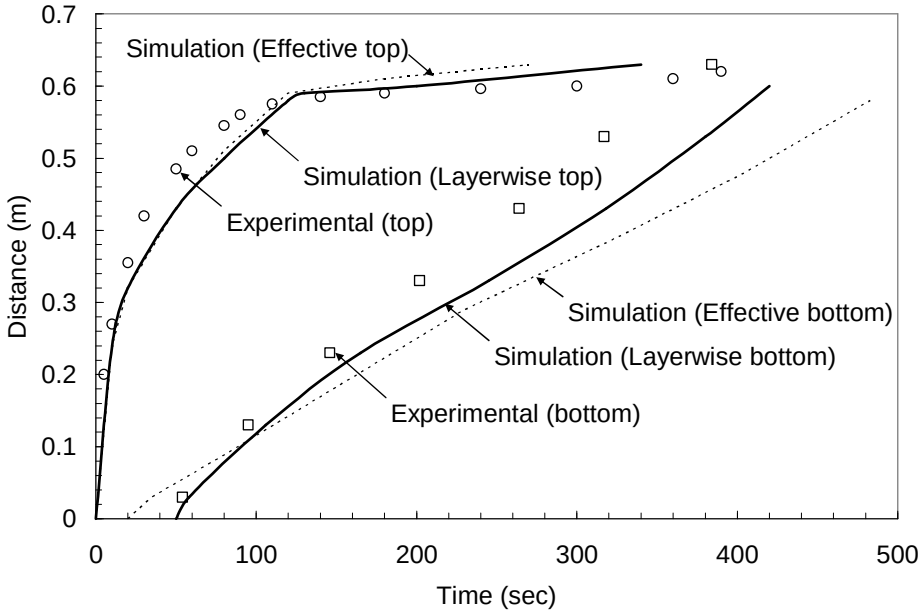

Figure 5-79 Plot of flow front location versus time for the top and bottom surfaces of the laminate using layerwise and effective models.

Contour plots showing the flow front profile for both the layerwise and effective models as well as photos of the flow front profile at 30, 120, and 240 seconds are given in Figure 5-81. From figure it is seen that the flow front profile for the layerwise model looks very similar to the actual profile from the flow experiment. However from the effective model it is seen that the predicted flow front greatly lags behind the experimental results.

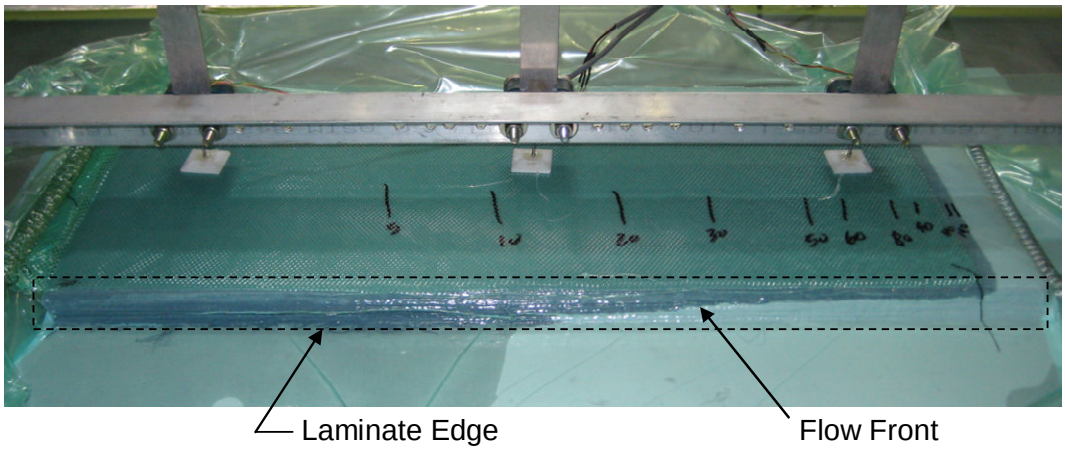

Figure 5-80 Photograph of the uni/triax laminate showing flow front profile through the thickness of the laminate during filling.

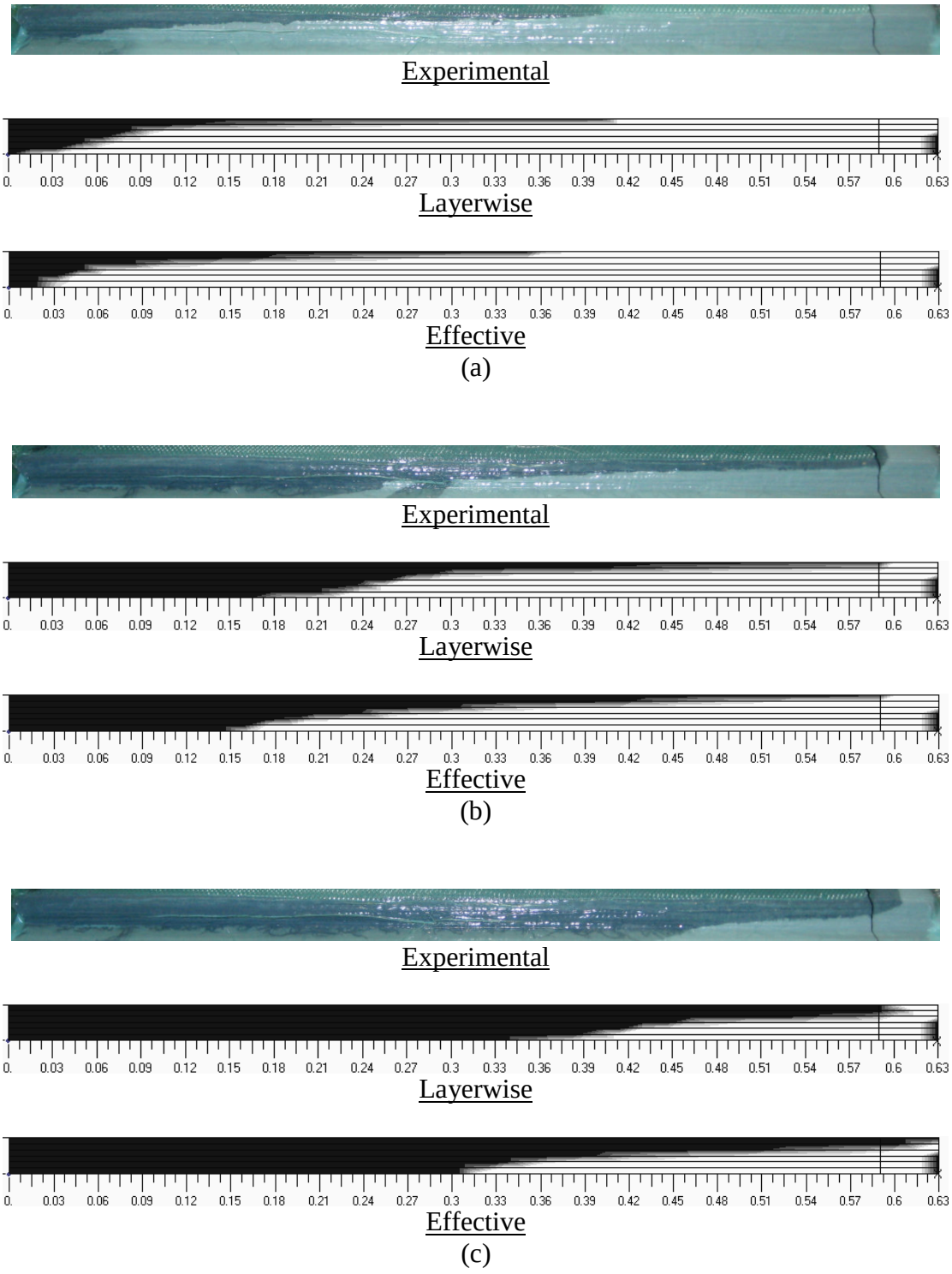

Figure 5-81 Photographs of the flow front at 30, 120, and 240 seconds are compared with simulation flow front results using both the layerwise and effective models.

Measured pressures at each sensor location during the filling operation are compared with predicted pressures using both the layerwise and effective models in Figure 5-82. From the plot it is observed that the predicted pressures from the Layer wise model at sensor P1, P2, and P3 show good agreement with experimental results. The predicted pressures at P4 through P6 under predict the actual pressure by approximately 5 to 10 kPa. Pressure predictions based on the effective model lags behind experimental measurements.

A plot of measured laminate thickness and predicted laminate thickness using both the layerwise and effective models at displacement sensor locations D1, D2, and D3 during filling is shown in Figure 5-83. From the plot it is seen that the predicted thicknesses agree well with experimental measurements using both models.

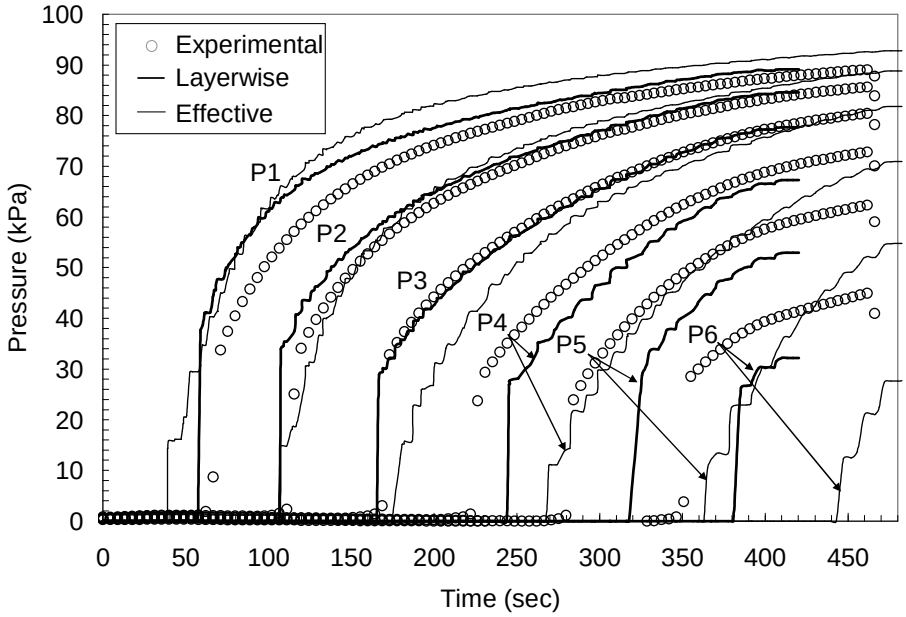

Figure 5-82 Plot of Pressure versus filling time at each pressure sensor (P1-P6) comparing experimental measurements with simulation results using the layerwise and effective models.

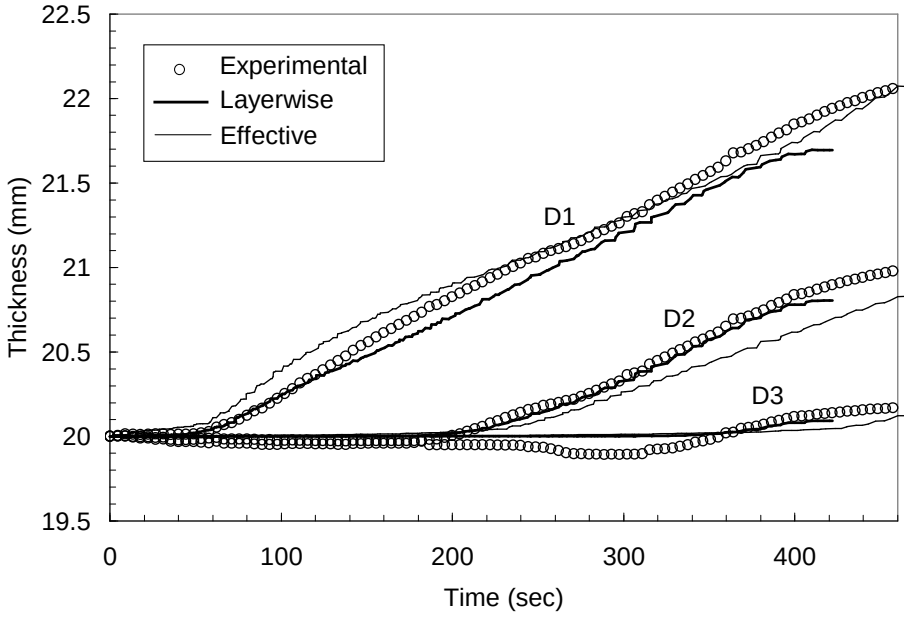

Figure 5-83 Plot of predicted laminate thickness during the filling phase.

Resin Bleeding (50 kPa Applied at Inlet)

This section compares experimental measurements with simulation results when a pressure of 50 kPa is applied at the inlet to bleed excess oil. A plot of the predicted pressures using the layerwise model and experimentally measured pressures along the length of the preform at different bleeding times is given in Figure 5-84. The simulation uses the compaction curves from the uni-directional and triax material constitutive models (Table 4-4). Overall the predicted pressure field at each bleeding time shows good agreement with the experimental measurements. However the initial (t=0) pressure is significantly lower than the experimental measurements. A plot of predicted pressures using the effective model is presented in Figure 5-85. From the plot it is observed that the effective model does a good job of predicting the initial pressure field but does a poor job of predicting pressures during the bleeding phase.

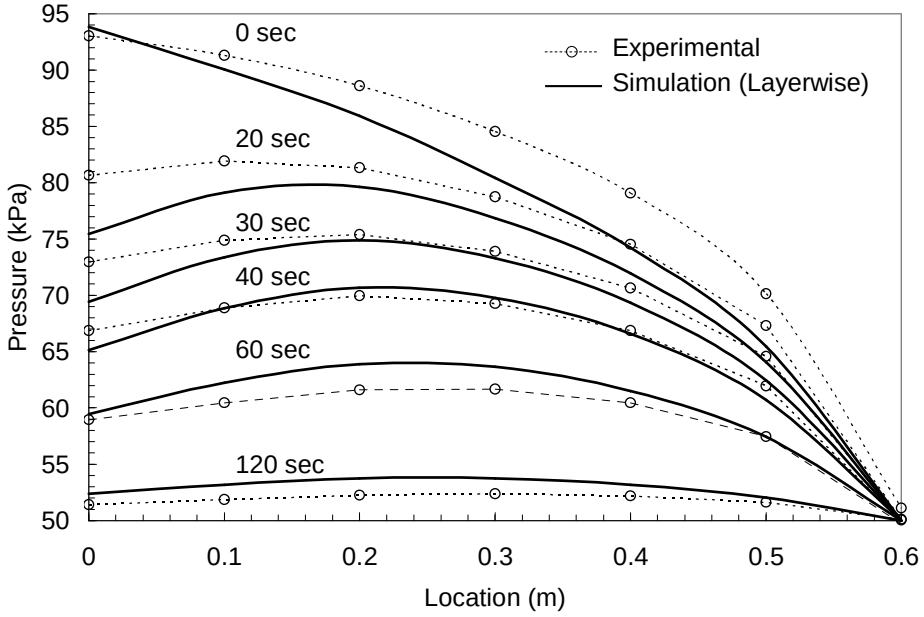

Figure 5-84 Plot of pressure versus location at different times comparing experimental measurements and layerwise simulation results for an applied pressure of 50 kPa at the inlet.

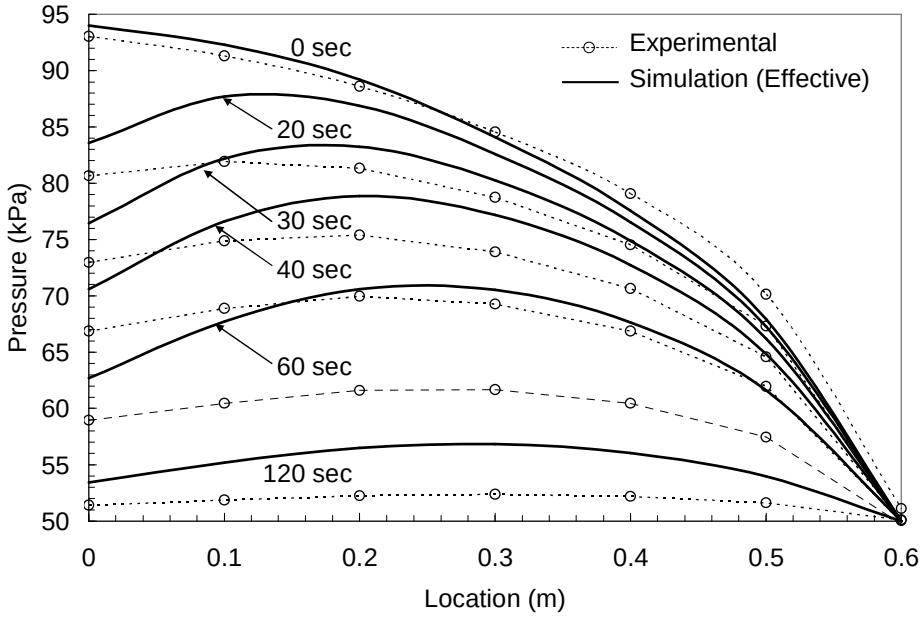

Figure 5-85 Plot of pressure versus location at different times comparing experimental measurements and effective simulation results for an applied pressure of 50 kPa at the inlet.

A plot of the pressure time history for pressure sensors P1 through P6 are given in Figure 5-86 through Figure 5-91 respectively. Each plot shows the experimental measurements along with simulation predictions using both the layerwise and effective models. From the plots it is observed that the layerwise model shows good agreement with the experimental results while the effective model over predicts the pressures at each sensor location. Again it is observed that the initial predicted pressure at each sensor location is lower than the experimental measurements. It is difficult to identify the exact cause for the under prediction of the initial pressure for sensor locations progressively further from the inlet. It is likely due to errors in the predicted permeability based on the constitutive models. For the layerwise model the permeability values are based on the individual constitutive models of the uni-directional and triax materials but do not consider any interaction at the interface between these materials. It has been shown by others [79] that the permeability of a preform consisting of multiple layers of different fiber architectures is dependent on the stacking sequence of the layers. This is due to the increase or decrease in flow at the layer interfaces due to surface undulations. It is possible that the permeability at the interfaces between the uni-direction and triax material us higher than the bulk permeability of the individual materials. Under prediction of the permeability would be one cause for under predicted pressures. In order to fully understand the issue additional pressure measurement are needed at the bag surface to understand how the pressures are changing through the thickness of the preform.

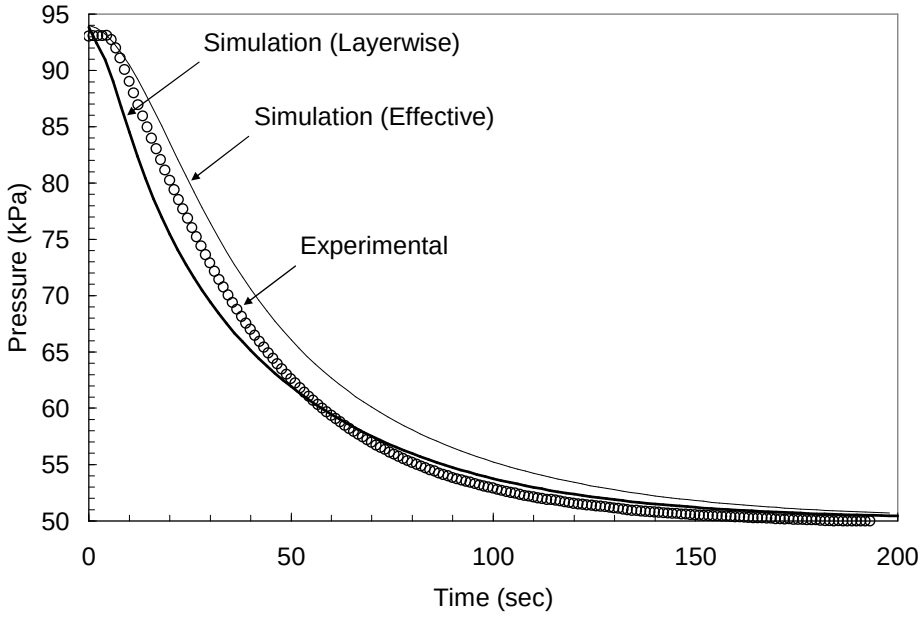

Figure 5-86 Plot of resin pressure versus time at sensor P1 (0.03 m) comparing the experimental measurements with the layerwise and effective models for an applied inlet pressure of 50 kPa.

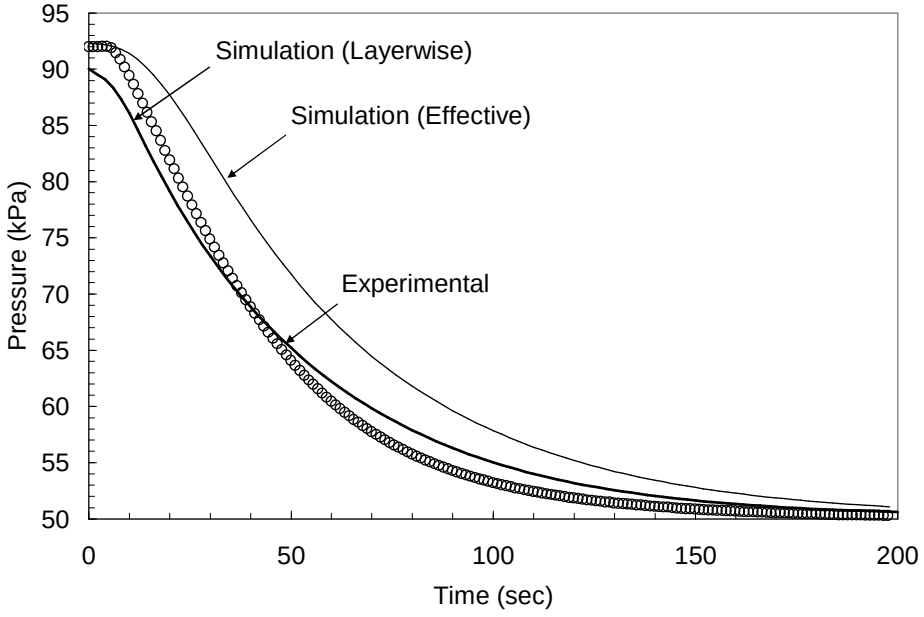

Figure 5-87 Plot of resin pressure versus time at sensor P2 (0.13 m) comparing the experimental measurements with the layerwise and effective models for an applied inlet pressure of 50 kPa.

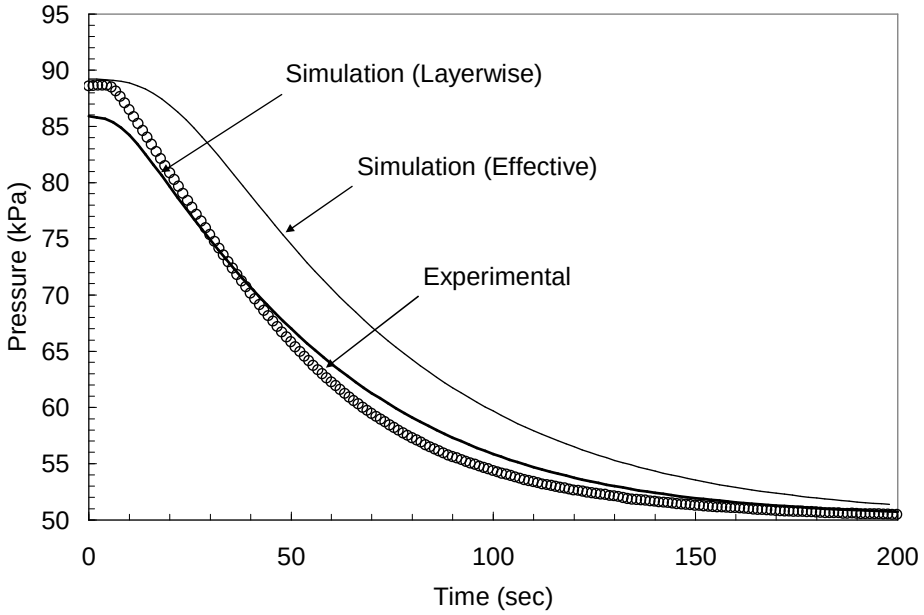

Figure 5-88 Plot of resin pressure versus time at sensor P3 (0.23 m) comparing the experimental measurements with the layerwise and effective models for an applied inlet pressure of 50 kPa.

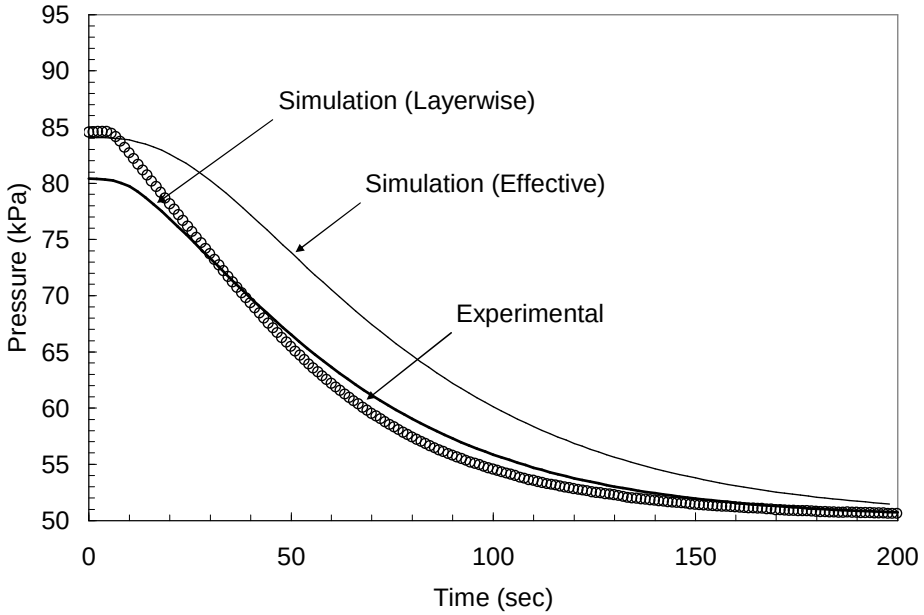

Figure 5-89 Plot of resin pressure versus time at sensor P4 (0.33 m) comparing the experimental measurements with the layerwise and effective models for an applied inlet pressure of 50 kPa.

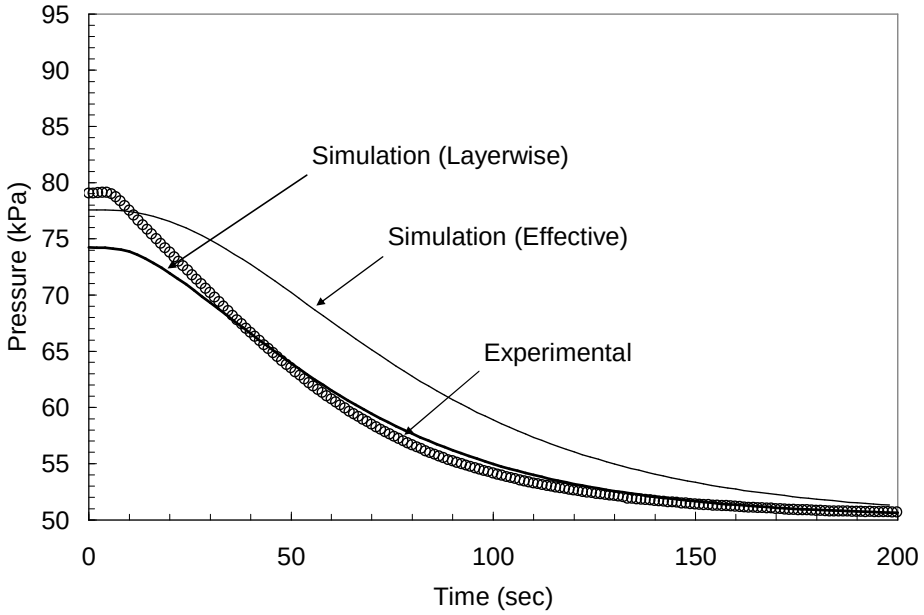

Figure 5-90 Plot of resin pressure versus time at sensor P5 (0.43 m) comparing the experimental measurements with the layerwise and effective models for an applied inlet pressure of 50 kPa.

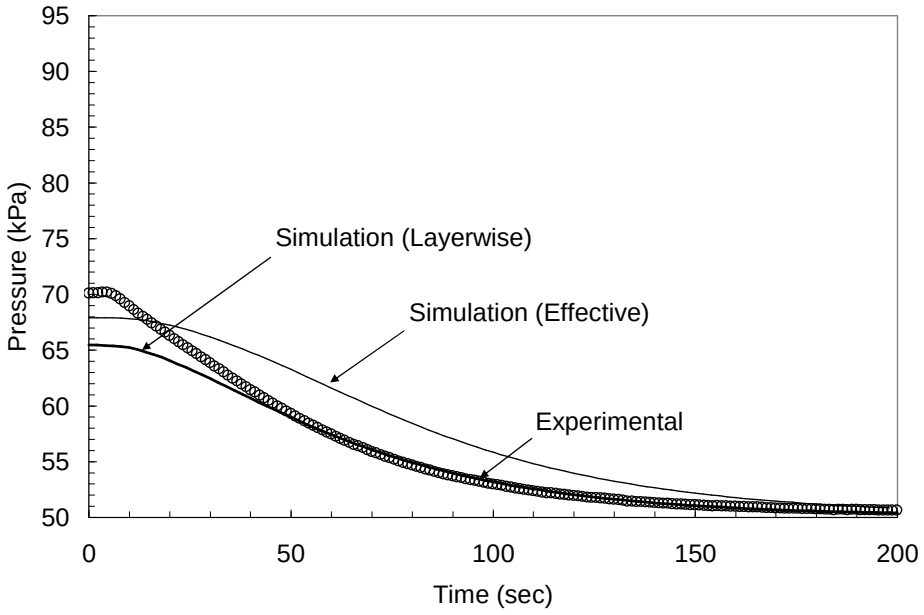

Figure 5-91 Plot of resin pressure versus time at sensor P6 (0.53 m) comparing the experimental measurements with the layerwise and effective models for an applied inlet pressure of 50 kPa.

Plots showing the pressure field and corresponding fiber volume fractions within the preform for elapsed bleeding times of 0, 20, 40, 60, and 90 seconds are given in Figure 5-92 and Figure 5-93 respectively. The plots are based on simulations using the compaction curves from the material constitutive models. As was seen for the uni-directional preform, it is observed that at the beginning of the bleeding process the pressure gradient through the thickness is minimal. Due to the high permeability of the flow distribution layer, as pressure is applied at the inlet there is a significant pressure drop in the flow distribution layer creating a pressure gradient through the thickness of the preform. This pressure gradient through the thickness allows resin to flow from the preform into the flow distribution mesh and then out the inlet hose greatly reducing the bleeding time. From the predicted fiber volume fraction seen in Figure 5-93 it is observed that the fiber volume fraction in the triax layers is much higher than that for the uni-directional material. This insight is lost when the effective model is used.

From the predicted fiber volume fractions the thickness of the laminate at sensor locations D1, D2, and D3 are predicted and compared with experimental results in Figure 5-94 through Figure 5-96 respectively. In all three cases the measured thickness falls between the thicknesses predicted using the compaction and relaxation curves of the constitutive model. At sensor locations D2, and D3 the magnitude of the measured thickness as well as the general shape of the curve seem to best match the predictions using the relaxation model. A summary of the predicted and measured change in thickness at each sensor location is given in Table 5-7. From the table it is seen that the layerwise model using the relaxation constitutive relationship shows the

best agreement with the experimental measurements with errors ranging from 0 to 33% with the maximum error at D3.

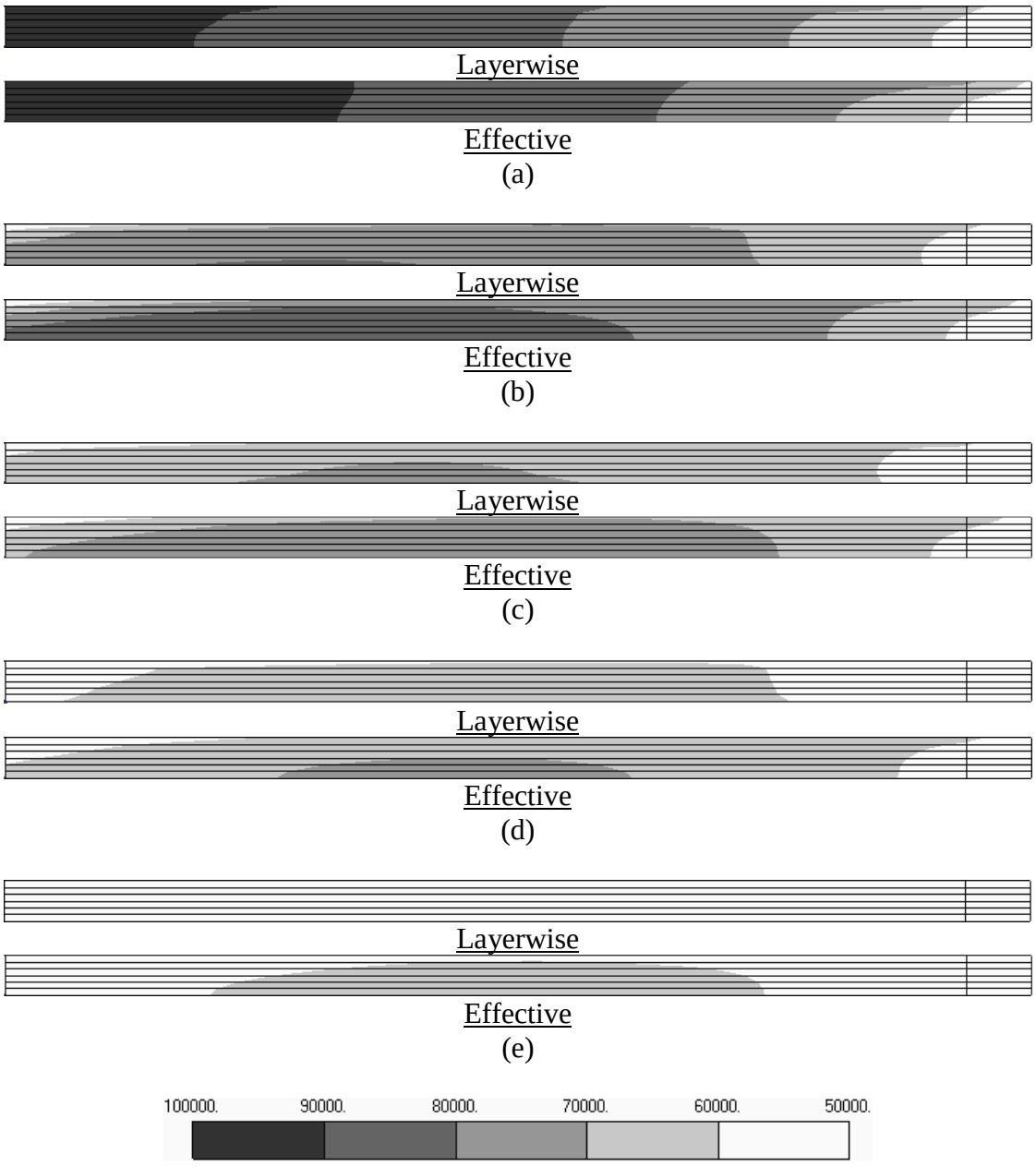

Figure 5-92 Contour plots of pressure for the uni/triax laminate during bleeding with an applied pressure of 50 kPa at the inlet showing pressures at (a) 0, (b) 20, (c) 40, (d) 60, and (e) 90 seconds for both layerwise and effective models.

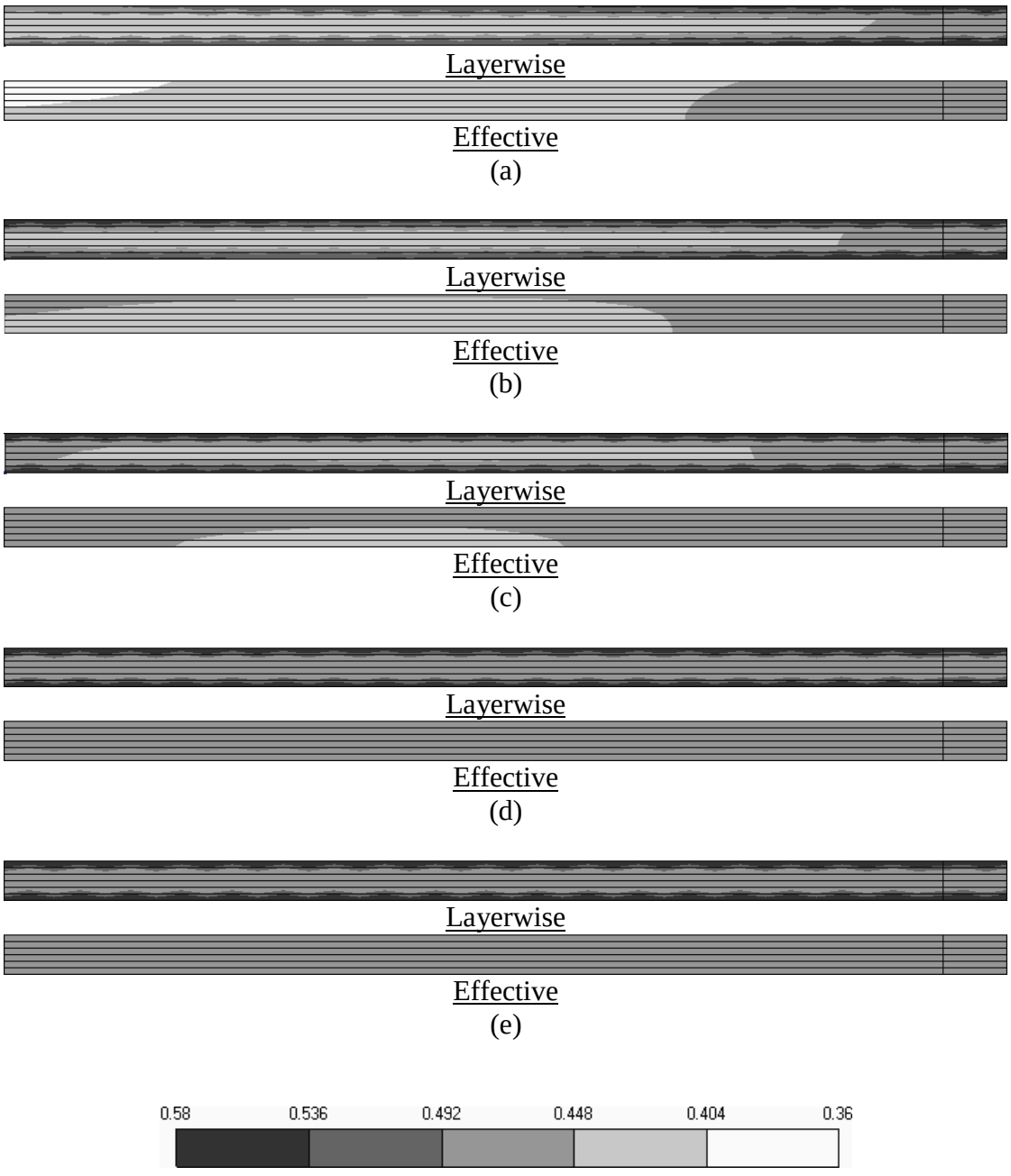

Figure 5-93 Contour plots of fiber volume fraction for the uni/triax laminate during bleeding with an applied pressure of 50 kPa at the inlet showing fiber volume fractions at (a) 0, (b) 20, (c) 40, (d) 60, and (e) 90 seconds for both layerwise and effective models..

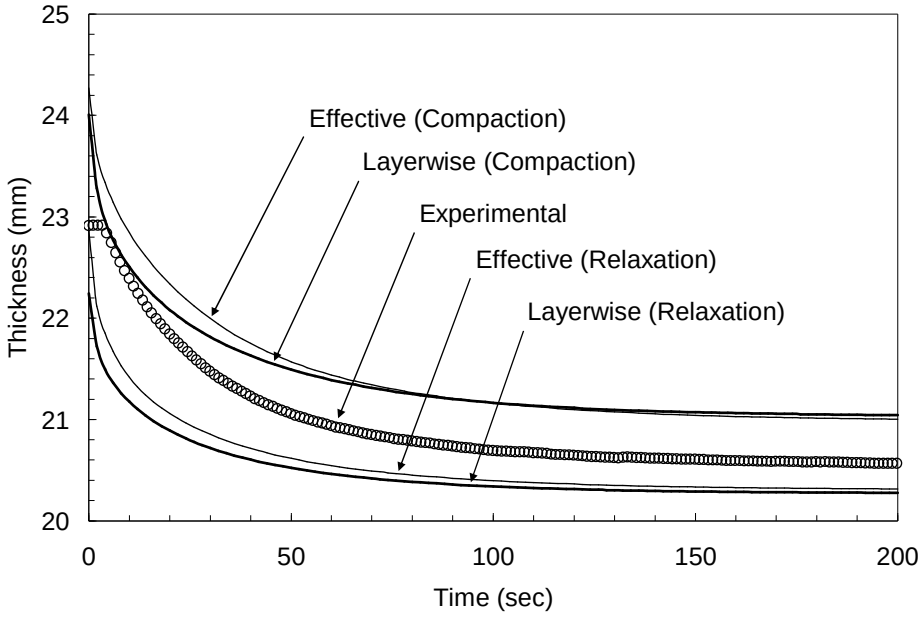

Figure 5-94 Plot of thickness versus bleeding time with 50kPa applied at the inlet comparing the predicted laminate thickness at sensor D1 with the experimentally measured thickness.

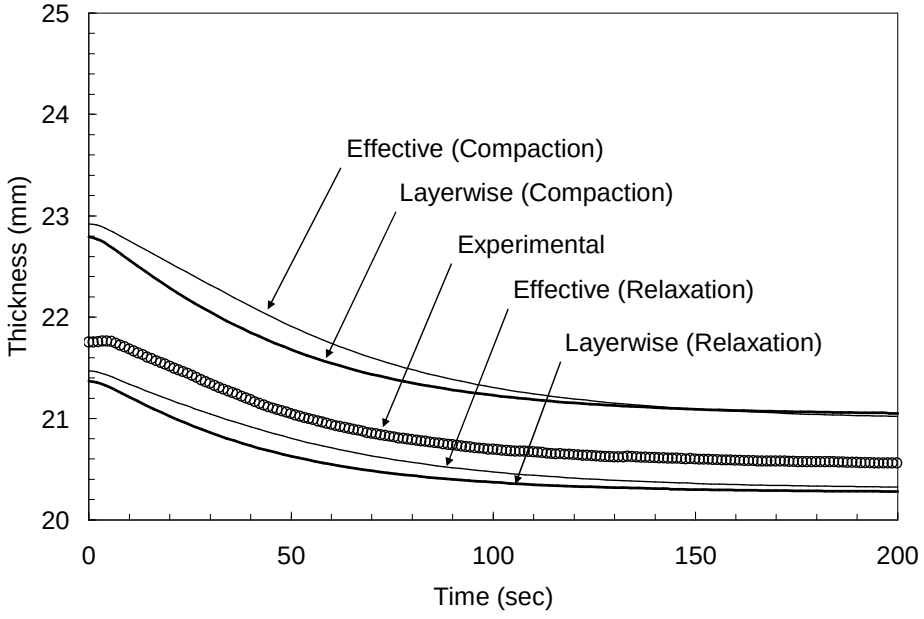

Figure 5-95 Plot of thickness versus bleeding time with 50kPa applied at the inlet comparing the predicted laminate thickness at sensor D2 with the experimentally measured thickness.

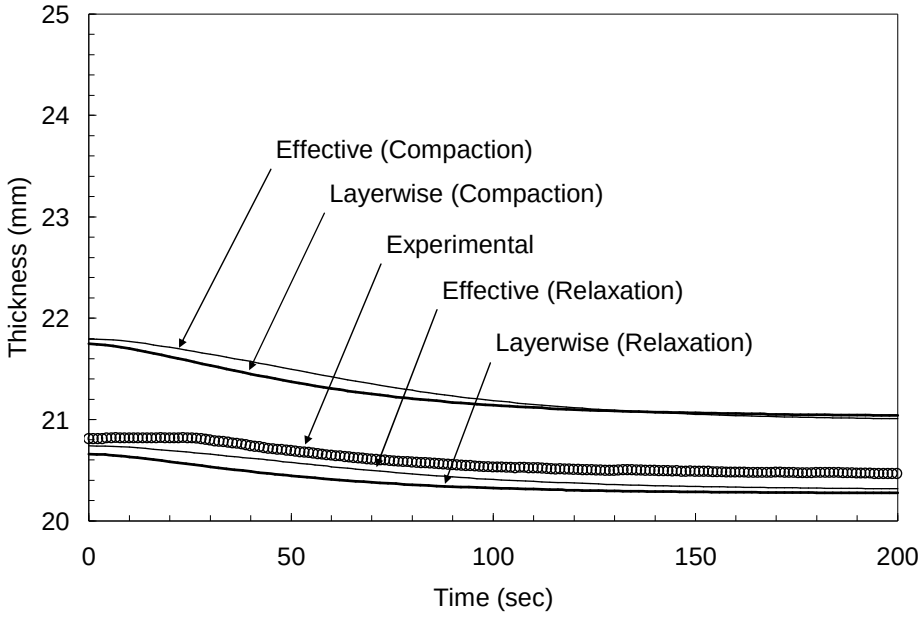

Figure 5-96 Plot of thickness versus bleeding time with 50kPa applied at the inlet comparing the predicted laminate thickness at sensor D3 with the experimentally measured thickness.

Resin Bleeding (Inlet Closed)

For the second bleeding experiment the inlet hose is closed and oil is only bled through the outlet hose. A plot of the predicted pressures for the layerwise model along with experimental measurements at different bleeding times is given in Figure 5-97. The predicted pressures show good agreement with experimental measurements with the exception of the prediction at 0 seconds. A plot of the predicted pressures using the effective model is given in Figure 5-98. From the plot it is seen that the effective model does a good job of capturing the initial (t=0) pressure field but does a poor job of predicting the pressure field during bleeding.

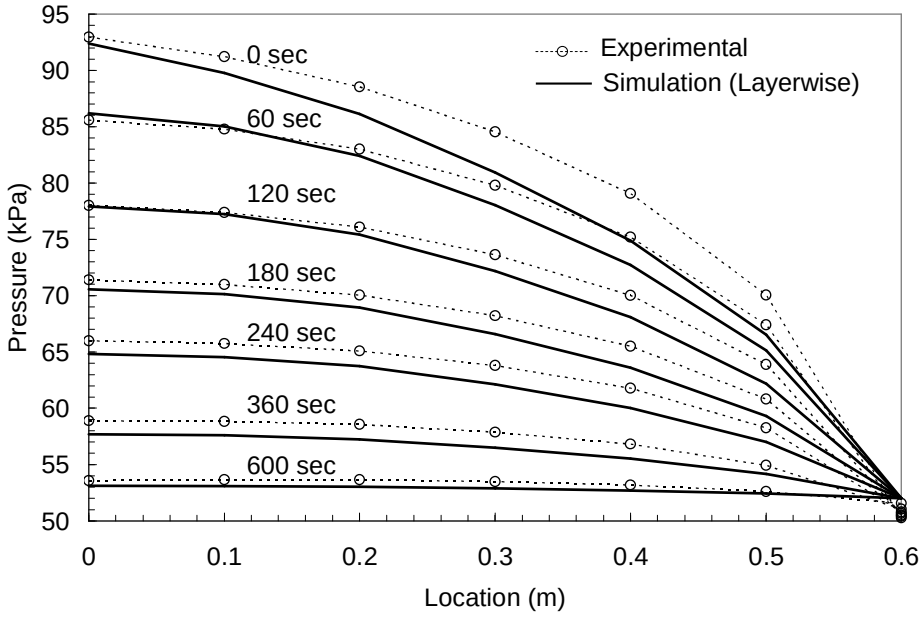

Figure 5-97 Plot of pressure versus location at different times during resin bleeding with the inlet closed comparing experimental measurements and simulation results using the layerwise model.

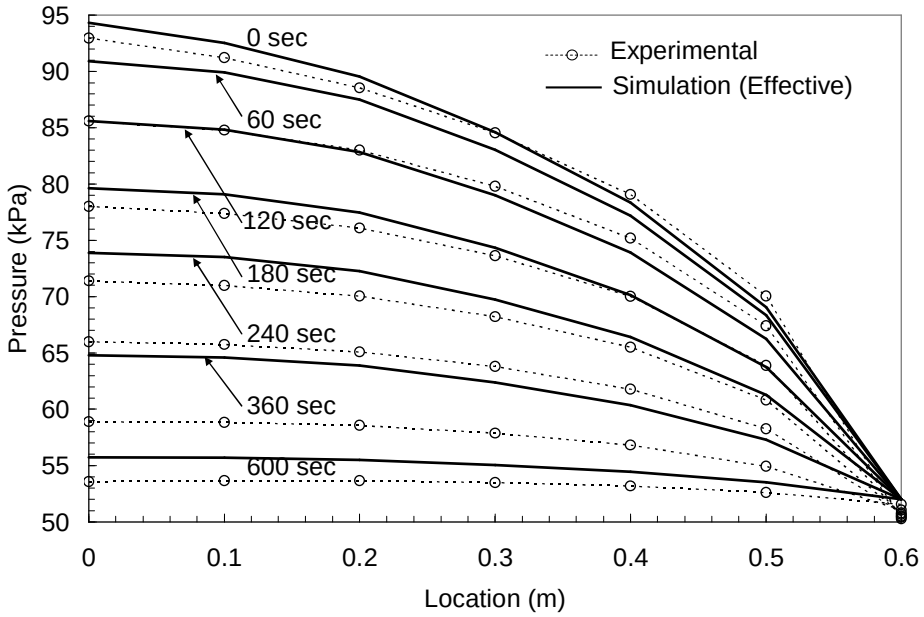

Figure 5-98 Plot of pressure versus location at different times during resin bleeding with the inlet closed comparing experimental measurements and simulation results using the effective model.

Time history plots of pressure versus bleeding times for each pressure sensor are given in Figure 5-99 through Figure 5-104. Each of the plots shows the experimentally measured pressures along with the predicted pressures using both the layerwise and effective models. From the plots it is seen that the layerwise model does a much better job of predicting the pressure in comparison to the effective model. As was observed for the first bleeding experiment the initial pressure predictions at sensors P3 through P6 using the layerwise model under predict the measured pressures. Again this is likely due to errors in the permeability values due to neglecting the multi-layer effects of the preform.

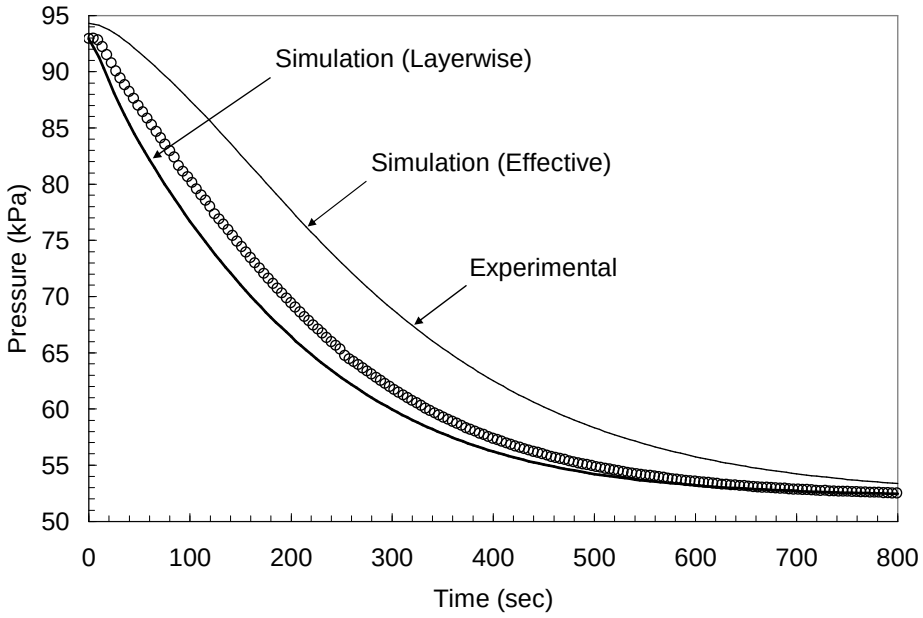

Figure 5-99 Plot of resin pressure versus time at sensor P1 (0.03 m) comparing the experimental measurements with the layerwise and effective models with the inlet closed.

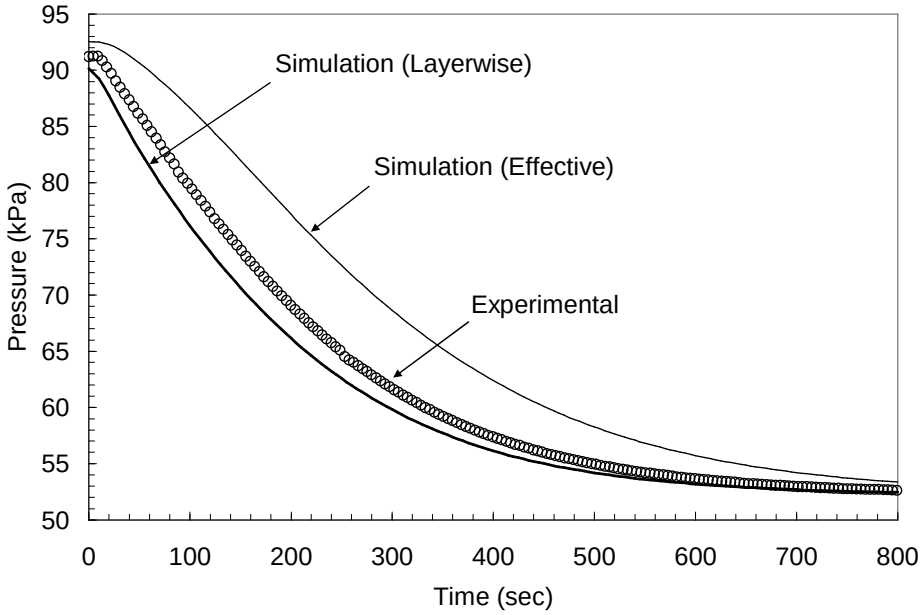

Figure 5-100 Plot of resin pressure versus time at sensor P2 (0.13 m) comparing the experimental measurements with the layerwise and effective models with the inlet closed.

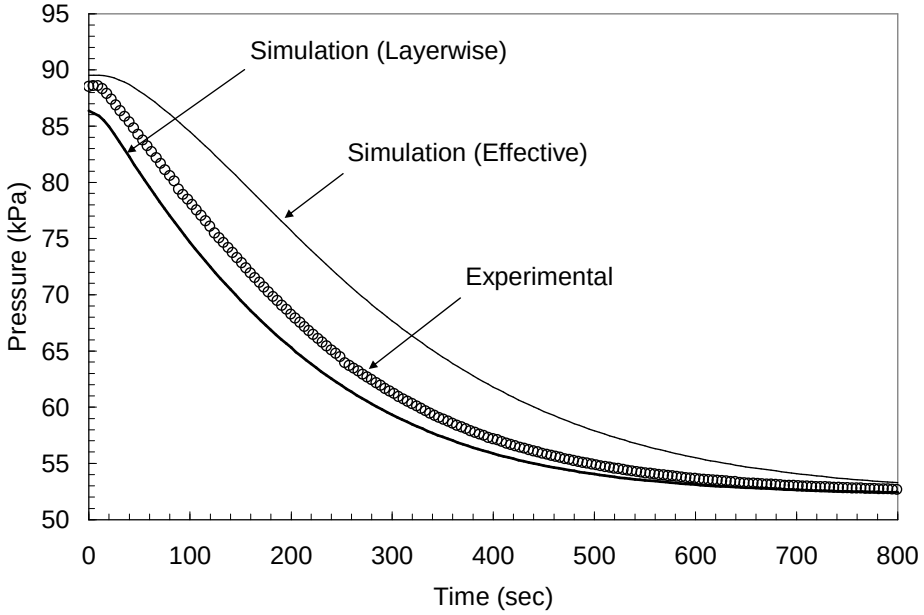

Figure 5-101 Plot of resin pressure versus time at sensor P3 (0.23 m) comparing the experimental measurements with the layerwise and effective models with the inlet closed.

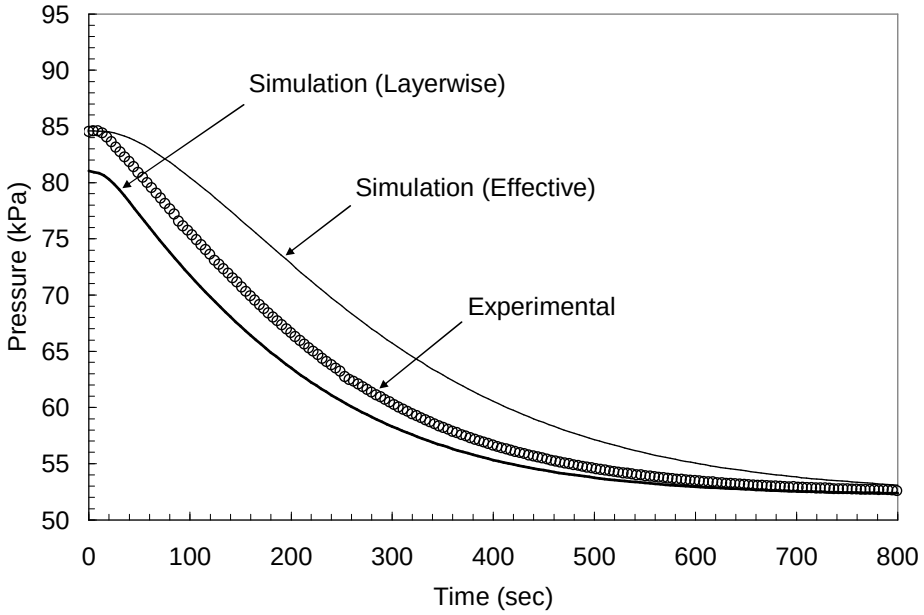

Figure 5-102 Plot of resin pressure versus time at sensor P4 (0.33 m) comparing the experimental measurements with the layerwise and effective models with the inlet closed.

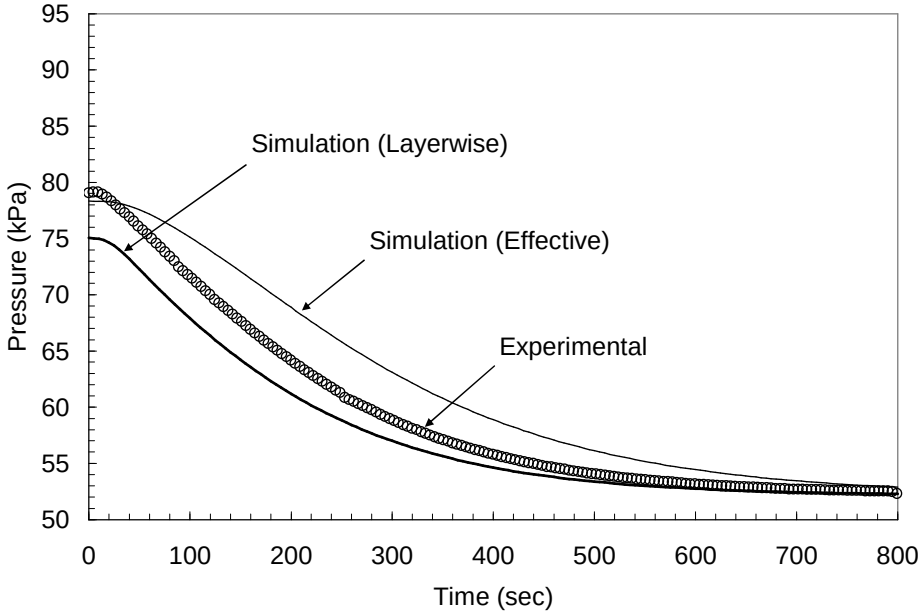

Figure 5-103 Plot of resin pressure versus time at sensor P5 (0.43 m) comparing the experimental measurements with the layerwise and effective models with the inlet closed.

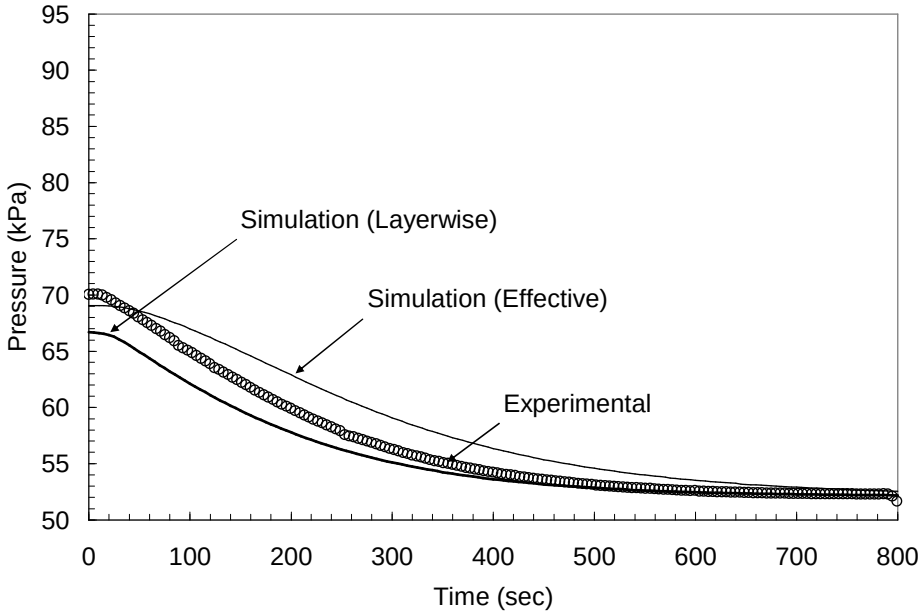

Figure 5-104 Plot of resin pressure versus time at sensor P6 (0.53 m) comparing the experimental measurements with the layerwise and effective models with the inlet closed.

Pressure as well as fiber volume fraction contour plots of the preform at bleeding times of 0, 60, 120, 240, and 360 seconds are given in Figure 5-105 and Figure 5-106 respectively. From Figure 5-105 it is seen that through out the bleeding process the pressure gradient is predominately along the length of the preform with a very small pressure gradient through the thickness. Due to the nature of the pressure gradient the flow of oil predominately occurs within the preform. For this bleeding experiment the time to reach equilibrium was approximately 600 seconds compared to 150 seconds for the case when vacuum pressure was applied at the inlet. It is also observed that while the effective model show smooth contours through the thickness of the preform the layerwise model shows a change in the contour profile as it moves

from the uni-directional to triax layers. Again the layerwise model is able to show the difference in the fiber volume fraction for the different layers while the effective model treats the preform as a single material.

From the predicted fiber volume fractions the laminate thicknesses are predicted at each displacement sensor location using both the layerwise and effective models with both the compaction and relaxation constitutive relationships. Plots of the predicted thickness along with experimental measurements for sensors D1, D2, and D3 are shown in Figure 5-107 through Figure 5-109 respectively. Again the experimental measurements fall between the predicted pressures using the compaction and relaxation constitutive models. The final thickness at all three sensor location is best predicted by the relaxation constitutive model with the effective model best fitting the shape of the experimental curve. A summary of the predicted and measured changes in thickness of the preform are presented in Table 5-7. From the table it is seen that the layerwise model using the relaxation constitutive relationship best matches the measured change in preform thickness with the prediction errors at D1, D2, and D3 being 5%, 0%, and 33% respectively.

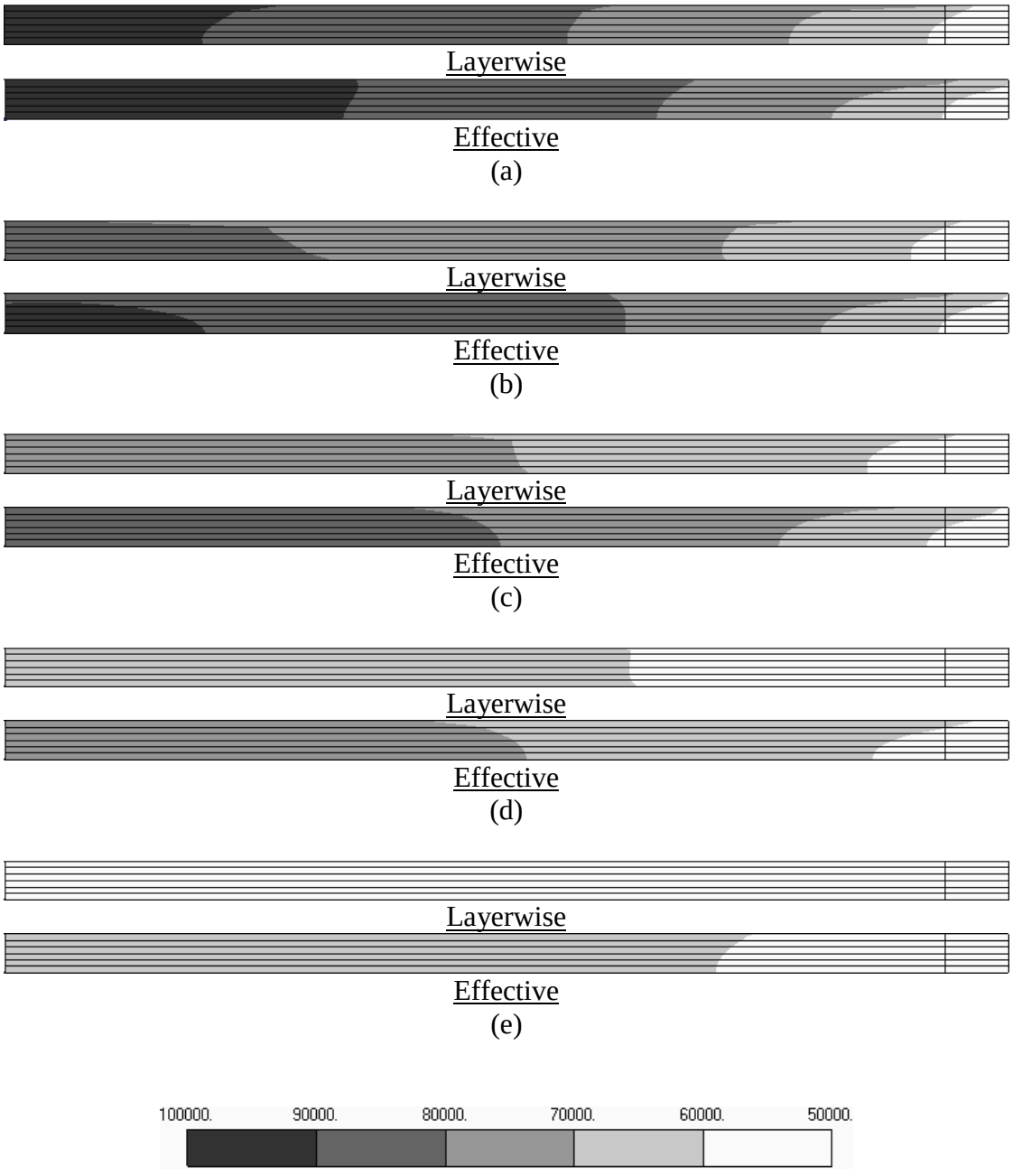

Figure 5-105 Contour plots of pressure for the uni/triax laminate during bleeding with the inlet clamped showing pressures at (a) 0, (b) 60, (c) 120, (d) 240,and (e) 360 seconds for both layerwise and effective models.

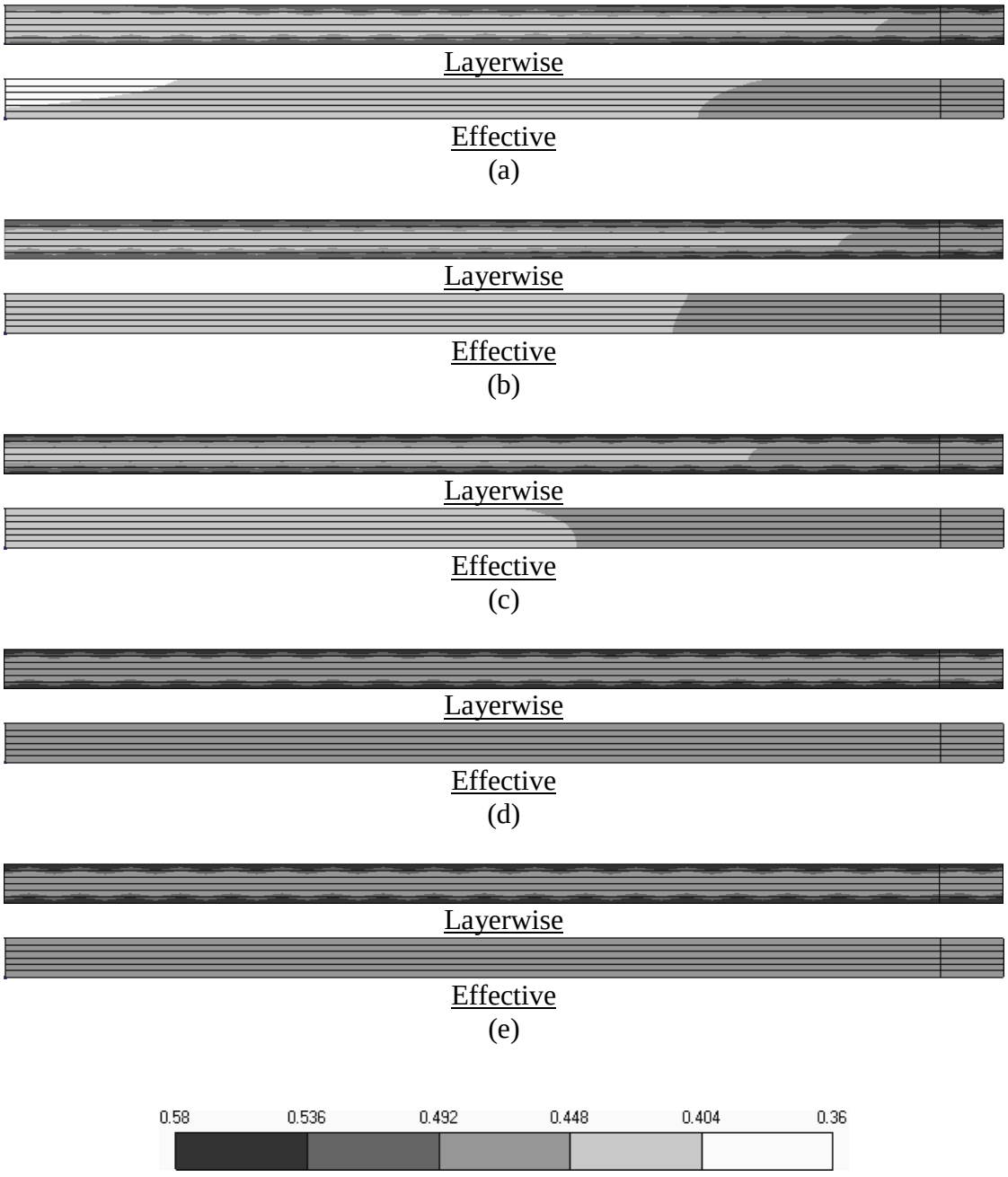

Figure 5-106 Contour plots of fiber volume fraction for the uni/triax laminate during bleeding with the inlet clamped showing the fiber volume fraction at (a) 0, (b) 60, (c) 120, (d) 240, and (e) 360 seconds for both layerwise and effective models.

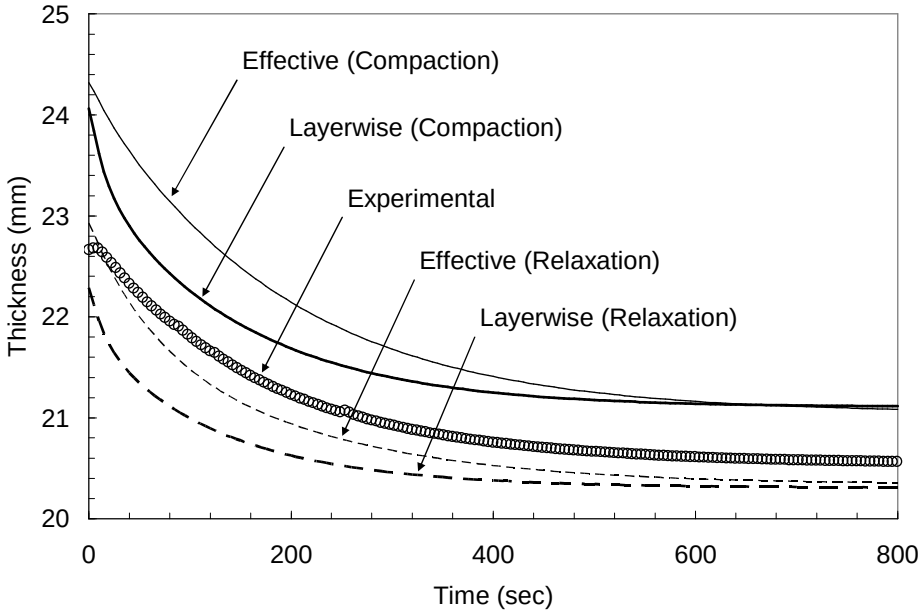

Figure 5-107 Plot of thickness versus bleeding time with the inlet clamped comparing the predicted laminate thickness at sensor D1 with the experimentally measured thickness.

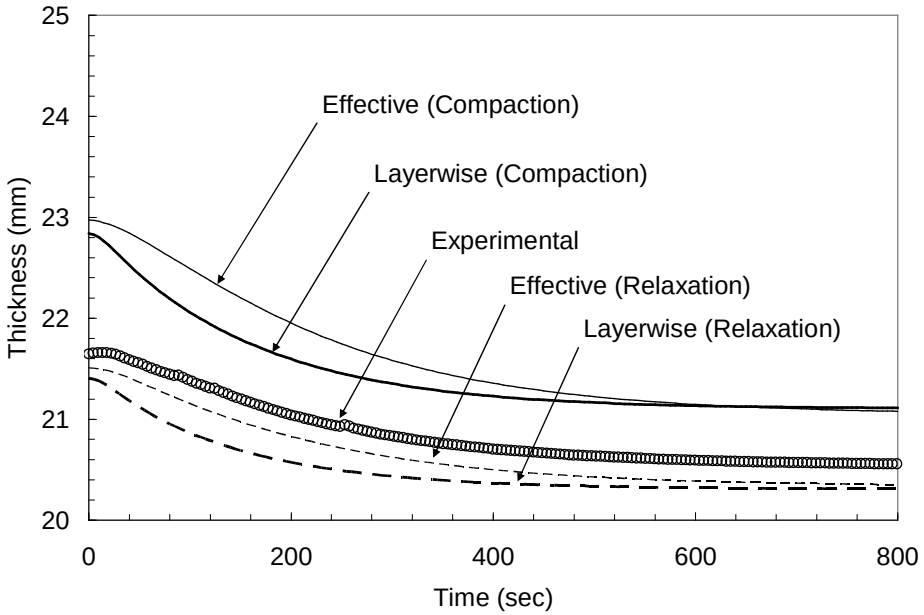

Figure 5-108 Plot of thickness versus bleeding time with the inlet clamped comparing the predicted laminate thickness at sensor D2 with the experimentally measured thickness.

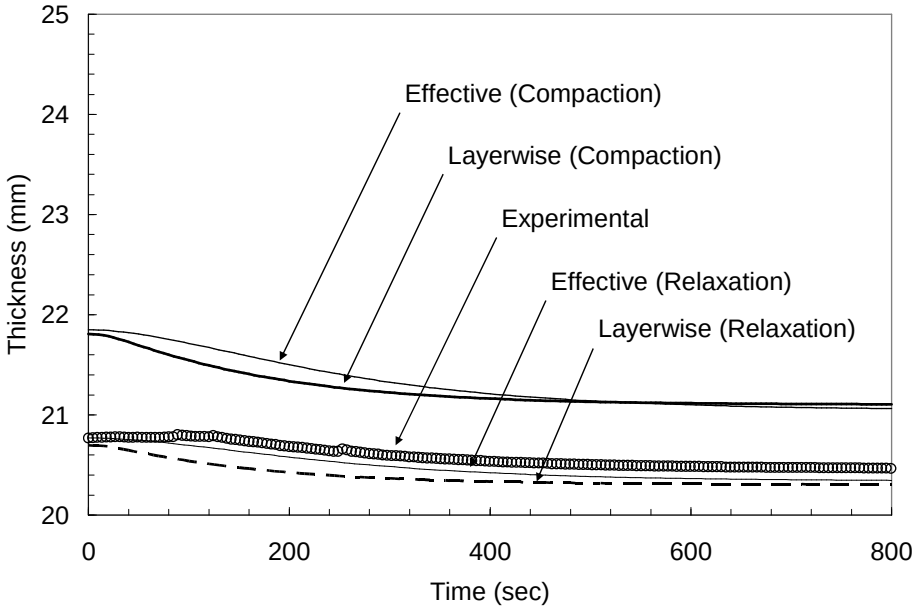

Figure 5-109 Plot of thickness versus bleeding time with the inlet clamped comparing the predicted laminate thickness at sensor D3 with the experimentally measured thickness.

Preform Relaxation (Atmospheric Pressure at the Inlet)

The final experiment is the relaxation of the preform. A plot of the pressure along the length of the preform during the relaxation process for is given in Figure 5-110. The plot shows experimental measurements as well as simulation results from both the layerwise and effective model using the relaxation curves from the respective constitutive models (Table 4-4). The plot shows the pressures for elapsed times of 0, 10, 20, 30, 60 and 120 seconds. From the plot it is seen that the simulations using both the layerwise and effective models do a fair job of capturing the shape of each pressure curve but consistently under predicts the magnitude of the pressures. Again this is likely due to error in the permeability values.

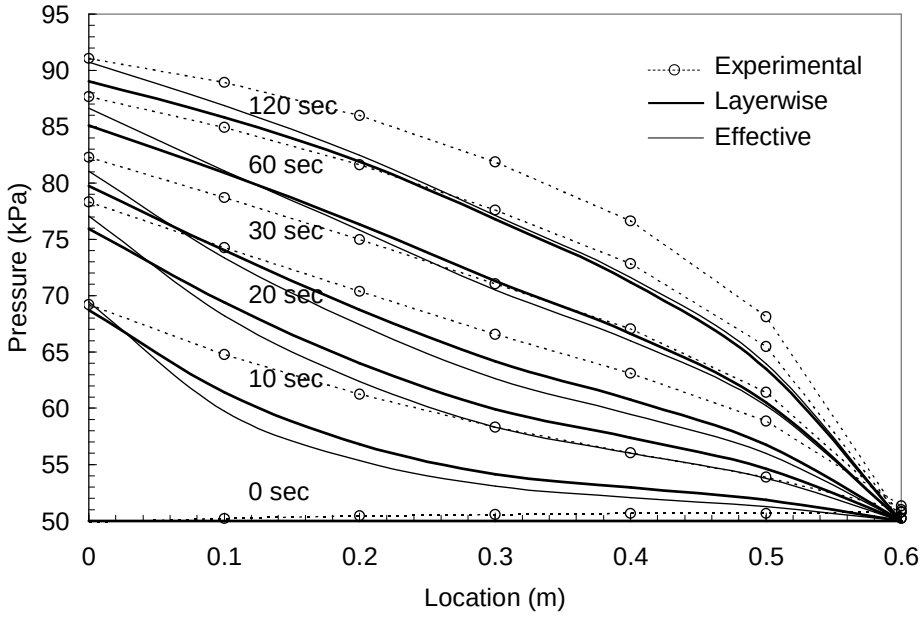

Figure 5-110 Plot of pressure versus location at different times during resin bleeding with 50 kPa applied at the inlet comparing experimental measurements and simulation results.

Time history plots of pressure versus relaxation time for pressure sensors P1 through P6 are given in Figure 5-111 through Figure 5-116 respectively. Each plot shows the experimental measurements as well as the simulation results using both the layerwise and effective models. The predicted pressures for sensors P1 and P2 show good agreement with experimental measurements with the layerwise model best representing shape of the experimental curve. At sensors P3 through P6 the layerwise model still does a good job of capturing the shape of the pressure versus time curve but under predicts the pressures.

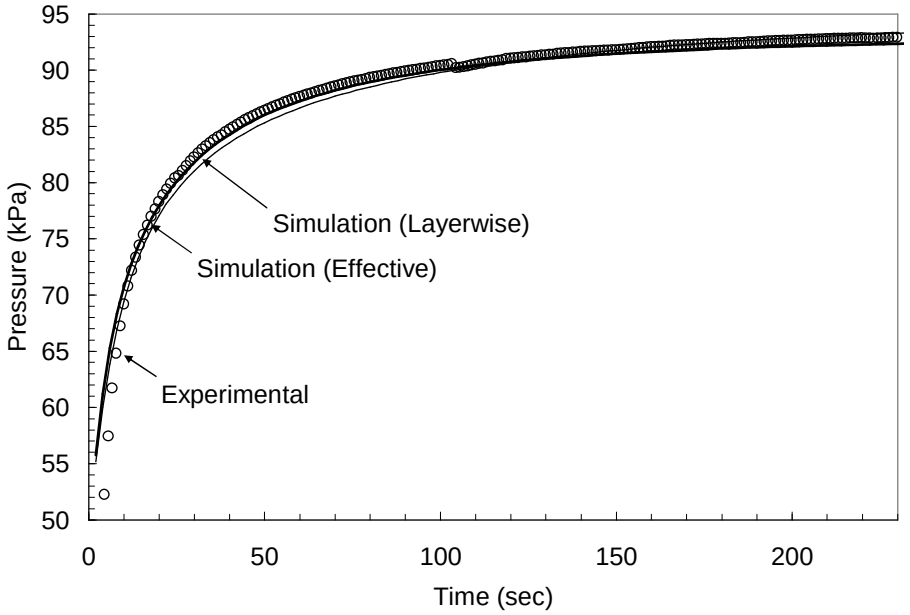

Figure 5-111 Plot of resin pressure versus time at sensor P1 (0.03 m) comparing the experimental measurements with the layerwise and effective models for an applied inlet pressure of 101 kPa.

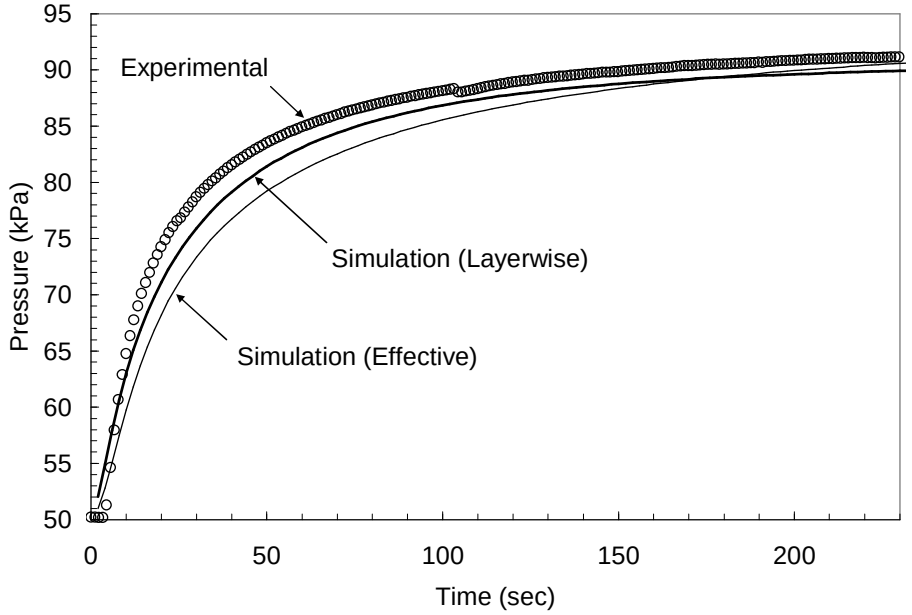

Figure 5-112 Plot of resin pressure versus time at sensor P2 (0.13 m) comparing the experimental measurements with the layerwise and effective models for an applied inlet pressure of 101 kPa.

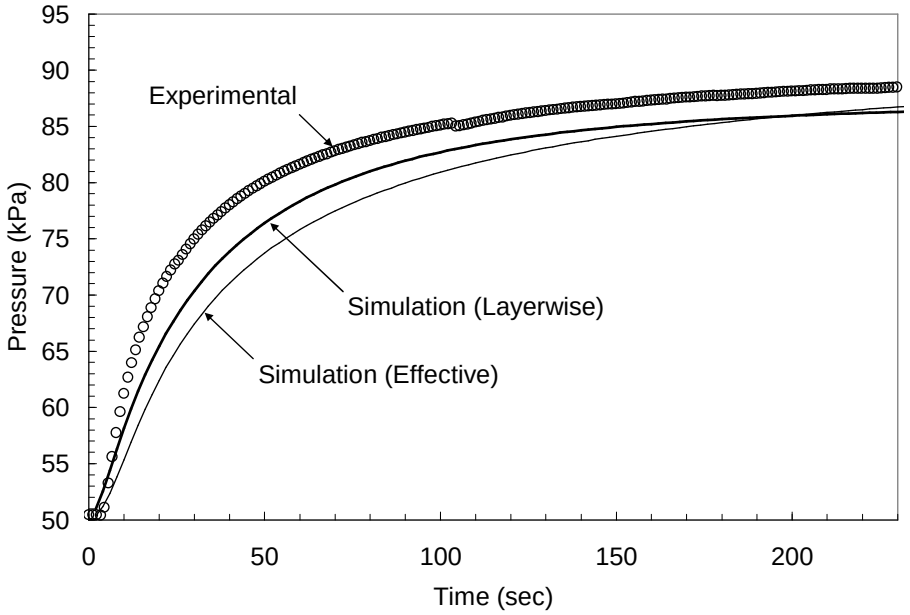

Figure 5-113 Plot of resin pressure versus time at sensor P3 (0.23 m) comparing the experimental measurements with the layerwise and effective models for an applied inlet pressure of 101 kPa.

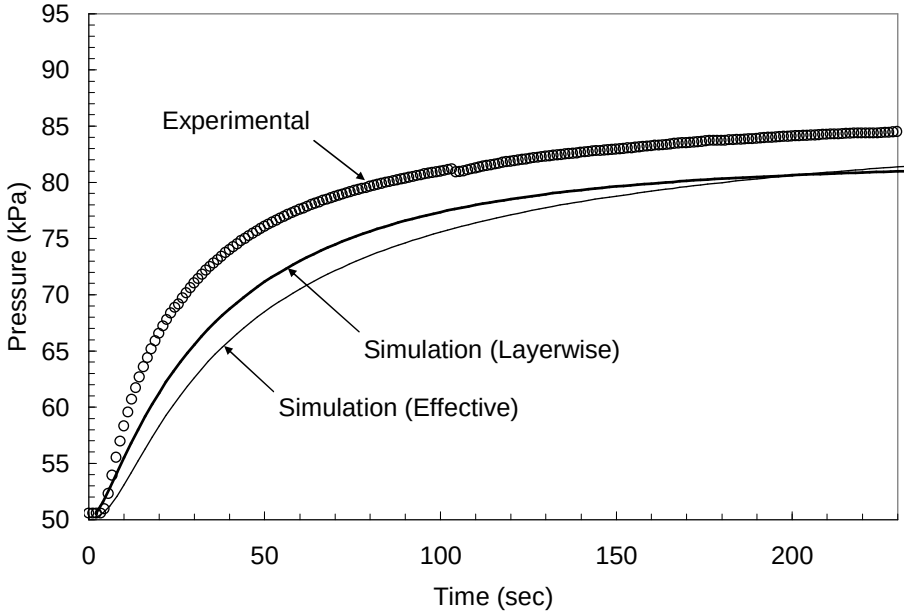

Figure 5-114 Plot of resin pressure versus time at sensor P4 (0.33 m) comparing the experimental measurements with the layerwise and effective models for an applied inlet pressure of 101 kPa.

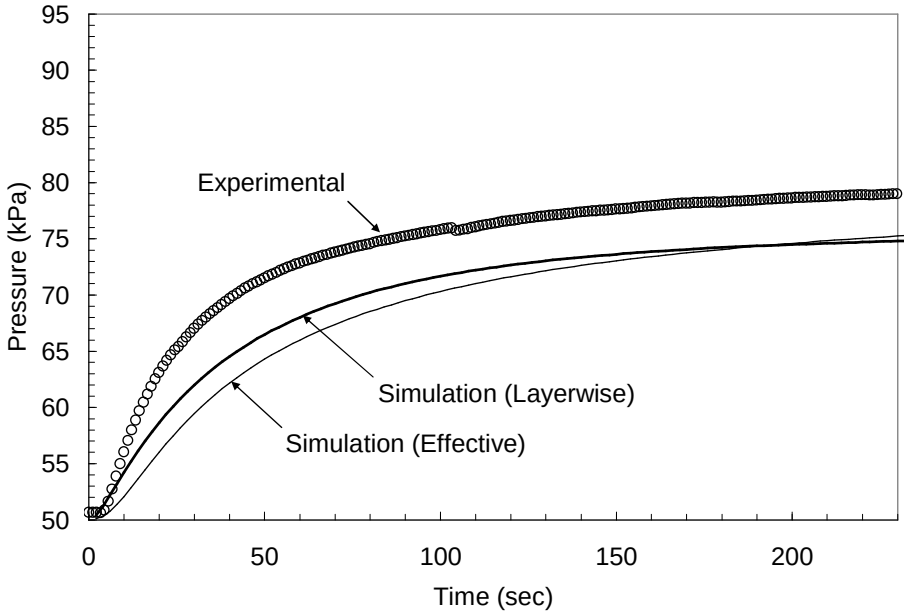

Figure 5-115 Plot of resin pressure versus time at sensor P5 (0.43 m) comparing the experimental measurements with the layerwise and effective models for an applied inlet pressure of 101 kPa

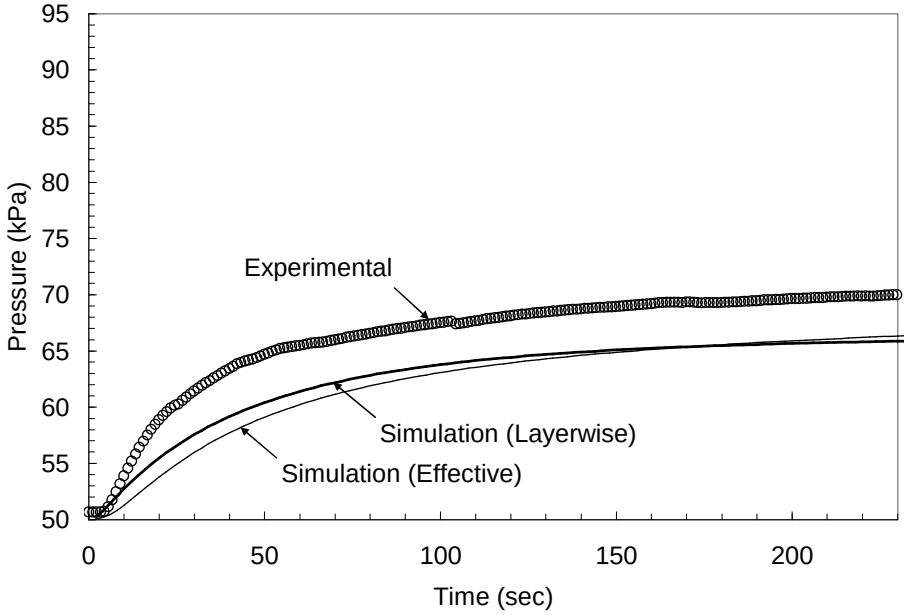

Figure 5-116 Plot of resin pressure versus time at sensor P6 (0.53 m) comparing the experimental measurements with the layerwise and effective models for an applied inlet pressure of 101 kPa

Contour plots of predicted pressures and fiber volume fractions during the relaxation process for elapsed times of 0, 20, 40, 60, and 120 seconds are given in Figure 5-117 and Figure 5-118 respectively. From the pressure contours it is again observed that while the effective model shows smooth contours the layerwise model gives contour curves which have discontinuities in the slope as it transitions between the different materials. Again the layerwise model is able to predict the fiber volume fractions for the different materials while the effective model treats the preform as a single material.

From the predicted fiber volume fractions the laminate thicknesses are predicted at each displacement sensor location using both the layerwise and effective models with the compaction and relaxation constitutive model curves for the respective materials (Table 4-4). Plots of the predicted thickness along with experimental measurements for sensors D1, D2, and D3 are shown in Figure 5-119 through Figure 5-121 respectively. From the plots it is seen that the predicted laminate thickness using the layerwise model and the relaxation curve from the constitutive model show excellent agreement with the experimental measurements. A summary of the predicted and measured changes in preform thickness are given in Table 5-7. From the table it is observed that the prediction error at sensor D1 and D2 did not exceed 5% with the error at D3 being 33%.

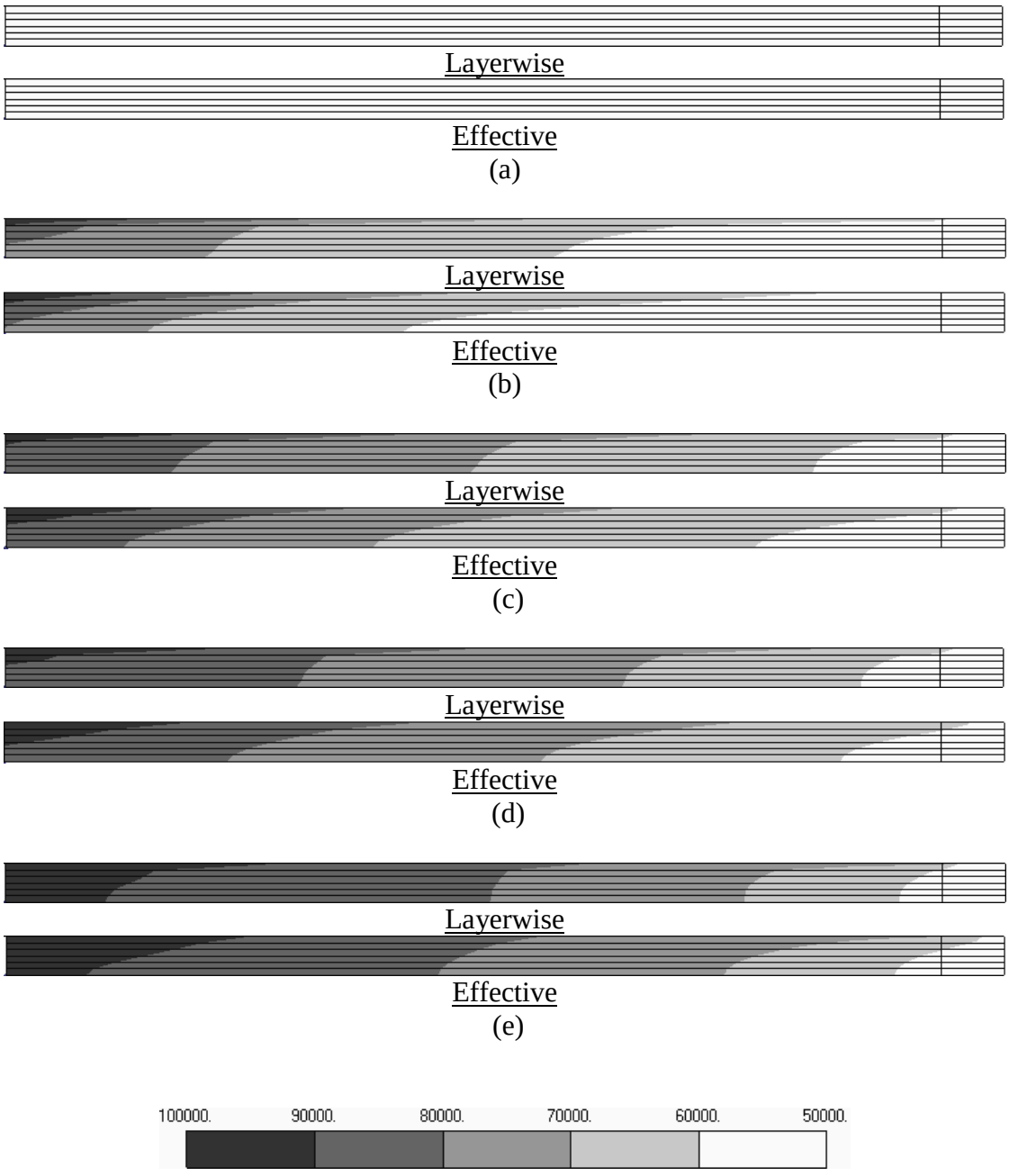

Figure 5-117 Contour plots of pressure for the uni/triax laminate during relaxation with the inlet open to the atmosphere showing pressures at (a) 0, (b) 20, (c) 40, (d) 60, and (e) 120 seconds.

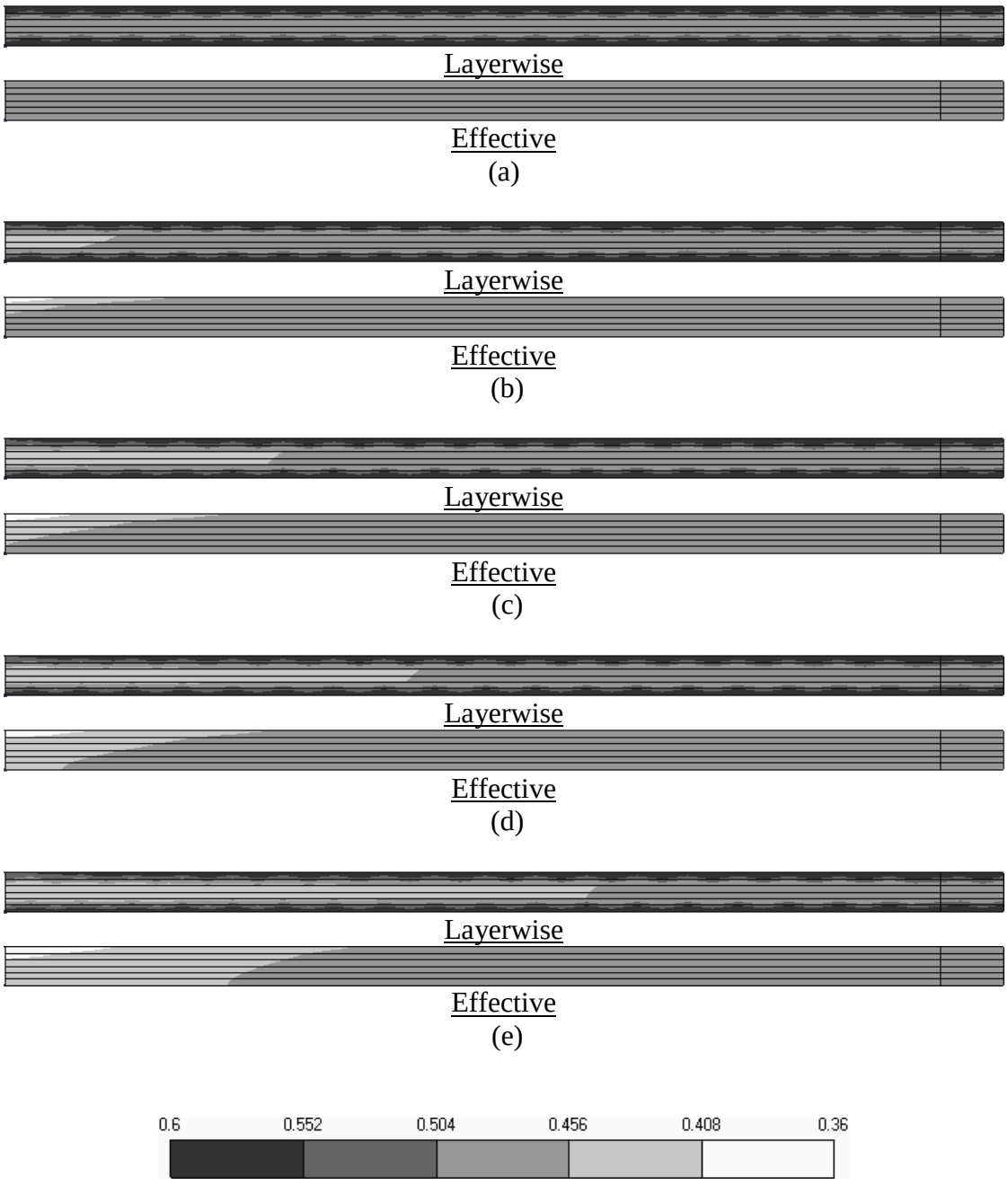

Figure 5-118 Contour plots of fiber volume fraction for the uni/triax laminate during relaxation with the inlet open to the atmosphere showing the fiber volume fraction at (a) 0, (b) 20, (c) 40, (d) 60, and (e) 120 seconds.

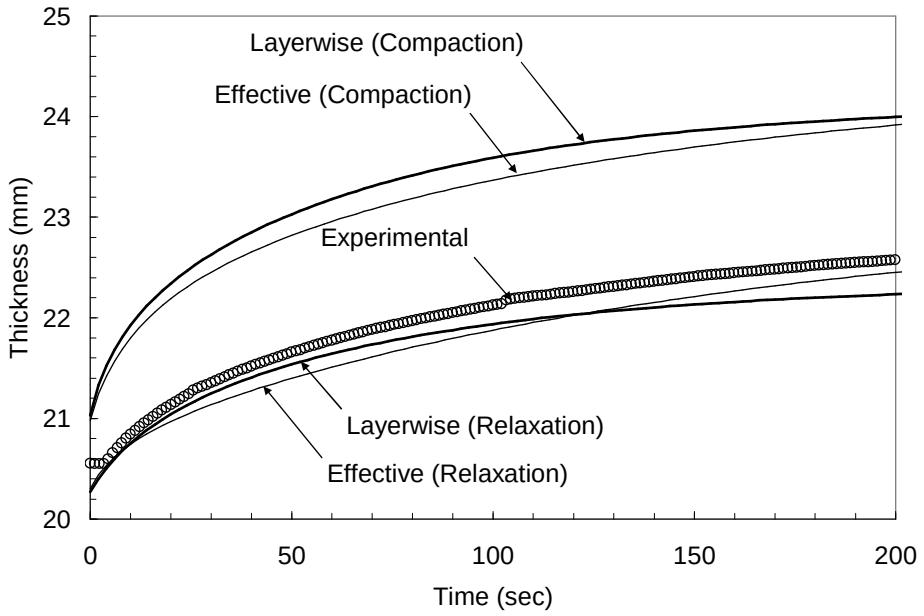

Figure 5-119 Plot of thickness versus time during relaxation comparing the predicted laminate thickness at sensor D1 with the experimentally measured thickness.

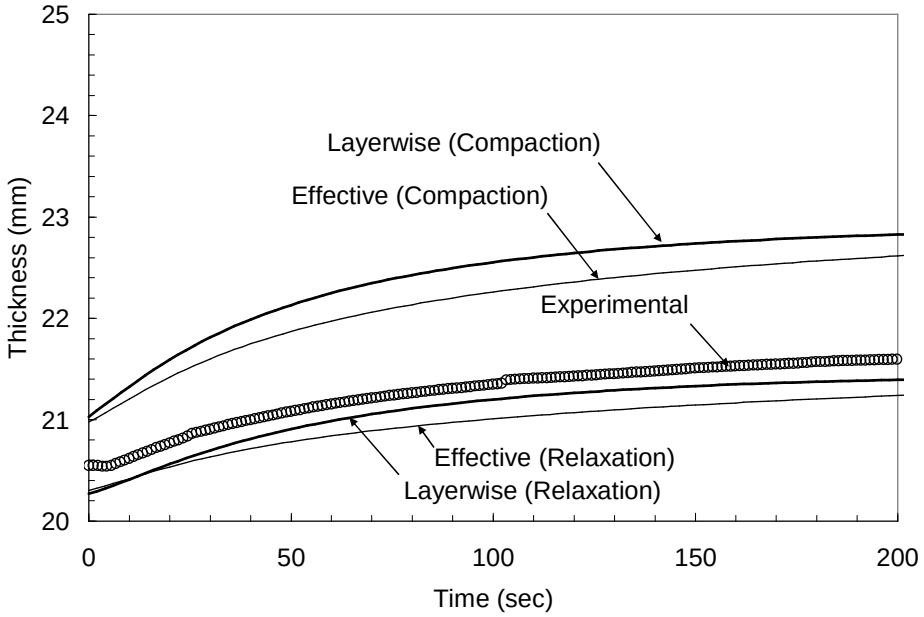

Figure 5-120 Plot of thickness versus time during relaxation comparing the predicted laminate thickness at sensor D2 with the experimentally measured thickness.

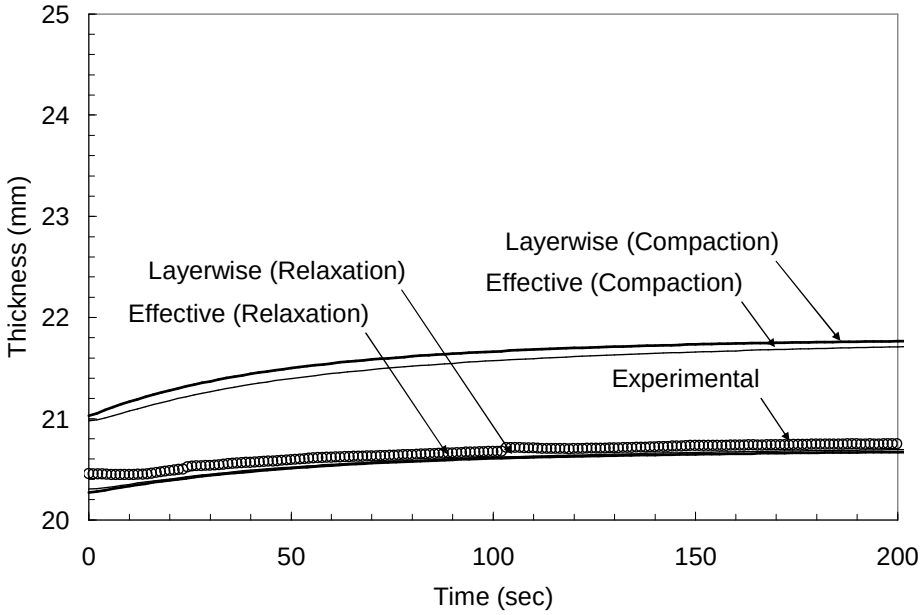

Figure 5-121 Plot of thickness versus time during relaxation comparing the predicted laminate thickness at sensor D3 with the experimentally measured thickness.

It is also of interest to note from Table 5-7 that the measured change in thickness progressively decreased at D1 for each of the experiments. For the first bleeding experiment the change in thickness was 2.3 mm which reduced to 2.1 mm for the second bleeding experiment and finally 2.0 mm for the relaxation experiment. This confirms nesting of the layers as the preform undergoes repeated compaction cycles.

Table 5-7 Summary of Thickness Predictions

	D1		*D2*		*D3*	
Case	Δt *(mm)*	*Error (%)*	Δt *(mm)*	*Error (%)*	Δt *(mm)*	*Error (%)*
			Bleed (50 kPa @ Inlet)			
Experimental	2.3	NA	1.2	NA	0.3	NA
Layerwise						
-Compaction	3.0	+30	1.8	+50	0.7	+133
-Relaxation	2.0	-13	1.1	-8	0.4	+33
Effective						
-Compaction	3.3	+44	1.9	58	0.8	+167
-Relaxation	2.6	+13	1.1	-8	0.5	+67
			Bleed (Inlet Closed)			
Experimental	2.1	NA	1.1	NA	0.3	NA
Layerwise						
-Compaction	3.0	+43	1.8	+64	0.7	+133
-Relaxation	2.0	-5	1.1	0	0.4	+33
Effective						
-Compaction	3.3	+57	1.9	+73	0.8	+167
-Relaxation	2.6	+24	1.1	0	0.5	+67
			Relax (100 kPa @ Inlet)			
Experimental	2.0	NA	1.1	NA	0.3	NA
Layerwise						
-Compaction	3.0	+50	1.8	+64	0.7	+133
-Relaxation	1.9	-5	1.1	0	0.4	+33
Effective						
-Compaction	2.9	+45	1.6	+45	0.7	+133
-Relaxation	2.2	+10	0.9	-18	0.4	+33

To gain further insight into using layerwise models versus effective models additional simulations were performed. The simulations consider the filling of a preform consisting of two materials in which the in-plane and through thickness

permeabilities of the two materials differ by a factor of 10. A typical example of this is the triax and uni-directional materials previously considered in this study. To simplify the study, the first material (Mat1) is defined by the uni-directional material with the flow parallel to the fibers where the compaction and permeability constitutive models are given in Table 4-4 and Table 4-5 respectively. The second material (Mat2) is defined by multiplying the permeability constitutive model of Mat1 by a factor of 0.1. The preform is comprised of these two materials such that the upper half of the preform thickness is composed of one material and the lower half of the preform laminate is composed of the second material. Two resin filling cases are considered. The first case compares the layerwise and effective models when no flow distribution layer is used and the flow is introduced at the preform edge, and the second case compares layerwise and effective models when a flow distribution layer is used.

For the first case study the layerwise model represents a preform in which the upper half of the preform consists of Mat1 and the lower half is Mat2. An illustration of the layerwise model is given in Figure 5-122. The effective permeability for the preform is obtained by the "Rule of Mixtures" where the in-plane permeability is defined as 0.55 times the in-plane permeability (κ_{11}) of the uni-directional material and the through thickness permeability is defined as 0.182 times the through thickness permeability (κ_{33}) of the of uni-directional material. An illustration of the effective model is given in Figure 5-123. The same finite element mesh used for the previous study is used in this study (see Figure 5-78).

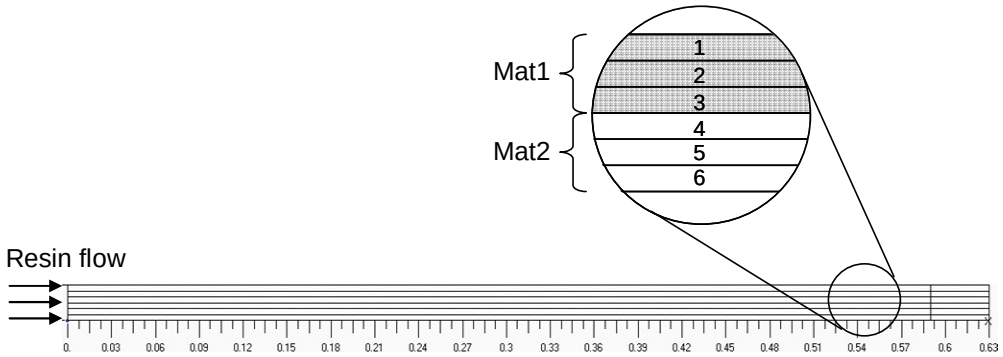

Figure 5-122 Illustration of the layerwise model in which a flow distribution mesh is not used where Mat1 is on top and Mat2 is on the bottom.

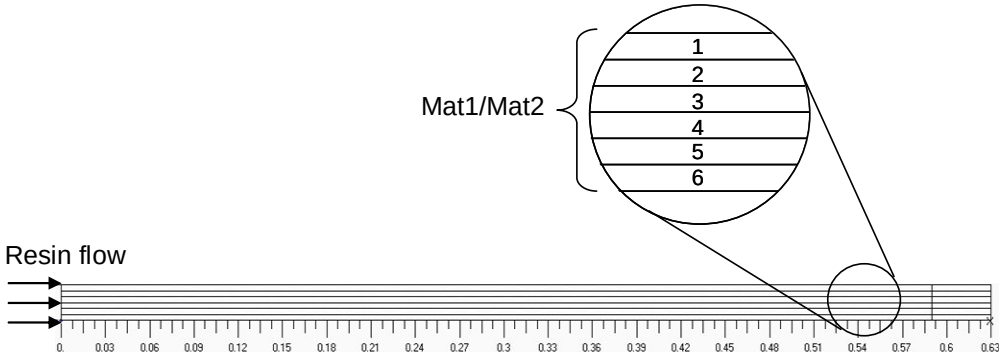

Figure 5-123 Illustration of the effective model in which a flow distribution mesh is not used.

Contour plots of the flow front at filling times of 30, 60, 180, 420, and 600 seconds are given in Figure 5-124. From the contour plots it is observed that the flow fronts for the layerwise and effective models are very different. The layerwise model shows a lead-lag of approximately 0.2 m between the flow front at the top and bottom surfaces of the preform. Due to the nature of the effective model it is incapable of

capturing this lag through the thickness of the preform. However the effective model does a good job of predicting the location of the flow front in an average sense. The predicted fill time for the layerwise model is 790 seconds where the fill time for the effective model is only 648 seconds (142 seconds shorter). Although the flow front for the layerwise model reaches the end of the preform first it takes a considerable amount of time to finishing wetting out the Mat2 layer which has very low permeability.

Contour plots of the pressure field for filling times of 30, 60, 180, 420, and 600 seconds are given in Figure 5-125. From the plots it is observed that near the flow front the pressure fields are very different for the layerwise and effective models. However, looking at the pressure field behind the flow front it is observed that the layerwise model shows constant pressure through the thickness of the preform and the layerwise and effective models are very similar.

The second case considers the same preform in which a flow distribution layer is used. Two layerwise models are considered in which the Mat1 and Mat2 layers are interchanged. Illustrations of the two layerwise models are given in Figure 5-126 and Figure 5-127 respectively. These two models are compared with an effective model utilizing the same flow distribution layer. An illustration of the effective model is given in Figure 5-128.

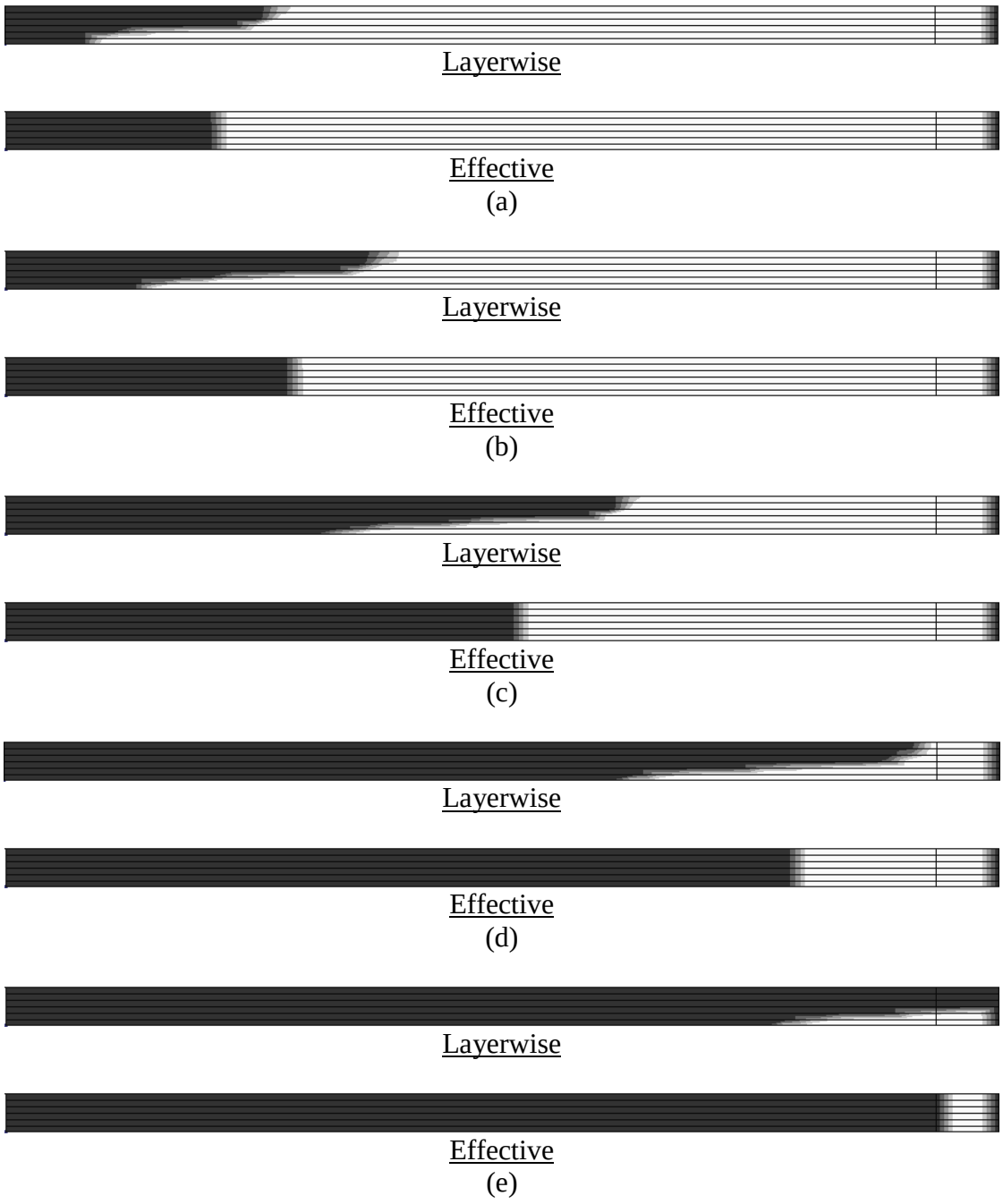

Figure 5-124 Plot of resin flow front during filling comparing layerwise and effective models at (a) 30, (b) 60, (c) 180, (d) 420, and (e) 600 seconds.

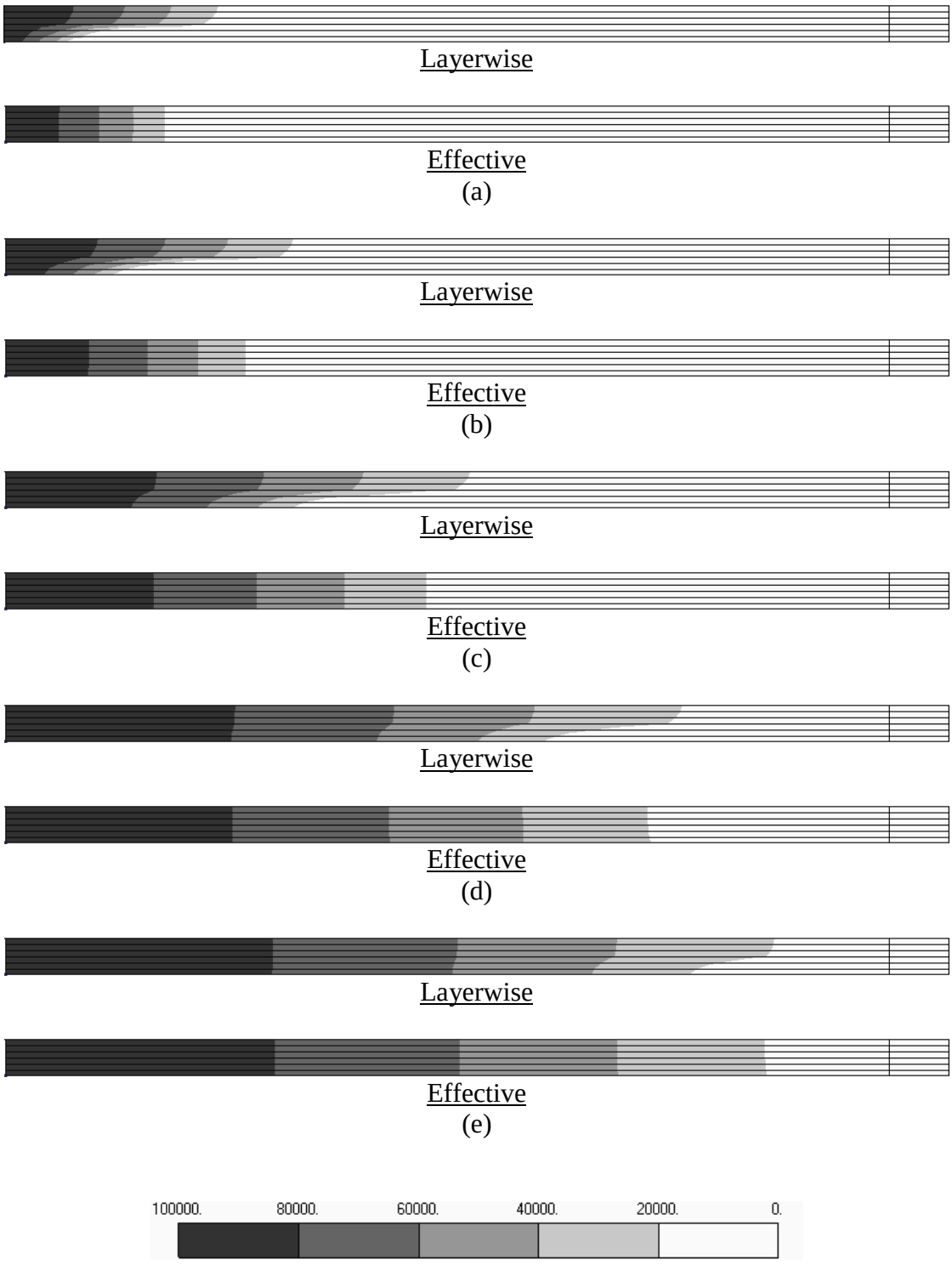

Figure 5-125 Plot of resin pressure during filling comparing layerwise and effective models at (a) 60, (b) 300, (c) 600, and (d) 900 seconds.

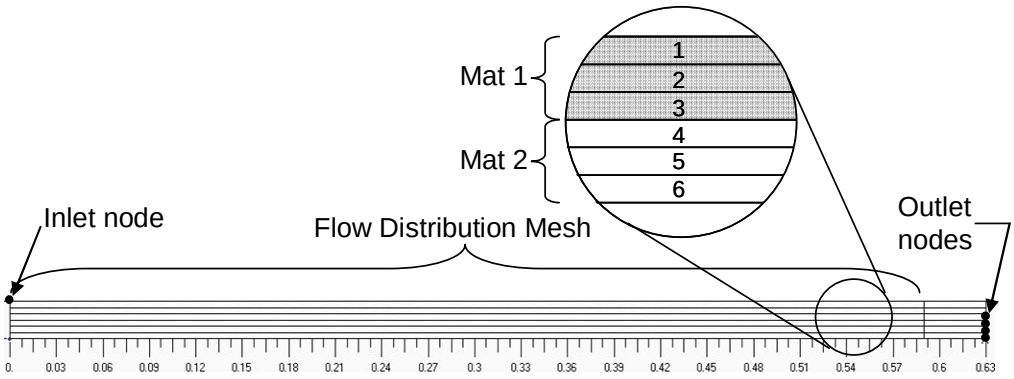

Figure 5-126 Illustration of the layerwise model with flow distribution layer in which the Mat1 material is on top and the Mat2 material is on bottom.

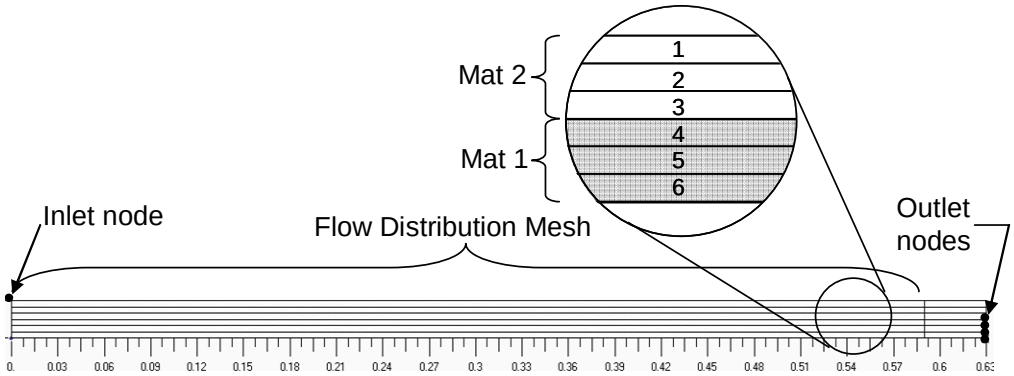

Figure 5-127 Illustration of the layerwise model with flow distribution layer in which the Mat2 material is on top and the Mat1 material is on bottom.

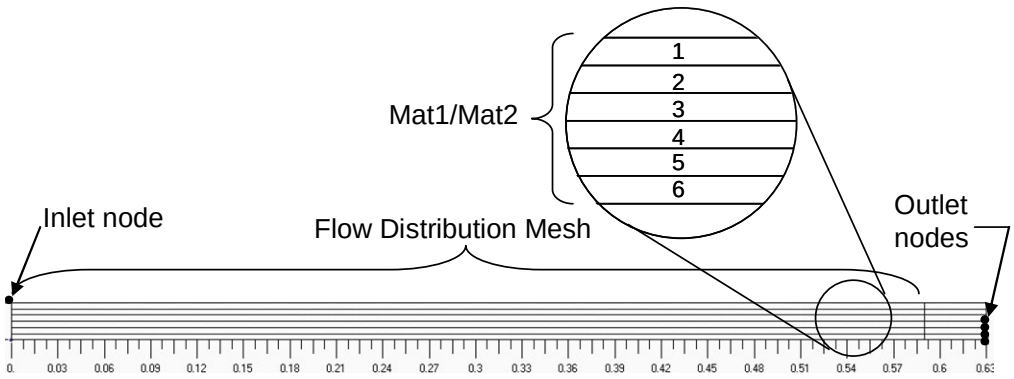

Figure 5-128 Illustration of the effective model with flow distribution mesh.

Contour plots of the flow front for the two layerwise models and effective model at filling times of 60, 120, and 300 seconds are given in Figure 5-129. From the contour plots it is observed that for the layerwise (Mat1/Mat2) model the lead-lag of the resin front is approximately 0.5 m. For the layerwise (Mat2/Mat1) and effective models it is seen that the flow of resin reaches the end of the flow distribution mesh well before the resin has penetrated through the thickness of the preform indicating that the lead-lag of the flow front through the thickness of the preform is longer than 0.6 m (the length of the flow mesh). It is predicted that the lead lag for the layerwise (Mat2/Mat1) model would be approximately 1.0 m while the lead-lag for the effective model would be 0.8 m. This large lead-lag is due to the low through thickness permeability of the Mat2 material which significantly stifles the flow of resin through the thickness of the preform. The total fill time for each of the models is given in Table 5-8. The effective model over predicts the fill time by 155 seconds when the Mat1 material is on top and under predicts the total filling time by 38 seconds when the Mat2 material is on top. The effective model predicts the location of the flow front in an average sense but is not able to capture the extreme difference in the lead-lag of the flow front when the Mat1 and Mat2 materials are interchanged. The ability to predict the lead-lag of the flow front is especially important when considering flow from a thick laminate to a thinner laminate in which residual air can become trapped at the mold surface due to the lead-lag phenomenon. Further consideration will be given to the infusion of laminates of varying thickness in the next chapter. Based on the observed filling patterns and predicted fill times it is seen that using a layerwise model which considers the specific lay up can be very important.

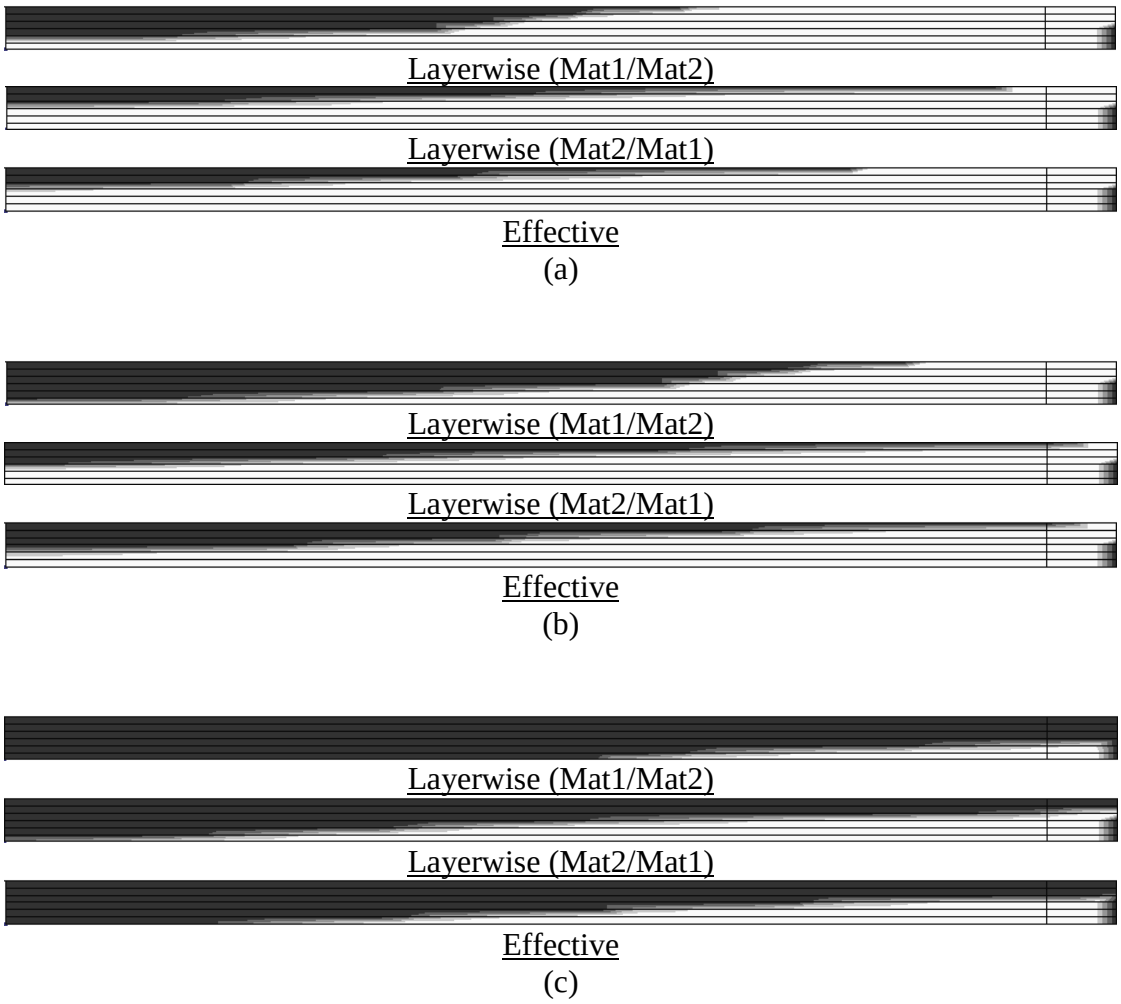

Figure 5-129 Plot of resin flow front during filling comparing layerwise models with the effective model at (a) 60, (b) 120, and (c) 300 seconds.

Table 5-8 Resin Fill Times

Model	*Fill Time (seconds)*
Layerwise (Mat1/Mat2)	410
Layerwise (Mat2/Mat1)	603
Effective	565

Contour plots of the pressure field for filling times of 60, 120, 300, and 500 seconds are given in Figure 5-130. From the plots it is observed the flow of resin near the flow front as well as behind the flow front is very different for each of the models. Since the flow is driven by the pressure gradient, the direction of the flow is normal to the contour lines. For the Layerwise (Mat1/Mat2) model it is seen that the flow in the top layer (Mat1) is largely along the length of the preform while the flow in the Mat2 layer is predominantly through the thickness. Conversely for the layerwise (Mat2/Mat1) model it is observed that the flow in the top layer (Mat2) is largely through the thickness while the flow in the lower layer (Mat1) is along the length of the preform (see contour plot at 500 seconds). Both layerwise models show discontinuities in the slope of the contour lines as they move across the interface between the two different materials. The contour lines for the effective model are smooth and continuous through the thickness of the preform. Again, as with the flow front profiles, it is observed that the pressure fields are very dependent on the preform lay up. It is clear from the pressure plots that if one desires to predict the pressure field during filling a layerwise model must be used.

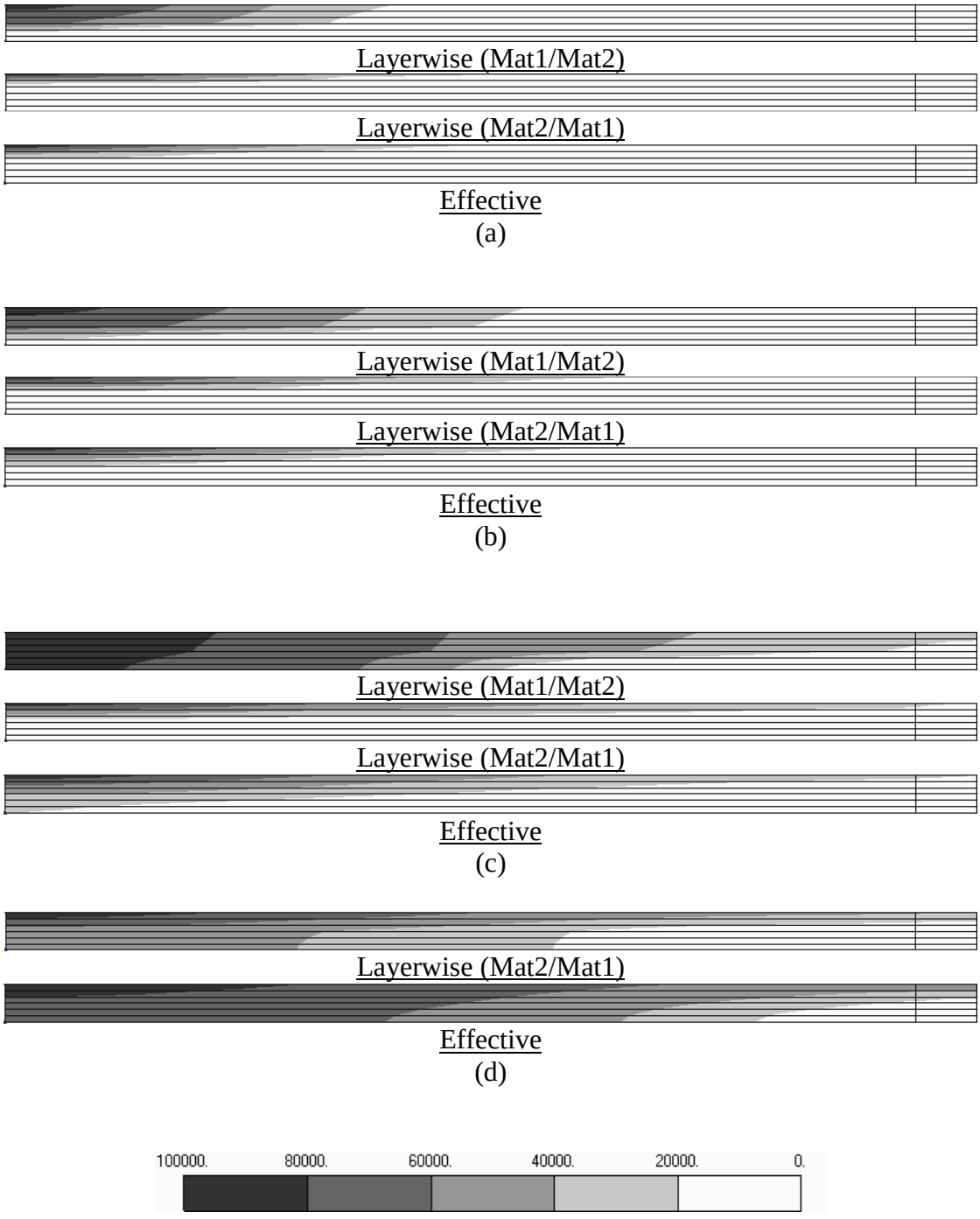

Figure 5-130 Plot of resin pressure during filling comparing layerwise models with the effective model at (a) 60, (b) 120, (c) 300, and (d) 500 seconds.

This study has investigated the extreme case of a 2-ply non-symmetric layup where it is observed that the order of the layup significantly affects the flow front profile through the thickness of the preform. It is common practice in composite design to almost always use symmetric layups in order to eliminate extension-shear-bend-twist coupling. Additional flow studies are performed to investigate the viability of the effective model for symmetric layups given by $[Mat1/Mat2]_{ns}$ and $[Mat2/Mat1]_{ns}$ where *n* equals 1, 2, and 3. It is expected that as *n* increases (plies become more blended through the thickness) that the results of the layerwise models will more closely match the effective model. The two different layups ($[Mat1/Mat2]_{ns}$ and $[Mat2/Mat1]_{ns}$) are considered to study the effects of the high (mat 1) and low (Mat 2) permeability layers when they are the outer plies of the laminate.

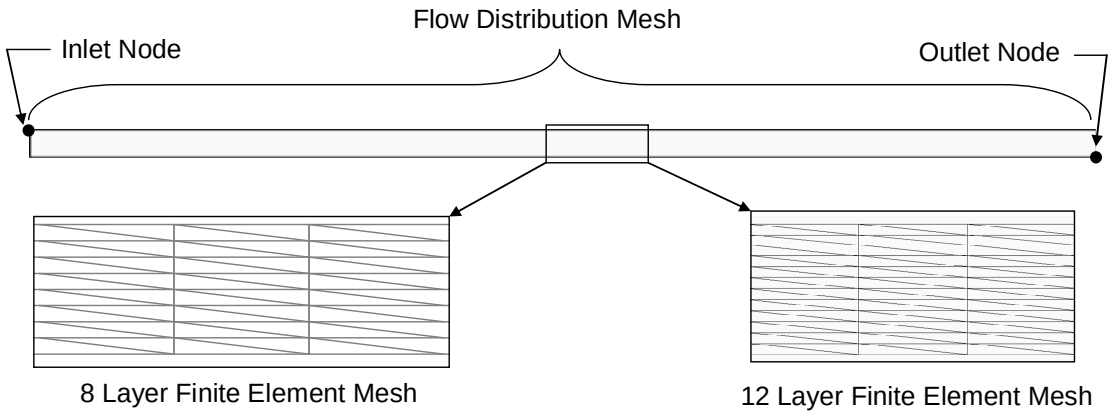

Figure 5-131 Illustration of the finite element model showing the inlet and outlet nodes as well as the 8 layer and 12 layer meshes used in the study.

In order to allow the lead-lag in the flow front to fully develop the model is extended to 1 m in length with the thickness being 0.024 m and the flow mesh running

the full length of the preform. An illustration of the finite element model showing the inlet and outlet node locations as well as the extent of the flow distribution mesh is given in Figure 5-131. The 4 and 8 ply layups ($[Mat1/Mat2]_s$, $[Mat1/Mat2]_{2s}$, $[Mat2/Mat1]_s$, and $[Mat2/Mat1]_{2s}$) are modeled using an 8 layer finite element mesh and the 12 ply layups ($[Mat1/Mat2]_{3s}$ and $[Mat2/Mat1]_{3s}$) are modeled using a 12 layer finite element mesh (Figure 5-131). The effective model uses the 8 layer finite element mesh. To assess the viability of the effective model the predicted fill time, lead-lag distance, and pressure distributions of the effective model are compared with each of the layerwise models. A summary of the total fill times and lead-lag distances for each model as well as fill time and lead-lag normalized by the effective model is given in Table 5-9.

Table 5-9 Summary of Fill Times and Lead-Lag Distances

Model Layup	*Total Fill Time (sec)*	*Normalized Fill Time*	*Lead-Lag Distance (m)*	*Normalized Lead-Lag*	*Flow Mesh Fill Time (sec)*
Effective	1016	1.00	0.55	1.00	470
$[Mat1/Mat2]_s$	962	0.95	0.45	0.82	530
$[Mat1/Mat2]_{2s}$	982	0.97	0.48	0.87	517
$[Mat1/Mat2]_{3s}$	987	0.97	0.50	0.91	494
$[Mat2/Mat1]_s$	1070	1.05	0.65	1.18	442
$[Mat2/Mat1]_{2s}$	1049	1.03	0.63	1.15	450
$[Mat2/Mat1]_{3s}$	1034	1.02	0.62	1.13	433

A comparison of the flow front profiles for each layup using the layerwise models is compared with the effective model in Figure 5-132. Each model shows the

flow front at the time in which the resin reaches the end of the flow mesh where these times are given in Table 5-9. For viewing convenience the thickness of the model has been scaled by a factor of 3. From the figure it is seen that as *n* increases the lead-lag distance and flow front profiles of the layerwise models more closely match that of the effective model. It is also observed that when the high permeability layer (Mat 1) is on the outside the lead-lag is shorter than that predicted by the effective model and when the low permeability layer (Mat 2) is on the outside the predicted lead-lag is larger than that predicted by the effective model. Plots of normalized fill time versus *n* and normalized lead-lag versus *n* are given in Figure 5-133 and Figure 5-134 respectively. From both plots it is seen that as n increases (more blended) the total fill time and lead-lag distance converge toward the effective model. It is also observed that the permeability of the outside plies plays a role in the fill time as well as the lead lag distance where the high permeability layer (Mat 1) on the outside leads to shorter fill times and lead-lag distances and the low permeability layer (Mat 2) on the outside leads to longer fill times and lead-lag distances with the effective model doing a good job of capturing the average of the two.

Pressure contour plots for each of the layerwise models and effective model are given in Figure 5-135. Like the flow front profile illustrations, each pressure contour plot is taken at the time in which the resin reaches the end of the flow mesh. From the figure it is seen that as *n* increases the pressure distribution of the layerwise models more closely match that of the effective model. Like the flow front profiles, it is observed that the presence of the high or low permeability layer on the outside affects the pressure distribution. A plot of pressure versus fill time at the mid-length

of the preform on the bottom surface is given in Figure 5-136. The plot shows the pressure history for each layerwise model as well as the effective model. From the plot it is observed that as *n* increases the pressure history converges toward the pressure history predicted by the effective model.

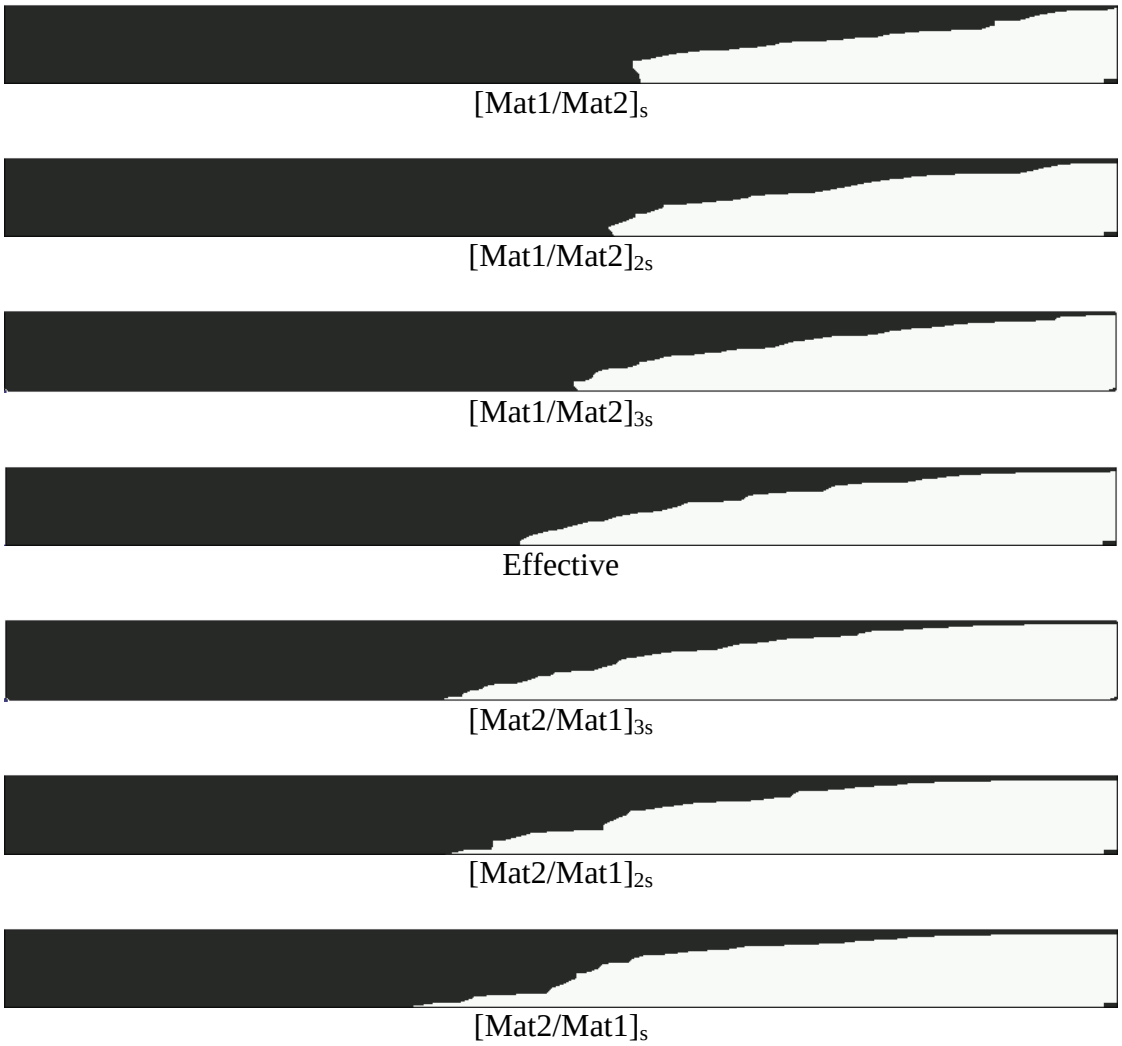

Figure 5-132 Illustration of the flow front for each of layerwise model along with the model using the effective properties. The images are scaled by a factor of 3 in the thickness direction for clarity.

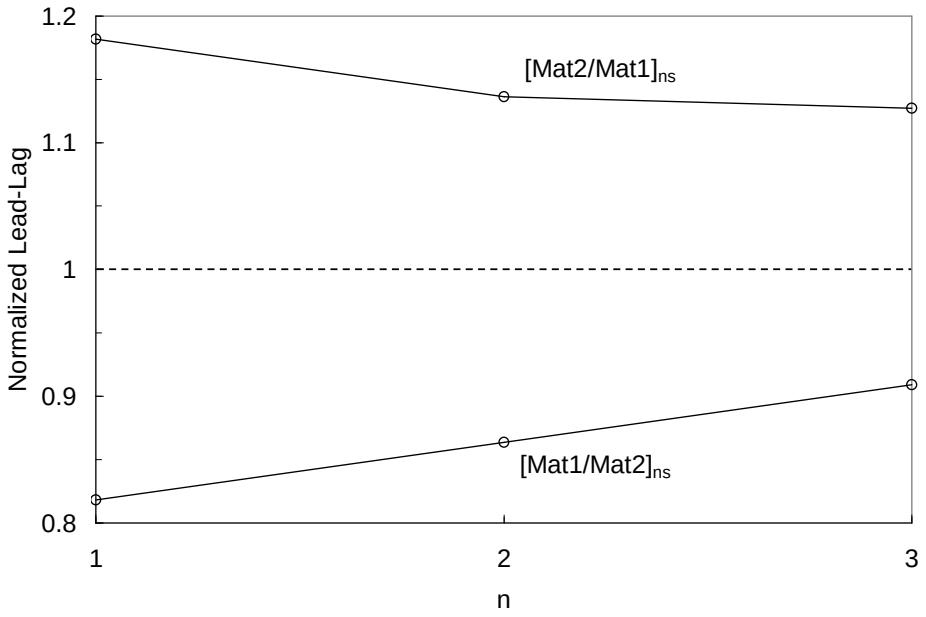

Figure 5-133 Plot of normalized lead-lag versus n for the cases in which the top and bottom plies are Mat 1 and when the top and bottom plies are Mat 2.

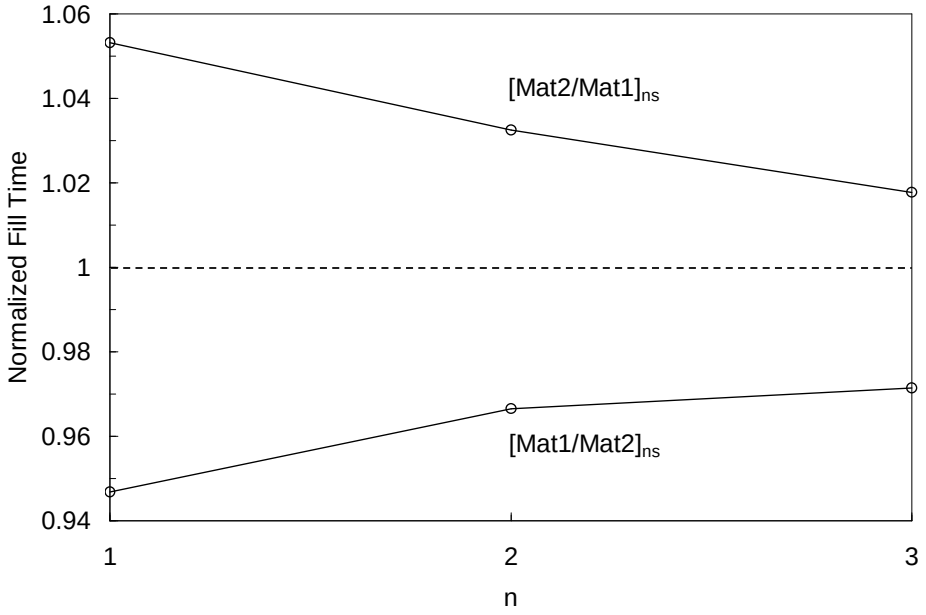

Figure 5-134 Plot of normalized fill time versus n for the cases in which the top and bottom plies are Mat 1 and when the top and bottom plies are Mat 2.

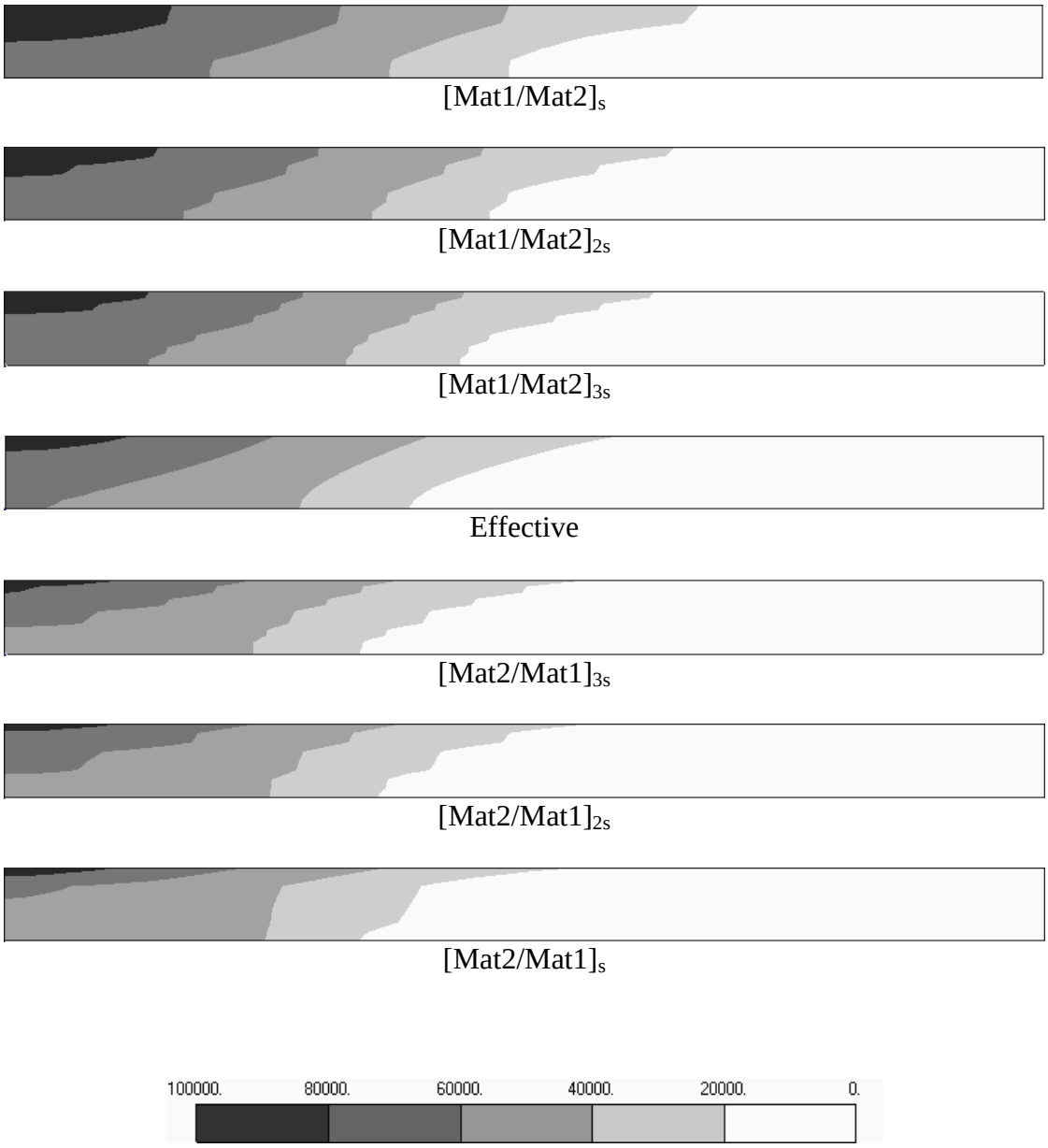

Figure 5-135 Contour plots of pressure when the flow front reaches the end of the flow mesh for each layerwise model and the effective model. The images are scaled by a factor of 3 in the thickness direction for clarity.

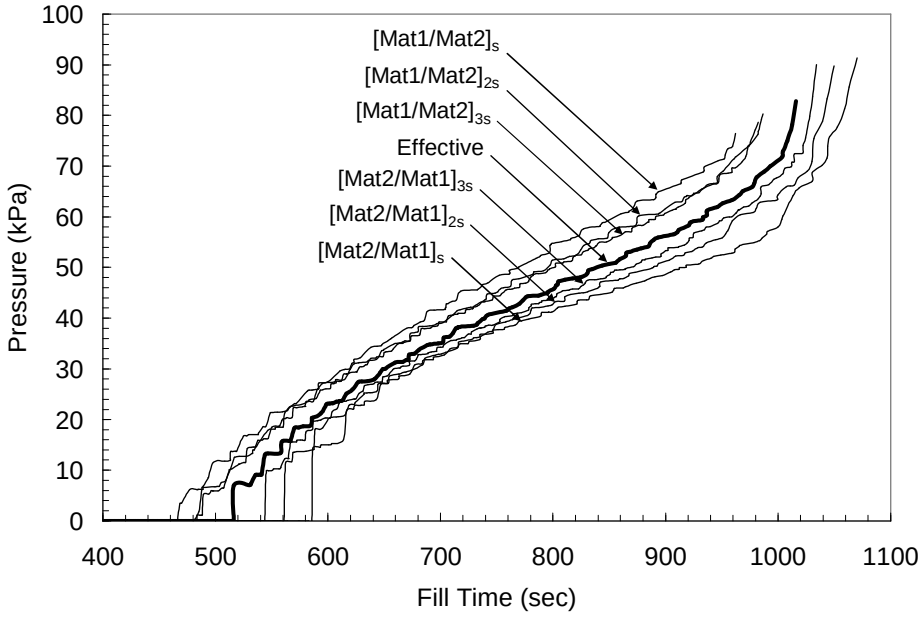

Figure 5-136 Plot of resin pressure versus fill time at the mid-length of the preform for each layerwise model and the effective model.

This last study has shown that for symmetric layups an effective model may be a viable tool for predicting fill time, flow front profiles, and pressure distributions for performs where the layers of differing permeability are interspersed through the thickness of the preform.

5.4 SUMMARY

This chapter has presented experimental results for three different flow experiments which were compared with simulation results. The Experiments were designed to study one-dimensional flow, two-dimensional flow through a preform consisting of one material type, and two-dimensional flow through a preform consisting of more than one material with differing permeabilities.

From the one-dimensional flow study it was observed that including transient thickness and fiber volume fraction effects during the filling phase had very little affect on the flow front progression or filling time. Pressure predictions during the resin filling phase showed excellent agreement with experimental measurements. The predicted pressures during the bleeding phase showed good agreement with the measurements, however while the predicted pressure was near symmetric about the mid point at bleeding time of 60 seconds, the measured pressure field was non symmetric with higher pressures toward the outlet end of the preform. It was shown that this is likely due to a non symmetric permeability field since each point along the preform is following a different compaction curve which lies between the established compaction and relaxation constitutive curves used in the simulation (see Figure 5-17).

The second experiment was performed to study in-plane and through thickness flow when a flow distribution layer is used. During the filling phase the predicted flow front progression along the top and mold surfaces showed good agreement with experimental measurements. The predicted pressures during the filling phase showed good agreement with measurements with the exception of the sensor location (P1) nearest the inlet where the pressure was under predicted. It was observed that the permeability along the vacuum bag/preform interface near the inlet was higher than the general through thickness permeability of the preform and must be considered. During the bleeding experiments simulation which utilized the compaction curve from the constitutive model showed good agreement with experimental measurements except at time zero where the pressures were under predicted. It was observed that

simulations which were run using the relaxation curve from the constitutive model did a good job of predicting the initial pressures at the beginning of the bleeding stage but were not as good as the bleeding progressed. In reality each point along the length of the preform follows a different compaction curve which originates along the relaxation curve and falls somewhere between the established compaction and relaxation curves depending on the starting point (see Figure 5-17).

The third study considered two-dimensional flow through a preform consisting of two different materials having different permeabilities. Simulations of flow during filling and bleeding were performed and compared using two different models. The first model was a layerwise model which modeled each material layer as separately in the preform and the second model was an effective model which treated the preform as a single material having an effective permeability which represented the lay-up under consideration. A comparison of experimental filling results and simulations using both the layerwise and effective models showed the layerwise model to best agree with the experimental measurements. The layerwise model did a much better job of predicting the experimental measurements for each of the bleeding experiments. The layerwise model did a good job of predicting the thickness of the laminate for all of the experiments when the relaxation curve from the constitutive model was used. A short study was performed to determine the necessity of using layerwise models. The study showed that for performs consisting of two different materials in which the in-plane and through thickness permeability are very different the use of a layerwise model can be critical in determining not only the total fill time but the length of the lead-lag of the flow front through the thickness of the preform. It was also shown that

when layers of differing permeability are interspersed through the thickness of the preform the effective model does a good job of representing the layerwise model and may be a viable tool for modeling the VARTM process.

CHAPTER 6

VARTM SIMULATION APPLICATIONS

This chapter presents the application of the flow simulation model in developing resin infusion and bleeding strategies for the beam hull section to be used in the composite modular bridge. A photograph of a completed composite beam section with attached deck is shown in Figure 6-1. The beam is 5 m long (197 in) and consists of a hull section with bulkheads and a top plate. The focus of this chapter is on the processing of the hull section. The beam hull is of particular interest since it consists of both thick and thin laminates in which the flow between these laminate thicknesses must be considered. A description of the hull section is given followed by an investigation of both infusion and bleeding strategies which will yield quality parts. Finally a summary of the findings is presented.

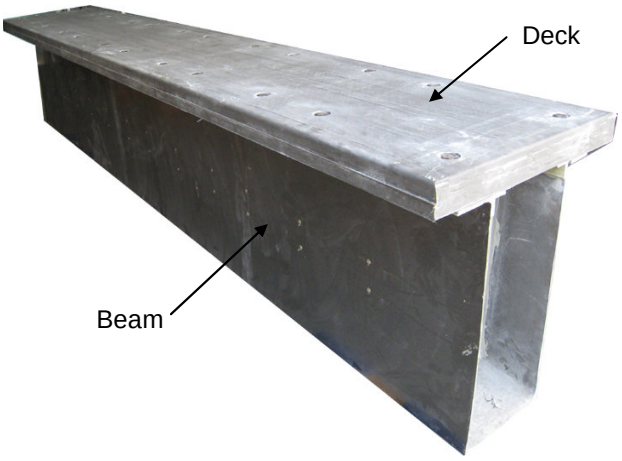

Figure 6-1 Photograph of a composite modular beam with attached deck.

6.1 BEAM HULL DESCRIPTION

The beam hull section is 5 m (197 in) long and 0.38 m (15 in) wide at the bottom. The total width at the top is 0.74 m with (29 in) with flanges which extend 0.18 (7 in) out on either side. The total depth of the section is 0.81 m (32 in). The section consists of three main regions: the tension rail, sidewalls, and flanges. The tension rail, which is 23 mm (0.9 in) thick, is primarily composed of uni-directional fibers oriented at 0° along the length of the beam to carry bending loads. The sidewalls are 7 mm (0.25 in) thick and are dominated by $\pm 45°$ oriented fibers to carry shear loads and 90° oriented fibers to resist buckling. The flanges are a continuation of the sidewall laminates and provide a surface for attachment of the beam top plate and deck. An illustration of the cross section of the beam hull is given in Figure 6-2. Each region of the hull section is composed of uni-directional and triax fabrics for which permeability and compaction characteristics have been established. The tension rail consists of 20 plies of uni-directional material and 6 plies of triax material where the layup is given by $[\text{triax}/\text{uni}_4/\text{triax}/\text{uni}_4/\text{triax}/\text{uni}_2]_S$. The sidewalls and flanges consist of 2 plies of uni-directional material and 4 plies of triax material where the layup is given by $[\text{triax}/\text{uni}/\text{triax}]_S$. The triax layers from the sidewalls are continuous through the tension rail. An illustration of the beam hull corner showing the transition of the layup from the sidewalls to tension rail is given in Figure 6-3.

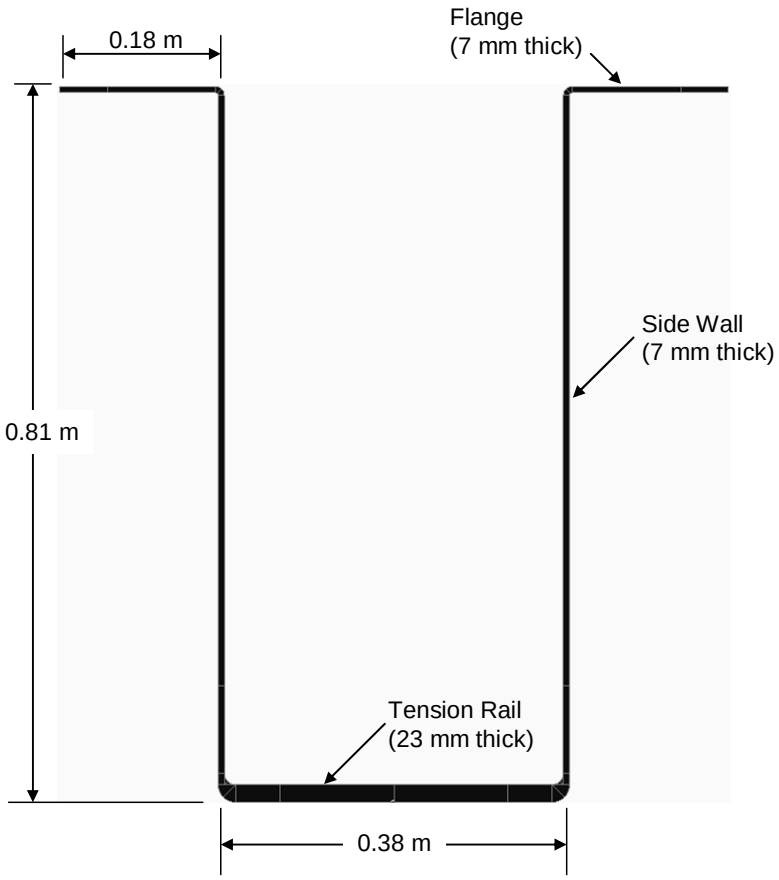

Figure 6-2 Illustration of the beam hull cross section showing dimensions.

The beam hulls are fabricated using the SCRIMP process where a series of photographs outlining the fabrication process are given in Figure 6-4. The process begins by placing the fiber reinforcing layers (preform) on a female aluminum mold. Great care is taken to ensure that each ply of the preform is properly placed to avoid excessive wrinkling of the fibers when vacuum pressure is applied. Following the placement of the fiber preform, a layer of release fabric is placed followed by the flow distribution mesh, flow springs, and inlet and vacuum (outlet) hoses. Finally the entire assembly is covered with a vacuum bag which is sealed around the perimeter of the

mold. Vacuum pressure is applied to the mold cavity after which resin is allowed to flow into the preform under atmospheric pressure. Following the completion of resin filling, excess resin is removed through resin bleeding and the part is cured at an elevated temperature (180° F cure with 250° F post cure). Following final cure, the vacuum bag, flow distribution mesh, and release fabric are removed and the final part is removed from the mold.

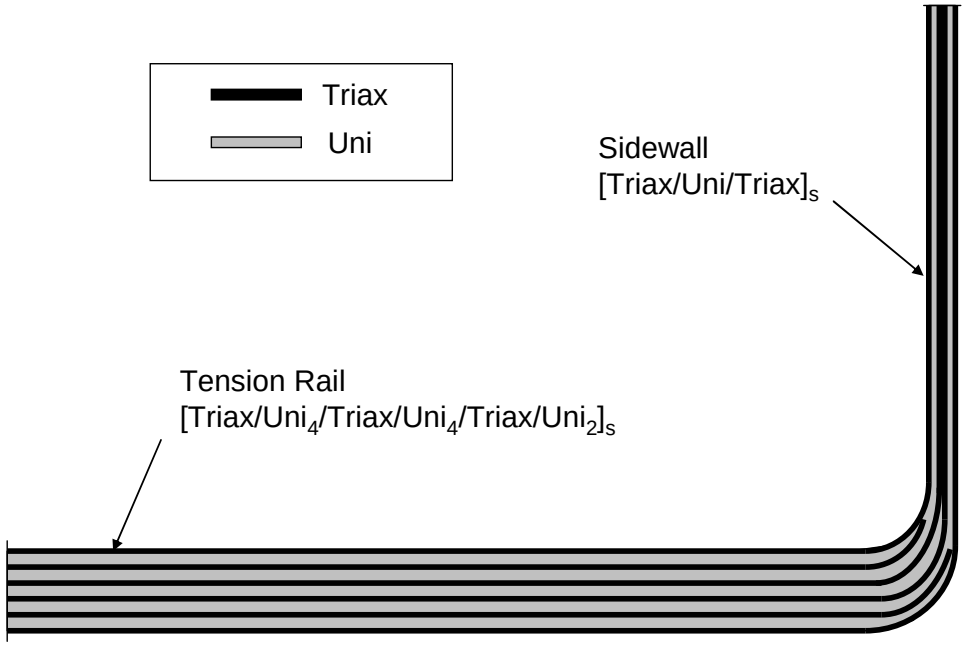

Figure 6-3 Illustration of the beam hull corner showing the layup of the tension rail and sidewall laminates.


(a)


(b)


(c)

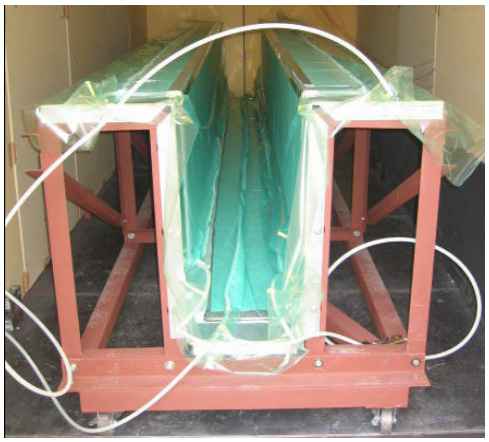
(d)


(e)

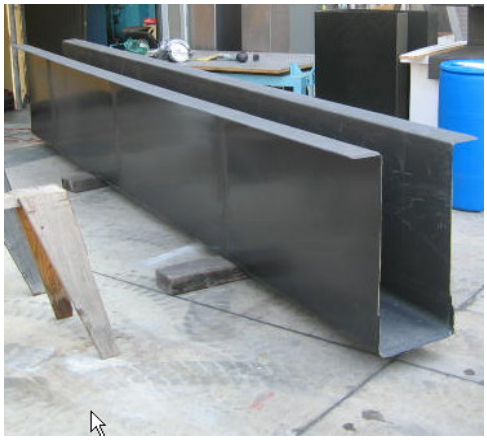
(f)

Figure 6-4 Photographs of beam hull fabrication: (a) Mold, (b) placement of fabric (preform), (c) placement of release fabric, flow mesh, flow springs, and hoses, (d) placement of vacuum bag and infusion, (e) vacuum bag and consumables removed, and (f) beam hull removed from mold.

In order to ensure that the final beam hull section is fully saturated with resin and air voids are minimized, an infusion strategy is developed through simulations of the filling process. In addition to an infusion strategy a method for removing excess resin must be determined so that excess resin can be removed in a timely manner such that the resin does not cure before the desired final part fiber volume fraction is reached. The following sections develop infusion and bleeding strategies based on insight provided by resin filling and bleeding simulations.

6.2 INFUSION STRATEGY

As a rule of thumb, for the resin filling stage of the VARTM process it is desirable to have the resin inlet at the lowest point of the part and the vacuum (outlet) lines at the highest points since any air trapped in the resin will have a tendency to migrate upward. Based on this fundamental rule two different infusion strategies are investigated to determine the strategy which will result in the shortest fill time and still offer a robust infusion which will minimize the presence of voids.

6.2.1 Resin Filling with Single Inlet

The first infusion strategy investigates the placement of a single inlet line along the length of the hull section centered on the tension rail with continuous flow distribution mesh extending up the sidewalls of the hull section and ending near the ends of the flanges were the outlet lines are located. An illustration of the infusion

strategy showing the locations of the inlet and vacuum (outlet) lines is given in Figure 6-5. The inlet and outlet lines are created using flow springs such that during the infusion process the resin quickly flows into the resin inlet line and then flows transverse to the length of the beam section. Due to the nature of the flow, the simulation model is reduced to a two-dimensional flow model where the flow transverse to the inlet line and through the thickness of the preform are considered. An illustration of the two-dimensional model as well as the finite element mesh are shown in Figure 6-6. Due to symmetry it is required to only model half of the beam hull section. The finite element model uses two-dimensional triangle elements to represent the preform and one-dimensional line elements representing the flow distribution mesh. The model consists of 749 elements and 443 nodes with the tension rail and sidewalls being modeled with three elements through the thickness of the laminates. A mesh refinement study comparing models with three elements through the thickness to a model using six elements through the laminate thickness showed good convergence using three elements through the thickness. The higher resolution model having six elements through the thickness is used to study the flow at the hull section corner.

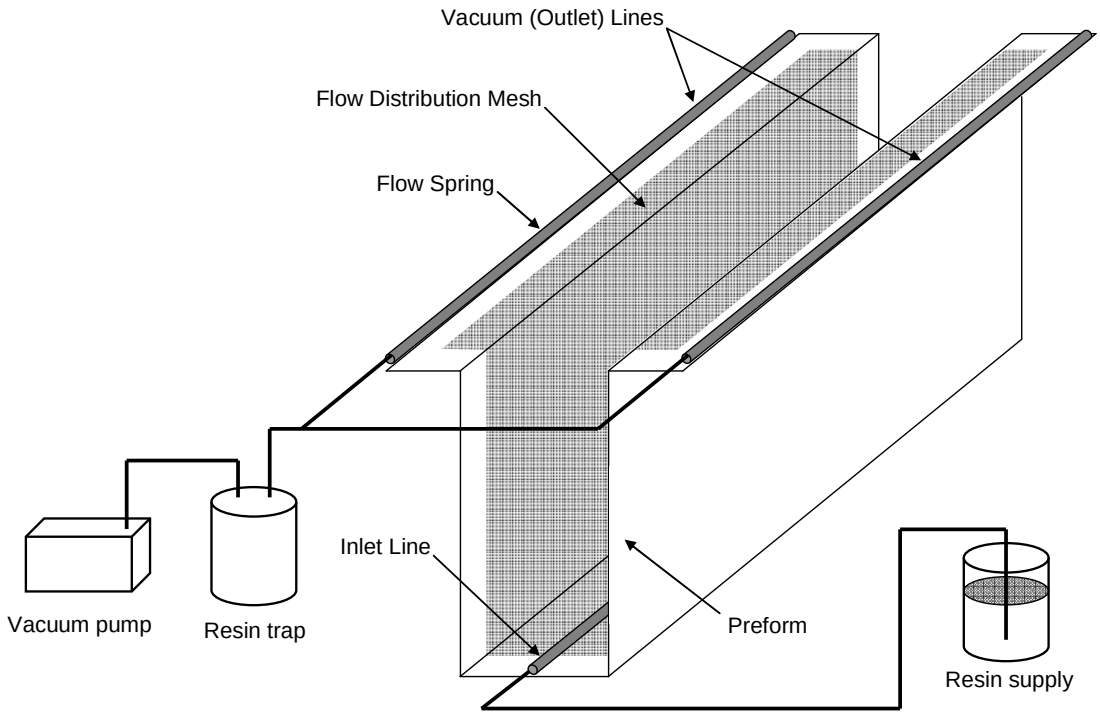

Figure 6-5 Illustration showing the infusion strategy in which a continuous flow distribution mesh is used with a single resin inlet line. Mold and vacuum bag not shown for clarity.

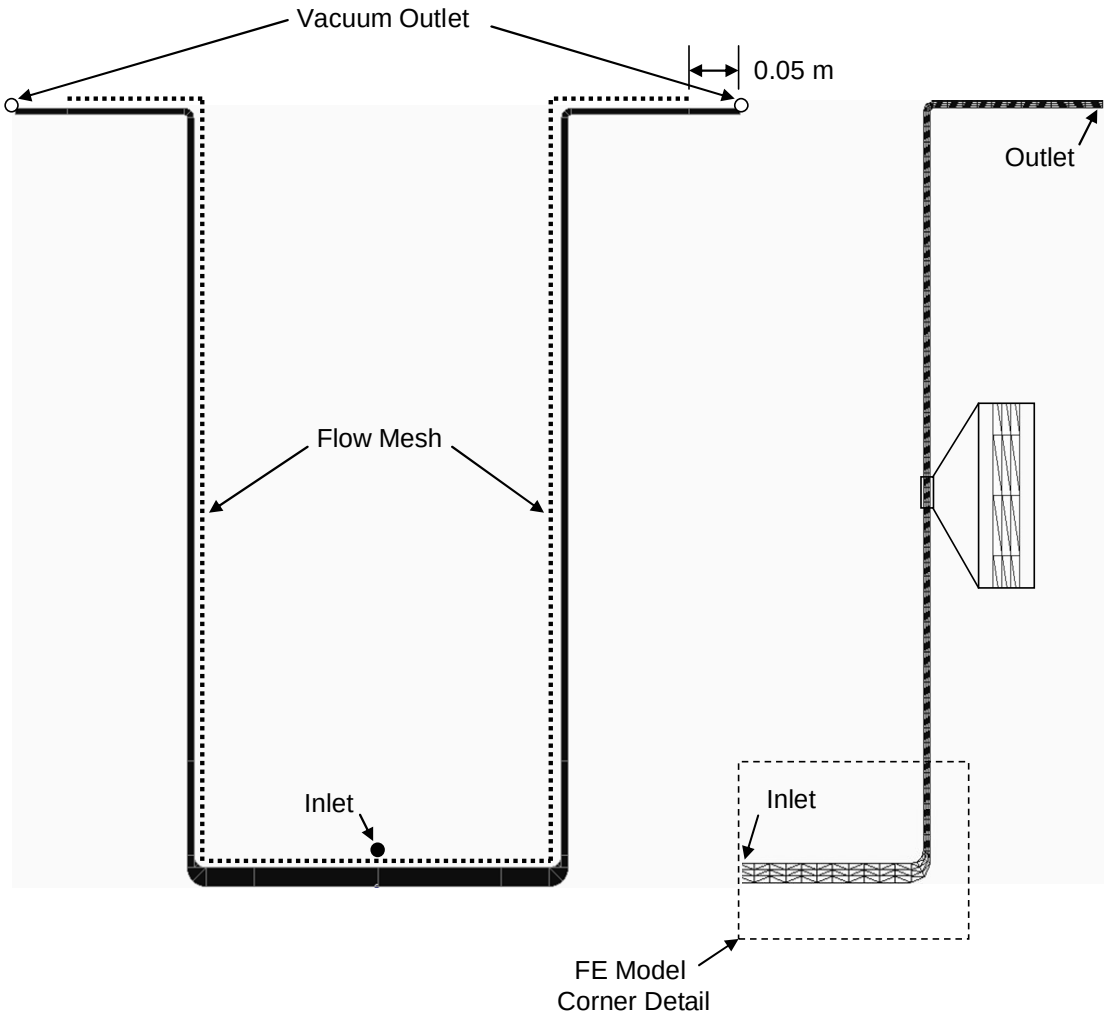

Figure 6-6 Illustration of (a) the hull cross section showing the infusion strategy in which a continuous flow distribution mesh layer is used with a single inlet as well as (b) the finite element mesh.

For purposes of simulation the permeability and compaction constitutive relations for the uni/triax preform are used for the tension rail portion of the hull section and the rule of mixtures is used to develop the permeability constitutive relationships for the sidewall and flange laminates. Based on constitutive models for

the uni and triax materials (Table 4-5) and the thickness fraction of each material in the sidewall laminate (23% uni and 77% triax) the in-plane (κ_{11}) and through thickness (κ_{33}) constitutive models are given by

$$\kappa_{11} = \left(2.28e^{-19.1V_f}\right)\left(10^{-6}\right) \tag{6.1}$$

$$\kappa_{33} = \left(7.56e^{-8.54V_f}\right)\left(10^{-11}\right). \tag{6.2}$$

The resin used in the composite beams is EPON 862 with Lindride 6 hardener which is infused at a temperature of 95° F. To account for the thickening of the resin as a function of time the viscosity versus time constitutive relationship given in Figure 4-9 is incorporated into the model. All filling simulations assume full vacuum (0 kPa) pressure at the outlet and near atmospheric pressure (100 kPa) at the inlet.

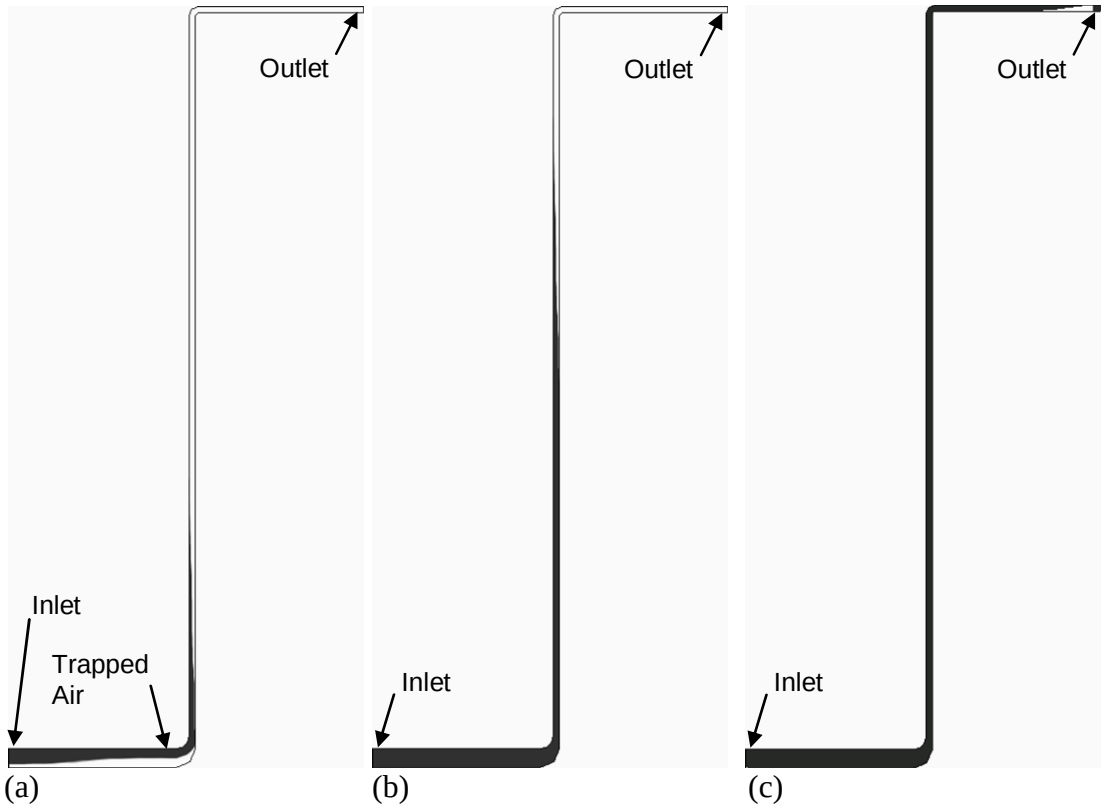

Figure 6-7 Contour plots showing the location of the flow front at (a) 300, (b) 1250, and (c) 3500 seconds for the case when a continuous flow mesh is used with a single inlet.

Contour plots of the flow front during infusion times of 300, 1250, and 3500 seconds are given in Figure 6-7. The total predicted filling time for the first infusion strategy is 3792 seconds. From Figure 6-7a it is seen that that due to the lead-lag of the flow front through the preform thickness, at a filling time of 300 seconds the resin has already penetrated through the thinner side wall laminate before the thicker tension rail laminate has become completely saturated. This is of concern since any residual air remaining in the tension rail does not have a path to the vacuum (outlet) line leading to the formation of voids within the tension rail laminate.

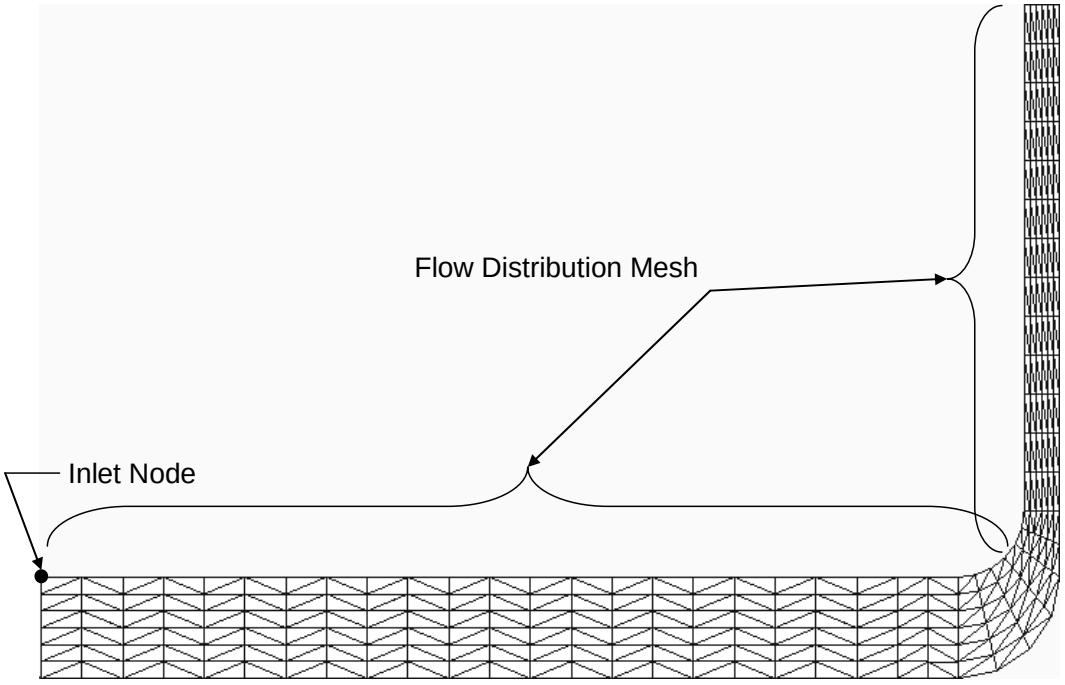

Figure 6-8 Illustration of the beam hull corner finite element model used to investigate the flow from the thick tension rail laminate to the thin sidewall laminate for the infusion strategy in which a continuous flow mesh layer is used.

To further investigate the entrapment of residual air in the tension rail laminate a higher resolution model of the corner between the tension rail and sidewall laminates was created. The model consists of 546 elements and 301 nodes in which six element are used through the preform thickness to provide higher resolution of the flow front. An illustration of the model showing the extent of the flow distribution mesh as well as the location of the inlet node is given in Figure 6-8. Contour plots of the flow front for filling times of 120, 280, 400, and 500 seconds are given in Figure 6-9. From the figure it is seen that there is a significant lag between the flow front at the preform

surface and the mold surface. At a time of 400 seconds it is observed that due to the large lead-lag of the flow front the resin has saturated through the thickness of the sidewall laminate while the resin front in the tension rail laminate has still not reached the mold surface. Since a true vacuum cannot be achieved there is now residual air trapped in the tension rail laminate which cannot escape through the sidewall due to the sidewall laminate being saturated with resin. As the resin continues to fill the tension rail laminate the residual air becomes more concentrated until a point at which the pressure of the residual air is equal to that of the resin and voids would form in the tension rail laminate (Figure 6-9d).

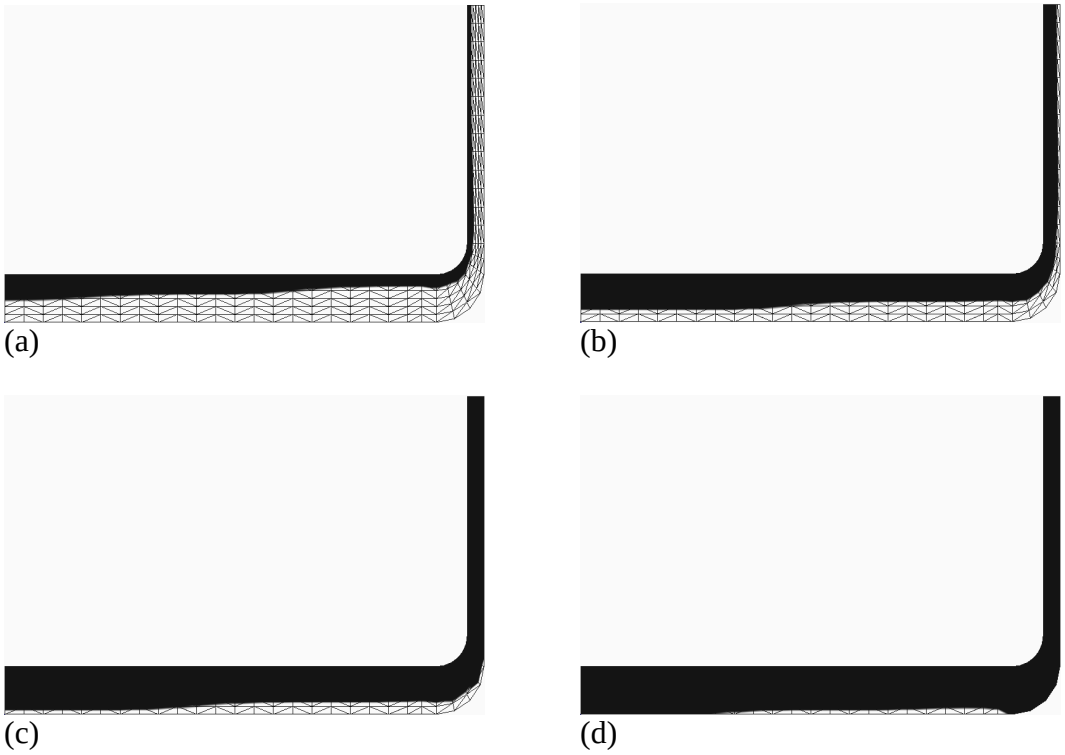

Figure 6-9 Illustrations of the flow front for the filling strategy using continuous flow mesh showing the flow front at (a) 120, (b) 280, (c) 400, and (d) 500 seconds.

To verify that the sidewall is becoming saturated prior to the tension rail laminate a simple flow experiment was set up where a flat panel was infused in which the flow went from a thicker laminate to a thinner laminate. Illustrations of the plan and side views of the test setup are given in Figure 6-10 and Figure 6-11 respectively. The test setup uses the same mold which was used for the experiments described in the previous chapter such that the flow font along the mold surface can be measured using the pressure transducers. The thicker portion of the laminate was 0.38 m long with the layup being the same as that for the tension rail (23 mm thick). The thinner laminates extended out 0.31 m on either side of the tension rail laminate with the layup being the same as that for the sidewalls (7 mm thick). Layers of release fabric and flow distribution mesh were placed over the preform with the flow mesh ending 50 mm short of the end of the preform. The infusion was performed using oil having a viscosity of 0.06 Pa•s. The oil was injected at the center of the thick portion of the laminate with a vacuum outlet at each end of the preform creating a symmetric infusion.

The infusion was perfumed with the full vacuum pressure (0 kPa) applied at the outlets and the inlet open to atmospheric pressure (101 kPa). During the infusion pressure data was recorded at each pressure sensor. A threshold pressure of 10 kPa was used to determine when the flow front had reached a given pressure sensor. A plot of the pressure at each sensor location versus time is given in Figure 6-12. A summary of the time at which the flow front reaches each sensor is given in Table 6-1. Although the flow should have been symmetric it was observed that the flow was much faster for the right half of the preform (sensor P6-P11) in comparison with the

left half of the preform (sensors P1-P6). This was believed to be due to a crease in the flow mesh on the left half of the preform at the inlet location. Although the flow was not symmetric the effects of flow from a thick to thin laminate are still observed in both halves of the preform.

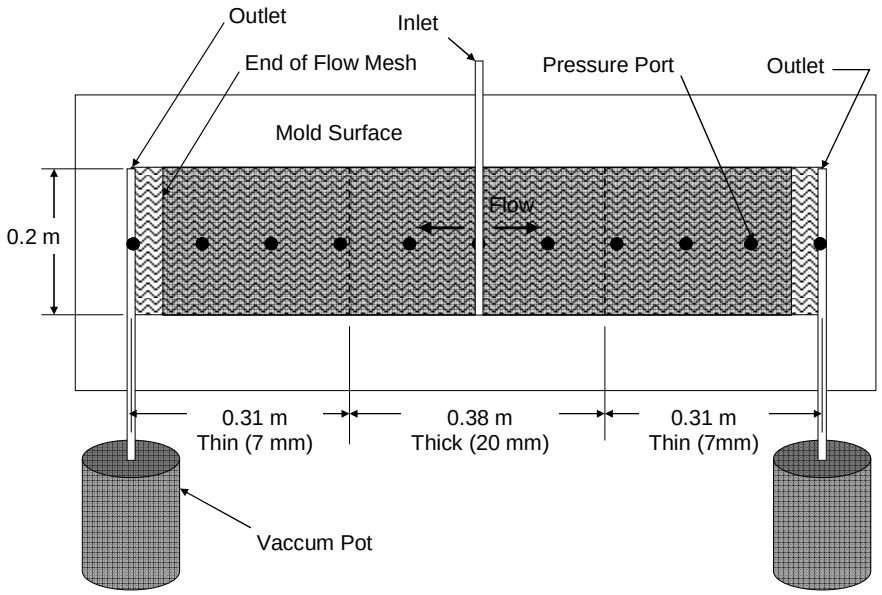

Figure 6-10 Illustration showing the plan view of the experimental setup to investigate resin flow from a thick laminate to a thin laminate when a flow distribution layer is used.

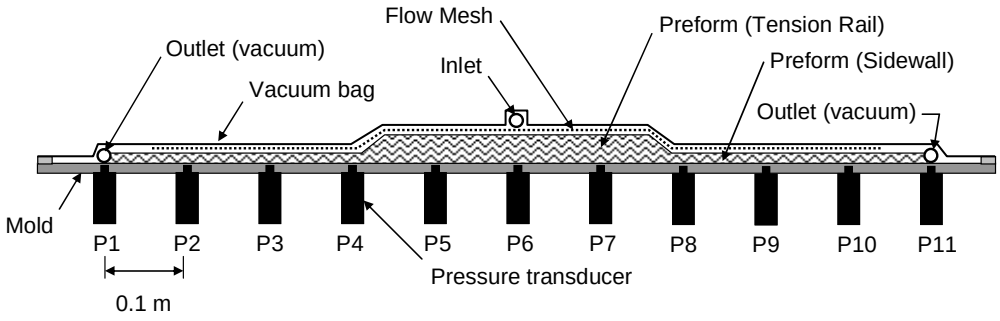

Figure 6-11 Illustration showing the side view of the experimental setup to investigate the nature of the flow front as the resin travels from a thick to a thin laminate.

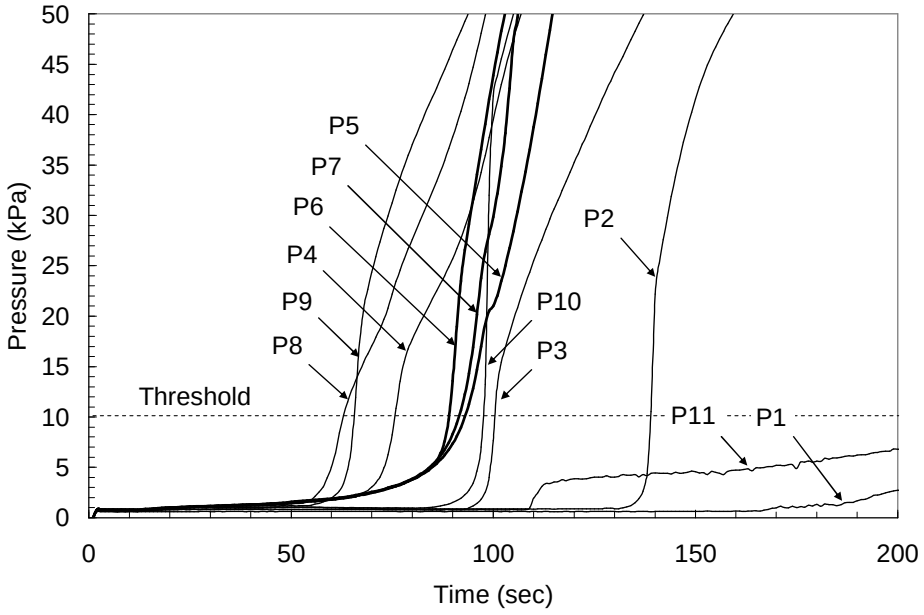

Figure 6-12 Plot of pressure versus time for sensors P1 through P11 showing the time at which the resin front reaches each pressure sensor location.

Table 6-1 Summary of Flow Front Arrival at each Pressure Sensor

Sensor	*Time (sec)*	*Laminate Thickness*	*Right or Left of Inlet*
P8	63	Thin	Right
P9	65	Thin	Right
P4	75	Thin	Left
P6	89	Thick	Center
P7	92	Thick	Right
P5	93	Thick	Left
P10	98	Thin	Right
P3	100	Thin	Right
P2	138	Thin	Right

From Figure 6-12 and Table 6-1 it is observed that the flow front has penetrated through the thickness of the laminate at sensors locations P8 and P9 on the right half of the preform and P4 on the left half of the preform prior to the thicker laminate (P5, P6, and P7) becoming fully saturated. At this point the path for residual air in the thicker laminate to escape to the vacuum outlet has been cut off forcing the residual air to remain in the thicker tension rail laminate. It takes an additional 20 to 30 seconds for the thicker tension rail to become saturated (see P5, P6, and P7). From Table 6-1 it is seen that the flow front reaches P10 at 98 seconds while it takes an additional 40 seconds for the flow front to reach P2. This is due to the nonsymmetric flow rate observed in the two halves of the preform. The experiment confirms what is observed in the simulation results that residual air may become trapped in thicker laminates when a continuous flow distribution mesh is used where a transition from a thicker to thinner laminate occurs.

6.2.2 Resin Filling with Multiple Inlets

To overcome the problem of residual air becoming trapped in the tension rail portion of the hull section a second infusion strategy is investigated in which multiple inlets are used and the continuous flow mesh across the transition from the tension rail to sidewall laminate is eliminated. For this infusion strategy the inlet at the center of the tension rail is preserved with the flow distribution mesh in the tension rail area terminating short of the hull corners. Additional inlets are located on each sidewall at 0.1 m from the bottom of the beam hull. From this point a layer of flow distribution mesh extends up each sidewall ending 50 mm before the vacuum outlet lines. An

illustration of the infusion strategy is given in Figure 6-13 with a cross section view being given in Figure 6-14. For purposes of discussion the inlet at the tension rail is referred to as inlet 1 with the sidewall inlets being referred to as inlet 2. The infusion is performed by allowing resin to flow in at inlet 1 where the resin flows across the surface of the tension rail and then permeates through the laminate thickness after which the flow front progresses to inlet 2. When the tension rail and sidewall laminates are completely saturated up to inlet 2 these secondary inlets are then opened and resin is allowed to flow up the sidewalls and to the outlet lines. To study the saturation of the tension rail area the high resolution model of the hull corner was used. The model is given in Figure 6-15 where the extent of the flow distribution mesh elements and inlet node are shown.

To study the effects of the width of the flow distribution mesh on the flow as it moves from the thicker tension rail laminate to thinner sidewall laminate, simulations were performed for three different flow mesh widths as well as a line infusion down the center of the tension rail. Flow studies using flow distribution mesh widths of 300 mm (12 in), 200 mm (8 in), 100 mm (6 in) were performed. Due to symmetry only half the flow mesh width is considered in the model (Figure 6-15).

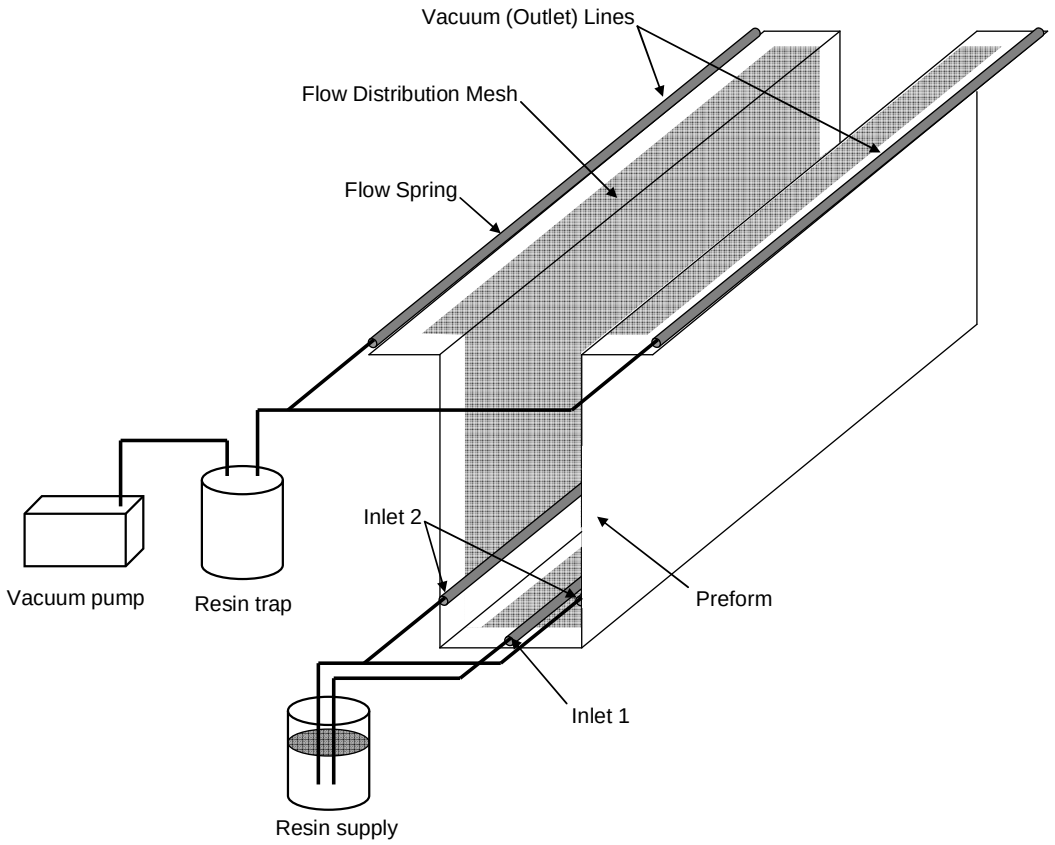

Figure 6-13 Illustration showing the infusion strategy in which a discontinuous flow distribution mesh is used with multiple resin inlet lines. Mold and vacuum bag not shown for clarity.

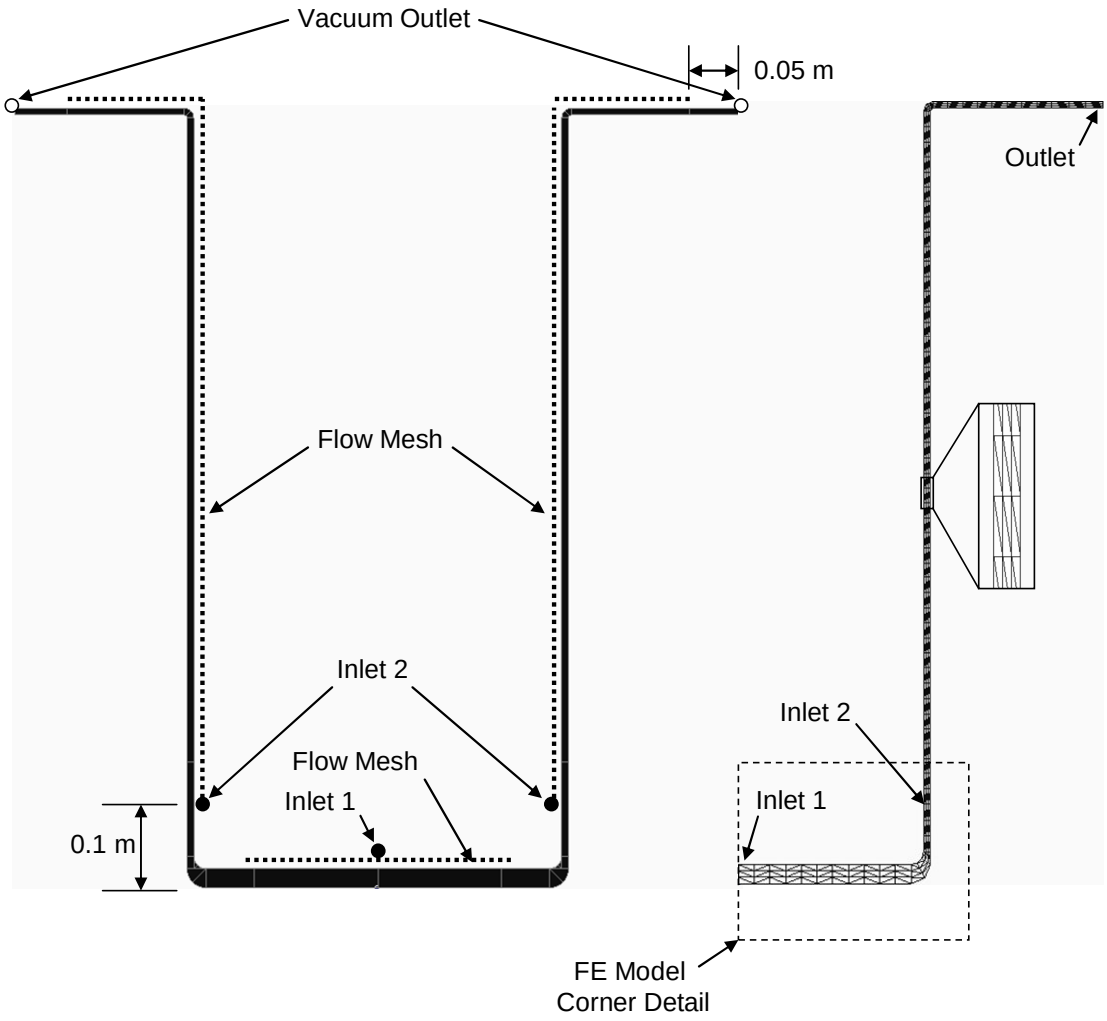

Figure 6-14 Illustration of (a) the hull cross section showing the infusion strategy in which a discontinuous flow distribution mesh layer is used with multiple inlets as well as (b) the finite element mesh.

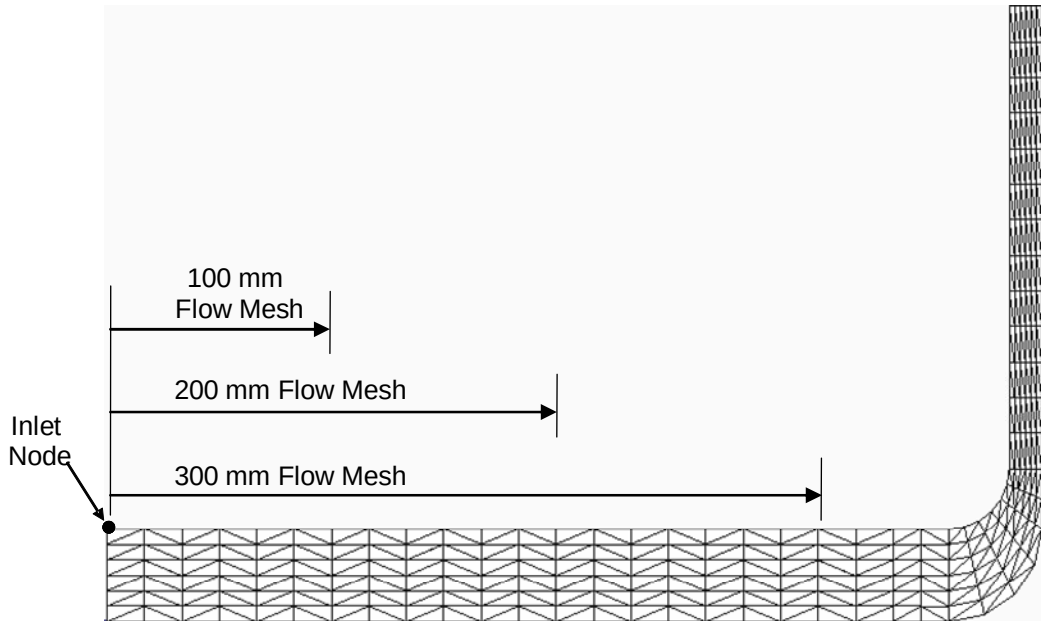

Figure 6-15 Illustration of the beam hull corner finite element model used to investigate the flow from the thick tension rail laminate to the thin sidewall laminate for the infusion strategy in which a discontinuous flow mesh layer is used. The flow mesh dimensions represent half of the total width of the flow mesh.

Contour plots showing the progression of the flow front using the 300 mm, 200 mm, and 100 mm wide flow distribution meshes are given in Figure 6-16, Figure 6-17, and Figure 6-18 respectively. Illustrations of the flow front for a line infusion are given in Figure 6-19.

From Figure 6-16 it is observed that when the 300 mm wide flow distribution mesh is used the lead-lag of the flow front is still significant as the flow moves through the corner from the thick to the thin laminate. Due to the magnitude of the lead-lag of the flow front it is observed that there is still potential for residual air to become entrapped in the tension rail laminate (Figure 6-16c).

From Figure 6-17 it is seen that by reducing the width of the flow mesh to 200 mm the lead-lag of the flow front is greatly reduced as the flow front moves through the corner of the hull section. From Figure 6-17c it is seen that although there is still a small lead-lag in the flow front at the corner there is no entrapment of residual air.

The risk of entrapping air is further reduced by using even a narrower flow distribution mesh as seen in Figure 6-18. From the illustrations it is seen that the lead-lag of the flow front is even further reduced when the 100 mm wide flow distribution mesh is used. The smallest lead-lag in the flow front is observed for the line injection shown in Figure 6-19. From these illustrations it is seen that the risk for air becoming trapped in the laminate is extremely low.

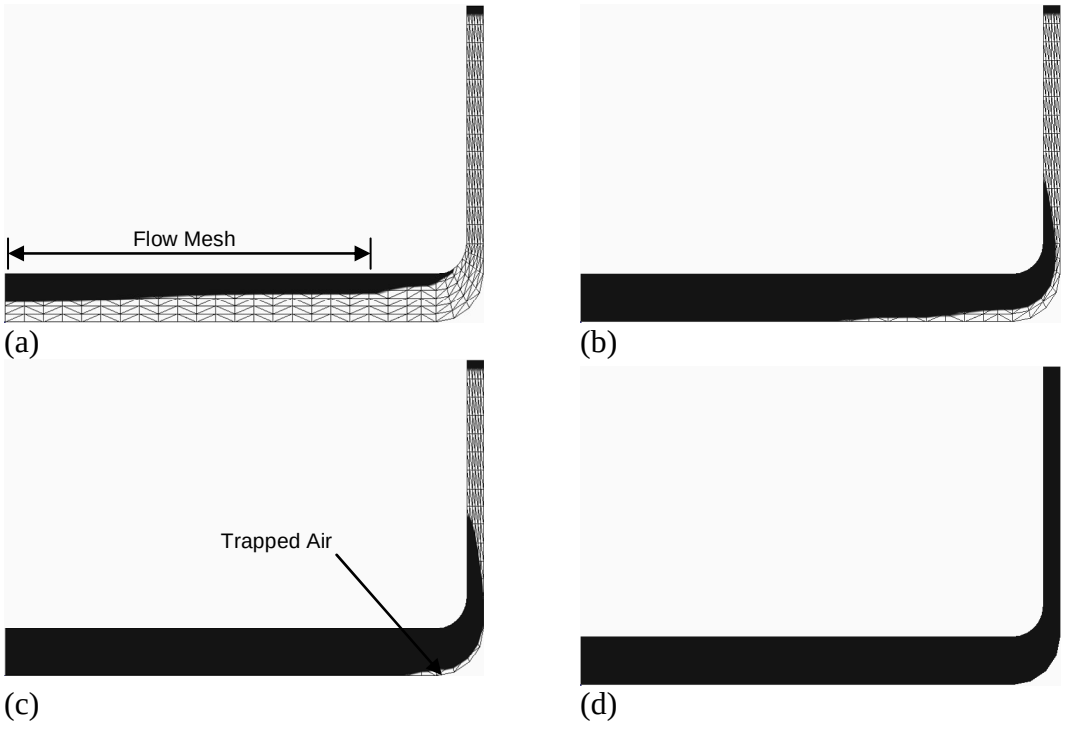

Figure 6-16 Illustrations of flow front locations using a 300 mm flow mesh for filling times of (a) 120, (b) 540, (c) 670, and (d) 1220 seconds.

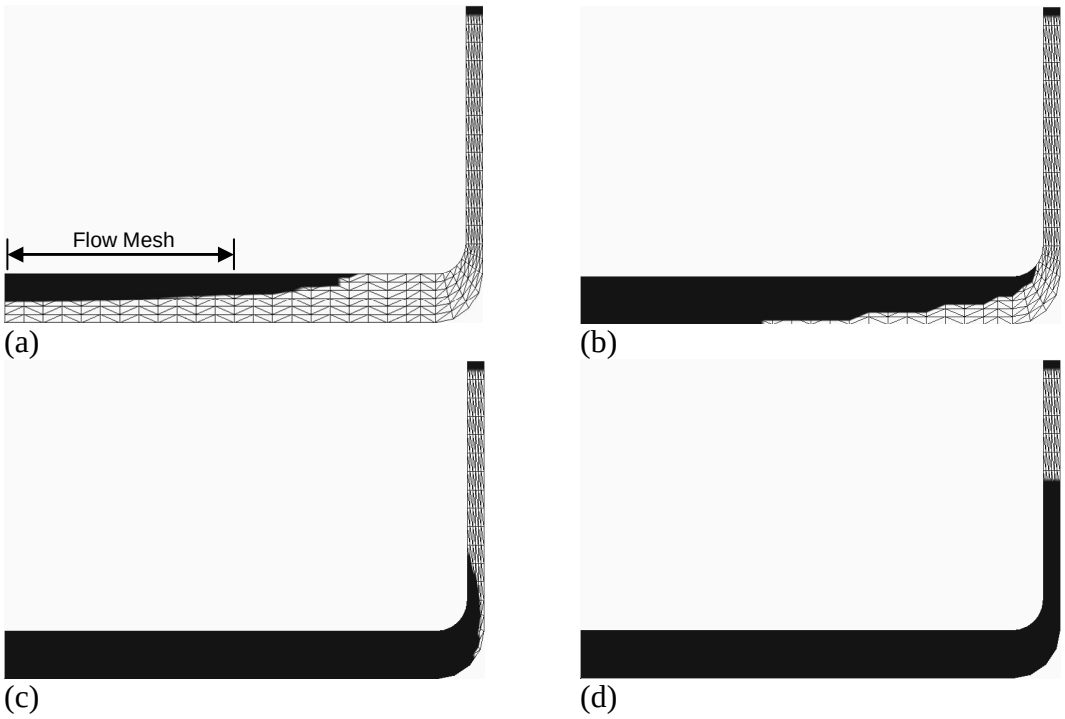

Figure 6-17 Illustrations of flow front locations using a 200 mm flow mesh for filling times of (a) 120, (b) 540, (c) 960, and (d) 1220 seconds.

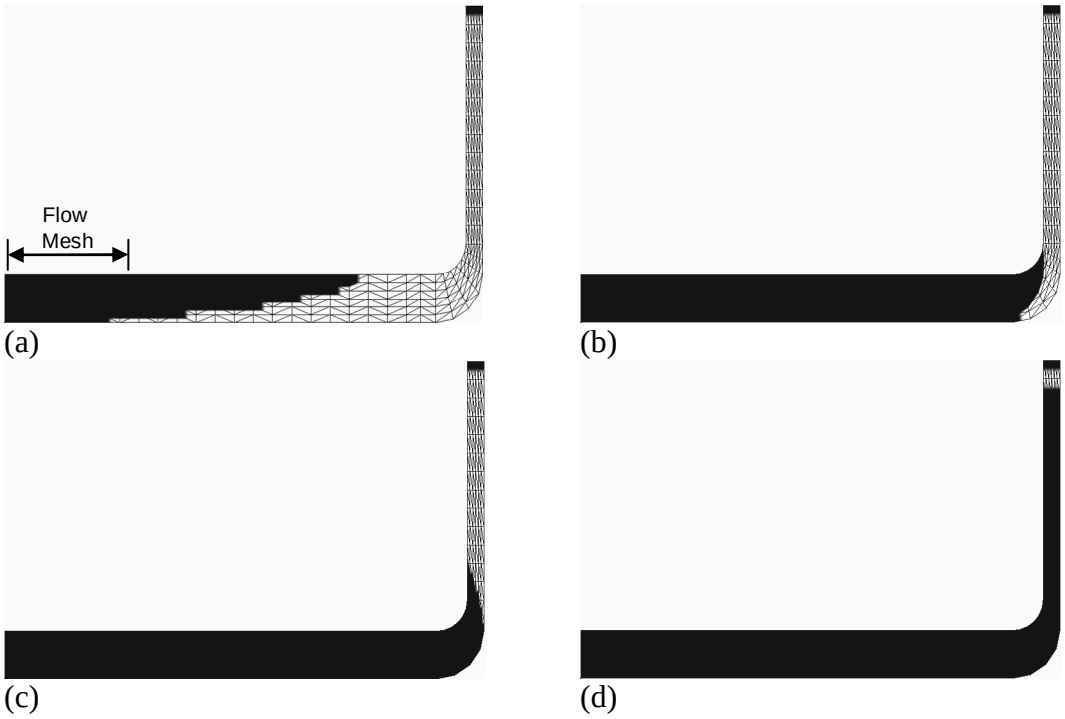

Figure 6-18 Illustrations of flow front locations using a 100 mm flow mesh for filling times of (a) 600, (b) 1330, (c) 1650, and (d) 2400 seconds.

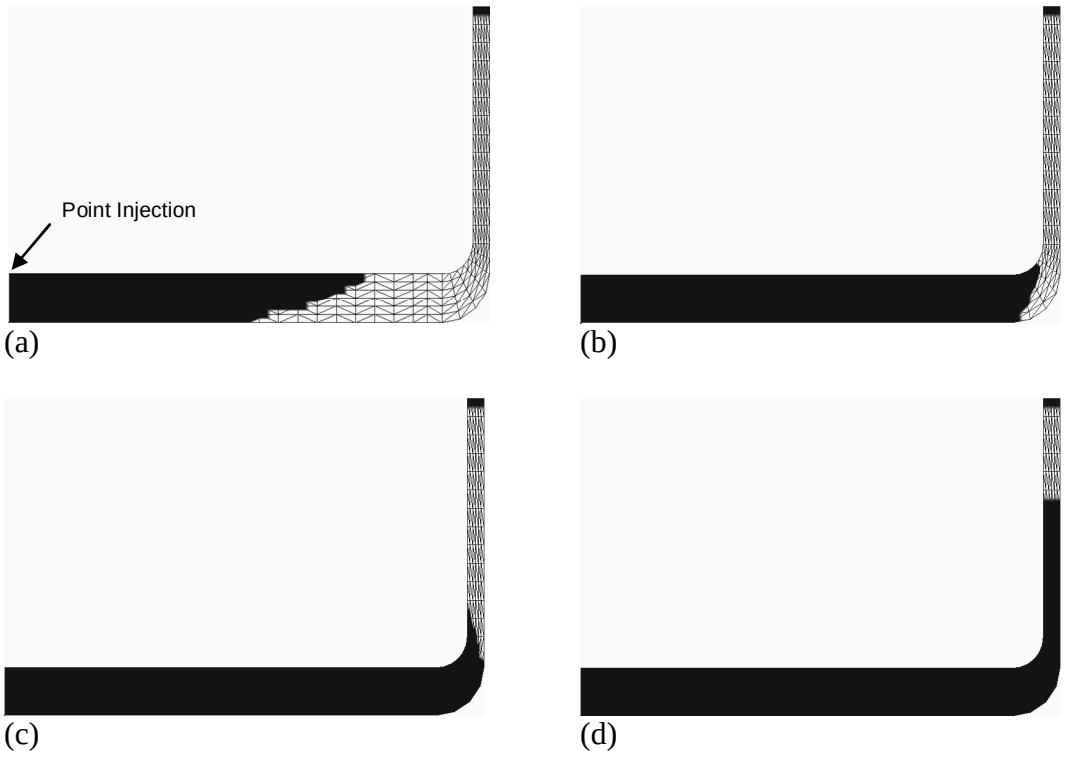

Figure 6-19 Illustrations of flow front locations using a point injection for filling times of (a) 2400, (b) 3500, (c) 4200, and (d) 5020 seconds.

Although the use of narrower flow distribution layers on the tension rail reduce the risk of voids due to air entrapment it also increases the required time to fill this section of the beam hull. For the 300 mm wide flow mesh a filling time of 1225 seconds was required to reach full saturation. When the 200 mm wide flow mesh was used a fill time of 1643 seconds was required and a fill time of 2498 seconds was required for the 100 mm wide flow mesh. The line injection required a fill time of 5781 seconds to reach full saturation. A plot of the required fill time versus flow mesh width is given in Figure 6-20. From the plot it is observed that the required fill time becomes increasingly greater as the flow mesh width decreases.

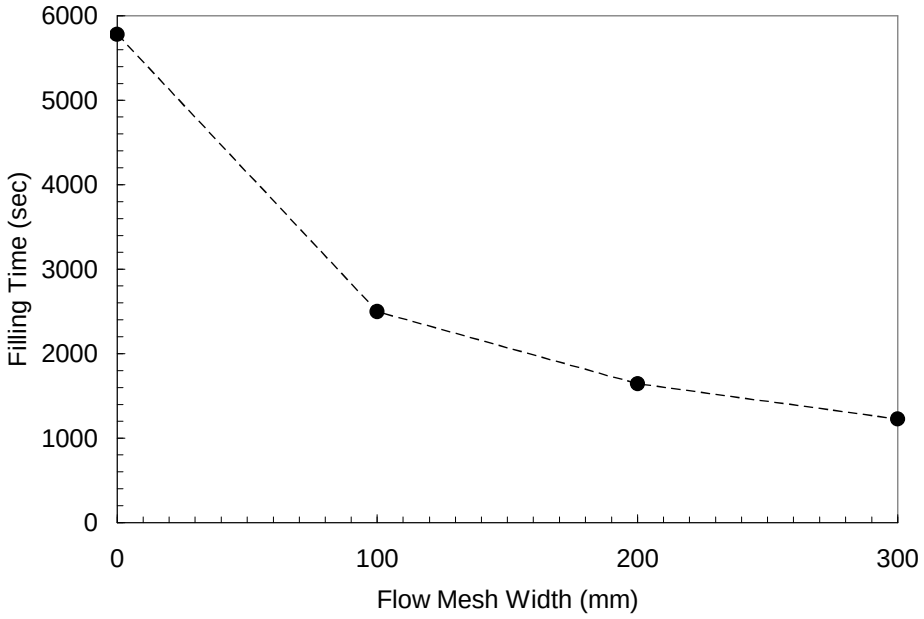

Figure 6-20 Plot of flow mesh width versus filling time for the beam hull corner.

.

To study the filling of the complete hull section using this infusion strategy the model from Figure 6-14 is used where full vacuum pressure (0 kPa) is applied at the outlet with atmospheric pressure (100 kPa) applied at inlet 1. Based on the study of the different flow mesh widths a flow distribution layer of 200 mm is used. At the time when the resin flow front reaches inlet 2 atmospheric pressure is then applied at inlet 2 and resin progression continues until the preform is completely saturated. Contour plots showing the progression of the flow front at 1020, 1700, and 3260 seconds is given in Figure 6-21. From the plots it is observed that the resin front reaches inlet 2 at a filling time of 1700 seconds at which time inlet 2 is opened. The total predicted filling time for this infusion strategy is 4077 seconds. Although the fill time is only 285 seconds longer than the filling time for the first infusion strategy

(3792 sec) it is much more robust in terms of eliminating the presences of voids in the tension rail laminate.

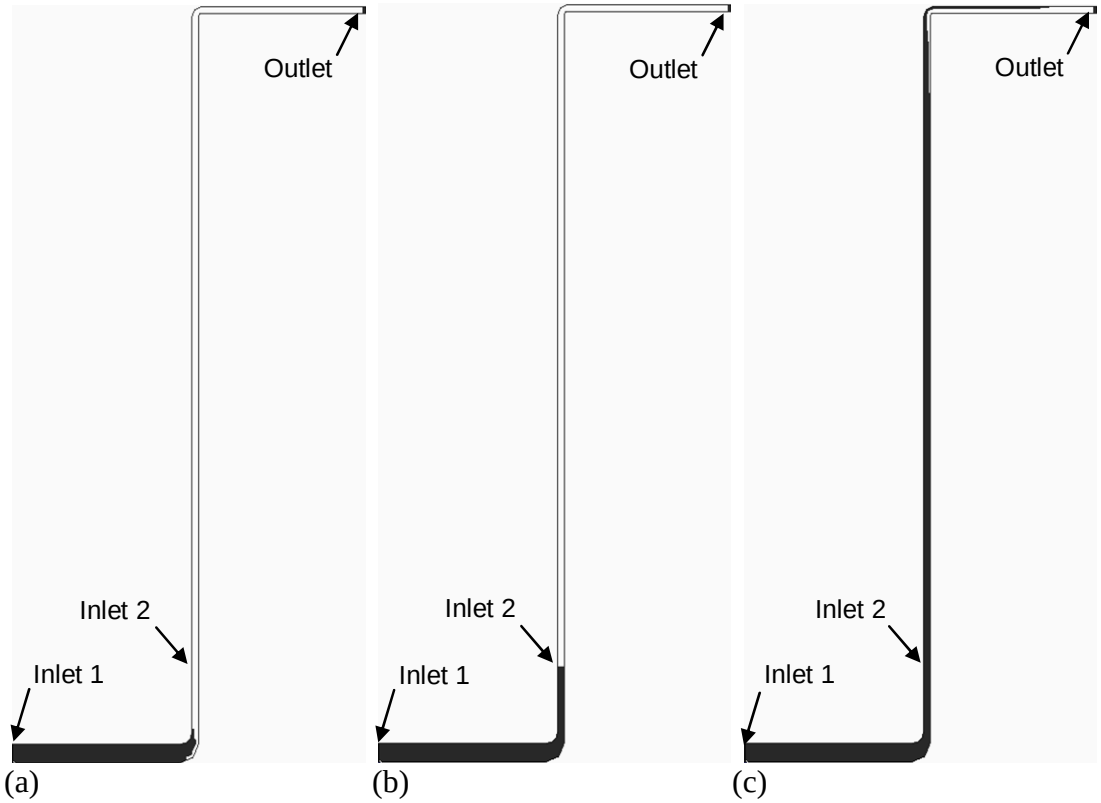

Figure 6-21 Contour plots showing the location of the flow front at (a) 1020, (b) 1700, and (c) 3260 seconds for the case when a discontinuous flow mesh is used with multiple inlets.

6.3 BLEEDING STRATEGY

At the end of resin filling it is common practice to reduce the vacuum pressure at the outlet to about half vacuum (50 kPa) and then to allow excess resin to be removed from the part. The most common method for removing resin is to simply close the inlet hose(s) and allow excess resin to bleed through the outlet. However

depending on the location of the inlets, outlets, and flow mesh layers the bleeding time may be extremely long. Based on the second infusion strategy using multiple inlets a bleeding strategy is developed through simulations. The study considers four different bleeding scenarios which investigate combinations of closing and/or applying vacuum pressure at the different inlets.

The first bleeding scenario considers closing both inlets and allowing resin to bleed through the outlet. The second scenario investigates closing inlet 2 and applying vacuum pressure at inlet 1 to bleed excess resin. The third scenario closes inlet 1 and applies vacuum pressure at inlet 2 and the fourth scenario considers applying vacuum pressure at both inlet 1 and inlet 2. A summary of the bleeding scenarios along with the conditions applied at each inlet and the outlet is given in Table 6-2.

Table 6-2 Summary of Bleeding Scenarios and Predicted Bleeding Times

Bleeding Scenarios	*Inlet 1*	*Inlet 2*	*Outlet*	*Bleeding Time (min)*
1	closed	closed	50 kPa	340
2	50 kPa	closed	50 kPa	73
3	closed	50 kPa	50 kPa	122
4	50 kPa	50 kPa	50 kPa	18

To investigate the resin bleeding process the resin pressure at seven locations along the hull section are considered. Each of the seven points is on the outer side (mold surface) of the hull section. An illustration of the beam hull section showing the seven reference locations is given in Figure 6-22. From the figure it is seen that points 1 and 2 are in the tension rail laminate with point 1 being directly below inlet 1

and point 2 being at the corner. Points 3 through 6 are along the sidewall with point 3 being directly below inlet 2 and point 7 is on the flange at the end of the flow mesh. Using these seven locations as reference points, simulations were performed and evaluated for the four different bleeding scenarios.

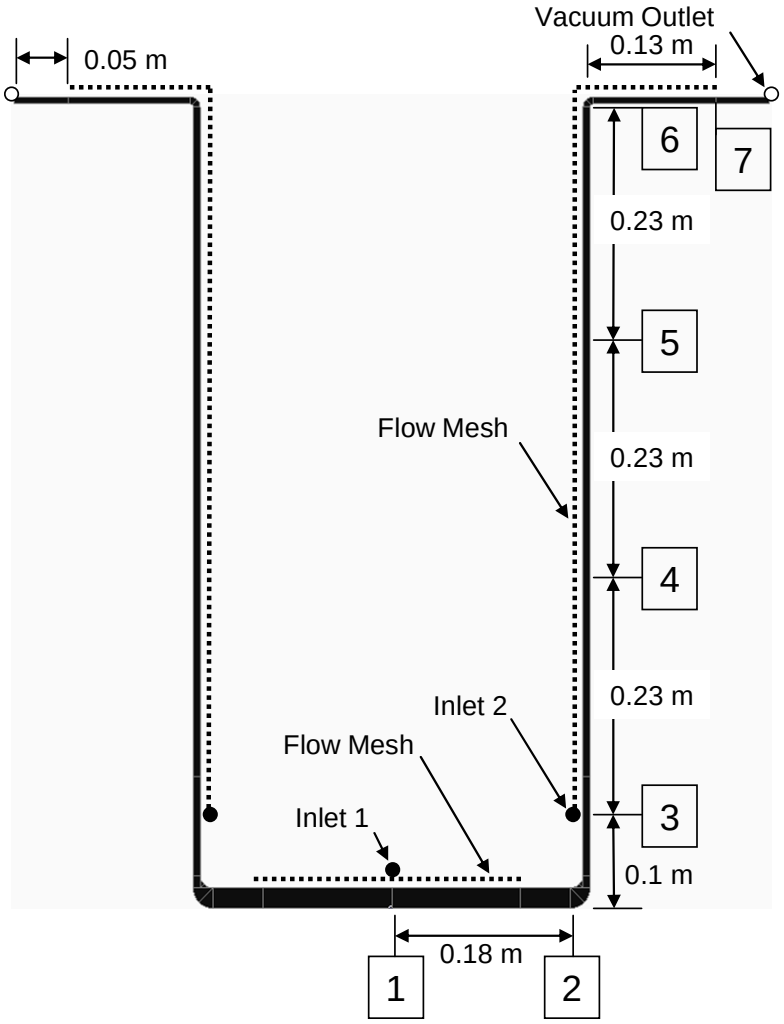

Figure 6-22 Illustration of the beam hull section showing the locations at which the pressures were monitored during the bleeding simulations.

6.3.1 Bleeding with Inlets Closed

Pressure contour plots for the first bleeding scenario are shown in Figure 6-23 with pressure contours at 0, 8000, and 17000 seconds being given. At time zero the pressure in the preform between inlet 1 and inlet 2 is uniform at atmospheric pressure. After the inlets are both closed a pressure gradient is developed from inlet 1 to the outlet and all the resin is bled through the outlet. The total bleeding time is predicted to be 20400 seconds (340 min) where bleeding is considered complete when the pressure is below 55 kPa. A plot of the pressure time history at each of the seven reference points is given in Figure 6-24. As expected, it is seen that point 1, which is furthest from the vacuum outlet, is the last to reach 55 kPa while point 7, which is nearest the outlet, is the first to reach 55 kPa.

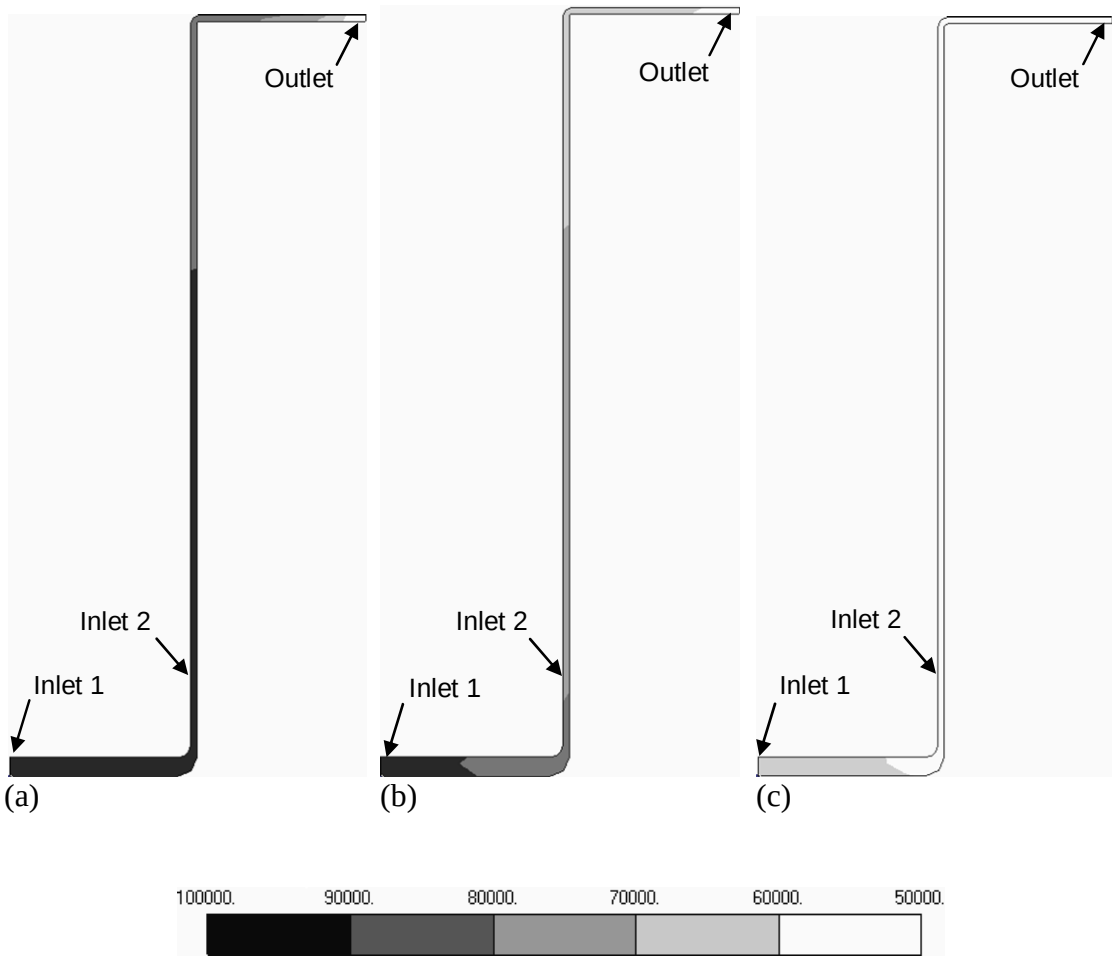

Figure 6-23 Contour plots of resin pressure for the bleeding case when the inlets are closed showing the pressures at bleeding times of (a) 0, (b) 8000, and (c) 17000 seconds.

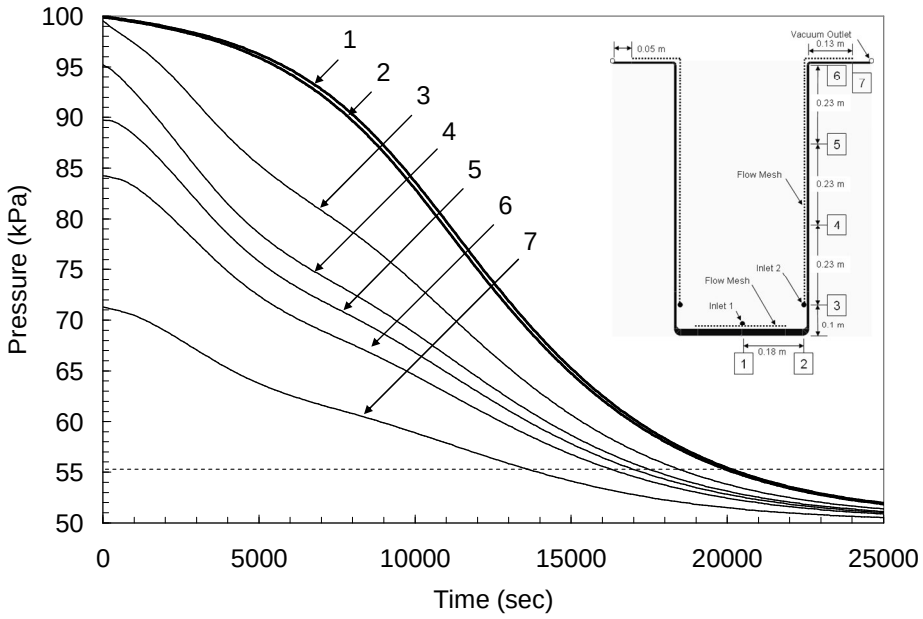

Figure 6-24 Plot of pressure versus time at locations 1 through 7 when the inlet hoses are closed and resin is allowed to bleed through the outlet hose.

6.3.2 Bleeding with Pressure Applied at Inlet 1 with Inlet 2 Closed

Pressure contour plots for the second bleeding scenario in which 50 kPa is applied at inlet 1 and inlet 2 is closed are given in Figure 6-25. The plots show pressure contours for bleeding times of 0, 800, and 2400 seconds. A time history plot of the predicted pressure at each of the six reference points is presented in Figure 6-26. From the figures it is observed that due to the vacuum pressure applied at inlet 1 the pressure in the tension rail laminate (points 1 and 2) quickly approach 50 kPa. The vacuum pressure applied at inlet 1 allows the resin to bleed through the thickness of the tension rail laminate and then out through the flow distribution mesh. As seen from Figure 6-26 the pressure in the sidewall and flange (points 3-7) decreases much

more slowly as the resin travels through the sidewall laminate to inlet 1 without the aid of a flow mesh layer. The total bleeding time for this scenario is 4380 seconds (73 min).

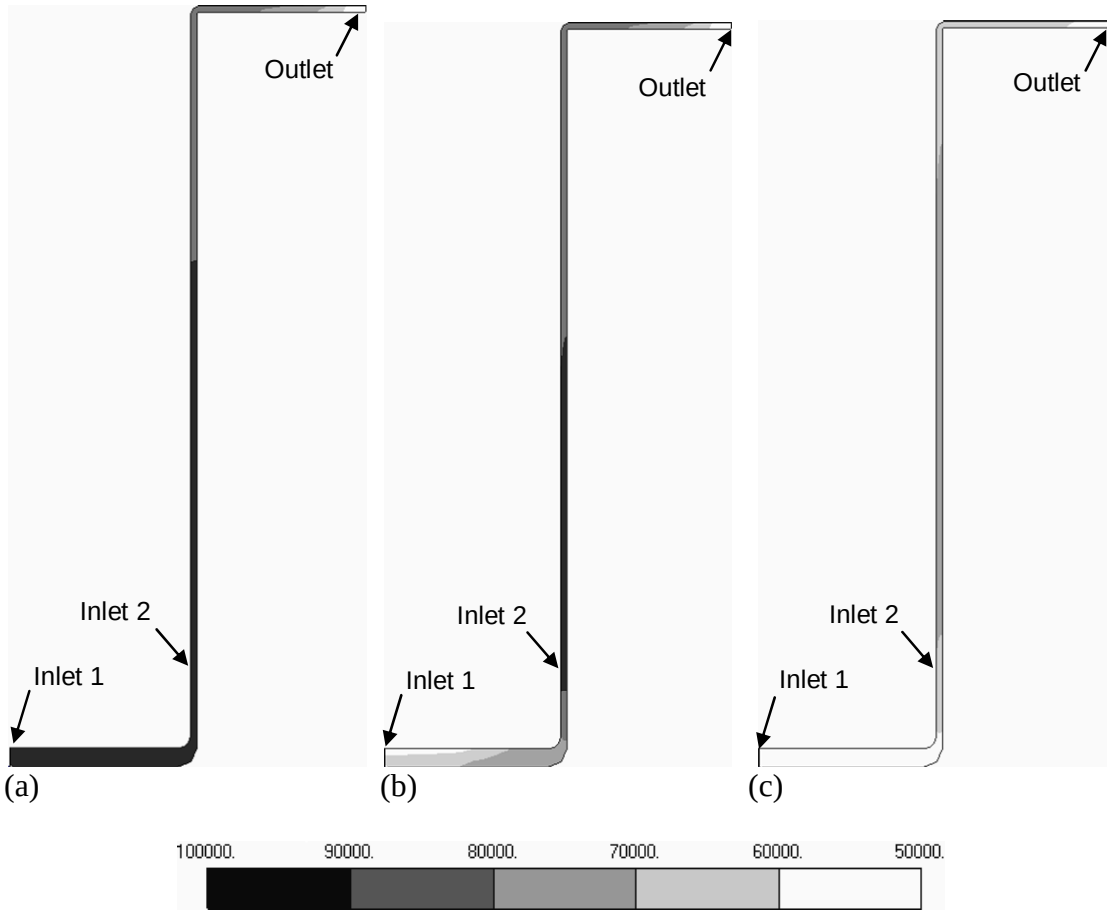

Figure 6-25 Contour plots of resin pressure for the bleeding case when vacuum pressure is applied at inlet 1 and inlet 2 is closed showing pressures at (a) 0, (b) 800, and (c) 2400 seconds.

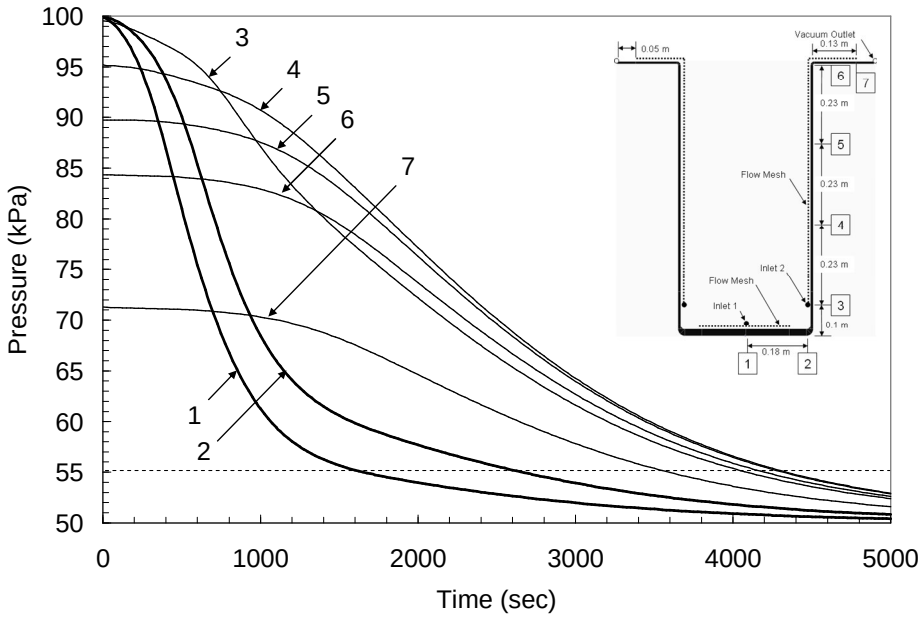

Figure 6-26 Plot of pressure versus time at locations 1 through 7 when inlet 2 is closed and vacuum pressure is applied at inlet 1 to bleed excess resin.

6.3.3 Bleeding with Pressure Applied at Inlet 2 with Inlet 1 Closed

Pressure contour plots for the third bleeding scenario in which 50 kPa is applied at inlet 2 and inlet 1 is closed are given in Figure 6-27. The plots show pressure contours for bleeding times of 0, 700, and 4700 seconds. A time history plot of the predicted pressure at each of the seven reference points is presented in Figure 6-28. From the figures it is observed that due to the vacuum pressure applied at inlet 2 the pressure in the sidewall and flange laminates (points 3-7) quickly approach 50 kPa. The vacuum pressure applied at inlet 2 allows the resin to bleed through the thickness of the sidewall laminate and then out through the flow distribution mesh. As seen from Figure 6-26 the pressure in the tension rail (points 1 and 2) decreases much more slowly as the resin travels from the tension rail and through the lower portion of the

sidewall without the aid of a flow mesh layer. The total bleeding time for this scenario is 7320 seconds (122 min), almost twice as long as when inlet 2 was closed and pressure was applied at inlet 1.

.

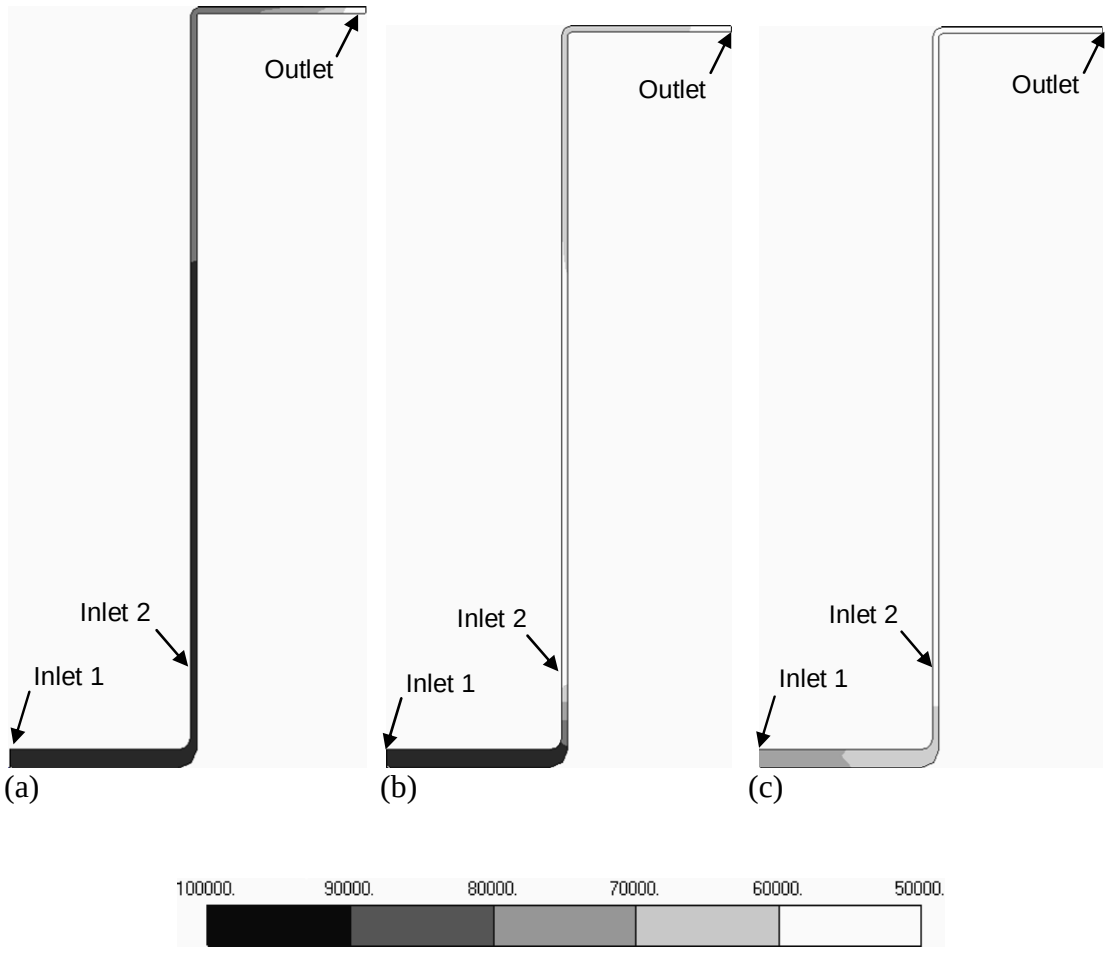

Figure 6-27 Contour plots of resin pressure for the bleeding case when vacuum pressure is applied at inlet 2 and inlet 1 is closed showing pressures at (a) 0, (b) 700, and (c) 4700 seconds.

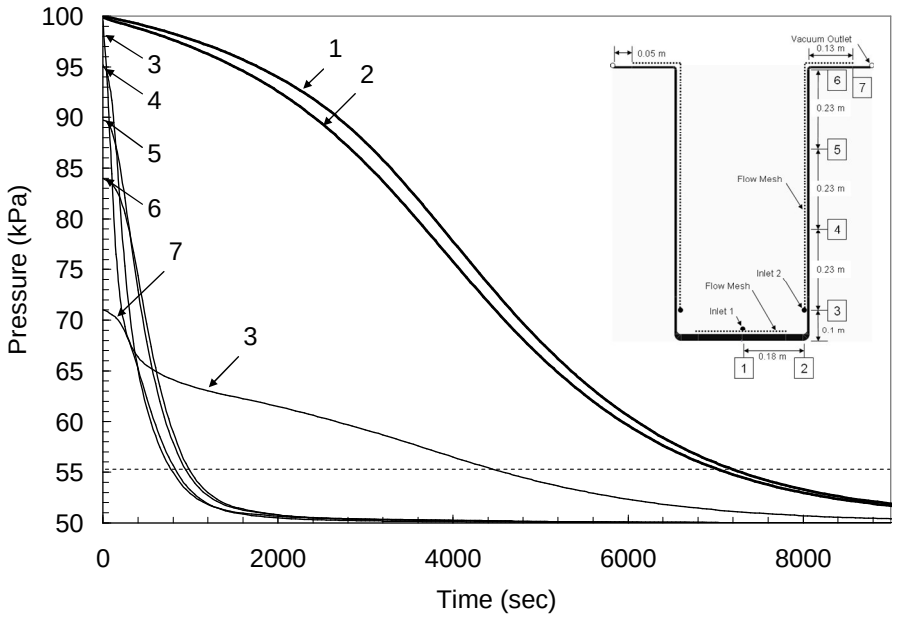

Figure 6-28 Plot of pressure versus time at locations 1 through 7 when inlet 1 is closed and vacuum pressure is applied at inlet 2 to bleed excess resin

6.3.4 Bleeding with Pressure Applied at Inlet 1 and Inlet 2

Pressure contour plots for the fourth bleeding scenario in which 50 kPa is applied at both inlets is given in Figure 6-29. The plots show pressure contours for bleeding times of 0, 400, and 800 seconds. A time history plot of the predicted pressure at each of the seven reference points is presented in Figure 6-30. From the figures it is observed that applying vacuum pressure at both inlets allows resin to quickly bleed from the preform due to the aid of the flow mesh layers. From Figure 6-30 it is seen that the tension rail corner (point 2) is the last place where the pressure reaches 55 kPa. This bleeding scenario predicts by far the shortest bleeding time at 1050 seconds (18 min).

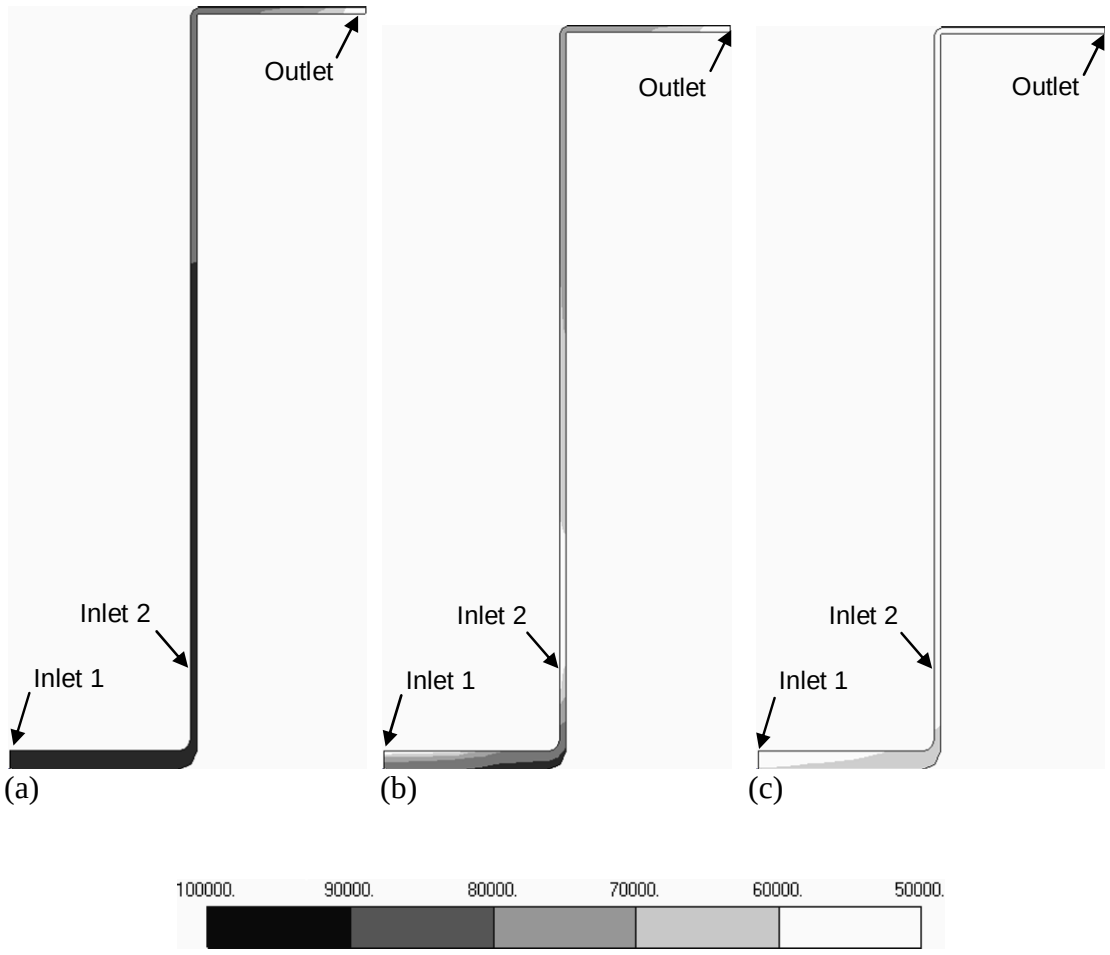

Figure 6-29 Contour plots of resin pressure for the bleeding case when vacuum pressure is applied at both inlets (inlet 1 and inlet 2) showing pressures at (a) 0, (b) 400, and (c) 800 seconds.

A summary of the bleeding time for each scenario is given in Table 6-2. From the table it is observed that just closing the inlet lines leads to a very long bleeding time (340 min) which for the case of the beam hull fabrication is unacceptable. The shortest bleeding time (18 min) is achieved by applying vacuum pressure at both inlets. It should be remembered that the filling and bleeding times are proportional to the viscosity of the resin and may be reduced by infusing and bleeding resin at higher temperatures.

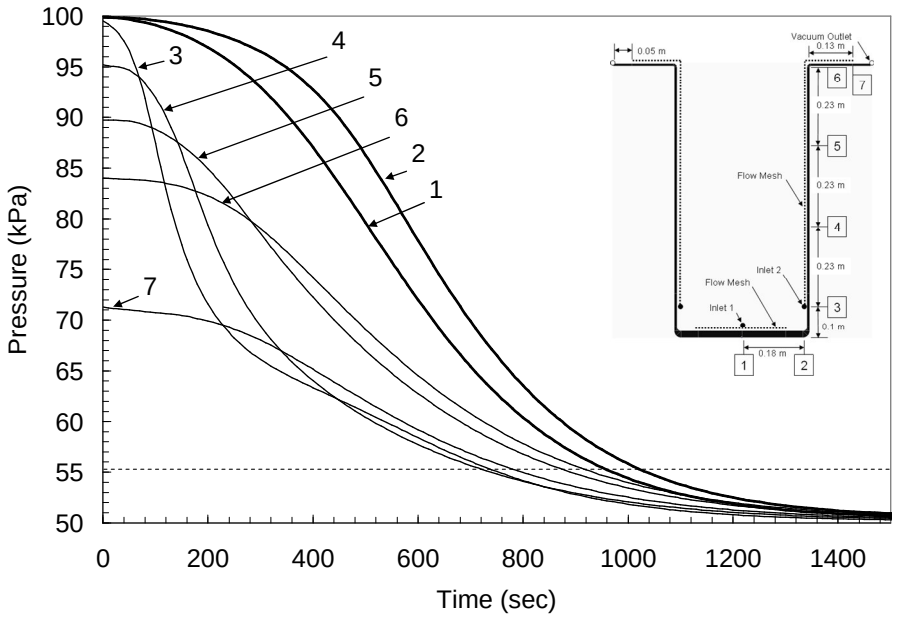

Figure 6-30 Plot of pressure versus time at locations 1 through 6 when vacuum pressure is applied at inlet 1 and inlet 2 to bleed excess resin.

6.4 FIBER BRIDGING

The compaction of fibers during the VARTM process can lead to some anomalies for complex geometries such as the corners of the beam hull. It is observed from a cured hull section that although the tension rail and sidewall thicknesses are uniform the areas near the corners show non uniform thickness where the laminate thicknesses increase as they approach the corner. A photograph of a corner showing the non uniform laminate thicknesses is given in Figure 6-31. This non uniform thickness is due to the interaction between the mold and preform during the compaction process. As vacuum pressure is applied the vacuum bag clamps the tension rail and sidewall fibers against the sides of the mold where friction forces prohibit them from moving in the plane of the laminates. Due to the high in-plane

stiffness of the fibers the preform is not able to conform to the corner of the mold and bridging occurs. Understanding this bridging phenomenon is necessary to properly predict the final laminate thickness in these areas as well as to predict the permeability of the preform in these regions.

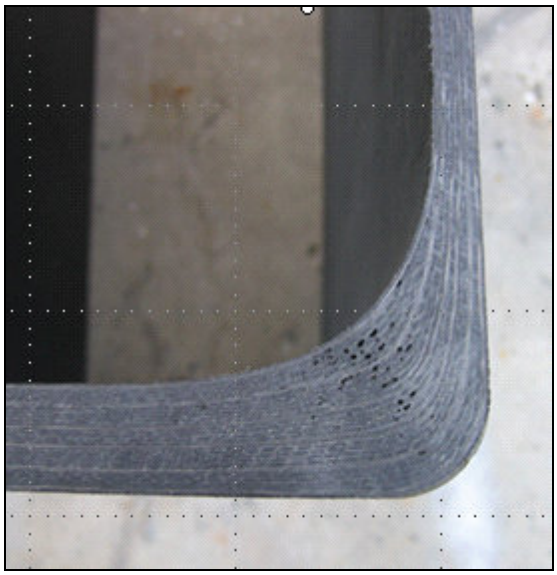

Figure 6-31 Photograph of the beam hull section corner showing the non uniform laminate thickness of the tension rail and sidewall near the corner.

To provide additional insight into the bridging of the preform layers across the hull corner a finite element model was developed. The finite element model showing the applied boundary conditions and loading is given in Figure 6-32. The through thickness stiffness of the preform was given a value of 500 kPa which was determined to mimic the compaction of the fibers under full vacuum pressure and the in-plane stiffness was given a value of 80 GPa representing the approximate in-plane stiffness

of the preform laminate. A compaction pressure of 100 kPa was applied normal to the surface of the preform with the outer surface of the preform being fixed. The ends of the tension rail and sidewall laminates are also fixed against translation in the plane of the laminate to simulate the clamping of the fiber layers under vacuum pressure. An illustration showing the absolute compaction displacements is given in Figure 6-33.

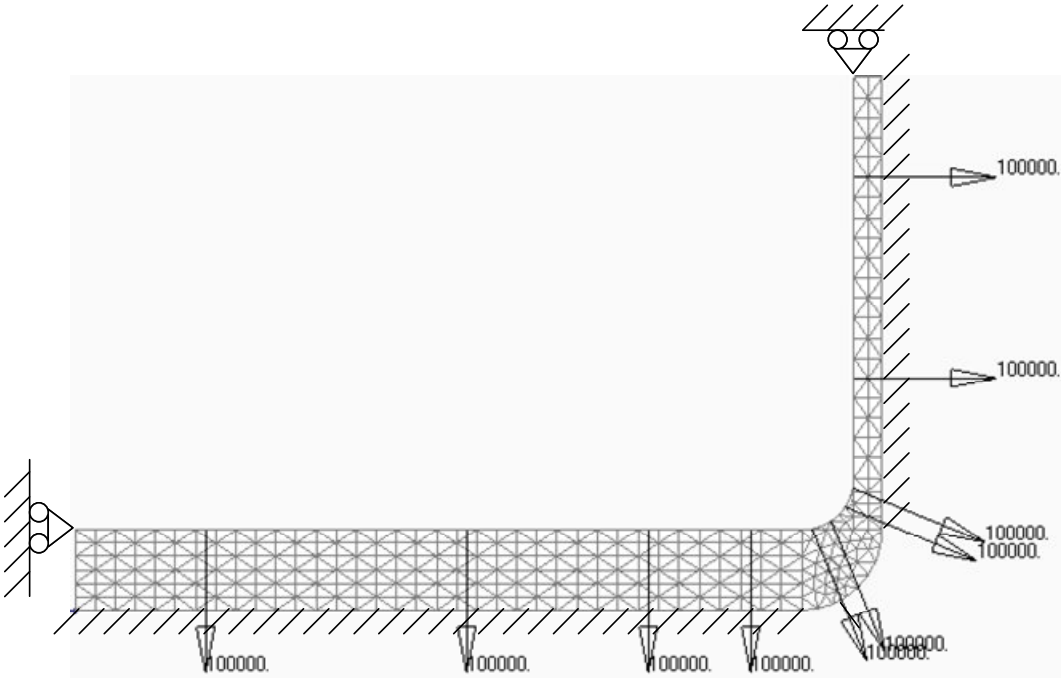

Figure 6-32 Illustration of the finite element model to study the bridging of the reinforcing fibers at beam hull corner.

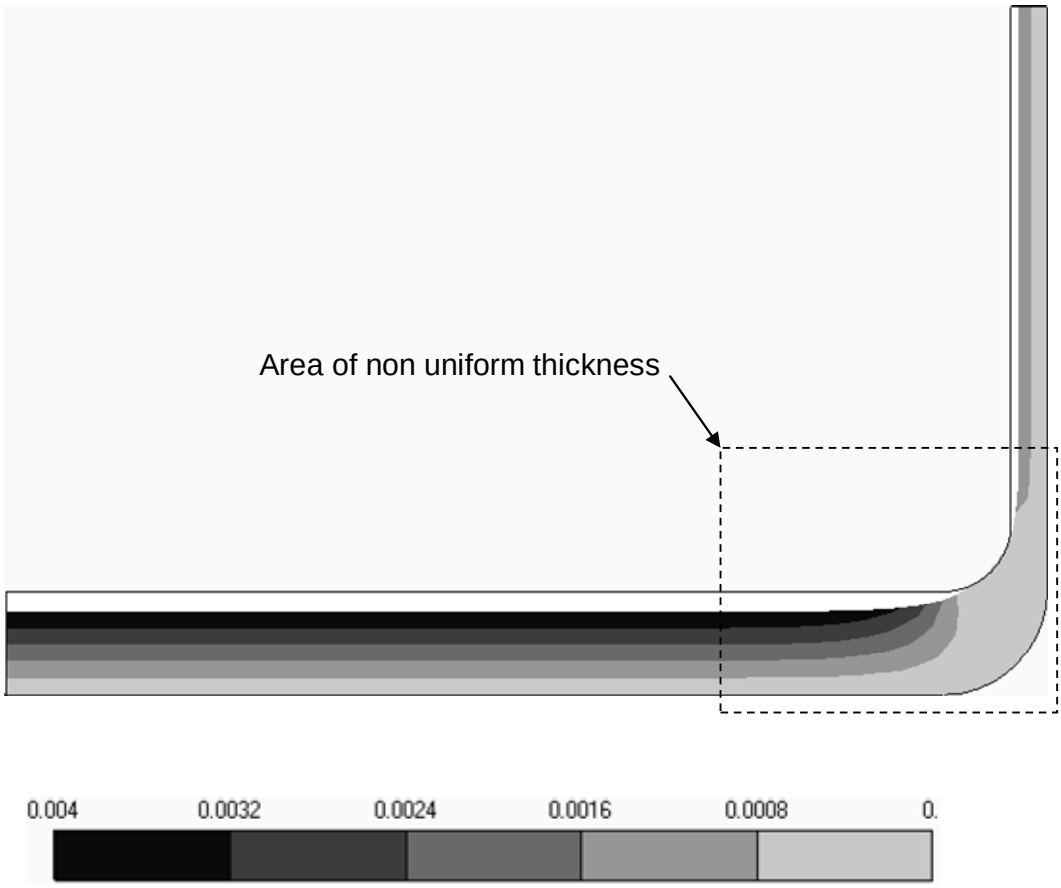

Figure 6-33 Finite element results of preform compaction under vacuum pressure showing the non uniform thickness at the corner of the hull section. Contours show absolute deformations.

From the model results it is observed that the tension rail and sidewall laminates exhibit a uniform thickness with the exception of the area near the corner (Figure 6-33). Due to this bridging effect it is observed that no compaction takes place at the corner where the laminate thickness actually increases. This phenomenon is not only important in predicting the final geometry of the part but it may also affect the flow in this region due to the increased porosity (increased permeability). Further

investigation is warranted to study the effects of fiber bridging on permeability and to develop fabrication methods to eliminate the occurrence of fiber bridging.

6.5 SUMMARY

This chapter has demonstrated the application of the simulation model in developing resin filling and bleeding strategies for a beam hull section to be used in composite modular bridging.

Two different bleeding strategies were investigated. The first strategy considered a continuous flow distribution mesh with a single resin inlet where the flow mesh was continuous from the thicker tension rail laminate to the thinner sidewall laminate. The second strategy used multiple inlets in which the flow distribution mesh was not continuous over the transition from the tension rail to sidewall laminates. Simulations of the first strategy revealed that due to the long lead-lag of the flow front the potential for residual air becoming trapped in the thicker tension rail laminate was very high. This was confirmed through experimental studies. The second infusion strategy using multiple inlets proved successful in minimizing the possibility for air becoming trapped in the laminate.

In addition to filling simulations, bleeding simulations were performed to develop a bleeding strategy for the beam hull section. Four different bleeding strategies were considered in which different combinations of closing and/or applying vacuum pressure at the inlets was considered. The bleeding simulations showed that

the shortest bleeding time could be achieved by applying vacuum pressure at both inlets.

Following the fabrication of a beam hull section it was observed that the tension rail and sidewall laminate thicknesses were uniform except at the area near the corners where the thickness gets progressively thicker moving toward the corner. A finite element study revealed the bridging of fibers across the corners. Further investigation is needed to understand the affects of fiber bridging on the permeability of the preform in these areas.

CHAPTER 7

PART I CONCLUSIONS

This section of the dissertation has presented the development of a flow simulation model capable of modeling both the filling phase as well as the bleeding phase of the VARTM process while considering the flow of resin through the thickness of the preform.

Chapter 3 focused on the development of the simulation model which accounts for both the transient nature of the fiber volume fraction during the VARTM process as well as the transient nature of the permeability as a function of fiber volume fraction. Algorithms which incorporate the finite element/control volume method were presented for both the resin filling and resin bleeding stages of the VARTM process.

Fiber volume fraction and permeability constitutive models were developed in Chapter 4. An alternative method for characterized perform materials was presented. The method utilizes a single sided rigid mold with a vacuum bag more closely representing the conditions during the VARTM process in comparison to other measurement techniques currently used in literature. Compaction and permeability models were developed for several performs to be considered in simulations. The study also found that it was critical to consider nesting affects of the flow distribution layer with the preform when developing the permeability constitutive model for the flow distribution mesh.

In Chapter 5 the resin flow model was validated through a series of flow experiments which considered one-dimensional flow and two-dimensional flow (including through-thickness flow) for preforms consisting a single material as well as a preform consisting of more than one material. The simulation model showed good agreement with the experimental results as well as simulation models proposed by others. However only the current model is capable of simulating the bleeding process for cased in which flow through the thickness is considered. Additional simulations were performed to assess the viability of using effective preform properties for performs composed of more than one material type as opposed to using a layerwise model which considers the properties of each layer. The study showed that as the different material become more blended through the preform thickness the layerwise model and effective model converge to the similar solutions.

Chapter 6 presented the application of the simulation model for developing an infusion strategy for a beam hull section to be used in composite bridging. The study revealed that due to the change in thickness of the preform from the thicker tension rail laminate to the thinner sidewall laminates the potential for air entrapment was high. The entrapment of air as resin flows from a thicker to thinner laminate when a flow distribution layer is used was confirmed through an experimental study. A Series of simulations in which different flow mesh configurations were used revealed a resin filling strategy which minimized the risk for air becoming trapped in the laminate. The simulation model was also used to study resin bleeding strategies to achieve the desired final fiber volume fractions for the part.

This research has demonstrated the developed simulation model and found it to be a viable tool in developing infusion strategies for composite structures.

PART II

COMPOSITE MODULAR BRIDGING

CHAPTER 8

INTRODUCTION

A continued desire for increased mobility in the aftermath of natural disasters, or on the battlefield, has lead to the need for improved light-weight bridging solutions. This chapter describes current deployable bridging systems used by the US Military and introduces a new light-weight composite bridging system designed to address the Military's entire gap crossing needs. As part of the new composite bridging system currently under investigation this research is focused on the development of composite bridge decking which is also designed to satisfy short-span (4 m) gap crossing needs. The design and testing of a composite bridge deck system with short-span gap crossing capabilities is described.

Deployable bridging falls into three general categories based on the mission which they are designed to accomplish. The first category is assault bridging which is designed to be rapidly emplaced to move military front line forces ahead as quickly as possible. Assault bridging is typically less than 25 m (82 ft) in length and emplaced in less than 10 minutes by an armored launch vehicle to minimize exposure of troops in hostile environments. Examples of assault bridges currently in use by the United States are the Armored Vehicle Launched Bridge (AVLB) and Wolverine Heavy Assault Bridge. The second category is tactical bridging which may be used to replace assault bridges which are required at other locations or to cross gaps which are too wide for available assault bridges. Tactical bridging is composed of light-weight

modular components which are assembled to span gaps up to 40 m (131 ft) and can be emplaced in less than two hours. Tactical bridges, such as the Medium Girder Bridge (MGB), may be completely built and launched without the aid of special launching equipment. Alternatively, as in the case of the Dry Support Bridge (DSB), special equipment to assemble and launch the bridge may be required. The last category of bridging is line of communication (LOC) bridging which is semi-permanent bridging used to producing routes for supply lines providing fuel, water, and other supplies. LOC bridging, such as the Bailey bridge produced by Mabey Johnson, may be used with intermediate piers to cross gaps of any length. A description of each of these bridges currently in use by the US Military is presented [107].

8.1 CURRENT MILITARY BRIDGING

Within the US Military the Marines and the Army currently utilize five different bridging systems to meet their bridging needs. To satisfy the need for assault bridging the Marines and Army use the AVLB with the Army more recently acquiring a number of Wolverine Heavy Assault Bridges. To satisfy tactical bridging needs both the Marines and Army use the MGB with the Army recently putting the DSB into service. Finally to fulfill line of communication needs both the Marines as well as Army rely on the Mabey Johnson “Bailey” bridge.

8.1.1 Armored Vehicle Launched Bridge (AVLB)

The AVLB, manufactured by General Dynamics Land Systems, is currently in use by both the Marines and Army [107]. The system consists of a scissor bridge mounted on a modified M60 tank chassis with a launching system. The bridge is composed of aluminum alloy having a length of 19.2 m (30 ft) and an overall width of 4.0 m (13.1 ft). The bridge consists of two parallel treadway each being 1.75 m (5.7 ft) wide. At a clear span of 18.3 m (60 ft) the bridge has a Military Load Class (MLC) rating of 60 (54,430 kg, 60 tons). The AVLB has a maximum depth at the mid span of 0.94 m (3.1 ft) and weighs a total of 13,290 kg (29,300 lbs). Photographs of the AVLB mounted on the launch vehicle as well as the launching of the bridge are shown in Figure 8-1 and Figure 8-2 respectively.

The AVLB takes only three minutes to launch and can be recovered from either end of the bridge. Recovery times are between 10 minutes and one hour depending on the site conditions. The biggest disadvantage of the AVLB is the MLC rating (MLC 60). The M1A1 Abrams tank currently in use weighs 60,780 kg (67 tons) and therefore cannot cross the AVLB under normal crossing conditions. The M1A1 is only allowed on the AVLB when a shorted span of 15.3 m (50 ft) is used and the tank performs a “cautionary crossing” at reduced speed. The Army is currently investigating solutions to increase the load carrying capacity of the AVLB.

Figure 8-1 Photograph of an AVLB.

Figure 8-2 Photograph of AVLB being launched.

8.1.2 Wolverine Heavy Assault Bridge (HAB)

Due to the deficient MLC rating of the AVLB, the US Army has acquired several Wolverine Heavy Assault Bridge systems manufactured by General Dynamics Land Systems and MAN Mobile Bridges [107]. The bridging system consists of a Leguan bridge provided by Man Mobile Bridges mounted on the Wolverine launching system (General Dynamics Land Systems) which is based on a M1 Abrams Chassis. The bridge is composed of aluminum alloy having a total length of 26 m (85 ft) and an MLC rating of 70 (63,500 kg, 70 tons). The bridge consists of two parallel treadways each being 1.6 m wide with a total bridge width of 4 m (13.1 ft). The bridge height is 0.9 m (3 ft) at the mid span and weighs 10,750 kg (23,700 lbs). Unlike the AVLB, the Wolverine launches in a horizontal fashion reducing the visible profile during launch. A photograph of the Wolverine during launch is shown in Figure 8-3. The wolverine offers a higher MLC rating with increased gap crossing length and reduced weight in comparison to the AVLB.

Figure 8-3 Photograph of the Wolverine Heavy Assault Bridge being launched.

8.1.3 Medium Girder Bridge

The Medium Girder Bridge (MGB), manufactured by Williams Fairey Engineering Limited, entered service in 1971 and is currently used by both the Marines as well as Army to serve their tactical bridging needs [107]. The MGB is a two-girder aluminum alloy bridge with decking supported between the two girders having a 4 m (13.1 ft) roadway width.

The MGB has a maximum MLC rating of 70 (63,500 kg, 70 tons) depending on the length and configuration. The MGB can be built in three different configurations: Single-storey (Figure 8-4), double-storey (Figure 8-5), and double-storey with link reinforcement (Figure 8-6). For the single-storey configuration the MGB has a height of 0.56 m (1.8 ft) and an MLC 70 rating for spans up to 9.9 m (32.5) in length. For the double-storey configuration the MGB has a height of 1.65 m (5.4 ft) and an MLC 70 rating for spans up to 31 m (102 ft) in length, and when the link reinforcement is used, gaps up to 45.8 m in length can be crossed with an MLC 70 rating. The link reinforcement hangs approximately 2 m (6.6 ft) below the bottom of the double storey bridge. The MGB can be launched by a crew of 25 soldiers in 45 minutes. Unlike other bridging systems, the MGB may be assembled and launched without the need of specialized assembly or launching equipment. All of the components with the exception of two are light enough (less than 230 kg, 500 lbs) to be carried by four men with the other two components requiring six men. A 45.8 m (150 ft) double-story bridge with link reinforcement weighs approximately 30,850 kg (68,000 lbs). A full MGB bridging asset (double-storey with link reinforcement) can be packaged on 16 shipping pallets which are 5 m (16 ft) in length.

During launching the MGB uses a launching nose beam attached to the front of the bridge such that as the bridge is constructed it is moved across the gap over rollers on the near bank utilizing the bridge weight as a counterbalance. Once the launching nose beam reaches the far bank a soldier crosses on the launching nose and sets us a roller on the far bank to bring the bridge across the gap. The bridge may be pushed across by hand or using a truck available at the site. A photograph of the MGB being launched is given in Figure 8-7.

Figure 8-4 Photograph of MGB single-storey configuration.

Figure 8-5 Photograph of MGB double-storey configuration.

Figure 8-6 Photograph of MGB double-story configuration with link reinforcement.

Figure 8-7 Photograph of the MGB with launching beam showing the bridge being pushed across the gap.

8.1.4 Dry Support Bridge (DSB)

The Dry Support Bridge (DSB) has recently been adopted by the US Army to replace the MGB [107]. The DSB is an aluminum alloy two girder bridge with a deck spanning between the girders. Each bridge module is 6 m long, 4.3 m (14.1 ft) wide, and 1.19 m (3.9 ft) high. The deck attaches to the girders through hinge connections such that the girders fold under the deck for storage and transportation. A photograph and illustration of a single bridge module being folded open for assembly are shown in Figure 8-8 and Figure 8-9 respectively. Tapered ramp modules are used at each end to bring traffic on and off the bridge. The DSB has a maximum clear span of 40 m (131 ft) with an MLC rating of 80 (track) and 100 (wheel) and a total weight of 37,110 kg (81,820 lbs). The DSB requires a special launch vehicle (Figure 8-8) for assembly and launching of the bridge. The bridge is launched by first placing a launch beam across the gap from which the assembled modules are suspended and moved across the gap. A photograph showing the launch beam and suspended bridge is shown in Figure

8-10. A crew of 8 can launch the bridge in less than 90 minutes. In addition to the launch vehicle the 40 m (131 ft) DSB can be carried on 4 Palletized Load System (PLS) flatracks. Two modules, when stacked for transportation are approximately equal to the size of a 6.1 m (20 ft) ISO container and therefore can be carried by most flatbed vehicles and trailers.

Figure 8-8 Photograph showing the DSB and specialized launch vehicle.

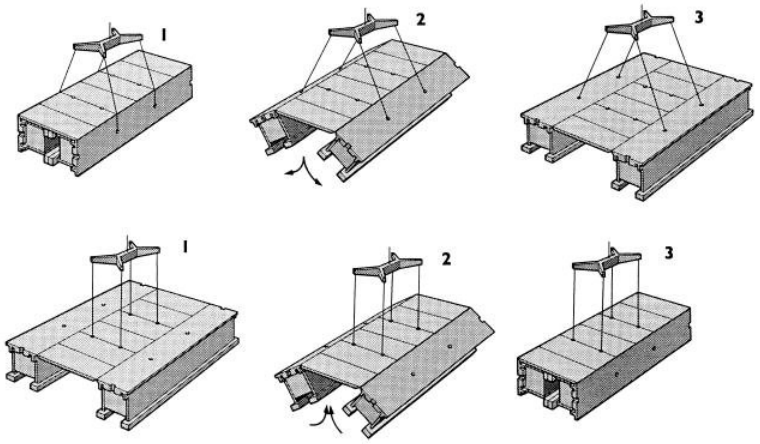

Figure 8-9 Illustration showing launching and retrieval of a bridge module.

Figure 8-10 Photograph showing the DSB being launched across a gap.

8.1.5 Mabey Johnson Bailey Bridge

The Bailey bridge is a steel truss type bridge with either steel or timber decking [107]. The Bailey bridge can be built with a roadway width ranging from 3.43 m (11.3 ft) (single-lane) to 7.23 m (23.7 ft) (two-lane). The Bailey bridge is designed to support MLC 80 (track) vehicles at a span of 39 m (128 ft). The bridge may be used with intermediate piers to cross gaps of any length. With 22 men a 39 m (128 ft) single lane bridge can be constructed and launched in 10 hours. Similar to the MGB, the Bailey bridge is launched using rollers and the bridge as a counterweight to move the bridge across the gap. No specialized equipment is required for construction or launching. A photograph of a Bailey bridge is shown in Figure 8-11.

Figure 8-11 Photograph of the Mabey Johnson Bailey bridge.

8.2 MODULAR COMPOSITE BRIDGING

To increase mobility in the aftermath of natural disasters, or on the battlefield and to reduce the need for multiple bridging assets to meet gap crossing needs, improved light-weight bridging solutions are being investigated. One proposed concept currently under investigation at the University of California, San Diego, through funding provided by the Office of Naval Research, is a family of bridges which utilize common components to satisfy assault, tactical, and line of communication bridging needs. In an effort to reduce weight and increase the service life, the bridge is composed of carbon/epoxy composite components. As seen from the plot in Figure 8-12 carbon/epoxy composites offer significant increases in strength and stiffness over conventional metallic materials used in current bridging. The composite bridging asset would consist of three basic building components which may be configured to meet the entire militaries gap crossing needs. The components

consist of tapered end ramp beams for access on and off the bridges, interior beams serving as the main load bearing elements, and deck sections attached to the tops of the beams. Each of the components is seen in Figure 8-13. The components are to be interconnected through metallic hinge joints which allow the components to be assembled in different configurations to satisfy assault, tactical, and line of communication bridging needs. Illustrations of each of the bridges produced within the family of bridges are given in Figure 8-14 . The reduced weight over conventional metallic bridges increases the capabilities of transporting the bridges by air and ground as well as the ease of launching. In addition, the use of composites with appropriate manufacturing processes lends itself to potential in field manufacturing.

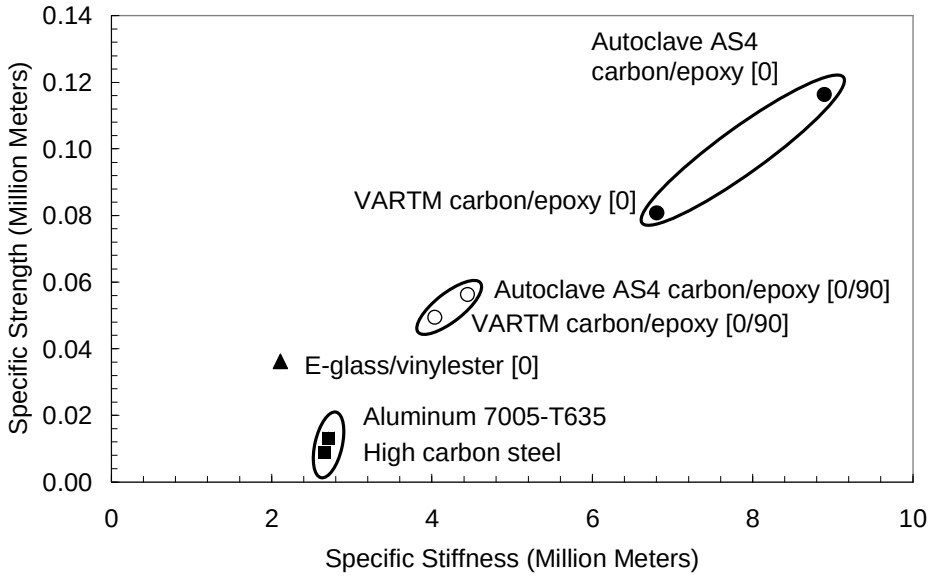

Figure 8-12 Plot showing the comparison of specific strength versus specific stiffness of common alloys used in military bridging with carbon/epoxy laminates.

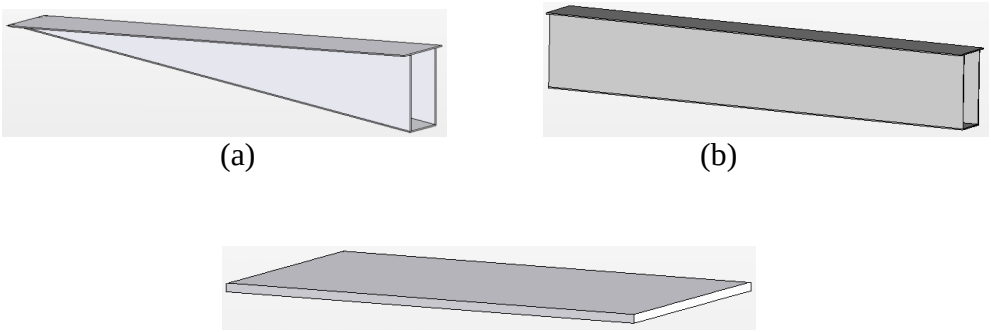

Figure 8-13 Illustration of the basic building blocks to construct the proposed composite modular bridging; (a) ramp beams, (b) interior beams, (c) deck sections.

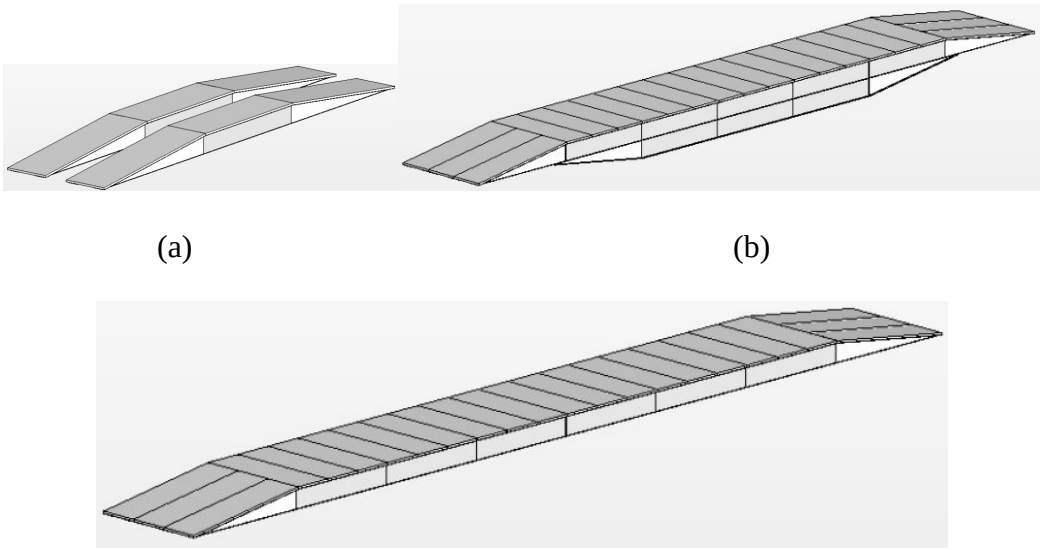

(a) (b) (c)

Figure 8-14 Illustration of proposed composite modular family of bridges: (a) assault, (b) tactical, and (c) line of communications.

The use of composites in the development of mobile bridging is not new. Since the mid nineties the US Army has been interested in developing new light-weight mobile bridging systems to replace existing heavier mobile bridging systems which are near the end of their service life. As part of this bridge replacement effort the Army desired a new bridging system which was capable of crossing gaps up to 12.2m (40 ft) in length while supporting track and wheel vehicles up to MLC 100 (90,700 kg, 200,000 lb). To meet this need, a bridging system known as the Composite Army Bridge (CAB) was developed and tested at the University of California, San Diego. The bridge is composed of a carbon/epoxy superstructure with a balsa core sandwich deck. During this bridge development program, an extensive research effort was performed to develop a light weight, high strength, deck core that was comparable with existing aluminum extruded decks. Although a wide range of cores were considered, none performed as well as balsa based upon weight, shear strength, and cost. The CAB proved to be a lighter alternative to existing bridging systems of the same load class and to date has experienced 20,000 actual or simulated crossings with no signs of damage. For more details about the Composite Army Bridge refer to papers by Kosmatka et al.[108, 5, and 109]. A photograph of the CAB as well as illustration showing the different components of the bridge are given in Figure 8-15 and Figure 8-16 respectively.

Figure 8-15 Photograph of an M1 Abrams tank crossing the Compos Army Bridge (CAB).

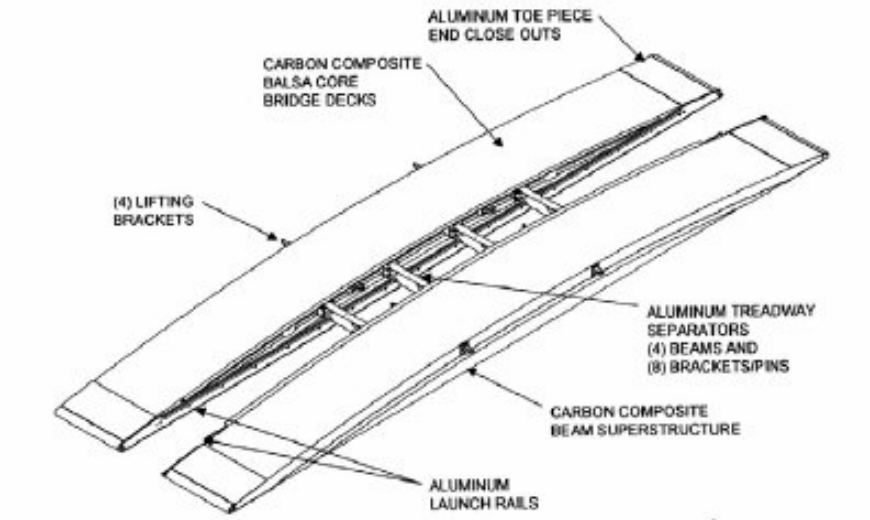

Figure 8-16 Illustration of the Composite Army Bridge (CAB).

More recently the US Army has expressed a need for a short-span bridging system for crossing gaps up to 4 m in length supporting MLC 30 (track) and fully loaded Palletized Load System (PLS) trucks. In order to address this short-span bridging need, the family of bridges concept is expanded such the bridge deck sections may be used for short-span bridging. A description of the development of the deck system followed by the development and testing of the short-span bridging system is presented in Chapters 9 and 10.

CHAPTER 9

DECK DEVELOPMENT

Over the past 15 years there has been a significant amount of research investigating the use of fiber reinforced polymer (FRP) decks for replacement of existing deteriorated bridge decks and for new bridge construction [6, 7, 8, 9, 110, 111, 112, and 113]. The current research investigates an alternative high performance FRP deck system which is defined by a high strength-to-weight ratio and performance under extreme loading conditions. Based on the success of the CAB program the research utilizes a similar carbon/epoxy sandwich core system looking at alternative core systems which will offer increased strength at a reduced weight in comparison to balsa

The research evaluates the performance of five different deck panels consisting of FRP webbed cores and compares them to the baseline balsa core deck used in the CAB. The design of the webbed cores as well as a detailed description of each of the five deck specimens is presented. Following a description of the core specimens, shear and compression testing procedures are outlined followed by a summary of the testing results. A finite element analysis is performed followed by design recommendations for FRP webbed deck systems. Finally an overall weight and performance comparison is made between the FRP deck/treadway systems tested and conventional extruded aluminum decking currently used within the military.

The FRP webbed cores considered in this study are limited to cores in which all of the webs are oriented in a single direction with webs at approximately 51 mm (2.0 in) on center in which only one way bending is considered. For most applications one way bending is sufficient, thus significant transverse bending stiffness is not required. Based on the loading requirements and limiting the overall deck thickness to 95 mm (3.75 in) (US Army requirement) it was determined that for one way bending a cross sectional shear strength of 5,100 kPa (740 psi) and a compressive strength of 9,240 kPa (1,340 psi) are required to match the performance of the baseline balsa core. To maximize the shear strength and stiffness of the core, the web laminates are predominately a $[\pm 45]$ lay up. Based on a 51 mm (2.0 in) web spacing and required cross section shear strength and compressive strength it is calculated that each web must carry a shear load of 259 kN/m (1,480 lb/in) and a compressive load of 469 kN/m (2,680 lb/in). Based on assumed laminate properties obtained from previous testing (see Table 9-1) minimum web thicknesses were determined to meet the shear and compression load demands. It was determined that a minimum web thickness of 0.8 mm (0.03 in) is required for shear and a web thickness of 2.5 mm (0.1 in) is required for compression. From a strength perspective it is evident that compression will govern the thickness of the web laminates. In addition to strength, the buckling capacity of the webs is also considered. A plot of the deck compressive strength and buckling loads for carbon and E-glass webs at 51 mm (2.0 in) centers is shown in Figure 9-1. Buckling load curves are given for both carbon and E-glass webs with and with out foam infill. The webs are treated as beams on elastic foundations where the buckling load for a beam with fixed ends is given by [114]

$$P_{cr} = 4\frac{\pi^2 E_b I}{l^2} + 2\sqrt{k_{foam} E_b I}\ , \tag{9.1}$$

where E_b is the flexural modulus of the web laminate, I is the moment of inertia of a unit length of the web, k_{foam} is the stiffness of the elastic foundation or in this case two times the elastic modulus of the foam since the foam is on both sides of the web, l is the depth of the web, and P_{cr} is the buckling load. The foam used in the deck panels is 48 kg/m^3 (3 pcf) polyisocyanurate foam having a modulus of 8,620 kPa (1,250 psi). Setting the foam stiffness k_{foam} to zero leads to the buckling solution without an elastic foundation (no foam infill). The bending modulus used for the carbon/epoxy and E-glass/epoxy webs is given in Table 9-1. From the plot in Figure 9-1 it is shown that for carbon webs with foam infill a thickness of 2.8 mm (0.11 in) is required to achieve the compressive strength of the balsa baseline. Similarly a thickness of 3 mm (0.12 in) is required for E-glass with foam infill, a thickness of 3.65 mm (0.14 in) is required for carbon without foam infill, and a web thickness of 3.85 mm (0.15 in) is required for E-glass without foam infill. Based on the web buckling load capacity, the thicknesses of the webs for the five different core test specimens range from 2.4 mm (0.1 in) to 4.2 mm (0.17 in). A detailed description of each of the core specimens is given in the following section.

Table 9-1 Web Laminate Properties

Laminate Type	*Modulus E_x (GPa) [Msi]*	*Shear Strength (MPa) [ksi]*	*Compressive Strength (MPa) [ksi]*
Carbon/epoxy	14.0 [2.03]	380 [55]	186 [27]
E-glass/epoxy	12.1 [1.75]	345 [50]	172 [25]

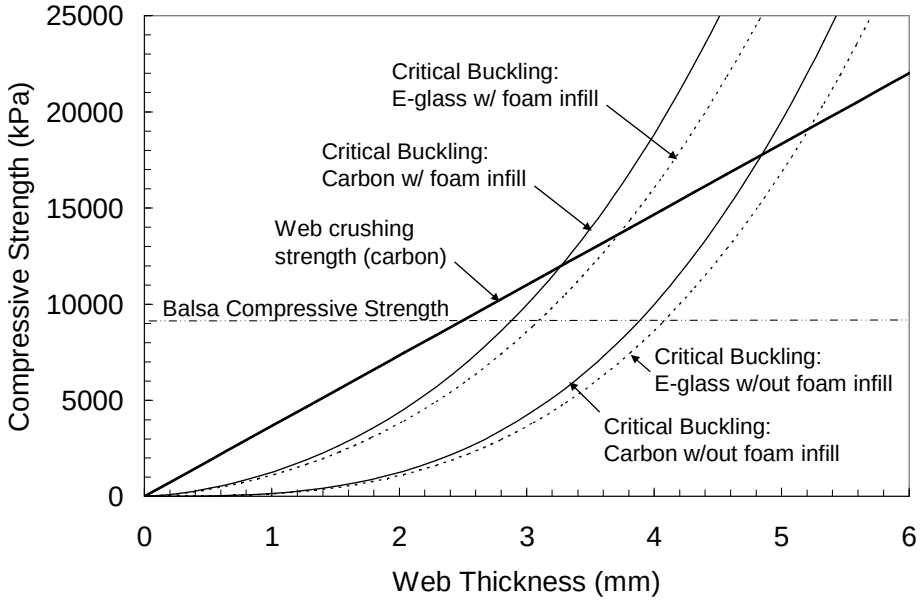

Figure 9-1 Analytical compressive strength vs. web thickness for carbon and E-glass [± 45] web laminates at 51 mm (2 in) on center.

9.1 CORE DESCRIPTION

Five different sandwich deck panels, each having a different core configuration, were fabricated and tested. Each core type is approximately 76 mm (3.0 in) thick and is composed of either carbon/epoxy webs or E-glass/epoxy webs with 10 mm (0.375 in) carbon/epoxy face sheets. The first three core types are fabricated using an automated winding process which wraps dry fiber tows around rectangular foam beams and then consolidates the individual beams and applies a

tackified scrim layer to the top and bottom surfaces which holds the beams together to form a sheet of webbed core material [115]. The final two core types are fabricated by hand wrapping and/or hand placing woven or stitched fabric between foam beams.

The baseline balsa core from the CAB project consists of two sheets of 248 kg/m^3 (15.5 pcf) balsa each being 38 mm (1.5 in) thick with an 0.61 kg/m^2 (18 oz/yd^2) layer of woven carbon at the mid plane. During the CAB project it was shown that thinner sheets of balsa contained less defects and that the shear strength of the balsa core could be increased using thinner plies of balsa with carbon splitters between the plies [108]. A matrix of holes was drilled through the core to allow the resin to infuse the splitter ply and face sheets during the VARTM process. The balsa surface was treated with a sealant to prevent any moisture escaping the balsa during the curing process. The final density of the core is approximately 290 kg/m^3 (18 pcf). Test results showed the balsa core to have a shear strength of 3,100 kPa (450 psi) and a compressive strength of 9,240 kPa (1,340 psi). The balsa core is essentially transversely isotropic and serves well in applications in which bi-directional bending stiffness and strength is required. An illustration of the balsa core is shown in Figure 9-2a.

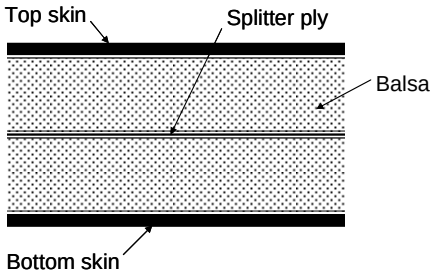

(A) Balsa

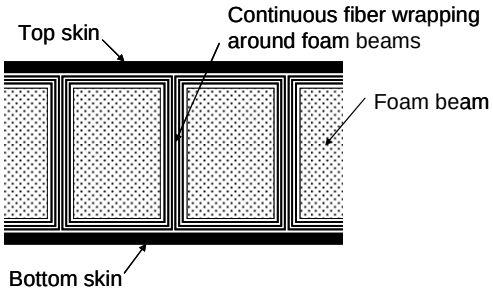

(B) C1-WCH and C2-WCL

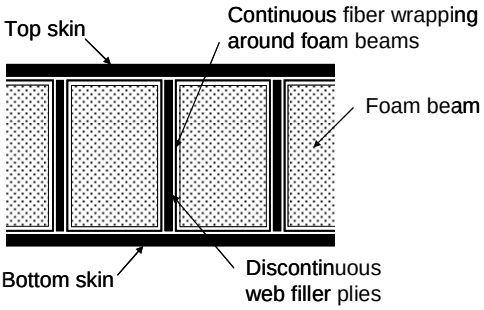

(C) C3-WE and C4-TC

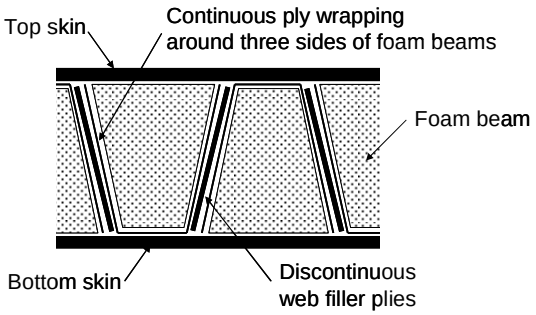

(D) C5-CC

Figure 9-2 Illustrations of the different core design configurations.

A description of the five FRP webbed core types is given as follows:

Core 1: Wound Carbon Heavy (C1-WCH).

The first core was fabricated using an automated winding process which wraps fiber tows around rectangular foam beams at prescribed winding angles. The foam used in this core is a 64 kg/m^3 (4 pcf) polyisocyanurate foam with a service temperature of 149° C (300° F) which is required for the processing temperatures during the final cure. The foam beams have cross section dimensions of 50 mm x 76 mm (1.95 in x 3.0 in). A 24k, T700 carbon tow was wound around each beam creating a $[\pm 45]_3$ laminate around each individual beam. Following the winding of the individual beams they are assembled together, consolidated, and held in place with a scrim layer which is applied to the top and bottom surfaces of the assembly to create a sheet of webbed core material. The assembly of the beams results in web laminates $[\pm 45]_6$ having a dry areal weight of approximately 2.58 kg/m^2 (76 oz/yd^2) and a final thickness of 3.4 mm (0.13 in). An illustration of this core is shown in Figure 9-2b.

Core 2: Wound Carbon Light (C2-WCL)

The second core, fabricated by the same winding process, is identical to the first core with the exception that 48 kg/m^3 (3 pcf) polyisocyanurate foam was used and half of the 24k tow was replaced with 12k tow resulting in webs which are 2.4 mm (0.094 in) thick having a dry areal weight of 1.94 kg/m^2 (57 oz/yd^2). Core 2 (C2-WCL) is used to investigate the effects of the foam on the buckling capacity of the webs under compression.

Core 3: Wound E-glass (C3-WE)

The third core was fabricated using the same winding process and foam dimensions as the first two cores with 48 kg/m^3 (3 pcf) polyisocyanurate foam. Core 3 (C3-WE) was wound with E-glass roving, having a yield of 500 m/kg (247 yd/lb), creating a single layer [$\pm$45] 0.54 kg/m^2 (16 oz/yd^2) around each foam beam. Four layers of 0.81 kg/m^2 (24 oz/yd^2) [$\pm$45] stitched E-glass fabric were inserted as a filler between each of the wrapped beams to build up the thickness of the webs for buckling stability. Following the placement of the filler layers the core proceeded through the consolidation and scrim processes as previously described. The final result of the process is a web dry fiber areal weight of 3.78 kg/m^2 (128 oz/yd^2) and a final web thickness of 4.0 mm (0.16 in). An illustration of this design is shown in Figure 9-2c. The use of E-glass along with filler layers as opposed to all winding is investigated as a low cost fiberglass alternative to the carbon of Core 1 (C1-WCH).

Core 4: Triax Carbon (C4-TC)

The fourth core consists of hand wrapping one layer of 0.41 kg/m^2 (12 oz/yd^2) [$\pm$45] stitched carbon fabric around 48 kg/m^3 (3 pcf) PVC foam (Baltek Airex R63) beams. Again the foam beams are rectangular having dimensions of 50 mm x 76 mm (1.95 in x 3.0 in). Special care was taken during the wrapping process to avoid wrinkling or bunching of the fabric. A spray adhesive was used to hold the fabric in place during wrapping. Following the wrapping of the fabric, two layers of 1.22 kg/m^2 (36 oz/yd^2) [0/$\pm$45] stitched carbon triax material were placed between the beams to build up the thickness of the webs for buckling stability. The 0° fibers in the

filler layers were oriented perpendicular to the core surface to increase the compressive strength of the core and provided better web stability as will be shown. The final web dry areal weight is 3.26 kg/m^2 (96 oz/yd^2) with a final web thickness of 4.0 mm (0.16 in). An illustration of this design is shown in Figure 9-2c.

Core 5: Corrugated Carbon (C5-CC)

The fifth core consists of 96 kg/m^3 (6 pcf) polyisocyanurate foam beams having a trapezoidal cross section with one ply of 0.61 kg/m^2 (18 oz/yd^2) balanced weave carbon fabric oriented at 45° wrapped around three sides of the beam. The foam beam dimensions are 60 mm (2.35 in) and 35 mm (1.35 in) at the wide and narrow edges respectively and 76 mm (3.0 in) deep. For ease of fabrication the fabric was only wrapped around the two vertical sides of the trapezoid and the narrow horizontal surface. Three plies of weaved carbon fabric oriented at 45° were placed between the assembled beams to build up the web thickness. The final dry areal weight of the webs is 3.81 kg/m^2 (90 oz/yd^2) and the final web thickness is 4.2 mm (0.17 in). An illustration of this design is shown in Figure 9-2d. A summary of the materials used in each core type is given in Table 9-2.

Table 9-2 Core Design

Core Type	*Fabrication Method*	*Material*	*Configuration (Figure 9-2)*	*Wrap Fiber*	*Filler Fiber*
C1-WCH	Winding	Carbon	B	T 700	NA
C2-WCL	Winding	Carbon	B	T 700	NA
C3-WE	Winding	E-glass	C	E-glass	E-BX 2400[a]
C4-TC	Hand	Carbon	C	C-BX 1200[a]	C-TLX 3600[a]
C5-CC	Hand	Carbon	D	G519[b]	G519[b]
Balsa	Hand	Balsa	A	NA	G519[b,c]

[a] Vectorply; [b]Fabric Development Inc.; [c]Splitter ply

Carbon skins were applied to each core and the SCRIMP process (a variant of the VARTM process) [18] was used to infuse the specimens with resin. Each of the specimens was cured at 82° C (180° F) and post cured at 121° C (250° F). Since the purpose of this study is to evaluate the shear strength of each of the core designs the top and bottom skin laminates were designed to ensure that the panel would fail in shear as opposed to bending. Fiber volume testing showed the fiber volume fraction of the webs for each specimen to be between 40% and 45%. The fiber volume fraction measurements were performed by matrix digestion using nitric acid in accordance with ASTM D3171.

9.2 TEST PROCEDURE

The main focus of this research is to quantify the shear strength and compressive strength of the five different cores. To assess the shear strength of the cores a three point bending test was performed and for the compressive strength a compression test was performed. The shear strength of the deck specimens was only

considered for one way bending with the webs running parallel to the length of the test specimen. The specimens were cut from fabricated panels which were 762 mm x 762 mm (30 in x 30 in) using an abrasive diamond tile saw such that the dimensions of each specimen are approximately 159 mm (6.25 in) wide by 762 mm (30 in) long with each specimen have three webs with the exception of Core 5 (C5-CC) which is 208 mm (8.20 in) wide such that the core cross section is symmetric with four webs. The exact specimen width, depth, web thickness, web spacing, and core areal weight are presented in Table 9-3.

9.2.1 Shear

The three-point bending test was conducted using a 490 kN (110 kip) MTS machine with a reaction beam held in the bottom grips which supported the test specimen by two roller supports with rubber pads spaced at 610 mm (24 in). A 152 mm x 254 mm (6 in x 10 in) steel loading nose with a 50 mm (2 in) thick rubber pad was held in the upper grips and used to apply the load at the mid span. Initial testing of Core 1 (C1-WCH) used a 50 mm x 254 mm (2 in x 10 in) loading nose which resulted in local crushing of the webs directly below the loading nose. This result prompted the use of the wider loading nose to avoid local crushing of the webs. A photo of the test setup is shown in Figure 9-3. A total of three specimens were tested for each core type. Three 10 mm (0.4 in) strain gages and six displacement transducers were applied to each specimen as shown in Figure 9-4. Two displacement transducers were used at each support as well as the mid-span to measure the relative

displacement of the mid-span to the support displacements as well as to detect any twisting which may occur during the test. The rubber pads were used to prevent the steel loading nose and roller supports from cutting into the skin laminate surfaces.

Table 9-3 Specimen Dimensions

Core Type	*Width (mm) [in]*	*Depth[a] (mm) [in]*	*Web Thickness (mm) [in]*	*Web Spacing (mm) [in]*	*Core Areal Weight (Kg/m^2) [psf]*
C1-WCH	160 [6.30]	98 [3.86]	3.4 [0.13]	53 [2.09]	15.7 [3.22]
C2-WCL	158 [6.21]	95 [3.74]	2.4 [0.09]	53 [2.07]	10.1 [2.07]
C3-WE	160 [6.30]	92 [3.62]	4.0 [0.16]	53 [2.09]	14.7 [3.00]
C4-TC	164 [6.45]	97 [3.82]	4.0 [0.16]	55 [2.17]	14.5 [2.97]
C5-CC	208 [8.20]	96 [3.78]	4.2 [0.17]	52 [2.05]	18.6 [3.81]
Balsa	181 [7.13]	92 [3.62]	NA	NA	22.0 [4.50]

[a] depth including face sheets.

Figure 9-3 Photograph of the three-point bending test.

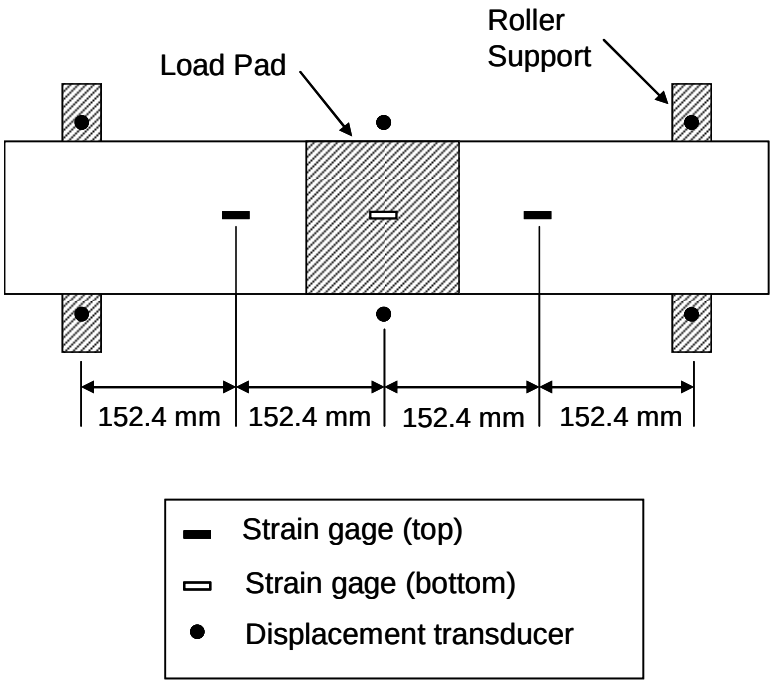

Figure 9-4 Illustration of the three-point bending test strain gage and displacement transducer locations.

9.2.2 Compression

For the compression test two specimens from each of the five core types were tested to failure. In addition, two specimens from Core 1 (C1-WCH), Core 2 (C2-WCL), and Core 3 (C3-WE) were tested without the foam infill to study the effects of the foam on the web buckling load. For the specimens tested without foam infill the foam was simply removed from the specimen prior to testing. The compression specimens were each the same width as the three point bending test specimens and 152 mm (6 in) long. The compression specimens were tested using a 2,670 kN (600 kip) SATEC compression machine. Hydrostone was applied to the non mold surface of the specimens to ensure that the top and bottom surfaces were smooth and parallel. The compression machine consists of upper and lower platens where the upper platen

is on a swivel to ensure that the load is evenly distributed. A photograph of the compression testing setup is seen in Figure 9-5.

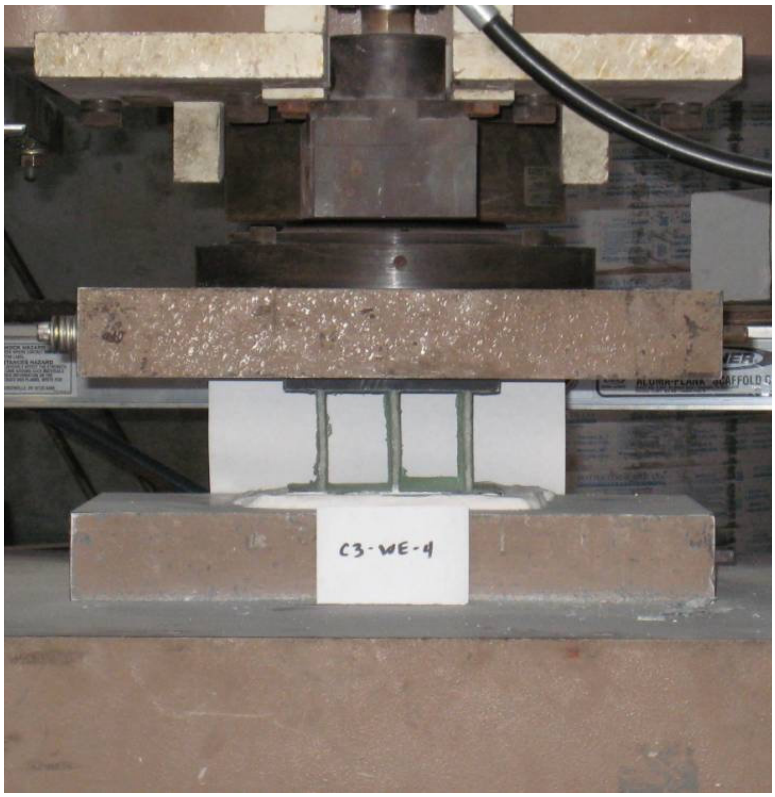

Figure 9-5 Illustration of compression test setup.

9.3 TEST RESULTS AND DISCUSSION

The results of the shear and compression testing are presented.

9.3.1 Shear

Shear failure of FRP webbed decks consist of four potential failure modes: (1) interlaminar shear between the core and the skins, (2) failure at the joint between the

webs and the skins, (3) shear failure of the webs, and (4) shear buckling of the webs. Of the four potential modes only two were observed. Core 1 (C1-WCH) and Core 5 (C5-CC) both failed in interlaminar shear between the core and skins, Core 3 (C3-WE) and Core 4 (C4-TC) failed in shear at the corner between the webs and the skins, and Core 2 (C2-WCL) did not experience shear failure but failed in local crushing of the webs directly below the loading nose. The webs of each of the core specimens were adequately thick to eliminate web shear failure or web shear buckling. An illustration of the two observed shear failures is presented in Figure 9-6. A plot of load versus deflection for each core type showing the relative stiffness of the cores is given in Figure 9-7. From this plot we see that Core 1 (C1-WCH) is the stiffest and the E-glass core (C3-WE) is the softest. A summary of the three point bending test results as well as the strength ratio of each core compared with the balsa baseline is given in Table 9-4. The shear strength reported is the average cross sectional shear strength and is determined by dividing the ultimate shear load by the total cross section of each specimen.

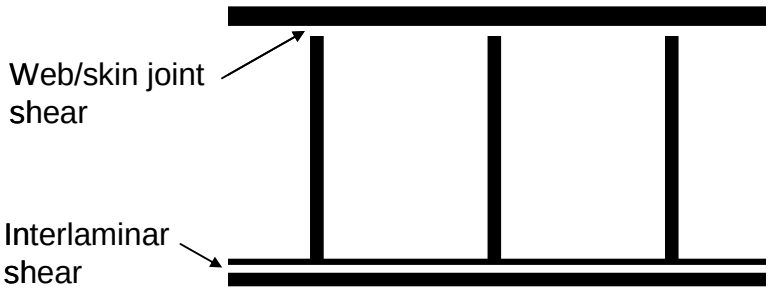

Figure 9-6 Illustration of potential shear failure mechanisms.

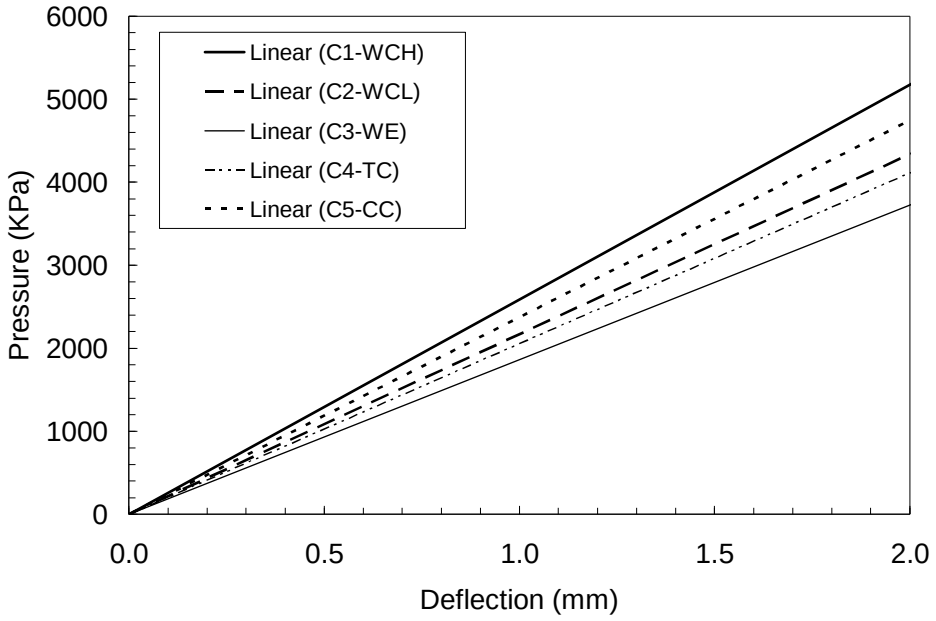

Figure 9-7 Plot of applied load versus deflection for each core type.

Table 9-4 Three-Point Bending Test Results

Core Type	*Failure Load (kN) [kips]*	*Shear Strength (kPa) [psi]*	*Failure Mode*	*Shear Strength Normalized wrt Balsa*
C1-WCH	315 [72.8]	10100 [1460]	Interlaminar shear	3.23
C2-WCL	148 [33.3]	4930 [716]	Local web crushing	1.59
C3-WE	160 [35.9]	5430 [788]	Web/skin joint shear	1.75
C4-TC	191 [42.9]	6000 [870]	Web/skin joint shear	1.93
C5-CC	201 [45.1]	5020 [729]	Interlaminar shear	1.62
Balsa	103 [23.2]	3100 [450]	Core shear	1.0

Core 1 (C1-WCL) and Core 5 (C5-CC) failed in interlaminar shear between the core and the skins. A photograph of a cut cross section of Core 5 (C5-CC) showing

this failure is seen in Figure 9-8. This type of failure occurs when the webs and web/skin joints have adequate strength to resist shear stresses and the interlaminar shear strength becomes the weakest point. From Table 9-4 we see that the shear strength of Core 1 (C1-WCH) (10,100 kPa, 1,460 psi) is about twice that of Core 5 (C5-CC) (5,020 kPa, 729 psi). The difference in the shear strength between these two cores can be explained by the illustration seen in Figure 9-9. From the illustration it is observed that for Core 1 (C1-WCH) the shear load path from the webs into the skins is equally distributed in each direction transverse to the webs while the corrugations of Core 5 (C5-CC) allow the shear to be transferred to the skins in only one direction thereby increasing the concentrated interlaminar shear stress by a factor of two and thus decreasing the shear strength by approximately one half compared to Core 1 (C1-WCH). It is expected that modifying Core 5 (C5-CC) by wrapping fabric around all four surfaces of the foam beams to allow the shear load to be transferred in both directions would greatly increase the shear strength. Core 1 (C1-WCH) represents the maximum shear strength for a web spacing of 51 mm (2 in). The shear strength could be increased by decreasing the web spacing thereby decreasing the required shear load to be transferred from each web into the skins.

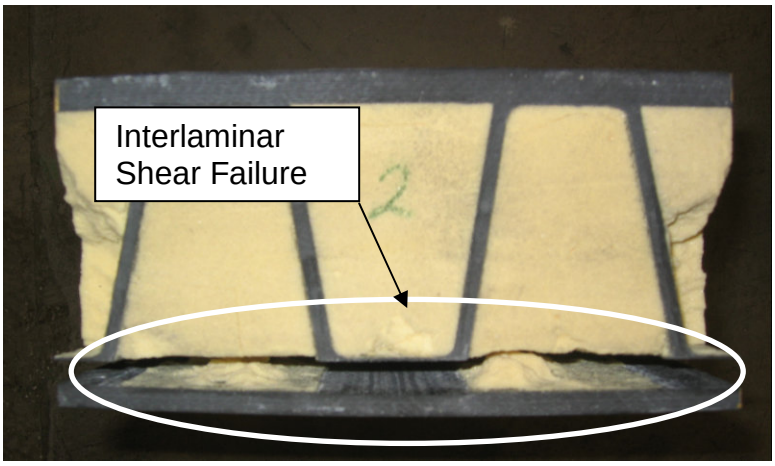

Figure 9-8 Photograph of the cross section of Core 5 illustrating the interlaminar shear failure.

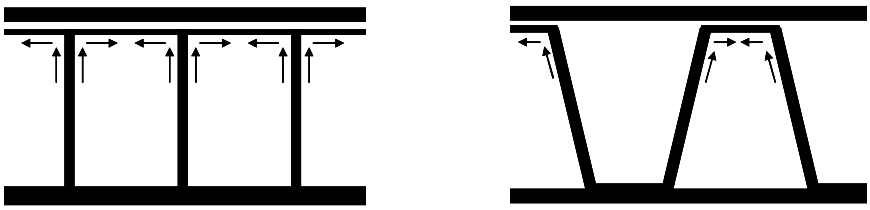

Figure 9-9 Illustration of the shear flow from the webs to the skins for (a) Core 1 (C1-WCH) and (b) Core 5 (C5-CC).

Core 3 (C3-WE) and Core 4 (C4-TC) both failed in shear at the joint between the webs and the skin. Both of these cores consist of webs in which a portion of the web thickness is produced by filler fabric which terminates at the web/skin joint and only a portion of the web thickness is continuous into the skin laminates. As a result the effective (continuous) web thickness at the web/skin joint is only a fraction of the total web thickness and therefore a location for potential shear failure. For Core 3 (C3-WE) and Core 4 (C4-TC) the effective web thickness at the web/skin joint is 25%

of the total thickness resulting in an effective web thickness of 1.0 mm (0.04 in) for each core. If we take all of the shear load to be carried in the webs and we use the effective thickness to determine the shear stresses in the web laminate we find that the web/skin joint of Core 3 (C3-WE) fails at a shear stress of 345,000 kPa (50 ksi) and Core 4 (C4-TC) fails at a shear stress of 414,000 kPa (60 ksi). These values correspond with the shear strength reported previously of 345 MPa to 380 MPa (50 ksi to 55 ksi) for a $[\pm 45]$ laminate having a fiber volume fraction of 40%. The shear strength of Core 3 (C3-WE) is 5430 kPa (788 psi) and the shear strength of Core 4 (C4-TC) is 6,000 kPa (870 psi). By increasing the effective thickness of the webs the shear strength could be increased up to the point that the failure mode transitions from web/skin joint failure to interlaminar failure between the core and the skins. Increasing the effective web thickness of Core 3 (C3-WE) by a factor of 1.85 would increase the effective shear stress to 10,000 kPa (1,460 psi) which is the shear stress at which interlaminar shear failure occurs as was seen in the case of Core 1 (C1-WCH). Similar results can be obtained for Core 4 (C4-TC) by increasing the effective web thickness by a factor of 1.67.

Core 2 (C2-WCL), which was identical to Core 1 (C1-WCH) with the exception of the webs being 33% thinner, failed in local web crushing directly below the loading nose and shear failure was not achieved. Based on this result we can say that Core 2 (C2-WCL) has a minimum shear strength of 4,930 kPa (716 psi).

A plot of the shear strength versus effective web thickness for webs spaced at two inches on center is given in Figure 9-10. On the plot the solid line represents the maximum shear strength where the failure mode is web/joint or web shearing and the

dashed line represents the upper shear strength limit at which the failure moves from web failure to interlaminar shear failure between the core and skins.

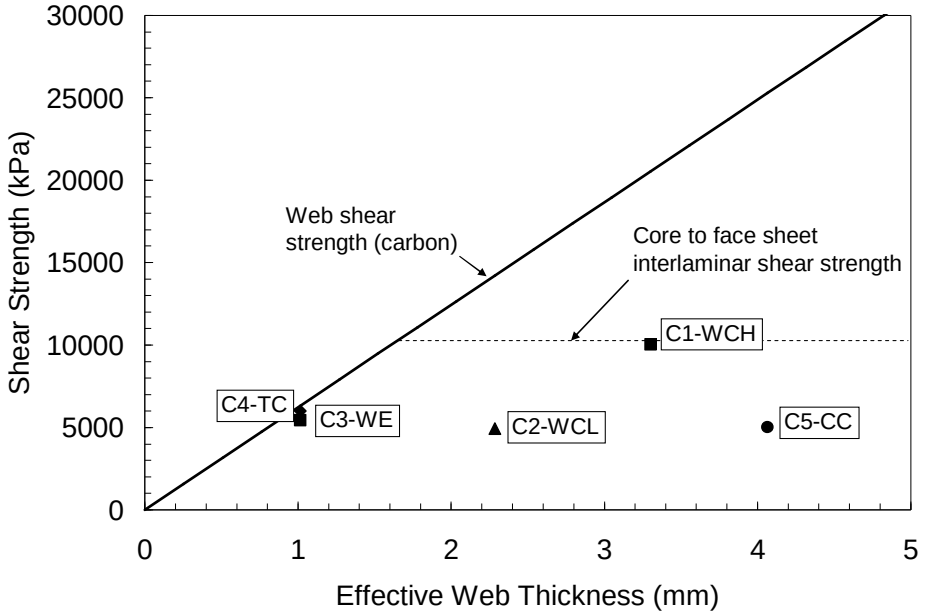

Figure 9-10 Plot of the shear strength versus effective web thickness for each core type with the predicted web shear strength.

9.3.2 Compression

The compression tests resulted in two different failure modes: (1) crushing of the webs and (2) buckling of the webs. Core 1 (C1-WCH), Core 2 (C2-WCL), and Core 3 (C3-WE) were each tested with and without the foam infill to study the effects of the foam on the stability of the webs. Core 4 (C4-TC) and Core 5 (C5-CC) were tested with the foam infill. A summary of the compression testing results including the compressive strength ratio of each core type with the baseline balsa core is given in Table 9-5. A plot of the compression test results with the analytical prediction of

web compression strength and web buckling load is given in Figure 9-11. The solid square symbols represent the experimental results with foam infill while the open squares represent finite element results with foam infill. Similarly the solid circles represent experimental results without foam infill and the open circles represent finite element results without the foam infill.

Table 9-5 Compression Test Results

Core Type	*Failure Load (kN) [kips]*	*Comp. Strength (kPa) [psi]*	*Failure Mode*	*Comp. Strength Normalized wrt Balsa*
C1-WCH w/ foam	307 [68.9]	12600 [1830]	Crushing	1.36
C1-WCH w/out foam	238 [53.5]	9770 [1420]	Buckling	1.06
C2-WCL w/ foam	115 [25.8]	4780 [693]	Buckling	0.52
C2-WCL w/out foam	64.1 [14.4]	2670 [387]	Buckling	0.29
C3-WE w/ foam	257 [57.8]	10600 [1530]	Buckling	1.14
C3-WE w/out foam	233 [52.4]	9590 [1390]	Buckling	1.04
C4-TC w/ foam	400 [90.0]	16100 [2330]	Crushing	1.74
C5-CC w/foam	242 [54.5]	15300 [2220]	Crushing	1.66
Balsa	254 [57.1]	9240 [1340]	Crushing	1.0

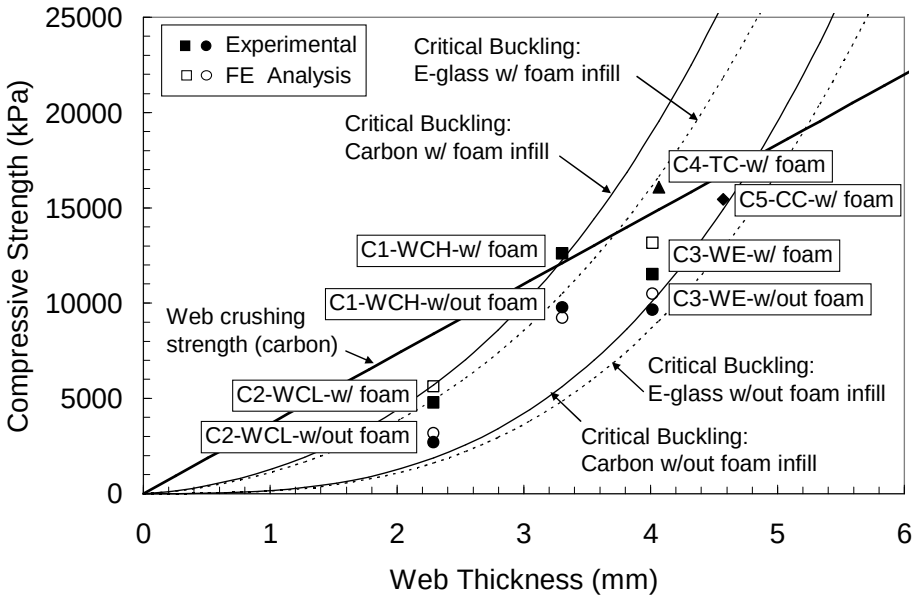

Figure 9-11 Plot of the compressive strength of each core type with the analytical and finite element predicted web compressive strength and web buckling strength for 51 mm (2 in) web spacing.

The Core 1 (C1-WCH) specimen with the foam infill failed in web crushing at a stress of 12,600 kPa (1,830 psi). Notice that from Figure 9-11 the predicted buckling load is just slightly higher than the web compressive strength agreeing with the observed failure. The specimen without the foam failed in buckling at a load of 9,790 kPa (1,420 psi). The presence of the light weight foam eliminated the web buckling failure mode so that the much higher web crushing failure was the critical load. Photographs of the failed specimens are seen in Figure 9-12.

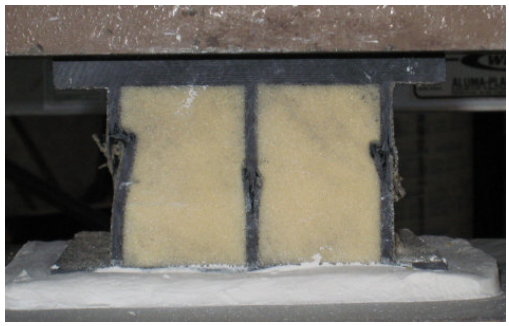

C1-WCH w/ foam

C1-WCH w/out foam

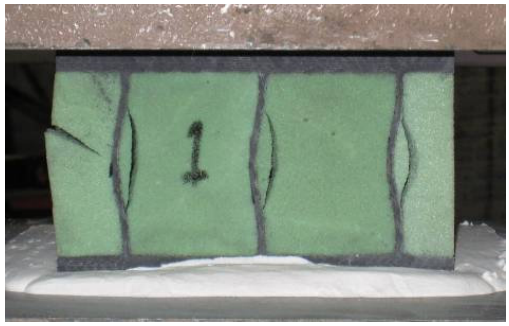

C2-WCL w/ foam

C2-WCL w/out foam

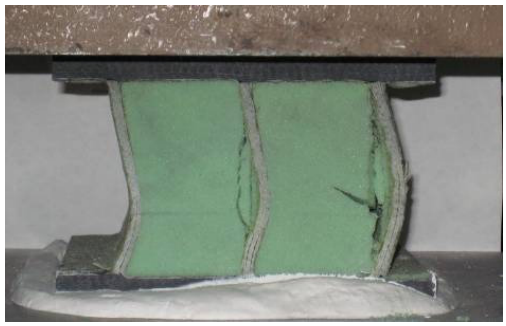

C3-WE w/ foam

C3-WE w/out foam

Figure 9-12 Photographs of compression specimens C1-WCH w/ foam, C1-WCH w/out foam, C2-WCL w/ foam, C2-WCL w/out foam, C3-WE w/ foam, and C3-WE w/out foam.

The test results for Core 2 (C2-WCL) showed the foam infill to have a significant effect on the buckling capacity of the webs. The compressive strength without the foam is 2,670 kPa (387 psi) and increases by a factor of 1.8 to 4,780 kPa (693 psi) with the foam present. Photographs of the test specimens are shown in Figure 9-12. From the photographs it is observed that the buckled shape resembles that of a beam with fixed ends.

Core 3 (C3-WE) was also tested with and without the foam infill with both tests resulting in buckling failure of the webs. Without the foam the compressive strength is 9,590 kPa (1,390 psi) which agrees well with the predicted compressive strength (see Figure 9-11). An increase in compressive strength to 10,500 kPa (1,530 psi) is observed for the specimens with the foam. As discussed previously, at the location where the webs meet skins only a portion of the web fibers are continuous and the remainder of the web is composed of filler layers which terminate at the web skin interface. It is believed that this discontinuity of fibers from the web to the skin reduces the stiffness of the web/skin joint (semi-rigid) resulting in a buckling load which is slightly less than the condition with fixed ends. The difference between the predicted and experimental compressive strength is due to the thickness of the edge foam as will be explained in the finite element analysis section of the paper.

Core 4 (C4-TC) and Core 5 (C5-CC) both failed in crushing of the webs. From Figure 9-11 it is observed that both of these cores fail near the web crushing strength for their respective web thicknesses. Recall that the webs of Core 4 (C4-TC) have some uni directional plies oriented perpendicular to the deck which slightly increases the capacity of the webs.

9.4 FINITE ELEMENT ANALYSIS

A finite element analysis was performed to compare measured deflections and strains from the three point bending test with those obtained from the finite element model to assess the reliability of the model for analyzing larger more complex FRP webbed deck structures. In addition finite element analysis of the compression testing was conducted to study the effects of the foam infill on the web buckling. The models were created and analyzed using MSC NASTRAN. The skin laminate and web laminates were modeled using four node quadrilateral composite laminate shell elements and the foam was modeled using solid eight node brick elements with isotropic material properties. The webs are modeled as $[\pm 45]_6$ laminates. The carbon/epoxy and E-glass/epoxy lamina properties used in the model are presented in Table 9-6. For the (3 pcf) polyisocyanurate foam a Young's modulus of 8,600 kPa (1,250 psi), a shear modulus of 1,724 kPa (250 psi), and a Poisson ratio of 0.04 are used. Foam mechanical properties were obtained from the manufacturer and an average of the compressive and tensile modulus in each direction was used. Each core was analyzed using the same model by adjusting the web thickness, material properties, and skin laminate offsets to accurately represent each specimen. The mesh was refined until convergence was achieved resulting in an element size used throughout the models of 12.7 mm (0.5 in).

Table 9-6 Lamina Properties

Lamina	E_{11} *(GPa) [Msi]*	E_{22} *(GPa) [Msi]*	G_{12} *(GPa) [Msi]*	*Poisson Ratio*
Carbon/epoxy	80.0 [11.6]	6.2 [0.9]	4.1 [0.6]	0.3
E-glass/epoxy	34.5 [5.0]	6.2 [0.9]	4.1 [0.6]	0.28

9.4.1 Shear

For the three-point bending finite element model, pinned boundary conditions were applied at the locations of the roller supports and the load was applied as a uniform pressure over an area equivalent to the loading nose used in the testing. A pressure of 5,943 kPa (862 psi), or 138 kN (31 kips) total load, was applied to the model for comparison to the experimental data. Table 9-7 presents a comparison of the experimental strains at the mid-span and quarter points as well as the deflection of each test specimen with values obtained from the finite element model. From the table it is seen that the model shows good agreement with the test data for the deflection and the quarter point strains (11.5% difference or less) with the exception of Core 5 and fair agreement for the mid-span strains which have differences that are 20% or less. Core 3 showed the best agreement with a max difference of 6.3%.

Table 9-7 Experimental and FE Three-Point Bending Test Results

	Deflection			*Mid-Span Strain*			*¼ Span Strain*		
Core Type	Exp. (mm) [in]	FE (mm) [in]	Diff. (%)	Exp. (με)	FE (με)	Diff. (%)	Exp (με)	FE (με)	Diff. (%)
C1-WCH	2.08 [0.082]	2.13 [0.084]	2.4	2730	2280	-16.5	-1160	-1030	-11.2
C2-WCL	2.62 [0.103]	2.46 [0.097]	-4.6	2830	2430	-14.1	-997	-1070	7.3
C3-WE	3.10 [0.122]	3.12 [0.123]	0.8	2770	2630	-5.1	-960	-1020	6.3
C4-TC	2.87 [0.113]	2.54 [0.100]	-11.5	2940	2370	-19.4	-1000	-1080	8.0
C5-CC	2.39 [0.094]	2.21 [0.087]	-7.4	2610	2370	-9.2	-773	-1080	39.7

9.4.2 Compression

For the compression test finite element model the bottom surface elements are fixed against translation in the direction of loading and at the top and bottom surfaces two corner nodes are fixed against translation in the plane of the skin laminates. A unit pressure is applied uniformly over the top surface and a buckling analysis is performed. A model of the compression test is shown in Figure 9-13. The buckling analysis showed the foam to play an important role in the buckling capacity of the webs. A comparison of the measured buckling capacities with the buckling capacity determined by the finite element analysis is presented in Table 9-8. A plot of the finite element results with the experimental results can be seen in Figure 9-11. From the table it is seen that the finite element analysis buckling loads showed good agreement with the measured buckling loads (less than 20% difference). However it was noticed that the buckling loads determined from the finite element model for the foam filled specimens was significantly lower than that predicted by the analytical solution. The analytical solution assumes that each web receives full support by the foam from each side. Looking at the actual test specimens the end webs had approximately 25 mm (1 in) of foam which was unconstrained on the outside. A finite element study was performed to investigate the effects of unconstrained foam thickness and stiffness on the buckling load of the web. A non dimensional plot showing the ratio of the critical buckling load with foam to the critical buckling load without foam ($P_{cr}/(4\pi^2 EI/l^2)$) versus different foam width to web height ratios (w/l) for different foam to web stiffness ratios (k^*) is given in Figure 9-14. The web stiffness ratio is defined as

$$k^* = \frac{k_{foam} l^4}{EI}. \tag{9.2}$$

The foam used in the test specimens (48 kg/m^3 polyisocyanurate) is represented by the stiffness ratio curve k^*= 700. From this curve it is noted that a foam thickness greater than 80 mm is required to reach the maximum buckling capacity of the web. The actual foam thickness of 25 mm used in the test specimens contributes only a small degree of additional stability to the webs. If a stiffer foam is used along the unconstrained edge, for example k^*= 2,000, an equivalent web buckling capacity can be obtained by using an edge foam infill which is only 20 mm wide. In cases where the edge foam of the deck is unconstrained, foam with a higher stiffness should be used to eliminate premature buckling of the edge webs.

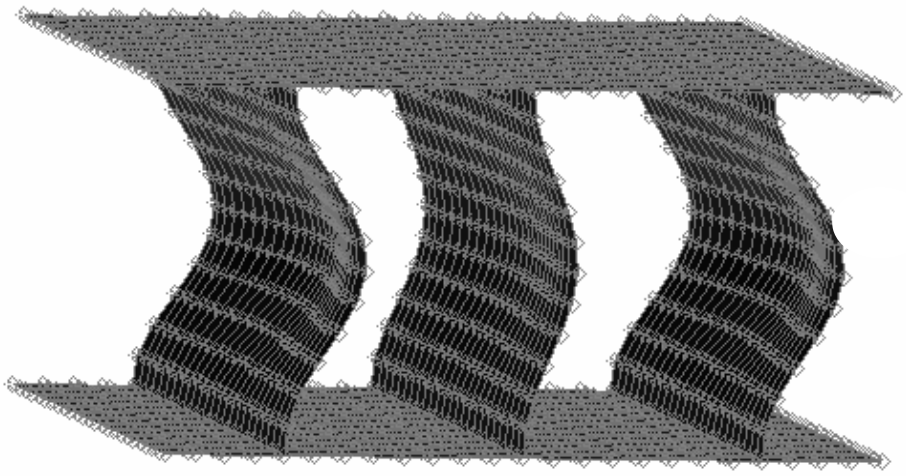

Figure 9-13 Finite element model of compression test showing buckled webs.

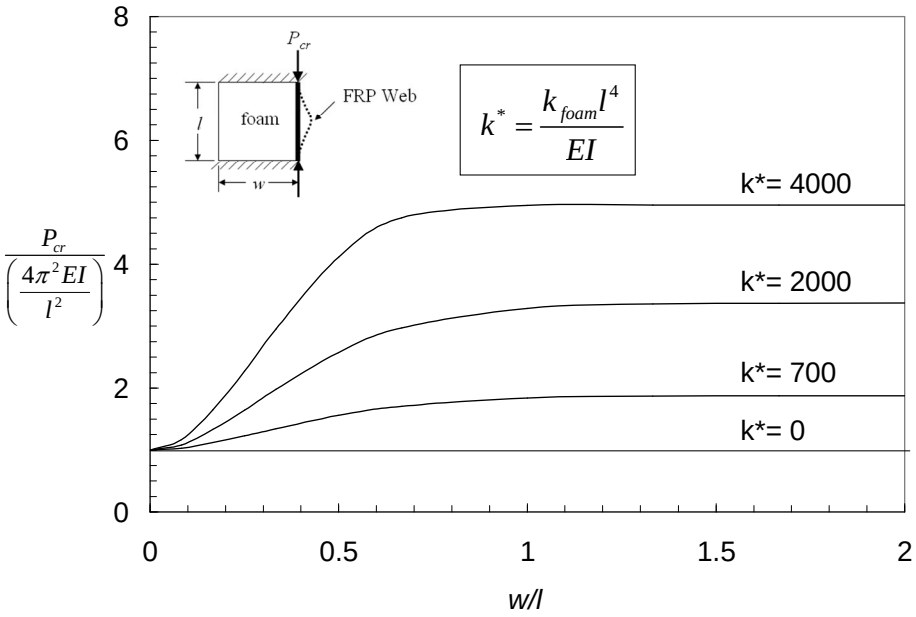

Figure 9-14 Plot of critical buckling load ratio versus foam width to web height ratio for various foam to web stiffness ratios.

Table 9-8 Experimental and FE Compression Test Results

	Buckling Load		
Core Type	*Exp (kPa) [psi]*	*FE (kPa) [psi]*	*Diff. (%)*
C1-WCH w/out foam	9770 [1417]	9610 [1400]	-1.6
C2-WCL w/ foam	4780 [693]	5620 [815]	17.6
C2-WCL w/out foam	2670 [387]	3180 [461]	18.4
C3-WE w/ foam	10600 [1530]	12300 [1780]	13.6
C3-WE w/out foam	9590 [1390]	10500 [1520]	8.5

9.5 DESIGN RECOMMENDATIONS

Based on the results of the shear and compression testing as well as the finite element analysis several recommendations are presented for the design of FRP webbed core sandwich composites.

From the shear tests it was shown that Core 1 (C1-WCH) failed in interlaminar shear between the core and the skins. As was discussed, this type of failure represents the highest load which can be carried by this core at the given web spacing. If higher shear strength is required the web spacing should be decreased to lower the shear load transfer demands for each web to the skins. As more webs are used the thickness of the webs can also be decreased while still considering web stability.

Core 5 (C5-CC) also failed in interlaminar shear between the core and skins at about one half the load of Core 1 (C1-WCH). As has been discussed this failure was a result of having continuous fibers from the webs to skin in only one direction. It is recommended that fibers be wrapped around all sides of the foam beams to provide shear load paths in both directions transverse to the webs.

It was shown that Core 3 (C3-WE) and Core 4 (C4-TC) both failed in shear of the web at the joint between the web and the skin. Because these two cores used filler fabric, only a portion of the fibers from the webs were continuous into the skins. In designing FRP webbed cores it is important to provide adequate continuous plies from the webs to the skins to carry the desired shear load. For design purposes the thickness of the webs considered for shear is only that portion of the plies which are continuous from the webs into the skins.

From the compression testing it was observed that the foam infill can have a significant effect on the buckling capacity of the webs. In cases where weight savings is critical, consideration should be given to using high modulus low weight foams in combination with thinner webs. Core 4 (C4-TC) which used filler fabric with fibers oriented perpendicular to the deck surface also proved effective in increasing the compressive capacity of the core.

To aid in core selection, a plot of the shear strength, compressive strength, and density of each core is given in Figure 9-15. From the figure we see that all of the cores with the exception of Core 2 (C2-WCL) meet or exceed the shear and compressive strength requirements. Core 1 (C1-WCH), which has the highest shear strength, exceeds the shear strength of the balsa core by a factor of 3.2 at a weight which is 28% lighter than the balsa.

A plot of the strength to weight ratio of each core is seen in Figure 9-16. For weight critical structures this plot is useful in determining which core offers the highest performance at the lightest weight. From the figure we see that Core 1 (C1-WCH) offers the greatest shear strength per unit weight while Core 4 (C4-TC) offers the highest compressive strength per unit weight. It is also noted from the plot that removal of the foam greatly increases the shear strength to weight ratio with Core 1 and Core 2 while little change was seen in the compressive strength to weight ratio. All of the cores exceeded the strength to weight ratio of the baseline balsa.

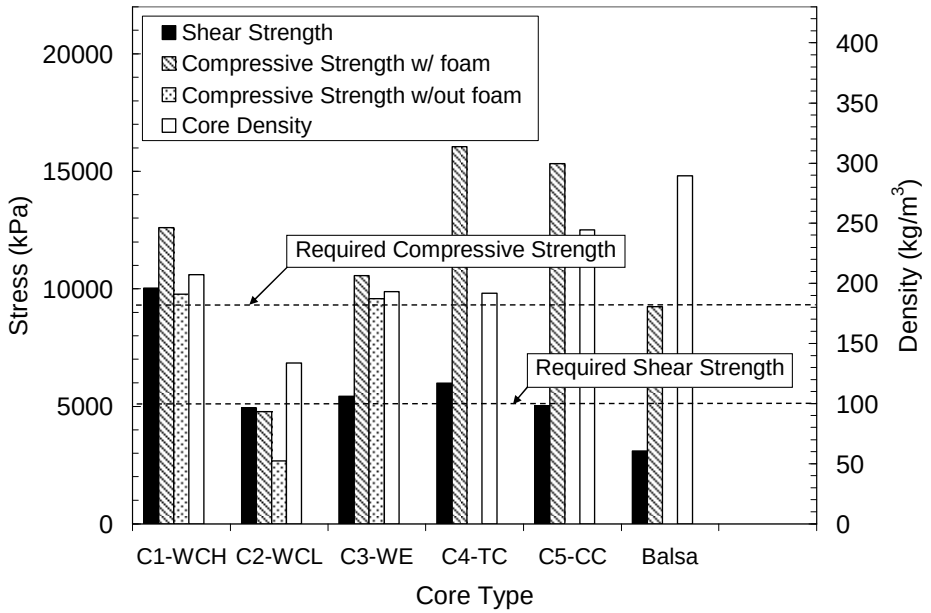

Figure 9-15 Plot of the shear strength, compressive strength, and density of each core type.

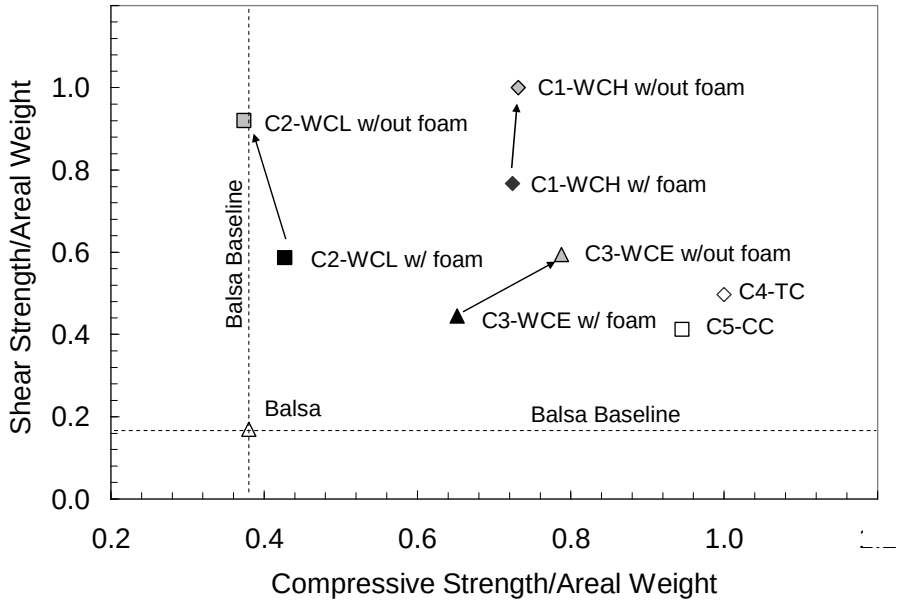

Figure 9-16 Plot of shear strength versus compressive strength normalized by areal weight for each core type.

9.6 PERFORMANCE CRITERIA

A comparison between the FRP decks considered in this study and conventional extruded aluminum decking currently used in the military is made to show the potential weight savings which can be realized through using FRP composites. The existing decking considered is from the Wolverine Heavy Assault Bridge developed by MAN Technologies of Germany and General Dynamic Land Systems of the U.S [107]. The deck has an overall depth of 79 mm (2.9 in) with 5 mm (0.2 in) thick webs spaced at 69 mm (2.7 in) on center with 5 mm (0.2 in) thick skins top and bottom (see Figure 9-17). The material used in the deck is 7005 T6 aluminum with properties given in Table 9-9. With the exception of Core 2 both the aluminum deck as well as the FRP composite decks meet all of the shear and compression strength requirements. The areal weight of the aluminum deck is 44 kg/m3 (9 psf) and the composite FRP decks have an areal weight ranging from 44 to 49 kg/m3 (9-10 psf). Thus, the composite decks are weight comparable to the existing aluminum deck design, but the existing aluminum deck can only span a 1.2 (48 inch) distance between supports and is not capable of spanning the 4 m gap of the currently designed composite FRP decks. In order to make a direct weight comparison between an aluminum deck and current FRP decks, the aluminum deck was redesigned to meet the current 4m gap requirement and overall deck thickness requirement by increasing the overall depth of the aluminum deck to 95 mm (3.75 in) and increasing the skin thickness to 10 mm (0.375 in). Thus, the redesigned aluminum deck has the same depth and matches the bending stiffness of the current FRP decks. The FRP deck skin laminate properties are given in Table 9-9. The resulting areal weight of the

aluminum deck is 68 kg/m^3 (14 psf), which represents a 30-35% weight savings for the current FRP decks over equivalent aluminum decking.

Table 9-9 Material Properties

Material	*Elastic Modulus E_x (GPa) [Msi]*	*Shear Modulus (GPa) [Msi]*	*Poisson's Ratio*	*Ult Strength (MPa) [ksi]*	*Ult Shear Strength (MPa) [ksi]*	*Density (kg/m^3) [1b/in^3]*
AL 7005 T6	71 [10.3]	27 [3.9]	0.33	350	190	2800
				[50.8]	[27.6]	[0.10]
Skin	74 [10.7]	10 [1.4]	0.37	607	NA	1600
Laminate				[88.0]		[0.058]

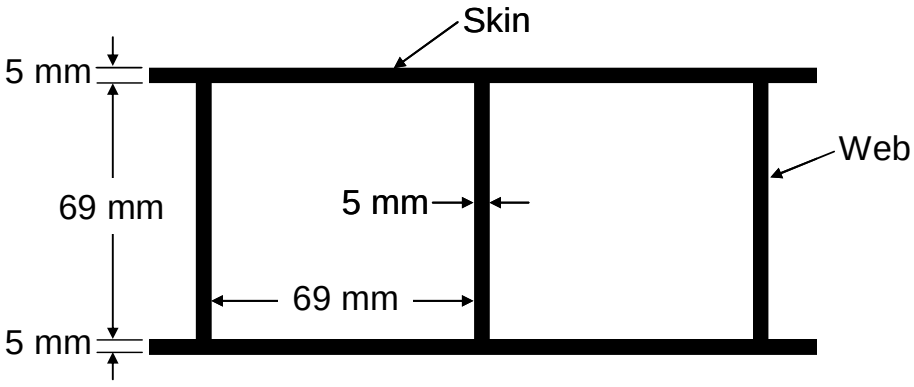

Figure 9-17 Illustration of the extruded aluminum deck with dimensions.

The chapter, in part, is a reprint of the material which appears in the *Journal of Composites for Construction* 2008 volume 12 issue 3 pages 344-354 titled “Light-Weight Fiber-Reinforced Polymer Composite Deck Panels for Extreme Applications.” The dissertation author was the primary investigator and author with advisor J. B. Kosmatka as co-author.

CHAPTER 10

SHORT-SPAN BRIDGING

Currently within the US military there is a need for a light-weight bridging system for crossing short-span gaps up to 4 m (157 in) in length. This bridge must also have a low profile constant thickness of 100 mm (4 in) or less, such that it can be used for other applications including decking for long span modular bridging, roadway matting, overlays for damaged bridge decks, and loading ramp systems for aircraft and ships. Moreover, it is required that the bridging system support Military Load Class 30 (MLC 30, 27,000 kg, 60,000 lbs) track vehicles and Palletized Load System (PLS) truck vehicles under extreme environmental and bank support conditions. For comparison purposes the HS-20-44 truck prescribed by the American Association of State Highway and Transportation Officials (AASHTO) [116] would have an MLC rating between 25 and 30 resulting in maximum moments and shears which are about 10% lower than that produced by an MLC 30 rated vehicle and 15% less than a fully loaded PLS truck.

To address the need for short-span bridging, MAN Mobile Bridges, located in Germany, has developed a commercially available mobile bridge known as the Short Track Bridge (STB) which is capable of spanning gaps up to 4 m in length while supporting MLC 30 vehicles [107]. The bridge is composed of two parallel treadways fabricated using high strength aluminum. Each treadway is 5.2 m (205 in) long and 0.6 m (24 in) wide, with the bridge depth varying along the length having a mid-span

maximum depth of 0.28 m (11 in). A single treadway weighs 250 kg (550 lbs) with the full bridge weighing 500 kg (1,100 lbs). A photograph of the Short Track Bridge is shown in Figure 10-1.

Figure 10-1 Photograph of the Short Track Bridge developed by MAN Mobile bridges.

Recently Wight et al. [117] presented the development and testing of an FRP short-span bridge developed for the Canadian Forces (CF). The bridge consists of two treadways fabricated from pultruded fiberglass tube sections and sheets which are bonded together to form a tapered box beam (treadway) which is 4.8 m (189 in) long and 1.2 m (48 in) wide. As with the aforementioned MAN bridge, the bridge depth varies along the length from 0.1 m (4 inches) at the ends to 0.5 m (20 inch) at the mid-span. A single treadway weighs 500 kg (1,100 lbs) and is designed to carry a vehicle weighing 27,000 kg (60,000 lbs). This weight does not include a wear surface or launching hardware. While both the MAN aluminum and Wight composite bridges

are different approaches for light-weight short-span emergency portable bridging, due to their large mid-span section depths neither of these satisfies the current US Army's requirements for low-profile, constant depth, versatile bridging considered in this study.

Based on the success of the webbed cores previously investigated, this research utilizes an FRP webbed core which offers increased strength at a reduced weight in comparison to balsa. The development of full scale bridge treadways using the webbed core is described in this study.

10.1 REQUIREMENTS

The design of the bridge treadway system is driven by performance requirements provided by the US Army and outlined in the Trilateral Design and Test Code for Military Bridging and Gap-Crossing Equipment (TDTC) [118]. The TDTC is a design and test code for military gap-crossing equipment which was developed through a cooperative effort between the United States, Germany, and the United Kingdom. The intent of the code is to provide a common set of design and testing procedures as well as requirements which allows equipment (bridges) tested in one country in accordance with the TDTC to be suitable for international acceptance. The requirements are (1) the bridge treadways must be light enough to be handled by military personnel without the assistance of heavy lifting equipment such as cranes or forklifts, (2) the treadways need to support both MLC 30 track and PLS truck vehicles over a 4 m (157 in) gap, (3) the treadways shall have a maximum constant depth of

100 mm (4 in), (4) the treadways must be wide enough to be safely crossed by the prescribed vehicles, (5) the maximum deflection of the treadways under full working load is to be limited to 152 mm (6 inches) (to maximize weight savings, allowable deflections for military bridges are significantly higher than those for civil bridges), (6) a minimum safety factor of 1.5 with respect to B-basis material strength properties shall be maintained for all components of the treadways, and (7) the treadways must be capable of performing under temperatures ranging from –46 °C (-50 °F) to 71 °C (160 °F). Additional gap crossing site criteria found in the TDTC [118] require that the bridge be designed to perform at sites in which (1) The bank soil maximum bearing pressure is 380 kN/m^2 (8 kips/ft^2), (2) the slope from the near to far bank is ±1:10, and (3) the transverse slopes of the near and far banks are up to 5% (10% relative slope if each banks slope in opposite directions). Due to the short length of the treadways the transverse bank slope requirement was relaxed to a total relative slope between the near and far banks of 5%.

10.2 DESIGN AND ANALYSIS

The design of the treadways involves first determining the critical vehicle loads, followed by calculating the critical internal moment and shear distributions and finally performing a detailed finite element analysis.

The design vehicles nominal axle loads and axle spacing are presented in Figure 10-2 (MLC 30) and Figure 10-3 (PLS truck). Due to the limited length of the treadways it was determined that the three rear axles of the PLS truck represented the

critical load case (see highlighted axles in Figure 10-3). The maximum (or working) axle loads are obtained by increasing the nominal axle loads to include the effects of (1) vehicle dynamic impact, (2) the bridge placed on a transverse slope which increases the loads on the lower (downhill) treadway and (3) the vehicle wheel load pads not centered with the treadway center line (commonly called eccentric loading). The impact (1.2) and side slope (1.05 MLC 30 and 1.063 PLS) load factors are included based upon TDTC requirements [118], where as the vehicle eccentricity effects are included within the finite element model applied loading.

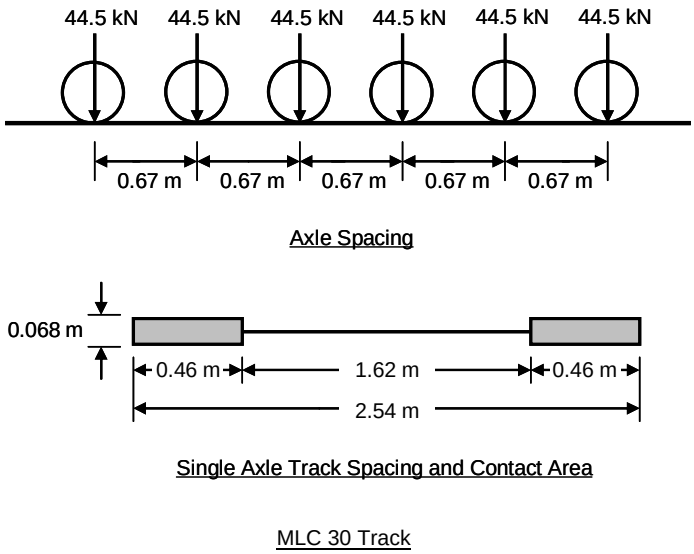

Figure 10-2 MLC 30 track nominal axle loads, spacing, and track contact areas.

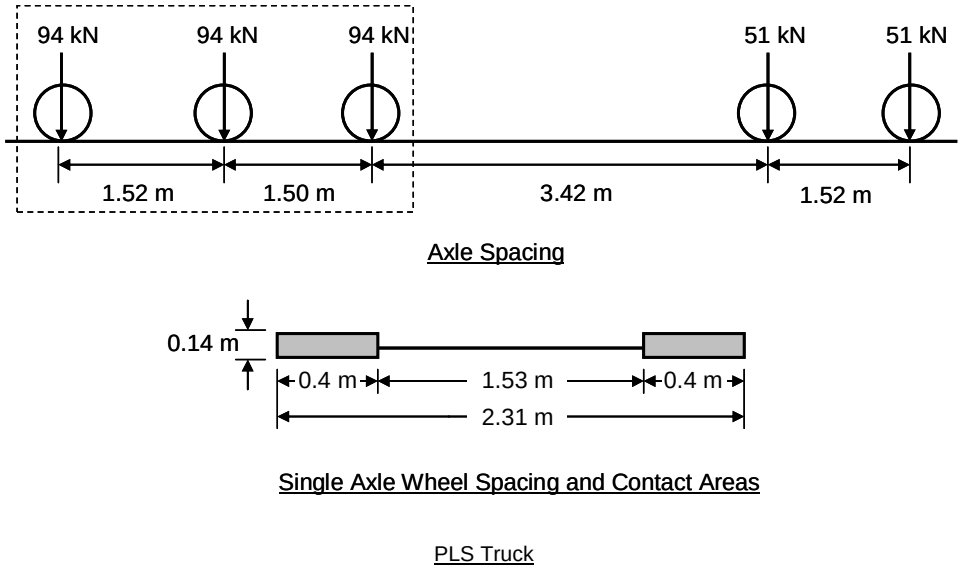

Figure 10-3 Fully loaded PLS truck nominal axle loads, spacing, and wheel contact areas.

The bridge length was determined to be 5.6 m (220 in) such that the bearing pressure at the bank seats due to the maximum vehicle load does not exceed the allowable bearing pressure given by the requirements. Each bridge treadway width was determined to be 0.76 m (30 in) such that the design vehicles can cross with 0.15 m (6 inches) clearance from either side. Due to the short crossing distance the US Army deemed the 0.76 m (30 in) treadway width to be adequate for safe crossing. The dimensions of a single bridge treadway are given in Figure 10-4.

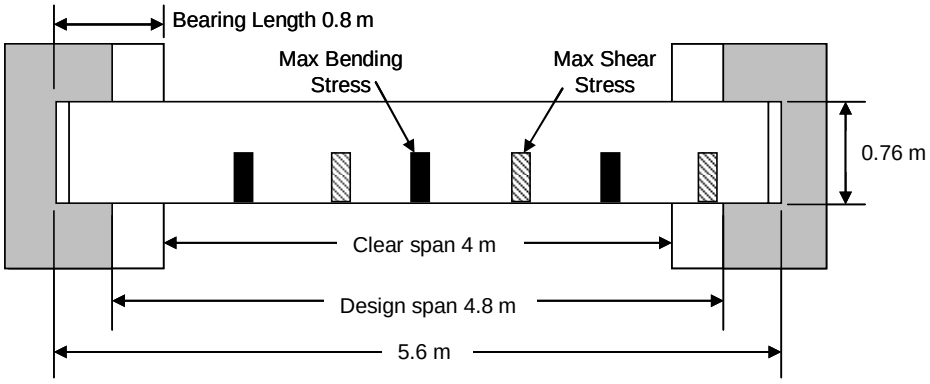

Figure 10-4 Illustration of treadway dimensions, gap geometry, and PLS truck locations for max bending and shear stress.

In accordance with the TDTC [118] the design span is taken to be the distance between the centroid of the bearing area at each bank. For a 4.0 m (157 in) clear span and a total bridge length of 5.6 m (220 in) the design span is 4.8 m (189 in) (see Figure 10-4). Based on the design span, maximum moment and absolute shear envelopes were produced for each design vehicle working load (Figure 10-5). The moment and shear envelopes were created by finding the maximum moment and shear created by each vehicle at each position on the treadway. It is seen that the PLS truck is the critical vehicle for design producing a maximum moment of 120 kN·m (88.5 k·ft) and a maximum shear of 122 kN (27.4 kips).

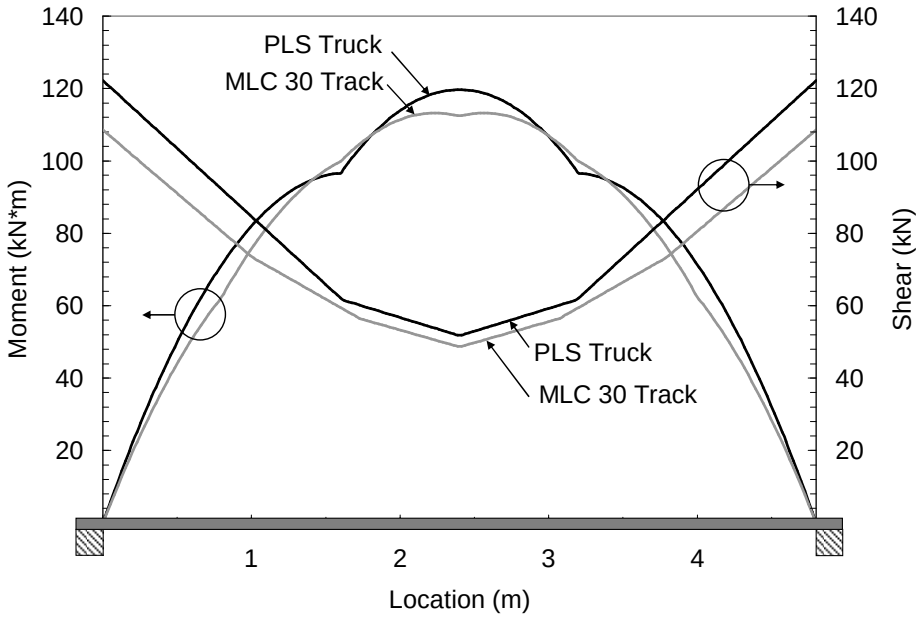

Figure 10-5 Plot of maximum moment and shear envelopes.

In order to meet the weight and bending stiffness requirements, the treadways have upper and lower skins consisting of carbon/epoxy laminates and a celled core composed of E-glass/epoxy webs spaced at 51 mm (2 in) on center. The core (C3-WE) was selected from a number of FRP webbed cores previously tested and evaluated. The core was shown to have adequate shear strength and compressive strength to resist global loading as well as local wheel or track loads. The core is a fiberglass webbed core which is produced by winding fiberglass roving around individual foam beams which are assembled together with filler fabric between the beams to increase the web thickness [115].

Based upon extending well correlated models of the webbed core deck a finite element model of a single treadway was created and analyzed using MSC NASTRAN. The model was created using four node composite shell elements for the skins and

four node single ply orthotropic elements for the vertical web core. See Figure 10-6. The material properties used in the model as well as the B-basis allowable strength properties given in Table 10-1 are based upon previous experimental testing of the carbon/epoxy skin laminates [108] and the E-glass/epoxy core. The carbon/epoxy top and bottom skins were sized as 11 mm (0.43 in) and 8 mm (0.3 in) thick, respectively, in order to meet the maximum deflection requirements of 152 mm (6 in), where the different thicknesses are a result of the differing tensile and compression strength of the carbon epoxy (see Table 10-1). A minimum skin laminate thickness of 8 mm (0.3 in) was used to prevent puncture failure due to concentrated rock loads based upon previous studies [108]. The skins consist of a 0.61 kg/m^2 (18 oz/yd^2) five harness (5H) satin weave and 0.61 kg/m^2 (18 oz/yd^2) unidirectional (uni) carbon. The layup of the treadway skins and core is given in Table 10-2.

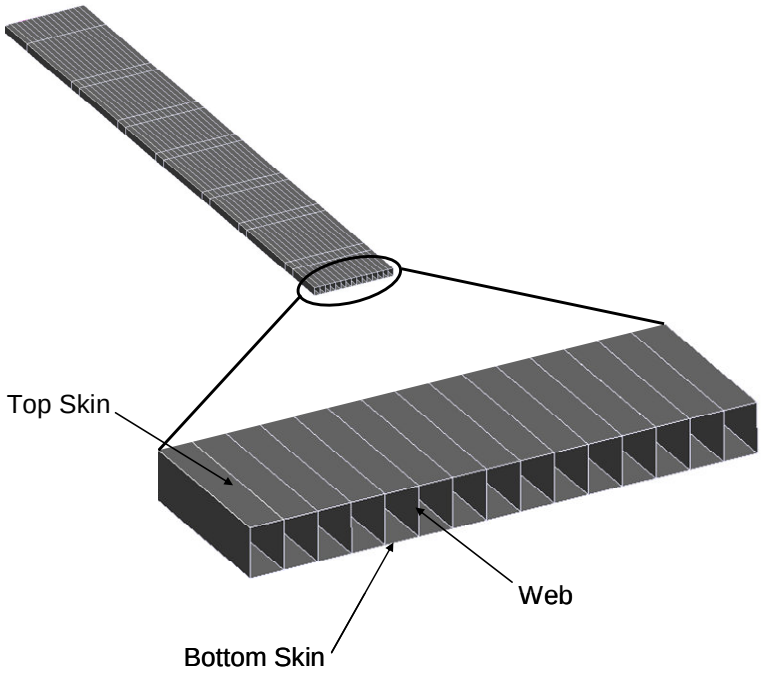

Figure 10-6 Illustration of a cross section of the finite element model showing the treadway skins and webs. End cap is not shown for clarity.

Table 10-1 Material Properties (B-basis Strength Properties)

Property	*5 Harness Satin Weave T300C-12k*	*Unidirectional Toho-24k*
E_{xt} (GPa) [Msi]	65.0 (9.4)	105.0 (15.2)
E_{xc} (GPa) [Msi]	58.0 (8.4)	91.0 (13.2)
E_{yt} (GPa) [Msi]	67.0 (9.7)	8.0 (1.1)
E_{yt} (GPa) [Msi]	57.0 (8.2)	8.0 (1.1)
G_{xy} (GPa) [Msi]	4.0 (0.6)	5.0 (0.7)
υ_{12}	0.04	0.32
X_t (MPa) [ksi]	616.0 (89.3)	883.0 (128.0)
X_c (MPa) [ksi]	381.0 (55.3)	536.0 (77.8)
Y_t (MPa) [ksi]	580.0 (84.1)	17.0 (2.4)
Y_c (MPa) [ksi]	378.0 (54.8)	79.0 (11.5)
S (MPa) [ksi]	39.0 (5.6)	32.0 (4.7)

Table 10-2 Deck Layup

No. of plies	*Material*	*Thickness (mm)*	*Orientation*
1 (top)	5H	0.7	0
1	5H	0.7	45
4	Uni	0.8	0
1	5H	0.7	0
4	Uni	0.8	0
1	5H	0.7	45
1	5H	0.7	0
2	Uni	0.8	0
core		76.0	0
2	Uni	0.8	0
1	5H	0.7	0
1	5H	0.7	45
2	Uni	0.8	0
1	5H	0.7	0
2	Uni	0.8	0
1	5H	0.7	45
1 (bottom)	5H	0.7	0

Several load cases were investigated using the finite element model to determine the maximum stresses produced in the skins and the core. The critical load case for the skins (maximum bending stress) is the PLS truck located at the treadway mid-span with the wheels located along one edge. The critical load case for core shearing is the PLS truck located such that the leading wheel is at the support with the wheels located along one edge. An illustration of the critical load cases is seen in Figure 10-4. Recall that the loads considered for the PLS truck are the rear three axles of the PLS truck. In addition to the vehicle load an additional mud load of 0.75 kN/m^2

(16 psf) is added per TDTC [118]. Both load cases are combined with 2.5% transverse bank slopes in opposite directions creating twisting in the treadway. A safety factor of 1.5 was used throughout the design along with experimentally measured B-basis allowable material properties for all composite laminates. From the critical load cases a ply by ply analysis using maximum stress criteria with respect to B-basis allowable material properties showed the upper skin to have a margin of safety (*MS*) of (+0.48) and the lower skin to have a margin of safety of (+0.92), where

$$MS = \left[\frac{\sigma_a}{\sigma_s \cdot FS} \right] - 1. \tag{10.1}$$

Here σ_a is the allowable stress for a given lamina (B-Basis allowable), σ_s is the stress in a given lamina at working load, and *FS* is the factor of safety (1.5). The shear load case showed the webbed core to be the critical component having a margin of safety of (+0.13). A summary of the critical lamina stresses, allowable B-basis strength properties, and margins of safety for each of the treadway components is given in Table 10-3.

Table 10-3 Margins of Safety

Location	*B-basis (MPa) [ksi]*	*Max Stress (MPa) [ksi]*	*Margin of Safety*
Top Skin	-536 (-77.8)	-243 (-35.2)	0.48
Bottom Skin	883 (128.0)	307 (44.5)	0.92
Webs (shear)	73 (10.6)	43 (6.3)	0.13

The bridge treadway ends experience high impact loads as vehicles enter and exit. To increase the treadway end durability, a 5 mm (0.1875 in) thick aluminum end cap was installed with a 9.5 mm (0.375 in) sacrificial tapered end ramp. The end cap extends 915 mm (36 in) on the bottom surface to protect the bearing surface and 760 mm (30 in) on the top surface to protect against vehicle wheel impact. In addition to the aluminum end caps, a 3 mm (0.125 in) thick polyurethane wear coating is applied to all surfaces of the treadways to protect the carbon/epoxy laminates. During the CAB project 14 different wear surface coatings were tested at extreme environmental conditions with numerous vehicle crossings with none performing as well as the polyurethane [5].

10.3 FABRICATION

Two treadways (one bridge) were fabricated using the Seemann Composite Resin Infusion Molding Process (SCRIMP) [18] method, a variant of the Vacuum Assisted Resin Transfer Molding (VARTM) process. The treadways are fabricated by laying up the top skin fabric on the mold followed by the core and then the placement of the bottom skin fabric plies. The plies from the top skin are interleafed with the bottom skin plies to provide a continuous load path from the top skin to the bottom skin along the treadway edges. Following the placement of the dry performs and core the assembly is covered with a layer of peel ply followed by a highly permeable SCRIMP layer and vacuum bag. The resin inlet is placed at the top of the treadway assembly and the vacuum outlets are placed along the edges. One advantage of using

the webbed core is that it provides a path for the resin to get from the top laminate to the bottom laminate without the need of drilling holes or providing other flow paths through the core thickness. An illustration of the SCRIMP process showing the cross section of the treadway is seen in Figure 10-7. Fiber volume fraction measurements of sub scale samples in accordance with ASTM D3171 showed the skins to have fiber volume fractions from 50-55% and the webs to have fiber volume fractions from 40-45%.

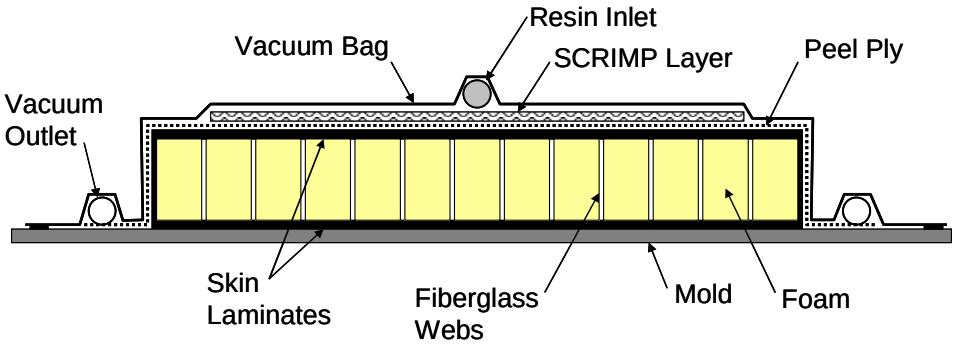

Figure 10-7 Illustration of SCRIMP process for infusing of treadways.

To satisfy the extreme temperatures which the treadway/deck must operate EPON 862 epoxy with Lindride 6 hardener is used which has a glass transition temperature exceeding 93°C (200°F) when properly post cured. Following the infusion of the treadways they were cured at a temperature of 82°C (180°F) and then post cured at 212° C (250°F). The resulting weight of each carbon/epoxy treadway was 204 kg (450 lbs).

Following the final cure of the treadways the aluminum end caps were bonded to the treadways using a high strength adhesive (Hysol 9394), where each aluminum

end cap weighed 28.5 kg (62.5 lbs). At the ends of the treadway where the end caps are installed a layer of fiberglass was placed on the surface during the infusion to eliminate potential galvanic corrosion between the carbon/epoxy and the aluminum.

Finally all surfaces (top, bottom, and edges) of the treadways were sand blasted, cleaned with a solvent, and then the polyurethane wear surface was applied by spraying a number of thin coats, where the final coat included embedded fine aggregate for improved traction for both foot traffic and vehicles. The thickness of the wear surface is 3 mm (0.125 inch) and the added weight is 80 kg (175 lbs) per treadway. The final weight of each bridge treadway is 340 kg (750 lbs). In the current study 24 strain gages were applied directly to the treadway carbon/epoxy surfaces before the wear surface was applied so that they would be protected from crossing vehicles.

In cases where the treadways are for temporary use and the wear surface and aluminum end caps are not required, the weight of each treadway may be significantly reduced. The skins could be reduced to 7 mm (0.3 in) top and bottom with the depth of the treadway still being limited to 0.1 m (4 in) giving a margin of safety of (+0.05). The estimated weight of each treadway is 177kg (390 lbs).

10.4 STRUCTURAL PROOF TESTING

Structural proof tests were performed on each treadway at the Powell Structural Laboratories on the University of California, San Diego campus to ensure that the performance requirements and design goals were achieved. The US Army

specified proof test requires that the critical working load moment and shear be reproduced as well as an overload (1.33 x working load) moment and shear. The working and overload shear loading is applied using a US Army supplied six-point whiffle tree fixture, where as the working and overload bending moment distribution is applied by converting it to a two-point load fixture. See Figure 10-8 for the load distribution produced by each of the load fixtures. The load pads are 0.66 m (26 in) long by 0.18 m (7 in) wide. To achieve the PLS working load moment (120 kN·m) and overload moment (169 kN·m) 128 kN and 170 kN loads respectively were applied using the two-point load fixture. To achieve the PLS working shear (122 kN) and overload shear (162 kN) 221 kN and 277 kN loads respectively were applied using the six-point whiffle tree load fixture.

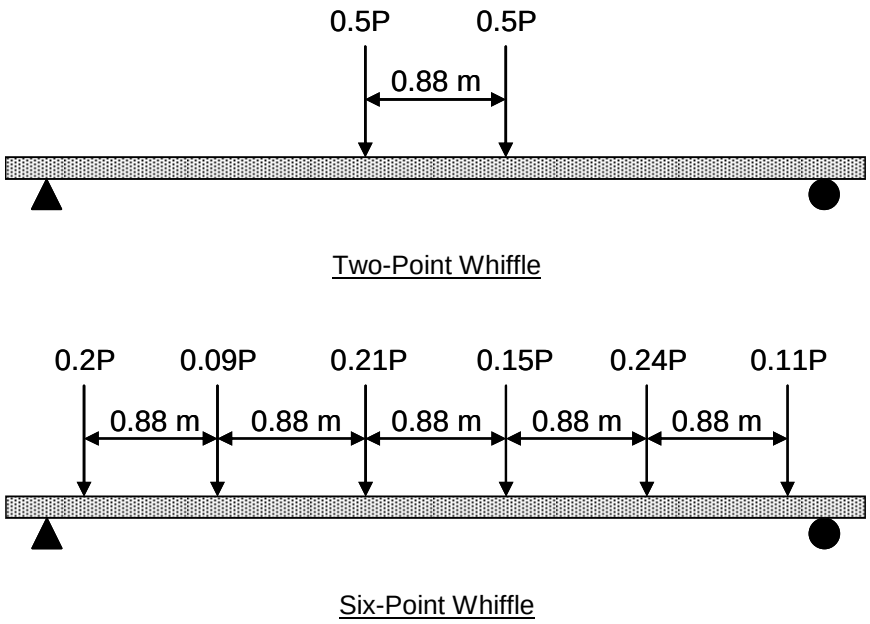

Figure 10-8 Illustration of two-point bent and six-point whiffle load fixtures.

Each treadway was instrumented with sixteen (6 mm) linear strain gages and eight strain gage rosettes, where the strain gages were installed prior to the application of the polyurethane wear surface. The strain gage locations are shown in Figure 10-9, where strain gages are located on the top and bottom surfaces at the mid-span and quarter spans. Gages are located both along the treadway center line as well as on either side of the center line to document unbalanced loading or treadway twisting. The rosettes located at the upper and lower treadway surface center points were used to measure longitudinal and transverse bending as well as in plane skin surface shear. Three rosette strain gages were also located along each side edge of the treadways to measure the shear strain at the supports and mid-span.

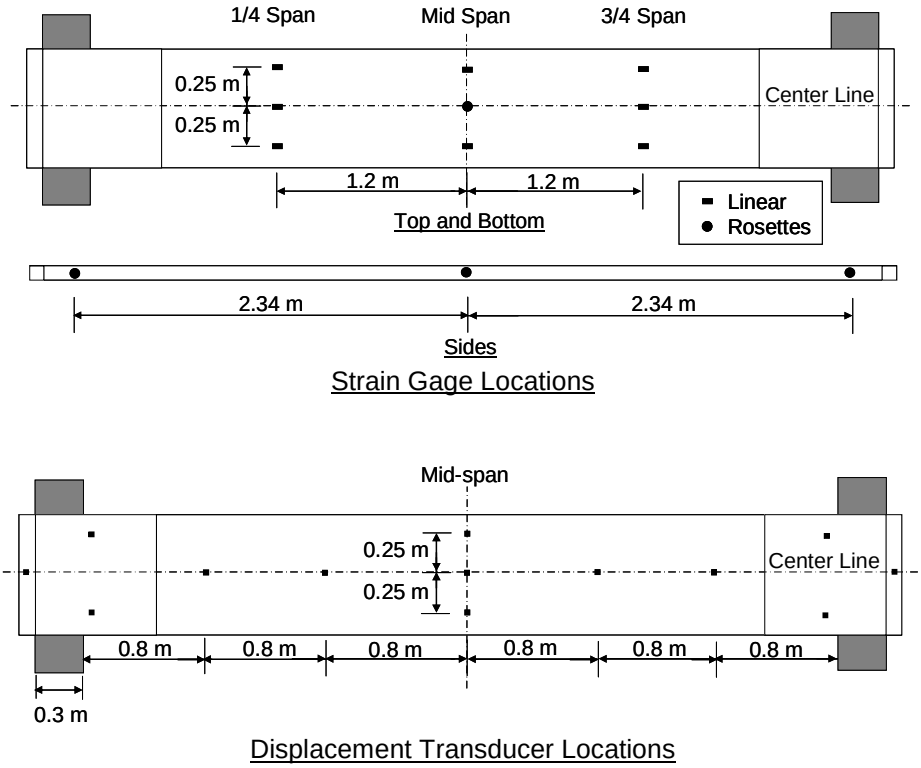

Figure 10-9 Strain gage and displacement transducer locations.

Each treadway was supported on floor mounted hardwood blocks and 38 mm (1.5 in) thick rubber bearing pads. The distance between the inside faces of the support blocks and rubber pads was the design span: 4.8 m (189 in). Thirteen linear potentiometer displacement transducers having a 300 mm (12 in) stroke were positioned as shown in Figure 10-9, where transducers were located along the center line to capture longitudinal treadway bending as well as along the mid-span to document treadway transverse bending and twisting. Moreover, displacement transducers were located on either side of the supports to measure compression or permanent settlement of the rubber bearing pads and support blocks. All test loads were applied with a 500 mm (20 in) stroke 660 kN (150 kip) actuator attached to a large overhead reaction frame. See Figure 10-10. The US Army specified proof test as described in the TDTC [118] requires that the bridge treadways first pass a working load test followed by an overload test without any permanent set or nonlinear response. The working load test involves applying increasing load increment cycles with two minute holds, up to the working load. The overload test consists of four load applications. The first application involves increasing load increments, with two minute holds, up to overload where a 30-minute hold is required. The second and third load cycles go from zero load to overload with a two minute hold and then unload. The fourth load application is a repeat of the first load application. The working load and overload tests were performed on each treadway using both the six-point and two-point load fixtures. A diagram showing the loading protocol for the bending proof test (two-point) is seen in Figure 10-11. A plot of the load versus mid-span displacement for all ten cycles of the two-point load test is shown in Figure

10-12, where both treadways behaved linearly through the entire proof test with the finite element model slightly over predicting the treadway stiffness by about 7%. The treadway displacement at each load increment for the two-point test is given in Figure 10-13, where the maximum displacement for the working load was 123 mm (4.8 in) and 160 mm (6.3 in) for the overload. The maximum displacement requirement was not exceeded. Strain and displacement measurements did not indicate any twisting or unbalanced loading throughout the testing.

Figure 10-10 Photo of proof test using whiffle tree.

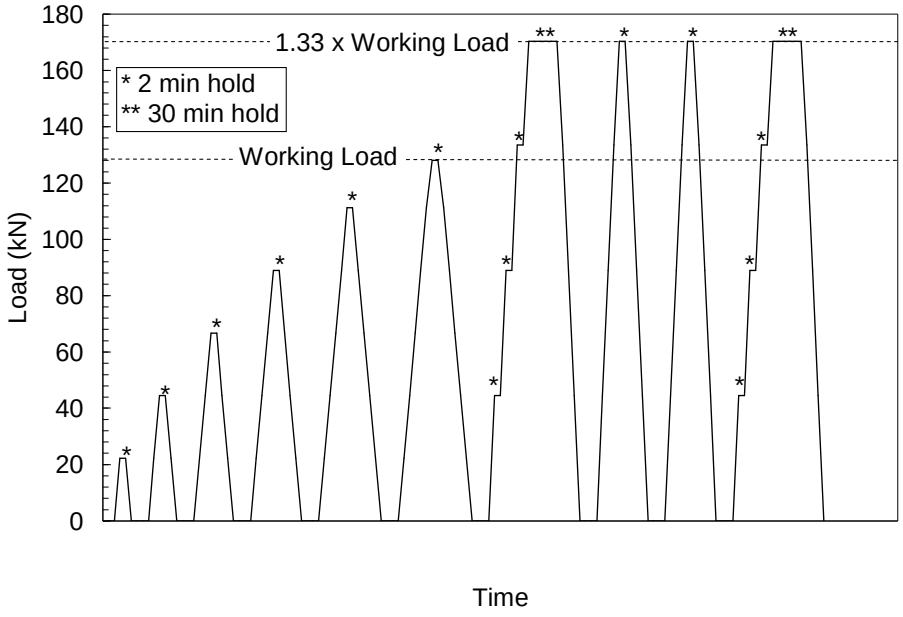

Figure 10-11 Bending proof test loading protocol.

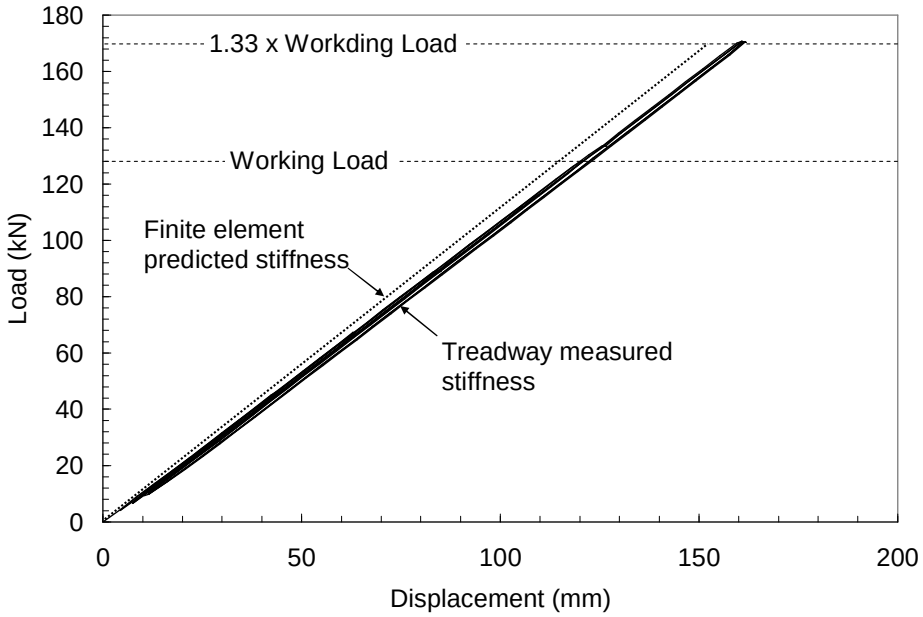

Figure 10-12 Plot of Load vs. mid-span deflection for two-point proof test.

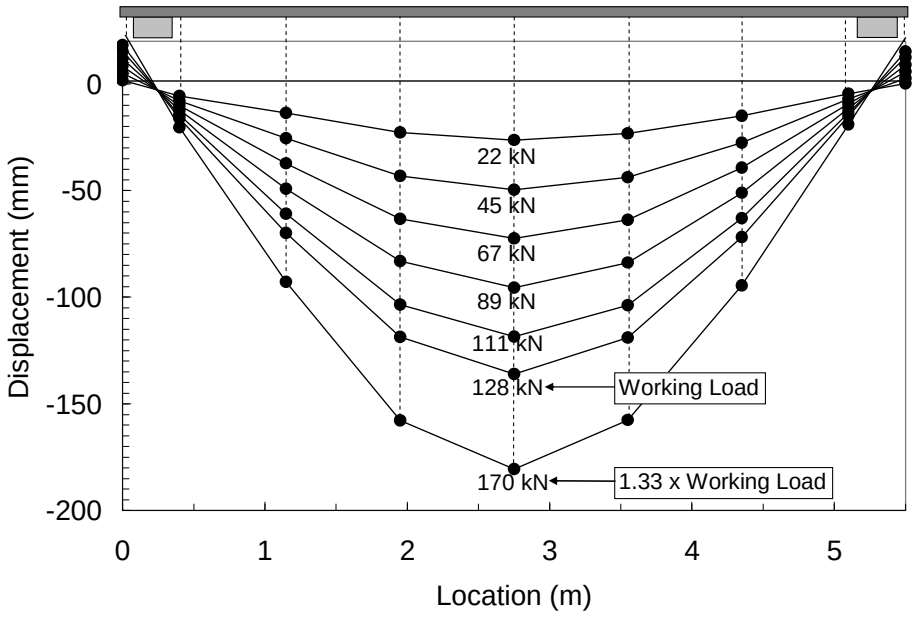

Figure 10-13 Two-point bend test measured deflections.

Comparisons of the working load moment and shear envelopes for the MLC 30 and PLS truck vehicles with the actual moments and shears achieved during the proof testing is seen in Figure 10-14 and Figure 10-15 respectively. From Figure 10-14 it is observed that the PLS truck working load moment was achieved at the center section of the treadway using the two-point fixture. As one moves toward the ends of the treadways it is observed that the two-point load fixture falls just short of reaching the PLS working load moment, however the six-point whiffle fixture is able to reach the working load moment in these regions. In a similar fashion, looking at Figure 10-15, it is seen that the maximum working shear is achieved at the ends of the treadways using the six-point whiffle fixture and the quarter points using the two-point load fixture. Although the working load shear is not achieved along the entire length of the

treadway the design is unchanged along the length of the treadway, thus the same bending and shear strength can be assumed along the entire treadway length.

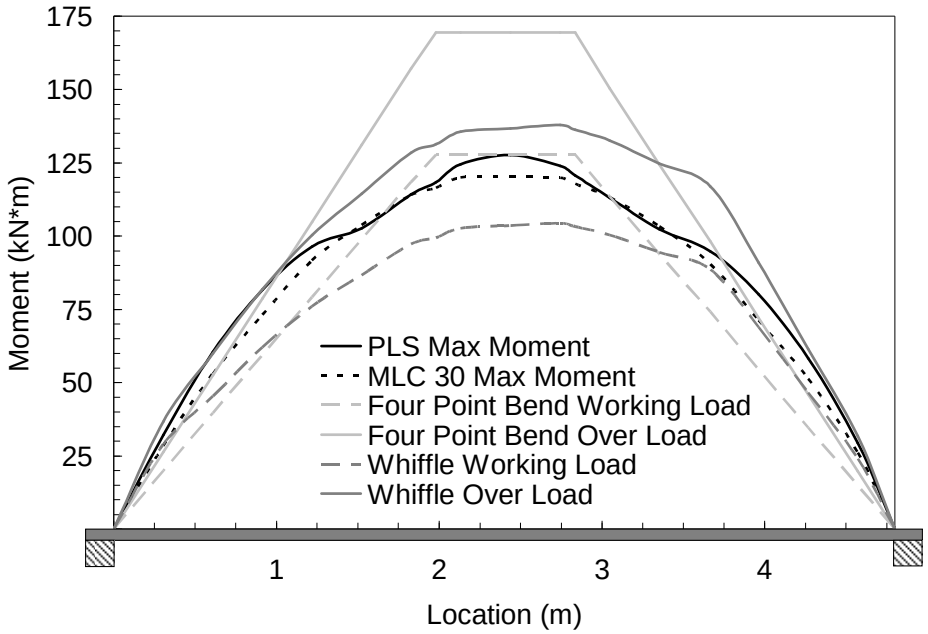

Figure 10-14 Plot of moment diagrams for design vehicles and proof testing.

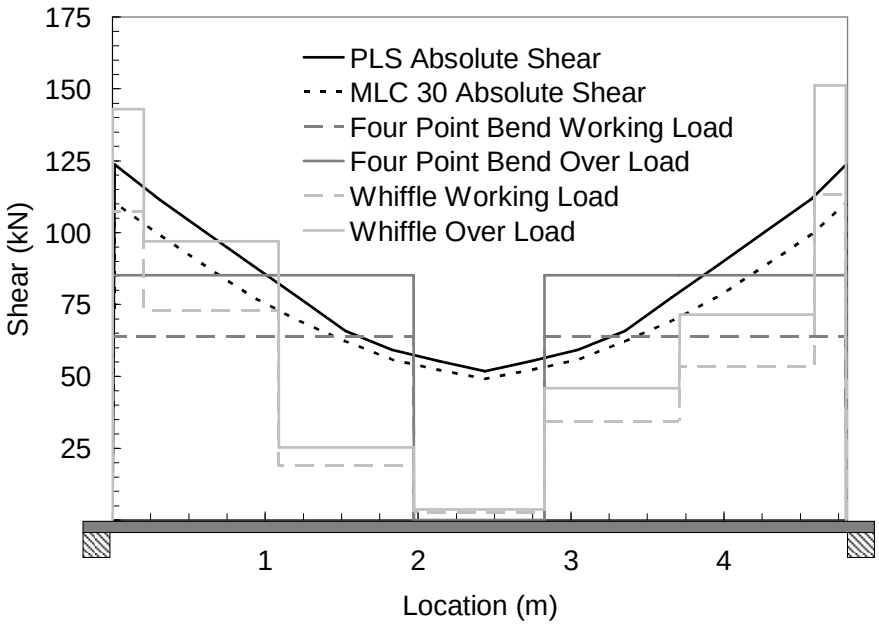

Figure 10-15 Plot of absolute shear diagrams for design vehicles and proof testing.

To validate the finite element model used in the design a comparison between the measured and predicted strains along the center line of the treadways as well as mid-span deflections are summarized in Table 10-4. All of the measurements with the exception of the mid-span strain on the top surface show differences which are less than 10%. In general the deflections were under predicted and the top skin strains were over predicted while the bottom skin strains were under predicted suggesting that the material compressive moduli used in the model may be slightly high.

Table 10-4 FE Model vs. Proof Testing Strains

		Treadway 1		*Treadway 2*	
Measurement Location	*Model*	*Exp.*	*Diff. (%)*	*Exp.*	*Diff. (%)*
¼ point top (μs)	-1400	-1317	6.3	-1346	4.0
¼ point bottom (μs)	1660	1803	-7.9	1667	-0.4
Center top (μs)	-2450	-1955	25.0	-2172	12.8
Center bottom (μs)	2900	2948	-1.6	3122	-7.1
¾ point top (μs)	-1400	-1278	9.5	-1369	2.3
¾ point bottom (μs)	1660	1833	-9.4	1822	-8.9
Center disp. (mm)	114	123	-7.4	123	-7.2

10.5 FIELD TESTING

Field testing of the treadways was performed at the Aberdeen Test Center (ATC), Aberdeen Proving Grounds, Maryland during the Spring of 2007. the focus of the field testing was two-fold. First, the treadway fatigue performance was studied

using fully loaded Palletized Load System (PLS) trucks crossing at speeds between 5 mph and 7 mph. 1,600 crossings were performed over a 5-day period. The second testing phase involved determining the dynamic impact load factors of the treadways as a function of vehicle type, crossing speed, and bridge bank (abutment) preparation.

A crossing site, which was prepared using earth moving equipment, was located in virgin soil with the gap measuring 20 cm (8 in) deep and 4.8 m (189 in) across. At each edge of the gap, a 20 cm x 20 cm (8 in x 8 in) timber abutment was emplaced such that it was level with the undisturbed soil surface. 10 cm x 10 cm (4 in x 4 in) separator timbers were placed between the abutments timbers to prevent any relative displacement between the two abutments during vehicle crossings. The two bridge treadways were placed on the abutments with a gap between the treadways of 122 cm (48 in). The treadway spacing was determined to allow the selected vehicles to cross safely with adequate inner and outer clearance from the treadway edges. The treadways were anchored to the soil at each corner to prevent them from moving during vehicle crossing. An illustration providing dimensions of the crossing site and treadways is seen Figure 10-16.

Each treadway is instrumented with 18 linear strain gages. Nine of the gages are located on the top surface with three gages across the width at the ¼-span, mid-span, and ¾-span locations with corresponding gages located on the bottom surface of the treadways. These are the same strain gages that were used in the proof testing. See Figure 10-9 (upper).

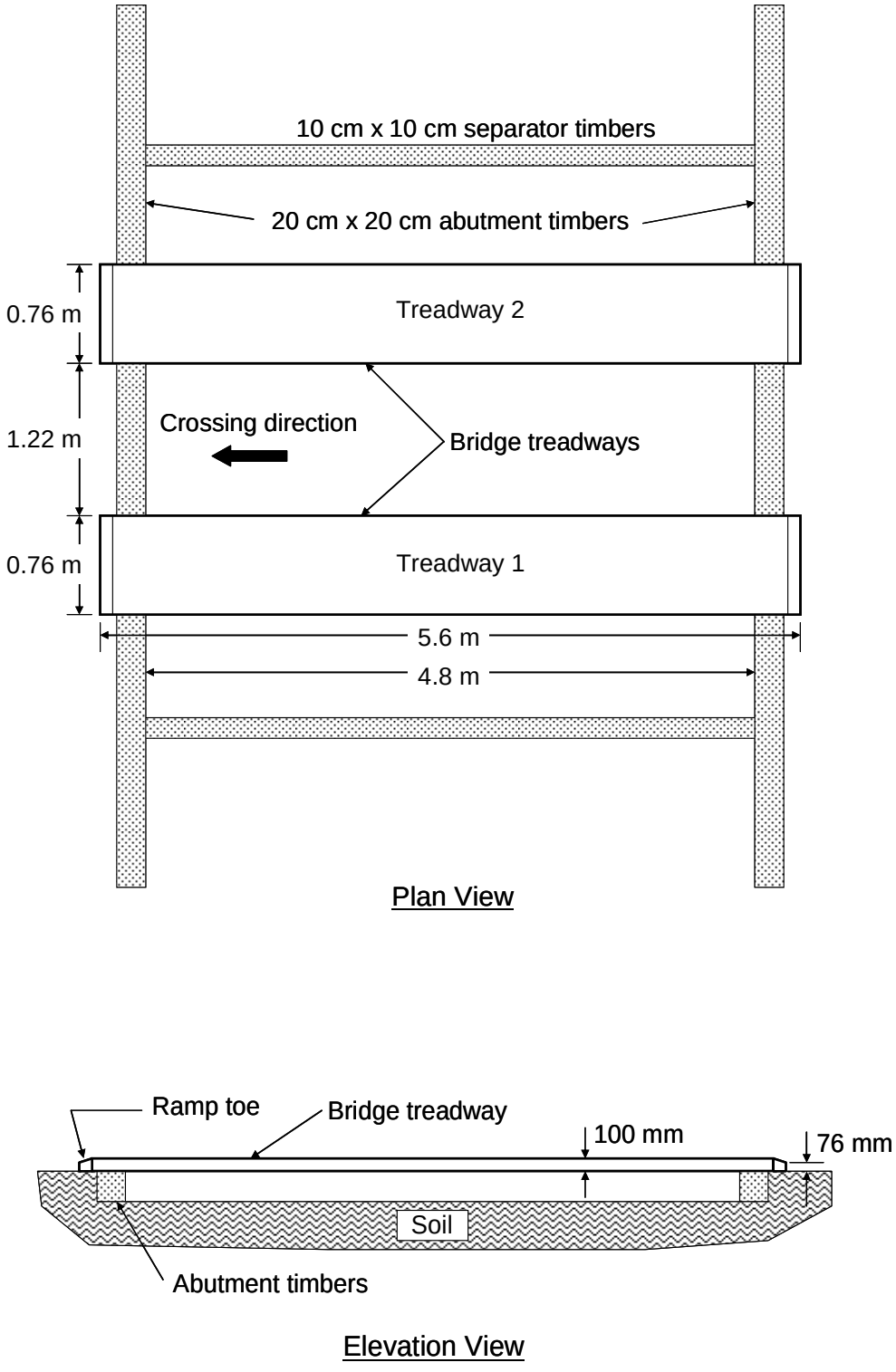

Figure 10-16 Illustration of the test setup showing the bridge treadways and gap dimensions.

Initially a PLS truck was slowly driven across the treadways and stopped for a period of 10 seconds with each axle positioned at the treadway mid-span (Figure 10-17). In Figure 10-18, a plot of the bottom mid-span skin strain is presented, where it is observed that the maximum strain occurs when the center of the rear three axles is at the mid-span. Prior to testing, the fully loaded PLS truck was weighed at 382 kN (86 kips) which is within 1% of the design PLS truck.

Figure 10-17 Photograph of PLS truck on treadways.

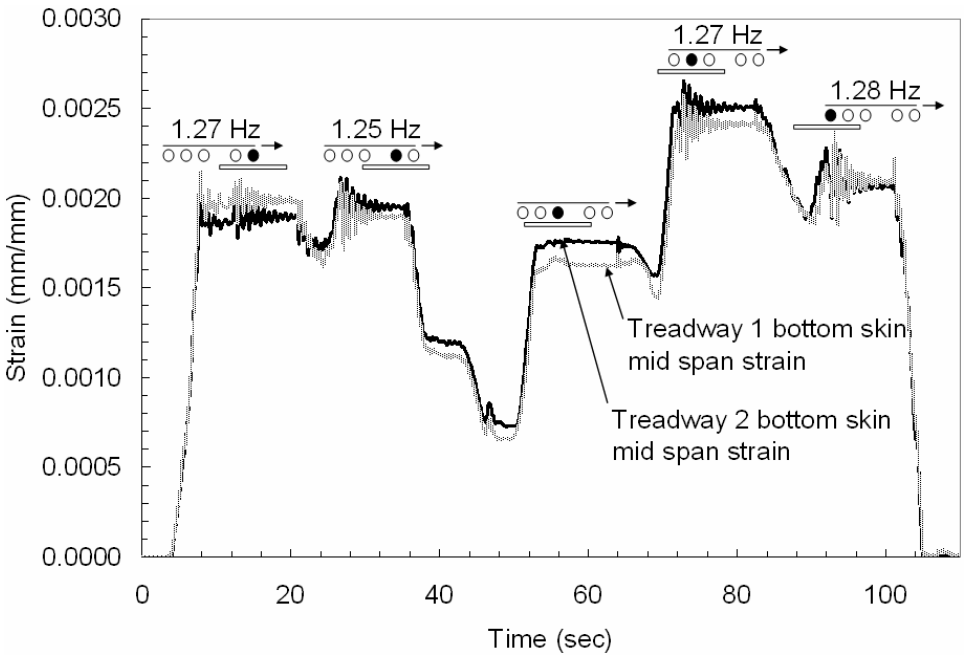

Figure 10-18 Plot of strain versus time for a fully loaded PLS truck with each axle positioned at the mid-span to obtain static strain measurements.

A comparison between measured strains and finite element predicted strains are presented in Table 10-5, where the strain measurements are taken with the PLS truck parked on the treadways with the rear three axles centered (critical design load). From the table it is seen that overall the measured strains and predicted strains show good agreement with the exception of the center top and ¾ bottom gages on treadway 2 which show differences from 17% to 22%. Similar differences were observed for the proof testing performed in the laboratory. For the case of the top center gage it is located directly below the center tire which may affect the measured strain. It should also be observed from Table 10-4 and Table 10-5 that the field test measured strains are lower than the laboratory measured PLS working load strains by a factor of approximately 1.2, which equals the assumed TDTC [118] dynamic load factor which is not present when the vehicle is parked (static load).

Table 10-5 Finite Element Model versus Field Testing Strains

		Treadway 1		*Treadway 2*	
Measurement Location	*Model*	*Exp.*	*Diff. (%)*	*Exp.*	*Diff. (%)*
¼ point top (μs)	-1290	-1310	-1.5	-1170	10.3
¼ point bottom (μs)	1530	1520	0.1	1510	1.3
Center top (μs)	-1940	-1870	3.7	-1590	22.0
Center bottom (μs)	2270	2620	-13.4	2340	-3.0
¾ point bottom (μs)	1530	1420	7.7	1310	17.0

10.5.1 Fatigue Testing

At the end of each test day, the PLS truck was parked with the center of the rear three axles located at the treadway mid-span. A plot of the strains on the bottom surface of the treadways at the ¼-span, mid-span, ¾-span, and the top surface at mid-span versus the total number of PLS crossings is presented in Figure 10-19. It is observed that the measured strains remain relatively constant throughout the 1,600 crossings period, where the slight scatter is most probably a result of vehicle load shifts, fuel burn, or vehicle placement on the bridge.

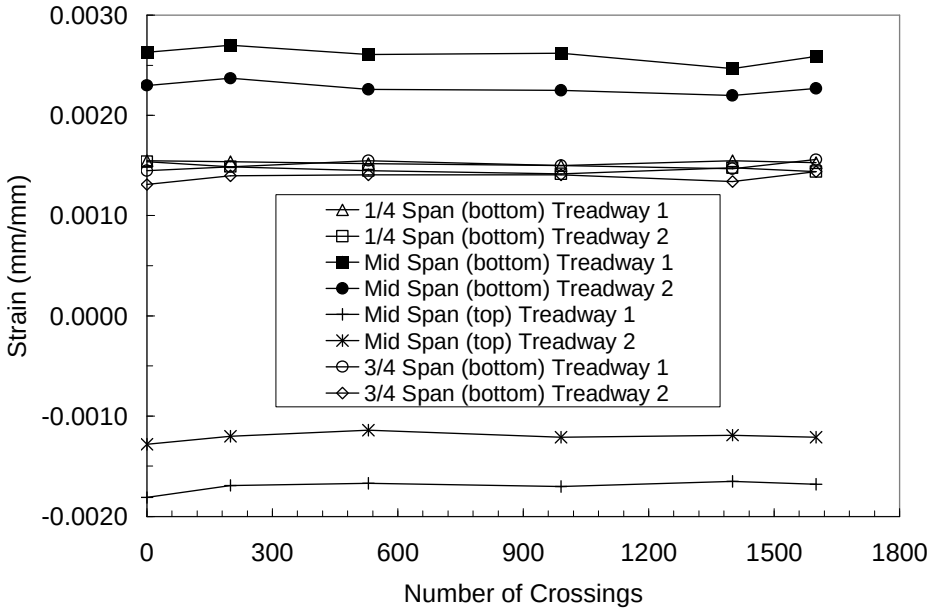

Figure 10-19 Plot of ¼-span, mid-span, and ¾-span strain versus total number of PLS crossings.

10.5.2 Dynamic Impact Testing

The second phase of the field testing involved determining the dynamic impact factors for the treadways as a function of vehicle type, crossing speed, and bank (abutment) preparation Due to the low mass of military and emergency response bridging systems the dynamic impact loads imparted by crossing vehicles can significantly increase the stresses within the structure beyond those experienced under static loads. The TDTC [118] requires that nominal vehicle loads be increased by a factor of 1.2 to account for dynamic impact. Previous work by Franklin et al. [119] investigated the dynamic loads on portable timber bridge systems with vehicles crossing at different speeds under both rough and smooth road conditions. The study

showed both the speed of the vehicle as well as the road conditions (smooth or rough) to greatly affect the dynamic loads experienced by the bridge systems. The study showed deflections which were 1.13 times higher than static deflections for smooth road entrance conditions while rough road entrance conditions resulted in deflections which were 1.44 times greater than the static deflection.

Five different vehicles were used during impact testing of the treadways, four wheel type vehicles and one track vehicle. The vehicles used were the 1) M113 Armored Personnel Carrier (track), 2) High Mobility Multipurpose Wheeled Vehicle (HMMWV), 3 Stryker, 4) Common Bridge Transport (CBT), and 5) Palletized Load System (PLS) truck. Photos of each of these vehicles are seen in Figure 10-20. All vehicles were tested fully loaded with the PLS truck being tested both loaded and unloaded. Prior to testing, each vehicle was carefully weighed to obtain both the total weight of the vehicle as well as the weight of each axle. A summary of the weights and axle spacing for each vehicle is given in Table 10-6 with Figure 10-21 showing the generic axle weights (P_i, i = 1-5) and axle spacing (L_i, i = 1-4).

Testing was conducted under both rigid soil support conditions as well as soft soil conditions with the approaches being unprepared (76 mm ramp toe height) or prepared. The approach was prepared by building up the area in front of the treadway ramp toe with gravel creating a smooth transition from the road to the treadway surface (see Figure 10-22). The field testing was conducted over a two day period. On the first day crossings were conducted with the fully loaded PLS truck and M113 Armored Personnel Carrier under rigid soil conditions and unprepared approaches. Between the first day and second day of testing there was a significant amount of

rainfall greatly softening the soil supporting the abutment timbers. Following the rain it was observed that the bank support timbers were deflecting as much as 37 mm (1.5 in) as the fully loaded PLS truck crossed. Under these conditions the fully loaded PLS truck again was tested along with the HMMWV, Stryker, CBT, and unloaded PLS. A matrix summarizing the vehicles tested with corresponding crossing speeds, soil condition, and approach condition is given in Table 10-7. The vehicles crossed speed at increments ranging from 8 kph (5 mph) up to 40 kph (25 mph) with three crossing performed at each speed increment. The fastest crossing speed for each vehicle was dictated by the confidence level of the driver. The first day of testing the temperature was 68°F with 78% humidity and the second day the temperature was 60°F with 92% humidity.

(a)

(b)

(c)

(d)

(e)

Figure 10-20 Photos of crossing vehicles: a) M113 Armored Personnel Carrier, b) HMMWV , c) Stryker, d) CBT, e) PLS (loaded).

Table 10-6 Vehicle Axle Spacing and Loads

Spacing/Loading	*M113*	*HMMWV*	*STRYKER*	*CBT*	*PLS (unloaded)*	*PLS (loaded)*
L1 (m) [in]	0.66 [26]	3.35 [132]	1.22 [48]	1.52 [60]	1.52 [60]	1.52 [60]
L2 (m) [in]	0.66 [26]	-	1.42 [56]	3.81 [150]	3.43 [135]	3.43 [135]
L3 (m) [in]	0.66 [26]	-	1.22 [48]	1.52 [60]	1.50 [59]	1.50 [59]
L4 (m) [in]	0.66 [26]	-	-	-	1.52 [60]	1.52 [60]
Width (m) [in]	2.51 [99]	2.08 [82]	2.59 [102]	2.39 [94]	2.39 [94]	2.39 [94]
P1 (kN) [lbs]	24.2 [5440]	22.5 [5060]	52.1 [11720]	60.5 [13600]	57.8 [13000]	75.1 [16880]
P2 (kN) [lbs]	24.2 [5440]	26.6 [5980]	53.2 [11950]	63.6 [14300]	57.8 [13000]	73.9 [16620]
P3 (kN) [lbs]	24.2 [5440	-	66.7 [14990]	77.3 [17380]	42.7 [9600]	60.8 [13660]
P4 (kN) [lbs]	24.2 [5440	-	66.3 [14900]	76.7 [17240]	42.7 [9600]	86.3 [19400]
P5 (kN) [lbs]	24.2 [5440	-	-	-	42.7 [9600]	86.7 [19480]
Total (kN) [lbs]	121 [27200]	49.1 [11040]	238.3 [53560]	278.1 [62520]	243.7 [54800]	382.8 [86040]

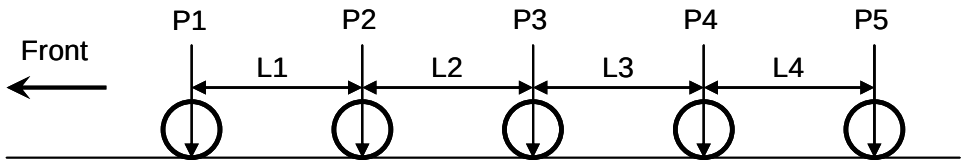

Figure 10-21 Illustration of generic axle spacing and axle loads.

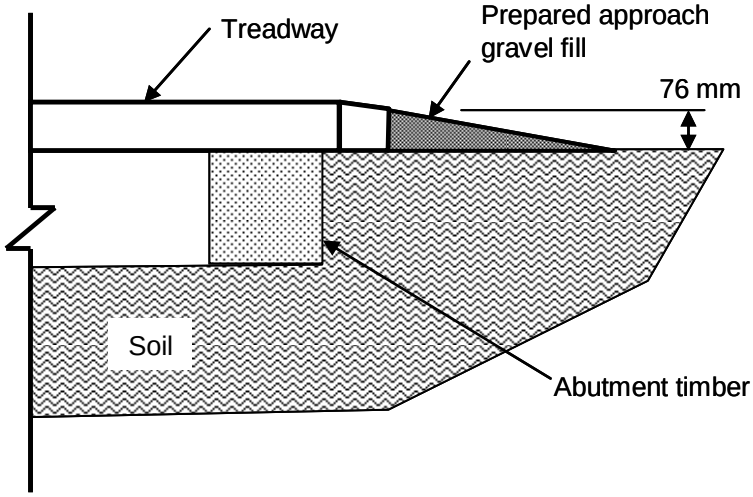

Figure 10-22 Illustration showing gravel fill area for prepared approaches.

Table 10-7 Vehicle/Condition Matrix

Condition	*M113 (kph) [mph]*	*HMMWV (kph) [mph]*	*Stryker (kph) [mph]*	*CBT (kph) [mph]*	*PLS (unloaded) (kph) [mph]*	*PLS(loaded) (kph) [mph]*
Rigid/unprepared	8-24 [5-15]	-	-	-	-	8-11 [5-7]
Soft/unprepared	-	8-32 [5-20]	8-40 [5-25]	8-24 [5-15]	-	8-24 [5-15]
Soft/prepared	-	8-32 [5-20]	8-40 [5-25]	8-32 [5-20]	8-32 [5-20]	8-32 [5-20]

Prior to beginning the crossings, a static strain measurement was taken for each vehicle. Each vehicle was slowly driven across the treadways stopping with each axle located at the mid-span for a period of time to allow the strains to reach equilibrium. Strain measurements were recorded to determine the maximum static strain created by each vehicle. Measurements were taken at a sampling frequency of 100 Hz allowing the natural frequency of the treadways as a function of vehicle position to be obtained as well. An example of the static strains and natural frequency measured for the fully loaded PLS truck on soft soil is shown in Figure 10-18.

10.5.3 Impact Factors

Impact factors (ratio of dynamic strain to static strain) as a function of speed as well as strain time histories were obtained for each vehicle. For this study the strain measurements were taken on the bottom surface at the center mid-span of each treadway. The crossing speed was determined by taking the sum of the length of the vehicle and the length of the treadways and dividing by the crossing time. Three crossings were performed at each speed from which the average crossing speed and impact factors were determined. Error bars in the plots indicate the maximum and

minimum impact factors at each crossing speed. From the calculated speed of each vehicle an illustration of the of the axle positions on the treadways is shown in each of the strain histories along with the maximum static strain of each treadway A description of each test vehicle and resulting impact factors is discussed.

M113 Armored Personnel Carrier

Having a cruising speed of 66 kph (41 mph), the M113 is a fully tracked, lightly armored vehicle used to transport personnel. The vehicle is 488 cm (192 in) long, 269 cm (106 in) wide and 221 cm (87 in) high having a curb weight of 10,830 kg (23,880 lbs) and a maximum weight of 14,060 kg (31,000 lbs). The M113 crossings occurred on rigid soil and unprepared approaches. A plot of the impact factor versus speed for each treadway is seen in Figure 10-23. From the plot it is observed that the impact is negligible up to a speed of 10 kph (6 mph) from which point the impact factor increases to a maximum of 1.12 at a speed of 18 kph (11 mph) and then reduces below 1.0 at speeds exceeding 22 kph (14 mph). A plot of the time history of the strains during the M113 crossing at a speed of 18 kph (11 mph) is shown in Figure 10-24. The shape of the strain response profile is unchanged for lower and higher speeds. Due to the close axle spacing (0.66 m) and load distribution of the track, the M113 shows a single strain impulse for each crossing.

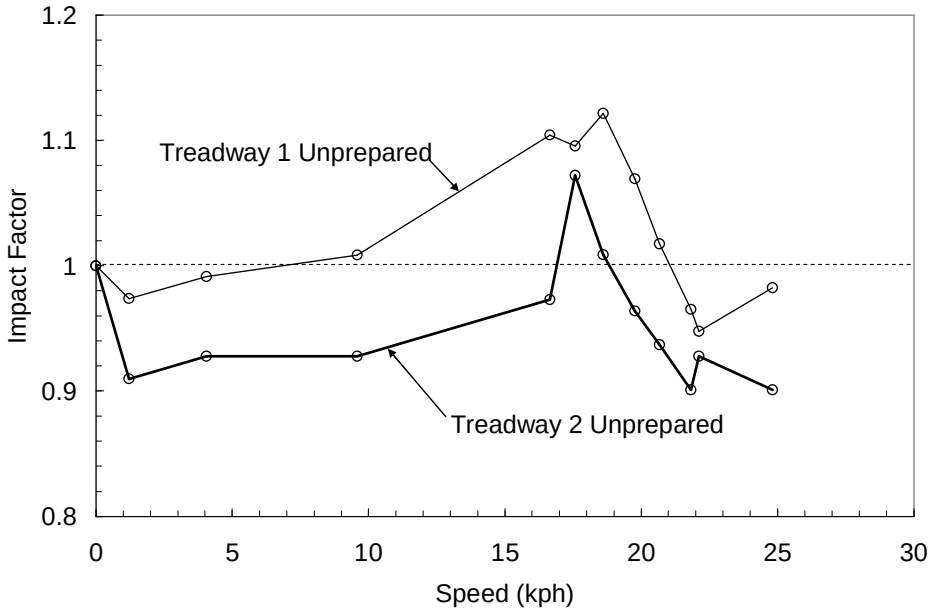

Figure 10-23 M113 Armored Personnel Carrier speed versus impact factor for unprepared approach on rigid abutments.

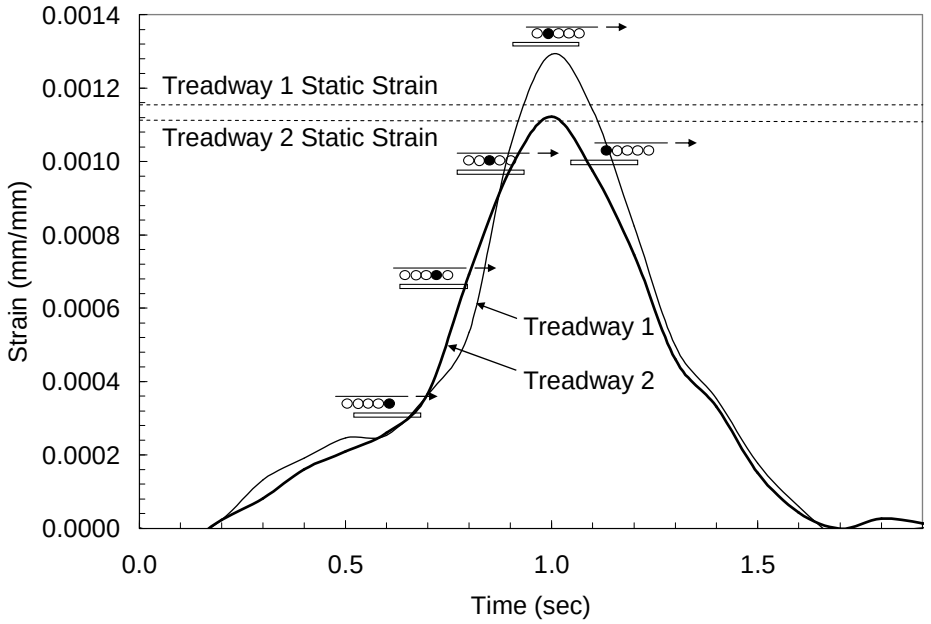

Figure 10-24 M113 mid-span strains versus time at a crossing speed of 18 kph.

High Mobility Multipurpose Wheeled Vehicle (HMMWV)

The MMMWV is a light, tactical, two-axle, wheeled vehicle used for command and control on the battlefield and transport of supplies up to 2,000 kg (4,400 lbs). The vehicle is 457 cm (180 in) long, 213 cm (84 in) wide, and 183 cm (72 in) tall having a curb weight of 3,500 kg (7,700 lbs) and a maximum fully loaded weight of 5,500 kg (12,100 lbs). The vehicle used in this study was 91% of maximum weight at 5,000 kg (11,040 lbs). The HMMWV has a cruising speed of 55 mph. The static strain measurements showed the maximum static strain to occur when the rear axle is at the mid-span. Crossings were performed on soft soil with both prepared and unprepared approaches. A plot of the impact factor versus speed for each treadway under both prepared and unprepared approach conditions is seen in Figure 10-25. From the plot it is observed that the maximum impact factor of 1.7 occurred at a crossing speed of 17 kph (11 mph) and unprepared approach conditions. For prepared approach conditions the maximum impact factor is 1.46. It is also observed that as the HMMWV crossing speed increases above 17 kph (11 mph) the impact factors decrease significantly approaching impact factors near 1.0 at 30 kph (19 mph). It is also noted that treadway 2 experienced significantly higher impacts in comparison to treadway 1. This is most likely due to the vehicle not being centered during crossings or static measurements. Time histories of the strains are given in Figure 10-26 and Figure 10-27 for unprepared approaches at crossing speeds of 17 kph (11 mph) and 30 kph (19 mph) respectively. From Figure 10-26 it is observed that there are two distinct strain impulses as the front and rear axles cross over the mid-span of the bridge, however from Figure 10-27 it is observed that at higher speeds there are many

low magnitude impulses with the maximum strains occurring when neither axle is at the mid-span.

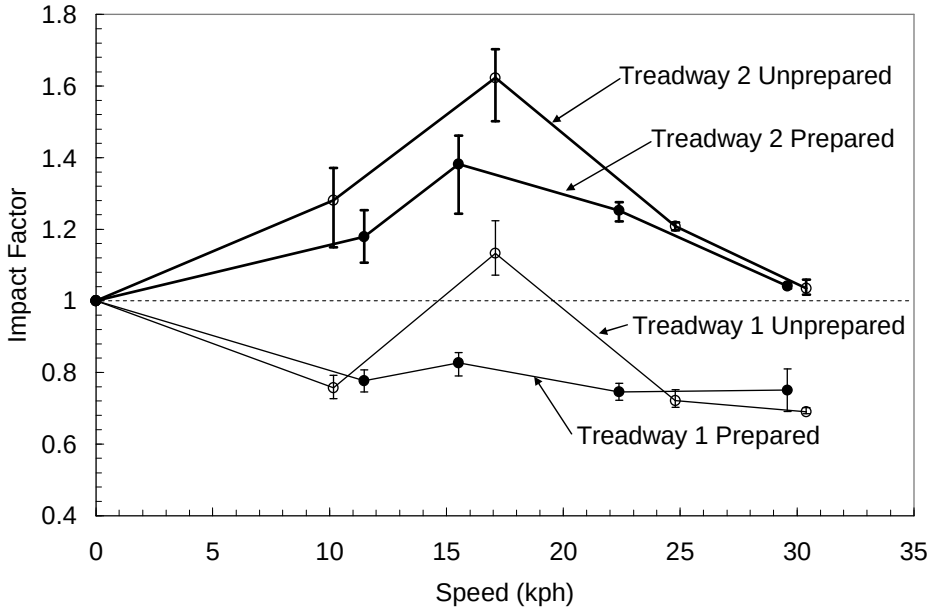

Figure 10-25 HMMWV speed versus impact factor for prepared and unprepared approach on soft abutments.

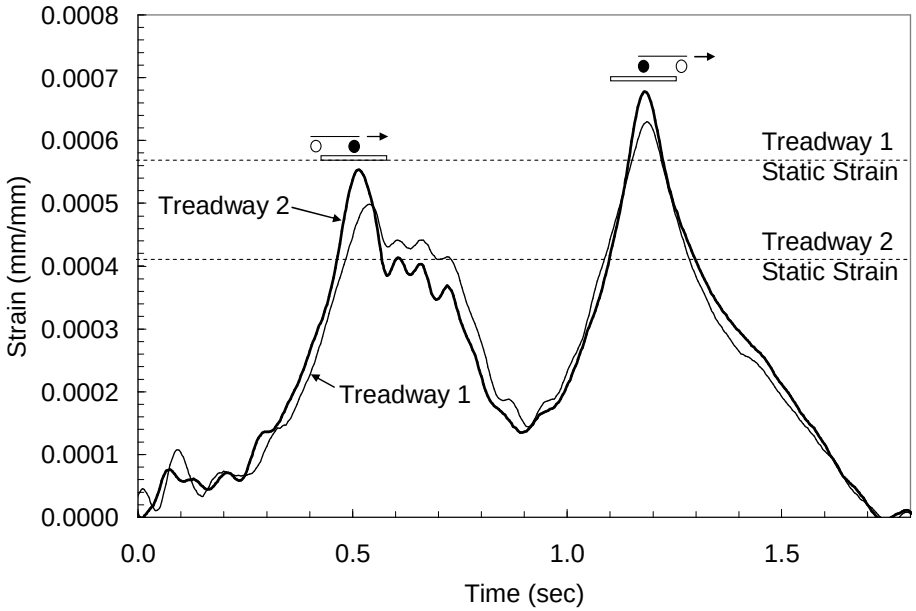

Figure 10-26 HMMWV mid-span stains versus time at a crossing speed of 17 kph.

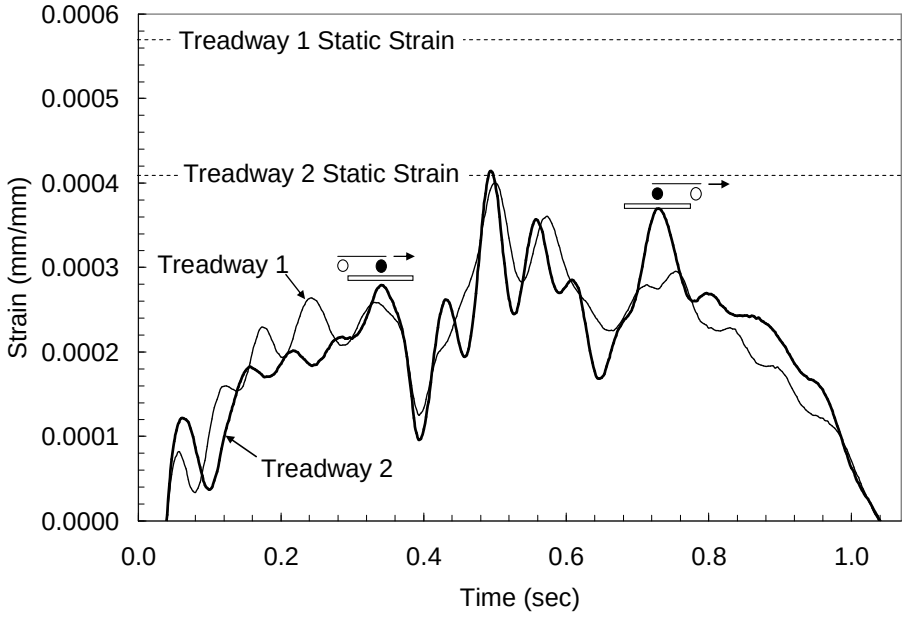

Figure 10-27 HMMWV mid-span stains versus time at a crossing speed of 30 kph.

Stryker

Having a road speed of 100 kph (62 mph), the Stryker is a four-axle, wheeled, all-terrain vehicle designed to fulfill a variety of missions from personnel carrier, to assault vehicle, to a medical evacuation vehicle. The Stryker is 700 cm (275 in) long, 272 cm (107 in) wide, and 264 cm (104 in) tall having a curb weight of 14,060 kg (31,000 lbs) and a maximum weight of 18,730 kg (41,300 lbs). The Stryker used in this study was an armored reconnaissance vehicle weighing 24,300 kg (53,560 lbs), which is 130% of the listed maximum vehicle weight. The static strain measurement showed the maximum static strains to occur when the third axle was positioned at the mid-span resulting in a measured natural frequency of 1.35 Hz. The Stryker was tested on soft soil with both prepared and unprepared approaches. A plot of the

impact factors versus speed is given in Figure 10-28. From the figure it is observed that impact factors of approximately 1.12 are observed for treadway 1 under both approach conditions at 10 kph (6 mph) and 20 kph (12 mph) with a maximum impact factor of 1.21 occurring at the maximum crossing speed of 40 kph (25 mph). It is observed that the approach condition has little effect on the maximum observed impact factors. Similarly as seen for the HMMWV, one treadway shows higher impact factors than the other. Again this is likely due to the vehicle not being centered during crossings. A time history of the impact factors for each treadway at a crossing speed of 40 kph (25 mph) with unprepared approaches is seen in Figure 10-29. From the figure it is observed that the strain response looks like one large strain impulse with individual axle effects being minimal. Similar to the M113 vehicle, the Stryker has closely spaced axles (1.2 m and 1.4 m) which results in a strain response which is similar to that observed for the M113 tracked vehicle.

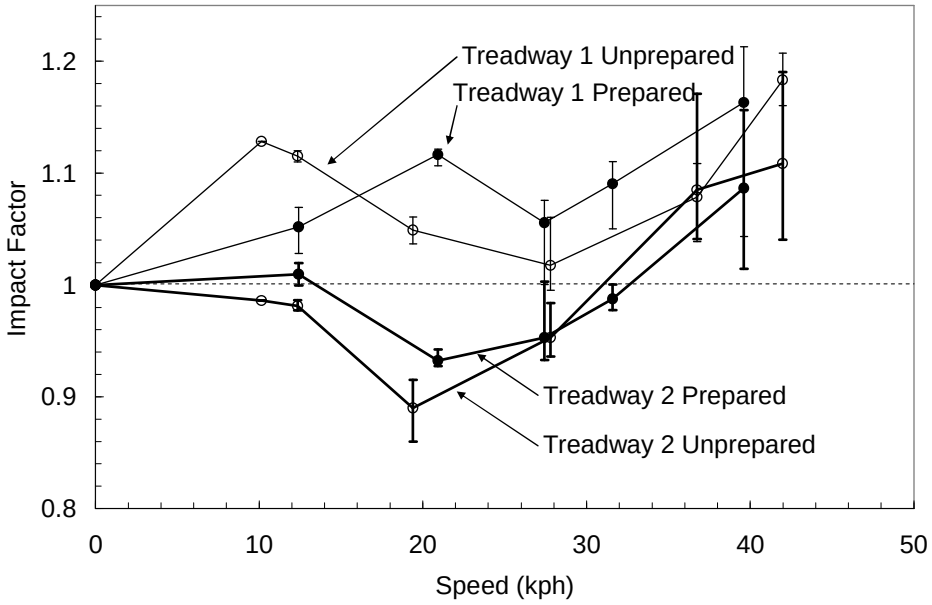

Figure 10-28 Stryker speed versus impact factor for prepared and unprepared approach on soft abutments.

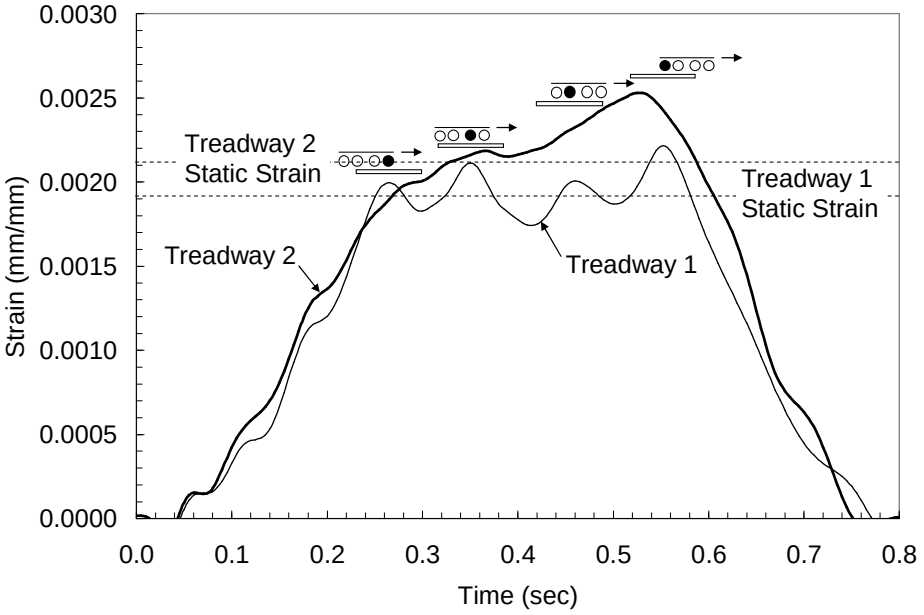

Figure 10-29 Stryker mid-span strains versus time at a crossing speed of 40 kph.

Common Bridge Transporter (CBT)

The CBT is a modified Heavy Mobility Tactical Truck (HEMTT) with a Load Handling System (LHS) having a maximum speed of 92 kph (57 mph). The CBT is designed to transport military bridging assets from Ribbon Bridging (RB) to Heavy Dry Support Bridging (HDSB). The CBT is 1,020 cm (401 in) long, 244 cm (96 in) wide, and 284 cm (112 in) tall having a curb weight of 17,600 kg (38,800 lbs) and a maximum weight of 27,600 kg (60,800 lbs) (10,000 kg payload for a maximum grade of 60%). The CBT considered in this study weighed 28,360 kg (62,530 lbs) (102% of listed maximum weight). The static measurement showed the third axle centered at the mid-span to produce the maximum static strain with a natural frequency of 1.56 Hz. A plot of the impact factor versus speed for soft soil conditions with both prepared and unprepared approaches is presented in Figure 10-30. From the plot it is seen that for speeds ranging from 10 kph (6 mph) to 27 kph (17 mph) the impact factors exceed 1.4 with a maximum of 1.5 occurring at 27 kph (17 mph). For low speed (7 kph) and high speed (35 kph) very low impact factors are observed. Strain time histories for crossing speeds of 10 kph (6 mph) and 27 kph (17 mph) are given in Figure 10-31 and Figure 10-32 respectively. At the slower crossing speed (10 kph) it is observed that there are four distinct strain impulses corresponding to each axle at the mid-span resulting in strains which are near or exceed the measured static strains with the maximum strain occurring for the second to last axle. At the faster speed (27 kph) it is seen that there are two strain impulses which approach or exceed the static strains corresponding to the second and last axles.

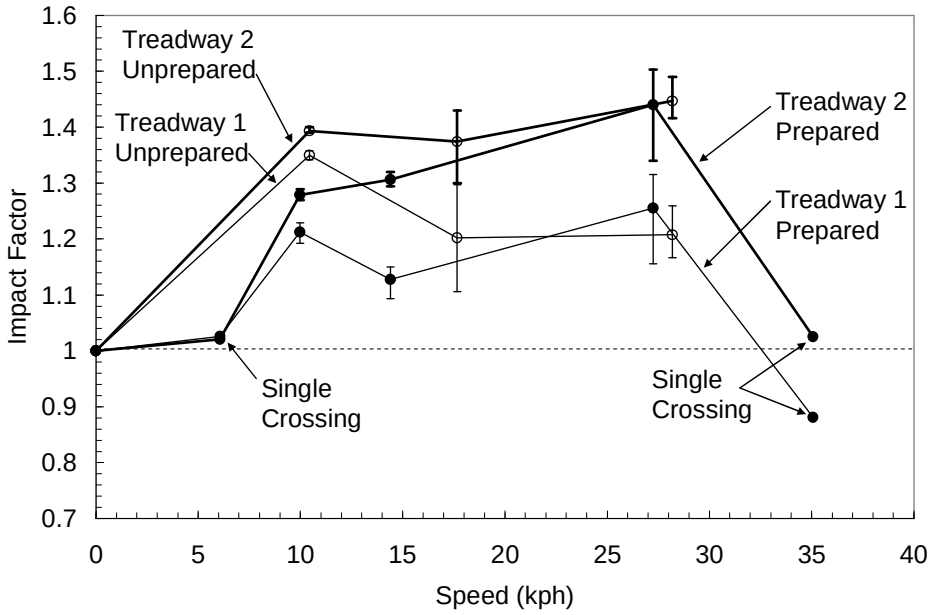

Figure 10-30 CBT speed versus impact factor for prepared and unprepared approach on soft abutments.

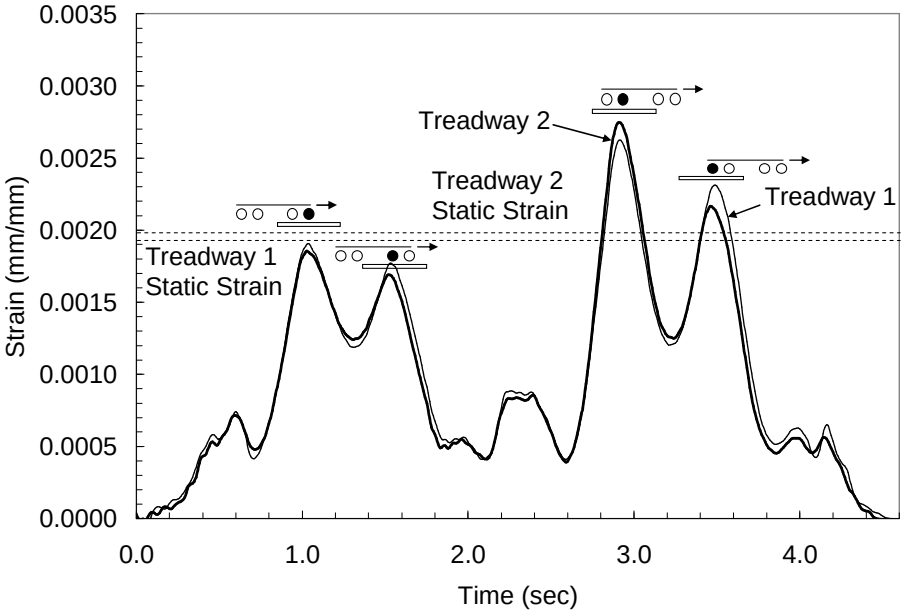

Figure 10-31 CBT mid-span strains versus time at a crossing speed of 10 kph.

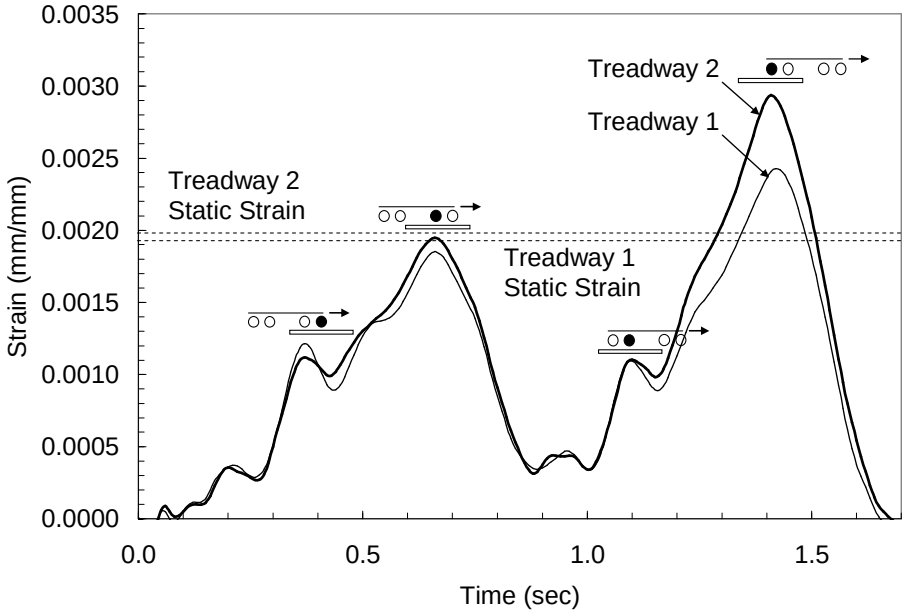

Figure 10-32 CBT mid-span strains versus time at a crossing speed of 27 kph.

Palletized Load System (PLS) Truck

The PLS truck is a five-axle supply transporter having a maximum speed of 92 kph (57 mph). The truck is 1,095 cm (431 in) long, 244 cm (96 in) wide, and 328 cm (129 in) tall having a curb weight of 24,830 kg (54,750 lbs) and a maximum weight of 39,280 kg (86,600 lbs). The PLS used in this research was tested both unloaded (24,830 kg) and fully loaded weighing 39,030 kg (86,040 lbs). The static measurements of the unloaded PLS showed the maximum static strain to occur when either the first or second axle is located at the mid-span with a natural frequency of 2.0 Hz. The loaded PLS produced maximum static strains when the fourth axle was located at the mid-span with rigid soil giving a natural frequency of 1.67 Hz and soft soil giving a frequency of 1.27 Hz. The decrease in frequency confirms the softening

of the soil. A plot of the impact factor versus speed for the unloaded PLS is shown in Figure 10-33. From the figure it is seen that the maximum impact factor (1.34) occurs at a speed of 23 kph (14 mph) with the impact decreasing at higher speeds. A strain time history for the unloaded PLS is given in Figure 10-34. From the plot it is seen that an impulse for each axle is observed with the highest strain occurring when the second axle is located at the mid-span. A plot of the impact factor versus speed for the fully loaded PLS under both rigid and soft soil conditions as well as prepared and unprepared approaches is seen in Figure 10-35. It is also observed that the maximum impact factor (1.71) occurs at a speed of 9 kph (6 mph) under the rigid soil conditions and unprepared approaches. It is observed that only a small increase in speed (12 kph) significantly reduces the impact factor to 1.24. A plot of the strain time history for the rigid soil case is seen in Figure 10-36. The plot shows distinct impulses for each axle, with three of the impulses exceeding the static strains, and the other two being only slightly less than the static strain level. The maximum strain occurred when the second to last axle was located at the mid-span. From Figure 10-35 it is observed that for soft soil conditions the maximum impact factor (1.25) occurred at a speed of 23 kph (14 mph). The strain time history at a crossing speed of 23 kph (14 mph) and unprepared approaches is given in Figure 10-37. The strain time history at this speed is much different that observed for the rigid soil case at 9 kph (6 mph) with impulses not always corresponding with axles at the mid-span and the maximum strain occurring when the last axle is a the mid-span.

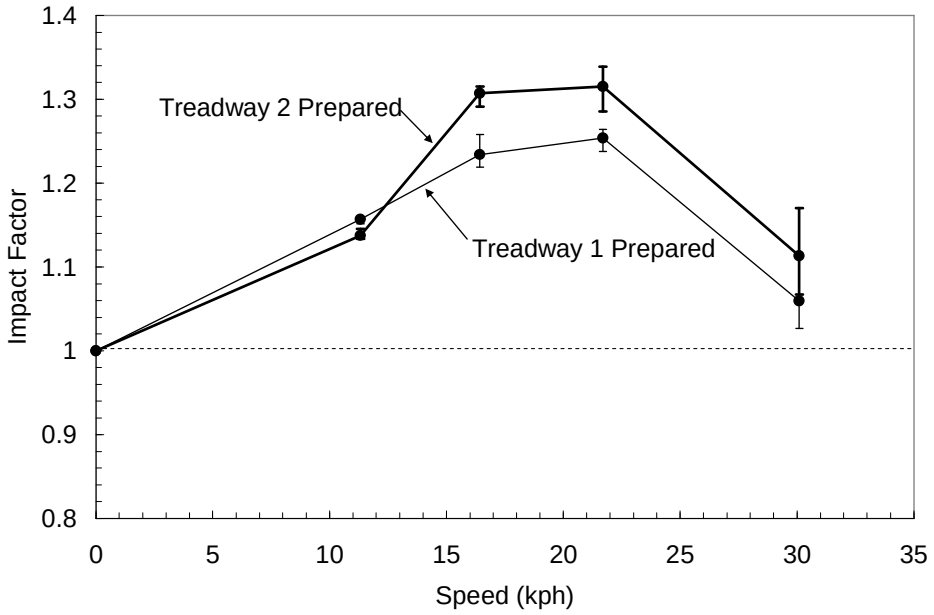

Figure 10-33 PLS (unloaded) speed versus impact factor for prepared approach on soft abutments.

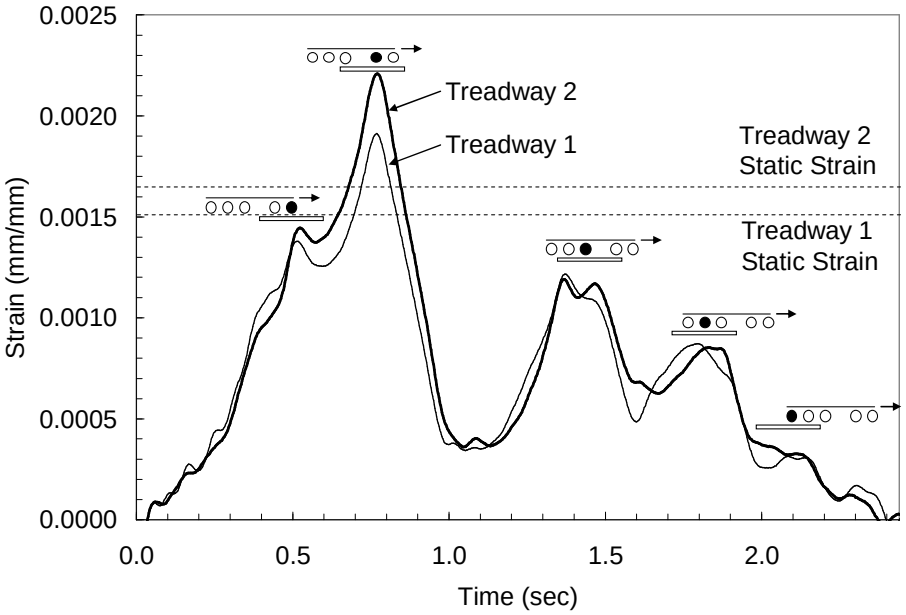

Figure 10-34 PLS (unloaded) mid-span strains versus time at a crossing speed of 23 kph.

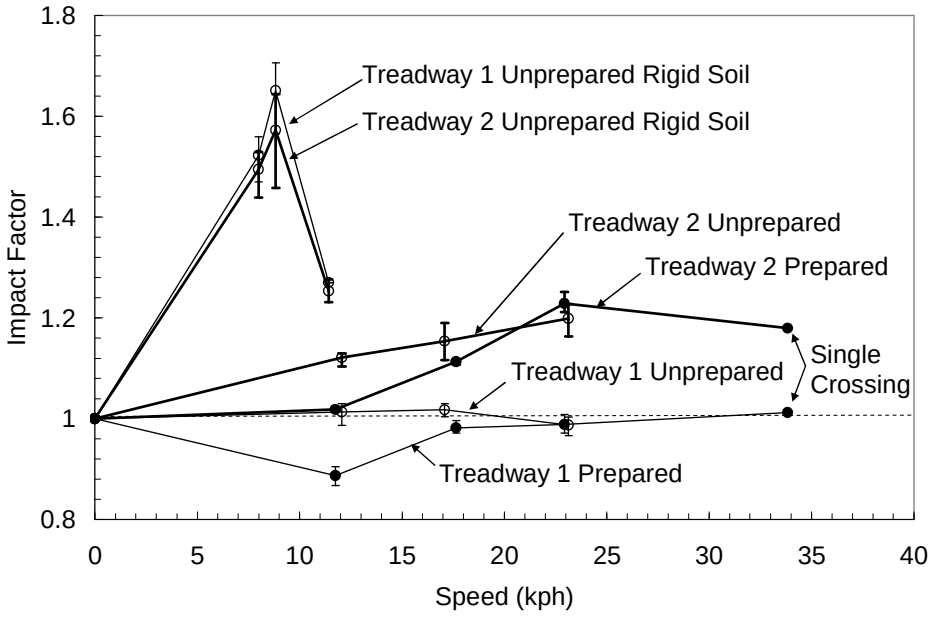

Figure 10-35 PLS (fully loaded) speed versus measured and analytical impact factors for prepared and unprepared approach on soft and rigid soil abutments.

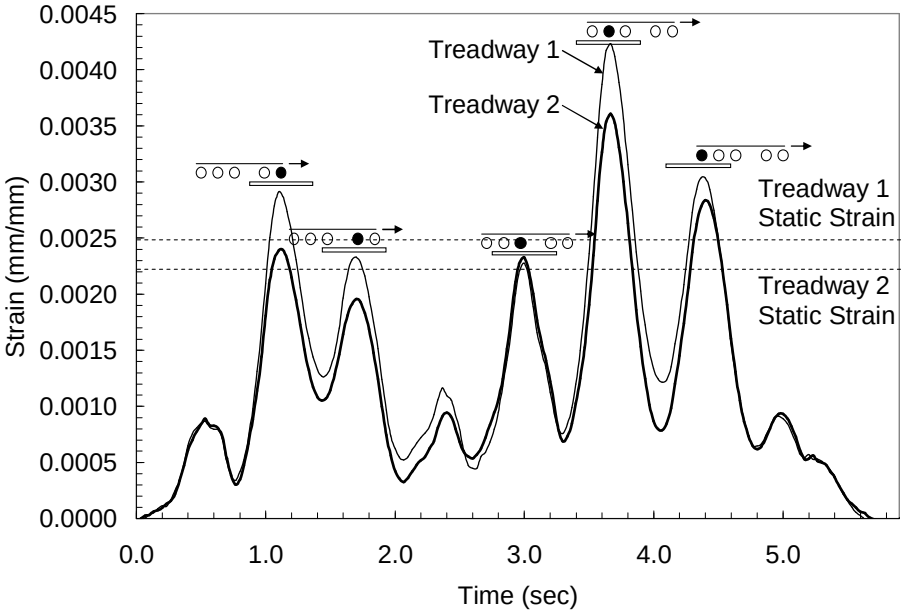

Figure 10-36 PLS (fully loaded) mid-span strains versus time at a crossing speed of 9 kph.

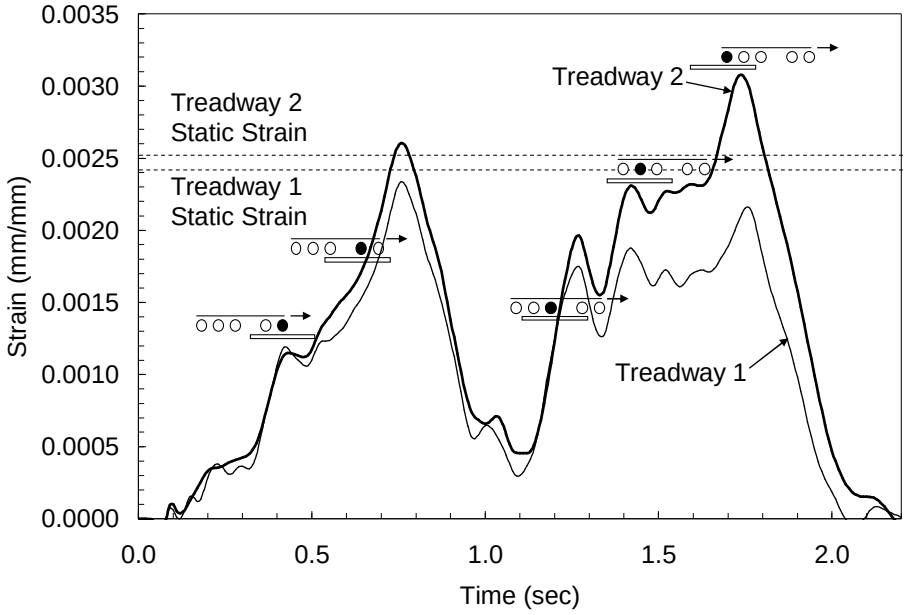

Figure 10-37 PLS (fully loaded) mid-span strains versus time at a crossing speed of 23 kph.

A summary of the maximum impact factor for each vehicle is given in Table 10-8. It is observed that the strain build-up for the tracked M113 appears as one impulse with the effects of individual axles being difficult to detect (Figure 10-24). In comparison, the strain build-up in the treadways from the wheeled vehicles is very different, where the strain response of each individual axle is clearly observed. At specific crossing speeds the HMMWV (Figure 10-26), CBT (Figure 10-31), and PLS truck (Figure 10-36) all produce strain responses in which each axle creates a distinct strain impulse where the strains exceed or are only slightly less than the maximum static strains. This knowledge is of importance in accessing the number of fatigue cycles over the bridge life. For example, the strain response of the fully loaded PLS at low speed, on rigid soil, should be treated as five separate load cycles. Similarly the

HMMWV should be treated as two load cycles and the CBT should be treated as four load cycles. In comparison, due to the close axle spacing of the four-axle wheeled Stryker, the strain build-up profile appears to be a combination of the observed tracked vehicle and wheeled vehicle and results in a single load cycle (Figure 10-29).

Table 10-8 Maximum Impact Factor and Vehicle Speed

Condition	*M113 (kph)*	*HMMWV (kph)*	*Stryker (kph)*	*CBT (kph)*	*PLS (unloaded) (kph)*	*PLS(loaded) (kph)*
Rigid/unprepared	1.12 (18)	-	-	-	-	1.71 (9)
Soft/unprepared	-	1.70 (17)	1.20 (40)	1.49 (27)	-	1.23 (23)
Soft/prepared	-	1.46 (15)	1.21 (40)	1.50 (27)	1.34 (23)	1.25 (23)

It is observed that the maximum impact factors for the HMMWV (1.7), CBT (1.5), and PLS (1.71) are all significantly higher than the design impact factor of 1.2 prescribed by the TDTC. While the impact factors for the wheeled Stryker (1.21) and the tracked M113 (1.12) agree with the TDTC assumptions. From the impact factor results it is observed that the approach condition (prepared versus unprepared) has very little affect on the impact factor with the exception of the HMMWV which shows an impact factor increase of 16% for the unprepared approaches. The vehicle configuration (weight and axle spacing) and crossing speed prove to be the parameters having the greatest effect on the dynamic impacts. From the M113 and Stryker it is observed that tracked vehicles, or vehicles with close axles spacing similar to tracked vehicles, have the lowest impact factors. In addition it is observed that the impact is very dependent on vehicle speed. For example the maximum impact for the Stryker

occurred at it's fastest crossing speed (40 kph) while the HMMWV, CBT and unloaded PLS all show impact factors which are near 1.0 at their fastest crossing speeds while showing impact factors much greater than 1.0 at slower speeds. The most critical loading on the bridge was produced by the fully loaded PLS on rigid soil at a crossing speed of 9 kph (6 mph). As was noted previously, a slight increase in speed greatly reduces the impact factor. Further testing is required to determine if the fully loaded PLS traveling slower across the bridge on soft soil would produce similar results. The extreme impact factor of the PLS on rigid soil is further considered in the following section.

10.5.4 Analytical Study

It was observed that the greatest impact factors for the loaded PLS occurred at very low crossing speeds. To aid in understanding these high impact factors a simple analytical solution of a point load moving across a simply supported beam is used [120]. The dynamic response is expressed by

$$z(t)=\begin{cases}\dfrac{2p_o}{mL}\dfrac{1}{\omega_n^2-(\pi v/L)^2}\left(\sin\dfrac{\pi v t}{L}-\dfrac{\pi v}{\omega_n L}\sin\omega_n t\right) & t\le L/v \qquad (10.2)\\[2ex] -\dfrac{2p_o}{mL}\dfrac{(2\pi v/\omega_n L)\cos(\omega_n L/2v)}{\omega_n^2-(\pi v/L)^2}\sin\left[\omega_n(t-L/2v)\right] & t\ge L/v \qquad (10.3)\end{cases}$$

where *z(t)* is the displacement response as a function of time, p_o is the moving point load, *m* is the mass per unit length of the bridge, *L* is the length of the bridge, ω_n is the fundamental bending natural frequency of the bridge, and *v* is the velocity of the point load. The response while the moving load is on the bridge ($t \le L/v$) is expressed by Eq. (10.2) and the response after the load has crossed the span (free vibration) ($t \ge L/v$) is given by Eq. (10.3). The solution assumes that the mass of the vehicle is negligible in comparison to the mass of the bridge which is true for most civil structures. However in the case of the short-span bridge considered in this study the mass of the bridge is small in comparison to the mass of the vehicle. To apply the solution an equivalent mass for the treadways is calculated based on the flexural stiffness of the treadways and the measured natural frequency from the static strain measurements. The equivalent treadway mass is determined by

$$m = \frac{\pi^4 EI}{L^4 \omega_n^2}, \tag{10.4}$$

where *EI* is the flexural stiffness of the bridge. The total response of the bridge due to vehicle crossing is found by superimposing the response of each individual moving axle load. The total displacement response is expressed by

$$u(x,t) = \sum_{n=1}^{k} z_n(t) \sin\frac{\pi x}{L}, \tag{10.5}$$

where *u* is the displacement at any location *x* along the treadway length at any instant in time, and *k* is the total number of axles of the vehicle.

Using the published solution, the impact response of the fully loaded PLS truck is investigated. From previous static loading of the treadways the flexural stiffness *EI* was determined to be 2,152 $kN \bullet m^2$ (7.5e8 $lb \bullet in^2$) and the measured natural frequency for the PLS truck on rigid soil was found to be 1.67 Hz. Using equation (3) the equivalent mass of the treadways was found to be 3,583 kg/m. The displacement response for a crossing speed of 9 kph (6 mph) was determined from Eq. (10.5) and divided by the calculated maximum static deflection to give an analytical impact factor as a function of time. The analytical impact factor time history is compared with the measured impact factor time history for the PLS truck in Figure 10-38. From the plot it is seen that the experimental and analytical results match reasonably well. Analytical impact factors versus crossing speed are compared with experimental results in Figure 10-39. For the soft soil conditions the measured natural frequency was 1.27 Hz with the equivalent mass being 6,195 kg/m. From Figure 10-39 it is observed that for the rigid soil condition the peak measured impact is captured by the analytical solution quite well. It is also observed that for soft soil a maximum impact was predicted at even a slower speed in comparison to the rigid soil conditions, however no experimental data was available at this speed to confirm the analytical results. Further understanding is gained by recognizing that at a crossing speed of 9 kph (6 mph), due to the typical axle spacing (1.52 m) of the PLS, the wheel loads are coming onto the treadway at a frequency of 1.67 Hz which matches the measured natural frequency of the treadway resulting in a resonance of the treadways.

Similarly for the soft soil conditions at a speed of 7 kph (4 mph) the wheel loads would be coming onto the treadways at a frequency of 1.27 Hz which again would result in a resonance of the treadways. It is recognized that this solution has limitations in that the mass is changing as the vehicle progresses and that inertial and damping effects are not included which could be significant especially for the soft soil conditions where settlement (friction) of the abutment timbers was observed. It was also seen that for higher speeds, above the first resonance described, the analytical solution greatly over predicts the impact factors. Although the solution has limitations, valuable insight may be gained concerning the high impacts observed at slow crossing speeds. The results show that for a given bridge flexural stiffness and soil stiffness the impact response can be very vehicle and speed dependent when excitation of resonant vibrations is considered.

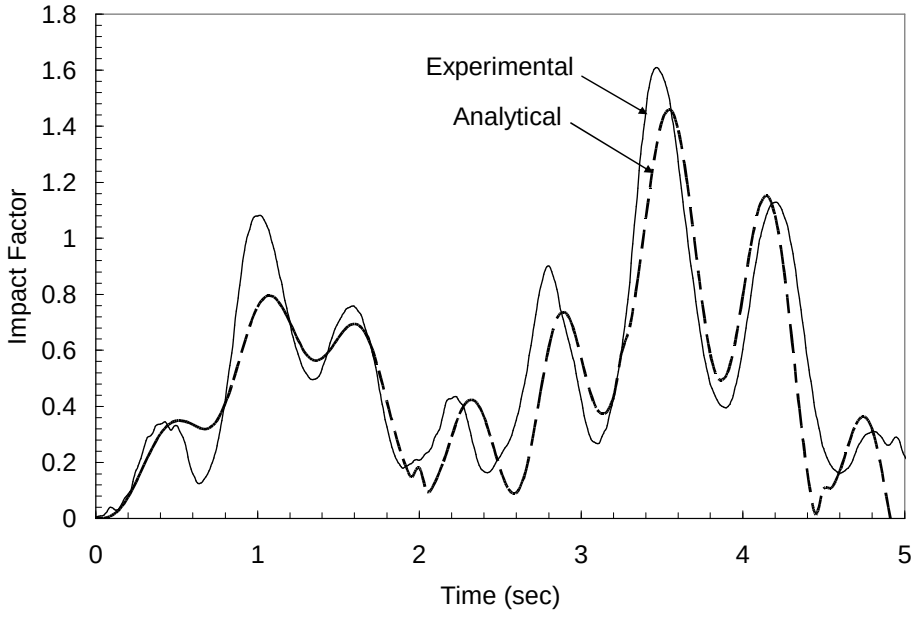

Figure 10-38 Comparison of Experimental and analytical impact factors for the PLS truck crossing at 9 kph.

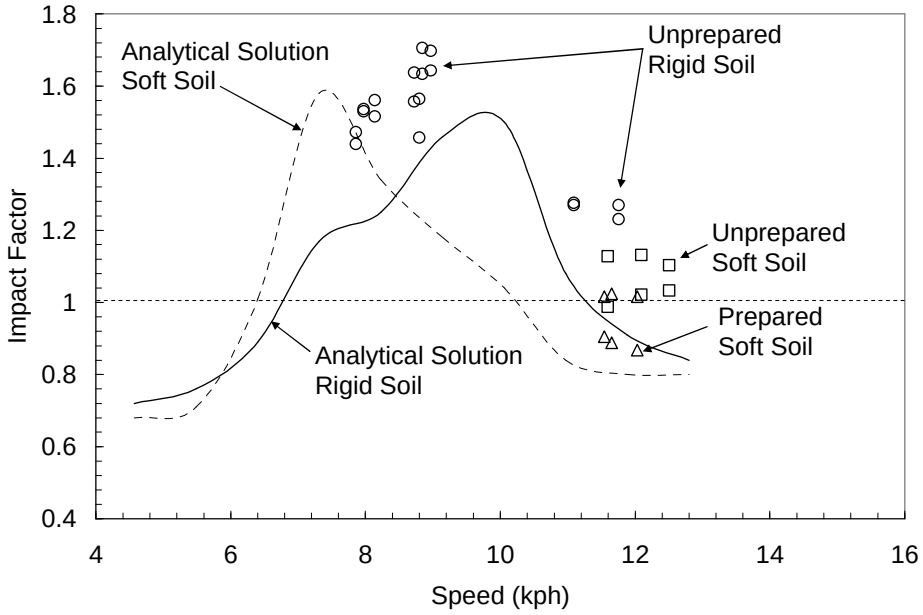

Figure 10-39 Analytical impact factors compared with experimental data.

This chapter, in part, is a reprint of the material which appears in the *Journal of Bridge Engineering* 2008 volume 13 issue 4 pages 388-397 titled "Development of a Short-Span Fiber-Reinforced Composite Bridge for Emergency Response and Military Applications." The dissertation author was the primary investigator and author with advisor J. B. Kosmatka as co-author.

CHAPTER 11

PART II CONCLUSIONS

This research has described the development and testing of five different FRP webbed core systems which are compared to an existing balsa core system developed as part of the Composite Army Bridge project. The new core system was used in the development of short-span bridging which underwent significant laboratory and field testing to prove the design.

All of the cores with the exception of Core 2 (C2-WCL) meet or exceed the shear and compressive strength requirements. Core 1 (C1-WCH), which has the highest shear strength, exceeds the shear strength of the balsa by a factor of 3.23 at a weight which is 28% lighter than the balsa. In terms of strength-to-weight performance it was found that all of the cores exceed the performance of the baseline balsa core.

Finite element modeling of the webbed deck showed good agreement with the test results and may be considered a viable tool for predicting deflections and strains as well as web buckling for larger more complex webbed core structures.

This research has shown that FRP webbed cores can exhibit increased strength and compressive properties at a significant weight savings in comparison to the balsa core used as the baseline for this study. In addition it has been shown that weight savings up to 35% can be realized by using FRP webbed decking in place of conventional aluminum decking.

The performance requirements for a short-span gap crossing bridge system have been set forth along with a description of the design, fabrication, and testing of a carbon/epoxy sandwich core treadway bridge system. During the design of the treadways several load cases were studied to determine the critical load cases for design. The analysis of the final design showed positive margins of safety for all of the components of the treadway with the critical component being the core having a margin of safety of +0.13. Laboratory proof testing was performed to ensure that the performance requirements were achieved and to validate the finite element model used in the design. The proof testing showed the treadways to behave linearly without any sign of permanent set or damage. A comparison of the test results and finite element model showed the model to be a very good representation of the treadway structures. Field testing of the treadways, consisting of 1,600 crossings of fully loaded PLS trucks, showed no decrease in stiffness or damage. The study has shown that the bridge treadways are capable of supporting vehicle loads up to MLC 30 including PLS vehicles and are a viable light-weight versatile bridging solution for use in emergency response and battlefield environments where short-span gaps are encountered.

Measured dynamic impact factors for five different military vehicles revealed values (for example, 1.71 for the fully loaded PLS) much greater than the 1.2 design impact factor prescribed by the TDTC. Moreover, the study showed that tracked vehicles and wheeled vehicles with closely spaced axles, such as the Stryker, result in impact factors which are 1.2 or less. The observed strain response for the HMMWV, CBT, and PLS revealed that each axle can produce a distinct strain impulse which comes near to or exceeds the maximum measured static strains. For these cases each

axle should be considered as a separate load cycles when accessing the number of fatigue cycles over the life of the bridge. For example, the strain response of the fully loaded PLS on rigid soil and low speed (9 kph) should be treated as five separate load cycles. An analytical study revealed that for a given vehicle weight and axle spacing vibration resonance of the treadways can be achieved as the frequency of the axles coming onto the treadway at a specific speed matches the natural frequency of the bridge.

APPENDIX A

ELEMENT AND CONTROL VOLUME FORMULATION

The finite element formulation for two-node line elements, four-node quadrilateral elements, four-node tetrahedral elements, six-node wedge elements, and eight-node hexahedral elements is presented. The isoparametric element approach described in Chapter 3 is used to derive the permeability "stiffness" matrix for each element type.

A.1 LINE ELEMENT

An isoparametric two-node line element is shown in Figure A-1. The element uses linear shape functions given by

$$\begin{bmatrix} N_1 \\ N_2 \end{bmatrix} = \begin{bmatrix} \frac{1}{2}(1-r) \\ \frac{1}{2}(1+r) \end{bmatrix}, \tag{A.1}$$

with the shape function derivatives given by

$$\begin{bmatrix} \frac{dN_1}{dr} \\ \frac{dN_2}{dr} \end{bmatrix} = \begin{bmatrix} -\frac{1}{2} \\ \frac{1}{2} \end{bmatrix}. \tag{A.2}$$

Following the isoparametric approach the element stiffness matrix is expressed by

$$[K]_e = \frac{1}{\mu}\int_{-1}^{1}[B]^T \kappa [B] J\, A_e dr, \qquad \textbf{(A.3)}$$

where A_e is the cross section area of the element. Recognizing that the shape function derivatives are constant and assuming the cross section is constant over the length of the element, the stiffness matrix is given by

$$[K]_e = \frac{\kappa A_e}{\mu L}\begin{bmatrix} 1 & -1 \\ -1 & 1 \end{bmatrix}, \qquad \text{(A.4)}$$

where L is the length of the element.

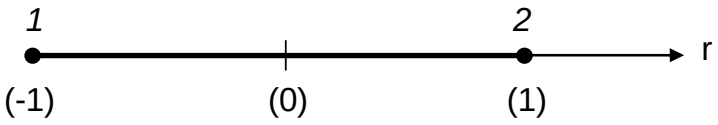

Figure A-1 Illustration of a two-node isoparametric line element.

The division of the line element into control volumes is given in Figure A-2. The shaded region of the element defined by points *1* and *a* illustrates the portion of the volume with contributes to the control volume associated with node 1.

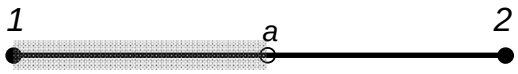

Figure A-2 Illustration of a two-node line element showing the control volume associated with node 1.

A.2 QUADRILATERAL ELEMENT

An isoparametric four-node quadrilateral element is shown in Figure A-3. The element uses linear shape functions given by

$$\begin{bmatrix} N_1 \\ N_2 \\ N_3 \\ N_4 \end{bmatrix} = \begin{bmatrix} \frac{1}{4}(1-r)(1-s) \\ \frac{1}{4}(1+r)(1-s) \\ \frac{1}{4}(1+r)(1+s) \\ \frac{1}{4}(1-r)(1+s) \end{bmatrix} \tag{A.5}$$

with shape function derivatives given by

$$\begin{bmatrix} \frac{\partial N_1}{\partial r} & \frac{\partial N_1}{\partial s} \\ \frac{\partial N_2}{\partial r} & \frac{\partial N_2}{\partial s} \\ \frac{\partial N_3}{\partial r} & \frac{\partial N_3}{\partial s} \\ \frac{\partial N_4}{\partial r} & \frac{\partial N_4}{\partial s} \end{bmatrix} = \begin{bmatrix} -\frac{1}{4}(1-s) & -\frac{1}{4}(1-r) \\ \frac{1}{4}(1-s) & -\frac{1}{4}(1+r) \\ \frac{1}{4}(1+s) & \frac{1}{4}(1+r) \\ -\frac{1}{4}(1+s) & \frac{1}{4}(1-r) \end{bmatrix}. \tag{A.6}$$

Following the isoparametric approach the element stiffness matrix is expressed by

$$[K]_e = \frac{1}{\mu}\int_{-1}^{1}\int_{-1}^{1}\left([B]^T[\kappa][B]|J|\right)h_e\,dr\,ds \tag{A.7}$$

Assuming that the thickness of the element (h_e) is constant the integral is solved using numerical integration (Gaussian quadrature) and the stiffness matrix is given as

$$[K]_e = \frac{h_e}{\mu}\sum_{i=1}^{n_{int}}[B(r_i,s_i)]^T[\kappa][B(r_i,s_i)]|J(r_i,s_i)|W_i \tag{A.8}$$

where n_{int} represents the number of integration points having coordinates (r_i, s_i) and associated weights W_i.

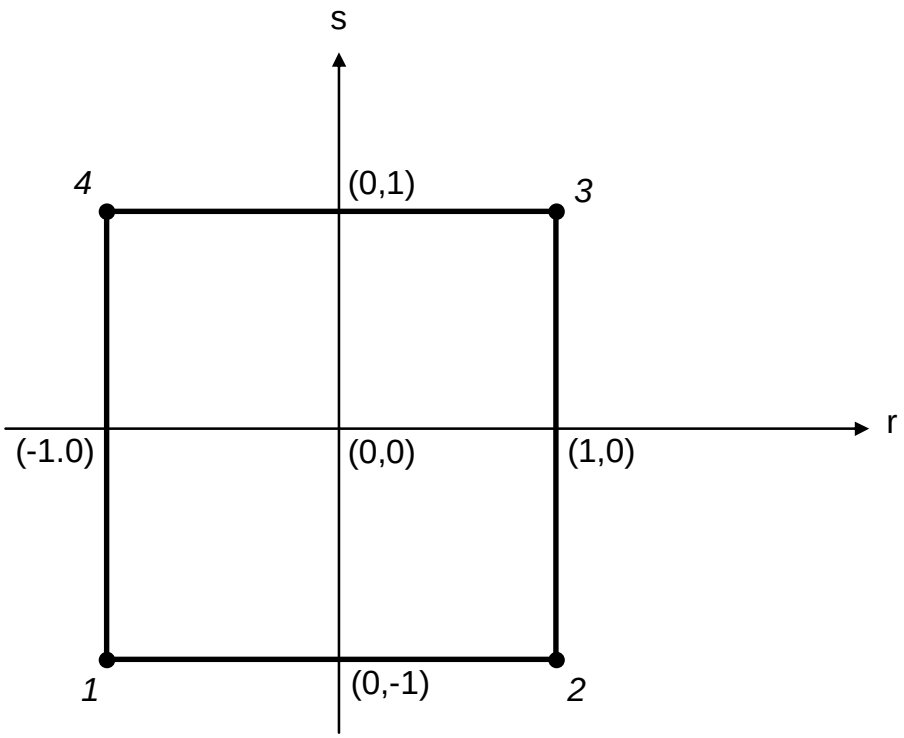

Figure A-3 Illustration of a four-node isoparametric quadrilateral element.

The division of the quadrilateral element into control volumes is given in Figure A-4. The shaded portion of the element defined by points *1*, *a*, *c*, and *b* (*1acb*) represents the portion of the element which contributes to the control volume associated with node 1.

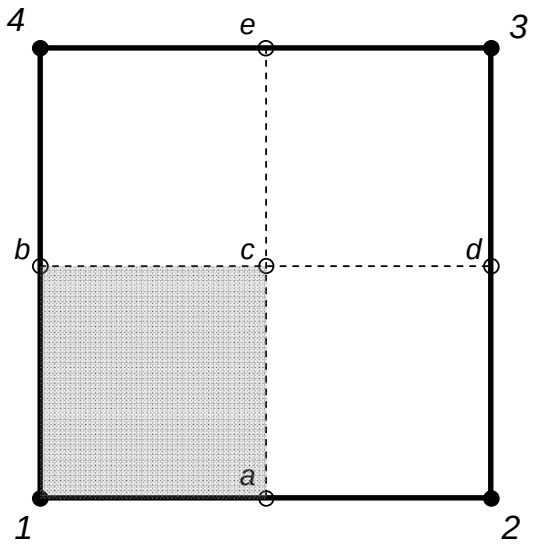

Figure A-4 Illustration of a four-node quadrilateral element showing the volume of the element which contributes to the control volume associated with node 1

A.3 TETRAHEDRAL ELEMENT

An isoparametric four-node tetrahedral element is shown in Figure A-5. The element uses linear shape functions given by

$$\begin{bmatrix} N_1 \\ N_2 \\ N_3 \\ N_4 \end{bmatrix} = \begin{bmatrix} r \\ s \\ t \\ 1-r-s-t \end{bmatrix} \tag{A.9}$$

where the shape function derivatives are constants given by

$$\begin{bmatrix} \frac{\partial N_1}{\partial r} & \frac{\partial N_1}{\partial s} & \frac{\partial N_1}{\partial t} \\ \frac{\partial N_2}{\partial r} & \frac{\partial N_2}{\partial s} & \frac{\partial N_2}{\partial t} \\ \frac{\partial N_3}{\partial r} & \frac{\partial N_3}{\partial s} & \frac{\partial N_3}{\partial t} \\ \frac{\partial N_4}{\partial r} & \frac{\partial N_4}{\partial s} & \frac{\partial N_4}{\partial t} \end{bmatrix} = \begin{bmatrix} 1 & 0 & 0 \\ 0 & 1 & 0 \\ 0 & 0 & 1 \\ -1 & -1 & -1 \end{bmatrix}. \tag{A.10}$$

Following the isoparametric approach the element stiffness matrix is expressed as

$$[K]_e = \frac{1}{6\mu} \int_0^1 \int_0^1 \int_0^1 \left([B]^T [\kappa][B] |J| \right) dr ds dt . \tag{A.11}$$

Since the shape function derivatives are constants the integration can be solved directly where the element stiffness matrix is given by

$$[K]_e = \frac{Vol_e}{\mu} [B]^T [\kappa][B]. \tag{A.12}$$

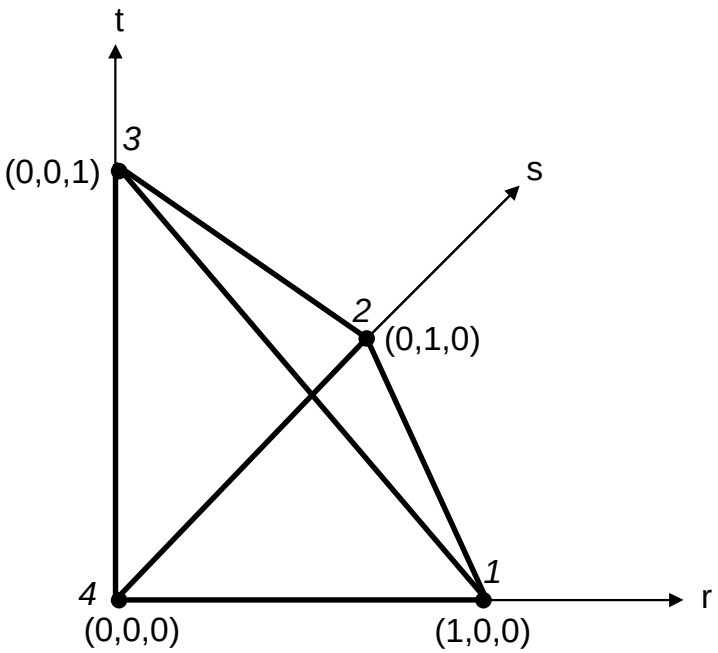

Figure A-5 Illustration of a four-node isoparametric tetrahedral element.

The division of the tetrahedral element into control volumes is given in Figure A-6. The tetrahedral is divided into four hexahedral volumes with each hexahedral contributing to the control volume associated with each of the four nodes. The shaded portion of the element volume (hexahedral) defined by corner points *1, a, j, f, c, g, k,* and *i* represents the volume of the tetrahedral which contributes to the control volume associated with node 1.

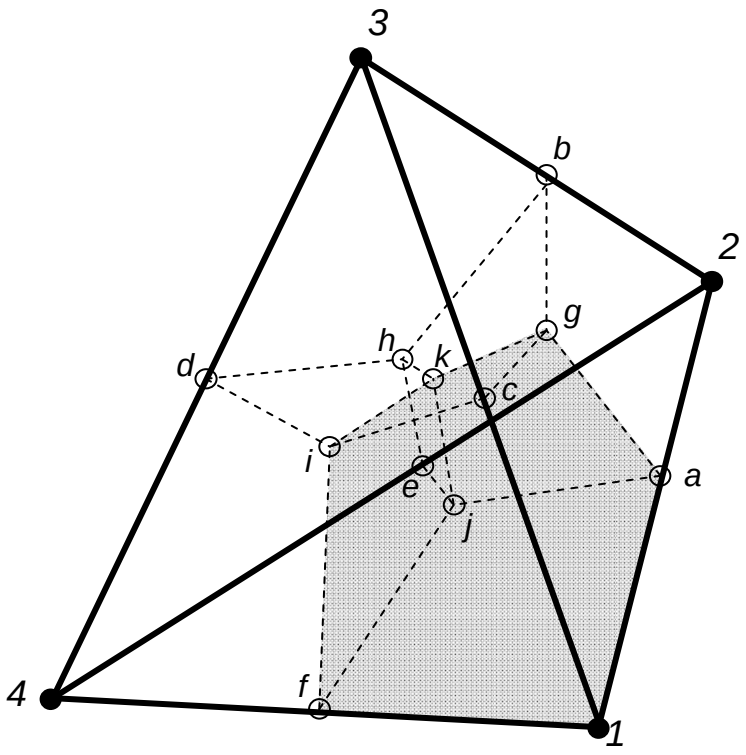

Figure A-6 Illustration of a four-node tetrahedral element showing the volume of the element which contributes to the control volume associated with node 1

A.4 WEDGE ELEMENT

An isoparametric six-node wedge element is shown in Figure A-7. The element uses linear shape functions given by

$$\begin{bmatrix} N_1 \\ N_2 \\ N_3 \\ N_4 \\ N_5 \\ N_6 \end{bmatrix} = \begin{bmatrix} \frac{r}{2}(1-t) \\ \frac{s}{2}(1-t) \\ \frac{1}{2}(1-r-s-t+rt+st) \\ \frac{r}{2}(1+t) \\ \frac{s}{2}(1+t) \\ \frac{1}{2}(1-r-s+t-rt-st) \end{bmatrix} \tag{A.13}$$

with the shape function derivatives given by

$$\begin{bmatrix} \frac{\partial N_1}{\partial r} & \frac{\partial N_1}{\partial s} & \frac{\partial N_1}{\partial t} \\ \frac{\partial N_2}{\partial r} & \frac{\partial N_2}{\partial s} & \frac{\partial N_2}{\partial t} \\ \frac{\partial N_3}{\partial r} & \frac{\partial N_3}{\partial s} & \frac{\partial N_3}{\partial t} \\ \frac{\partial N_4}{\partial r} & \frac{\partial N_4}{\partial s} & \frac{\partial N_4}{\partial t} \\ \frac{\partial N_5}{\partial r} & \frac{\partial N_5}{\partial s} & \frac{\partial N_5}{\partial t} \\ \frac{\partial N_6}{\partial r} & \frac{\partial N_6}{\partial s} & \frac{\partial N_6}{\partial t} \end{bmatrix} = \begin{bmatrix} \frac{1}{2}(1-t) & 0 & -\frac{r}{2} \\ 0 & \frac{1}{2}(1-t) & -\frac{s}{2} \\ -\frac{1}{2}(1-t) & -\frac{1}{2}(1-t) & \frac{1}{2}(r+s-1) \\ \frac{1}{2}(1+t) & 0 & \frac{r}{2} \\ 0 & \frac{1}{2}(1+t) & \frac{s}{2} \\ -\frac{1}{2}(1+t) & -\frac{1}{2}(1+t) & \frac{1}{2}(1-r-s) \end{bmatrix}. \tag{A.14}$$

Following the isoparametric approach the element stiffness matrix is expressed as

$$[K]_e = \frac{1}{2\mu} \int_0^1 \int_0^1 \int_{-1}^1 \left([B]^T [\kappa][B] |J| \right) drdsdt . \tag{A.15}$$

The integral is solved using numerical integration (Gaussian quadrature) and the stiffness matrix is expressed by

$$[K]_e = \frac{1}{2\mu}\sum_{i=1}^{n_{\text{int}}}[B(r_i,s_i,t_i)]^T[\kappa][B(r_i,s_i,t_i)]|J(r_i,s_i,t_i)|W_i \qquad \text{(A.16)}$$

where n_{int} represents the number of integration points having coordinates (r_i, s_i, t_i) and associated weights W_i.

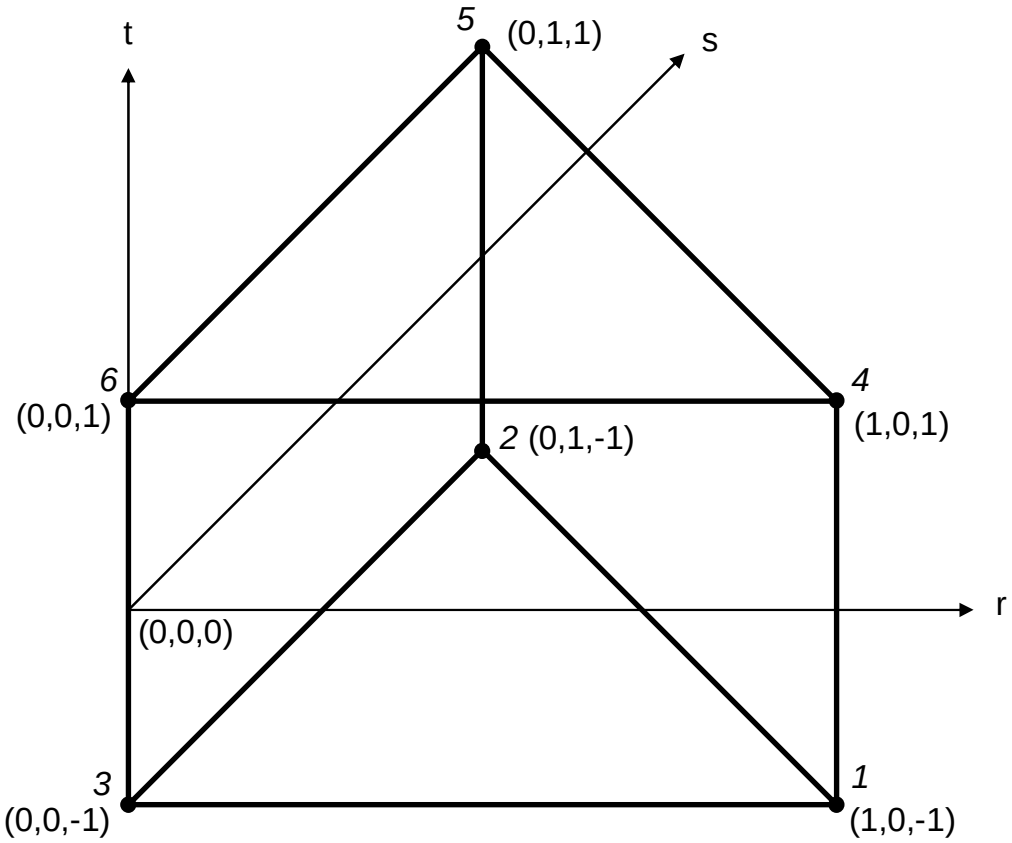

Figure A-7 Illustration of a six-node isoparametric wedge element.

The division of the wedge element into control volumes is given in Figure A-8. The wedge is divided into six hexahedral volumes with each hexahedral contributing to the control volume associated with each of the six nodes. The shaded portion of the element volume (hexahedral) defined by corner points *1*, *a*, *d*, *c*, *e*, *f*, *k*, and *j* represents the volume of the wedge which contributes to the control volume associated with node 1.

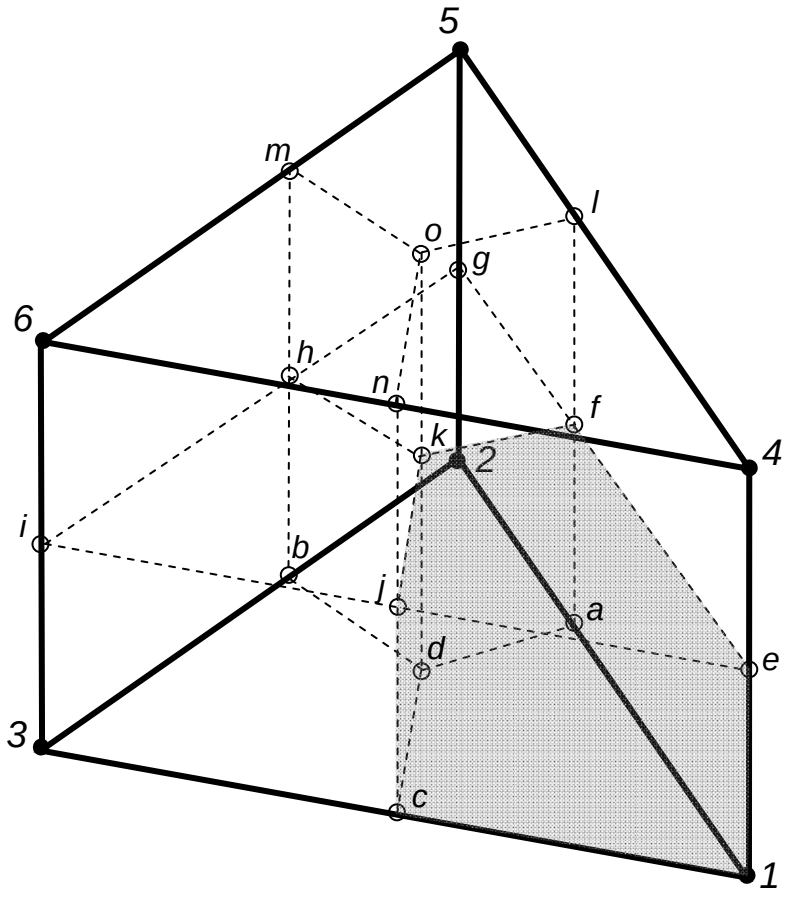

Figure A-8 Illustration of a six-node wedge element showing the volume of the element which contributes to the control volume associated with node 1

A.5 HEXAHEDRAL ELEMENT

An isoparametric eight-node hexahedral element is shown in Figure A-9. The element uses linear shape functions given by

$$\begin{bmatrix} N_1 \\ N_2 \\ N_3 \\ N_4 \\ N_5 \\ N_6 \\ N_7 \\ N_8 \end{bmatrix} = \begin{bmatrix} \frac{1}{8}(1+r)(1-s)(1-t) \\ \frac{1}{8}(1+r)(1+s)(1-t) \\ \frac{1}{8}(1-r)(1+s)(1-t) \\ \frac{1}{8}(1-r)(1-s)(1-t) \\ \frac{1}{8}(1+r)(1-s)(1+t) \\ \frac{1}{8}(1+r)(1+s)(1+t) \\ \frac{1}{8}(1-r)(1+s)(1+t) \\ \frac{1}{8}(1-r)(1-s)(1+t) \end{bmatrix} \tag{A.17}$$

with the shape function derivatives given by

$$\begin{bmatrix} \frac{\partial N_1}{\partial r} & \frac{\partial N_1}{\partial s} & \frac{\partial N_1}{\partial t} \\ \frac{\partial N_2}{\partial r} & \frac{\partial N_2}{\partial s} & \frac{\partial N_2}{\partial t} \\ \frac{\partial N_3}{\partial r} & \frac{\partial N_3}{\partial s} & \frac{\partial N_3}{\partial t} \\ \frac{\partial N_4}{\partial r} & \frac{\partial N_4}{\partial s} & \frac{\partial N_4}{\partial t} \\ \frac{\partial N_5}{\partial r} & \frac{\partial N_5}{\partial s} & \frac{\partial N_5}{\partial t} \\ \frac{\partial N_6}{\partial r} & \frac{\partial N_6}{\partial s} & \frac{\partial N_6}{\partial t} \\ \frac{\partial N_7}{\partial r} & \frac{\partial N_7}{\partial s} & \frac{\partial N_7}{\partial t} \\ \frac{\partial N_8}{\partial r} & \frac{\partial N_8}{\partial s} & \frac{\partial N_8}{\partial t} \end{bmatrix} = \begin{bmatrix} \frac{1}{8}(1-s)(1-t) & -\frac{1}{8}(1+r)(1-t) & -\frac{1}{8}(1+r)(1-s) \\ \frac{1}{8}(1+s)(1-t) & \frac{1}{8}(1+r)(1-t) & -\frac{1}{8}(1+r)(1+s) \\ -\frac{1}{8}(1+s)(1-t) & \frac{1}{8}(1-r)(1-t) & -\frac{1}{8}(1-r)(1+s) \\ -\frac{1}{8}(1-s)(1-t) & -\frac{1}{8}(1-r)(1-t) & -\frac{1}{8}(1-r)(1-s) \\ \frac{1}{8}(1-s)(1+t) & -\frac{1}{8}(1+r)(1+t) & \frac{1}{8}(1+r)(1-s) \\ \frac{1}{8}(1+s)(1+t) & \frac{1}{8}(1+r)(1+t) & \frac{1}{8}(1+r)(1+s) \\ -\frac{1}{8}(1+s)(1+t) & \frac{1}{8}(1-r)(1+t) & \frac{1}{8}(1-r)(1+s) \\ -\frac{1}{8}(1-s)(1+t) & -\frac{1}{8}(1-r)(1+t) & \frac{1}{8}(1-r)(1-s) \end{bmatrix} \quad \text{(A.18)}$$

Following the isoparametric approach the element stiffness matrix is expressed as

$$[K]_e = \frac{1}{\mu}\int_{-1}^{1}\int_{-1}^{1}\int_{-1}^{1}\left([B]^T[\kappa][B]|J|\right)drdsdt\,. \quad \text{(A.19)}$$

The integral is solved using numerical integration (Gaussian quadrature) and the stiffness matrix is expressed by

$$[K]_e = \frac{1}{\mu}\sum_{i=1}^{n_{\text{int}}}[B(r_i,s_i,t_i)]^T[\kappa][B(r_i,s_i,t_i)]\left|J(r_i,s_i,t_i)\right|W_i \quad \text{(A.20)}$$

where n_{int} represents the number of integration points having coordinates (r_i, s_i, t_i) and associated weights W_i.

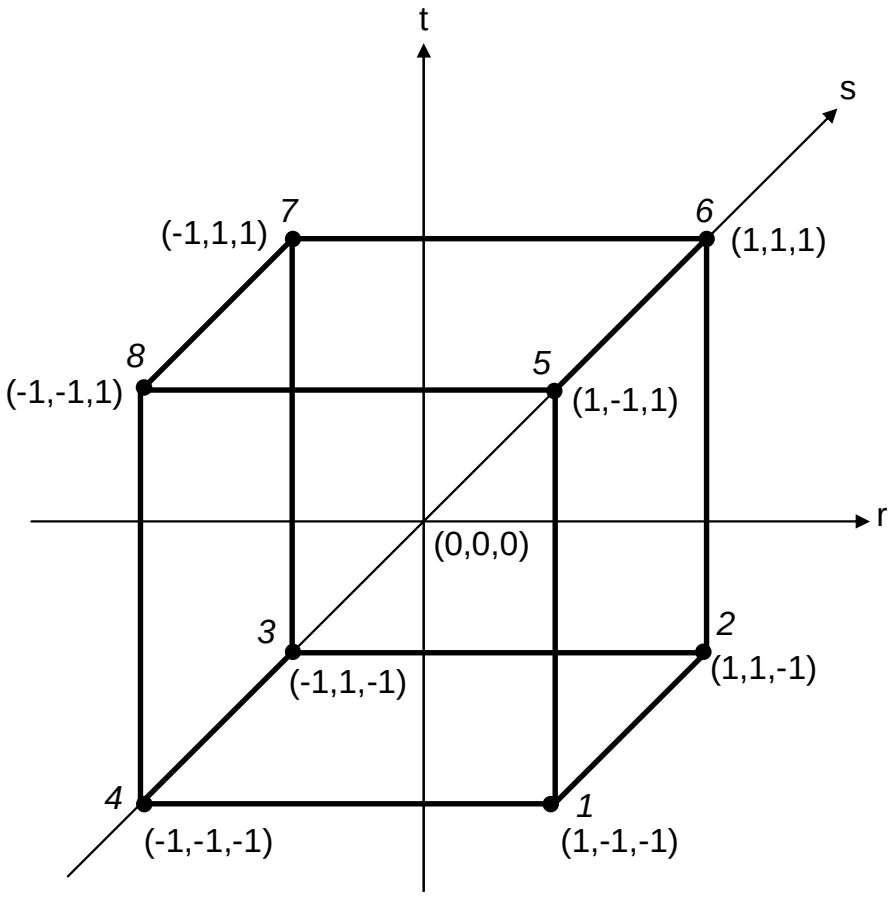

Figure A-9 Illustration of an eight-node isoparametric hexahedral element.

The division of the hexahedral element into control volumes is given in Figure A-10. The element is divided into eight hexahedral volumes with each hexahedral contributing to the control volume associated with each of the eight nodes. The shaded portion of the element volume (hexahedral) defined by corner points *1, a, c, b,*

f, *g*, *j*, and *i* represents the volume of the element which contributes to the control volume associated with node 1.

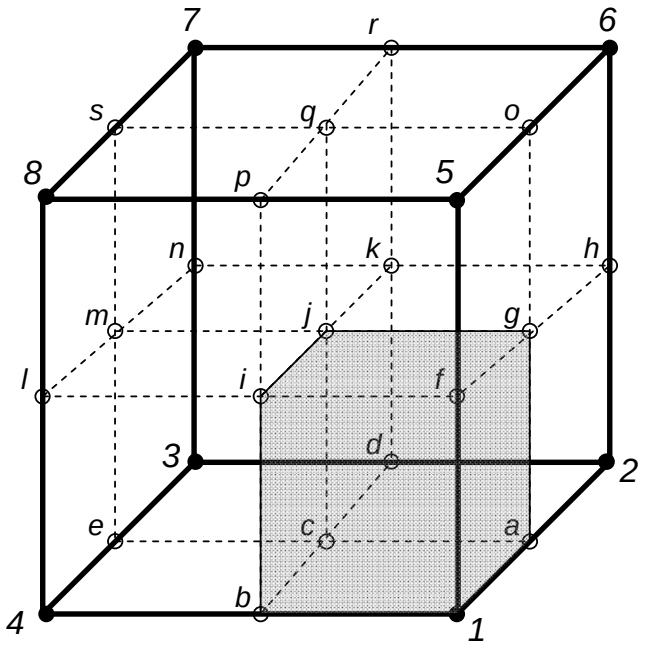

Figure A-10 Illustration of an eight-node hexahedral element showing the volume of the element which contributes to the control volume associated with node 1

APPENDIX B

COORDINATE TRANSFORMATION

For models which use two-dimensional elements, where the flow is in the plane of the element, it is necessary to transform from the global coordinate system to the local element coordinate system. This transformation occurs through a rotation about the *x*-axis followed by a rotation about the *y*-axis such that the element *z*-axis coincides with the element normal. An illustration of an element showing the surface normal with the global coordinate system is given in Figure B-1. The normal vector ($\hat{n}$) is expressed in global coordinates by the coordinates of the three corners by

$$\hat{n} = \frac{\left(\overline{x}_3 - \overline{x}_1\right) \times \left(\overline{x}_2 - \overline{x}_1\right)}{\left|\left(\overline{x}_3 - \overline{x}_1\right) \times \left(\overline{x}_2 - \overline{x}_1\right)\right|} \tag{B.1}$$

where $\overline{x}$ are the coordinate vectors given by

$$\overline{x}_i = \begin{Bmatrix} x(i) \\ y(i) \\ z(i) \end{Bmatrix} \quad i = 1, 2, 3. \tag{B.2}$$

First the rotation about the *x*-axis is determined such that the element normal lies within the *x*-*z* plane. This rotation angle is given by

$$\theta_x = \cos^{-1}\left(\frac{n(3)}{\sqrt{n(3)^2 + n(2)^2}}\right). \tag{B.3}$$

The transformation about the *x*-axis is given by

$$\begin{Bmatrix} n'(1) \\ n'(2) \\ n'(3) \end{Bmatrix} = \begin{bmatrix} 1 & 0 & 0 \\ 0 & \cos\theta_x & -\sin\theta_x \\ 0 & \sin\theta_x & \cos\theta_x \end{bmatrix} \begin{Bmatrix} n(1) \\ n(2) \\ n(3) \end{Bmatrix}, \tag{B.4}$$

where the prime indicates the normal in the transformed coordinate system. Next the required rotation about the *y*-axis is given by

$$\theta_y = \cos^{-1}\left(\frac{n'(3)}{\sqrt{n'(1)^2 + n'(3)^2}}\right) \tag{B.5}$$

By combining the transformations about the *x* and *y*-axis the transformation from the global coordinate system to the local element coordinate system is given by

$$\begin{Bmatrix} x' \\ y' \\ z' \end{Bmatrix} = \begin{bmatrix} \cos\theta_y & -\sin\theta_x \sin\theta_y & -\sin\theta_y \cos\theta_x \\ 0 & \cos\theta_x & -\sin\theta_x \\ \sin\theta_y & \sin\theta_x \cos\theta_y & \cos\theta_x \cos\theta_y \end{bmatrix} \begin{Bmatrix} x \\ y \\ z \end{Bmatrix} \tag{B.6}$$

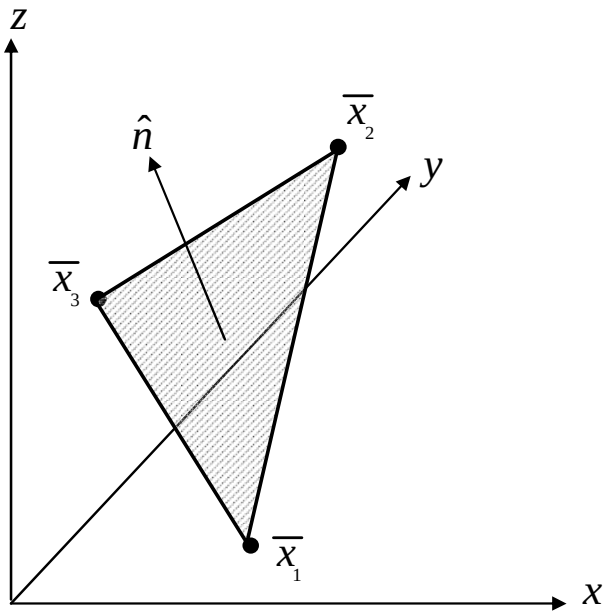

Figure B-1 Illustration of a two-dimensional element showing the element normal in relationship to the global coordinate system.

REFERENCES

1. Walz, M. 2006. The Dream of Composites. Advantage Business Media, www.rdmag.com, Issue November 2006, (accessed July 2008).

2. Nguyen, L. B., Juska, T., and Mayes, J. S. 1997. Evaluation of Low Cost Manufacturing Technologies for Large Scale Composite Ship Structures, Collection of Technical Papers, AIAA/ASME/ASCE/AHS/ASC Structures, Structural Dynamic and Materials Conference 2: 992-1001.

3. Lewit, S. M., and Jakubowski, J. C. 1997. Low Cost VARTM Process for Commercial and Military Applications. 42nd International SAMPE Symposium 99: 1173-1187.

4. Pike, T., McArthur, M., and Schade, D. 1996. Vacuum Assisted Resin Transfer Molding of a Layered Structural Laminate for Application on Ground Combat Vehicles. International SAMPE Technical Conference 28: 374-380.

5. Kosmatka, J. B. 1999. Structural Testing of DARPA/BIR Composite Army Bridge. *Composite Structures* 44 (2-3): 99-115.

6. Alagusundaramoorthy, P., Harik, I., and Choo, C. 2006. Structural Behavior of FRP Composite Bridge Deck Panels. *Journal of Bridge Engineering* 11 (4): 384-393.

7. Ehlen, M. 1999. Life-Cycle Costs of Fiber-Reinforced-Polymer Bridge Decks. *Journal of Materials in Civil Engineering* 11 (3): 224-230.

8. Davalos, J., Qian, P., Frank, Xu X., Robinson, J., and Barth, K. 2001. Modeling and Characterization of Fiber-Reinforced Honeycomb Sandwich Panels for Highway Bridge Applications. *Composite Structures* 52 (3-4): 441-452.

9. GangaRao, H., Thippeswamy, H., Shekar, V., and Craigo, C. 1999. Development of Glass Fiber Reinforced Polymer Composite Bridge Deck. *SAMPE Journal* 35 (4): 12-24.

10. Brouwer, W. D., Van Herpt, E. C. F. C., and Labordus, M. 2003. Vacuum Injection Moulding for Large Structural Applications. *Composites Part A.* 34: 551-558.

11. Military Handbook 17-1F: Composite Materials Handbook, Volume 1 Polymer Matrix Composites Guidelines for Characterization of Structural Materials, Department of Defense, 2002.

12. Williams, C., Summerscales, J, and Grove, S. 1996. Resin Infusion Under Flexible Tooling (RIFT): a Review. *Composites Part A* 27:517-524.

13. Muskat, I. 1950. Method of Molding. US Patent No. 2495640.

14. Adams, A. 1972. Vacuum Molding Patent, GB Patent No. 1432333.

15. Gotch, T. M. 1978. Improved Production Process for Manufacture of GRP on British Rail. 11th Reinforced Plastics Conference, BPF, RPG, Brighton, Paper 4: 33-39.

16. Gotch, T. M. 1980. Developments and Potential of Vacuum Impregnation Techniques for GRP Manufacture. 12th Reinforced Plastics Conference, BPF, RPG, Brighton 7 Paper 7: 25-31.

17. Gotch, T. M. 1985. Low Investment Alternatives to Hand Lay GRP Production. Hands Off GRP II Conference Plastic and Rubber Institute: 1-11.

18. Seemann, W. 1990. Plastic Transfer Molding Techniques for the Production of Fiber Reinforced Plastic Structures. US Patent No. 4902215.

19. Seemann, W. 1994. Unitary Vacuum Bag for Forming Composite Articles. US Patent No. 5316462.

20. Rigas, E. J. and Mulkern, T. J. 2006. Process and Apparatus for Improved Composite Fiber Volume Fraction and Dimensional Stability by Removal of Accumulated Excess Resin Using the Vacuum Assisted Resin Transfer Molding (VARTM) Process. US Patent No. 7147818.

21. Woods, J., Modin, A., Hawkins, R., and Hanks, D. 2008. Controlled Atmospheric Pressure Resin Infusion Process, US Patent No. 7334782.

22. Filsinger, J., Lornez, T., Stadler, F., and Utecht, S. 2001. Method and Device for Producing Fiber-reinforced Components Using an Injection Method, German Patent WO 01/68353 A1.

23. Li, W., Krehl, J., Gillespie, J. W., Heider, D., Endrulat, M., Hochrein, K., Dunham, M. G., and Dubois, C. J. 2004. Process and Performance Evaluation of the Vacuum-Assisted Process. *Journal of Composite Materials* 38 (20): 1803-1814.

24. Walsh, S. 2003. Apparatus and Method for Selectively Distributing and Controlling a Means for Impregnation of Fibrous Articles. US Patent No. 6586054.

25. Allende, M., Mohan, R., and Walsh, S. 2004. Experimental and Numerical Analysis of Flow Behavior in the FASTRAC Liquid Composite Manufacturing Process. *Polymer Composites* 25 (4): 384-396.

26. Darcy, H. 1856. *Les Fontaines Publiques de la Villa de Dijon.*

27. Dave, R. 1990. A Unified Approach to Modeling Resin Flow During Composite Processing. *Journal of Composite Materials* 24: 22-41.

28. Pillai, K. M. and Advani, S. G. 1998. A model for Unsaturated Flow in Woven Fiber Preforms during Mold Filling in Resin Transfer Molding. *Journal of Composite Materials* 32 (19): 1753-1783.

29. Coulter, J. P., Smith, B. F., and Guceri, S. I. 1988. Experimental and numerical analysis of resin impregnation during the manufacturing of composite materials. Proceedings of the American Society for Composites, Second Technical Conference: 209-217.

30. Friedrichs, B. and Guceri, S. I. 1995. A Hybrid Numerical Technique to Model 3-D Flow Fields in Resin Transfer Molding Process. *Polymer Engineering and Science* 35 (23): 1834-1851.

31. Yoo, Y. E. and Lee, W. I. (1996). Numerical Simulation of the Resin Transfer Mold Filling Process Using the Boundary Element Method. Polymer Composites 17(3), 368-374.

32. Wang, H. P. and Lee, H. S. 1989. *Fundamental of Computer Modeling for Polymer Processing*, Chapter 8, ed. C. L. Tucker. New York: Hanser Publishers.

33. Fracchia, C. A., Castro, J., and Tucker, C. L. 1989. A Finite Element/Control Volume Simulation of Resin Transfer Mold Filling. Proceedings of the American Society for Composites, Fourth Technical Conference: 157-166.

34. Bruschke, M. V., and Advani, S. G. 1990. A Finite Element/Control Volume Approach to Mold Filling in Anisotropic Porous Media. *Polymer Composites* 11 (6): 398-405.

35. Simacek, P., Advani, S. G., and Binetruy, C. 2004. LIMS: A Comprehensive Tool. *JEC Composites* 8: 143-146.

36. Young, W. B., Han, K., Fong, L. H., Lee, L. J., and Liou, M. J. 1991. Flow Simulation in Molds with Preplaced Fiber Mats. *Polymer Composites* 12 (6): 391-403

37. Young W.B., Rupel K., Han K., and Lee L.J. (1991) Analysis of Resin Injection Molding in Molds With Preplaced Fiber Mats. II: Numerical Simulation and Experiments of Mold Filling, *Polymer Composites* 12(1) pp 30-38.

38. Calhoun, D. R., Yalvac, S., Wetters, D. G., Wu, C. H., Wang, T. J., Tsai, J. S., and Lee, L. J. 1996. Mold Filling Analysis in Resin Transfer Molding. *Polymer Composites* 17 (2): 251-264.

39. Koorevaar, A., 2002. Simulation of Liquid Injection Molding Delivering on the Promise. SAMPE 2002, JEV in Paris.

40. Young, W. B. 1994. Three-Dimensional Nonisothermal Mold Filling Simulations in Resin Transfer Molding. *Polymer Composites* 15 (2): 118-127.

41. Trochu, F., Gauvin, R., and Gao, D. M. 1993. Numerical Analysis of the Resin Transfer Molding Process by the Finite Element Method. *Advances in Polymer Technology* 12 (4): 329-342.

42. Trochu, F., Gauvin, R., Gao, D. M., and Boudreault, J. F. 1994. RTMFLOT-An Integrated Software Environment for the Computer Simulation of the Resin Transfer Molding Process. *Reinforced Plastics and Composites* 12: 262-270.

43. Mohan, R. V., Ngo, N. D., and Tamma, K. K. 1999. On a Pure Finite-Element-Based Methodology for Resin Transfer Mold Filling Simulation. *Polymer Engineering and Science* 39 (1): 26-43.

44. Mohan, R. V., Ngo, N. D., and Tamma, K. K. 1999. Three Dimensional Resin Transfer Molding: Isothermal Process Modeling and Explicit Tracking of Moving Fronts for Thick Geometrically Complex Composites Manufacturing Applications Part I. *Numerical Heat Transfer, Part A* 35: 815-838.

45. Mohan, R. V., Ngo, N. D., Tamma, K. K, and Shires, D. R. 1999. Three Dimensional Resin Transfer Molding: Isothermal Process Modeling and Explicit Tracking of Moving Fronts for Thick Geometrically Complex Composites Manufacturing Applications Part II. *Numerical Heat Transfer, Part A* 35: 839-858.

46. Pillai, K. M. and Advani, S. G. 1998. Numerical Simulation of Unsaturated Flow in Woven Fiber Preforms During the Resin Transfer Molding Process. *Polymer Composites* 19 (1): 71-80.

47. Kempner, E A, 1997. *Process Simulations for Manufacturing of Thick Composites*. Dissertation, UCLA, Los Angeles, California.

48. Kang, M. K., Lee, W. I., and Hahn, H. T. 2001. Analysis of Vacuum Bag Resin Transfer Molding Process. *Composites Part A* 32: 1553-1560

49. Joubaud, L., Achim, V., and Trochu, F. 2005. Numerical Simulation of Resin Infusion and Reinforcement Consolidation Under Flexible Cover. *Polymer Composites* 26 (4): 417-427.

50. Correia, N. C., Robitaille, F., Long, A. C., Rudd, C. D., Simacek, P., and Advani, S. G. 2004. Use of Resin Transfer Molding Simulation to Predict Flow, Saturation, and Compaction in the VARTM Process. *Journal of Fluids Engineering* 126: 210-215.

51. Young, S. S. 2006. Mathematical Analysis of Resin Flow Through Fibrous Porous Media. Applied Composite Materials 13: 335-343.

52. Lopatnikov, S., Simacek, P., Gillespie, J., and Advani, S. G. 2004. A Closed Form Solution to Describe Infusion of Resin Under Vacuum in Deformable Fibrous Porous Media. *Modeling and Simulation in Materials Science and Engineering* 12: 191-204.

53. Walsh, S. M. and Freese, C. E. 2005. Numerical Model of Relaxation During Vacuum Assisted Resin Transfer Molding (VARTM). Polymer Composites 26 (5): 628-635.

54. Song, X. 2003. *Vacuum Assisted Resin Transfer Molding (VARTM): Model Verification*. Dissertation, Virginia Polytechnic Institute and State University, Blacksburg, Virginia.

55. Song, X., Loos, A., Grimsley, B. W., Cano, R. J., and Hubert, P. 2004. Modeling the VARTM Composite Manufacturing Process. SAMPE 2004 Long Beach.

56. Grimsley, B. W., Hubert, P., Song, X., Cano, R. J., Loos, A. C., and Pipes, B. 2001. Flow and Compaction During the Vacuum Assisted Resin Transfer Molding Process. SAMPE Technical Conference 2001.

57. Grimsley, B. W., Cano, R. J., Hubert, P., Loos, A. C., Kellen, C. B., and Jensen, B. J. 2004 Preform Characterization in VARTM Process Model Development. SAMPE 36th ISTC San Diego CA Nov. 15-18.

58. MacRae, J. D. 1994. *Development and Verification of a Resin Film Infusion/Resin Transfer Molding Simulation Model for Fabrication of Advanced Textile Composites*. Thesis, Virginia Polytechnic Institute and State University, Blacksburg, Virginia.

59. Caba, C. A. 1998. *Verification of a Three-Dimensional Resin Film Infusion Process Simulation Model*. Thesis, Virginia Polytechnic Institute and State University, Blacksburg, Virginia.

60. Hsiao, K-T., Mathur, R., Advani, S. G., Gillespie, J. W., and Fink, B. K. 2000. A Closed Form Solution for Flow During the Vacuum Assisted Resin Transfer Molding Process. *Journal of Manufacturing Science and Engineering* 122: 463-475.

61. Yoon, M-K. and Doan, D. F. 2008. Homogeneous Modeling of VARTM Processes with Hybrid Layer Media. Journal of Composite Materials 42(8): 805-824.

62. Sun, X., Li, S., and Lee, L. J. 1998. Mold Filling Analysis in Vacuum-Assisted Resin Transfer Molding. Part I: SCRIMP Based on a High-Permeable Medium. *Polymer Composites* 19 (6): 807-817.

63. Jun, N. Shoujie, L., Sun, X., and Lee, L. J. 1998. Mold Filling Analysis in Vacuum-Assisted Resin Transfer Molding. Part II: SCRIMP Based on Grooves. *Polymer Composites* 19 (6): 818-829.

64. Song, Y. S. and Youn, J. R. 2008. Numerical Investigation on Flow through Porous Media in the Post-infuison Process. *Ploymer Composites* published on-line July 2008: 1-7.

65. Kozeny, J. 1927. Ueber kapillare Lietung des Wassers im Boden Sitzungsperichte Wiener Akademie, 136(2a): 271-306.

66. Carman, P. C. 1937. Fluid Flow Though Granular Beds, Tansacations. Institution of Chemical Engineering, London, 15: 150-166.

67. Gutowski, T. G. 1985. A Resin Flow/Fiber Deformation Model for Composites. *SAMPE Quarterly* 16 (4): 58-64.

68. Gutowski, T. G., Cai, Z., Kingery, J., and Wineman, S. J. 1986. Resin Flow/Fiber Deformation Experiments. *SAMPE Quarterly* 17 (4): 54-58.

69. Gutowski, T. G., Morigaki, T., and Cai, Z. 1987. The Consolidation of Laminate Composites. *Journal of Composite Materials* 21: 172-188.

70. Stadtfeld, H. C., Erninger, M., Bickerton, S., and Advani, G., 2002. An Experimental Method to Continuously Measure Permeability of Fiber Preforms as a Function of Fiber Volume Fraction. *Journal of Reinforced Plastics and Composites* 21 (10): 879-899.

71. Parnas, R. S., Flynn, K. M., and Dal-Favero, M. E. 1997. A Permeability Database for Composite Manufacturing. *Polymer Composites,* 18 (5): 623-633.

72. Lai, Y. H., Khomami, B., and Kardos, J. L. 1997. Accurate Permeability Characterization of Preforms Used in Polymer Matrix Composite Fabrication Processes. *Polymer Composites* 18 (3): 368-377.

73. Chan, A. W. and Hwang, S. T. 1991. Anisotropic In-Plane Permeability of Fabric Media, *Polymer Engineering and Science* 31 (16): 1233-1239.

74. Han, K., Lee, C. W., and Rice, B. P. 2000. Measurements of the Permeability of Fiber Preforms and Applications. *Composites Science and Technology* 60: 2435-2441.

75. Gauvin, R., Trochu, F., Lemmen, Y., and Diallo, L. 1996. Permeability Measurement and Flow Simulation Through Fiber Reinforcement. *Polymer Composites* 17 (1): 34-42.

76. Jeffrey, A. A., Pavel, S., and Advani, S. G. 2003. The Implications of Fiber Compaction and Saturation on Fully Coupled VARTM Simulation. *Composites Part A* 35: 159-169.

77. Lekakou, C., Johari, M. A. K. B., and Bader, M. G. 1996. Compressibility and Flow Permeability of Two-Dimensional Woven Reinforcements in the Processing of Composites. *Polymer Composites* 17 (5): 666-672.

78. Luce, T., Advani, S., Howard, J., and Parnas, R. 1995. Permeability Characterization. Part 2: Flow Behavior in Multiple-Layer Preforms. *Polymer Composites* 16 (6): 446-458.

79. Adams, K. L. and Rebenfeld, L. 1991 Permeability Characteristics of Multilayer Fiber Reinforcements Part I: Experimental Observations. *Polymer Composites* 12 (3): 179-185.

80. Mogavero, J. and Advani, S. G. 1997. Experimental Investigation of Flow Through Multi-Layered Preforms. *Polymer Composites* 18 (5): 649-655.

81. Tackitt, K. D. and Walsh, S. M. 2005. Experimental Study of Thickness Gradient Formation in the VARTM Process. *Materials and Manufacturing Process* 20: 607-627.

82. Dave, R., Kardos, J. L., and Dudukovic, M. P. 1987. A Model for Resin Flow during Composite Processing: Part 1-General Mathematical Development. *Polymer Composites* 8 (1): 29-38.

83. Acheson, J. A., Simacek, P., and Advani, S. G. 2003. The Implications of Fiber compaction and Saturation on Fully Coupled VARTM Simulation, *Composites Part A* 35: 159-169.

84. Sozer, E. M., Chen, B., Graham, P. J., Chou, T-W, and Advani, S. G. 1999. Characterization and Prediction of Compaction Force and Preform Permeability of Woven Fabrics During the Resin Transfer Molding Process. Plymouth, U.K. Proceedings of the Fifth International Conference on Flow Processes in Composite Materials: 25–36.

85. Chen, B, Chou, T-W. 1999. Compaction of Woven-Fabric Preforms in Liquid Composite Molding Processes: Single-Layer Deformation. *Composites Science and Technology* 59: 1519–1526.

86. Chen, B, Chou, T-W. 1999. Compaction of Woven-Fabric Preforms: Nesting and Multi-layer Deformation. *Composites Science and Technology* 60: 2223–2231.

87. Chen B, Cheng AH-D, Chou T-W. 2001 A Nonlinear Compaction Model for Fibrous Preforms. *Composites Part A* 32: 701–707.

88. Chen B., Lang, E. J., and Chou, T-W. 2001. Experimental and Theoretical Studies of Fabric Compaction Behavior in Resin Transfer Molding. Materials. *Science and Engineering A* (317)1: 188–196.

89. Robitaille, F., and Gauvin, R. 1998. Compaction of Textile Reinforcements for Composites Manufacturing I: Review of Experimental Results. *Polymer Composites.* 19 (2): 198–216.

90. Saunders, R A., Lekakou, C., and Bader, M. G. 1999. Compression and Microstructure of Fibre Plain Woven Cloths in the Processing of Polymer Composites. *Composites Part A.* 29: 443–454.

91. Saunders, R A., Lekakou, C., and Bader, M. G. 1999. Compression in the Processing of Polymer Composites. 1. A Mechanical and Micro Structural Study of Different Glass Fabrics and Resins. *Composites Science and Technology* 59: 983–93.

92. Luo, Y., and Verpoest, I. 1999. Compressibility and Relaxation of a New Sandwich Textile Preform for Liquid Composite Molding. *Polymer Composites* 20 (2): 179–191.

93. Advani, S. G., and Sozer, E. M. 2003. *Process Modeling in Composite Manufacturing*. New York: Marcel Dekker AG.

94. Huebner, K. H., Dewhirst, D. L., Smith, D. E., and Byrom, T. G. 2001. *The Finite Element Method for Engineers*. New York: John Wiley and Sons.

95. Castro, J. M. and Macosko, C. W. 1982. Studies of Mold Filling and Curing in the Reaction Injection Molding Process. *AICheE Journal* 28 (2): 250-260.

96. Wang, V., Hieber, C. A., and Wang, K. K. 1986. Dynamic Simulation and Graphics for the Injection Molding of Three-Dimensional Thin Parts. *Journal of Polymer Engineering* 7 (1): 21-45.

97. Mase, G. T., and Mase, G. E. 1999. *Continuum Mechanics for Engineers*. Boca Raton: CRC Press.

98. Nedanov, P. B., and Advani, S. G. 2002. A Method to Determine 3D Permeability of Fibrous Reinforcements. *Journal of Composite Materials* 36 (2): 241-254.

99. Parnas, R. S., and Salem, A. J. 1993. A Comparison of the Unidirectional and Radial In-Plane Flow of Fluids through Woven Composite Reinforcements. *Journal of Polymer Composites* 14 (5): 383-394.

100. Sayre, J. R. 2000. *Vacuum-Assisted Resin Transfer Molding (VARTM) Model Development, Verification, and Process Analysis*. Dissertation, Virginia Polytechnic Institute and State University, Blacksburg, Virginia.

101. Carman, P. C. 1939. Fluid Flow Through Granular Beds. *Journal of Agricultural Science* 29: 351.

102. Gebart, B. R. 1992. Permeability of unidirectional reinforcements for RTM. *Journal of Composite Materials* 26 (8): 1100–33.

103. Bruschke, M. V., Advani, S. G. 1003. Flow of generalized Newtonian fluids across a periodic array of cylinders. *Journal of Rheology* 37 (3): 479–98.

104. Lazurus, P. 1994. Infusion. *Professional Boat Builder*, 30: 42-45.

105. Draper, N. R., and Smith, H. 1998. *Applied Regression Analysis*. New York: Wiley and Sons.

106. Herakovich, C. T. 1998. *Mechanics of Fibrous Composites.* New York: John Wiley and Sons.

107. Connors, S. C., and Foss, D. F 2005. *Jane's Military Vehicles and Logistics.* Jane's Information Group.

108. Kosmatka, J., Grippo, W., Policelli, F., Charbonnet, S., Randolph, B., and Hegimier, G. 2000. Advanced Composites for Bridge Infrastructure Renewal-Phase II DARPA. Report No. SSRP-2000/06, Department of Structural Engineering, UCSD.

109. Kosmatka, J. B. and Policelli, F. J. 1999. Development of the DARPA/BIR Composite Army Bridge: Phase I Accomplishment. *Journal of Advanced Materials* 31 (3): 23-36.

110. Hutcheson, D. and Sheppard, M. 2003. Optimizing Sandwich Panel Performance with 3-D Fiber Reinforcing core Architecture. *SAMPE Journal* 39 (6): 68-75.

111. Stoll, F., Campbell, S., Day, S., and Sheppard, M. 2004. High-Performance, Low-Cost Infusion Cores for Structural Sandwich Panels. Proceedings of SAMPE 2004, Long Beach Convention Center Long Beach CA.

112. Williams, B., Shehata, E., and Rizkalla, S. 2003. Filament-Wound Glass Fiber Reinforced Polymer Bridge Deck Modules. *Journal of Composites for Construction* 4 (3): 266-273.

113. Zureick, A., Shif, B., and Munley, E. 1995. Fiber-Reinforced Polymeric Bridge Decks. *Structural Engineering Review* 7 (3): 256-266.

114. Hetenyi, M. 1964. *Beams on Elastic Foundation.* Ann Arbor: The University of Michigan Press.

115. U.S. Pat. 6,740,381, 2000. Fiber Reinforced Composite Cores and Panels. Webcore Technologies Inc.

116. AASHTO LRFD Bridge Design Specifications. 1998. Washington D.C.: American Association of State Highway and Transportation Officials.

117. Wight, R. G., Erki, M. A., Shyu, C. T., Tanovic, R., and Heffernan, P. J. 2006. Development of FRP Short-Span Deployable Bridge-Experimental Results. *Journal of Bridge Engineering* 11 (4): 489-498.

118. Trilateral Design and Test Code for Military Bridging and Gap-Crossing Equipment. 2005. US Army Tank-automotive and Armaments Command.

119. Franklin, J. M., Taylor, S. E., Morgan, P. A., and Ritter, M. A. 1999. Design Criteria for Portable Timber Bridge Systems: Static Versus Dynamic Loads. ASAE and CSAE-SCGR Annual International Meeting, Toronto, Ontario, Canada July 18-21.

120. Chopra, A. K. 2001. *Dynamics of Structures, Theory and Applications to Earthquake Engineering.* New Jersey: Prentice Hall Inc.